

https://dspace.org/

Mineralogy and geochemistry of the impact breccias of the Bosumtwi impact structure, Ghana : genesis and secondary proccesses

Coney, Louise

2009-05-28T10:56:53Z
http://hdl.handle.net/10539/6991

Downloaded from a DSpace repository. https://dspace.org/

MINERALOGY AND GEOCHEMISTRY OF THE IMPACT BRECCIAS OF THE BOSUMTWI IMPACT STRUCTURE, GHANA: GENESIS AND SECONDARY PROCESSES.

Louise Coney

A thesis submitted to the Faculty of Science, University of the Witwatersrand, Johannesburg, in fulfillment of the requirements for the degree of Doctor of Philosophy.

Johannesburg, 2009.

DECLARATION

I declare that this dissertation is my own, unaided work. It is being submitted for the Degree of Doctor of Philosophy in the University of the Witwatersrand, Johannesburg. It has not been submitted before for any degree or examination in any other University.

_____.

Louise Coney

_____day of_____2009

Abstract

The 10.5 km diameter and 1.07 Ma old Bosumtwi structure in Ghana is a complex impact structure that displays a variety of preserved impactites from both within and outside of the crater and that is associated with the Ivory Coast tektite strewn field. Consequently, this crater structure provides a rare opportunity to examine a wide range of impact-related deposits, including within-crater deposits and proximal as well as distal ejecta. Access to the within-crater deposits was provided by two drill cores obtained by a 2004 drilling project of the International Continental Scientific Drilling Program (ICDP). The focus of the present study has been to determine the petrographic and geochemical characteristics of the different impactites, inside and outside of the crater and how these relate to the regional target rocks / drilled crater basement with the aim of understanding how the impactites formed during the cratering process.

Two hard rock cores were recovered from the ICDP drilling project: one through the thickest section of the crater fill (LB-07A) outside of the central uplift and one into the flank of the central uplift (LB-08A). The former has been the focus of this study. No coherent melt sheet was intersected and the shock state of the impactites is lower than expectations from pre-drilling numerical modeling (2.6 – 3.9 km^3 expected; <0.2 km^3 melt encountered). Suevites from south and north of the crater have also been examined in a similar manner to those from within the crater.

The LB-07A core has been subdivided on the basis of different impactite types into: An upper impactite section (333.28 - 415.67 m depth), which consists of seemingly alternating polymict lithic and suevitic breccias; this sequence is underlain by a lower impactite section (415.67 - 470.55 m depth) consisting of monomict breccias (after metagreywacke, phyllite or shale), which, in turn, is underlain by basement metasediments (470.55 - 545.08 m depth). The

basement metasediments are dominated by shale over metagreywacke. Both the lower impactites and basement metasediments contain cm-scale thin dykes (at 430.13 m, 445.22 m, 483.00 m and 513.90 m depths) with suevitic fill. The matrices of all the suevites are clastic and contain discrete and tiny (50 – 100 µm) melt fragments. A 30 cm thick granophyric-textured lithology, interpreted to represent a hydrothermally altered granitioid intrusion, occurs at 487.12 m (in the basement metasediments). The subdivision of the core has provided a useful correlative tool for geophysical and geochemical observations.

The target rock variety comprises metasediments (mostly metagreywacke, shale and phyllite) that form the bulk (ca. 95%) of the material from which the impactites were derived, and granite that forms a minor component (< 0.5 %). The metagreywacke and shale (together with phyllite) form near equal contributions (44 and 47 % respectively) to the target stratigraphy. Additionally carbonate, in the form of calcite bands, contributes to the target rock composition (ca. 2 %). Other contributors include schists and quartz derived from argillitic or greywacke metasedimentary precursors (6.5 % overall).

The impactites within the crater are chemically quite homogeneous. Platinum group element (PGE) and osmium isotope analysis failed to detect an unequivocal contribution from the meteoritic projectile in the within-crater breccias. It is concluded that the meteoritic signature is masked by the high abundances of siderophile and platinum group metals in the target lithologies (associated with the regional, pre-impact gold mineralization).

The degree of shock of clasts in the impactites of the within-crater deposits is lower than expected from pre-drilling numerical modeling (in that no melt layer is in evidence). A maximum of 3 PDF sets in quartz clasts are noted. On average, only 5.9 % of all quartz grains display 1 or more PDF sets in the upper impactites, with this number

decreasing to 4.4 % in the lower impactites, and 1.8 % in the basement metasediments. No PDFs in feldspar have been noted. Diaplectic quartz glass is present in the upper and lower impactites, with a distinct absence of this shock feature in the basement metasediments. Rare diaplectic feldspar glass has been observed. A general decrease in shock pressure, in terms of proportions of melt and shocked quartz, is noted along both cores. Melt particles reach a maximum of 1 cm in size, and a maximum proportion of 36 vol% in a non-representative sample, but are generally less than 5 vol% in abundance. Melt particles of the different core sequences differ in terms of colour and, to a lesser degree, chemical composition. The particles are chemically heterogeneous at the single particle scale. The melt particles consist of mixes of minerals derived from the target lithologies (quartz, feldspars, phyllosilicates).

Small areas of suevites have been found to both the north and south of the crater (1.5 km^2). The suevites from outside of the crater have a larger proportion of granite - and a distinct absence of carbonate – clasts. Overall, the suevites from the south have clast populations dominated by shale, phyllite and slate, followed by granitoid, metagrewacke and schist; those from the north are dominated by granitoid, schist, and relatively smaller proportions of phyllite, slate and shale. The clast populations are notably different from those of the within-crater suevites that are dominated by metagreywacke and shale, though more similarities can be observed between those from the south and the within-crater suevites. Additionally, the out-of-crater suevites are distinct from the within-crater suevites in terms of their geochemical signature (which reflects the different clast populations), and – particularly - shock degree of clasts (up to 4 PDF sets in quartz, presence of ballen cristobalite and higher proportions of diaplectic glass in the out-of-crater suevite). Melt particle sizes range up to 40 cm and melt is volumetrically more significant (18 – 37 vol%) than in suevite within the crater. Melt particles outside the crater are more vesiculated. Additionally, some melt particles from

the north contain microlites. The particles also display internal heterogeneity (particularly noticeable for those from south of the crater), and those from the north are relatively enriched in Al_2O_3 and depleted in FeO and MgO, in comparison to those from south of the crater. The particle compositions from south of the crater are more similar to the within-crater melt analyses than to those from north of the crater. The melt compositions indicate that these melt particles also formed from mineral mixes.

The impactite distribution (out-of-crater suevites occur to the north and south of the crater, but are absent from the east and west) is consistent with a low-angle oblique bolide impacting from the east. Due to the differing petrographic and shock characteristics of the suevites, it has been concluded that the within-crater and out-of-crater suevites formed by different mechanisms. A method of formation involving relatively less shocked material and derivation from metagreywacke and shale involves either slumping off the crater walls or lateral movement of melted and displaced target rock within the crater. Limited admixture of fallback material from the ejecta plume is proposed to explain the accretionary lapilli layer found above the impactite sequence. The out-of-crater suevites were formed by fallout from the ejecta plume (thus resulting in higher proportions of shocked material). However, the ejecta plume itself was differentiated laterally, which resulted in the manifestation that the clast populations of the suevites outside of the crater are different to each other. A weak post-impact hydrothermal system affected the crater fill, as testified by calcite veins and pods, quartz and chlorite veins, and sulphide formation in the breccia matrices. This constrains the hydrothermal system to lower greenschist facies conditions, as no minerals from higher metamorphic assemblages have been found.

The present study has indicated that the impactites from Lake Bosumtwi are distinct from each other in terms of petrographic and

geochemical characteristics. Furthermore it is proposed that these impactites formed by different mechanisms. This study has provided petrographic and geochemical data against which to correlate pre-drilling expectations.

DEDICATION

For Luke, Marylyn and Ron, whose support was unequalled. My appreciation will never cease.

ACKNOWLEDGEMENTS

Drilling at Lake Bosumtwi was supported by the International Continental Drilling Program (ICDP), the U.S. NSF-Earth System History Program (U.S. NSF) under grant no. ATM-0402010, Austrian FWF (project P17194-N10), the Austrian Academy of Sciences and by the Canadian NSERC. Drilling operations were performed by DOSECC.

Analytical and travel expenses for this work were funded through a grant from the National Research Foundation of South Africa, the International Scientific and Continental Drilling Program, a National Research Foundation Scarce-Skills Bursary from the NRF (to L.C.), a Jim and Gladys Taylor Trust award (to L.C.), and an Austrian Science Foundation (FWF) grant (Project P17194-N10).

I would like to thank my Supervisors, Roger Gibson (School of Geosciences, University of the Witwatersrand, Johannesburg, South Africa) and Uwe Reimold (Museum of Natural History, Humboldt-University, Berlin, Germany) for their patience and guidance over the duration of my PhD. Uwe and Roger provided the necessary objective eye for this thesis and have always pushed me to achieve my personal best. Additionally I would like to thank my unofficial Supervisor, Christian Koeberl (Department of Lithospheric Research, Centre for Earth Sciences, University of Vienna, Vienna, Austria), who has guided me through paper submissions and supported me in conference presentations. I would also like to thank Dona Jalufka for her support during my research trip to Vienna. I have been exceptionally lucky in that I have had the opportunity to work in a number of laboratories in South Africa and Europe, and this has been facilitated by Uwe, Roger and Christian. I would also like to thank Iain McDonald (School of Earth, Ocean and Planetary Sciences, Cardiff

University, Cardiff, Wales) who provided fantastic assistance, input and motivation for the PGE analyses and hosted me in Wales.

The assistance by a number of individuals in terms of analytical preparation and guidance has been much appreciated. Freddie Roelofse (Council for Geoscience, Pretoria, South Africa), Alex Mathebula (School of Geosciences, University of the Witwatersrand, Johannesburg, South Africa) and the team at SGS Lakefields (Johannesburg, South Africa) are thanked for thin-section preparation. Sharon Turner (School of Geosciences, University of the Witwatersrand, Johannesburg, South Africa) and Ralf-Thomas Schmitt (Humboldt-University, Berlin, Germany) are thanked for their assistance in the XRF analyses, and Dieter Mader (University of Vienna, Vienna, Austria) is thanked for his assistance with the INAA analyses. Allan Wilson and Janine Naicker (School of Geosciences, University of the Witwatersrand, Johannesburg, South Africa) are thanked for their assistance in the ICP-MS analyses. Bernard Peucker-Ehrenbrink (Woods Hole Oceanographic Institution) supervised the osmium isotope analyses. Lutz Hecht, Peter Czaja and Kirsten Born (Museum of Natural History, Humboldt-University, Berlin, Germany) are thanked for their assistance with the scanning electron microscopy and electron microprobe analyses in Berlin; Caroline Larkham (Electron Microscope Unit, University of the Witwatersrand, Johannesburg, South Africa) is thanked for her assistance with the scanning electron microscopy in Johannesburg. The staff at the GeoForschungsZentrum, Potsdam, Germany are thanked for allowing me to view the core on more than one occasion.

Forson Karikari, Daniel Boamah, Moses Quainoo and David Okyeame are thanked for their assistance in the preparation and undertaking of the field work at Lake Bosumtwi. This sampling trip was truly an experience to be remembered.

I am particularly appreciative to a number of individuals from the Bosumtwi “team” who have fielded discussions and provided much input over the course of this project: Ludovic Ferrière, Alex Deutsch, Jared Morrow, Steve Goderis, Bernd Milkereit, Sabine Luetke, Hernan Ugalde, Kai Wünnemann and Horton Newsom.

I have been fortunate to have published some of the results of this work in Meteoritics and Planetary Science: Melissa Nelson, Horton Newsom and Wright Horton, Jr., are thanked for detailed reviews for the lithostratigraphic paper; Jared Morrow and David King are thanked for their constructive reviews of the geochemical paper. Bernd Milkereit provided the editorial handling for both papers.

A number of individuals in the impact-cratering field have given me much input and support: in particular I would like to thank Axel Wittmann, Paula Ogilvie, Tanja Mohr-Westheide, Martin Tuchscherer and Cristiano Lana as well as everyone at the Museum of Natural History, Humboldt-University, Berlin.

As always, the contribution of friends (some of whom also happen to be geologists) cannot go unrecognized. I have had two very supportive office-mates: Fiona Scholes (for the first half) and Paula Ogilvie (for the second half). I would like to extend my appreciation to the following individuals: Lew Ashwal, Paul Cook, Roger Dixon, Paul Franklyn, Guy Freemantle, Madelein Gerber, Rhiannon Gwyn, Richard & Janet Hornsey, Judith Kinnaird, Luke Longridge, Shawn Letts, Paul Nex, Robyn Pickering, Lindi Richer, Peter Ringdahl, James Roberts, Johanna Salminen, Libby Sharman-Harris, Anika Solanki, Sue Webb and Stefanie Weise.

My parents, as always, have been very supportive in all ways possible, but most of all in their constant encouragement of my work. My partner, Luke Longridge, has not only been a sounding board for all manner of ideas. I will always be thankful for his help, advice, motivation and cups of coffee!

CONTENTS

DECLARATION ii
ABSTRACT iii
DEDICATION viii
ACKNOWLEDGEMENTS ix
LIST OF FIGURES xx
LIST OF TABLES xxxix
LIST OF APPENDICES xliii

Chapter One: Introduction

1.1 Introduction to this Project 1
1.2 Impact Crater Formation 2
1.2.1 Contact and Compression Phase 4
1.2.2 Excavation Phase 5
1.2.3 Modification Phase 7
1.2.3.1 Simple craters 7
1.2.3.2 Complex craters 8
1.2.3.3 Multi-ring basins 10
1.2.4 Ejecta Dispersal 11
1.2.5 Impactites 13
1.2.5.1 Subcrater rocks 14
1.2.5.2 Impactites of the crater interior 16
1.2.5.3 Impactites of the crater rim region and proximal ejecta 18
1.2.5.4 Distant regions and distal ejecta 19
1.3 Impact-Induced Shock Effects in Minerals and Rocks 20
1.3.1 Planar Microstructures in Quartz 21
1.3.2 High Pressure Polymorphs 24
1.3.3 Diaplectic Glasses 24
1.3.4 Mineral and Rock Melting 25
1.4 The Bosumtwi Impact Structure, Ghana 25
1.4.1 Historical Background 26
1.4.2 Link to the Ivory Coast Tektite Strewn Field 28

1.5 Regional Geology 28
1.6 Geochemical Studies 35
1.7 Geophysical Studies 36
1.8 International Continental Scientific Drilling of Lake Bosumtwi 42
1.8.1 The Palaeoclimatic Record 45
1.8.2 Impactite Cores LB-07A and LB-08A 47
1.9 This Study 48

Chapter Two: Methodology

2.1 Sampling Procedure 51
2.2 Thin Section Preparation 51
2.3 Scanning Electron Microscopy 52
2.4 Universal Stage Microscopy 52
2.5 Geochemical Methods 53
2.5.1 X-Ray Fluorescence Spectrometry 53
2.5.2 Instrumental Neutron Activation Analysis 55
2.5.3 X-ray Diffraction 59
2.5.4 Inductively Coupled Plasma-Mass Spectrometry 61
2.5.4.1 Platinum group element analyses 61
2.5.4.2 Trace element analysis of the out-of-crater suevites 62
2.5.5 Electron Microprobe Analysis 63
2.5.6 Osmium Isotope Analysis 64

Chapter Three: Lithostratigraphy and Petrography of the LB-07A Core

3.1 Macroscopic Observations on Core LB-07A 67

3.1.1 Contact Relationships 74
3.1.2 Hydrothermal Alteration of Core LB-07A 76
3.1.3 Upper Impactites - Breccia Characteristics 76
3.1.4 Lower Impactites - Breccia Characteristics 78
3.2 Microscopic Observations 78
3.2.1 Upper Impactite Unit (333.38–415.67 m) 80
3.2.2 Lower Impactite Unit (415.67–470.55 m) 89
3.2.3 Basement Metasediments (470.55–545.08 m) 90
3.2.4 Oxide and Sulphide Phases 93
3.3 Summary 93

Chapter Four: Geochemistry of the LB-07A core

4.1 Introduction 96
4.1.1 Previous Assessment of Meteoritic Component for the Bosumtwi Crater and the Ivory Coast Tektites 98
4.2 Methodology 99
4.3 Major Element Compositions 99
4.3.1 Polymict Lithic Breccias 101
4.3.2 Suevites 102
4.3.3 Monomict Breccias 103
4.3.4 Basement Lithologies 104
4.3.5 Granophyric-Textured Lithology 105
4.3.6 Comparison of Upper and Lower Suevite Occurrences 105
4.3.7 Hydrothermal Alteration 105
4.3.8 Polymict Lithic Breccia *vs.* Suevite Compositions 108
4.3.9 Polymict Breccia (Upper Impactites) *vs.* Monomict Breccia Compositions 108
4.3.10 Monomict Breccia *vs.* Basement Lithology Compositions 108
4.3.11 Matrix Compositions 109
4.3.12 Alteration of the Impactites 110

4.4 Trace Element Characteristics 110
4.4.1 Polymict Lithic Breccias 112
4.4.2 Suevites 113
4.4.3 Monomict Breccias 113
4.4.4 Basement Lithologies 115
4.4.5 Granophyric-Textured Lithology 115
4.4.6 Rare Earth Element Data 116
4.5 Cluster Analysis 117
4.6 Variations in Geochemical Characteristics Between the LB-07A Impactites and Those of Target Rocks 122
4.6.1 Basement Metasediments *vs*. Target Rock Types 122
4.6.2 Polymict/Monomict Impact Breccias *vs*. Target Rocks 126
4.7 Siderophile Element Compositions and Possible Meteoritic Component 127
4.7.1 Meteoritic Component 129
4.8 Summary 131

Chapter Five: Shock Metamorphism

5.1 Introduction 134
5.1.1 Shock Pressure Dependence of Orientations of PDFs in Quartz 135
5.1.2 Shock Dependence of Diaplectic Glasses, High-Pressure Polymorphs and Mineral Melts 135
5.2 Methodology 136
5.3 Shock Variation in the LB-07A Core 137
5.3.1 Quartz and Feldspar – Shock Metamorphic Effects 137
5.3.2 PDF Crystallographic Orientations 142
5.3.3 PDF Crystallographic Orientations – Comparison with Morrow (2007) 147
5.3.4 Diaplectic Glass 149
5.3.5 Carbonate Minerals 150

5.4 Suevite Melt Particle Characteristics in the LB-07A Core 151
5.4.1 Melt Particle Characteristics in the Upper Impactites 153
5.4.2 Melt Particle Characteristics in the Lower Impactites 154
5.4.3 Melt Particle Characteristics in the Basement Suevites 166
5.4.4 Possible Sources of Alteration in Suevites 166
5.4.5 Suevite Melt Particle Compositions 168
5.4.5.1 Melt particle comparison to the Ivory Coast tektites 180
5.5 Summary 180

Chapter Six: Out-of-Crater Suevites

6.1 Introduction 183
6.2 Methodology 184
6.3 Target Rock Lithologies 184
6.4 Suevite Outcrop Locations 190
6.4.1 Suevite from South of the Crater – Outcrop Description 191
6.4.2 Suevite from North of the Crater – Outcrop Description 191
6.4.3 Suevite from South of the Crater – Microscopic Features 195
6.4.4 Suevite from North of the Crater – Microscopic Features 195
6.4.4.1 Comparison to previous work on the out-of-crater suevites from the north of the crater 196
6.4.5 Shock Metamorphism of the Out-of-Crater Suevites 198
6.4.5.1 Melt particle characteristics 199
6.5 Chemical Signatures of the Out-of-Crater Suevites 203
6.5.1 Whole Rock Analysis 207
6.5.1.1 Major element differences between the out-of-crater suevites and the within-crater suevites 210
6.5.1.2 Comparison of the major element results for

The out-of-crater suevites with previous studies 210
6.5.2 Trace Element Analysis 211
6.5.2.1 Rare earth elements 212
6.5.2.2 Trace element differences between the out-of-crater suevites and the within-crater suevites 215
6.5.2.3 Comparison of the trace element results for the out-of-crater suevites with previous studies 220
6.5.3 Suevite Melt Particle Compositions 222
6.5.3.1 Melt particles from suevites from south of the crater 222
6.5.3.2 Melt particles from suevites from north of the crater 234
6.5.3.2.1 Comparison to previous studies 242
6.5.3.3 Comparison of melt particle phases from north of the crater and south of the crater 242
6.5.3.4 Cluster analysis 243
6.6 Summary 246

Chapter Seven: Discussion and Conclusions

7.1 Petrographic Characterisation and Comparison of the Impactites in the LB-07A Core, LB-08A Core and the Out-of-Crater Suevites 250
7.2 Geochemical Characterisation and Comparison of the Impactites in the LB-07A Core, LB-08A Core and the Out-of-Crater Suevites 254
7.3 Composition of the Target Volume 258
7.4 Shock Petrographic Comparison of the LB-07A and LB-08A Cores and the Out-of-Crater Suevites 260
7.4.1 Melt Particle Characteristics 264
7.5 Petrographic and Geochemical Characterisation of Alteration of Impactites in the LB-07A Core 270

7.5.1 Pre-impact Hydrothermal Mineralization 270
7.5.2 Post-impact Alteration 271
7.6 Presence of a Meteoritic Component in the Impactites of the LB-07A Core 273
7.7 The Bosumtwi Cratering Event 275
7.7.1 Impactite Distribution 275
7.7.1.1 Average volume of melt in the proximal ejecta – assessment with respect to the numerical modeling 278
7.7.2 Assessment of Other Ideas Pertaining to the Degree of Shock of Clasts in the Basement Material at Lake Bosumtwi 284
7.7.3 Model Constraints 285
7.7.3.1 Constraint 1: Petrographic differences 286
7.7.3.2 Constraints 2 and 3: Shock petrographic and melt volume differences 288
7.7.4 Proposed Model for the Formation of the Bosumtwi Impactites 289
7.8 Suevites of the Bosumtwi and Ries Craters – a Comparison 291
7.9 Conclusions 296
7.10 Recommendations 299

LIST OF FIGURES

Fig. 1.1: Location of the Bosumtwi impact structure, Ghana, and the Ivory Coast tektite and microtektite strewn fields, Côte d'Ivoire and offshore. Locations of deep-sea cores given by circles – red circles indicate where microtektites have been recovered, whereas yellow circles indicate places of no recovery of microtektites. Modified after Koeberl et al. (2007a)…..3

Fig. 1.2: Complex impact crater formation: A) Contact and compression, B) and C) excavation and D) modification stages (modified after French, 1998). The idealised form of the final structure is indicated in E.....5

Fig. 1.3: Schematic cross-sections through A) simple and B) complex impact craters, indicating the positions of various impactites. Dashed lines indicate listric faults. Simple crater modified after Grieve (1987); complex crater modified after Reimold and Gibson (2006)……..8

Fig. 1.4: Graph of flow parameter (= $g^{1/2}\rho D^{3/2}/\eta$) versus strength parameter (=$\rho gH/c$), where g = surface gravity, ρ = target density, D = crater diameter, H = crater depth, and Bingham parameters η = viscosity and c = cohesion (modified after Melosh, 1982, 1989). See text for discussion.....…10

Fig. 1.5: Examples of lunar craters: A) Euler crater, showing the ejecta blanket; crater diameter is 28 km (source: Lunar and Planetary Institute, Apollo 17 Metric photograph AS17-2923). B) Copernicus crater, with central uplift and secondary crater; Copernicus crater diameter is 93 km (towards front of the image; source: NASA, Apollo 17 metric photograph AS17-151-23260). C) Mare Orientale, a multi-ring basin; crater diameter is 960 km (source: NASA, Lunar Orbiter 4, part of frame M-187)……11

Fig. 1.6: Simplified schematic diagram showing the ejecta curtain and vapour plume expansion during the early stages of an impact event (modified after Melosh, 1989). The ejecta curtain is shown by the dashed lines, and its movement is shown by the dashed arrows. The vapour plume is shown by the solid line, and its expansion is shown by the solid arrows.....13

Fig. 1.7: Schematic cross section showing an idealised impactite distribution in a complex crater.....15

Fig. 1.8: Pressure-temperature (P-T) conditions of shock metamorphic processes (modified after French, 1998). Red curves indicate the P-T boundaries for the conversion of quartz to its high-pressure polymorphs and the blue curve indicates the conversion of carbon from graphite to diamond……22

Fig. 1.9: False colour Spot satellite image of the Bosumtwi impact crater. Scale bar is 8 km in length. Red colours indicate vegetation, while main roads and settlements are shown in light green. Image courtesy of Jeff Plescia, John Hopkins University……27

Fig. 1.10: Simplified geological map of Ghana, showing the distribution of the Birimian Supergroup (modified after Kesse, 1985). Belt-type granitoids form late-orogenic unfoliated intrusions in the Birimian volcanic belts; basin-type granitoids form synorogenic foliated batholiths in the central portions of the Birimian basins (Leube et al., 1990)…..30

Fig. 1.11: Simplified regional geological map, showing Lake Bosumtwi and surroundings (modified after Jones et al., 1981; Koeberl and Reimold, 2005).....31

Fig. 1.12: Cross-section showing the Reimold et al. (1998) traverse and zonation of the north-western part of the crater rim of the Bosumtwi impact structure. Each zone is characterised by different structural components (modified after Reimold et al., 1998).....33

Fig. 1.13: Elevation of the Bosumtwi region, showing the crater rim and the elevation of the Obuom Range (front right of image, trending NE-SW). Image is a combination of an Aster satellite image (band combination 7, 3 and 1, contrast enhanced) overlaid with a projection of grey-shaded Shuttle Radar Topography Mission data. Image from Koeberl et al. (2007a).....37

Fig. 1.14: Lake Bosumtwi Bouguer gravity anomaly. Data have been corrected for water depth and integration with land data. Contour interval is 1 mGal, with black triangles indicating the more negative anomalies. Coordinate system is UTM Zone 30N, WGS84. Image from Ugalde et al. (2007a).....37

Fig. 1.15: Total magnetic field over Lake Bosumtwi. Data collection lines and lake outline are indicated in black, with the location of the

ICDP cores indicated as stars. Contour interval is 2 nT. Data from Danuor (2004), image from Ugalde et al. (2007b).....38

Fig. 1.16: Lake Bosumtwi velocity model derived from seismic reflection data (modified after Karp et al., 2002). The three boundaries indicate approximate positions of the lake floor, base of sediments and base of the impactite sequence, from top to bottom.....38

Fig. 1.17: Bathymetric map (A) and seismic profile (B) across ICDP boreholes LB-07A and LB-08A. Thick black lines represent seismic profiles (reflection and refraction data), and the thin black lines are bathymetric contour lines. Contour interval is 5 m (modified after Scholz et al., 2002; Karp et al., 2002; Koeberl et al., 2006a).....43

Fig. 1.18: Map of Africa showing the position of Lake Bosumtwi relative to the maximum seasonal variation of the position of the intertropical convergence zone (ITCZ; modified after Shanahan et al., 2006)……..46

Fig. 3.1: Detailed lithostratigraphic column for the LB-07A core. Upper impactites: alternating polymict lithic breccia and suevite. Lower impactites: upper unit (415.67–430.13 m) consists of metagreywacke; middle unit (430.33–445.22 m) consists of phyllite for 4 m, underlain by metagreywacke with occasional pods of phyllite; lower unit (445.52–470.55 m) consists of metagreywacke ending in 3.6 m of mylonitic, shale-rich, thinly banded lithologies. Basement rocks are highly disaggregated and partially powdered. Also shown is the sample density over the entire core.....68

Fig. 3.2: Hand specimen photographs. A) Sample KR7-51, upper impactite unit, sample depth = 383.14 m; matrix-supported suevite with sub-cm- to cm-sized lithic fragments: sub-rounded carbon-rich shale (S), metagreywacke (MGW); melt particles are microscopic. B) Sample KR7-15, upper impactite unit, sample depth = 402.73 m; matrix-supported suevite with sub-cm- to dm-sized lithic fragments: laminated shale (S) with cross-cutting pre-impact veinlet, laminated shale clast (S2) with a cross-cutting pre-impact veinlet, metagreywacke (MGW), quartz-rich metagreywacke (QMGW), quartz (Qtz); melt particles are microscopic. Shale clasts are angular, metagreywacke and quartz clasts are sub-rounded. C) Sample KR7-11, upper impactite unit, sample depth = 383.74 m; matrix-supported suevite with sub-cm- to cm-sized fragments: large metagreywacke clast in centre (MGW), matrix to left and right of the clast, phyllite

clast (P). Matrix on left side of sample shows distinctive flow texture around metagreywacke clasts. D) Sample KR7-43, upper impactite unit, sample depth = 384.84 m; matrix-supported suevite with sub-cm- to cm-sized fragments: large metagreywacke clast dominates the sample, and the breccia matrix forms a distinctive flow texture on the left side; post-impact calcite pod at the left edge of hand specimen……70-71

Fig. 3.3: Hand specimen photographs. A) Sample KR7-27, lower impactite unit, sample depth = 468.28 m; mylonitic metagreywacke monomict breccia with cross-cutting quartz veinlets (Qtz). B) Sample KR7-74, lower impactite unit, sample depth = 430.13 m; matrix-supported suevite with sub-cm- to cm- sized lithic fragments: metagreywacke (MGW), shale (S) and quartz (Qtz)……72

Fig. 3.4: Core box image of basement metasediments (Box no. 45, depth range = 512.80 – 517.65 m) indicating the difference between the metagreywacke (MGW)-rich sediments (light grey), and the shale (S)-rich sediments (dark grey). Horizontal length of core box is 60 cm……73

Fig. 3.5: Core box image of the sharp contact (Box no. 26, depth range = 413.04 – 415.82 m) between the upper and lower impactites. Contact is indicated by arrow. Horizontal length of core box is 60 cm……75

Fig. 3.6: Pre- and post-impact alteration. A) Core box image of secondary carbonate veins (C) and a fold structure (F) in suevites of upper impactites (Box no. 25, depth range = 410.21 - 413.04 m). B) Core box image of carbonate pods (C) in shales of the basement metasediments (Box no. 48, depth range = 530.39 – 539.29 m)…..77
Fig. 3.7: Macro-photographs of impactite textures. A) Sample KR7-11, suevite, upper impactites, sample depth = 383.74 m; angular metagreywacke, laminated shale (with rutile inclusions and pre-impact quartz veins), rounded quartz clasts. B) Sample KR7-52, polymict lithic breccia, upper impactites, sample depth = 392.00 m; sub-angular to rounded clasts of metagreywacke (MGW), shale, quartz (Qtz) showing flow texture (particularly apparent in bottom left corner)……79

Fig. 3.8: Main lithic and mineral clast and matrix abundance variations throughout the upper section of impactites in drill core LB-07A……..81

Fig. 3.9: Photomicrographs of lithic phases in suevites observed throughout LB-07A core. A) Sample KR7-1, mylonitic metagreywacke clast in polymict lithic breccia, upper impactites, sample depth = 334.91 m; main minerals are quartz, K-feldspar and phyllosilicates (P); image width = 3 mm, cross polarized light (CPL). B) Sample KR7-7, suevite, upper impactites, sample depth = 363.20 m; laminated shale with rutile (R) growing in direction of lamination. Metagreywacke on left side of the image; image width = 3 mm, plane polarized light (PPL). C) Sample KR7-35, suevite, upper impactites, sample depth = 359.33 m; phyllite clast (Ph); image width = 3 mm, CPL. D) Sample KR7-41, suevite, upper impactites, sample depth = 408.72 m; "boiled" shale clast (see text for details); image width = 1.5 mm, PPL. E) Sample KR7-36, suevite, upper impactites, sample depth = 364.45 m; a considerably altered granite clast (G); image width = 3 mm, CPL. F) Sample KR7-41, suevite, upper impactites, sample depth = 408.72 m; breccia clast (possibly pre-impact) in the suevite (line separates the two phases); image width = 1.5 mm, CPL……..84

Fig. 3.10: Photomicrographs of phyllosilicate textures. A) Sample KR7-8, polymict lithic breccia, upper impactites, sample depth = 370.34 m; chlorite displaying an acicular habit; image width = 1mm, CPL. B) Sample KR7-8, polymict lithic breccia, upper impactites, sample depth = 370.34 m; kinked muscovite; image width = 0.75 mm, CPL……85

Fig. 3.11: Photomicrographs of calcite – pre- and post-impact phases. A) Sample KR7-8, polymict lithic breccia, upper impactites, sample depth = 370.34 m; pre-impact calcite (Cal) crystal; image width = 2 mm, CPL. B) Sample KR7-27, shale monomict breccias, lower impactites, sample depth = 468.28 m; post-impact calcite veinlet which cross-cuts the monomict breccia; image width= 1.31 mm, PPL……86

Fig. 3.12: Clast shape and size variation throughout the upper impactites. Maximum clast size in mm is given, measured on the long axis of clasts. A = angular, S-A = sub-angular, S-R = sub-rounded, R = rounded……87

Fig. 3.13: Backscattered electron images. The lightest fragments correspond to rutile, the grey fragments correspond to quartz (moderately grey indicates silica-rich lithologies), with darker grey indicating the mixed matrix, black indicates cracks in the thin section. A) Matrix of polymict lithic breccia; sample KR7-9, polymict lithic

breccia, upper impactites, sample depth = 377.46 m; width of scale bar = 200 µm. B) Vesiculated melt particle in matrix of suevite; sample KR7-14, suevite, upper impactites, sample depth = 398.44 m; width of scale bar = 80 µm. C) Round quartz-rich melt particle (indicated by arrow) in clastic matrix; width of scale bar= 10 µm……..88-89

Fig. 3.14: Photomicrographs of granophyric intergrowth (g) of quartz and feldspar; carbonate (Carb) and muscovite (Ms), quartz (Qtz) indicated. A) Sample KR7-83, suevite, basement metasediments, sample depth = 513.90 m; clast in suevite; image width = 3 mm, CPL. B) and C) Sample KR7-82, granophyric-textured lithology, basement metasediments, sample depth = 487.12 m: B) image width = 1.75 mm, CPL; C) image width = 3.00 mm, CPL…….92

Fig. 3.15: Reflected light photomicrographs of sulphide phases. Darker phases indicate silicate minerals. A) Sample KR7-46, shale, basement metasediments, sample depth = 530.63 m; primary agglomerate of euhedral pyrite crystals overgrown on the left lower side by a network of fine grained, post-impact, partially acicular pyrite; image width = 1.31 mm. B) Sample KR7-11, suevite, upper impactites, sample depth = 383.74 m; pyrrhotite relicts (circled) within rutile in a shale clast in suevite, upper impactites; image width = 0.25 mm……..94

Fig. 4.1: Profiles of the abundances of the major elements A) SiO_2; B) TiO_2; C) Fe_2O_3 (total Fe); D) MgO; E) K_2O; F) Na_2O; G) Al_2O_3 and H) CaO, plotted versus depth for the LB-07A core. Data in wt%. Shading indicates the ranges of abundances for each element…..100

Fig. 4.2: Shale (vol%; determined from modal point-counting) vs. A) Fe_2O_3 and MgO contents (in wt%) and B) V contents (in ppm) for suevites from the LB-07A core……..103

Fig. 4.3: A) CaO content and B) K_2O content versus Loss on Ignition (LOI) for the impactites and basement metasediments of LB-07A core. All data in wt%.....106

Fig. 4.4: Ternary discrimination diagrams for the electron microprobe analyses (10 µm defocused beam) of matrix of upper impactite polymict breccia samples from core LB-07A. A) Al_2O_3-(FeO+MgO)-SiO_2. B) AK(FM). Fields for common minerals in the LB-07A core are indicated (after Deer et al., 1971). Average target rock

compositions (phyllite-greywacke, shale, granite dykes, Pepiakese granite; after Koeberl et al., 1998) are also plotted……111

Fig. 4.5: Chemical Index of Alteration calculated from XRF analyses of LB-07A core samples……112

Fig. 4.6: Profiles of the abundances of the trace elements A) Cr; B) Ni; C) Co; D) Rb; E) Sr and F) Zr, plotted versus depth for the LB-07A core. Shading indicates the ranges of abundances for each element. All data in ppm……114

Fig. 4.7: Selected C1 chondrite-normalized rare earth element patterns (normalization factors after Taylor and McLennan, 1985). A) Upper impactite polymict lithic breccias. B) Upper impactite suevite. C) Lower impactite monomict breccias. D) Basement lithologies. E) La/Th ratios for all samples against depth. F) La/Lu ratios for all samples against depth……..…118-119

Fig. 4.8: Geochemical plots showing the results of the cluster analysis: 5 clusters produced by cluster analysis of 93 cases and 26 variables and the Euclidean Sum of Squares (k-means): A) Ternary diagram of Co-Ni-Cr. B) Ternary diagram of Sr-Zr-Rb. C) Binary diagram of MgO vs. Fe_2O_3. All data in wt%. D) Binary diagram of CaO vs. K_2O. All data in wt%.....123-124

Fig. 4.9: Harker plots for the LB-07A core samples versus "regional target rocks" (Koeberl et al., 1998). Fields delineate the positions of the compositions of the polymict lithic breccias, suevites, monomict breccias and basement metasediments of the LB-07A core. Symbols indicate the positions of LB-07A breccia outliers, the granophyric-textured lithology (of core LB-07A) and the regional target rocks (shale, greywacke-phyllite, granite dyke and Pepiakese granites; Koeberl et al., 1998). All data in wt%.....128

Fig. 4.10: Chondrite-normalized PGE abundance patterns for selected samples from the LB-07A core. Normalization data from Jochum (1996), except for Pd - from Anders and Grevesse (1989)……131

Fig. 4.11: Plot of inverse ^{188}Os concentration ($1/^{188}Os$) versus $^{187}Os/^{188}Os$ for the Bosumtwi drill core samples and target rocks. A straight mixing line between radiogenic, Os-poor (i.e, upper crustal) target rocks (Koeberl and Shirey, 1993) and an unradiogenic, Os-rich component (i.e., carbonaceous chondrites) is shown in order to

indicate the ideal mixing line for meteorite and upper continental crust mixing (Peucker-Ehrenbrink and Jahn, 2001)……132

Fig. 5.1: Photomicrographs of planar deformation features in quartz grains. A) Sample KR7-35, suevite, upper impactites, sample depth = 359.33 m; 2 PDF sets, oriented NW-SE and WNW-ESE (indicated with solid lines) and 3 sets of sub-parallel fractures oriented ESE-WNW, ENE-WSW and NW-SE (indicated with dashed lines); image width = 0.25 mm, cross-polarised light (CPL). B) Sample KR7-1, polymict lithic breccia, upper impactites, sample depth = 334.38 m; 2 grains with 1 PDF set each, oriented NE-SW and WNW-ESE (indicated with solid lines), and 3 sets of sub-parallel fractures oriented NNE-SSW, ENE-WSW and NNW-SSE (indicated with dashed lines); image width = 0.25 mm, CPL……..138

Fig. 5.2: Photomicrograph of decorated planar deformation features and one set of planar fractures in quartz grains. Sample KR7-41, suevite, upper impactites, sample depth = 408.72 m; one set of planar fractures (PF, indicated with dashed line), oriented NNW-SSE; three sets of decorated PDFs in toasted quartz (2 sets oriented NNE-SSW and 1 set oriented NE-SW, indicated with solid lines); image width = 0.20 mm, CPL……139

Fig. 5.3: Photomicrographs of various shock features in quartz. A) and B) Photomicrographs of reduced birefringence in quartz grains, with shock fractures (formed at ca. 5 GPa). Sample KR7-41, suevite, upper impactites, sample depth = 408.72 m; image width = 2 mm, CPL. C). Photomicrograph of mosaic extinction in a quartz grain, with 2 sets of sub-parallel fractures oriented NE-SW and NW-SE. Sample KR7-44, suevite, upper impactites, sample depth = 407.77 m; image width = 2 mm, CPL. D) Photomicrograph of toasted quartz. Sample KR7-18, suevite, upper impactites, sample depth = 411.34 m; image width = 1 mm, plane polarized light (PPL)……..141

Fig. 5.4: Variation of the proportion of shocked quartz grains with depth through the LB-07A core. % quartz grains with PDFs refers to the relative % of all quartz grains studied for their shock features (compare Table 5.2)……142

Fig. 5.5: Histograms of crystallographic orientations of planar deformation features in quartz: A) upper impactites, B) lower impactites and C) basement metasediments. Absolute frequencies calculated after von Engelhardt and Bertsch (1969)……146

Fig. 5.6: Histograms of crystallographic orientations of planar deformation features in quartz: A) upper impactites (this study) B) upper impactites (Morrow, 2007). Absolute frequencies calculated after von Engelhardt and Bertsch (1969)……...149

Fig. 5.7: Photomicrographs of diaplectic glass. A) and B) Sample KR7-16, suevite, upper impactites, sample depth = 404.26 m; diaplectic quartz glass (marked by arrows); image width = 1 mm: A) PPL; B) CPL. C) and D) Sample KR7-16, suevite, upper impactites, sample depth = 404.26 m; diaplectic K-feldspar glass (marked by arrow); image width = 1 mm: C) PPL; D) CPL……151

Fig. 5.8: Photomicrographs of fractured and twinned calcite. A-D) Sample KR7-83, suevite, basement metasediments, sample depth = 513.90 m. A) Central grain displays 2 cleavages (indicated with solid lines) oriented NNE-SSW and NW-SE, and one fracture set (indicated with dashed lines) oriented E-W; second grain in lower right corner displays 2 fracture sets oriented NNE-SSW and ENE-WSW; other minerals include quartz and feldspar in image; image width = 1 mm, PPL. B) Close-up of central calcite grain in A); image width = 0.20 mm, PPL. C) Close-up of lower right grain in A); image width = 0.075 mm, PPL. D) Calcite grain with cleavage oriented NE-SW and 1 fracture set oriented NNW-SSE; image width = 0.075 mm, PPL……152

Fig. 5.9: Photomicrographs of melt particles from the upper impactites. A) and B) Sample KR7-6, suevite, upper impactites, sample depth = 360.65 m; angular shard; image width = 3 mm: A) PPL; B) CPL. C) and D) Sample KR7-36, suevite, upper impactites, sample depth = 364.45 m; felsic (f) and mafic (m) melt particles (indicated with arrows); image width = 3 mm: C) PPL; D) CPL. E) - F) Backscattered electron images of melt clasts in upper impactite suevite: the grey fragments correspond to quartz (moderately grey indicates silica-rich lithologies), with lighter white-grey and dark grey indicating the mixed melts. E) and F) Sample KR7-6, suevite, upper impactites, sample depth = 360.65 m; angular shard: E) Angular shard (outlined and indicated by arrow) with highly variable composition indicated by SEM imagery; width of scale bar = 900 µm. F) Enlarged area from E), showing the boundary between felsic and mafic phases in the melt particle, with both phases characterized by quartz inclusions; width of scale bar = 100 µm. G) and H) Sample KR7-36, suevite, upper impactites, sample depth = 364.45 m: G) Felsic melt particles which are highly vesiculated; width of scale bar = 400 µm. H) Partially melted metagreywacke clast; width of scale bar

= 800 µm. I) – K) Sample KR7-14, suevite, upper impactites, sample depth = 398.44 m: highly vesicular melt particles in clastic matrix which consists of mixed lithologies and minerals; I) and J) width of scale bar = 80 µm. K) width of scale bar = 60 µm. L) Sample KR7-43, suevite, upper impactites, sample depth = 384.84 m; melt particle which consists of flow bands. The particle is more mafic than the surrounding matrix and the centre of the particle is characterized by numerous quartz clasts; width of scale bar = 400 µm……...155-159

Fig. 5.10: Macrophotographs of the lower impactite suevites. Melt particles (indicated with arrows) are brown in colour. A) and B) Sample KR7-23; suevite, lower impactites, sample depth = 430.13 m; distinct flow structures can be noted in many of the melt particles. C) Sample KR7-45; suevite, lower impactites, sample depth = 445.22 m……160

Fig. 5.11: Photomicrographs of melt particles (indicated with arrows) from the lower impactites. Sample KR7-23, suevite, lower impactites, sample depth = 430.13 m. A) and B) Part of the largest recorded melt particle in core LB-07A; image width = 3 mm: A) PPL; B) CPL. C) and D) Melt particle with distinct colour variation and large quartz clasts; image width = 3 mm: C) PPL and D) CPL. E) – H) Backscattered electron images of melt clasts in lower impactite suevite: the grey fragments correspond to quartz (moderately grey indicates silica-rich lithologies), with lighter white-grey and dark grey indicating the mixed melts. Sample KR7-23, suevite, lower impactites, sample depth = 430.13 m. E) Sub-rounded melt particle with variable composition. Matrix is composed of fine-grained clastic phases, and is not molten; width of scale bar = 100 µm. F) Entire image consists of part of a single melt particle with distinctive sub-rounded quartz clasts and numerous rounded pores; width of scale bar = 10 µm. G) and H) Discrete melt particle in clastic matrix (indicated by arrow). I) - L) Sample KR7-45, suevite, lower impactites, sample depth = 445.22 m; matrix consists of sub-rounded to angular fragments of target rocks and minerals. I) Sub-angular melt particle (indicated by arrow) with a distinct lack of vesicles; width of scale bar = 900 µm. J) Entire image consists of part of a single melt particle with sub-rounded to angular inclusions; width of scale bar = 40 µm. K) Droplet-shaped melt particle (indicated by arrow) with flow structures of variably mafic composition; width of scale bar = 900 µm. L) Homogeneous melt particle which contains few vesicles; width of scale bar = 400 µm……..161-165

Fig. 5.12: A-D) Photomicrographs of melt particles (indicated with arrows) from the suevite injections into the basement metasediment. A) and B) Sample KR7-81, suevite, basement metasediments, sample depth = 483.00 m; image width = 1.75 mm: A) PPL; B) CPL. C) and D) Sample KR7-83, suevite, basement metasediments, sample depth = 513.90 m; image width = 1.75 mm: C) PPL; D) CPL. E)-F) Backscattered electron image of melt clasts in basement suevite: the single light grey-white fragment is pyrite, grey fragments correspond to quartz (moderately grey indicates silica-rich lithologies), with dark grey indicating the mixed melts. Sample KR7-81, suevite, basement metasediments, sample depth = 483.00 m; E) Highly vesicular melt particle (circled) in clastic matrix; width of scale bar = 40 µm. F) Vesicular material, with the analysed points (by EMPA; red points) indicated; width of scale bar = 1 µm……...167

Fig. 5.13: Ternary plots of Al_2O_3-(MgO+FeO)-SiO_2 for A) analyses of melt particles from the upper impactites and B) analyses of melt particles from the lower impactites obtained by electron microprobe analysis (10 µm defocused beam). Cut-off points for the totals are indicated in the legend, in order to test the validity of the melt particle analyses……170

Fig. 5.14: Binary plots of the electron microprobe analyses (10 µm defocused beam): Melt particle phases in the within-crater suevites from core LB-07A. A) SiO_2 vs. TiO_2; B) Al_2O_3 vs. CaO; C) K_2O vs. Na_2O; D) MgO vs. FeO. Data in wt%.....172

Fig. 5.15: Ternary discrimination diagrams for the electron microprobe analyses (10 µm defocused beam) of the melt particles from core LB-07A. A) Al_2O_3-(MgO+FeO)-SiO_2. B) K_2O-Na_2O-CaO. C) AK(FM) diagram. Fields for common minerals in the LB-07A core are indicated (after Deer et al., 1971). Average target rock compositions (phyllite-greywacke, shale, granite dykes, Pepiakese granite; after Koeberl et al., 1998) and the Ivory Coast tektites (after Koeberl et al., 1997a) are also plotted……..175-176

Fig. 5.16: Ternary discrimination diagram for the electron microprobe analyses (10 µm defocused beam) of the melt particles from core LB-07A. AK(FM) diagram……178

Fig. 6.1: Sampling locations of the suevites from north and south of the crater, superimposed onto the regional geological map of Koeberl and Reimold (2005; Appendix 1). Outcrops 1-4 indicate the positions of the suevites sampled in this study. Points T1-8 indicate the

locations where target rocks were collected by W.B. Jones or by W.U. Reimold and C. Koeberl……...185

Fig. 6.2: Photomicrographs of target rock lithologies sampled outside of the crater. A) Sample LB-32, phyllite; main minerals are quartz, feldspar and biotite; image width = 3 mm, PPL. B) Sample J-492, greywacke; main minerals are quartz, feldspar and biotite, with a preferred orientation of grains from the top to the bottom of the image; image width = 2.75 mm, PPL. C) Sample J-497, slate, with crenulation cleavage defined by quartz; image width = 2.5 mm, PPL. D) Sample J-505, granite dyke; main minerals are quartz, feldspar, biotite and chlorite, image is dominated by fine-grained quartz-feldspar intergrowth; image width = 2.75 mm, PPL. E) Sample LB-35, Pepiakese granite; main minerals are quartz, sericitized plagioclase, microcline and biotite; image width = 3 mm, CPL……187-188

Fig. 6.3: Out-of-crater breccia from the south. A) Outcrop 1: GPS UTM coordinates: 0673437, 0713135 (UTM Zone = 30N). Person for scale. The exposure is located adjacent to a stream bed and consists entirely of suevite, except for the 0.5 m weathering horizon capping the exposure. Maximum clast size is 10 cm, circled, and indicated by arrow. Stars indicate the sampling positions. B) Outcrop 2: GPS UTM coordinates: 0672300, 0714393. GPS for scale. The exposure consists of a 1 m^2 pavement in a stream bed……192

Fig. 6.4: Out-of-crater breccia from the north. A) Outcrop 3: GPS UTM coordinates: 0676968, 0725874 (UTM Zone = 30N). Hammer (30 cm long) for scale. The exposure consists entirely of suevite, with clasts up to 25 cm in diameter. A hole from a 15 cm granite clast which has been removed is circled, and indicated by arrow. B) Outcrop 4: GPS UTM coordinates: 0677361, 0725615. The exposure consists of a single boulder, 2.5 m high and 2 m wide……....193

Fig. 6.5: Hand specimen images of suevites from south of the crater. A) Sample BS-1, outcrop 1. B) Sample BS-2, outcrop 1. Both samples are characterised by a medium dark grey matrix. Post-alteration Fe-oxides/-hydroxides are evident on the left side of sample BS-1 (indicated by Fe). Melt particles are indicated (Me). Scale bar in cm……195

Fig. 6.6: Hand specimen images of suevites from north of the crater. A) Sample BS-12, outcrop 3. B) Sample BS-9, outcrop 3. C) Sample BS-14, outcrop 3. Both samples are characterised by a yellow to

yellowish-green matrix. Melt particles are indicated (Me). Scale bar in cm……196

Fig. 6.7: Photomicrographs of various features in the out-of-crater suevites. A) Sample BS-5, 3 PDF sets in a quartz grain, oriented NNW-SSE, E-W and NE-SW (indicated with solid lines), 1 set of sub-parallel fractures oriented NW-SE (indicated with dashed lines); image width = 0.52 mm, PPL. B) Sample LB-31; ballen quartz; image width = 0.5 mm, PPL……..200

Fig. 6.8: Hand specimen images of large melt particles in suevites from north of the crater (outlined, indicated by Me). A) Sample BS-16, Outcrop 3; irregular to elongate-shaped melt particle, with quartz-filled vesicles. B) Sample BS-13, Outcrop 3; sub-rounded to sub-angular melt particles. Scale bar in cm. C) Sample BS-5, Outcrop 4; entire sample consists of a pancake-shaped melt particle (oriented horizontally in outcrop). D) Sample BS-4, Outcrop 3; entire sample consists of a melt particle with definitive flow structures (of different composition), defined by slightly different colouring of melt bands. Scale bar in cm……201-202

Fig. 6.9: Thin section images of the suevites from A) south of the crater (sample BS-1; outcrop 1) and B) north of the crater (sample BS-5; outcrop 4). Melt particles are circled and indicated by arrows. Note the extensive and variable size of vesiculation in the melt particle from the north of the crater……..203

Fig. 6.10: A) Photomicrograph consists entirely of a melt agglomerate from suevite from north of the crater with white, sub-rounded vesicles (indicated by arrow). Sample BS-4; image width = 0.52 mm, PPL. B) Photomicrograph of microlites (indicated by arrow) in melt in suevite from north of the crater. Sample BS-4; image width = 0.52 mm, PPL. C) – F) Backscattered electron images of melt with microlites in Fe-rich melt from north of the crater: the grey fragments correspond to quartz (moderately grey indicates silica-rich melt), with lighter white-grey and dark grey indicating the mixed melts, and black for the vesicles. Sample BS-14B. C) Width of scale bar = 400 µm. D) Entire image shows microlites in melt (mesostasis); width of scale bar = 50 µm. E) Extensive development of microlites in melt agglomerate. In parts, the microlites form radiating fans; width of scale bar = 100 µm. F) Melt agglomerate with flow texture between vesicles; width of scale bar = 300 µm. G) – L) Backscattered electron images of melt particles from south of the crater. Sample BS-2A. G) Discrete melt particle in clastic matrix from south of the crater; width of scale bar =

100 µm. H) Flow banding of different compositions in melt particle. Width of scale bar = 10 µm. I) Melt particle with large vesicles, mafic composition in clastic matrix; width of scale bar = 100 µm. J) Angular melt particle containing large glassy areas, internally variable in composition; width of scale bar = 100 µm. K) Melt particle with highly variable composition; width of scale bar = 100 µm. L) Close up of an area of the melt particle in G, showing the flow textures with different composition; width of scale bar = 10 µm……..……..204-206

Fig. 6.11: Harker plots for the out-of-crater suevites, indicating the differences between the suevites from the south and north of the crater. Data for the LB-07A suevites, average of the LB-08A suevites (Ferrière et al., 2007b), and out-of-crater suevites from the studies of Karikari et al. (2007) and Boamah and Koeberl (2003) are indicated. All elements are plotted against SiO_2. A) TiO_2; B) Al_2O_3; C) Fe_2O_3; D) MnO. E) MgO; F) CaO; G) Na_2O and H) K_2O. All data in wt%.....208-209

Fig. 6.12: Trace element plots for the within-crater and out-of-crater suevites, indicating the differences between the suevites from the south and north of the crater. A) Sc vs. V; B) Cu vs. Zn; C) Cr vs. Co; D) Rb vs. Sr; E) Th vs. U and F) Ba vs. Zr. All data in ppm…….213

Fig. 6.13: Selected C1 chondrite-normalized rare earth element patterns (normalization factors after Taylor and McLennan, 1985). A) Out-of-crater suevites from south of the crater. B) Out-of-crater suevites from north of the crater……...214

Fig. 6.14: Trace element ternary plots. A) Hf-Co-Th. B) Cr-Zr-La. For A) and B) analyses from all impactite lithologies from LB-07A core, together with the out-of-crater suevites (this study) are indicated as well as averages of the target rock types of Koeberl et al. (1998) and the average Ivory Coast tektite composition (Koeberl et al., 1997a).
C) Hf-Co-Th. D) Cr-Zr-La. For C) and D) only suevite analyses from LB-07A core, together with the out-of-crater suevites (this study) are indicated as well as out-of-crater suevite analyses of Karikari et al. (2007), Boamah and Koeberl (2003) and the average of the LB-08A suevite analyses from core LB-08A (Ferrière et al., 2007b)….216-217

Fig. 6.15: C1 chondrite-normalized average rare earth element patterns (normalization factors after Taylor and McLennan, 1985). A) LB-07A polymict lithic, suevitic and monomict breccias and basement lithologies. B) LB-07A impactites with average target rocks (Koeberl et al., 1998). C) LB-07A impactites with Ivory Coast tektites (Koeberl

et al., 1997a). D) LB-07A impactites with out-of-crater average suevites from north of the crater (this study; Boamah and Koeberl, 2003) and south of the crater (this study)……219

Fig. 6.16: Binary plots of trace element analyses of within-crater (LB-07A from this study; LB-08A average from Ferrière et al., 2007b) and out-of-crater suevites (this study; Karikari et al., 2007; Boamah and Koeberl, 2003). A) Sc vs. V; B) Cu vs. Zn; C) Cr vs. Co; D) Rb vs. Sr; E) Th vs. U and F) Ba vs. Zr. All data in ppm…….221

Fig. 6.17: Backscattered electron images of melt particles analysed from sample BS-1, thin section BS-1A suevite from south of the crater: the lightest fragments correspond to rutile, moderately grey indicates silica-rich lithologies, with lighter white-grey and dark grey indicating the mixed melts, and black for the vesicles. A) Area of melt particle analyses, showing two portions analysed; width of scale bar = 100 µm. B) Enlargement of portion 1; width of scale bar = 100 µm. C) Enlargement of portion 1; showing melt particles 1-3; width of scale bar = 10 µm. D) Enlargement of portion 2, showing points analysed on melt particle 4; width of scale bar = 10 µm. E) Points analysed on melt particle 1; width of scale bar = 10 µm. F) Points analysed on melt particle 3; width of scale bar = 10 µm. G) Points analysed on melt particle 2; width of scale bar = 10 µm……...224-225

Fig. 6.18: Thin section and backscattered electron images of melt particles analysed from sample BS-1, thin section BS-1B, suevite from south of the crater: the lightest fragments correspond to rutile, moderately grey indicates silica-rich lithologies, with lighter white-grey and dark grey indicating the mixed melts, and black for the vesicles. Three grains were identified in thin section. A) Grain 1. B) Grain 2. C) Grain 3, area 1. D) Grain 3, area 2. E) Grain 3, area 3. The points analysed are indicated in red (see text for details). Width of scale bar = 100 µm…….226-227

Fig. 6.19: Element maps from sample BS-2, melt particles 2 and 3. Element maps produced by electron microprobe analysis at a current of 10 kV. A) Backscattered electron image of melt particle 2; width of scale bar = 10 µm. B) Si for particle 2; width of scale bar = 20 µm. C) Al for particle 2; width of scale bar = 20 µm. D) Fe for particle 2; width of scale bar = 20 µm. E) Mg for particle 2; width of scale bar = 20 µm. F) Ca for particle 2; width of scale bar = 20 µm. G) Na for particle 2; width of scale bar = 20 µm. H) K for particle 2; width of scale bar = 20 µm. I) Si for particle 3; width of scale bar = 20 µm. J) Al for particle 3; width of scale bar = 20 µm. K) Fe for particle 3; width of scale bar =

20 µm. L) Mg for particle 3; width of scale bar = 20 µm. M) Ca for particle 3; width of scale bar = 20 µm. N) K for particle 3; width of scale bar = 20 µm. O) Na for particle 3; width of scale bar = 20 µm……..……228-231

Fig. 6.20: Binary plots of the electron microprobe analyses for melt particles (10 µm defocused beam): melt particles in the out-of-crater suevites from south of Lake Bosumtwi. A) SiO_2 vs. TiO_2; B) Al_2O_3 vs. CaO; C) K_2O vs. Na_2O; D) MgO vs. FeO. Data in wt%.....233

Fig. 6.21: Ternary discrimination diagrams for the electron microprobe analyses (10 µm defocused beam) of melt particle phases in the out-of-crater suevites from south of Lake Bosumtwi. A) Al_2O_3-(MgO+FeO)-SiO_2. B) K_2O-Na_2O-CaO. C) AK(FM) diagram. Fields for common minerals in the suevites are indicated (after Deer et al., 1971). Average target rock lithologies (phyllite-greywacke, shale, granite dyke and Pepiakese granite; after Koeberl et al., 1998) and the average composition of the Ivory Coast tektites (after Koeberl et al., 1997a) are also plotted…….235-236

Fig. 6.22: Al_2O_3-(MgO+FeO)-SiO_2 diagrams showing the various phases analysed from melt particles using the electron microprobe (10 µm defocused beam) from A) sample BS-14B; B) sample BS-16B; C) sample BS-8. The phases were identified from assessment of spots analysed with the microprobe, and include where the area % of mesostasis present is greater than the area % of microlites (mesostasis>microlites); where both phases are equal in abundance (mesostasis = microlites), and where only mesostasis is present……..237-238

Fig. 6.23: Binary plots of the electron microprobe analyses (10 µm defocused beam): Melt particle phases in the out-of-crater suevites from north of Lake Bosumtwi. A) SiO_2 vs. TiO_2; B) Al_2O_3 vs. CaO; C) K_2O vs. Na_2O; D) MgO vs. FeO. Data in wt%.....239

Fig. 6.24: Ternary discrimination diagrams for the electron microprobe analyses (10 µm defocused beam) of melt particle phases in the out-of-crater suevites from north of Lake Bosumtwi. A) Al_2O_3-(MgO+FeO)-SiO_2. B) K_2O-Na_2O-CaO. C) AK(FM) diagram. Fields for common minerals in the suevites are indicated (after Deer et al., 1971). Average target rock lithologies (phyllite-greywacke, shale, granite dyke and Pepiakese granite; after Koeberl et al., 1998) and the average composition of the Ivory Coast tektites (after Koeberl et al., 1997a) are also plotted…….241-242

Fig. 6.25: An AK(FM) discrimination diagram for the electron microprobe analyses (10 µm defocused beam) of melt particle phases in the out-of-crater suevites from south and north of Lake Bosumtwi……..244

Fig. 7.1: Comparison of the LB-07A and LB-08A stratigraphies (LB-08A after Ferrière et al., 2007a); t = thickness……..252

Fig. 7.2: Harker plots of Fe_2O_3 and CaO (wt%) comparing polymict lithic, suevitic and monomict breccias, granophyric-textured lithologies, metagreywacke and phyllite, slate and shale of LB-07A (this work) and LB-08A (data from this study and Ferrière et al., 2007b), shown together with the out-of-crater suevite averages of this study……..256

Fig. 7.3: Rare earth element comparisons. A) Averages calculated for polymict lithic, suevitic, monomict breccias as well as basement lithologies from core LB-07A (this study), out-of-crater suevites (this study) and regional target rock lithologies (Koeberl et al., 1998). B) Averages for polymict lithic breccias and suevites, metagreywacke, phyllite-slate and light greenish-grey metagreywacke from core LB-08A (data from Ferrière et al., 2007b)…….258

Fig. 7.4: Ternary discrimination diagrams for the electron microprobe analyses (10 µm defocused beam) of melt particle phases from within and out of the crater. A) Al_2O_3-(MgO+FeO)-SiO_2 and B) K_2O-Na_2O-CaO. C) AK(FM) discrimination diagram…….……...268-269

Fig. 7.5: Ejecta patterns caused by oblique impact. Large circle indicates the crater, and small circles indicate the ejecta distribution. A) Oblique impact angle between 60 and 90°. B) Oblique impact angle between 45 and 60°. C) Oblique impact angle between 20 and 45°. D) Oblique impact angle between 0 and 20°. E) Ejecta pattern of the Bosumtwi crater (modified after Koeberl et al., 2007a)……277

Fig. 7.6: Model for the emplacement of the impactites at the Bosumtwi crater. A) An oblique impact, travelling from east to west makes contact with the Birimian target rocks. Note the heterogeneous nature of the target geology. B) Ejection of the Ivory Coast tektites and microtektites; formation of ejecta curtain and/or ejecta plume; fracturing and brecciation of the target rocks by the progression of the shock wave. C) Formation of the central uplift and out-of-crater and within-crater suevites by contributions from the

ejecta curtain and/or ejecta plume and ground surge/slumping, respectively. D) Formation of the uppermost impact fallback layer (fine-grained material from the ejecta plume). E) Post-impact hydrothermal system affects entire crater fill. ……..……..292

LIST OF TABLES

Table 1.1: Shock pressures with corresponding mineral and rock deformation features for porous and non-porous rocks (adapted after French, 1998; Koeberl and Martínez, 2003). Data from Stöffler (1984); Melosh (1989); Stöffler and Langenhorst (1994); Montanari and Koeberl (2000); Koeberl (2002)……...21

Table 2.1: Analytical precision for major and trace elements by XRF analysis at the University of the Witwatersrand (S. Farrell-Turner, pers. comm., 2004)……...55

Table 2.2: Analytical precision for major and trace elements by XRF analysis at the Humboldt-University in Berlin (R-T. Schmitt, pers. comm., 2007)……56

Table 2.3: Typical precisions for elements analysed in the Vienna INAA Laboratory (C. Koeberl, pers. comm., 2004). All elemental abundances in ppm, unless otherwise stated……...60

Table 2.4: Trace element compositions of standards used for the ICP-MS at the University of the Witwatersrand, Johannesburg (A. Wilson, pers. comm., 2007.)……63

Table 2.5: Major element compositions of standards used for the electron microprobe analysis at the Humboldt-University in Berlin (P. Czaja, pers. comm.)……..64

Table 2.6: Rock standard and procedural blank $^{187}Os/^{188}Os$ data, with 95% confidence limits, obtained from the Wood Hole Oceanographic Institute……65

Table 3.1: LB-07A core: Lithostratigraphic subdivision……..72

Table 3.2: Modal analyses (data in vol%) by optical microscopy on thin sections of selected, representative samples of polymict lithic breccia and suevite……82-83

Table 4.1: Averages and ranges for major element abundances for the LB-07A polymict lithic breccias, suevites, monomict breccias and basement metasediments, as well as the major element abundances for the granophyric-textured lithology (data in wt%)……..101

Table 4.2: Compositional data (major elements, all data in wt%) from defocused electron microprobe analysis of matrix from two breccia samples from the upper impactites……..110

Table 4.3: Cluster analysis results for 5 cluster groups using 93 cases (i.e., samples) and 26 variables (a combination of major and trace elements, see text for details) and the Euclidean Sum of Squares (k-means). The means, standard deviations of the groups are indicated……121

Table 4.4: Distribution of the LB-07A lithologies into the 5 clusters produced by cluster analysis of 93 cases and 26 variables and the Euclidean Sum of Squares (k-means). See text for details……..122

Table 4.5: Averages and ranges in major element abundances for the target rocks of the Bosumtwi structure and the Ivory Coast tektites (data in wt%), after Koeberl et al. (1997a, 1998)……125

Table 5.1: Typical crystallographic orientations of planar deformation features in shocked quartz. Minimum pressures for the generation of some of these features are indicated (modified after Stöffler and Langenhorst, 1994; Langenhorst, 2002)……136

Table 5.2: Summary of shock features in quartz grains and melt particle statistics for upper impactite polymict lithic breccia and suevite, lower impactite monomict breccia and suevite and basement metasedimentary lithologies. The basement suevites show no PDFs……..……140

Table 5.3: Shock analysis of the basement metasediments. All samples were examined (using the 50x magnification) for evidence of PFs and PDFs in quartz grains, and the orientation of PDF sets were measured using a U-Stage……144

Table 5.4: Number of PDF sets and absolute frequencies (%) of specific PDF orientations in quartz grains from the basement metasediments, lower impactites and upper impactites of core LB-07A……145

Table 5.5: Comparison between the U-stage data of Morrow (2007; upper impactites) and averages of data collected in this study (upper impactites, lower impactites, basement metasediments). All data in absolute frequencies (%)……...148

Table 5.6: Differences between suevites along the LB-07A core…153

Table 5.7: Cluster analysis results for 5 cluster groups using 90 cases (i.e., samples) and 9 variables (major elements, see text for details) and the Euclidean Sum of Squares (k-means). The means and standard deviations of the groups are indicated (all data in wt%)……..179

Table 5.8: Distribution of the clusters in the different melt particles from the within-crater suevites, produced by cluster analysis of 90 cases and 9 variables and the Euclidean Sum of Squares (k-means). See text for details……..180

Table 6.1: Modal analysis data (in vol%) obtained by pointcounting of selected, representative samples of the out-of-crater suevites…...197

Table 6.2: Comparison between the petrographic data for the northern out-of-crater suevites of this study and that of Boamah and Koeberl (2006). All populations in vol%.....198

Table 6.3: Summary of shock features in quartz grains of selected, representative samples of the out-of-crater suevites……199

Table 6.4: Comparison of major element ranges of out-of-crater suevites in this study to those of Boamah and Koeberl (2006) and Karikari et al. (2007)……211

Table 6.5: Cluster analysis results for 5 cluster groups using 216 cases (i.e. samples) and 9 variables (major elements, see text for details) and the Euclidean Sum of Squares (k-means). The means and standard deviations of the groups are indicated. All data in wt%.....245

Table 6.6: Distribution of the clusters in the different melt particles from the out-of-crater suevites, produced by cluster analysis of 216 cases and 9 variables and the Euclidean Sum of Squares (k-means). See text for details……..246

Table 7.1: Average modal analyses of within-crater suevites from the LB-07A core (this study), the LB-08A core (Ferrière et al., 2007a) and the out-of-crater suevites (this study). All data in vol%.....253

Table 7.2: Averages and standard deviations (in wt%) for the LB-07A suevites (this study), LB-08A suevites (Ferrière et al., 2007b) and the suevites from south and north of the crater collected in this study……..257

Table 7.3: Comparison of the overall proportions of principal lithologies in the LB-07A (this study) and LB-08A (Ferrière et al., 2007a) cores (bulk stratigraphies)……259

Table 7.4: Comparison of proportions of regional target lithologies.....260

Table 7.5: PDF associations in the LB-07A core……...264

Table 7.6: Melt particle differences for the suevites from the LB-07A (this study) and LB-08A (Ferrière et al., 2007a) cores, as well as the out-of-crater suevites from the south and north of Lake Bosumtwi (this study)……265

Table 7.7: Parameters used for the calculation of the average melt volume in the proximal ejecta at Lake Bosumtwi. Data for the suevites from the crater moat is estimated from the LB-07A core (this study); for the central uplift from the LB-08A core (Ferrière et al., 2007a)……..279

LIST OF APPENDICES

Appendix 1: Bosumtwi impact crater: Geological Map; prepared by Christian Koeberl and Wolf Uwe Reimold. *Originally published as part of:* Koeberl C. and Reimold W.U. (2005). Bosumtwi impact crater, Ghana (West Africa): An updated and revised geological map, with explanations. Jahrbuch der Geologischen Bundesanstalt, Wien (Yearbook of the Geological Survey of Austria) Vienna, **145**, 31-70 and 1 map, 1:50,000.

Appendix 2: Full sample list for this study: LB-07A core (KR7-), and samples of the out-of-crater suevites (BS-).

Appendix 3a: Main lithologies recognized throughout the LB-07A core, and their defining characteristics.

Appendix 3b: Hand-specimen and thin section descriptions of samples from the LB-07A core and out-of-crater suevites collected by L. Coney; out-of-crater suevites and target rock lithologies collected by W.U. Reimold and C. Koeberl ; target rock lithologies collected by W.B. Jones.

Appendix 4a: Geochemical Data: Major (wt%) and trace element (ppm, unless indicated otherwise) data for samples from the LB-07A core determined by XRF and INAA (trace elements only).

Appendix 4b: PGE and Os isotope data measured by ICP-MS for analyzed samples from the LB-07A core.

Appendix 5a: Universal stage data

Appendix 5b: Selected SEM (backscattered electron) imagery of melt particles obtained in this study for the within-crater suevites.

Appendix 5c: X-Ray Diffraction Results for samples from the LB-07A core.

Appendix 5d: Microprobe data for melt particles from the LB-07A core and from the out-of-crater suevites.

Appendix 6a: Geochemical data: Major (wt%) and trace element (ppm) data for the out-of-crater suevites collected in this study, determined by XRF and ICP-MS.

Appendix 6b: Selected SEM (backscattered electron) imagery, element maps and thin section images of melt particles obtained in this study for the out-of-crater suevites.

Appendix 7: Peer-reviewed papers.

Chapter One: Introduction

1.1 Introduction to this Project

Impact cratering is a fundamental geological process not only on Earth, but throughout the Solar System (see e.g., Melosh, 1989; French, 1998; Reimold et al., 2005). It is widely accepted among Earth scientists that collisions of extraterrestrial objects with Earth have played a significant role in altering the Earth's crust (e.g., French, 1968, 1990; Shoemaker, 1977; Grieve, 1987, 1990, 1991; Pesonen and Henkel, 1992; Dressler et al., 1994). The Earth Impact Database provides a current list (see http://www.unb.ca/passc/ImpactDatabase/index.html) of 174 recognised impact structures. In Africa, 19 impact structures have been confirmed (Master and Reimold, 2000).

During an impact cratering event, the short-lived and high intensity pressure and temperature conditions create a variety of impactites (impact-generated rocks). These impactites can either be ejected from the crater to various distances, or remain within the crater. Their final position is dependent, in part, to their original position relative to the point of impact and their physical response to the impact event. Classification schemes of impactites have been made (e.g., Stöffler and Reimold, 2006; Stöffler and Grieve, 2007) according to proximity to the crater, mode of genesis, melt proportion and shock characteristics of clasts; however, few craters allow the study of the full spectrum of impactites, largely because of incomplete preservation or exposure.

The Bosumtwi impact crater (Fig. 1.1) in Ghana is a 1.07 Ma old (Koeberl et al., 1997a), medium-sized, complex (see Melosh, 1989) crater. The crater is one of the best preserved impact structures in its size and age class, and is one of 3 impact craters worldwide which have associated tektite strewn fields (the Ivory Coast tektite strewn field; Lacroix, 1934; see Koeberl et al., 1997a). In 2004, the

International Continental Scientific Drilling Program (ICDP) facilitated the drilling of two cores through the thickest section of the crater fill (LB-07A) and the central uplift (LB-08A) in the Bosumtwi crater.

The focus of this study is to examine and understand the genesis of various impactite lithologies in the Bosumtwi crater that have been made accessible by this drilling, and to compare these with the impact-related deposits in the immediate environs of the crater. These observations will be combined with published work on the Ivory Coast tektites and microtektites linked to the crater (Glass, 1968, 1969; Koeberl et al., 1997a), in order to reconstruct the formation, modification and distribution of impactites of the Bosumtwi crater.

This project investigates the primary formation and post-impact modification (hydrothermal alteration) of the impact breccias by examining their mineralogical characteristics and their geochemical signatures. The crystallization history of the melt clasts, together with any compositional differences between the breccias and glasses, is examined. Stratigraphic variations in the LB-07A core have been determined. A study to investigate the presence of meteoritic projectile has been undertaken. Impact breccia development of the within-crater breccias has been compared and contrasted with that of the out-of-crater breccias (in particular melt component contrasts and shock metamorphism of clasts). A comparison of the breccias at the Bosumtwi crater with those of the Ries Crater, Germany has been discussed.

1.2 Impact Crater Formation

Impact craters are formed by projectiles that are large and coherent enough to travel through the Earth's atmosphere with little or no deceleration and that strike the ground at approximately the original cosmic velocity (> 11 km/s) (French, 1998). Such projectiles tend to

be large – generally > 20 m for a coherent iron meteorite, and > 50-100 m for a stony one (French, 1998).

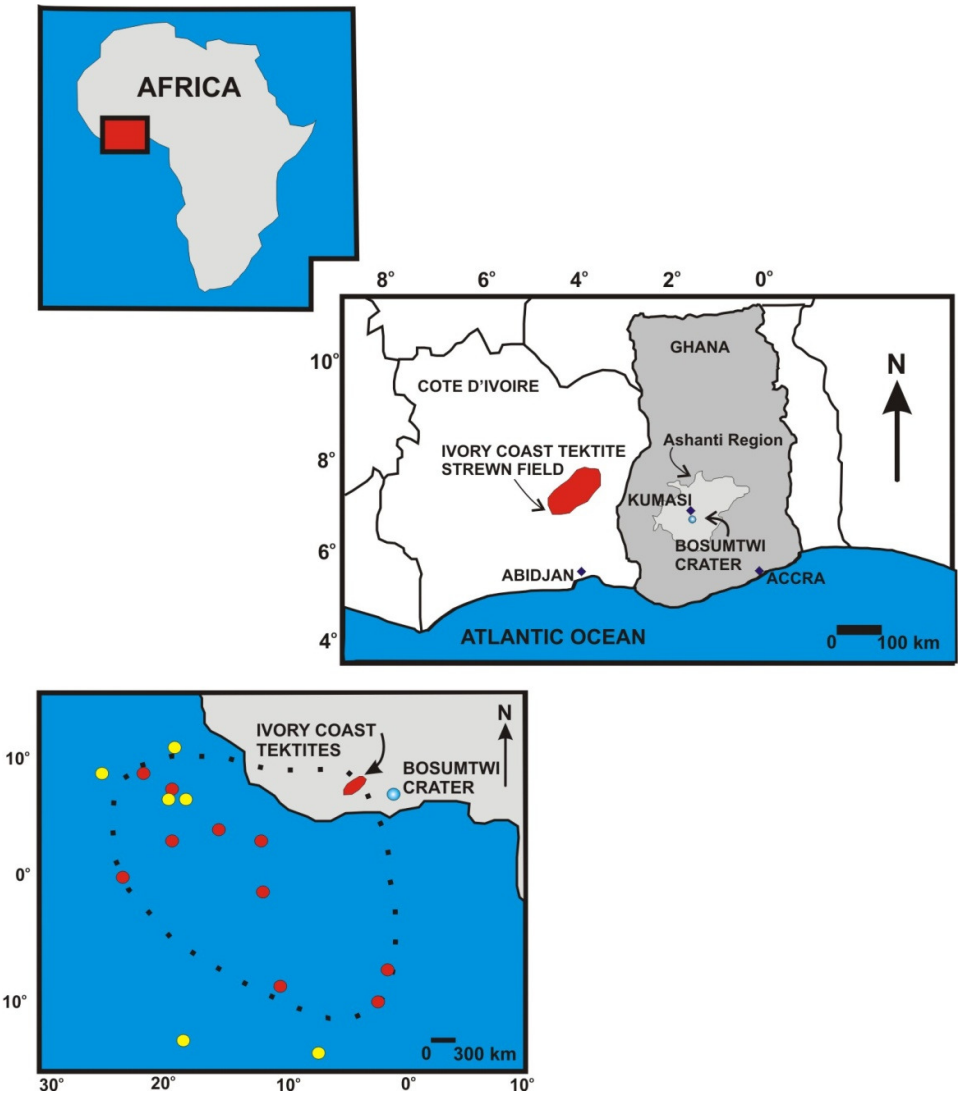

Fig. 1.1: Location of the Bosumtwi impact structure, Ghana, and the Ivory Coast tektite and microtektite strewn fields, Côte d'Ivoire and offshore. Locations of deep-sea cores given by circles – red circles indicate where microtektites have been recovered, whereas yellow circles indicate places of no recovery of microtektites. Modified after Koeberl et al. (2007a).

As the bolide hits the ground, its kinetic energy is transferred by high-pressure shock waves into the target (Melosh, 1989; Montanari and Koeberl, 2000), which heat and compress the rock. These transient shock waves are characterised by high pressures (up to 100s of

GPa) and velocities (> 10 km/s; French, 1998), which cannot be produced by internal geological processes (Melosh, 1989); they compress the target rocks to pressures above the Hugoniot Elastic Limit (HEL; see Melosh, 1989). The effects of these shock waves are irreversible. Although the cratering process is continuous, three stages (Fig. 1.2) are used to describe it (Gault et al., 1968; Grieve, 1987, 1991; Melosh, 1989; Melosh and Ivanov, 1999; Fig. 1.2):

1.2.1 Contact and Compression Phase

This stage (Fig. 1.2 A) commences upon contact of the projectile with the surface, producing a number of shock waves (which move as a supersonic front) as the result of velocity contrasts between the impacting and the target material (Melosh, 1989). Melting or vaporisation of the target rock and projectile may take place upon contact (Melosh, 1989). This phase is characterised by structural and phase changes in the minerals of the target rocks (Montanari and Koeberl, 2000).

The maximum pressures, temperatures and velocities in the target rocks are largely confined to a region comparable in size to the volume of the projectile (Melosh, 1989). The distribution of shock pressures is established by the end of this stage, and as this ends, the shock pressures form a series of approximately hemispherical shells around the impact point, decreasing in intensity outward from the point of impact (Fig. 1.2). The duration of this stage is influenced by the size, composition and original cosmic velocity of the projectile and lasts as long as the shock wave and the subsequent rarefaction wave ("release wave"; a wave which reduces the rock density and results in the melting and vaporisation of the projectile; see Montanari and Koeberl, 2000) take to traverse the projectile (between 10^{-3} and a few seconds; Melosh, 1989).

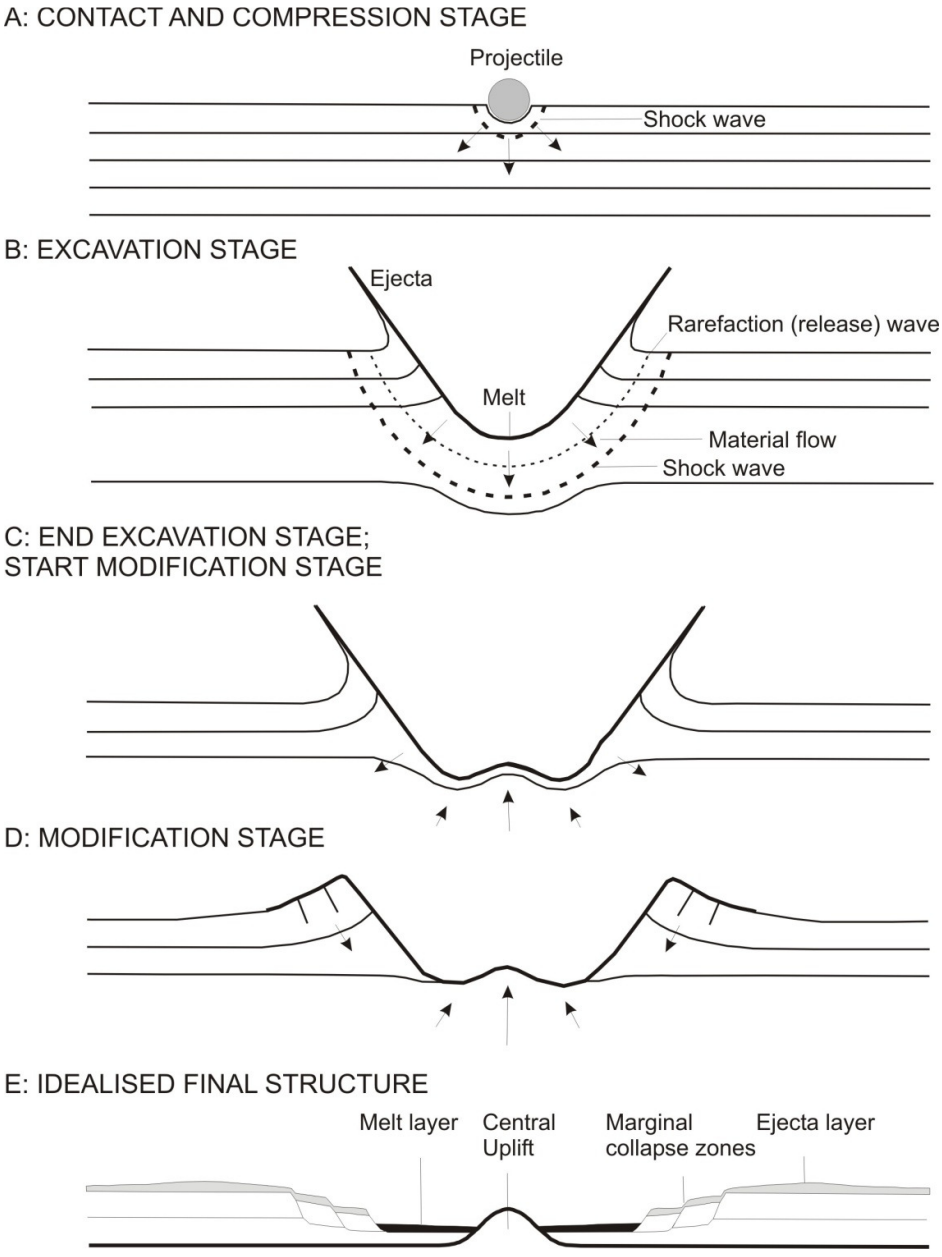

Fig. 1.2: Complex impact crater formation: A) Contact and compression, B) and C) excavation and D) modification stages (modified after French, 1998). The idealised form of the final structure is indicated in E.

1.2.2 Excavation Phase

The contact and compression phase is followed by the longer excavation phase (Fig. 1.2 B, C). In this stage, a roughly hemispherical shock wave moves into the target rocks, which compresses the target (Melosh, 1989). The shock waves transmitted into the target rocks lose their energy rapidly as they move away

from the point of impact (Melosh, 1989). This is because the shock wave expands into an increasing volume of rock and energy is lost to the target in the form of heat, deformation and acceleration. The shock wave variably shocks target rocks according to their strength. Ultimately, the shock pressure drops to 1-2 GPa (with a velocity of 5-8 km/s; Kieffer and Simonds, 1980), at which point the shock wave becomes a regular elastic wave (seismic wave). This point is typically reached at a radial distance corresponding to the edge of the transient crater (French, 1998). The transient crater is the cavity formed immediately after the end of crater excavation (French, 1998; Melosh, 1989). This crater later undergoes collapse and modification to form the final impact crater.

The progression of the shock wave sets the target material in motion, and this initiates an excavation flow (Melosh, 1989; O'Keefe and Ahrens, 1999; Wünnemann and Ivanov, 2003) that opens up the transient crater (the diameter of which is far larger than that of the projectile). The volume and temperatures of the zones of melted and vaporized rock are controlled almost entirely by the dynamics of the shock wave. The amount of melt will be approximately ten times the amount of vapour (Melosh, 1989).

The transient crater can be divided into two zones: the upper ejection zone and the displacement zone (French, 1998). The upper ejection zone is characterised by rocks that have high velocities and are ejected beyond the crater rim (this includes the vapour plume, see section 1.2.4). The displacement zone, on the other hand, experiences lower tensional stresses and excavation flow velocities; this material is driven downwards and outwards.

The shape (and size) of the final crater is determined by the interaction of the excavation flow and the strength of the target material (i.e., crystalline *vs*. sedimentary rocks), as well as the force

of gravity (Melosh, 1989). Structural controls, such as regional joint planes will also play a role in the ultimate crater shape.

The excavation phase ends when the transient crater reaches its maximum size (theoretically before the forces of gravity and rock mechanics are initiated). In contrast to the contact and compression stage, this phase may last up to several minutes, for large structures.

1.2.3 Modification Phase

Following the excavation phase, broadening and shallowing of the transient crater takes place in two ways: debris slides and slumping off the crater walls under the influence of gravity and elastic rebound of the shock compressed rocks occurs below the central parts of the crater (see Fig. 1.1 D; French, 1998; Melosh, 1989). Additionally, deposition of ejected material into and around the crater takes place. This phase lasts only slightly longer than the excavation stage: less than one minute for a small structure, and a few minutes for a larger one (Melosh, 1989). Only once normal terrestrial processes of erosion, uplift and sedimentation take place is this stage considered to be over (French, 1998). The size of the crater, as well as elastic parameters, will determine the ultimate type of crater that is formed. Three types of crater morphology can be recognised:

1.2.3.1 Simple craters

Simple craters (Fig. 1.3 A) occur as bowl-shaped depressions, which are ≤ 2 to 4 km in diameter depending on the strength of the target rock (Montanari and Koeberl, 2000). In this case, only minor collapse of the transient crater walls takes place during modification (increasing the crater diameter by up to 20 %). The crater is filled with a mixture of variably shocked rock fragments with melt, forming a “breccia lens” (Fig. 1.3 A). Examples of simple craters include Meteor Crater, Arizona, U.S.A. (e.g., Kring, 2007), Tswaing, South Africa (Brandt, 1999; Brandt and Reimold, 1995), Lonar, India (Fredriksson et al., 1973; Osae et al., 2005) and Brent, Canada

(Grieve, 1987; Koeberl and Milkereit, 2007). For terrestrial structures, the transition between simple and complex craters occurs at a diameter of 4 km in massive crystalline rocks, and 2 km in sediments (French, 1998).

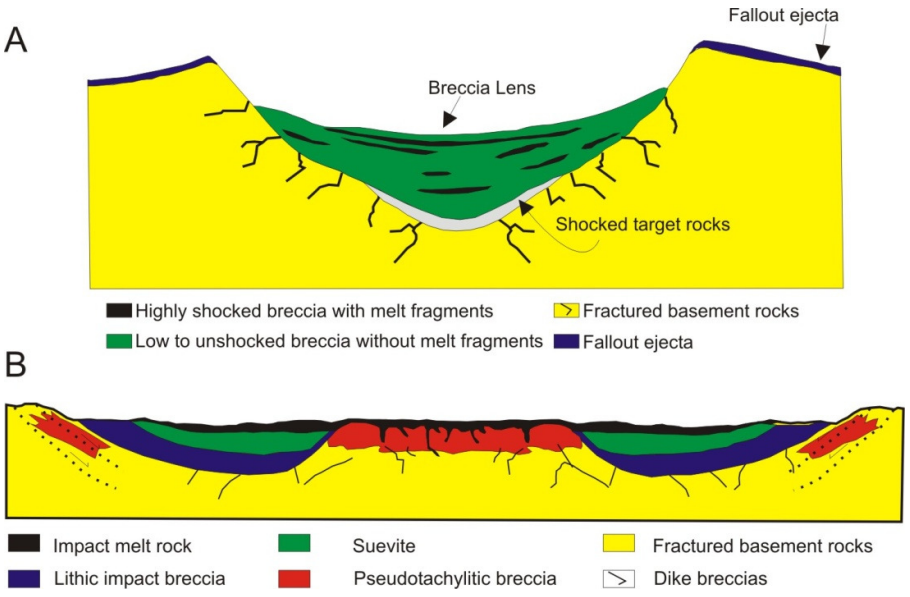

Fig. 1.3: Schematic cross-sections through A) simple and B) complex impact craters, indicating the positions of various impactites. Dashed lines indicate listric faults. Simple crater modified after Grieve (1987); complex crater modified after Reimold and Gibson (2006).

1.2.3.2 Complex craters

Complex craters (Fig. 1.1 E; Fig. 1.3 B) are characterised by a centrally uplifted region (either a central peak or one or more peak rings). Complex craters have an apparent crater depth of a fifth to a sixth of the crater diameter (Montanari and Koeberl, 2000).

In complex craters, slump terraces form on the walls and on the central peaks (areas of deformed and fractured rocks that originally lay below the transient crater; Dence, 1968; Grieve et al., 1981; Fig. 1.3 B). The slump terraces are formed by rocks around the periphery of the crater which collapse downward and inward along concentric faults (Melosh, 1989). The central peak may be unstable and

collapse, initiating the rise of mountains around the place where the central peak once was – this is known as a peak ring. As complex crater size increases, a central peak will be replaced by a peak-ring system, and then by a series of concentric rings and basins. Complex craters are also filled with a mixture of variably shocked impact breccia (fallback breccia; Montanari and Koeberl, 2000) and clastic debris of the collapsed crater rim.

The final form of the crater is governed by the so-called “flow” and “strength” parameters, and is based on observations that shocked material behaves both as a viscous fluid but has a definite plastic yield stress (“Bingham Fluid”; see Melosh, 1982). A Bingham fluid supports applied stresses without a great amount of strain until the shear stress exceeds its cohesion after which it flows as a viscous fluid. The “flow parameter” (Fig. 1.4) encompasses surface gravity, target density, crater diameter and viscosity, and the “strength parameter” incorporates target density, surface gravity, crater depth and cohesion (Fig. 1.4; Melosh, 1982). Cohesion and viscosity are dimensionless Bingham parameters. The combination of the strength and flow parameters allows a good quantitative description of the formation of complex craters as the result of gravity-driven collapse, and indicates the complex interaction of forces that govern the final form of a complex crater.

Central-peak structures (diameters of ca. 4-22 km on Earth; French, 1998), e.g., Bosumtwi crater, Ghana (Koeberl and Reimold, 2005; Koeberl et al., 2007a); central-peak-basin structures (diameters of ca. 22-30 km on Earth; French, 1998), e.g., Ries crater, Germany (Stöffler et al., 2001 and references therein) and peak-ring basin structures (diameters of ca. 30-62 km on Earth; French, 1998), e.g., Siljan crater, Sweden (Henkel and Pesonen, 1992) are the three types of complex impact structures that can be distinguished in terms of increasing crater diameter (Grieve et al., 1981; Melosh, 1989). Erosional processes on Earth make the preservation of original

morphologies difficult; however, on the Moon, where there is a lack of erosional and depositional processes, the characteristics are well preserved (Fig. 1.5).

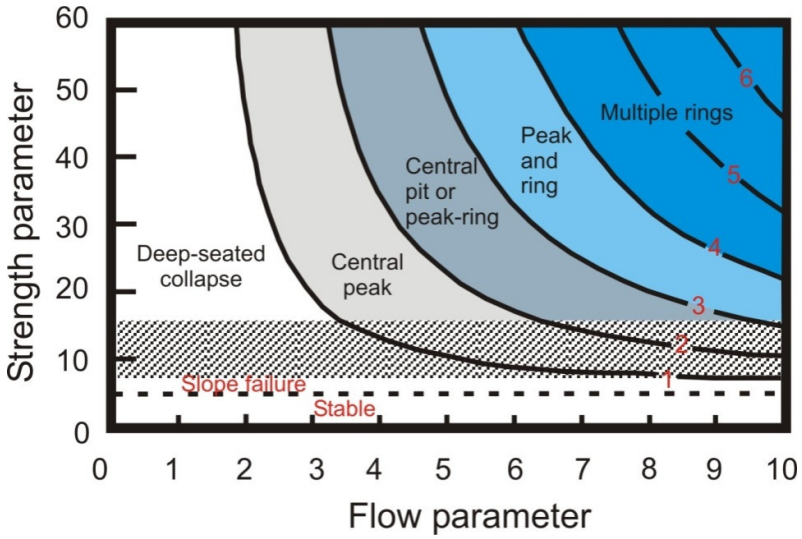

Fig. 1.4: Graph of flow parameter (= $g^{1/2}\rho D^{3/2}/\eta$) versus strength parameter (=$\rho gH/c$), where g = surface gravity, ρ = target density, D = crater diameter, H = crater depth, and Bingham parameters η = viscosity and c = cohesion (modified after Melosh, 1982, 1989). See text for discussion.

1.2.3.3 Multi-ring basins

Multi-ring basins are the largest impact-produced structures and consist of multiple (two or more) concentric, uplifted rings and alternating down-faulted valleys (ring graben), in addition to the outer rim of the structure (Fig. 1.5). Multi-ring basins are produced by projectiles which are tens to hundreds of kilometres in diameter (see Spudis, 1993; Melosh, 1989; Morgan et al., 1997). On Earth, multi-ring basins have diameters greater than 100 km, and though it has been difficult to identify these structures on Earth due to surface alteration processes, three structures are considered as multi-ring basins (Poag et al., 2004; Grieve and Therriault, 2000). Chicxulub crater, Mexico (diameter of ca. 180 km; Hildebrand et al., 1991; Sharpton et al., 1992; Morgan et al., 1997), Sudbury crater, Canada (diameter of ca. 200-250 km; Grieve and Therriault, 2000) and

Vredefort crater, South Africa (diameter of ca. 250-300 km; Grieve and Therriault, 2000; Reimold and Gibson, 2001) have been proposed as multi-ring basins. Smaller basins, with only two structural rings could be the Chesapeake Bay crater, U.S.A. (ca. 90 km) and the Popigai crater, Russia (ca. 100 km; Poag et al., 1999, 2004; Masaitis et al., 1999a; Whitehead et al., 2002a).

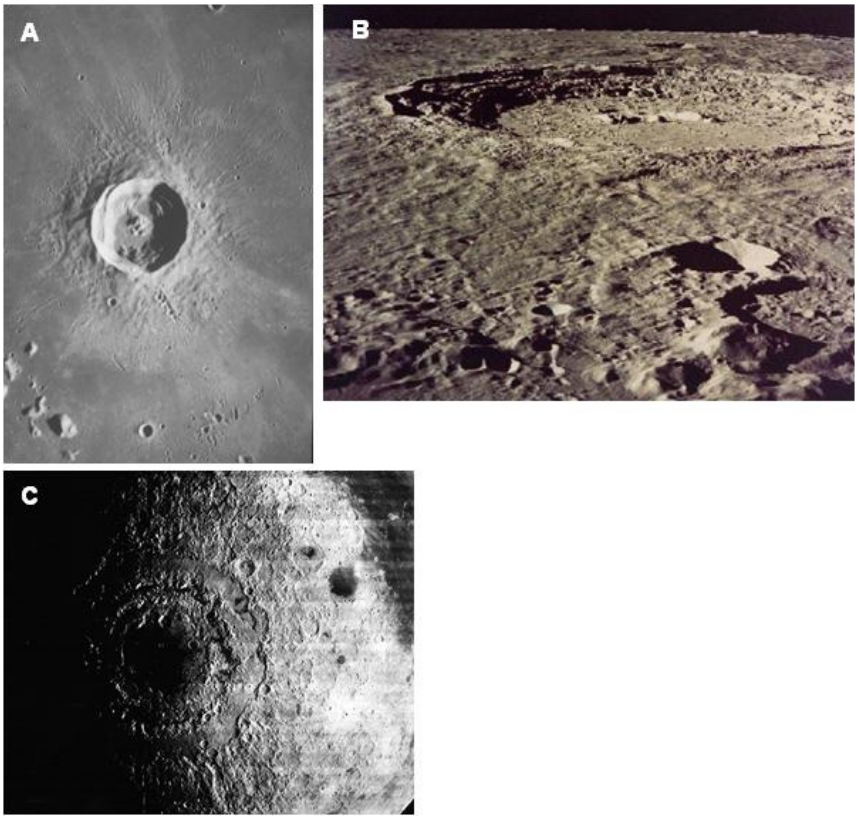

Fig. 1.5: Examples of lunar craters: A) Euler crater, showing the ejecta blanket; crater diameter is 28 km (source: Lunar and Planetary Institute, Apollo 17 Metric photograph AS17-2923). B) Copernicus crater, with central uplift and secondary crater; Copernicus crater diameter is 93 km (towards front of the image; source: NASA, Apollo 17 metric photograph AS17-151-23260). C) Mare Orientale, a multi-ring basin; crater diameter is 960 km (source: NASA, Lunar Orbiter 4, part of frame M-187).

1.2.4 Ejecta Dispersal

Material from a large impact is thought to be dispersed by two different mechanisms: as part of the ejecta curtain and by vapour plume expansion (Melosh, 1989; Alvarez, 1996). The ejecta curtain

disperses debris in a short-range zone, and consists of a front of particles (Alvarez, 1996). Each particle moves with its own ballistic trajectory, and the ejecta curtain has been observed in laboratory experiments to form a downward-pointing cone centred on the point of impact (Schultz and Gault, 1982). Some material may not leave the central cavity, but will flow around turbulently as ground-surge. The vapour plume (a.k.a. fireball) consists of vapour together with some of the earliest and fastest moving ejecta (Melosh, 1989). This rapidly accelerates upwards, and blows out of the top of the atmosphere (Alvarez, 1996).

Vapour plume expansion and spallation (the ejection of tiny fragments of material) involves both the forces of stress wave expansion and excavation flow (Fig. 1.6; Melosh, 1989). The vapour plume has the ability to transport vast amounts of material to great distances, such as seen for the ejecta blanket associated with the Cretaceous-Palaeogene extinction which scattered iridium-rich dust all over the world (see Melosh, 1989). Vapour plume expansion begins during the contact and compression phase when the projectile makes contact with the target, and high pressures are generated (Melosh, 1989). The unloaded projectile and target can begin to expand upward and outward at high velocities, once they are vaporised. The plume is a mixture of variably shocked components, each with different temperatures. The expansion is dominated by the components with the highest temperatures (which may move at velocities potentially exceeding 10 km/s; Melosh, 1989). It will overtake the ejecta curtain, and will enclose the crater in a transient atmosphere composed of vaporized projectile and target rock fragments. Large pieces of ejecta could be crushed by the aerodynamic pressures exerted by the plume. It is thought that the shape of this plume would be hemispherical until it begins to condense. Currently the only way to investigate ejecta plume formation is by numerical modeling (see Ivanov et al., 1996; Pierazzo et al., 1998, 2003; O'Keefe and Ahrens, 1999; Melosh and Ivanov,

1999; Pierazzo and Melosh, 1999, 2000; Collins et al., 2002; Shuvalov, 2003; Wünnemann and Ivanov, 2003; Shuvalov and Dypvik, 2004; Stöffler et al., 2004), in comparison with textural observations on impact ejecta.

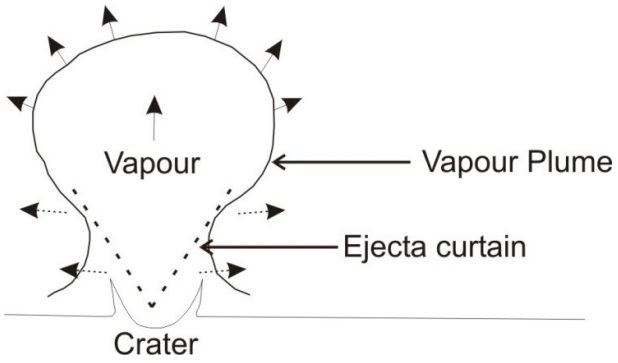

Fig. 1.6: Simplified schematic diagram showing the ejecta curtain and vapour plume expansion during the early stages of an impact event (modified after Melosh, 1989). The ejecta curtain is shown by the dashed lines, and its movement is shown by the dashed arrows. The vapour plume is shown by the solid line, and its expansion is shown by the solid arrows.

1.2.5 Impactites

In impact structures, a variety of distinctive rock types can be observed, which are known as impactites. An impactite is defined as "a collective term for all rocks affected by one or more hypervelocity impact(s) resulting from collision(s) of planetary bodies" (Stöffler and Grieve, 2007). They are produced by shock wave movement through the target rock, and occur at different depths beneath, within and around the final impact crater. Rocks may either be allochthonous (rock that has been moved from its original location), autochthonous (rock that has been deformed in its original location) or parautochthonous (an intermediate type to allochthonous and autochthonous). Impact ejecta are those impactites occurring around, on and as part of the crater rim. These impactites are thought to be mostly emplaced by ballistic processes (Melosh, 1989; Ahrens and O'Keefe, 1978) and may be divided into proximal and distal ejecta. The distribution of impact ejecta depends on the

distance from the impact site, crater size, the underlying lithologies and the presence or absence of volatiles (see Melosh, 1989).

Recently Stöffler and Grieve (2007) provided a classification scheme of impactites, on behalf of the Subcommission on the Systematics of Metamorphic Rocks of the International Union of Geological Sciences. Impactites (Fig. 1.7) can be divided on the basis of their location with respect to the crater structure:

1. Subcrater – parautochthonous rocks, cross-cutting allogenic rocks, and pseudotachylitic breccia
2. Crater interior – allogenic crater-fill deposits (e.g., lithic breccia, suevite, impact melt rock)
3. Crater rim region – proximal ejecta deposits (e.g., fallout breccia) and breccia injections into the crater rim strata
4. Distant from crater – distal ejecta (e.g., tektites)

1.2.5.1 Subcrater rocks

Subcrater rocks occur within the crater below the zone of excavation. These rocks are driven downward and outward initially during the impact event, and can be blocks of tens to hundreds of metres in size. Regions adjacent to the crater, however, may not be displaced at all. In this region, shock pressures vary widely; the highest pressures will be found towards the centre of the structure, dropping off further away. Thus, a wide variety of shock-metamorphosed effects may be observed.

In general, rocks will be fractured and cataclased, and polymict (multiple clast types) or monomict (single clast type) lithic breccias may be produced that have or lack high-pressure shock-metamorphic effects. In other words, rock and mineral fragments occur in a clastic matrix of smaller but similar fragments, which are derived from the local target rocks.

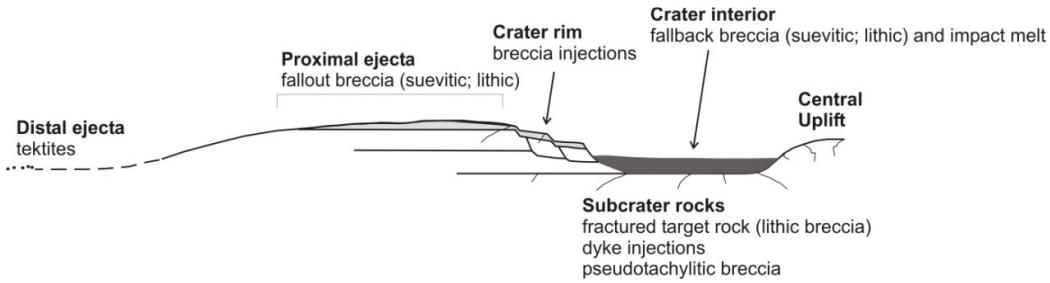

Fig. 1.7: Schematic cross section showing an idealised impactite distribution in a complex crater.

Shatter cone development may also take place – these features provide a macroscopic indicator of impact deformation (see Roddy and Davis, 1977; Sharpton et al., 1996; Dressler and Sharpton, 1997; Nicolaysen and Reimold, 1999; Wieland et al., 2006). They can form in a variety of rock types (French, 1998; Koeberl and Martínez-Ruiz, 2003), though they are best developed in fine-grained rocks. They comprise curved, striated fractures that form partial to complete cones. The origin and timing of these features is still not yet fully resolved – an evaluation of the different hypotheses and new findings has been reported recently in Wieland et al. (2006).

Large fractures in this zone could be intruded by allogenic materials (rock fragments and/or melt) to form cross-cutting bodies (e.g., Lambert, 1981; Bischoff and Oskierski, 1987; Dressler and Sharpton, 1997; Dressler and Reimold, 2001, 2004). The allogenic breccias are frequently polymict, with lithologically diverse fragments, indicating that mixing has taken place over considerable distance. The breccias can be lithic (melt-free), melt-fragment breccias (containing fragments of heterogeneous glass, rocks and minerals, in a clastic matrix; i.e., suevites), impact melt rocks (rock and mineral fragments in a matrix of glassy or crystalline melt) or impact melt rocks (composed of glassy or crystalline melt with few or no inclusions; see Dressler and Reimold, 2001; Fig. 1.3).

Pseudotachylite, a friction-produced melt, has also been observed in impact settings (see Reimold, 1995, 1998), though this is also a tectonically-produced phase (e.g., Philpotts, 1964; Sibson, 1975; Spray 1995; Dressler and Reimold, 2004). However, the occurrence of pseudotachylite-like material, in great volumes, has been observed in the large impact structures such as the Vredefort and Sudbury craters (Reimold, 1995, 1998; Reimold and Gibson, 2005, 2006), part of which is likely to have some form of origin by shock (Reimold and Gibson, 2006). On this basis, the term "pseudotachylitic breccia" (Reimold, 1995, 1998; Reimold and Gibson, 2006; cf. Fig. 1.3) has now been proposed to describe pseudotachylite-like material of impact origin. These breccias consist of variably sized rounded clasts of target material set in a crypto- to microcrystalline matrix (Reimold and Gibson, 2006).

1.2.5.2 Impactites of the crater interior

In the crater interior, "crater-fill breccias" are found. These allogenic breccias consist of ejected material or material moved by ground-surge. This includes large and small bodies of melt and variably sized fragments of shocked and unshocked target rock that do not travel beyond the crater rim; impact breccia deposited near the crater rim that fell back into the crater under gravity collapse (see Melosh, 1989; French, 1998) or mobilized as ground surge. Post-impact debris flows off the crater rim can also contribute to the crater fill.

In small, simple craters, this material is usually thoroughly mixed, and may fill the crater to half its depth, in what is known as the breccia lens (Fig. 1.3; Melosh, 1989). On the other hand, this material may form discrete units in larger, complex craters (see Stöffler et al., 1988; French, 1998). These crater-fill deposits may be subsequently buried beneath younger crater-fill sediments, which may help to preserve the underlying breccias (e.g., Bosumtwi crater, Ghana; Koeberl et al., 2007a). Fragments in the breccias may preserve shock pressures ranging from about 5 GPa to > 100 GPa

(see Table 1.1). Three types of breccia are recognized as crater-fill breccias (see Stöffler and Grieve, 2007; Stöffler and Reimold, 2006): lithic breccias, melt-fragment-bearing breccias (suevites) and melt-matrix breccias (impact-melt rocks).

Lithic breccias are melt-free breccias and form a distinctive lithology in both large and small impact structures (e.g., Bunte Breccia in the Ries crater; Hörz et al., 1983). They consist of rock and mineral fragments (clasts) in a matrix of finer-grained material that generally consists of the same rock and mineral fragments. These breccias are poorly sorted, and clast sizes vary from < 1 mm to tens of metres. Clast shapes can be rounded to angular, and the clasts may or may not be highly shocked, depending on from where they originated in the impact structure. These breccias are mostly polymict, as their components are extracted from a wide range of target rocks. They can be associated, both vertically and horizontally (French, 1998), with melt-fragment-bearing breccias (suevites). Suevite is defined as a "polymict impact breccia that includes melt particles (glassy or crystallized) in a mostly clastic matrix containing lithic and mineral clasts in various stages of shock metamorphism" (see Stöffler and Grieve, 2007; Stöffler and Reimold, 2006). There is some debate about the minimum amount of melt fragments (A. Deutsch, pers. comm., 2006) needed to constitute a suevite rather than a lithic breccia. In this study, all breccias which contain any amount of melt are regarded as melt-fragment (suevitic) breccias. The type-locality for suevites is the ca. 14.5 Ma Ries crater, Germany (e.g., von Engelhardt et al., 1969; von Engelhardt and Graup, 1984; von Engelhardt, 1990, 1997). These breccias occur as both fallback and fallout deposits. The melt particles can be compositionally heterogeneous and may show flow-structures. The glass particles from fallout suevites may show grooved and lobate structures due to their aerodynamic transport, while those within the crater are usually smaller and lack such structures (von Engelhardt and Graup, 1984; von Engelhardt, 1990; French, 1998).

Recently, Osinski et al. (2004) proposed that constituents in the groundmass of suevites from the Ries crater were molten at the time of deposition, and that certain minerals were crystallized out of the groundmass. This observation indicated that these breccias were in fact melt-matrix breccias, rather than melt-fragment breccias (Osinski et al., 2004). More investigation into the genesis of the Ries crater suevites is underway.

Melt-matrix breccias (impact melt breccias) are those breccias that do not contain individual melt fragments, but whose matrix was originally molten. The matrix can vary from glassy material to textures of a crystalline rock. The rock and mineral fragments may be shock deformed or melted. As the percentage of melt increases, the melt breccia type grades into impact melt rock.

1.2.5.3 Impactites of the crater rim region and proximal ejecta

The crater rim is composed of uplifted substrata, overturned target rocks and overlying ejecta debris (Melosh, 1989). The uplift is caused by the plastic deformation of rocks underneath the rim as well as the injection of subhorizontal breccia dykes. The rim is also composed of overturned target rocks. The crater rim region is subjected to lower shock pressures (typically <2 GPa; Kieffer and Simonds, 1980) than some of the materials inside the crater. Thus, the autochthonous target rocks are generally fractured and brecciated, but only rarely contain shock-deformation features.

Proximal ejecta occur in the immediate vicinity of the crater (< 5 crater radii from the rim; Melosh, 1989). At further distances, a near-continuous blanket of ejecta, which thins with distance from the crater (McGetchin et al., 1973; Stöffler et al., 1975; Melosh, 1989) covers the environs of the crater (the so-called “ejecta blanket”). The proximal ejecta comprise ca. 90% of all material excavated during the impact event (Koeberl and Martínez-Ruiz, 2003). These ejecta

may be shocked and even molten. The blanket is not homogeneous, but is made up of the same distinct lithologies as the crater-fill rocks.

The morphology of ejecta blankets may be affected by factors such as the angle of impact (see Melosh, 1989; Cintala et al., 1999; Schultz, 1996). At impact angles of 60° – 90°, the ejecta blanket will be roughly circular in shape (Gault and Wedekind, 1978). As the angle decreases, the ejecta blanket will concentrate downrange of the crater (see Gault and Wedekind, 1978). The ejecta deposits from an oblique impact are always bilaterally symmetric as the ejecta may concentrate towards either side of the crater (Gault and Wedekind, 1978).

1.2.5.4 Distant regions and distal ejecta

A small amount of the material ejected from the crater may travel significant distances (> 5 crater radii; see Melosh, 1989) from the crater. The mechanism for emplacement of these deposits is still not fully understood, but it has been accepted that ballistic deposition will have played a substantial role (see Melosh, 1989; Koeberl and Martínez-Ruiz, 2003). In terrestrial events, where atmosphere is present, a combination of ballistic ejection as well as atmospheric transport can distribute distal ejecta to regional or global distances (Alvarez et al., 1995). Distal ejecta contain distinct evidence for meteorite impact – shocked rock and mineral fragments, and unusual glassy objects (e.g., tektites, microtektites and spherules; see Koeberl and Martínez-Ruiz, 2003).

Tektites are chemically homogeneous bodies which are up to a few centimetres in size (Koeberl and Martínez-Ruiz, 2003) and represent melts of surficial material from an impact target sequence. They are formed only during hypervelocity events. Four tektite strewn fields have been identified on Earth, with three linked to known impact craters: the Ivory Coast (Bosumtwi crater), North American (Chesapeake Bay crater), Central European (Ries crater) and

Australasian strewn fields. The chemical and isotopic compositions of tektites have been used to link the tektites to their source craters, such as in the case of the Ivory Coast tektite and microtektite strewn field (see section 1.4.2; Glass, 1968, 1969; Glass et al., 1991; Koeberl et al., 1997a). Microtektites are tektites that are less than 1 mm in diameter and have been recovered from deep-sea cores (see Koeberl and Martínez-Ruiz, 2003). Another important occurrence of microtektites has been in the sediments of the boundary layer of the Cretaceous-Palaeogene boundary (formerly Cretaceous-Tertiary; see Smit, 1999) which provided crucial evidence that this boundary was associated with a large meteorite impact event (see Montanari and Koeberl, 2000; Koeberl and Martínez-Ruiz, 2003).

1.3 Impact-Induced Shock Effects in Minerals and Rocks

Shock metamorphic effects are crucial to the identification of impact structures, as the effects produced are unique to such craters. The physical conditions that produce these effects are well known, and have been established through practical experiments (e.g., French and Short, 1968; Roddy et al., 1977; Stöffler, 1972, 1974; Kieffer and Simonds, 1980; Melosh, 1989; Stöffler and Langenhorst, 1994; Huffman and Reimold, 1996; Koeberl, 2002), in comparison with observations in natural impact structures.

Peak shock pressures and temperatures in the impact event vary from ≤ 2 GPa near the crater rim to ≥ 100 GPa near the point of impact. Temperatures may be as much as 10 000 ^{o}C near the point of impact, and are typically in the range of 500–3000 ^{o}C, though they can be much lower (ca. 100 ^{o}C). Post-shock temperatures increase with increasing shock pressure. Shock pressures are far outside the range of normal geological processes (see Fig. 1.8). For example, regional and contact metamorphic processes usually produce pressures in the range of < 2 GPa, and temperatures of ≤ 1200 ^{o}C in the crust (see Koeberl and Martínez-Ruiz, 2003). Strain rates in contact and regional metamorphic processes range from 10^{-3} s^{-1} to

10^{-6} s^{-1} over long periods of time (10^5 to 10^7 years), whereas in impact events strain rates are between 10^4 s^{-1} and 10^6 s^{-1} and are produced essentially instantaneously (see Fig. 1.8; French, 1998). The release of shock pressure produces diagnostic mineral and rock deformation effects at different pressures (Table 1.1).

Table 1.1: Shock pressures with corresponding mineral and rock deformation features for porous and non-porous rocks (adapted after French, 1998; Koeberl and Martínez, 2003). Data from Stöffler (1984); Melosh (1989); Stöffler and Langenhorst (1994); Montanari and Koeberl (2000); Koeberl (2002).

Shock pressure range (GPa)	Effects
2-45	Shatter cone and breccia formation, rock fracturing.
5-45	Planar fractures and planar deformation features $\{0001\}$, $\{10\bar{1}1\}$, $\{10\bar{1}3\}$, $\{10\bar{1}2\}$ in quartz; also in feldspar, olivine and zircon. Quartz and feldspar with reduced refractive indices and birefringence.
15-50	High-pressure polymorph formation: Quartz → stishovite, coesite; graphite → diamond; olivine → ringwoodite
30-40	Diaplectic quartz and feldspar glasses (isotropization through solid-state transformation with crystal habit preservation)
45->70	Mineral melts (quartz, feldspar)
>60	Rock melts
>100	Complete rock vaporisation

It should be emphasized at this point that not all rocks (and therefore minerals) in the vicinity of the impact site will experience all shock effects, as the passage of the shock wave through the target rock is not homogeneous. Quartz is able to preserve a range of unique shock effects (Grieve et al., 1996; French, 1998; Stöffler 1971a, 1971b, 1972, 1974; Stöffler and Langenhorst, 1994; Langenhorst, 2002; Fig. 1.8). It is also abundant in a wide variety of terrestrial crustal rock types, and therefore has become the most important shock indicator mineral.

1.3.1 Planar Microstructures in Quartz

Planar fractures (PFs) and planar deformation features (PDFs) are deformation features that can be produced by shock.

Planar fractures are parallel sets of multiple planar cracks (or cleavages) in quartz or other mineral grains. They develop at shock pressures below the HEL (~5-8 GPa; French, 1998). The fractures are typically 5-10 µm wide and have a spacing of 20 µm or more in individual grains (Langenhorst, 2002). These structures are highly suggestive of an impact origin, when accompanied by other shock-induced features (Robertson et al., 1968; Stöffler and Langenhorst, 1994; Grieve et al., 1996; French et al., 1997), but have also been observed as non-impact deformation.

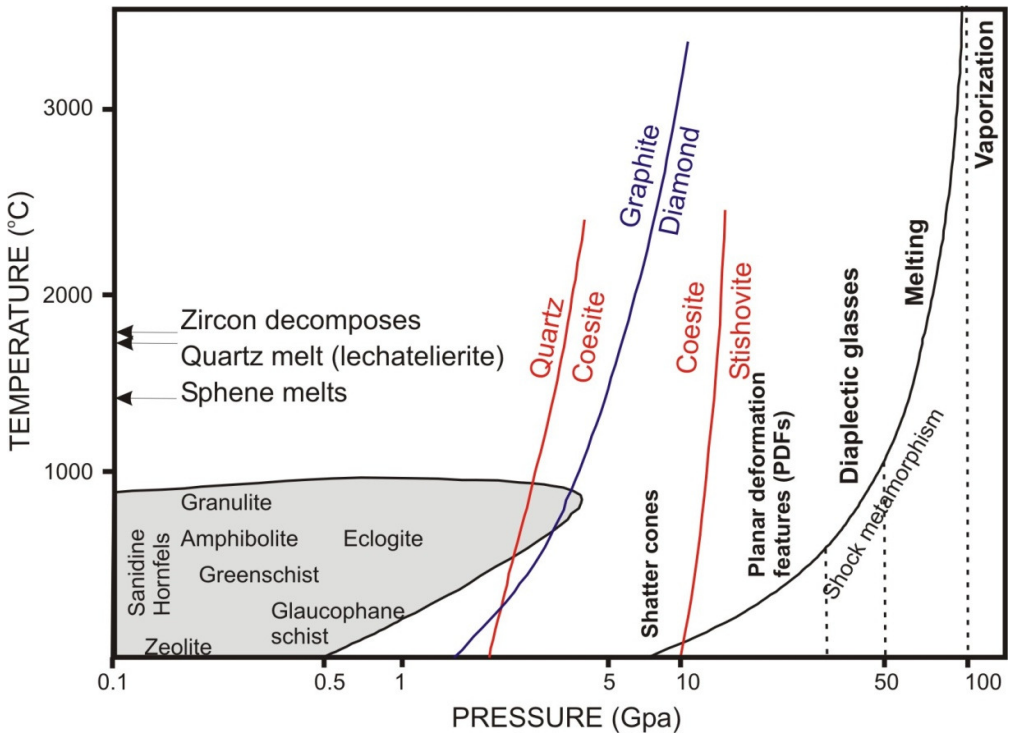

Fig. 1.8: Pressure-temperature (P-T) conditions of shock metamorphic processes (modified after French, 1998). Red curves indicate the P-T boundaries for the conversion of quartz to its high-pressure polymorphs and the blue curve indicates the conversion of carbon from graphite to diamond.

Planar deformation features (PDFs) occur as single or multiple sets of extremely narrow (< 2-3 µm), parallel planar features, which are closely spaced (typically 2-10 µm). These are not open cracks, unlike planar fractures. Optical and TEM studies have shown that, within individual PDFs, the structure of the original crystalline quartz is

severely deformed, so that the quartz has transformed into a distinct amorphous phase (Kieffer et al., 1976; Goltrant et al., 1991, 1992; Gratz et al., 1992; Langenhorst, 1994, 2002). These features are only produced under shock-metamorphic conditions and are thus diagnostic of meteorite impact. The PDFs are generally oriented parallel to specific rational crystallographic planes in the host quartz crystal – especially to base c (0001) or to low-index rhombohedral planes such as ω $\{10\bar{1}3\}$, π $\{10\bar{1}2\}$and r $\{10\bar{1}1\}$. The specific crystallographic orientations of PDFs have been linked to specific pressure ranges (French, 1998).

In thin section, unaltered PDFs form multiple sets of continuous planes that extend across most or all of the host grain, and are generally found in younger, well preserved, impact structures. However, the presence of fresh, continuous PDFs depends on geological conditions since their formation, including cooling rate and post-impact temperatures. In altered, geologically old, or metamorphosed samples, PDFs are also distinctive, but may be discontinuous in comparison. The amorphous material may be recrystallized, and in the process fluid inclusions may develop along the original planes (called “decorated PDFs”; Robertson et al., 1968; Stöffler and Langenhorst, 1994), which will preserve the original orientation of the PDFs. Thus, this fabric can still be recognized in rocks that have undergone alteration, and even metamorphism (e.g., greenschist facies at Sudbury crater, Canada). More intense recrystallization can produce arrays of small mosaic quartz crystals along the PDF orientations (Leroux et al., 1994).

In other minerals (e.g., feldspar) similar planar microstructures are also produced by shock (e.g., Stöffler, 1972, 1974). These features are less studied and not as well characterised as those in quartz as feldspars are more optically diverse (optically biaxial versus optically uniaxial in quartz). For a comprehensive discussion of such effects, refer to Langenhorst (2002).

1.3.2 High Pressure Polymorphs

High pressure mineral polymorphs are shock-formed at pressures above 15 GPa (see Table 1.1, Fig. 1.8; see Montanari and Koeberl, 2000). Quartz can be transformed into coesite (Chao et al., 1961) and stishovite (Chao et al., 1962) under high shock pressures, although the transformation is not direct (Langenhorst, 2002). Quartz is converted to diaplectic glass or melted under high shock-produced temperatures (see Langenhorst and Poirier, 2000) and then, during decompression, coesite and/or stishovite crystallize. Post-stishovite phases have also been reported, but these are not fully characterised as yet (El Goresy et al., 2000; Sharp et al., 1999).

Similar changes for the following minerals to their high pressure polymorphs may also take place: olivine to ringwoodite (see Langenhorst et al., 1995; Chen et al., 1996), graphite to diamond (Masaitis et al., 1990, 1999b; Koeberl et al., 1997b; Hough et al., 1997) and zircon may form reidite (Glass et al., 2002).

1.3.3 Diaplectic Glasses

Shock-produced diaplectic glass (see French, 1998; Table 1.1, Fig. 1.8) is entirely different to conventional glasses that are produced by melting of a mineral to a liquid at temperatures above its melting point. Diaplectic glasses do not melt or flow – they preserve the original texture of the crystal and original fabric of a rock, despite having been transformed into an amorphous phase (von Engelhardt et al., 1967; Stöffler, 1984). These glasses are optically isotropic (i.e., they do not show birefringence under cross polarized light). Common diaplectic glasses of minerals include those of quartz and feldspar (for plagioclase - maskelynite; Bunch et al., 1967). When a mineral is transformed to diaplectic glass, the refractive index decreases, but the density increases (Langenhorst and Deutsch, 1994).

Mafic minerals do not appear to form diaplectic glasses, as the temperatures needed to achieve this are higher than those needed

for traditional mineral melting (French, 1998). It must be noted that diaplectic quartz and feldspar glasses are metastable, and will be destroyed if they are exposed to relatively mild post-impact temperatures (French, 1998). In such cases, the quartz and feldspar will recrystallize to microcrystalline aggregates that replace the original crystal, and are commonly accompanied by the development of spherulitic textures (French, 1998). The formation of diaplectic glass is still not fully understood; it may represent a solid-state collapse (Stöffler, 1984) or high-pressure liquid quenching (Langenhorst, 1994).

1.3.4 Mineral and Rock Melting

At higher shock pressures than those needed to produce diaplectic glass (Table 1.1) and higher post-shock temperatures (≥ 1000°C), the melting-points of rock-forming minerals are exceeded, and localized melting takes place (French, 1998). In shock-produced melting the entire mineral is instantaneously raised to the post-shock temperature. If the temperature exceeds the individual mineral's melting point, melting of that mineral will take place (French, 1998). The mineral melt thus has the same composition as the original mineral before any flow or mixing takes place. At higher shock pressures, where temperatures are higher and cooling times longer, selective mineral melting in addition to normal eutectic melting may take place, and thus the rock will yield a mixture of heterogenous melts, some of which may preserve the original shapes and compositions of precursor grains (Peredery, 1972).

Eventually, with higher shock pressures, melting takes place throughout the rock, producing an impact melt body which may have a more homogeneous composition, and that displays flow textures.

1.4 The Bosumtwi Impact Structure, Ghana

The Bosumtwi impact structure is located in Ghana, approximately 32 km south-southeast of the town of Kumasi, Ashanti Province (Fig.

1.1). The crater is centered at 06°32' N and 01°25' W. It is one of only 19 confirmed impact structures in Africa (Koeberl, 1994a; Master and Reimold, 2000; Koeberl and Reimold, 2005). It is 1.07 ± 0.05 Ma old (Koeberl et al., 1997a), and has a diameter of ca. 10.5 km (e.g., Wagner et al., 2002). The crater is one of the best preserved impact structures of such size. It is filled with the 8.5 km diameter and up to 80 m deep Lake Bosumtwi (Fig. 1.9) and underlying lake sediments (see section 1.8.1). Outside the crater rim at a radial distance of between 7 and 8.5 km from the crater centre is a slight, near-circular depression and an outer ring of minor topographic elevation with a diameter of about 20 km (Jones et al., 1981; Garvin and Schnetzler, 1994; Reimold et al., 1998; Wagner et al., 2002). As already noted, the Bosumtwi crater is associated with the Ivory Coast tektite and microtektite strewn field (Fig. 1.1; Glass, 1968, 1969; Glass et al., 1991; Koeberl et al., 1997a).

The Bosumtwi structure was drilled in July to October 2004 by the ICDP in order to recover a series of sedimentary cores to investigate the sedimentary fill (as the sediments preserve a complete 1 Ma palaeoenvironmental record) as well as two cores through the impactite sequence (LB-07A and LB-08A; e.g., Koeberl et al., 2005, 2006a, 2007a; see section 1.8).

1.4.1 Historical Background

Lake Bosumtwi was first studied scientifically in the early 1900s. Initially, much debate about the origin of this structure took place. Fergusson (1902) suggested that the crater was not of volcanic origin. Kitson (1916) interpreted it as a subsidence feature, whereas MacLaren (1931) was the first to favour impact. Rohleder (1936) supported an explosive origin for the lake. He had been studying the impact structures of Steinheim, Germany and Tswaing, South Africa, and believed them to be impact-generated, but could not find similarities between those structures and Lake Bosumtwi.

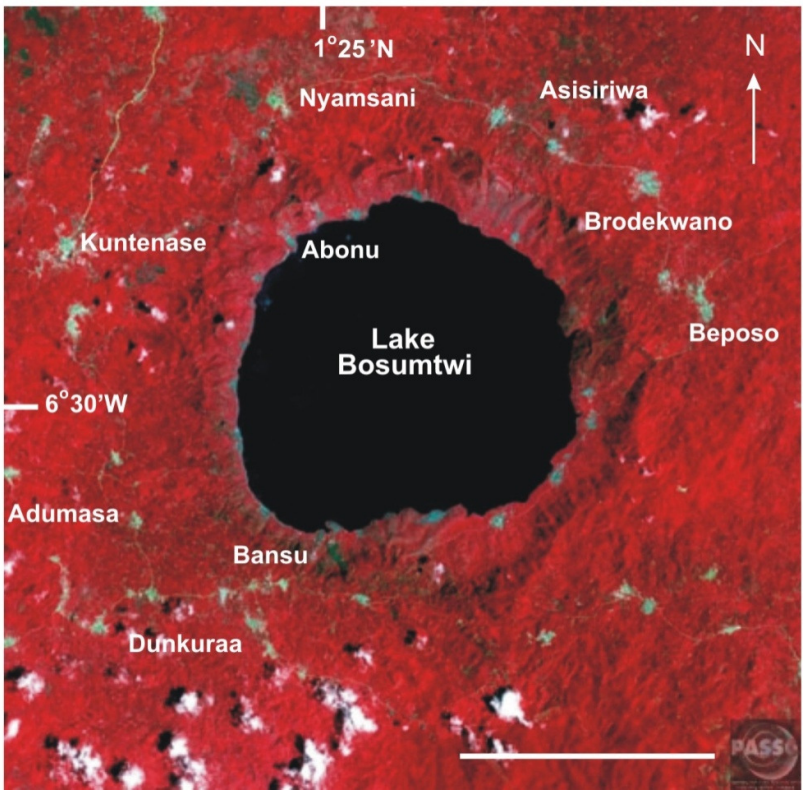

Fig. 1.9: False colour Spot satellite image of the Bosumtwi impact crater. Scale bar is 8 km in length. Red colours indicate vegetation, while main roads and settlements are shown in light green. Image courtesy of Jeff Plescia, John Hopkins University.

Junner (1937) believed the crater to be of volcanic origin. However, when outcrops of suevite around the crater rim (Chao, 1968; Jones et al., 1981), as well as coesite (Littler et al., 1961) and Ni-rich iron spherules and baddeleyite (a high temperature modification of zircon; El Goresy, 1966; El Goresy et al., 1968), were found in glasses from the crater rim, the impact hypothesis was favoured by these authors. Subsequently, shocked quartz with planar deformation features in suevite was described by Koeberl et al. (1998), and this provided unequivocal proof of the origin of Lake Bosumtwi as the product of bolide collision. The presence of a meteoritic component in the Ivory Coast tektites was confirmed by Koeberl and Shirey (1993) by Os isotopic investigation.

1.4.2 Link to the Ivory Coast Tektite Strewn Field

The Bosumtwi impact structure is also of special interest as it is one of only a few impact structures that retain their original ejecta fields. The Ivory Coast tektites were first reported in 1934 (Lacroix, 1934) from an area of about 40 km radius in the Ivory Coast territory (see Fig. 1.1). The tektites are centimetre-sized, mostly spherically-shaped black glasses. Additionally, microtektites have been recovered from deep-sea cores off the coast of West Africa (Fig. 1.1; see Glass, 1968, 1969). The microtektites are smaller than the glass bodies from the tektite strewn field, measuring up to 1 mm in diameter, and have a greater variety of shapes (e.g., dumbbell shaped, tear-drops, ropes, spheres). The Ivory Coast tektites were linked to the Bosumtwi crater using a variety of methods. The tektites have been found to have similar geochemical signatures (Schnetzler et al., 1967; Jones, 1985a) as well as similar isotopic compositions (Schnetzler et al., 1966; Lippolt and Wasserburg, 1966; Kolbe et al., 1967; Shaw and Wasserburg, 1982) to rocks from the Bosumtwi impact structure. Ages for the tektites and Bosumtwi impact glasses were determined and found to agree (e.g., Gentner et al., 1964, 1967; Durrani and Khan, 1971; Storzer and Wagner, 1977), but the most convincing age dating linking the structure and the tektites was reported by Koeberl et al. (1997a). Koeberl et al. (1997a) used both fission track and ^{40}Ar-^{39}Ar dating, and found both the tektites and the Bosumtwi crater to date to 1.07 ± 0.05 Ma.

1.5 Regional Geology

The Bosumtwi crater was excavated in the 2.1-2.2 Ga metamorphosed supracrustal rocks of the Birimian Supergroup (Junner, 1937; Woodfield, 1966; Moon and Mason, 1967; Wright et al., 1985; Leube et al., 1990; Watkins et al., 1993; Hirdes et al., 1996; Koeberl and Reimold, 2005; Feybesse et al., 2006; Fig. 1.10; Fig. 1.11; Appendix 1). The Birimian Supergroup in Ghana occurs as a number of parallel, evenly spaced, volcanic belts, several hundred kilometres in length, that are separated by basins containing dacitic

volcaniclastics, argillitic sediments, granitoids and greywackes (cf. Wright et al., 1985; Leube et al., 1990; Fig. 1.10). The Birimian rocks consist of both metasediments and metavolcanics, that have been metamorphosed to lower greenschist facies (c.f. Wright et al., 1985; Leube et al., 1990; Davis et al., 1994; Hirdes et al., 1996; Oberthür et al., 1998; Watkins et al., 1993). The Supergroup was originally divided into the Lower Birimian (dominated by the metasediments) and the Upper Birimian (dominated by greenstone-type metavolcanics), but it was later shown that both units were, in fact, contemporaneous (Leube et al., 1990) at 2.17 ± 0.07 Ga (Leube et al., 1990; Taylor et al., 1992; Davis et al., 1994; Hirdes et al., 1996).

Granitoids are associated with both the Birimian metasedimentary basins and the volcanic belts (Fig. 1.10). “Basin-type” or “Cape Coast type” granitoids occur in the basins (Fig. 1.10), and form synorogenic foliated batholiths (Leube et al., 1990). These granitoids are peraluminous and granodioritic in composition. The belts have been intruded by “belt-type” or “Dixcove” granitoids (Fig. 1.10) and form mostly late-orogenic unfoliated intrusions which are metaluminous and have a tonalitic composition (Leube et al., 1990).

Metavolcanic rocks occur southeast of the crater (Fig. 1.11). The metasediments consist of interbedded metapelites and meta-tuffs, together with (meta)greywackes and quartzitic greywackes, shales and slates (Koeberl and Reimold, 2005). The metapelites comprise a varied assemblage of phyllites, mica-schists, shales and slates. These rocks are characterised by a strong regional northeast-trending fabric with steep dips to either the northwest or southeast. Local variations in both strike and dip are seen around Lake Bosumtwi and have been interpreted as the result of macro-deformation related to the impact event (Reimold et al., 1998; Boamah and Koeberl, 2003).

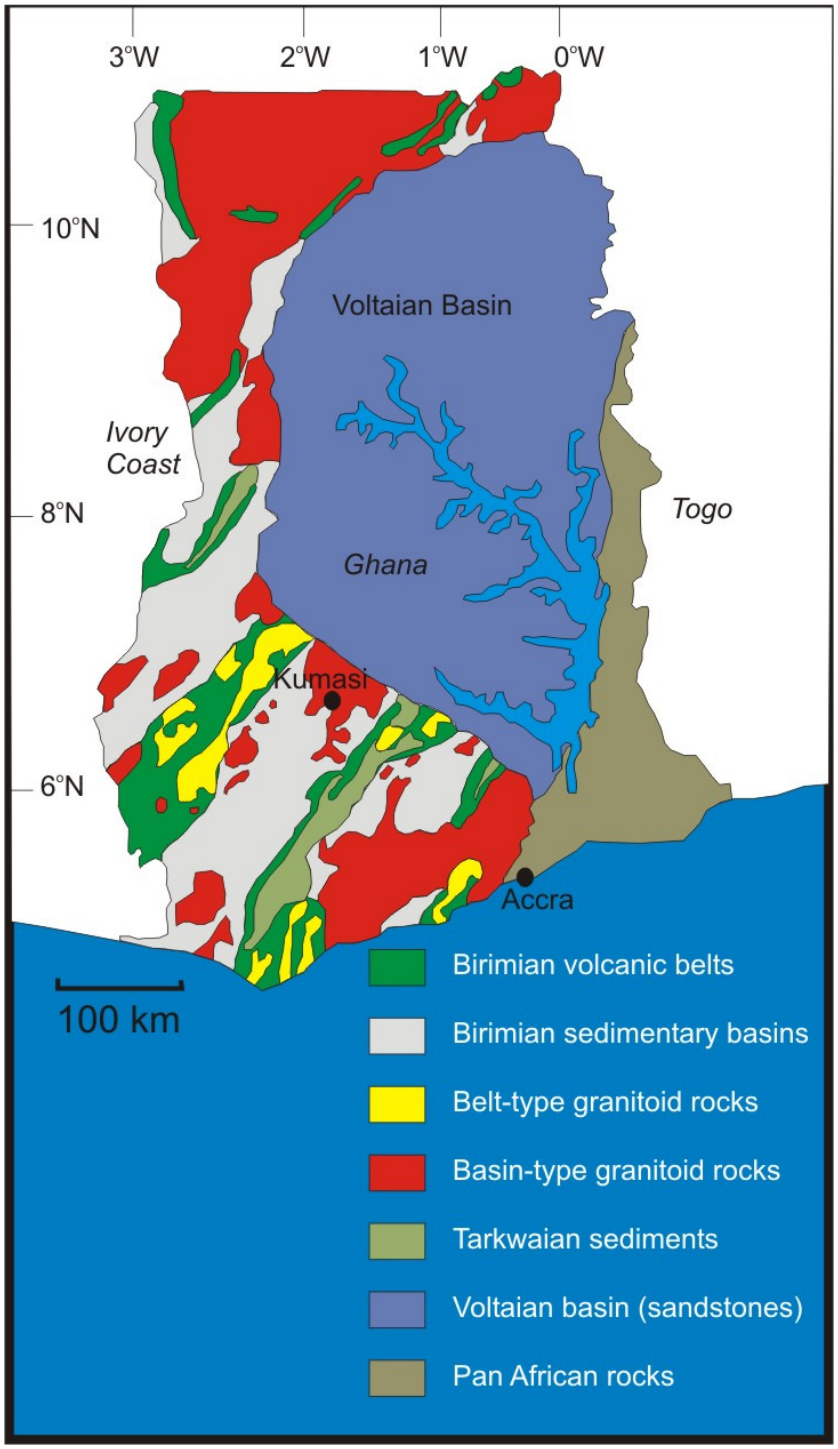

Fig. 1.10: Simplified geological map of Ghana, showing the distribution of the Birimian Supergroup (modified after Kesse, 1985). Belt-type granitoids form late-orogenic unfoliated intrusions in the Birimian volcanic belts; basin-type granitoids form synorogenic foliated batholiths in the central portions of the Birimian basins (Leube et al., 1990).

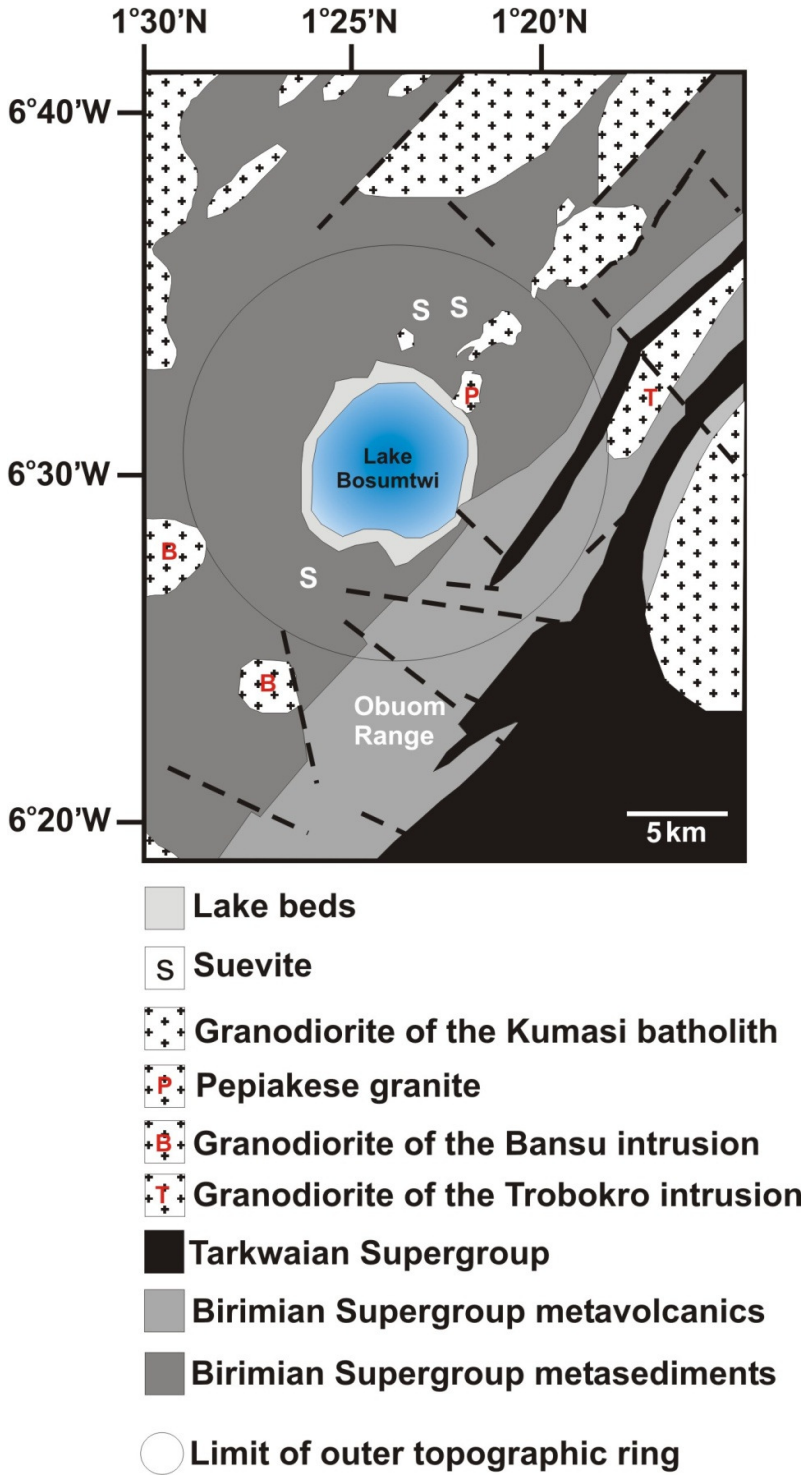

Fig. 1.11: Simplified regional geological map, showing Lake Bosumtwi and surroundings (modified after Jones et al., 1981; Koeberl and Reimold, 2005).

Apart from the Obuom mountain range to the southeast of the crater (Fig. 1.11), and locations along some stream channels in the environs of the crater, exposure is generally poor in the area around Lake Bosumtwi.

Country rock in the immediate environs of the crater is dominated by metagreywacke, phyllite and some meta-sandstone, but shale (including graphitic shale) and mica-schist were also observed by Woodfield (1966), Moon and Mason (1967) and Reimold et al. (1998); also see Appendix 1. The crater rim rocks are locally intensely folded and/or faulted. A number of granitoid intrusions (mainly biotite- and amphibole-bearing granites, but also including albitite and diorite; Appendix 1; Fig. 1.11) were mapped by Junner (1937) and Moon and Mason (1967); see also Reimold et al. (1998).

Reimold et al. (1998) conducted a structural analysis of the northwestern crater rim in order to compare it to other crater rim structures. They divided the rim into four zones, with zone 1 furthest away from the lake, and zone 4 closest to the lake (Fig. 1.12). Zone 1 was found to be dominated by polymict lithic breccia, intercalated with secondary weathering products. Zone 2 was characterised by a variety of thrust planes, folds, and fractures, together with overturned target rocks. Zone 3 was thought to represent a megabreccia zone, in which decreasing block size was observed toward the rim crest. Finally, zone 4 had evidence of variably oriented thrust faults. Reimold et al. (1998) noted that this zonation, also seen at the Tswaing crater (Brandt and Reimold, 1995), could be characteristic of bowl-shaped impact structures.

Reimold et al. (1998) reported the occurrence of a number of biotite-granite dykes intruding the metasediments along the crater rim, and Koeberl et al. (1998) drew attention to the existence of a granophyric-textured lithology of then uncertain origin (cf. Chapter 3). The overall granite component in the vicinity of the crater and, by

implication in the impact target, was estimated at less than 2 % (Reimold et al., 1998).

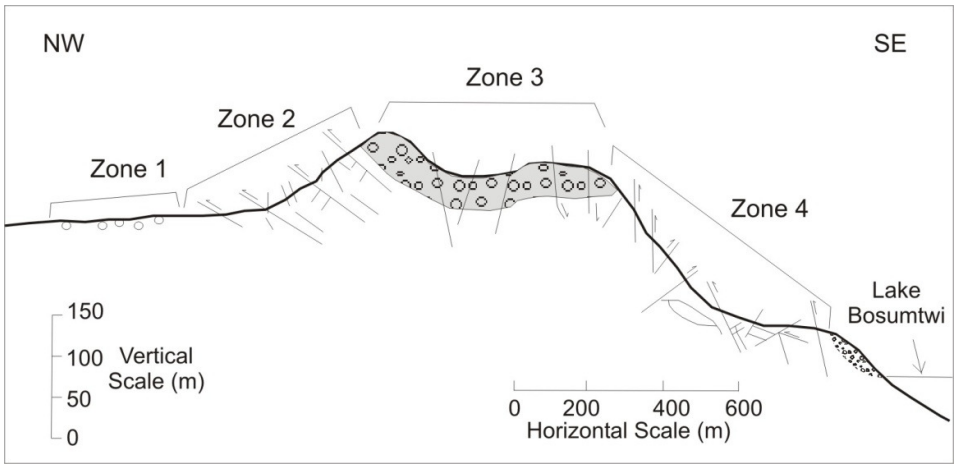

Fig. 1.12: Cross-section showing the Reimold et al. (1998) traverse and zonation of the north-western part of the crater rim of the Bosumtwi impact structure. Each zone is characterised by different structural components (modified after Reimold et al., 1998).

The Pepiakese granite forms an intrusive body on the northeastern side of Lake Bosumtwi (see Fig. 1.11). It differs from the other granite intrusions in the region in being variably altered, and in having a dioritic component that contains a substantial proportion of mafic minerals, including amphibole (Koeberl et al., 1998; Boamah and Koeberl, 2003).

To the southeast of the Bosumtwi crater, younger clastic sedimentary rocks of the ~2.1 – 2.13 Ga Tarkwaian Supergroup (Hirdes and Nunoo, 1994; Fig. 1.10, 1.11) are present. These strata are regarded as detritus of the Birimian rocks and are also metamorphosed to greenschist-facies grade (Leube et al., 1990; Koeberl and Reimold, 2005).

The youngest deposits found at the crater include breccias associated with the Bosumtwi impact and the Bosumtwi lake beds (cf. Junner, 1937; Moon and Mason, 1967; Jones et al., 1981; Jones,

1985b; Koeberl et al., 1997c; Reimold et al., 1998). Monomict and polymict lithic impact breccias, as well as suevite have been described by Koeberl and Reimold (2005 and references therein). Suevite deposits have been mapped and studied around the crater by Koeberl et al. (1998), Boamah and Koeberl (2003, 2006) and Koeberl and Reimold (2005). These latter authors also provide further details regarding the geology of the Bosumtwi structure and a detailed geological map (Appendix 1) based on earlier mapping reports.

Boamah and Koeberl (2003, 2006) reported results from a 1999 shallow drilling program to the north of the crater rim that identified a number of different types of impactite, including glass-rich suevite (which occurs as discrete blocks) and polymict lithic breccia (which commonly grades into unbrecciated rock and may be mixed with secondary mass wasting products). In agreement with Koeberl et al. (1998), they proposed that greywacke-phyllite lithologies and granite dykes, together with a minor amount of the Pepiakese granite phase found to the northeast of Lake Bosumtwi (Fig. 1.11, Appendix 1), were the dominant contributors to the suevite. Boamah and Koeberl (2006) also reported petrographic information for the suevite from the short drill cores and from outcrops. Macroscopically, they found that suevite comprised up to 70 vol% matrix (all material smaller than 1 cm) and up to 20 vol% impact melt fragments, together with ~8 vol% greywacke, ~5 vol% metapelite, up to 3 vol% granite and less than 1 vol% mineral clasts (quartz and feldspar). Upon microscopic examination, the matrix, defined as all material < 0.05 mm in size, was composed of quartz, feldspar, biotite and rock fragments, together with rare impact melt particles. Common shock metamorphic features of clasts included planar fractures, planar deformation features (PDFs, up to 5 sets per grain) in quartz (none noted in feldspar), diaplectic quartz and feldspar glasses, kink-banded biotite and ballen quartz (Boamah and Koeberl, 2006). The

main shock features are consistent with shock pressures between 20 and >60 GPa (Boamah and Koeberl, 2006).

1.6 Geochemical Studies

Target rock compositions (major and trace element compositions) have been estimated by Koeberl et al. (1998). They identified four target rock groups: phyllite-greywacke, shale, granite dykes (unaltered) and the Pepiakese granite. They found that the chemical distinction between phyllites and greywackes was not well defined and, thus, included them as one group. The phyllite and greywacke samples studied by Koeberl et al. (1998) have variable chemical compositions, but are distinct from the shales in that they have higher SiO_2 and lower Al_2O_3, Fe_2O_3 and MgO contents.

Koeberl et al. (1998) analyzed a number of the rocks from around the Bosumtwi crater structure for their O, Sr and Nd isotopic compositions. The measured Rb-Sr isotopic ratios of selected target rocks were similar to those previously obtained for Birimian granitoid intrusions (Taylor et al., 1992). Taylor et al. (1992) used the Rb-Sr, Sm-Nd and Pb-Pb isotopic systems to constrain the rock-forming events, and found that the results from the various isotope systems were generally in agreement with each other and that the Birimian magmatic crust-forming event took place over the time interval from ~2.3 to 2.0 Ga by differentiation from slightly depleted crust. The isotopic data of Shaw and Wasserburg (1982) and Koeberl et al. (1998) supported the interpretation that the Ivory Coast tektites are related to the rocks exposed in the vicinity of the Bosumtwi impact structure (Koeberl et al., 1998).

Boamah and Koeberl (2002) measured major and trace element concentrations of a number of soil samples from around the Bosumtwi structure. They found that the soil samples showed considerable variation relative to the parent rocks from which they had been derived but that values remained within the range obtained

for the source rocks. Boamah and Koeberl (2002) concluded that the variable geochemical signature reflected the extensive chemical weathering that had taken place in the tropical environment.

Karikari et al. (2007) recently re-investigated the chemical compositions and petrographic characteristics of the Bosumtwi target rocks; they found that these rocks were characterised by two phases of alteration (see also Chapter 3). The first, a pre-impact hydrothermally-produced alteration, was identified as concentrated along shear zones. This resulted in the growth of secondary minerals such as chlorite, sericite, sulphides and quartz, as well as the sericitization of plagioclase and chloritization of biotite. The second phase was a post-impact argillic alteration that is mainly associated with the suevites, and specifically targets the melt particles within the suevites (alteration of glass clasts to phyllosilicates). Karikari et al. (2007) also reported the Bosumtwi granites to have tonalitic to quartz-dioritic compositions, and that they, together with the metasedimentary rocks, are of volcanic-arc tectonic provenance.

Ferrière et al. (2007a, b) has performed both geochemical and petrographic analysis of core LB-08A, obtained from the central uplift. Their results will be discussed in detail in Chapter 7.

1.7 Geophysical Studies

The Bosumtwi region has been characterised extensively in terms of its geophysical characteristics, including elevation (Fig. 1.13), gravity (Fig. 1.14), magnetic (Fig. 1.15) and seismic surveys (Fig. 1.16). The first magnetic studies were reported by Jones et al. (1981) who interpreted a central negative anomaly of ~40 nT as caused by a lens of low-density crater-fill breccia below lake sediments. Jones et al. (1981) also collected gravity data, but these were limited to the land area around the Bosumtwi crater, and thus were interpreted to represent regional trends only.

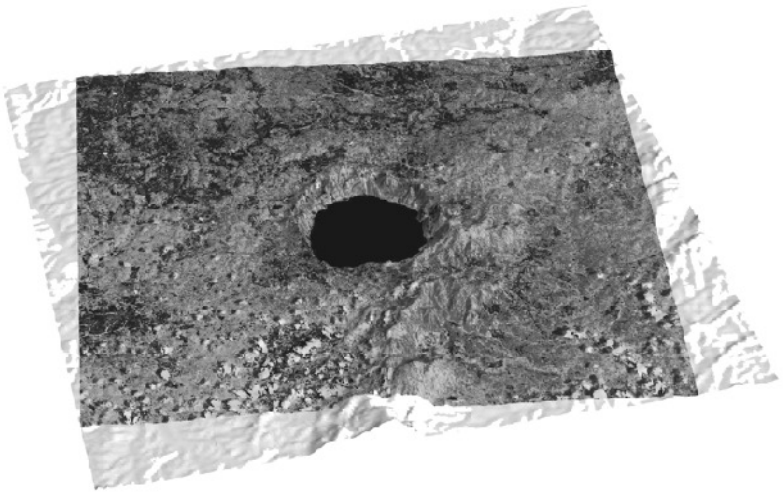

Fig. 1.13: Elevation of the Bosumtwi region, showing the crater rim and the elevation of the Obuom Range (front right of image, trending NE-SW). Image is a combination of an Aster satellite image (band combination 7, 3 and 1, contrast enhanced) overlaid with a projection of grey-shaded Shuttle Radar Topography Mission data. Image from Koeberl et al. (2007a).

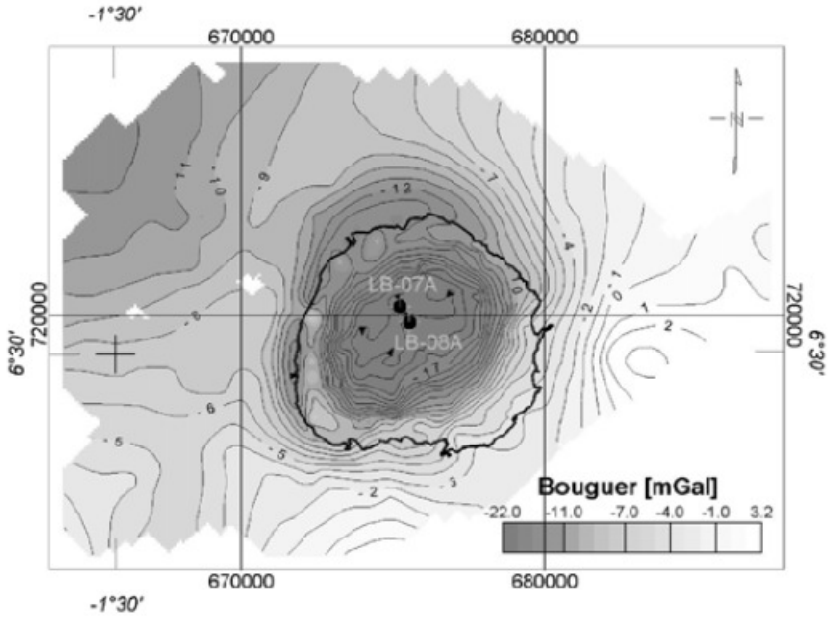

Fig. 1.14: Lake Bosumtwi Bouguer gravity anomaly. Data have been corrected for water depth and integration with land data. Contour interval is 1 mGal, with black triangles indicating the more negative anomalies. Coordinate system is UTM Zone 30N, WGS84. Image from Ugalde et al. (2007a).

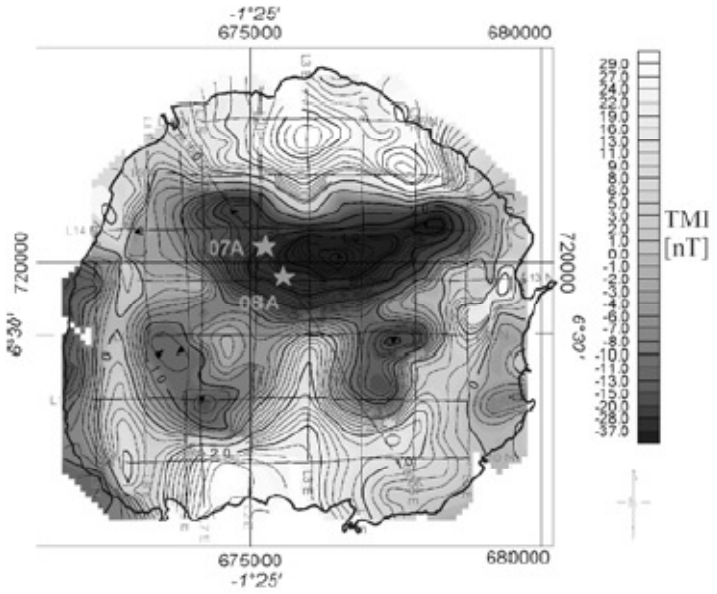

Fig. 1.15: Total magnetic field over Lake Bosumtwi. Data collection lines and lake outline are indicated in black, with the location of the ICDP cores indicated as stars. Contour interval is 2 nT. Data from Danuor (2004), image from Ugalde et al. (2007b).

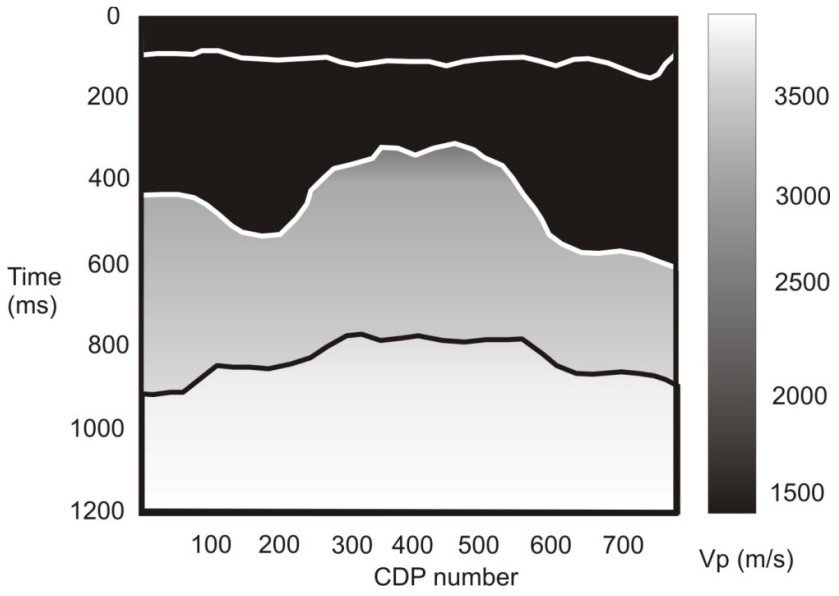

Fig. 1.16: Lake Bosumtwi velocity model derived from seismic reflection data (modified after Karp et al., 2002). The three boundaries indicate approximate positions of the lake floor, base of sediments and base of the impactite sequence, from top to bottom.

In 1997, a high-resolution airborne geophysical survey was conducted by the Geological Surveys of Ghana and Finland together with the University of Vienna (Ojamo et al., 1997; Pesonen et al., 1998, 1999). This produced total magnetic field, electromagnetic and gamma radiation patterns over the Bosumtwi structure. Plado et al. (2000) utilized data from this survey to produce a magnetic model for the Bosumtwi structure. The data revealed that a circumferential magnetic halo occurs outside the crater, at a radial distance of ~6 km from the centre.

Additionally, a central negative magnetic anomaly with two smaller positive anomalies was located over the central-north part of the lake (Fig. 1.15). Weaker negative anomalies were found in the eastern and western parts of the lake (Fig. 1.15). Plado et al. (2000) interpreted all the anomalies as encircling a central uplift, and suggested that the central anomaly was caused by one or several strongly magnetic impact melt bodies in the structure. It was suggested that the strong airborne radiometric anomaly around and to the north of the central crater rim (Plado et al., 2000) was caused by a local enrichment of potassium. This was geochemically investigated by Boamah and Koeberl (2002) who suggested that the potassium anomaly was either caused by potassium mobilization owing to the impact event or the local presence of high-potassium bearing target rocks (see section 1.6).

Plado et al. (2000) also measured the petrophysical properties of impactites and country rocks, and demonstrated that clear differences exist between them. The suevites had comparatively higher magnetization, lower densities and higher porosities than the pre-impact lithologies. Remanent magnetization dominated over induced magnetization in the suevites. Plado et al. (2000) suggested that the magnetic body below the lake was normally magnetized and, from these results, that the normally magnetized remanence was acquired during the Jaramillo normal polarity epoch (starting at ca.

1.07 Ma; see Channell et al., 2002). In their studies of the Ivory Coast tektites, Glass et al. (1991) noted that the tektites had been deposited following the onset of this epoch – consistent with the findings of Plado et al. (2000). A reverse polarity remanence component, which was superimposed onto the normal component, was most likely caused by acquisition of secondary remanence (Plado et al., 2000). Danuor and Menyeh (2007) and Ugalde et al. (2007b) also reported more magnetic results from the Bosumtwi crater, which agreed with those collected by Plado et al. (2000). The main features included a negative anomaly (minimum of 55 nT) to the north and a smaller positive anomaly to the south. Danuor and Menyeh (2007) and Ugalde et al. (2007b) interpreted the magnetic signatures as produced by a causative body located north of the central uplift, although the ICDP drilling did not intersect an appreciable amount of melt. Ugalde et al. (2007b) interpreted this as bodies that correspond to a lithology south of the Kumasi batholith, rather than an impactite, as suggested by Danuor and Menyeh (2007). This interpretation is also favoured by Morris et al. (2007a) who suggested that the magnetic anomalies were mainly sourced in undetected or covered bedrock intrusions.

Lower gravity signatures (Fig. 1.14) over the crater (a negative Bouguer anomaly of about -18 mgal) relative to the surrounding region were suggested to reflect the presence of lower-density breccia within the crater (Danuor, 2004). Within this gravity low, a small relative maximum of 2 mgal was evident over the area of the central uplift. After utilizing seismic results as further constraints, it was determined that the central uplift occurred at a depth of 250 m below the lake surface. Danuor and Menyeh (2007) suggested that the negative gravity anomaly reflects a combination of the fractured and brecciated nature of the rocks in the rim area and below the crater floor, the impact breccias within the crater and the sedimentary and water infilling of the lake.

Karp et al. (2002) and Scholz et al. (2002) published the results of several seismic studies undertaken to characterise the interior of the crater in preparation for the 2004 ICDP Drilling Program (Fig. 1.16; section 1.8). These seismic reflection and refraction studies helped to define the position of a small central uplift structure (Fig. 1.16). The central uplift structure has a maximum diameter of 1.9 km and a maximum height of 130 m above the floor of an annular moat. It has experienced much faulting activity, which partially took place during or after lacustrine deposition in the structure, as seen by lake bed disturbance. Karp et al. (2002) produced a velocity model (Fig. 1.16) from seismic reflection and refraction data consisting of 3 layers: Layers 1 and 2 represent the lake water and the post-impact sediments, and a third layer is referred to as the "bedrock" layer (in order to contrast to the 2 layers above). Interestingly, the apparent crater depth (ca. 550 m) was shown to be deeper than classical scaling laws (Cintala and Grieve, 1994) had predicted. Also notable from the velocity model was the increase in seismic velocity with depth (Karp et al., 2002; Fig. 1.16). The velocity gradient was substantially larger under the central uplift than beneath the annular moat, and has been interpreted as the result of material difference – the central uplift was formed by deformed and rebounded target rock, whereas the annular moat was thought to be filled by "fallback" breccias (Karp et al., 2002; Scholz et al., 2007).

The digital elevation model (Fig. 1.13) has been further refined using multichannel seismic reflection data as well as regional topographic data from outside the lake (Scholz et al., 2007). It was found that the post-impact sediments are 180 – 300 m thick and have seismic velocities of 1.5 – 1.65 km/s (Scholz et al., 2007). The central uplift has an overall irregular surface with a small graben structure. A number of normal faults which extend from the central uplift into the post-impact sediments were noted, and are interpreted as a consequence of continuing compaction of the central uplift, which consists of high-porosity materials.

L'Heureux and Milkereit (2007) obtained sonic velocity and density logs from cores LB-07A and LB-08A in order to estimate the degree of heterogeneity and fracturing in the target rocks. They determined that the Bosumtwi impactites fall into the so-called "quasi-homogeneous scattering regime" – i.e., seismic energy is able to propagate through the medium with minimum disruption. They were not able to estimate the total extent of the damage beneath the structure (due to the core depth constraints), but were able to conclude that the features observed here are characteristic of fractured impactites. Morris et al. (2007a) also examined the fracture-density of the two cores, and found that the depth extent of fracture-related density reduction is much greater in the central uplift (i.e., in core LB-08A) than in the crater moat (LB-07A).

Artemieva et al. (2004) used numerical modeling of an oblique impact of 30-45° to predict the amount of melt and the nature of the impacting projectile. The drilling project has since revealed that the amount of melt predicted by Artemieva et al. (2004) was incorrect (as far less melt was intersected than predicted). Artemieva (2007) attempted to explain this discrepancy utilizing factors such as impact velocity and angle and target composition. Artemieva (2007) concluded that the impactites were turbulently dispersed due to the vaporisation of pore water, which was not included in the model of Artemieva et al. (2004). See also chapter 7, for discussion against the new drilling results and findings of this study.

1.8 International Continental Scientific Drilling of Lake Bosumtwi

The Bosumtwi structure was the subject of an interdisciplinary drilling effort by the ICDP in late 2004, which led to the recovery of a series of 14 cores through the sedimentary crater fill, as well as two cores (LB-07A and LB-08A; Fig.1.17) through the impact breccia fill and into underlying crater basement (e.g., Koeberl et al., 2005, 2006a, 2007a).

The primary reasons for drilling the Bosumtwi crater were: 1) to obtain a complete, 1 million-year palaeoenvironmental record, and 2) to study the subsurface structure and crater fill (see Koeberl et al., 2007a). In addition, the cores were also used to provide new constraints on the previously obtained geophysical data across the crater and its environs (see Koeberl et al., 2005, and papers from Meteoritics and Planetary Science 42, issues 4 and 5).

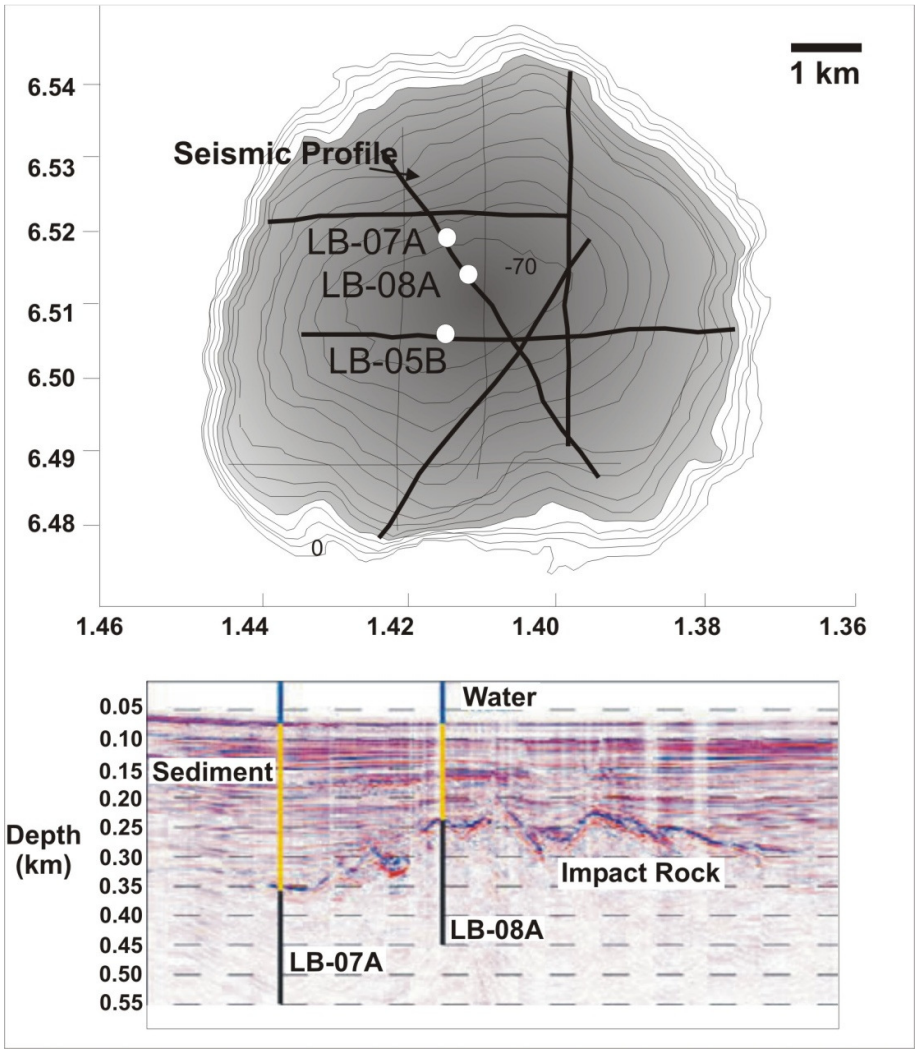

Fig. 1.17: Bathymetric map (A) and seismic profile (B) across ICDP boreholes LB-07A and LB-08A. The position of LB-05B is also shown. Thick black lines represent seismic profiles (reflection and refraction data), and the thin black lines are bathymetric contour lines. Contour interval is 5 m (modified after Scholz et al., 2002; Karp et al., 2002; Koeberl et al., 2006a).

The Bosumtwi crater was also selected as a drilling target because it is one of the few craters on Earth that has both proximal and distal ejecta, and because the crater itself is well-preserved. Lake Bosumtwi is one of only two known young craters of this size (the other being El'gygytgyn in Siberia; see Koeberl and Milkereit, 2007) and may have a crucial diameter near the changeover from a complex crater with a central peak to a crater that has a central peak-ring system (as seen, for instance, at the Ries Crater, Germany, which is twice the size of the Bosumtwi crater). A synthesis between geophysical, geochemical and petrographic studies was made possible by the drilling.

An initial drilling proposal was submitted to the ICDP in January 2002, and was accepted. Pre-drilling site preparation took place thereafter, which included construction of an access road and pier, as well as obtaining permission from government and tribal authorities. This was completed by July 2004 (Koeberl and Milkereit, 2007). Additionally, a seismic survey (see section 1.7) was undertaken in order to choose the optimum positions for the boreholes (Karp et al., 2002; Scholz et al., 2002). The hard rock drilling phase, in addition to borehole logging and geophysical studies, was completed in October, 2004. The hard rock samples (122 core boxes) were stored at the Geoforschungszentrum (GFZ) in Potsdam, Germany, where they were also scanned and documented. A first sampling party took place in January 2005. First results of the various studies were presented at the Lunar and Planetary Science conference in a special session dedicated to the drilling project in March 2006, and the participants in this consortium study published the first results in a special volume of Meteoritics and Planetary Science in 2007 (see Meteoritics and Planetary Science 42, issues 4 and 5).

1.8.1 The Palaeoclimatic Record

The Bosumtwi crater has been examined for the record it contains of palaeoclimatic change since its formation 1.07 Ma ago. The crater, due to its excellent preservation, young age and location, is well suited to provide a record of tropical climate change for West Africa. A number of studies have recorded palaeoclimatic changes using short sediment cores (lake level, lake chemistry, climate and vegetation history) for the previous 27, 500 years (e.g., Talbot and Delibrias, 1977, 1980; Hall et al., 1978; Talbot et al., 1984; Talbot and Kelts, 1986). These results not only served to characterise the climatic history of the crater, but also provided detailed understanding of tropical climate changes and vegetation stability (Talbot et al., 1984) and indicated that Lake Bosumtwi would be an ideal environment for conducting palaeoenvironmental studies.

The lake is hydrologically-closed (owing to its high crater rim) and, thus, the lake sediments can be used as an indicator of the precipitation and evaporation balance (see Peck et al., 2004). Groundwater sources are thought to be negligible (see Koeberl et al., 2007a). The steep crater wall and the depth of the lake limit wind-related wave mixing of the water column, and the deep water of the lake is anoxic, limiting bioturbation, and enhancing preservation of laminated sediment varves. Thus, the lake provides an ideal area for lake sediment studies (see Brooks et al., 2005).

The Bosumtwi structure also lies in the path of the seasonal migration of the Intertropical Convergence Zone (ITCZ). The ITCZ forms the atmospheric boundary between northeasterly continental trade winds and southeasterly onshore trade winds (Shanahan et al., 2006; Fig. 1.18), which is important for hurricane formation (those hurricanes that reach Central and North America). The lake sediments provide a million year record of change of the North African monsoon strength and Harmattan (dry, aerosol-rich

northeasterly continental trade winds from the Sahara and Sahel) strength.

Other studies of the lake sediments estimated the level of lake overflow (Turner et al., 1996a, 1996b), which is about 100 m above the present lake level, and is the highest position where lake sediments occur along the inner crater rim. It is apparent that the lake has fluctuated significantly in the last 20, 000 years (Turner et al., 1996a, 1996b; Peck et al., 2004; Brooks et al., 2005). Peck et al. (2004) assessed the magnetic parameters of minerals from an 11 m sediment core (which spanned 26 000 years of deposition) and found that sudden shifts in magnetic parameters represented arid conditions when the effect of the summer monsoon was weakened (determined by variable concentrations of the magnetic mineral greigite).

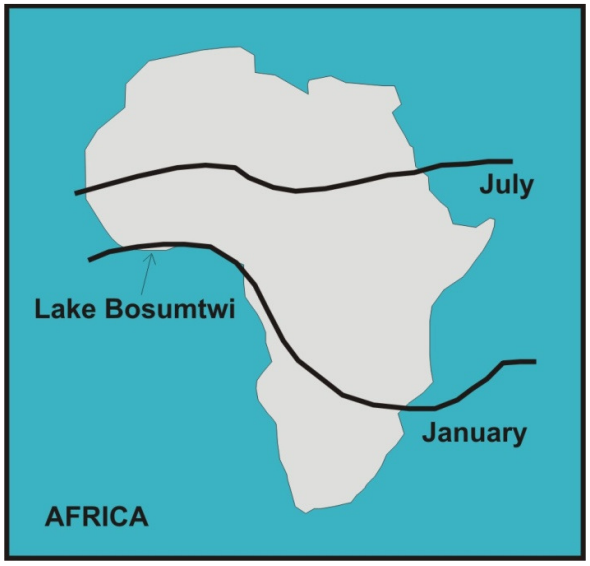

Fig. 1.18: Map of Africa showing the position of Lake Bosumtwi relative to the maximum seasonal variation of the position of the intertropical convergence zone (ITCZ; modified after Shanahan et al., 2006).

Brooks et al. (2005) utilized a combined seismic reflection and sedimentological study and found four seismic sequence boundaries as well as an exposure surface in a number of sediment cores

(between 3 and 11 m in length). They interpreted these as erosional surfaces formed during lowstands of the lake, which are potentially a response to increased aridity in the equatorial tropics.

Shanahan et al. (2006) combined radiocarbon dating and geomorphological studies of palaeo-shorelines. They found a number of a lake level high- and lowstands, and the data indicate that these correspond to the timing of glacial events in Africa and the northern hemisphere. Thus, these periods were controlled by the northern hemisphere palaeoclimatic conditions during northern hemisphere glaciation events.

Sediment cores (totaling 1833 m) were recovered from 5 different drill sites (including LB-07A; Fig. 1.17) along the primary seismic profile which covers the complete 1 million year old lacustrine sediment fill.

1.8.2 Impactite Cores LB-07A and LB-08A

The impactite cores were chosen in accordance with field and seismic data (Fig. 1.17) that define the Bosumtwi impact structure (Karp et al., 2002; Scholz et al., 2002). Both drill sites were constrained by good-quality seismic profiles (Fig. 1.17). Core LB-07A is from the crater moat surrounding the central uplift and was drilled to a depth of 545.08 m below lake level, whereas LB-08A (e.g., Ferrière et al. 2007a) was drilled to a depth of 451.33 m below lake level on the flank of the central uplift (Fig. 1.17; Koeberl et al., 2007a). Additionally, samples from another core, LB-05B, have also been examined, as they contain material from the cross-over between the base of the sediments and top of the impactite sequence. A thin, impact-glass-bearing, “accretionary lapilli”-rich fallout layer has been identified in this core (Koeberl et al., 2006b; Koeberl et al., 2007b).

Diamond coring tools were utilized from the top of the impactite sequence. Unfortunately, in both holes the topmost impactite (ca. 3 m) could not be recovered. Drilling progressed through the impact breccia layer into the fractured bedrock. Acquisition of zero-offset and multi-offset vertical seismic profile data in the holes established a link with previously obtained seismic data (Schmitt et al., 2007).

1.9 This Study

The hard rock core LB-07A (drilled through the deepest part of the crater fill) is the primary material used for this study. The study involved producing the full lithostratigraphic profile, and a full assessment of the core in terms of petrography and geochemistry. In addition, limited field work in Ghana took place in 2007, in order to collect samples from exposures of out-of-crater suevites located to the north and south of the crater rim to facilitate a comparison between within-crater and out-of-crater suevites.

Objectives of this study included the following:

- The production of the LB-07A lithostratigraphic profile.
- Petrographic characterisation and comparison of the different impactites in the LB-07A core.
- Geochemical characterisation and comparison of the different impactites in the LB-07A core.
- Petrographic and geochemical characterisation of post-impact modification (hydrothermal alteration) of the impactites.
- Determining the target rock lithologies (petrography, geochemistry) and mixing relationships for the impactites of the LB-07A core.
- Geochemical study to investigate the presence of meteoritic projectile in the impactites of the LB-07A core.
- Petrographic and geochemical comparison of the within-crater suevites and the out-of-crater suevites.
- Comparison between the lithostratigraphic profile and geochemical variation between the LB-07A and LB-08A cores.
- Production (if possible) of a sequence of events that took place

during the formation and modification of the impactites in the Bosumtwi event.

Chapter 2 details the methodology and analytical conditions used in this study. Chapter 3 presents the lithostratographic profile, as well as detailed petrographic characteristics of the core. Chapter 4 presents the detailed geochemical analysis of samples from core LB-07A, which includes major (by X-ray Fluorescence) and trace element (by Instrumental Neutron Activation Analysis) data and a study to assess whether a meteoritic component is present by platinum group element (PGE) analysis and osmium isotope analysis. Chapter 5 presents the shock metamorphic findings for the LB-07A core, based on detailed microscopic observations of quartz and feldspar grains, universal stage measurements of quartz grains from all levels of the core and a detailed description and analysis of the various suevites intersected in core LB-07A (in particular the melt particle characteristics). Chapter 6 presents macroscopic, microscopic and geochemical data for the out-of-crater suevites. Finally, Chapter 7 presents the discussion and conclusions of the findings of this project (see the objectives above), including a comparison of the various impactite types exposed at the Bosumtwi crater, and those at the Ries crater, Germany.

Three peer-reviewed papers (Appendix 7) have been published from this PhD project in Meteoritics and Planetary Science:

Coney, L., Gibson, R.L., Reimold, W.U., Koeberl, C. (2007). Lithostratigaphic and Petrographic Analysis of ICDP Drill Core LB-07A, Bosumtwi impact structure, Ghana. Meteoritics and Planetary Science, **42**, 569-590.

Coney, L., Reimold, W.U., Gibson, R.L., Koeberl, C. (2007). Geochemistry of impactites and basement lithologies from ICDP Borehole LB-07A, Bosumtwi Impact Structure, Ghana. Meteoritics and Planetary Science, **42**, 667-688.

McDonald, I., Peucker-Ehrenbrink, B., **Coney, L.**, Ferrière, L., Reimold, W.U., and Koeberl, C. (2007). Search for a meteoritic component in drill cores from the Bosumtwi impact structure, Ghana: Platinum-group element contents and osmium isotopic characteristics. Meteoritics and Planetary Science, **42**, 743-754.

Co-authors Roger Gibson (University of the Witwatersrand, South Africa) and Uwe Reimold (Humboldt-University in Berlin, Germany) were the supervisors for this PhD project. Christian Koeberl is a collaborator at the University of Vienna, Austria, and facilitated geochemical analyses in Vienna. Iain McDonald is a collaborator at Cardiff University, and supervised the Platinum Group element analysis for the third paper. In order to learn techniques and acquire these data, I spent time at both the University of Vienna and Cardiff University performing these analyses, and time was also spent at the Humboldt-University in Berlin performing scanning electron microscopy and electron microprobe analysis. Bernhard Peucker-Ehrenbrink analysed the osmium isotopic content of a number of samples at the Woods Hole Institute, U.S.A. Ludovic Ferrière has examined core LB-08A for similar features to those investigated by this study in core LB-07A. He also obtained Os isotopic results for core LB-08A, which are compared to those of the LB-07A core in the third paper.

Chapter Two: Methodology

2.1 Sampling Procedure

Detailed logging of the LB-07A core took place during the sampling party at the Geoforschungszentrum (GFZ) in Potsdam, Germany, in January 2005, and then again during a second visit in March 2006. These results have been used in combination with petrographic analysis of representative samples to compile the lithostratigraphy of the LB-07A core presented here. Logging involved identification of the various lithostratigraphic types as well as noting any macroscopic changes throughout the core. Eighty-five quarter-core samples were obtained, photographed and described before the samples were prepared for thin sectioning and geochemical analysis. Samples of suevites were collected from both south (3 samples) and north of the crater rim (13 samples) in February 2007. A number of samples from the suevites from south of the crater had been previously collected by Uwe Reimold (WUR) and Christian Koeberl (CK), and were made available for this project. All samples collected are presented in Appendix 2. Guidelines for identifying the main clast phases for the suevites are presented in Appendix 3a, while hand specimen and petrographic summary descriptions and photographs are presented in Appendix 3b. All mineral abbreviations are after Kretz (1983).

2.2 Thin Section Preparation

Polished thin sections from core LB-07A samples were prepared at the Council for Geoscience (Pretoria, South Africa). Eighty-five samples, primarily of the impact breccias, were selected for preparation of 120 polished thin sections that were examined in both transmitted and reflected light. Additionally, 20 polished thin sections were prepared from the out-of-crater suevite sample suite to augment the collection of previously collected samples of WUR and CK. Point-counting of a number of breccia thin sections took place (according to the traditional method of Chayes, 1949), whereby approximately 500 to 1000 observations are made over 4 to 5 cm^2

areas. A number of coherent thin sections of impact breccia were subjected to “shock point-counting,” whereby all observable quartz and feldspar grains were examined for shock features while rastering whole thin sections on a petrographic microscope. Thin sections from the out-of-crater suevites were prepared at the SGS Lakefield Laboratories (Johannesburg, South Africa). A number of thin sections were first embedded in epoxy owing to their friable state.

2.3 Scanning Electron Microscopy

Scanning electron microscopy (SEM) was applied to further characterise the suevites (both within-crater and out-of-crater) for their matrix modal composition (clastic or melted phases), to examine clast phases, and to ascertain the proportion of microscopic melt particles, as well as examine the texture of the melt particles identified by optical microscopy. SEM work was performed at Humboldt University in Berlin, using a JEOL-JSM 6300 instrument at 15 kV acceleration voltage coupled with a RÖNTEC X-Ray energy-dispersive analytical system for semi-quantitative chemical characteristics.

Polished thin sections were coated with carbon prior to SEM analysis. The same procedure was followed for the electron microprobe analysis (see section 2.5.5). Samples were observed in the backscattered electron mode, and spots were checked for their major element composition using energy-dispersive spectroscopy.

2.4 Universal Stage Microscopy

The Universal stage (U-stage) was used in this study to measure the crystallographic orientations of planar deformation features (PDFs). The procedure involved measuring, in a single quartz grain, both the orientation of the pole to the crystallographic plane parallel to each set of PDFs as well as the c-axis orientation (optic axis orientation) of the grain. The data were then plotted on a standard stereonet, and the relative angle between the c-axis and the pole to the PDF set

was measured. A number of repeat measurements on each PDF set were made in order to ensure precision. Langenhorst (2002) provides a full review of this method.

2.5 Geochemical Methods

In order to examine the compositions of the LB-07A impactites, their possible source rocks, the mixing of target rocks in formation of the impact breccias, a suite of 85 LB-07A within-crater impactites and 9 out-of-crater suevites were subjected to major and trace element geochemical analysis. Additionally, selected samples from the LB-07A core were assessed for the possible presence of a meteoritic projectile. All samples (LB-07A core samples of 5 to 10 cm length; quarter cores of 3 cm radius) were first crushed and milled to a powder (after pre-contamination of crushing instruments with sample powder). All samples were milled in tungsten carbide swing mills, or, where possible, in an agate mill, in order to avoid contamination from the equipment.

2.5.1 X-Ray Fluorescence Spectrometry

X-ray fluorescence (XRF) spectrometry is used to determine both major and trace element compositions of a sample. XRF spectrometry is based on the excitation of secondary X-rays within a sample by primary X-rays (e.g., Rollinson, 1995). The primary X-ray ionizes the component atoms which involves the ejection of 1 or more electrons from the atom. The atoms are then unstable, and electrons in higher orbitals will “fall” into the lower orbitals, and in doing so, release energy in the form of X-rays (the energy is equal to the energy difference between the orbitals). Thus, the radiation emitted is characteristic of the atoms present in the material.

All samples from LB-07A core and the out-of-crater suevites from Ghana were analyzed using standard XRF procedures at the University of the Witwatersrand (Johannesburg; see Reimold et al., 1994, for details on the procedures, precision, and accuracy; Table

2.1) or at the Humboldt-University (Berlin; see Schmitt et al., 2004, for details on the procedures, precision and accuracy; Table 2.2). A number of duplicate analyses were obtained for samples from core LB-07A, producing a total of 91 chemical results.

Pressed powder pellets (used for trace element analysis) were prepared by combining the powder with glue (Mowiol 40-88^{TM}) in aluminium cups. Fusion discs (used for major element analysis) were made using 1.26 g of sample with 1.5 g flux (a mixture of lithium tetraborate, lithium carbonate and lanthanum oxide) and sodium nitrate (an oxidising agent). A PW 1400 XRF machine was used at the School of Geosciences, University of the Witwatersrand, where the rhodium X-ray tube was run at 50 kV and 50 mA.

At the Humboldt-University in Berlin, powders were dried for 4 hours at 105 ^{o}C. Then 0.6 g of sample was mixed with 3.6 g of di-lithiumtetraborate and between 0.5 and 2.0 g of NH_4NO_3 and fusion discs were produced. For loss on ignition values (LOI), 1 g of material was dried for 4 hours at 1000 ^{o}C, and the weight difference pre- and post-drying was calculated. A Siemens SRS 3000 machine was used, where the rhodium X-ray tube was run between 30 and 60 kV and between 50 and 100 mA.

Standards (University of the Witwatersrand) used for major element analysis were NIM-S (syenite), AN-G (anorthosite), NIM-D (dunite), MICA-FE (biotite), NIM-N (norite) and NIM-G (granite). At the Humboldt-University in Berlin, a Geoquant programme based on the following international standards was used for calibration: CR-2CAS1, HG-BAH, MRG-1, NIM-D, NIM-G, NIM-L, NIM-N, NIM-P, NIM-S, SY-3, UN-SPS, VS-813, VS-2116, VS-2117, VS-2119, VS-2120, VS-2121, VS-2122, VS-2123, VS-2125, VS-2889, VS-5370, VS-7126, VS-7176, VS-MO7, VS-MO13, VS-MO15, X-39, X-41, X-44, X-45, X-48, X-50, Z-AN, Z-BM, Z-FK, Z-GM, Z-GNA, Z-KH, Z-SW, Z-TB and Z-TS.

Analytical precisions for major and trace element analyses at the University of the Witwatersrand XRF facility are listed in Table 2.1 and those for the Humboldt-University analyses in Table 2.2.

Table 2.1: Analytical precision for major and trace elements by XRF analysis at the University of the Witwatersrand (S. Farrell-Turner, pers. comm., 2004).

Major Element	Standard Deviation	Absolute Error (%)	Relative Error (%)	Standard Range (wt%)
SiO_2	0.36	0.06	-0.09	34.40-76.31
TiO_2	0.07	-0.04	13.7	0.00-2.69
Al_2O_3	0.07	0.07	1.3	0.30-30.04
Fe_2O_3	0.09	-0.03	-3.7	0.09-26.65
MnO	0.01	-0.009	4.8	0.01-0.35
MgO	0.18	-0.05	-6.1	0.03-43.18
CaO	0.04	0.003	0.2	0.11-16.03
Na_2O	0.13	-0.05	-6.8	0.04-6.57
K_2O	0.07	0.005	-5.6	0.01-15.40
P_2O_5	0.02	-0.02	14.2	0.01-1.40
LOI	0.26	-0.21	7.1	
Total	0.58	-0.18	0.2	
Trace Element	**Standard Deviation**	**Absolute Error (ppm)**	**Relative Error (%)**	**LLD (ppm)***
V	9	-3.8	-12.7	12
Cr	7	0.7	5.2	12
Co	2	0.7	-10.7	6
Ni	2	0.6	-9.3	6
Cu	5	1.9	-0.3	6
Zn	2	2.8	-6.2	6
As	2	4.7		15
Rb	2	1.0	-1.9	3
Sr	2	1.3	0.4	3
Y	2	-0.7	-3.7	3
Zr	3	4.3	1.2	8
Nb	1	-2.4	-8.5	3
Ba	7	12.0	3.1	20
Pb	2	3.1		10

**LLD = lower limit of detection.*

2.5.2 Instrumental Neutron Activation Analysis

Instrumental neutron activation analysis (INAA) is a method that can be used for the simultaneous determination of about 25-40 major, minor and trace elements in small geological samples (Koeberl, 1993, 1994b). This method allows selective determination of elements in the ppm or ppb range without chemical treatment, and is based on the 'activation' of powdered rock samples with neutrons. All samples from the LB-07A core were analysed for their trace element contents using INAA at the University of Vienna, Austria.

Table 2: Analytical precision for major and trace elements by XRF analysis at the Humboldt-University in Berlin (R-T. Schmitt, pers. comm., 2007).

Major Element	Analytical error (wt%)	Standard Range (wt%)
SiO_2	0.50	1.00-100
TiO_2	0.01	0.01-4.00
Al_2O_3	0.10	0.50-50.00
Fe_2O_3	0.05	0.05-25.00
MnO	0.01	0.01-0.50
MgO	0.05	0.01-50.00
CaO	0.05	0.01-50.00
Na_2O	0.05	0.01-10.00
K_2O	0.05	0.01-10.00
P_2O_5	0.01	0.01-2.50
SO_3	0.1	0.10-0.50
Trace Element	**Analytical error (ppm)**	**LLD (ppm)***
V	5	15
Cr	5	15
Co	5	15
Ni	5	15
Cu	25	30
Zn	25	30
Rb	5	15
Sr	5	15
Y	5	10
Zr	5	15
Nb	5	10
Mo	10	10
Ba	30	30
Ce	20	30
Pb	20	15
Th	5	10
U	10	10

**LLD = lower limit of detection.*

During the irradiation with neutrons, naturally occurring stable isotopes of the constituent elements are transformed into higher-mass unstable isotopes by neutron capture reactions. Prompt gamma radiation is also produced and this can be used as the analytical signal if measured during irradiation (prompt-gamma INAA); this is not to be confused with the analytical signal in standard INAA (as used here). After irradiation, the activated nuclei decay, emitting beta and gamma rays, the latter with one or more characteristic energies (in the range between 60 and 2000 keV). The amount of the radioactive nuclide is then determined by measuring the intensity of these emissions, using a gamma-ray detector. As irradiated geological samples contain radionuclides of different half-lives, the gamma spectra change with time and, thus, three counting

cycles are recorded over a period of two weeks in order to detect and quantify all the isotopes present in the sample.

A nuclear reactor is used as the source of neutrons for the irradiation of samples. Neutrons emitted during the fission of ^{235}U (the most commonly used element for nuclear reactors) are too energetic (too fast) to be used for INAA (or to sustain a chain reaction). They are therefore slowed down (or moderated, usually by water), which leads to a loss in the kinetic energy and to a different energy spectrum. This process of moderation is essential to keep the chain reaction in the reactor fuel going. There are three groups of neutrons (based on energy) produced, and INAA makes use of the so-called thermal neutrons which have an energy range of 0.001-0.5 eV. In a standard research reactor, these neutrons have the highest neutron flux, which is essential for the interaction between the reactor neutrons and the target nuclei (the probability of which is known as the neutron capture cross-section). The larger the cross-section of an isotope, the more neutron capture reactions take place, and the ease with which an isotope can be detected by neutron activation analysis is increased (Koeberl, 1994b).

The instrumentation for INAA consists of three main parts: the gamma ray detector, the electronic signal processing and amplification part and a multi-channel analyser (for storage of all measured signals). The multi-channel analyser is used together with a computer system for data evaluation.

Aliquots of powders (200 mg) were weighed into polyethylene vials. The vials were then heat-sealed, together with geological standards [AC-E, a granite standard from France (Govindaraju, 1989); ALL, the Allende Meteorite sample (Jarosewich et al., 1987); G2, a granite from the United States Geological Survey (Govindaraju, 1989), and WMG1, a PGE reference material (CANMET, 1994)]. The samples were packed into aluminium foil and then placed into a larger

irradiation vial and irradiated at the Atomic Institute of the University of Vienna in a TRIGA Mark II type reactor for ~ 8 hours at a flux of 2.10 x 10^{12} $ncm^{-2}s^{-1}$. After a cooling period of one day, the samples were transferred to the INAA laboratory at the Department of Lithospheric Research, Centre for Earth Sciences at the University of Vienna. After decontamination (washing with HCl, NaOH and distilled H_2O), the samples were counted in three cycles using HpGe (high-purity germanium) detectors. The first counting period (to detect short-lived isotopes; e.g., Na, K, Ga, As, Br, Mo, Sb, W, Au) was performed 1-3 days after irradiation, and the duration was 45 minutes per sample. The second counting period (to detect medium-lived isotopes; e.g., Cr, Fe, Rb, Sb, Zr, Ba, rare earth elements) took 2-4 hours per sample and was performed 3-7 days after irradiation. A third counting cycle (for the long-lived isotopes; e.g., Sc, Co, Ni, Zn, Se, Sr, Ir) was performed 2-3 weeks after the end of the second cycle, and involved a 12-24 hour counting period for each sample.

Data evaluation was performed after all three measurement cycles had been completed. This included calibration of the spectra and correction for errors using the computer software (adapted after CanberRA Genie 2000 Work Station™), and calculation of the concentrations of the elements using comparison with standard data, whilst correcting for peak interferences.

The precision and accuracy of this method can be very good, if procedures are followed correctly. Factors affecting precision are (1) weighing errors, (2) geometry errors during counting, (3) flux variation during irradiation, (4) poor counting statistics in the peak area determination and (5) sampling errors. On the whole, these errors should not create much of a problem, as the first 3 errors can be taken into account and corrected for by using the computer software, and sampling errors can be avoided by using standard techniques. The fourth error (which is generally affected by small sample quantities) was avoided here, as enough sample material

was available, and counting times were adjusted in order to ensure that these were correct. Some analyses were duplicated to check for precision. For most elements there was ~ 5% relative precision in the INAA data (Table 2.3), although in some cases it reached 10 or 15 relative percent.

Accuracy is affected by (1) interfering nuclear reactions involving different parent elements yielding the same product nuclide, (2) spectral interferences from overlapping peaks, (3) self-shielding in the samples due to the presence of high cross-section elements, (4) dead-time errors (the detector and electronic system processing one pulse and missing another) and (5) problems with standards. These factors can be quantified and corrected for: thus this method of analysis is very accurate. Accuracy was checked by treating standard reference materials with known compositions the same way as unknown samples.

Detection limits for INAA are difficult to estimate because there are many factors involved, including matrix composition, counting times and geometry, detector characteristics and sample sizes. Typical detection limits range from 10^{-3} to 10^{-10} g/g (i.e., sub-parts per billion) for different elements (Koeberl, 1994b). Iridium detection limits are dependent upon the nature of the sample, in that they are ca. 2 ppb for carbonate-poor samples, and ca. 0.5 ppb for carbonate-rich samples.

2.5.3 X-ray Diffraction

X-ray diffraction (XRD) was performed on 18 samples (16 bulk samples, and 2 “matrix-only” samples, in order to check if the bulk samples were representative of the matrix compositions) from the LB-07A core.

Table 2.3: Typical precisions for elements analysed in the Vienna INAA Laboratory (C. Koeberl, pers. comm., 2004). All elemental abundances in ppm, unless otherwise stated.

Element	Precision (rel. %)	Element	Precision (rel. %)
Na (wt %)	2	La	2
K (wt %)	5	Ce	3
Sc	2	Nd	5
Cr	3	Sm	2
Fe (wt %)	4	Eu	2
Co	2	Gd	5
Ni	15	Tb	2
Zn	3	Tm	5
As	10	Yb	2
Se	10	Lu	2
Br	10	Hf	2
Rb	2	Ta	2
Sr	5	W	10
Zr	10	Ir (ppb)	Dependent on detection limit
Sn	2	Au (ppb)	15
Sb	5	Th	2
Cs	2	U	10
Ba	10		

Seven suevites (from different stratigraphic positions), 3 polymict lithic breccias, 2 monomict breccias and 4 metasediments from the basement were analysed at the School of Geosciences (University of the Witwatersrand, Johannesburg), on a Philips PW 1830 machine (CuK alpha radiation, operated at 50 kV and 50 mA), in order to investigate possible alteration phases (i.e., the presence of phyllosilicate minerals). The powder grain size was approximately 50 µm.

The samples were crushed and milled to a powder (after pre-contamination of crushing instruments) using tungsten carbide swing mills. The powders were moulded into aluminium frames that were then mounted in the machine. The samples were scanned through 70 degrees (2θ). Measurements of various angles were used to determine inter-planar spacings which are characteristic of the diffracting crystal and, thus, to determine the composition of the minerals in the sample.

2.5.4 Inductively Coupled Plasma-Mass Spectrometry

2.5.4.1 Platinum group element analyses

Inductively Coupled Plasma-Mass Spectrometry (ICP-MS) was used in the current study to determine the PGE (Platinum Group Element) signatures of 10 samples in order to investigate if any meteoritic component was present within the Bosumtwi core rocks. These analyses were performed at the School of Earth, Ocean and Planetary Sciences, Cardiff University. The method relies upon the pre-analysis concentration of the PGEs followed by chemical analysis of these elements.

The first part of the procedure involved the preparation of pre-concentrate of the PGE and gold within the samples using Nickel Sulphide Fire Assay. Nickel sulphide has been found to be an effective collector of PGEs (Iain McDonald, pers. comm., 2006). The metals were concentrated into a dense collector phase (insoluble in the silicate melt) which sank to the bottom of a crucible where it was collected after the material had solidified. Initially, the furnace was heated to 1100 ^{o}C, and the crucibles were marked using a copper rod. The copper oxidised to a black copper oxide in the furnace, thus preserving the label. The samples were then combined with a sodium borate-based flux (consisting of 6 g of sodium carbonate and 12 g of borax) and other collector components (0.9 g of sulphur, 1.08 g of nickel, 5 g of silica powder). Approximately 15 g of sample were added to this standard mixture, which were then mixed within a labelled plastic bag to ensure homogeneity. The mixtures were later transferred to the marked crucibles. A blank assay was also prepared from silica powder, and a standard assay was prepared: WITS-1 reference material (see McDonald and Viljoen, 2006) was used in this case.

Samples were heated for approximately 90 minutes once the furnace had reached 1050 ^{o}C. The samples were then removed and allowed to cool overnight, then the crucibles were broken, and a golden

sulphide bead was tapped out. The mass of each assay bead was determined, and the beads were then subjected to acid digestion to remove nickel and copper. Each of the eight beads were placed into individual 400 ml beakers, covered with watch glasses, and taken to the fume cupboard. The beakers were arranged on halogen hotplates and 150 ml of AR grade concentrated HCl were added to each beaker. The beakers were covered and heated. Some of the nickel sulphide beads dissolved within 4 hours, others took up to 24 hours. Additional HCl was added to the beakers when the level fell to 100 ml or less. Once the reaction was completed, around 100 ml of cold de-ionised water was added, and the beakers were cooled.

Once a sample had cooled, 1 ml of tellurium chloride stock solution was added, followed by 3 ml of tin chloride solution. Tin reduced the tellurium to metal, and a black precipitate was formed. This step is called 'co-precipitation'. The beakers were covered with a watchglass and heated for about 45 – 60 minutes in order for the precipitate to coagulate. The solution was then cooled and filtered through 0.45 µm pore-size membrane filters on the Sartorius filtration system. The filtrate was washed with copious amounts of de-ionised water. The filter paper and filtrate were deposited into labelled teflon screw-top vials. The samples were then analysed through the ICP-MS.

2.5.4.2 Trace element analysis of the out-of-crater suevites

The out-of-crater suevites were analysed for their trace element contents by ICP-MS at the University of the Witwatersrand, Johannesburg. A Perkin Elmer DRC-e machine was used and samples were analysed against certified primary solution standards. The international reference materials AGV-2, BCR-1 and BIR-1 were used (Table 2.4). Agreement with accepted values of the standards was better than 10 %, and in many cases better than 5 %. For each sample, 50 mg of powder was used. Each sample powder was individually digested in a microwave with a 60:40 high purity $HF:HNO_3$ solution. They were digested using a MARS microwave

digester. The sample mixture was then made up to 50 ml using 5% HNO_3-solution containing 50 ppb Rh, Re, Bi and In, before an aliquot was run on the ICP-MS.

Table 2.4: Trace element compositions of standards used for the ICP-MS at the University of the Witwatersrand, Johannesburg (A. Wilson, pers. comm., 2007).

Element	AGV-2 (ppm)	BCR-1 (ppm)	BIR-1 (ppm)
Sc	13.0	32.6	44.0
V	120	407	313
Cr	17.0	16.0	382
Co	16.0	37.0	51.4
Ni	19.0	13.0	166
Cu	53.0	19.0	126
Zn	86.0	130	71.0
As	0.00	0.65	0.40
Rb	68.6	47.2	0.25
Sr	658	330	108
Y	20.0	38.0	16.0
Zr	230	190	15.5
Nb	15.0	14.0	0.60
Ba	1140	681	7.00
La	38.0	24.9	0.62
Ce	68.0	53.7	1.95
Pr	8.30	6.80	0.38
Nd	30.0	28.8	2.50
Sm	5.70	6.59	1.10
Eu	1.54	1.95	0.54
Gd	4.69	6.68	1.85
Tb	0.64	1.05	0.36
Dy	3.60	6.34	2.50
Ho	0.71	1.26	0.57
Er	1.79	3.63	1.70
Tm	0.26	0.56	0.26
Yb	1.60	3.38	1.65
Lu	0.25	0.51	0.26
Hf	5.08	4.95	0.60
Ta	0.89	0.81	0.04
W	0.00	0.44	0.007
Pb	13.0	13.6	3.0
Th	6.10	5.98	0.03
U	1.88	1.75	0.01

2.5.5 Electron Microprobe Analysis

Electron microprobe analysis (EMPA) was performed at the Museum of Natural History, Humboldt-University in Berlin to obtain quantitative major element analyses on melt particles and matrix compositions from core LB-07A and the out-of-crater suevites. A JEOL JXA 8800 machine was used for the analyses of the within-crater suevites, with

four wavelength-dispersive spectrometers, operated at 15 kV voltage and 15 nA beam current. For the out-of-crater suevite analyses, a JEOL JXA 8500F machine with five wavelength-dispersive spectrometers, operated at 15 kV voltage and 15 nA beam current. For all analyses, the beam diameter used was 10 µm. Standards used were the international standard materials basalt glass (USNM 111240) and tektite (USNM 2213). Table 2.5 shows the major element compositions of the standards used for the microprobe analysis.

Table 2.5: Major element compositions of standards used for the electron microprobe analysis at the Humboldt-University in Berlin (P. Czaja, pers. comm., 2007).

Element	Basalt Glass (wt%)	Std Error* (wt%)	Tektite (wt%)	Std Error* (wt%)
SiO_2	50.81	0.12	75.75	2.21
Al_2O_3	14.06	0.03	11.34	0.52
Fe_2O_3	2.23		0.64	
FeO	9.83	0.23	4.32	0.77
MgO	6.71	0.02	1.51	0.92
CaO	11.12	0.09	2.66	0.86
Na_2O	2.62	0.01	1.06	0.94
K_2O	0.19	0.19	1.88	0.91
TiO_2	1.85	0.04	0.50	0.96
P_2O_5	0.20		0.00	
MnO	0.22	0.01	0.11	0.96
H_2O	0.02		0.10	

**Std error = standard error = standard deviation/√number of samples; after Bajpai et al. (1974).*

After samples were carbon-coated, they were analysed using the SEM. During SEM analysis, spots that were to be analysed by EMPA were identified, and these were then marked on the sample using a water-resistant marker. Samples were then mounted and placed in the microprobe, and spots were then chosen manually, and coordinates entered into the computer.

2.5.6 Osmium Isotope Analysis

Two samples with high siderophile contents from the LB-07A core were sent for analysis to the Woods Hole Oceanographic Institute in order to further assess whether any meteoritic component was

present in the Bosumtwi rocks. Five rock standards and three procedural blanks were analysed together with the samples (Table 2.6) in order to check the precision and accuracy of the analysis.

The samples were prepared for analysis by NiS fire assay (Ravizza and Pyle, 1997; Hassler et al. 2000). A few grams of rock powder were spiked with a mixed PGE tracer enriched in ^{99}Ru, ^{105}Pd, ^{190}Os, ^{191}Ir and ^{198}Pt.

Table 2.6: Rock standard and procedural blank $^{187}Os/^{188}Os$ data, with 95% confidence limits, obtained from the Wood Hole Oceanographic Institute.

Sample name	Rock type	$^{187}Os/^{188}Os$ ± 2σ	$^{187}Os/^{188}Os$ ± 2σ	$^{187}Os/^{188}Os$ ± 2σ
		Average	95% confidence limit	Relative 95% confidence limit (%)
BHVO-1	Hawaiian Basalt	0.1314	0.0018	1.4
EN026 10D-3	MORB*, Mohns Ridge	0.160	0.013	8.4
TDB-1	Diabase, Canada	0.83	0.04	4.6
WGB-1	Wellgreen Gabbro	0.187	0.012	6.7
Procedural blanks	Borax, Ni, S	0.61	0.06	

**MORB = Mid Oceanic Ridge Basalt.*

The sample powder was then mixed with a flux mixture (sodium tetraborate, high-purity Ni powder, sublimed elemental sulphur) and placed into a glazed ceramic crucible. The mixture was fused at 1000 ^{o}C for ca. 90 minutes. After cooling, a sulphide bead was separated from the glass and dissolved in 6.2N HCl at ca. 150 ^{o}C. The solution containing insoluble PGE-rich particles was then filtered through a 0.45 µm cellulose filter and the filter paper was transferred to a Teflon vial and digested in 1 ml concentrated HNO_3. In order to oxidize the Os to OsO_4, the closed Teflon vial was heated to ca. 100 ^{o}C for about 60 minutes. After chilling the vial in water and diluting the solution five-fold with Millipore water, the Teflon lid was replaced with a two-port cap. One cap was connected to an argon supply for

plasma generation, and the other to the torch of a multicollector ICP-MS (ThermoElectron NEPTUNE). Volatile OsO_4 was carried with the argon stream into the plasma, allowing the determination of osmium. Osmium isotopic compositions were determined using 3 channeltrons in a multi-dynamic acquisition routine that corrects for variable channeltron counting efficiencies and instrumental mass fractionation. Osmium concentrations were calculated using at least 2 isotope ratios to check for consistency. Concentrations agree within a few percent of each other, and were not reported when the standard deviation exceeded 20%. Precision, accuracy and procedural blanks are listed in Table 2.6 (see also Peucker-Ehrenbrink et al., 2003).

Chapter Three: Lithostratigraphy and Petrography of the LB-07A Core

3.1 Macroscopic Observations on Core LB-07A

The LB-07A drill core lithostratigraphy produced from this study is shown in Fig. 3.1, and a summary description is provided in Table 3.1. All depths indicated are depths below lake level, which was constant during the drilling period. The drill core was recovered between 333.38 m and 545.08 m depth. Recovery of the core varied between 10 and 100%, with an average of 65%, and the highest recovery was recorded in the upper part of the borehole (to a depth of ca. 414 m). The coherence of the core deteriorates with depth, with mainly friable and strongly fractured material (some disking) recovered below a depth of ca. 455 m. Consequently, the density of sampling for this work is highest in the upper part of the core (Fig. 3.1), where preservation is best.

Figure 3.1 shows the subdivision of the LB-07A core, and the number of samples taken at various stratigraphic depths, together with information on the detailed lithological variation within the core. The core has been divided into three parts: an *upper impactite* unit (333.28 m to 415.67 m depth), a *lower impactite* unit (415.67 m to 470.55 m depth) and *basement metasediments* (470.55 m to 545.08 m depth).

The upper impactites (Fig. 3.1) comprise polymict lithic impact breccia (see Appendix 3a) alternating with up to 21.89 m of suevite (Fig. 3.2 A, B). The distinction between these two breccia types is based on detailed petrographic analysis (see below), but essentially the suevite contains melt particles whereas the polymict lithic breccias lack melt particles. The lower impactite sequence comprises monomict impact breccia formed either from metagreywacke or shale or phyllite.

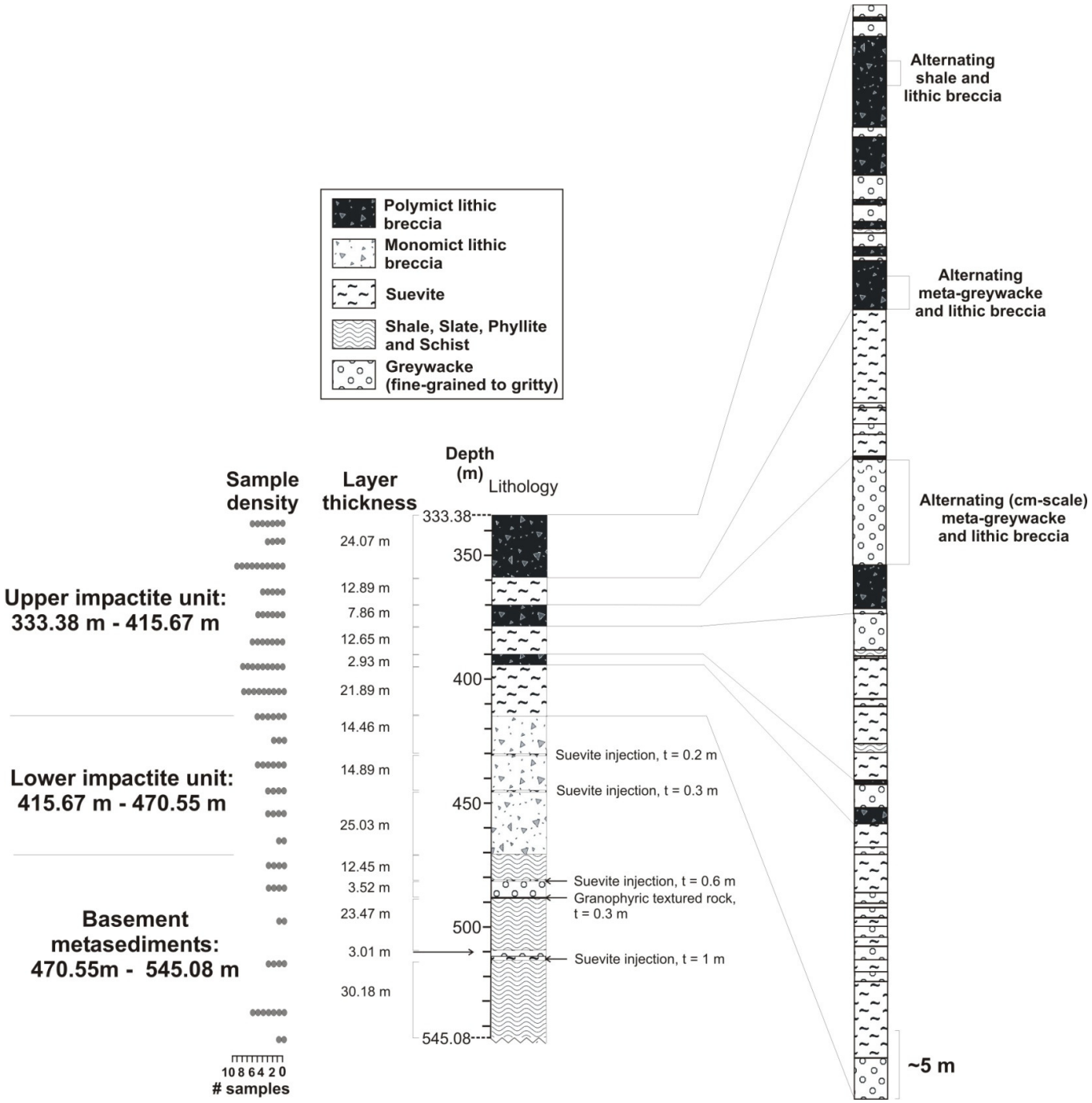

Fig. 3.1: Detailed lithostratigraphic column for the LB-07A core. Upper impactites: alternating polymict lithic breccia and suevite. Lower impactites: upper unit (415.67–430.13 m) consists of metagreywacke; middle unit (430.33–445.22 m) consists of phyllite for 4 m, underlain by metagreywacke with occasional pods of phyllite; lower unit (445.52–470.55 m) consists of metagreywacke ending in 3.6 m of mylonitic, shale-rich, thinly banded lithologies. Basement rocks are highly disaggregated and partially powdered. Also shown is the sample density over the entire core.

Metagreywacke is the dominant phase and phyllite and shale form minor components of this unit (Fig. 3.3; Appendix 3a, b).

Two thin (centimetre-scale), grey suevite intercalations were intersected in this unit at 430.13 and 445.13 m depth, respectively. The first suevite intersection is 20 cm width, and the second is 30 cm in thickness (see Table 3.1). Below the lower impactites, the borehole intersected metasediments (Fig. 3.4) from 470.55 m to 545.08 m depth. The metasediment colour varies from dark grey to white. The grey zones comprise highly altered shales with rare remnants of graphitic shale, which is thought to be the source of the dark colour. The white zones contain metagreywacke fragments. The metasediments are dominantly altered shale (followed in abundance by metagreywacke) with two thin (<1 m thick; see Table 3.1), light to dark grey suevite intercalations at 483.00–483.60 m and 513.90–514.90 m depth, respectively, and a single intercalation of a distinct, granophyric-textured lithology at 487.12–487.42 m depth (Fig. 3.1). In the absence of any indication that it could be a megablock of target rock within impact breccia, it is thought that the lowermost sequence represents crater floor (basement).

Pre-impact features include folding (soft-sediment), veining (Fig. 3.2 B) and lamination in clasts. There is some deformation (folding) of suevites which is clearly post-impact (see Fig. 3.2 C, D), which is most likely caused by post-impact slumping. Only a single, 1 cm diameter, macroscopic melt particle was observed at 430.13 m depth. It has been debated in our group that the entire upper impactite sequence should be considered suevite and that the lack of melt fragments in samples from specific depths could be the result of accidental sampling bias.

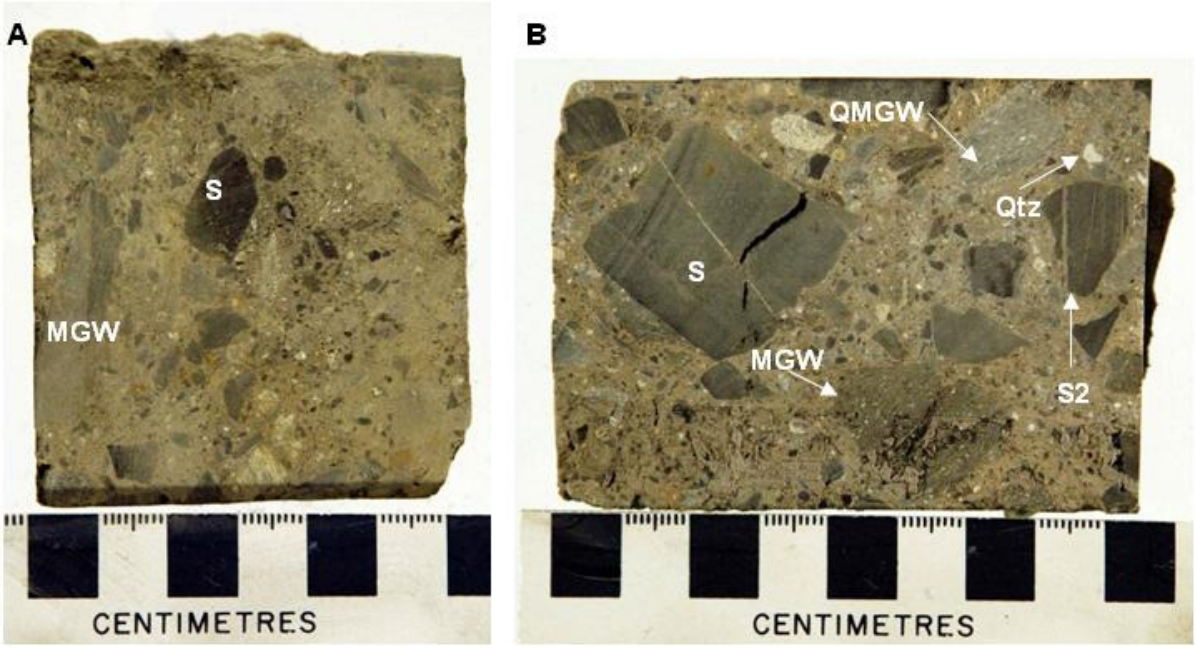

Fig. 3.2: Hand specimen photographs. A) Sample KR7-51, upper impactite unit, sample depth = 383.14 m; matrix-supported suevite with sub-cm- to cm-sized lithic fragments: sub-rounded carbon-rich shale (S), metagreywacke (MGW); melt particles are microscopic. B) Sample KR7-15, upper impactite unit, sample depth = 402.73 m; matrix-supported suevite with sub-cm- to dm-sized lithic fragments: laminated shale (S) with cross-cutting pre-impact veinlet, laminated shale clast (S2) with a cross-cutting pre-impact veinlet, metagreywacke (MGW), quartz-rich metagreywacke (QMGW), quartz (Qtz); melt particles are microscopic. Shale clasts are angular, metagreywacke and quartz clasts are sub-rounded. Continued on next page.

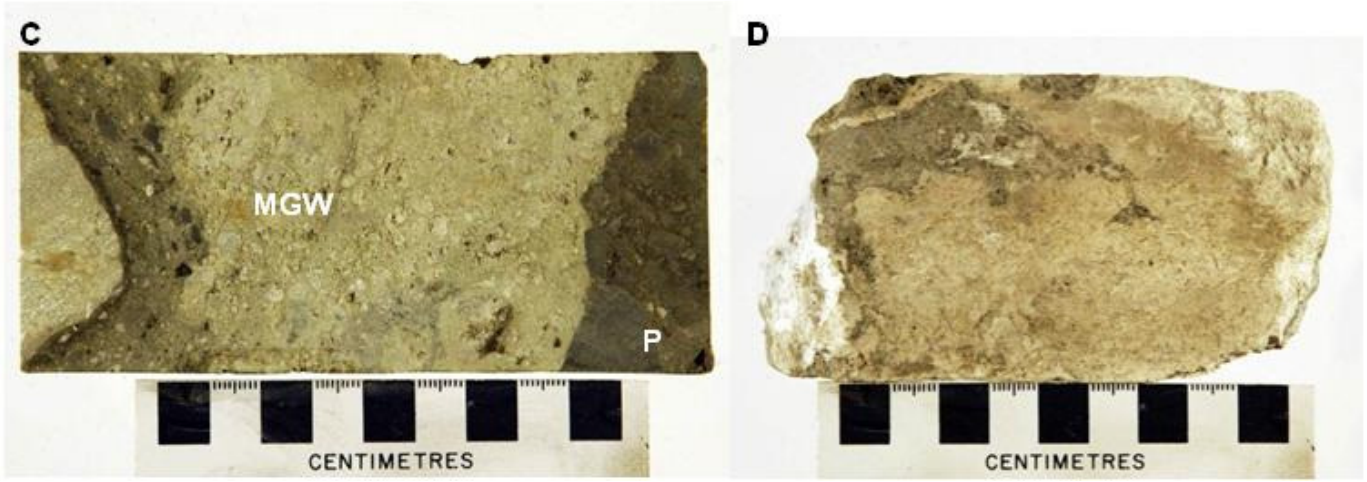

Fig. 3.2 (cont'd): Hand specimen photographs. C) Sample KR7-11, upper impactite unit, sample depth = 383.74 m; matrix-supported suevite with sub-cm- to cm-sized fragments: large metagreywacke clast in centre (MGW), matrix to left and right of the clast, phyllite clast (P). Matrix on left side of sample shows distinctive flow texture around metagreywacke clasts. D) Sample KR7-43, upper impactite unit, sample depth = 384.84 m; matrix-supported suevite with sub-cm- to cm-sized fragments: large metagreywacke clast dominates the sample, and the breccia matrix forms a distinctive flow texture on the left side; post-impact calcite pod at the left edge of hand specimen.

Table 3.1: LB-07A core: Lithostratigraphic subdivision.

Unit	Lithology	Sample depth (m)
Upper Impactites	Polymict lithic breccia	333.38 - 357.45
	Suevite	357.45 - 370.34
	Polymict lithic breccia	370.34 - 378.20
	Suevite	378.20 - 390.85
	Polymict lithic breccia	390.85 - 393.78
	Suevite	393.78 - 415.67
Lower Impactites	Monomict lithic breccia	415.67 - 430.13
	Suevite (~20 cm)	430.13
	Monomict lithic breccia	430.33 - 445.22
	Suevite (~30 cm)	445.22
	Monomict lithic breccia	445.52 - 470.55
Basement Metasediments	Shale, slate, phyllite, schist	470.55 - 483.00
	Suevite (~60 cm)	483.00
	Metagreywacke	483.60 - 487.12
	Granophyric-textured rock (~30 cm)	487.12
	Shale, slate, phyllite and schist	487.42 - 510.89
	Metagreywacke	510.89 - 513.90
	Suevite (~1 m)	513.90
	Shale, slate, phyllite and schist	514.90 - 545.08

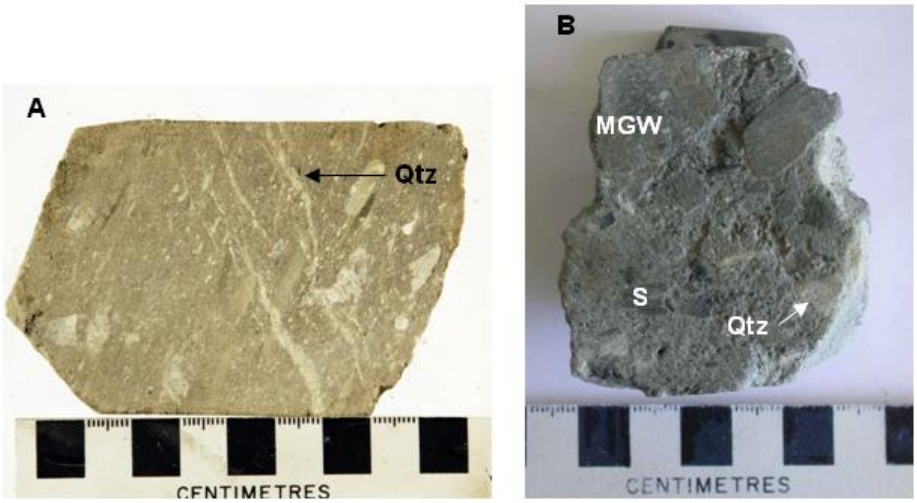

Fig. 3.3: Hand specimen photographs. A) Sample KR7-27, lower impactite unit, sample depth = 468.28 m; mylonitic metagreywacke monomict breccia with cross-cutting quartz veinlets (Qtz). B) Sample KR7-74, lower impactite unit, sample depth = 430.13 m; matrix-supported suevite with sub-cm- to cm-sized lithic fragments: metagreywacke (MGW), shale (S) and quartz (Qtz).

However, it is also possible that the turbulent processes during and after impact (slumping producing debris flows) could have caused the intercalation of polymict lithic breccias and suevite (see Chapter 7).

The lower part of the core displays a feature known as disking—where centimetre-wide pieces have broken essentially perpendicular to the core axis (apparent dip of 10 – 20°), with fracturing generally parallel to metasediment bedding orientations. This disking effect is clearly related to the well-laminated and lithologically diverse (at a scale of centimetres to decimetres) nature of this section, with many, if not all, fractures originating on lithological contacts and bedding-planes. The effect is thought to be caused by the drilling-induced shear stress (see also Deutsch et al., 2007).



Fig. 3.4: Core box image of basement metasediments (Box no. 45, depth range = 512.80 – 517.65 m) indicating the difference between the metagreywacke (MGW)-rich sediments (light grey), and the shale (S)-rich sediments (dark grey). Horizontal length of core box is 60 cm.

The stratigraphic subdivision of the LB-07A core has been supported by concurrent geophysical studies. Morris et al. (2007b) were able to subdivide the polymict and monomict breccias on the basis of shape, orientation and size of clasts. They found that the monomict breiccas had a more uniform and smaller clast size in comparison to the polymict breccias. The polymict breccias show an interbedding of layers with a mixed clast fabric, locally variable clast ellipticity (reflecting the different components) and an increased clast size

which shows a complex variation with depth. Elbra et al. (2007) performed petrophysical and palaeomagnetic studies of a number of samples from both cores, and were able to differentiate between the impactites and basement sequence. The polymict lithic breccias and suevites have lower bulk densities and significantly higher porosities (up to 38%) than the metapelitic target rocks. Schell et al. (2007) also performed petrophysical measurements for both cores, as well as determining the magnetic properties of these samples. Both magnetic anisotropy and magnetic susceptibility were used to distinguish between the various lithologies. Schell et al. (2007) used the parameters of foliation (the “dominant layered structure”) and lineation (features produced through “flow processes”) to distinguish the rocks. Shales, slates, phyllites and schists displayed high degrees of anisotropy (owing to an intense foliation), metagreywacke and polymict lithic breccia display intermediate degrees of anisotropy (more lineation than foliation) while suevites showed low degrees of anisotropy.

3.1.1 Contact Relationships

Contact relationships between the different lithologies are generally indistinct in the upper impactites. Contacts between the polymict lithic breccias and suevite in the upper impactite sequence could not be resolved on the macroscopic scale and could be gradational, as the polymict lithic breccias and suevite are similar but for the fact that the suevite contains minor amounts of microscopic melt particles. The contact between the upper and lower impactite sequences at 415.67 m depth is sharp (Fig. 3.5). The contacts between the thin suevite intercalations and monomict breccia also appear distinct, indicating that likely these suevites represent injections into the monomict breccia, although it must be noted that the deterioration of the core is already substantial in the lower impactites, so that detailed analysis of contact zones is somewhat hampered.

The basement metasediments are extensively fractured and occur in the subcrater (i.e., parautochthonous zone; Fig. 1.7; section 1.2.5), where the chief disturbance is structural. Any breccia phase (be it lithic, suevitic, or melt-rock) will occur either as a dyke (i.e., a cross-cutting phase; see section 1.2.5.1) or a layer-parallel injection (i.e., one which exploits contact weaknesses) in the basement metasediments. The first suevite intercalation occurs at a boundary between metagreywacke monomict breccia and phyllite monomict breccia (i.e., a strength contrast; Fig. 3.1), where the comparative weakness would allow the injection of impactite.



Fig. 3.5: Core box image of the sharp contact (Box no. 26, depth range = 413.04 – 415.82 m) between the upper and lower impactites. Contact is indicated by arrow. Horizontal length of core box is 60 cm.

The second suevite occurs in the middle of a metagreywacke monomict breccia unit, and the metagreywacke on either side of the suevite is identical macroscopically and microscopically. Also, both suevite units in the monomict breccia contain “foreign” material (e.g., shale, phyllite in the metagreywacke unit) to that seen in the monomict breccias, and thus, must have originated elsewhere and been injected.

The metagreywacke and shales of the basement metasediment are intercalated on millimetre to metre scales. Contacts are commonly sharp but typically undulating, presumably owing to the low-amplitude folding that is noted throughout the metasediment sequence both in the core and in outcrop outside of the crater (Reimold et al., 1998).

3.1.2 Hydrothermal Alteration of Core LB-07A

Alteration thought to be of post-impact age is most pronounced in the upper impactites (above 415.67 m depth). Throughout the core calcite pods and millimetre- to centimetre-wide calcite and quartz veins (Fig. 3.6), as well as rare sulphide occurrences, are observed. Post-impact veins display variable dips with respect to the core axis, ranging from moderately steep to shallow.

These veins are distinct from pre-impact quartz veins that are restricted to large clasts and, on the microscopic scale, display evidence of shock deformation (see Chapter 5). A number of such pre-impact quartz veins occur parallel to bedding in metagreywacke or altered shale. The lower impactites show less evidence of pre-impact alteration (both macroscopically and microscopically) but the relatively poor state of the core has hampered a full investigation of this aspect. Local pods of cross-cutting calcite are observed in the lower impactites. Calcite pods of up to 10 cm size and sulphide-filled fracture networks up to 1 cm wide are observed in the underlying metasediments.

3.1.3 Upper Impactites - Breccia Characteristics

The polymict lithic breccia and the suevites of the upper impactites are very similar in hand specimen. Both polymict breccias consist of submillimetre- to decimetre-sized clasts, and the main clasts observable on the macroscopic scale include metagreywacke, shale, quartz and sandstone.



Fig. 3.6: Pre- and post-impact alteration. A) Core box image of secondary carbonate veins (C) and a fold structure (F) in suevites of upper impactites (Box no. 25, depth range = 410.21 - 413.04 m). B) Core box image of carbonate pods (C) in shales of the basement metasediments (Box no. 48, depth range = 530.39 – 539.29 m).

All polymict breccias of the upper impactites have a light grey to grey matrix (Fig. 3.2 A - D), the abundance of which varies between 40 % and 70 %. Clasts show a variety of shapes (Fig. 3.7 A, B) between angular and rounded, but most of the shale (sometimes laminated)

clasts are angular (Fig. 3.2 B; Fig. 3.7 A), whereas the metagreywacke clasts are more rounded (Fig. 3.2 B, Fig. 3.7 B). Other clasts noted in hand specimen include quartz (Fig. 3.2 B), phyllite and minor schist. A number of samples show flow textures, which are generally observed around large (>2 cm) clasts (Fig. 3.2 C, D). Maximum clast size in the sample set is 10 cm. Calcite overprint in the form of pods and veins is apparent (Fig. 3.2 D).

3.1.4 Lower Impactites - Breccia Characteristics

The lower impactites consist of both monomict breccias and suevites (Fig. 3.1; Appendix 3b). The monomict breccias either consist of metagreywacke, phyllite or shale. The metagreywacke monomict breccias are white to light grey, and locally have minor shale intercalations. The shale monomict breccias are grey. The phyllite monomict breccias are similar to the shale monomict breccias, but have a characteristic sheen caused by the abundance of phyllosilicate minerals, and are fissile. All monomict breccias consist of angular to sub-rounded clasts.

The suevites in the lower impactites consist of between 30 % and 40 % matrix with shale, quartz, phyllite and schist clasts. The upper suevite injection (430.13 m) has sub-rounded clasts; the lower suevite (445.22 m) injection has more angular clasts. In both suevites, minor ovoid, light brown to green melt particles are observed. The maximum melt particle size observed in hand specimen is 0.5 cm, but most particles are millimetre sized.

3.2 Microscopic Observations

The microscopic findings, to some degree, mirror the macroscopic observations in that evidence of both pre- and post-impact secondary alteration is apparent and that the clast compositions noted in the microscopic study reflect the findings of the macroscopic study (see Appendix 3b). Metasedimentary lithic clasts

dominate throughout the impactite sequence, with a trace of granitic clasts. Significantly, no evidence of metavolcanic clasts was found.

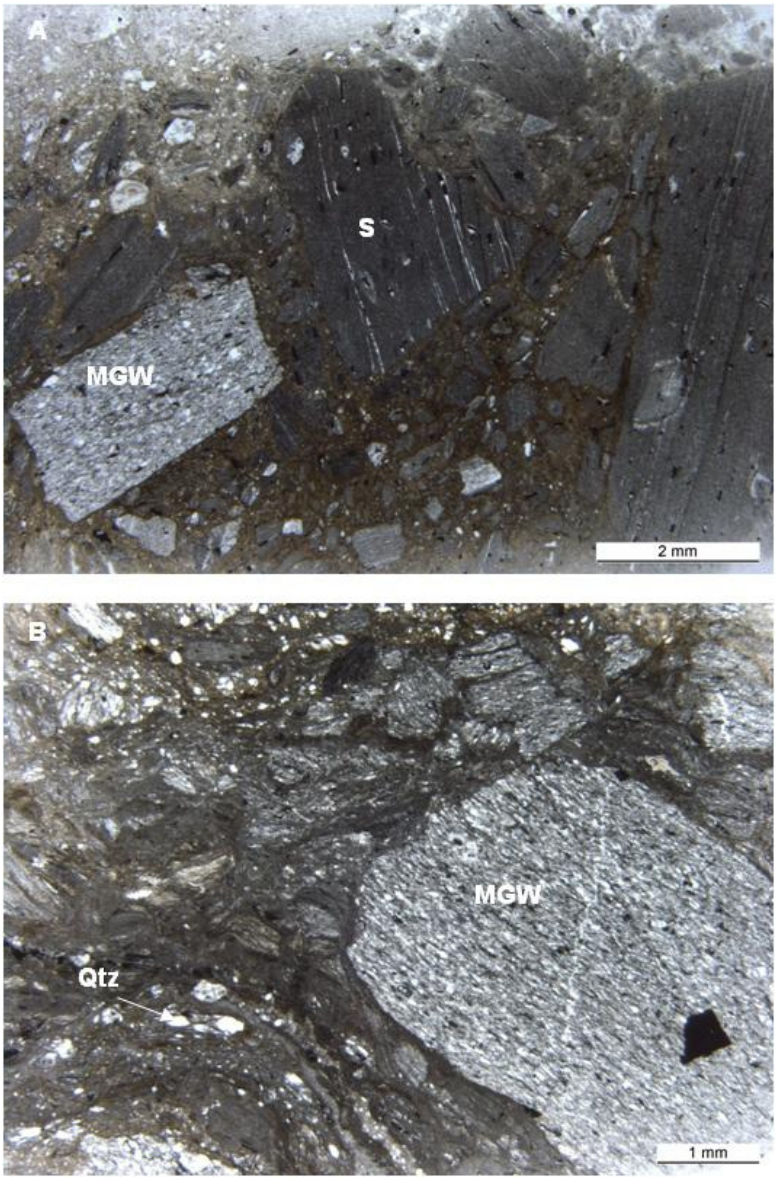

Fig. 3.7: Macro-photographs of impactite textures. A) Sample KR7-11, suevite, upper impactites, sample depth = 383.74 m; angular metagreywacke, laminated shale (with rutile inclusions and pre-impact quartz veins), rounded quartz clasts. B) Sample KR7-52, polymict lithic breccia, upper impactites, sample depth = 392.00 m; sub-angular to rounded clasts of metagreywacke (MGW), shale, quartz (Qtz) showing flow texture (particularly apparent in bottom left corner).

3.2.1 Upper Impactite Unit (333.38–415.67 m)

The upper impactite unit is well preserved and contains three lithic breccia sections that alternate with three suevite sections (Fig. 3.1; Table 3.1). All these breccias are microscopically very similar, but the suevites can be distinguished from the polymict lithic breccias by the presence of melt fragments. No sharp contacts are seen between the polymict lithic breccias and the suevites, and they are, thus, treated as a single sequence. Melt particles comprise between 1.6 and 6.8 vol% in the suevites (see the modal data in Table 3.2; Fig. 3.8). The breccias are mostly matrix-supported, though a few are clast-supported, with no discernible trend between these types with depth.

The clast populations of both the polymict lithic breccias and suevites are dominated by metagreywacke clasts. These are commonly mylonitic with a mineralogy dominated by quartz, with feldspar and phyllosilicates (Fig. 3.9 A). Phyllite, mica-schist, quartzite and well-laminated shale (Fig. 3.9 A, B) are the other significant lithic clast phases (Table 3.2). Phyllites (Fig. 3.9 C) are fine-grained but characterised by a schistose fabric defined by fine-grained sericite. Mica-schists are similar in texture to the phyllites, but contain larger grains of muscovite and biotite. Quartzite is composed of interlocking, rounded to sub-rounded, equigranular quartz grains.

Shales occur as fine-grained phases (particles are sub-microscopic) that appear dark grey to black in thin section, and which are generally laminated, and locally iron-stained. Partial destruction of features such as lamination (giving the clasts a “boiled” appearance; Fig. 3.9 D) has taken place in some of the lithic clasts, and is thought to have been caused by shock melting. Kink bands of 200 µm wavelength are observed in the shales (and some slates) and the phyllites and are well known from the Birimian rocks collected outside the crater (e.g., Koeberl and Reimold, 2005).

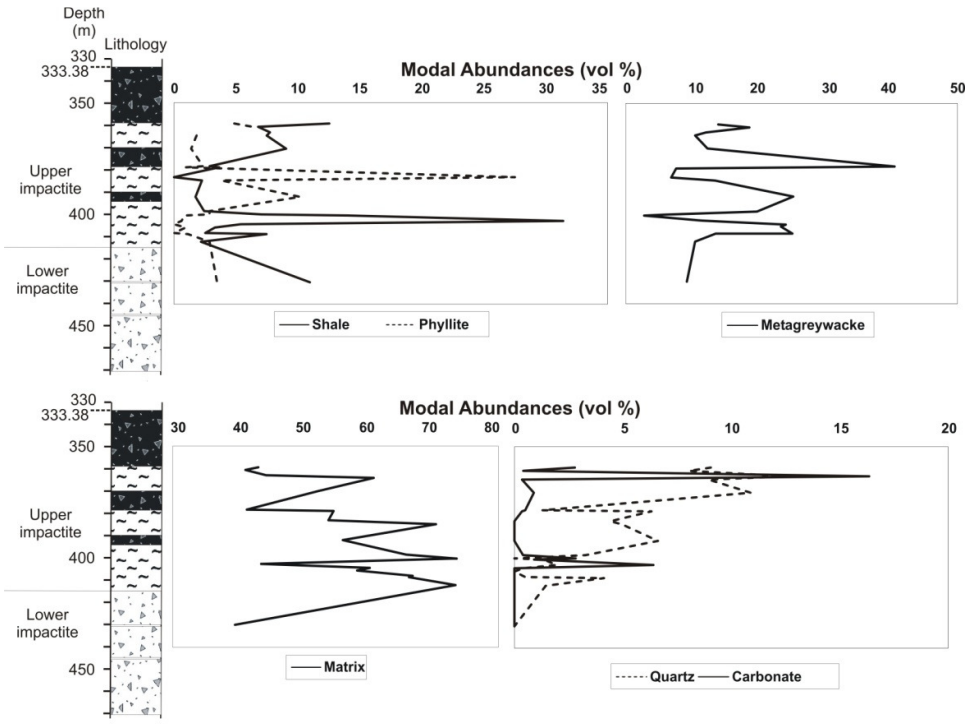

Fig. 3.8: Main lithic and mineral clast and matrix abundance variations throughout the upper section of impactites in drill core LB-07A.

Other minor (generally <0.1 vol%) lithic clast components include leucogranite (Fig. 3.9 E), graphitic schist, limestone and discrete but rare clasts of lithic impact breccia (breccia-in-breccia; Fig. 3.9 F; see Table 3.2). Amongst mineral clasts, quartz, plagioclase, K-feldspar, various phyllosilicates (biotite, chlorite, muscovite and sericite; Fig. 3.10) and calcite clasts are significant.

The phyllosilicate minerals display two textures: they either occur as acicular needles (e.g., chlorite, Fig. 3.10 A; all lithic clasts) or may be kinked (e.g., muscovite, Fig. 3.10 B; none observed in lithic clasts). The kinking is related to the impact event, as it is confined to discrete phyllosilicate grains.

Traces of amphibole (tremolite-actinolite) and sphene were noted during point-counting. Biotite and chlorite are the main phyllosilicate phases, though muscovite has been noted, and sericite is common as a replacement texture in plagioclase.

Table 3.2: Modal analyses (data in vol%) by optical microscopy on thin sections of selected, representative samples of polymict lithic breccia and suevite. Continued on next page.

Sample No.	**KR7-35**	**KR7-6**	**KR7-7**	**KR7-36**	**KR7-8**	**KR7-50**	**KR7-37**	**KR7-51**	**KR7-43**	**KR7-52**
Depth (m)	**359.33**	**360.65**	**363.20**	**364.45**	**370.34**	**378.20**	**379.09**	**383.14**	**384.84**	**392.00**
Breccia type*	**Suevite**	**Suevite**	**Suevite**	**Suevite**	**Lithic**	**Suevite**	**Suevite**	**Suevite**	**Suevite**	**Lithic**
Matrix	43.1	43.3	44.4	61.8	52.3	43.0	68.8	56.4	72.2	56.2
Metagreywacke	13.9	19.6	12.1	10.5	12.3	42.2	9.6	7.1	13.7	25.2
Shale	12.5	7.1	7.7	7.6	9.1	2.9	4.6	x	2.4	1.8
Phyllite	4.9	6.7	x	1.8	1.4	2.4	1.3	28.4	3.9	10.2
Schist	4.5	12.1	x	x	x	x	2.5	x	x	x
Breccia	4.9	x	x	x	x	x	x	x	x	x
Leucogranite	x	x	x	6.5	0.5	3.2	x	1.0	x	x
Phyllosilicates*	x	x	1.0	0.4	13.6	x	0.4	x	x	x
Quartz	9.0	8.5	12.6	9.1	10.9	1.3	7.9	4.6	5.1	6.6
Total feldspar*	0.4	0.4	0.5	x	0.5	0.5	2.5	0.5	x	x
Carbonate	2.8	0.4	16.4	0.4	0.9	0.5	0.4	x	x	x
Sphene	0.7	x	x	x	x	x	x	x	x	x
Diaplectic glass*	x	x	x	x	x	x	x	x	x	x
Melt	3.5	1.8	5.3	1.8	x	3.7	2.1	2.5	2.7	x
Total	100.2	99.9	100	99.9	101.5	99.7	100.1	100.5	100	100

**Breccia type: lithic = polymict lithic breccia; Total feldspar = plagioclase + K-Feldspar, where plagioclase>K-feldspar; Phyllosilicates = chlorite + biotite + muscovite (primary and secondary); Diaplectic glass = diaplectic quartz glass and diaplectic feldspar glass. Approximately 500 grains counted per section over 1.5 cm^2 areas. x = traces (< 0.1 vol%). Matrix consists of grains which are less than 50 µm in size.*

Table 3.2 (cont'd): Modal analyses (data in vol%) by optical microscopy on thin sections of selected, representative samples of polymict lithic breccia and suevite.

Sample No.	**KR7-14**	**KR7-40**	**KR7-53**	**KR7-15**	**KR7-16**	**KR7-17**	**KR7-20**	**KR7-41**	**KR7-42**	**KR7-23a**
Depth (m)	**398.44**	**400.06**	**400.58**	**402.73**	**404.26**	**405.57**	**408.32**	**408.72**	**412.17**	**430.13**
Breccia type*	**Suevite**	**Suevite**	**Suevite**	**Suevite**	**Suevite**	**Suevite**	**Suevite**	**Suevite**	**Suevite**	**Suevite**
Matrix	66.9	73.6	76.3	43.6	60.2	58.3	66.8	66.2	73.5	39.6
Metagreywacke	20.1	6.1	2.8	11.5	24.1	23.4	25.1	13.6	10.5	9.3
Shale	2.5	7.1	14.7	31.4	5.4	3.3	2.5	7.5	2.2	11.0
Phyllite	2.9	2.8	0.9	0.6	x	1.0	x	1.1	2.9	3.5
Schist	x	X	x	x	x	x	x	x	x	x
Breccia	x	X	x	x	x	x	x	0.4	x	x
Leucogranite	x	X	x	x	x	x	x	x	x	x
Phyllosilicates*	x	X	x	x	x	4.8	x	3.8	x	x
Quartz	3.3	X	1.4	1.9	0.4	x	0.5	4.1	1.5	x
Total feldspar*	0.8	0.5	x	1.3	x	x	1.5	0.8	0.4	x
Carbonate	0.4	2.8	0.9	6.4	x	x	x	x	x	x
Sphene	x	X	x	x	x	x	x	x	x	x
Diaplectic glass*	x	1.4	0.9	x	3.7	2.4	x	x	4.0	x
Melt	2.9	5.7	1.9	3.2	6.2	6.8	3.5	2.6	4.4	36.1
Total	99.8	100	99.8	99.9	100	100	99.9	100.1	100.1	99.9

**Breccia type: lithic = polymict lithic breccia; Total feldspar = plagioclase + K-Feldspar, where plagioclase>K-feldspar; Phyllosilicates = chlorite + biotite + muscovite (primary and secondary); Diaplectic glass = diaplectic quartz glass and diaplectic feldspar glass. Approximately 500 grains counted per section over 1.5 cm^2 areas. x = traces (< 0.1 vol%). Matrix consists of grains which are less than 50 µm in size.*

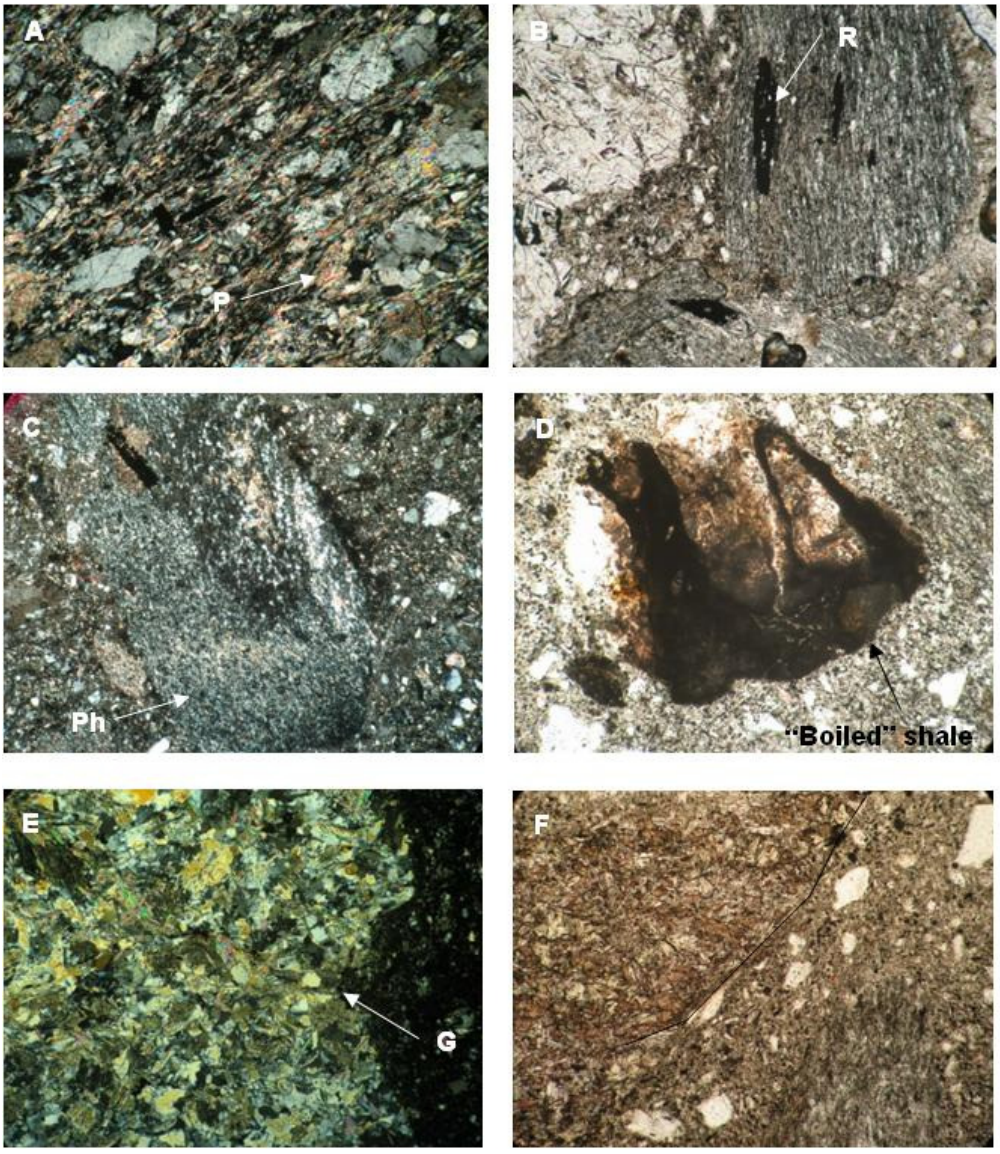

Fig. 3.9: Photomicrographs of lithic phases in suevites observed throughout LB-07A core. A) Sample KR7-1, mylonitic metagreywacke clast in polymict lithic breccia, upper impactites, sample depth = 334.91 m; main minerals are quartz, K-feldspar and phyllosilicates (P); image width = 3 mm, cross polarized light (CPL). B) Sample KR7-7, suevite, upper impactites, sample depth = 363.20 m; laminated shale with rutile (R) growing in direction of lamination. Metagreywacke on left side of the image; image width = 3 mm, plane polarized light (PPL). C) Sample KR7-35, suevite, upper impactites, sample depth = 359.33 m; phyllite clast (Ph); image width = 3 mm, CPL. D) Sample KR7-41, suevite, upper impactites, sample depth = 408.72 m; "boiled" shale clast (see text for details); image width = 1.5 mm, PPL. E) Sample KR7-36, suevite, upper impactites, sample depth = 364.45 m; a considerably altered granite clast (G); image width = 3 mm, CPL. F) Sample KR7-41, suevite, upper impactites, sample depth = 408.72 m; breccia clast (possibly pre-impact) in the suevite (line separates the two phases); image width = 1.5 mm, CPL.

Chlorite is present as both discrete mineral grains as well as a secondary alteration product of biotite, intergrown with the latter.

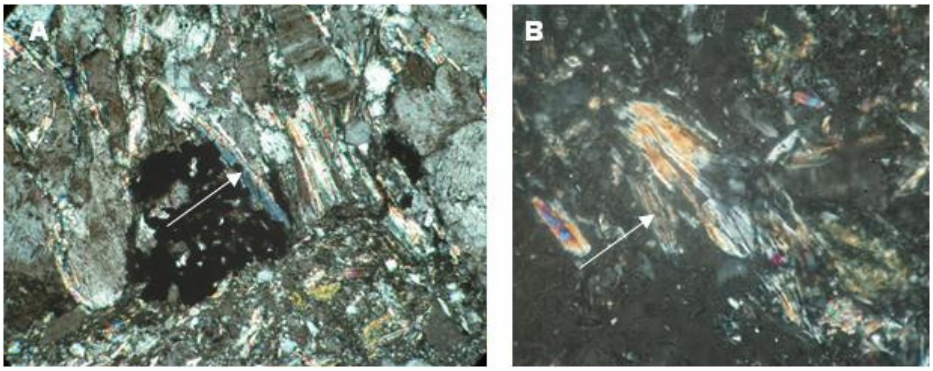

Fig. 3.10: Photomicrographs of phyllosilicate textures. A) Sample KR7-8, polymict lithic breccia, upper impactites, sample depth = 370.34 m; chlorite displaying an acicular habit; image width = 1mm, CPL. B) Sample KR7-8, polymict lithic breccia, upper impactites, sample depth = 370.34 m; kinked muscovite; image width = 0.75 mm, CPL.

Hydrothermal effects are observed in the form of fine (up to 1 mm wide) quartz veining and sericitization of plagioclase, and secondary chlorite after biotite. Discrete bands, up to several mm in width, of pre-impact calcite (Fig. 3.11 A; distinguished from post-impact calcite pods by larger grain size and well-developed mosaic texture) occurs in the upper impactites and throughout the LB-07A core. Up to now, calcite was not considered a significant component of the target volume, but carbonate has been recognized here as a distinct lithology in large coherent basement rock sections (metasediment units) of the lower sequence. This material is also present as clasts of euhedral calcite crystals in the impact breccias (<5 vol%; up to 1 mm sized clasts). In addition, calcite occurs as aggregates of ~100–700 µm size grains in post-impact veinlets (Fig. 3.11 B).

The lithic and mineral clast size varies from 0.1 mm to 2 cm throughout the impact breccia interval. Clast shapes vary from sub-rounded to angular, with an overall tendency towards angularity (Fig. 3.7 A, B). The shapes of microscopic melt fragments also vary from

well-rounded to angular. No systematic size or shape variation has been recognized with increasing depth within the upper impactite sequence (Fig. 3.12).

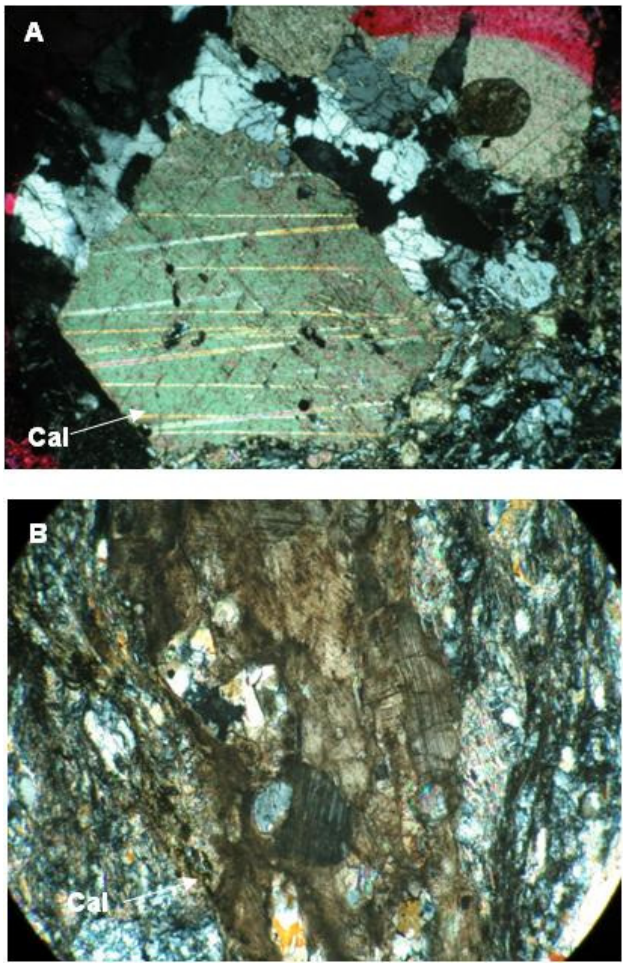

Fig. 3.11: Photomicrographs of calcite – pre- and post-impact phases. A) Sample KR7-8, polymict lithic breccia, upper impactites, sample depth = 370.34 m; pre-impact calcite (Cal) crystal; image width = 2 mm, CPL. B) Sample KR7-27, shale monomict breccias, lower impactites, sample depth = 468.28 m; post-impact calcite veinlet which cross-cuts the monomict breccia; image width= 1.31 mm, PPL.

Microscopically, the matrices (here considered as everything with a grain size of less than 50 µm) of these breccias is rather heterogeneous in terms of size and shape of the fragments: there is strong variation in the colour of the matrix as a whole from light to dark grey-brown (colours after the Munsell system; Munsell, 1912),

presumably relating to iron content (see Chapter 4). Flow structures have been observed in a few samples in the breccia matrix, in both the polymict lithic breccias and suevites of the upper impactite section. Flow is indicated by minerals and matrix flowing around clasts larger than 1 mm in diameter. It is, however, also possible that this feature was produced by compaction of the deposit. Scanning electron microscope (SEM) analysis shows that the matrix grains are highly angular (Fig. 3.13 A), and matrix composition is dominated by quartz, with minor feldspar and mafic minerals (including some biotite). It was noted in Chapter 1 (section 1.2.5.2) that Osinski et al. (2004) reported that the matrices of the Ries suevites were formed from melts, and that these breccias are in fact melt-matrix breccias. The matrices of the Bosumtwi suevites were examined for similar features (i.e., recrystallised minerals) and no evidence was found. Locally, small particles with vesiculated structure are present in the matrix of suevite samples and are interpreted as tiny (50 – 100 μm) melt fragments (Fig. 3.13 B, C; see section 5.3). Their abundance is estimated at <5% of the matrix. The differences between the observations made by Osinski et al. (2004) for the Ries suevites those made in this study for the Bosumtwi suevites will be addressed more fully in Chapter 7.

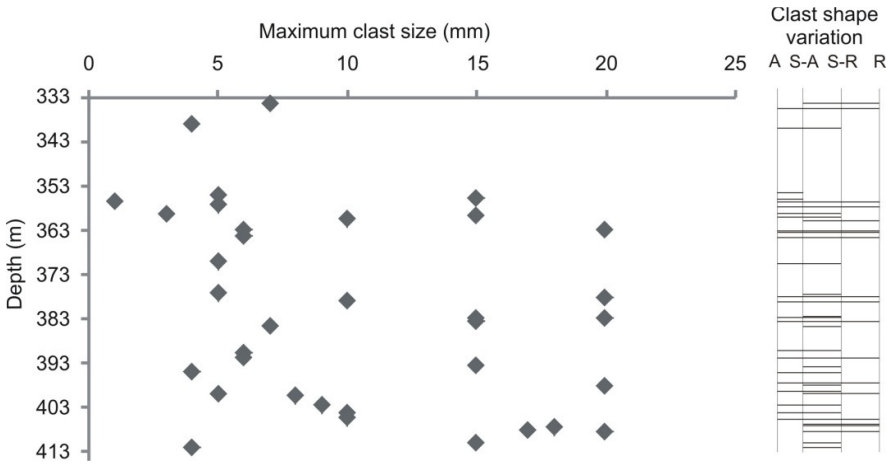

Fig. 3.12: Clast shape and size variation throughout the upper impactites. Maximum clast size in mm is given, measured on the long axis of clasts. A = angular, S-A = sub-angular, S-R = sub-rounded, R = rounded.

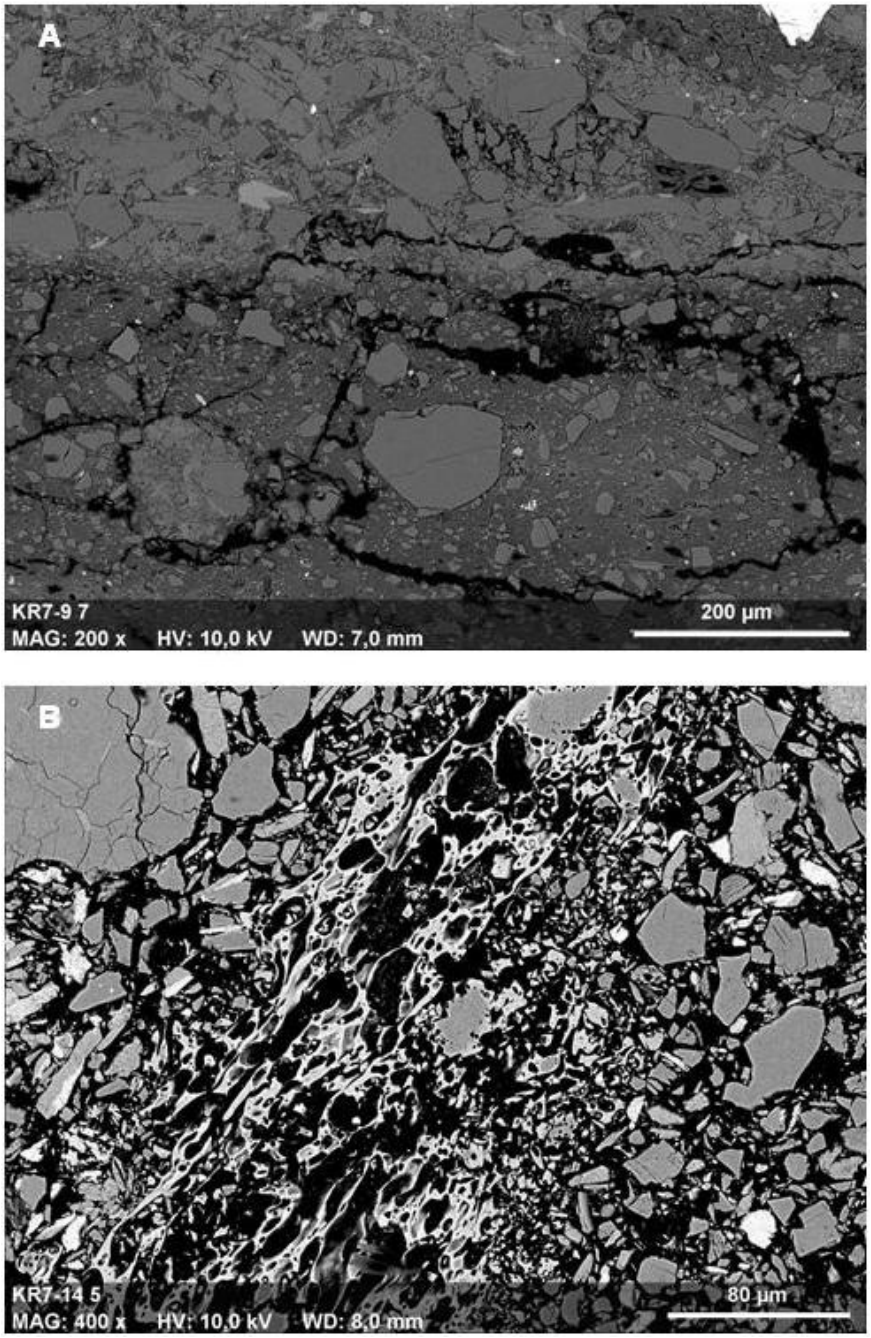

Fig. 3.13: Backscattered electron images. The lightest fragments correspond to rutile, the grey fragments correspond to quartz (moderately grey indicates silica-rich lithologies), with darker grey indicating the mixed matrix, black indicates cracks in the thin section. A) Matrix of polymict lithic breccia; sample KR7-9, polymict lithic breccia, upper impactites, sample depth = 377.46 m; width of scale bar = 200 µm. B) Vesiculated melt particle in matrix of suevite; sample KR7-14, suevite, upper impactites, sample depth = 398.44 m; width of scale bar = 80 µm. Continued on next page.

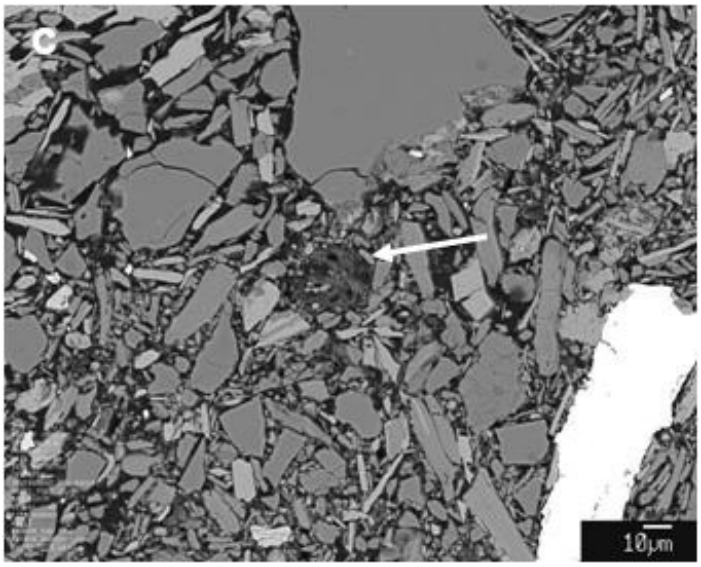

Fig. 3.13 (cont'd): Backscattered electron images. C) Round quartz-rich melt particle (indicated by arrow) in clastic matrix; width of scale bar = 10 µm.

3.2.2 Lower Impactite Unit (415.67–470.55 m)

The breccias in this interval are well preserved (massive) for part of the interval, but below 455 m depth they are disaggregated. Alternation between metagreywacke and shale breccia types is on a decimetre- to metre-scale. Suevite intercalations are found at 430.13 m (~20 cm thick) and 445.13 m (~30 cm thick).

The metagreywacke monomict breccias are characterised by angular to sub-rounded clasts, which are very fine-grained (~0.1–0.2 mm) at the top of the sequence. With increasing depth, the clast size increases to ~0.4 mm and locally to 1 mm; but no consistent change in clast size occurs with depth. The matrix consists of very fine (< 50 µm), angular clasts of metagreywacke. The matrix-to-clast content is variable and increases with increasing depth from approximately 40 to 60 vol%. Clasts in the metagreywacke monomict breccias consist of quartz, K-feldspar, plagioclase, muscovite and sericite. The phyllosilicates are generally bladed in shape, and are the smallest phases present. The clasts are internally weakly to strongly mylonitized in the interval 454.35–470.55 m.

Locally, post-impact rounded pods of calcite (which overprint and cross-cut the breccias) up to ~0.5 mm in diameter, and calcite veinlets (0.2 to 0.5 mm thick) are evident. The suevite intercalations in the lower impactites differ from the suevites of the upper impactites in that the matrix colour is moderate greenish-yellow (Munsell colour chart). Kinked shale, phyllite and mylonitic metagreywacke form the dominant lithic clast types in the suevites, and quartz and plagioclase mineral clasts are common in both suevite intercalations. The lithic/mineral clasts are angular to sub-rounded, and vary in size from <0.1 mm to 0.5 mm, which is smaller than the clasts seen in the upper impactite suevites.

3.2.3 Basement Metasediments (470.55–545.08 m)

Owing to the highly disaggregated nature of this sequence - many samples provided were completely pulverized - only grain mounts could be prepared. Thus, only randomly preserved fragments (mostly quartz-rich) were studied, with some doubt as to whether or not these grain mounts are fully representative of the lithological composition of these strata. However, it is reasonably certain that altered shale dominates in this interval.

Shale lithologies contain quartz, sericitised plagioclase and phyllosilicate minerals (biotite and muscovite), together with rare sulphides. Some of the shale lithologies are mylonitic. Grain size varies from sub-micrometre to 500 µm, and grain shape varies from angular to sub-rounded (see Appendix 3b). Metagreywacke-dominated lithologies contain varying amounts of quartz, feldspar and phyllosilicates, which occur at sizes up to 500 µm. A number of these samples have secondary calcite overprint. One sample (KR7-31) contains some amphibole (hornblende), and may be a poorly preserved granite clast; the thin section, however, is very fragmented. The hand specimen, unfortunately, does not provide any further clarification, as the sample is nearly entirely powderised. The geochemical analysis of this sample does not differentiate it

from the other metasediments (Appendix 4; section 4.3.4). Given the nature of the target rocks, it is possible that a granitic dyke may have intersected the sampled section.

The two suevite intercalations in the basement (at 483.00 and 513.90 m depths) show different characteristics to the suevites of the upper and lower impactites, and from each other, particularly in terms of the colour of the matrix and clast type. The clast size is substantially smaller than the clast size seen in the upper and lower impactite suevites. Similarities between these two suevites include variable clast size ranging from 0.1 to 1 mm and clast shape (elongated/flattened). The clasts are angular to sub-rounded, but rarely round. The suevite intercalation at 483.00 m is ~60 cm wide, dark grey, and characterised by a dense, homogeneous, grey-black matrix. Metagreywacke and laminated shale form the dominant lithic clasts, with quartz dominating the mineral clast population. In general, all mineral and lithic clasts are approximately 0.1 to 0.5 mm in size, with the lithic clasts being slightly larger than the mineral clasts (expected as the quartz clasts are likely derived from the lithic components, i.e., metagreywacke and shale). The suevite at 513.90 m is ~1 m thick and is characterised by a light grey matrix together with an abundance of lithic fragments that are predominantly metagreywacke, followed by shale; however, it also includes one clast of felsic granophyre ~2 mm in size (Fig. 3.14 A). The granophyre clast is dominated by kinked muscovite, together with subsidiary quartz-feldspar granophyric intergrowth, as well as plagioclase and secondary calcite which occur as patchy intergrowths. The mineral clasts in the suevite include quartz, kinked muscovite, rare plagioclase and a single ~1 mm-size elongate clast of actinolite-tremolite amphibole.

A granophyric-textured igneous rock is found in the interval from 487.12 m to 487.42 m. It consists of quartz-feldspar intergrowth, muscovite and post-impact calcite (Fig. 3.14 B, C).

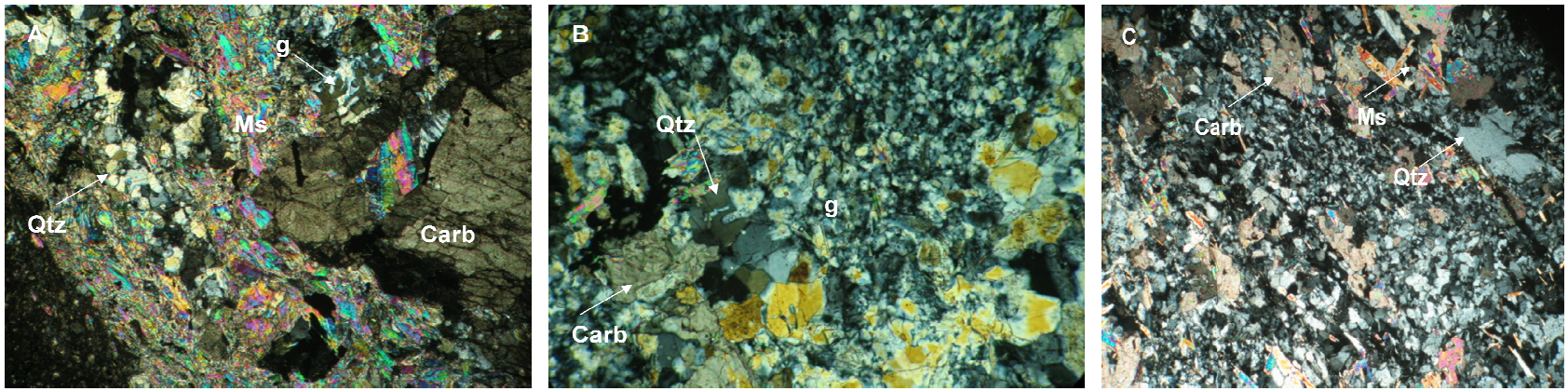

Fig. 3.14: Photomicrographs of granophyric intergrowth (g) of quartz and feldspar; carbonate (Carb) and muscovite (Ms), quartz (Qtz) indicated. A) Sample KR7-83, suevite, basement metasediments, sample depth = 513.90 m; clast in suevite; image width = 3 mm, CPL. B) and C) Sample KR7-82, granophyric-textured lithology, basement metasediments, sample depth = 487.12 m: B) image width = 1.75 mm, CPL; C) image width = 3.00 mm, CPL.

The calcite is interpreted as post-impact, as it occurs as ca. 1 mm wide rounded masses (showing little twinning, 1 set maximum) which overprint the granophyric texture. The rock is slightly different from the clast found in the suevite at 483.00 m in that it is more quartz-feldspar rich. The quartz-feldspar granophyric intergrowth is dominant, followed by post-impact calcite which occurs as rounded masses (~1 mm in diameter), likely after plagioclase. Muscovite is present as platy crystals (0.1 mm long). After examination of the hand specimen, it was concluded that this lithology may represent a hydrothermally altered intrusion of the granophyric granitoid lithology first described by Reimold et al. (1998) from the northwestern rim of the crater.

3.2.4 Oxide and Sulphide Phases

Rutile is a trace component in a number of shale clasts and is considered to be of pre-impact origin (see Fig. 3.9 B). Sulphide minerals (pyrite > chalcopyrite >> arsenopyrite > pyrrhotite; Fig. 3.15 A, B) occur as both pre- and post-impact phases (Fig. 3.15 A, B). They can occur within shale clasts, usually parallel to the lamination, indicating that these occurrences likely formed pre-impact. Pyrrhotite occurs as a minor component of the sulphide assemblage within brecciated rutile grains (Fig. 3.15 B; also noted by Kontny et al., 2007). Additionally, networks of these minerals have been noted in the breccias, and are considered of post-impact hydrothermal origin (Fig. 3.15 A).

3.3 Summary

The lithostratigraphy of core LB-07A has been divided macroscopically into three units: the *upper impactites*, *lower impactites* and the crater *basement metasediment* sequence. The overall abundance of different lithologies is as follows: 16.5% polymict lithic breccia, 23.4% suevite, 25.7% monomict lithic breccia, 31.2% shale and 3.2% metagreywacke (the last two comprise the basement metasediments).

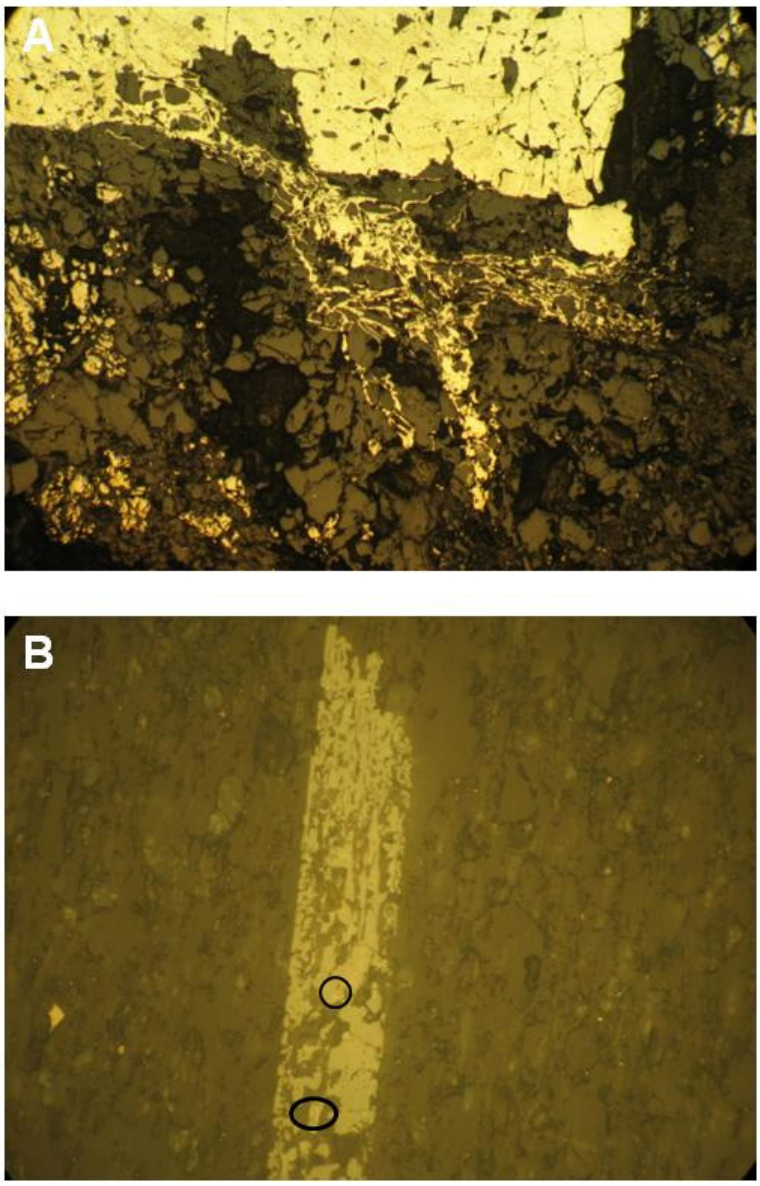

Fig. 3.15: Reflected light photomicrographs of sulphide phases. Darker phases indicate silicate minerals. A) Sample KR7-46, shale, basement metasediments, sample depth = 530.63 m; primary agglomerate of euhedral pyrite crystals overgrown on the left lower side by a network of fine grained, post-impact, partially acicular pyrite; image width = 1.31 mm. B) Sample KR7-11, suevite, upper impactites, sample depth = 383.74 m; pyrrhotite relicts (circled) within rutile in a shale clast in suevite, upper impactites; image width = 0.25 mm.

The upper impactites consist of alternating polymict lithic impact breccia and suevite, with the presence of melt particles identified as the main difference between the two breccia types. Evaluation of the

possibility that the entire upper impactite unit comprises suevite is rejected as extensive sampling was undertaken to evaluate this possibility. The suevite and polymict lithic breccia are interfingered, which may have been caused by turbulent processes during and after impact (producing debris flows). The polymict lithic breccias and suevite of the upper impactites, together comprising ~40% of the LB-07A core, yielded the following average clast compositions: 45 vol% metagreywacke, 20 vol% shale, 12 vol% quartz (presumably also mostly derived from argillitic or greywacke metasedimentary sources) and 10 vol% phyllite are chief contributors to the clast population. Approximately 4 vol% carbonate (calcite) is noted (this reflects both pre- and post-impact carbonate, where pre- > post-carbonate). The remaining 9 vol% of the total clast composition consists of minor amounts of phyllosilicates, feldspar, schist, rare granite and impact breccia.

The matrices of the suevites are composed of clastic material – both lithic and mineral fragments of less than 50 µm. The matrices were not molten, and show no evidence of recrystallised minerals, as is the case with the Ries suevites. Discrete melt particles of 50 – 100 µm occur in the matrix and are estimated at less than 5 % of the total matrix.

The lower impactites represent monomict impact breccia after either metagreywacke (86 vol%), shale (6.6 vol%) or phyllite (7.4 vol%). Suevite injections, which are distinct from those of the upper impactites, are found in the lower impactites and the basement metasediments, as well as a granophyric-textured lithology in the basement metasediments. The basement rocks (shale and metagreywacke) constitute ~35% of the sequence, throughout which difficulties with observation have been experienced owing to the poor state of preservation of the core and relatively lower core recovery in the lowermost parts of the core.

Chapter Four: Geochemistry of the LB-07A core

4.1 Introduction

Geochemical characterisation of impactites is an important tool utilized in the study of impact craters in order to investigate the source(s) of the breccias and mixing relationships of the target rocks in the different impactite types (see Chapter 3; Koeberl, 2007). Geochemical studies have also been successfully utilized in several craters to investigate the possible presence of a meteoritic component in the impactites (Morgan et al., 1975; Palme et al., 1978; Palme, 1982; Koeberl, 2007).

The presence of a meteoritic component in impact breccias is an important diagnostic criterion for the impact origin of a crater. Approximately 45 impact craters on Earth have been conclusively shown to display evidence of meteoritic components (Koeberl, 2007). Recently, Maier et al. (2006) reported finding a number of fossil meteorite fragments (the largest piece is 25 cm) in the melt rock of the Morokweng structure, South Africa, which has not been observed in any other impact crater to date. In general, a small amount of meteoritic component (in the form of a melt or vapour) is mixed with a large volume of target rock vapor. This mixture may also be incorporated into impact melt rock, suevite or impact glass. The percentage of meteoritic component is usually very small (less than 1 %) and is thus difficult to detect (see McDonald et al., 2007; Koeberl, 2007). Procedures utilized include analyzing the abundances of elements which have high concentrations in meteorites but low concentrations in the Earth's crust (Palme et al., 1978; Evans et al., 1993; McDonald et al., 2001). PGE concentrations together with interelement ratios can be used to resolve the type or class of meteorite (see Koeberl, 2007; Morgan et al., 1975; Palme et al., 1978, 1979; Evans et al., 1993). For example, chondrites have narrower and higher abundances of Ir and Os contents than achondrites (Koeberl, 2007).

Difficulties arise in detecting a meteoritic component in impact breccias for a number of reasons. First, meteorites have variable compositions (for compositional ranges for each class of meteorite; see McDonald, 2002) and also target rocks have variable siderophile element concentrations. Additionally, impactites may have low siderophile target element compositions. The PGE patterns of mantle and related rocks can be similar to the signatures of chondrites, as mantle rock PGE contents are higher than those in the crust by factors of 10^2 to 10^3 (see Koeberl, 2007). If gold and PGEs are present in high indigenous abundances in crustal rocks, low Ir/Au ratios could be observed, seemingly indicative of a nonchondritic source (Koeberl, 2007).

Another possibility is that siderophile element fractionation can take place in the impact melt while it is still molten (Koeberl, 2007). This effect is obviously most significant for larger craters (e.g., Sudbury impact structure; see Dressler and Reimold, 2001), as the melt will take longer to solidify, on the order of many thousands of years. A number of mineral phases may incorporate PGEs and related siderophiles into their structures (e.g., magnetite, chromite; see Koeberl, 2007), which leads to a heterogeneous distribution of these elements (e.g., East and West Clearwater structures, see Palme et al., 1979; Chicxulub structure, see Koeberl et al., 1994a). Post-impact hydrothermal fluid activity may also affect the PGE abundances (Dressler and Reimold, 2001). Given these variables, meteoritic components are most likely heterogeneously distributed in an impact structure (e.g., Palme et al., 1979; Koeberl et al., 1994a, b; Schuraytz et al., 1994).

Even where a meteoritic chemical component is evident, its presence can only be identified if a well-constrained mixing relationship exists between the target rocks and the impactor that can be plotted as a regression with a lower intercept that accurately

reflects the average PGE concentration in the target rocks (see McDonald et al., 2001; Tagle and Claeys, 2005).

4.1.1 Previous Assessment of the Meteoritic Component for the Bosumtwi Crater and the Ivory Coast tektites

The possible presence of a meteoritic component in tektites and impact breccias and the indigenous siderophile element component of the target rocks of the Bosumtwi structure has been investigated by a number of workers (Palme et al., 1978; Jones, 1985a; Koeberl and Shirey, 1993; Dai et al., 2005).

Palme et al. (1978) found that the Ivory Coast tektites have high concentrations of siderophile elements – in particular Ir and Os (on the order to 0.3-0.4 ppb). They interpreted this as evidence of meteoritic contamination and related this signature to an iron meteorite composition. Jones (1985a) also noted high siderophile element abundances, but suggested this could be due to the high indigenous contents of PGEs in the target rocks, owing to local ore mineralization. Koeberl and Shirey (1993) measured the concentrations and isotopic ratios of Os and Re for a number of Ivory Coast tektite samples as well as for various country rocks from the Bosumtwi structure. The Os isotopic ratios of the tektites (0.155 – 0.213) were close to meteoritic values, whereas the rocks of the Bosumtwi structure showed values (1.52 – 5.01) more typical of older continental crust (see DePaolo and Wasserburg, 1979). Koeberl and Shirey (1993) concluded that the Re-Os isotopic signatures of the tektites provided unambiguous evidence for contamination with 0.1–0.6 % meteoritic component. A meteoritic component in the Ivory Coast tektites was also confirmed by Cr isotope measurements (Koeberl et al., 2004). However, no clear meteoritic component has been distinguished in the fallout suevites (Dai et al., 2005), as the target rock PGE concentrations are highly variable and can be very high (e.g., Ir up to 3 ppb and Pt up to 39 ppb). There are also several gold mines and prospects in the greater

region around Lake Bosumtwi, and extensive gold exploration has been carried out in the immediate environs of the crater. Elevated siderophile element abundances are found in many of the country rocks in the Ashanti region (Osae et al., 1995; Jones, 1985a; Dai et al., 2005), which presents difficulties for verification of a meteoritic component.

The LB-07A core provides a unique opportunity to assess the meteoritic component of the Bosumtwi crater as it intersects a variety of only weakly altered impactites. Additionally, as noted in section 4.1, many impact structures show heterogeneous distribution of a meteoritic component within impactites. The borehole core provides an opportunity to analyse any vertical variation in such a component within the crater and compare this with the lateral variation documented previously.

4.2 Methodology

Major and trace element data for the LB-07A core were obtained using X-Ray Fluorescence spectrometry (at the University of the Witwatersrand and Humboldt-University) and Instrumental Neutron Activation Analysis (at the University of Vienna). Platinum group element concentrations of 10 samples were obtained using Inductively Coupled Plasma Mass Spectrometry (ICP-MS) at Cardiff University. Samples with high siderophile contents were also analyzed for their Os isotope ratios at the Woods Hole Oceanographic Institution. The XRF and INAA results are presented in Appendix 4a. Platinum group element data and Os isotopic data are presented in Appendix 4b.

4.3 Major Element Compositions

The major element abundances, plotted against depth in order to investigate the respective compositions of the different lithologies, are shown in Fig. 4.1. Table 4.1 gives the overall ranges in the major element contents for the various lithologies.

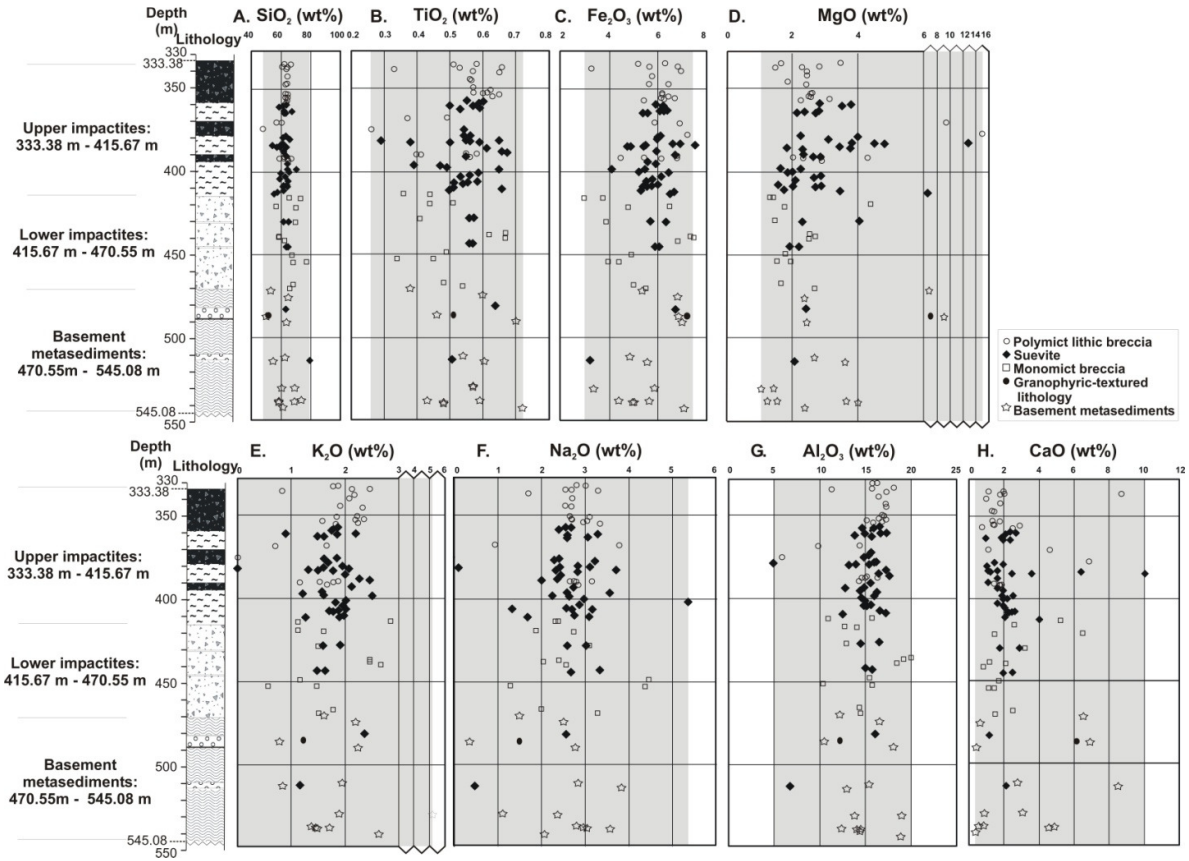

Fig. 4.1: Profiles of the abundances of the major elements A) SiO_2; B) TiO_2; C) Fe_2O_3 (total Fe); D) MgO; E) K_2O; F) Na_2O; G) Al_2O_3 and H) CaO, plotted versus depth for the LB-07A core. Data in wt%. Shading indicates the ranges of abundances for each element.

Table 4.1: Averages and ranges for major element abundances for the LB-07A polymict lithic breccias, suevites, monomict breccias and basement metasediments, as well as the major element abundances for the granophyric-textured lithology (data in wt%).

	Polymict lithic breccia (Average) n = 24	**Polymict lithic breccia (Range)**	**Suevite (Average) n = 42**	**Suevite (Range)**	**Monomict breccia (Average) n = 12**	**Monomict breccia (Range)**
SiO_2	61.5±4.19	46.4 - 66.2	62.3±4.03	53.8 – 70.0	65.9±6.36	56.0 – 77.0
TiO_2	0.53±0.11	0.26 – 0.66	0.55±0.07	0.38 - 0.67	0.49±0.11	0.34 - 0.67
Al_2O_3	15.1±2.67	6.0 – 17.7	14.7±2.30	5.0 - 17.0	14.8±0.30	10.9 -19.0
Fe_2O_3*	5.98±0.86	3.3 - 7.5	5.87±0.76	4.7 - 7.5	5.13±1.51	3.0 - 7.4
MnO	0.05±0.02	0.03 - 0.14	0.06±0.02	0.02 - 0.12	0.05±0.02	0.03 - 0.12
MgO	3.54±2.94	1.5 – 15.0	3.04±1.82	1.6 - 12.7	2.08±0.88	1.3 - 4.4
CaO	2.27±1.86	0.8 - 8.6	2.35±1.57	0.95 - 10.1	2.37±1.59	0.8 - 6.5
Na_2O	2.64±0.78	0.9 –3.8	2.63±0.81	0.11 - 5.4	2.62±0.95	1.3 - 4.5
K_2O	1.76±0.58	d.l. - 2.3	1.73±0.43	d.l. - 2.5	1.73±0.72	0.57 - 2.9
P_2O_5	0.10±0.02	0.05-0.14	0.11±0.07	0.04 -0.43	0.09±0.03	0.06 - 0.14
LOI	5.98±3.22	3.6-17.2	6.19±2.32	2.7 -15.1	3.96±1.81	2.1 - 4.9

	Basement meta-greywacke (Average) n = 3	**Basement meta-greywacke (Range)**	**Basement shale (Average) n = 11**	**Basement shale (Range)**	**Granophyric-textured lithology n = 1**
SiO_2	56.7±6.35	49.7 – 62.2	62.7±6.31	52.7 – 73.3	51.2
TiO_2	0.49±0.04	0.46 – 0.54	0.56±0.10	0.38 - 0.72	0.51
Al_2O_3	13.1±2.48	10.4 – 15.2	15.0±2.44	12.1 - 18.7	12.1
Fe_2O_3*	5.58±1.12	4.5 – 6.9	5.58±1.13	3.4 - 7.1	7.2
MnO	0.08±0.03	0.05 - 0.11	0.06±0.03	0.03 - 0.11	0.12
MgO	5.20±3.57	2.7 – 9.3	2.66±1.62	1.0 – 6.6	6.8
CaO	4.85±2.06	2.8 – 6.9	2.53±2.80	0.4 - 8.5	6.2
Na_2O	2.08±1.49	0.4 – 3.0	2.61±0.83	1.1 - 3.8	1.5
K_2O	1.39±0.58	0.8 – 1.9	2.06±1.15	0.8 - 5.2	1.2
P_2O_5	0.12±0.02	0.10 – 0.14	0.10±0.05	0.03-0.22	0.15
LOI	9.47±4.15	5.6 – 13.9	5.56±3.00	2.7-12.3	12.3

** All Fe as Fe_2O_3.*

4.3.1 Polymict Lithic Breccias

The polymict lithic breccias have TiO_2 and K_2O contents within small ranges, with few outliers (see Table 4.1; Fig. 4.1 B, E; Appendix 4a). The SiO_2 contents vary between 46.4 and 66.2 wt%, and show little extraordinary scatter (Fig. 4.1 A). The Al_2O_3 contents show a fair amount of scatter (Fig. 4.1 G). The CaO contents vary mainly between 0.76 and 2.89 wt%, with a maximum of 8.59 wt % - owing to the combined presence of anorthite as well as calcite in this specific sample (Fig. 4.1 H). The Na_2O contents vary between 0.94 and 3.78 wt% (Fig. 4.1 F). The Fe_2O_3 (all Fe calculated as Fe^{3+})

contents vary between 3.26 and 7.53 wt%, and positively correlate with MgO values (between 1.5 and 15.0 wt%; Fig. 4.1 C, D). The MnO and P_2O_5 values both vary within small ranges: MnO values vary between 0.03 and 0.14 wt%, with most samples having values lower than 0.06 wt%; P_2O_5 contents vary between 0.05 and 0.14 wt%, with the majority of samples varying between 0.10 and 0.14 wt% (see Table 4.1, Appendix 4a).

4.3.2 Suevites

The majority of the SiO_2 contents for the suevites are in the range from 53.76 to 66.21 wt%, which is similar to that of the polymict lithic breccias, although a few more siliceous suevite samples (up to 70 wt%; Fig. 4.1 A) are in evidence. The TiO_2, K_2O and Fe_2O_3 contents vary within ranges similar to those of the polymict lithic breccias (Fig. 4.1 B, C, E). The highest Fe_2O_3 values could not be correlated with high shale contents (only a weak correlation with some samples could be made), so it is clear that another component is controlling the Fe_2O_3 composition, such as the variable sulphide or mica contents (Fig. 4.2 A). MgO contents are again correlated positively to the Fe_2O_3 contents. The Al_2O_3 values range from 12.44 to 17.04 wt% (Fig. 4.1 G), with a single outlier at 5.02 wt% (within a sample of high carbonate content). The CaO contents are highly variable and the full range is between 0.95 and 10.06 wt% (high values corresponding to high calcite contents), with most values lying in the range of 0.95 to 2.89 wt% - which is comparable to the values observed for the polymict lithic breccias (Fig. 4.1 H). The Na_2O abundances vary between 0.11 and 5.38 wt%, with most values falling into the range of 0.11 to 3.71 wt% (Fig. 4.1 F). These fluctuations are related to feldspar abundance, which varies between 0.7 and 8.5 vol% in the suevite samples (Table 3.2). As with the polymict lithic breccias, the MnO contents vary in a small range: 0.02-0.12 wt%. The P_2O_5 values vary between 0.04 wt% and 0.37 wt%.

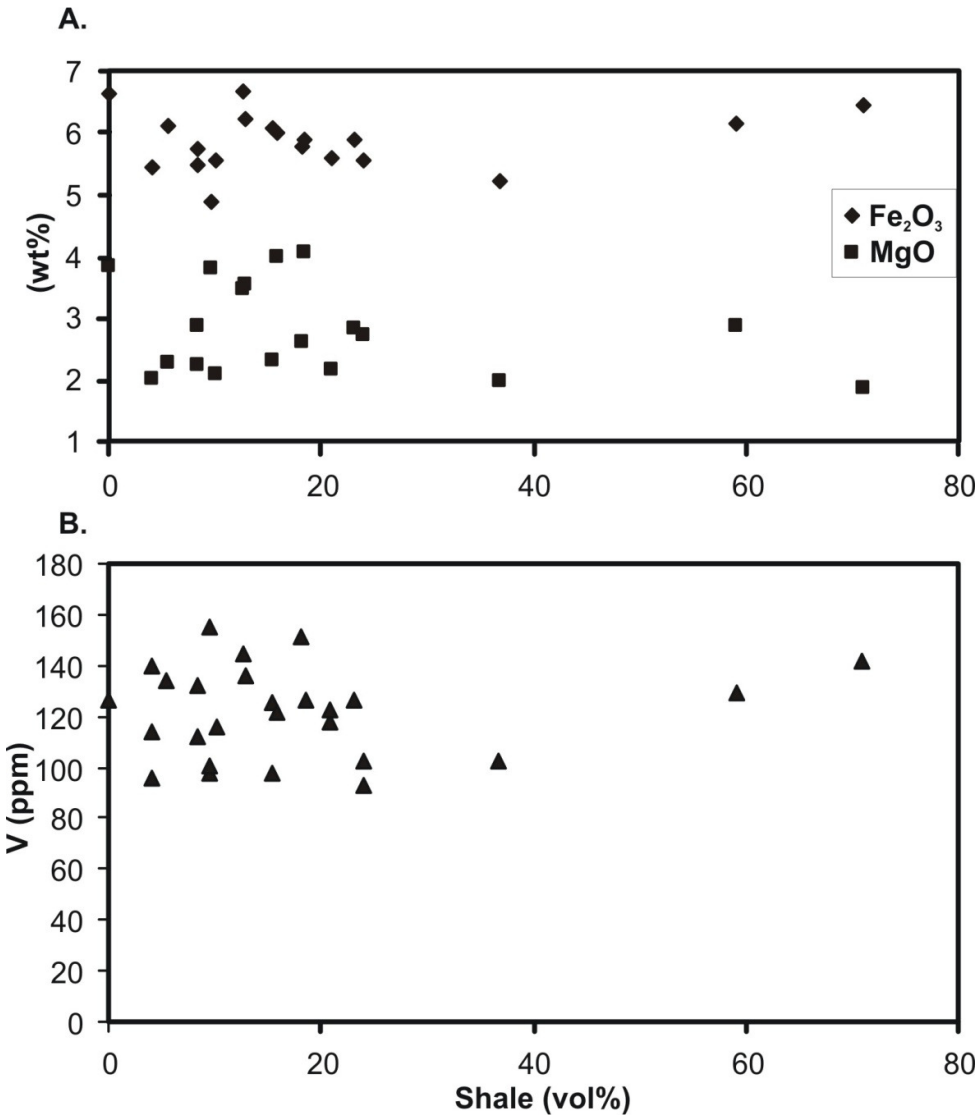

Fig. 4.2: Shale (vol%; determined from modal point-counting) vs. A) Fe_2O_3 and MgO contents (in wt%) and B) V contents (in ppm) for suevites from the LB-07A core.

4.3.3 Monomict Breccias

In the monomict breccias (lower impactites) SiO_2 content varies between 56.01 and 76.95 wt% (Fig. 4.1 A), which is a slightly wider range than that for the polymict impact breccias of the upper impactites. K_2O and TiO_2 values are similar to those observed for the upper impactites (Fig. 4.1 B, E). The Al_2O_3 contents vary between 10.90 and 18.96 wt%, which is the same range as observed for the basement lithologies (see 4.3.4; Fig. 4.1 G), but a smaller range than that seen for the suevites and polymict lithic breccias. As with the

other lithologies, CaO contents show extensive variation – mostly from 0.82 to 2.10 wt%, to a maximum value to 6.48 wt% (corresponding again to high calcite contents; Fig. 4.1 H). The Fe_2O_3 abundances of monomict breccias show the most scatter out of all the lithologies (Fig. 4.1 C). The Na_2O and MgO contents vary within a much smaller range than seen for the polymict breccias (Fig. 4.1 D, F). The monomict breccias have similar ranges of MnO (0.03 – 0.12 wt%) and P_2O_5 (0.06 – 0.14 wt%) to the polymict lithic breccia (see Table 4.1).

4.3.4 Basement Lithologies

In the basement rocks the SiO_2 as well as K_2O contents vary within significantly larger ranges than those for the impactites (Table 4.1; Fig. 4.1 A, E); however, the bulk of the values fall into ranges similar to those for the impactites. No correlation of K_2O contents with LOI values exists – which indicates that a significant proportion of carbonate must be responsible for the high LOI values (Fig. 4.3), in addition to other minerals which would contribute to the total LOI content, such as the hydrous ferromagnesian minerals (e.g., phyllosilicates, amphibole). Amphibole (specifically hornblende) has been noted in one of the metagreywacke dominated samples (KR7-31), and the geochemical signature of this sample indicates a slight enrichment in K_2O and Na_2O relative to other basement metasediments. It was suggested that this sample represented a poorly preserved granite dyke (see section 3.2.3) but the geochemical signature of this sample (Appendix 4a) does not support this – it is most similar to the regional chemical signature of the phyllite-greywackes rather than to those of the granite dykes and the altered Pepiakese granite (Koeberl et al., 1998), so it is concluded that the sample must have contained a granite-derived fragment in a metagreywacke.

The CaO contents vary between 0.39 and 8.49 wt%, similar to the overall range in the other lithologies (Fig. 4.1 H). The altered shales

have lower SiO_2, Al_2O_3, Na_2O and P_2O_5, and higher Fe_2O_3, MnO, MgO and K_2O contents than the metagreywackes (Appendix 4a). This agrees with the observations made by Koeberl et al. (1998) for phyllite samples from their regional study.

4.3.5 Granophyric-Textured Lithology

The granophyric-textured lithology at 487.12 m depth has a distinct chemical signature. It has low SiO_2, Na_2O and K_2O abundances together with notably higher CaO (6.16 wt%; correlated with a high LOI of 12.30 wt%; Fig. 4.3), Fe_2O_3 and MgO contents, in comparison to the overall major element compositions of the basement rocks (Fig. 4.1 A, C, D, E, F, H). The Al_2O_3, TiO_2, MnO and P_2O_5 contents are within the overall ranges observed for the other basement lithologies (Fig. 4.1 B, G).

4.3.6 Comparison of Upper and Lower Suevite Occurrences

In general, the suevites show similar geochemical signatures (Fig. 4.1). The lowermost suevite intercalation in the basement metasediments (at 513.90 m depth) has comparatively higher SiO_2 and lower Al_2O_3, Fe_2O_3, Na_2O, K_2O and P_2O_5 contents than the average (see Fig. 4.1 and Appendix 4a) suevite values. The major element compositions of the lower impactite (at 430.03 m and 445.13 m depth) and upper basement (at 483.00 m depth) suevites fall within the ranges for the upper impactite major element signatures, which agrees with the observations (see Table 3.2) of similar metagreywacke, shale and phyllite contents. The lowermost suevite consists mostly of granophyric-textured clasts and muscovite. Very little metagreywacke and a near-complete absence of shale characterise this suevite.

4.3.7 Hydrothermal Alteration

In order to further constrain the extent of hydrothermal alteration in core LB-07A, as indicated by the presence of post-impact carbonate, plots of LOI versus CaO (Fig. 4.3 A) and K_2O (Fig. 4.3 B) contents

were made. Most of the samples have CaO contents in the range 0.5–3 wt% and LOI contents between 2 and 9 wt%. However, some outliers exist, and these high CaO contents correlate with relatively high LOI contents. These high CaO contents together with high LOI values are evident in all lithologies throughout the core.

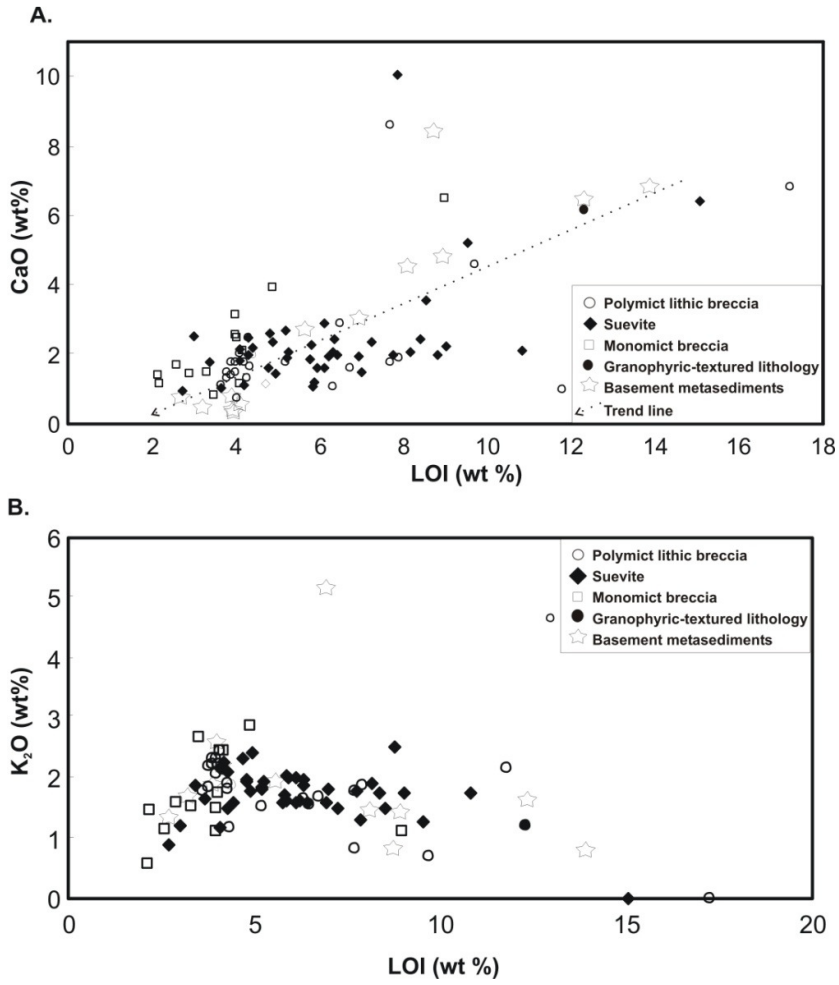

Fig. 4.3: A) CaO content and B) K_2O content versus Loss on Ignition (LOI) for the impactites and basement metasediments of LB-07A core. All data in wt%.

If these signatures represent the effect of post-impact carbonate precipitation from hydrothermal solutions, this indicates that hydrothermal alteration did take place throughout the LB-07A core (rather than in isolated lithologies). This is supported by petrographic findings (macroscopic and microscopic carbonate segregations, veins and pods; see section 3.1.2). Care was taken to separate any

> 2 cm sized carbonate pods (Fig. 3.6 B) from the samples crushed for geochemical analysis to ensure that the CaO results are representative of the bulk rock composition, rather than an artifact of random sampling of isolated carbonate-rich areas. However, it was impossible to separate thin (mm-wide) pre- and post-impact carbonate bands and small (< 0.5 cm) carbonate pods that are present locally in the target rock, sometimes in significant amounts (up to 16.4 vol%, see Table 3.2).

A small number of samples from all lithologies have high CaO and moderate LOI values and seemingly form a negative trend (indicted by trend line) in Fig. 4.3 A. This feature is most likely related to the presence of the feldspar (in particular plagioclase) in metagreywacke, which would result in a contribution of CaO content but no contribution to the LOI signature.

There are two cases (polymict lithic breccia sample KR7-2 from 339.22 m depth and suevite sample KR7-6 from 360.65 m depth) where LOI contents are relatively high (>10 wt%) but CaO contents are low (2 wt% or less). This implies that the total LOI values do not always relate only to CO_2, but other sources of secondary volatiles (e.g., SO_x from sulphide, H_2O and hydroxide from alteration phases, primary target rock minerals, and post-impact phyllosilicates) should be taken into consideration. Petrographic analysis (see Chapter 3) indicates that the LOI contents may be related to H_2O from alteration phases (e.g., chlorite, sericite) and other phyllosilicates, as these minerals are in evidence throughout the core. In order to check this, a plot of K_2O versus LOI was made (Fig. 4.3 B), and some correlation is evident, but clearly indicative that phyllosilicate contents are not the sole control factors. The two samples in which LOI contents are high but CaO contents are low contrast with the other samples with high LOI contents in that they have minor carbonate (<1 vol%) and abundant phyllite and mica-rich schist (> 30 vol%) clasts.

4.3.8 Polymict Lithic Breccia *vs.* Suevite Compositions

Similar ranges of abundances are seen for the polymict lithic breccia and suevite with respect to SiO_2, TiO_2, Al_2O_3 and CaO contents (higher maximum values for the suevite samples). Both polymict breccia types also have similar K_2O and Na_2O contents. More variation in Fe_2O_3 content is observed in the polymict lithic breccias as opposed to the suevites. Comparable variation is observed for the MgO contents in both polymict breccias, and this element shows the largest overall variation in the borehole. No correlation with the amount of shale, or total phyllosilicates, in the breccias can be made, and it is probable that a combination of minerals controls the geochemical signature. The MnO content variance is almost the same for both data sets, and the P_2O_5 values have a slightly larger range for the suevites than the polymict lithic breccias (see Table 4.1).

4.3.9 Polymict Breccia (Upper Impactites) *vs.* Monomict Breccia Compositions

The range of SiO_2 values of the monomict breccias are only slightly higher than that of the suevites. The TiO_2, CaO and K_2O abundance ranges are the same for both the polymict and monomict breccias. The range in Al_2O_3 contents observed for the monomict breccias is similar to that of the upper impactites. The Na_2O contents vary within a smaller range for the monomict breccias than for the polymict breccias. Very little variation in the monomict breccias occurs in MgO contents compared to the polymict breccias. Overall, there is generally more scatter of abundances for the monomict breccias than for the polymict breccias.

4.3.10 Monomict Breccia *vs.* Basement Lithology Compositions

The SiO_2, Al_2O_3, CaO and TiO_2 contents are similar for the monomict breccias and the basement lithologies. Abundances of Na_2O, K_2O and MgO show wider scatter in the basement lithologies, whereas the Fe_2O_3 content has more scatter in the monomict breccias.

Considering that both sequences are made up of the same lithologies, although locally at different proportions, this overall similarity is not surprising.

4.3.11 Matrix Compositions

The composition of the matrix was studied here using geochemistry as this is extremely fine-grained and cannot be resolved with the petrographic microscope (see section 3.2.1). The composition of the matrix samples were initially studied using XRD. Clasts (>0.5 cm) were separated from their matrices in a number of breccia samples and a bulk sample and the corresponding "clast-free" sample were analysed using XRD. No differences could be ascertained between the two samples. It was then decided to use defocused electron microprobe analysis of matrices of two polymict breccia samples (KR7-54, polymict lithic breccia, 334.48 m; KR7-6, suevite, 360.65 m) from the upper impactites in order to obtain major element compositions of the matrix. A number of spots (10 µm diameter) across the samples (chosen as traversing more matrix than clasts) were analysed, and points intersecting clasts larger than 50 to 100 µm were discarded. All samples with totals lower than 90 wt% were discarded as these were interpreted to have intersected holes in the thin section. Unfortunately, due to the porous nature of the thin sections, this yielded 90% of the data invalid. The remaining data is reported in Table 4.2. The compositional ranges of the data (plotted in Fig. 4.4; Table 4.2) of the polymict lithic breccia and suevite are comparable and indicate that the matrix consists primarily of fine-grained quartz, alkali feldspar, biotite, chlorite and other phyllosilicates. It is also clear that a number of the compositions represented by the matrix are more similar to mixes of minerals – some compositions are directly comparable to the mineral compositions of granite and shale (Fig. 4.2 A). These compositions most likely represent microscopic melts (c.f. section 3.1.2; Fig. 3.12).

Table 4.2: Compositional data (major elements, all data in wt%) from defocused electron microprobe analysis of matrix from two breccia samples from the upper impactites.

	SiO_2	TiO_2	Al_2O_3	CaO	MgO	K_2O	Na_2O	FeO	MnO	Total
KR7-6	99.36	0.01	0.04	0.03	0.02	0.03	0.02	0.28	0.00	99.79
KR7-6	24.99	0.01	23.16	0.10	10.65	0.27	0.36	31.38	0.08	91.00
KR7-6	93.69	0.03	0.18	0.03	0.00	0.13	0.27	0.06	0.01	94.41
KR7-54	91.70	0.02	0.04	0.03	0.00	0.03	0.05	0.00	0.02	91.90
KR7-54	73.43	0.04	14.52	0.26	0.04	0.03	8.80	0.01	0.02	97.15
KR7-54	93.79	0.00	1.18	0.04	0.04	0.23	0.07	0.17	0.00	95.51
KR7-54	89.84	0.03	0.18	0.02	0.06	0.07	0.07	0.23	0.00	90.49
KR7-54	84.61	0.00	3.88	0.08	1.02	0.06	1.00	2.80	0.00	93.44
KR7-54	45.90	0.12	24.27	0.07	4.25	2.16	4.18	11.77	0.02	92.74
KR7-54	97.68	0.01	0.01	0.03	0.01	0.00	0.01	0.09	0.00	97.83
KR7-54	45.46	0.00	21.09	0.30	5.81	0.03	6.30	14.46	0.04	93.48
KR7-54	92.33	0.01	0.23	0.07	0.09	0.02	0.03	0.29	0.00	93.06
KR7-54	96.20	0.01	0.05	0.04	0.01	0.02	0.04	0.12	0.00	96.48
KR7-54	86.74	0.91	4.10	4.63	0.03	0.01	0.04	1.25	0.02	97.74
KR7-54	95.98	0.00	0.11	0.01	0.01	0.03	0.03	0.02	0.00	96.19
KR7-54	94.16	0.05	2.40	0.02	0.20	0.56	0.03	0.74	0.00	98.16
KR7-54	92.38	0.00	1.25	0.08	0.02	0.04	0.8	0.15	0.00	94.71
KR7-54	97.17	0.00	0.05	0.00	0.02	0.00	0.03	0.05	0.00	97.32

4.3.12 Alteration of the Impactites

The Chemical Index of Alteration (CIA; Nesbitt and Young, 1982) was calculated for the XRF analyses for the impactites. The CIA is calculated as $[Al_2O_3/(Al_2O_3+K_2O+Na_2O+CaO)]*100$, where a ratio of 100 represents the most altered material.

The CIA values (Fig. 4.5) indicated no substantial differences between the various impactites. The results show that most samples are indeed altered. However, the pre-impact and post-impact alteration cannot be distinguished using this index. There is little change of the CIA with depth (Fig. 4.5) – the only trend that can be identified is a slight increase in the upper impactites towards the top of the core – this would be related to possible alteration on and just beneath the lake beds.

4.4 Trace Element Characteristics

All eighty-six samples from core LB-07A were analyzed by XRF and INAA for their trace element contents (Appendix 4a). Selected trace element values have been plotted against depth in Figure 4.6.

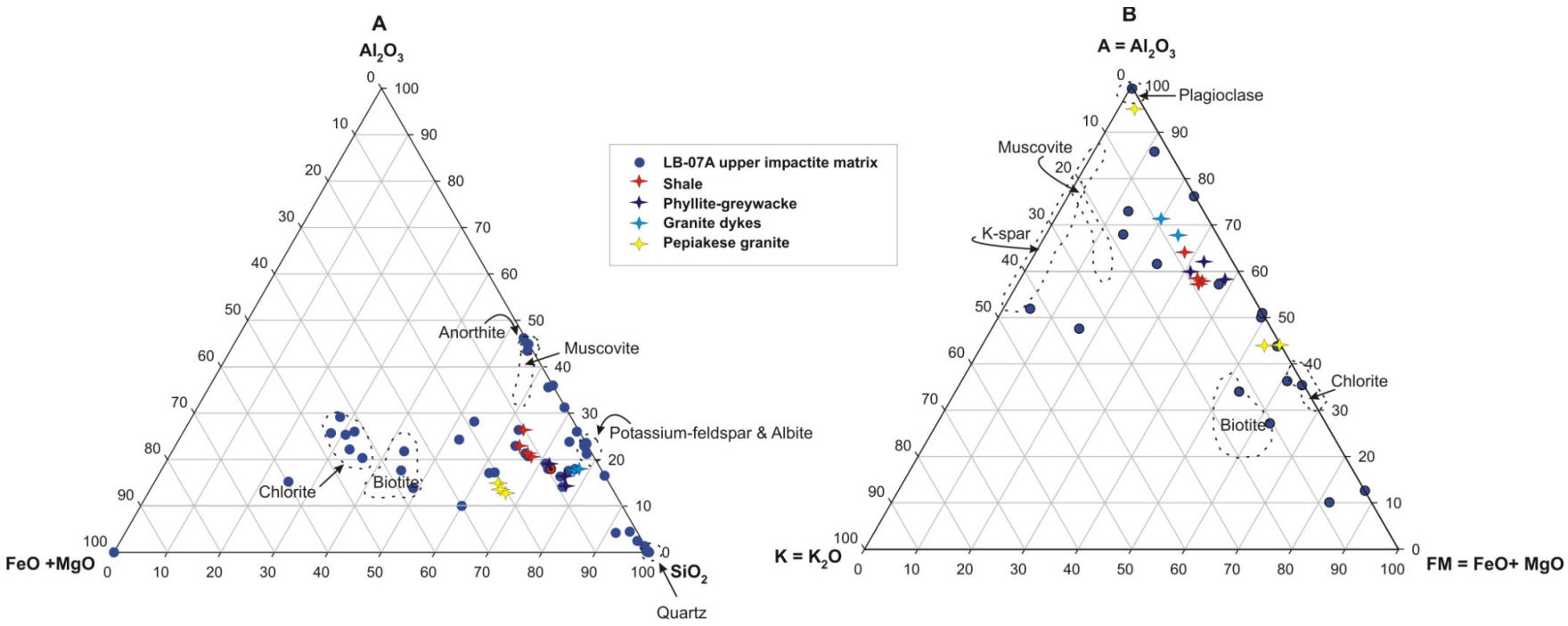

Fig. 4.4: Ternary discrimination diagrams for the electron microprobe analyses (10 µm defocused beam) of matrix of upper impactite polymict breccia samples from core LB-07A. A) Al_2O_3-(FeO+MgO)-SiO_2. B) AK(FM). Fields for common minerals in the LB-07A core are indicated (after Deer et al., 1971). Average target rock compositions (phyllite-greywacke, shale, granite dykes, Pepiakese granite; after Koeberl et al., 1998) are also plotted.

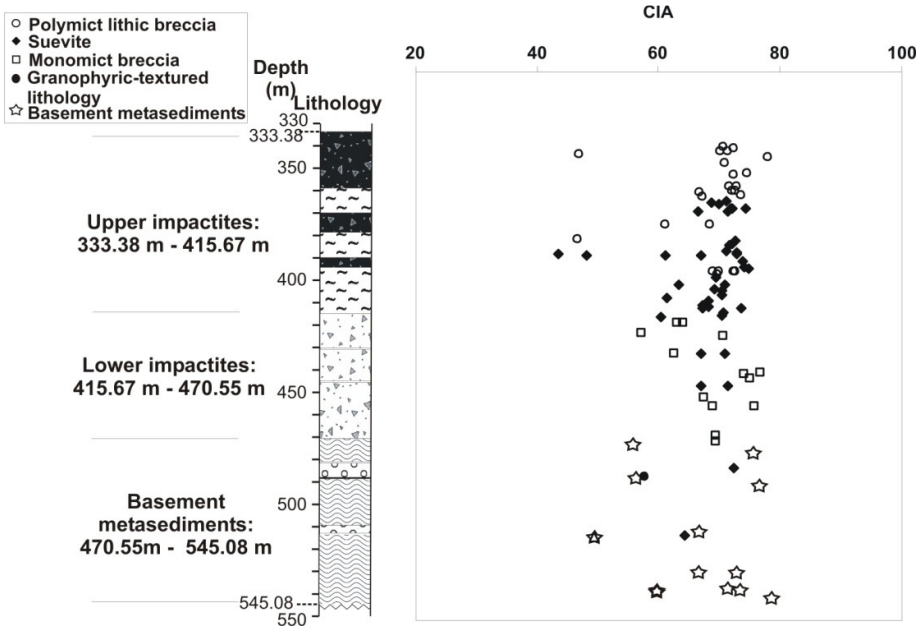

Fig. 4.5: Chemical Index of Alteration calculated from XRF analyses of LB-07A core samples.

Niobium, Br, and Y values are generally either below the respective detection limits or very low (close to the limit of detection), and thus indicate that these elements are present only as minor substitution components for major elements in the common mineral phases (e.g., feldspars, phyllosilicates, oxides) or in trace minerals.

4.4.1 Polymict Lithic Breccias

The polymict lithic breccias show narrow ranges in concentration for Rb, Zr, Sr and V (Fig. 4.6 D-F). The concentration range for V in the polymict lithic breccia is larger than that observed for the suevites. Much scatter is seen in Ba content. The chalcophile elements Zn and Cu show much scatter throughout the sequence. Nickel, Co and Cr values vary within small ranges (Fig. 4.6 A-C), and only two samples show substantially higher concentrations (at 370.39 and 377.46 m depth), which are associated with higher siderophile element variations (i.e., Fe_2O_3 and MgO contents). These two samples also show substantial enrichment in As (401 ppm and 728 ppm, respectively; Appendix 4a). It is thought that these enrichments might be caused by the presence of arsenopyrite or other sulphides;

however, the only phase that has been optically identified in these samples (less than 50 μm in size) is pyrite.

4.4.2 Suevites

The suevites have similar geochemical signatures to the polymict lithic breccias. Little variation is seen for Rb, Zr and V, with much scatter observed in Sr, Ba, Zn and Cu values (Fig. 4.6 D-F). As with the polymict lithic breccias, the Ni, Co and Cr contents are positively correlated (Fig. 4.6 A-C).

Only a few outliers with very high Ni and Co abundances are observed. Interestingly, these very high Ni abundances correlate with different major element abundances. The first, at 383.74 m depth, coincides with very high MgO contents (12.07 wt%), but only moderate Fe_2O_3 contents. This may reflect enrichment of the sample with Fe-poor (phlogopitic) biotite, occurrences of which have been observed in the LB-07A core.

The second, at 398.44 m depth, correlates with no specific major element enrichment except for Al_2O_3. This sample shows some evidence of hydrothermal alteration, which would leach most major elements except for Al_2O_3. However, this section contains arsenopyrite and pyrite, both of which would potentially result in an enrichment of Ni. The third enrichment of Ni, at 413.14 m depth, correlates with high Fe_2O_3 and MgO contents.

4.4.3 Monomict Breccias

The monomict breccias show more variation in Rb, Sr and Zr concentrations than the upper impactite polymict breccias (Fig. 4.6 D-F; Appendix 4a). The monomict breccias have no substantially elevated concentrations in the siderophile elements, and very little variation is observed throughout this part of the sequence (see Fig. 4.6 A-C).

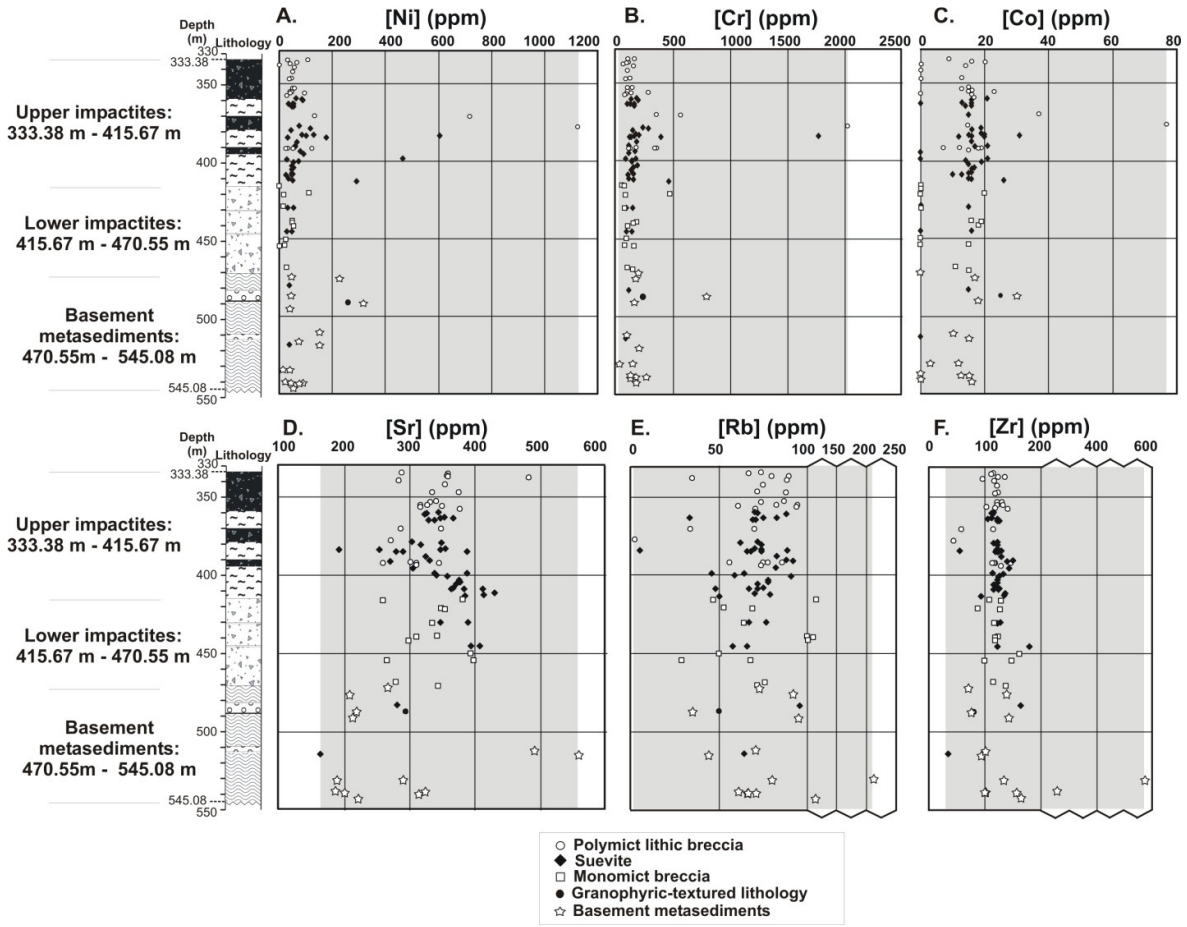

Fig. 4.6: Profiles of the abundances of the trace elements A) Cr; B) Ni; C) Co; D) Rb; E) Sr and F) Zr, plotted versus depth for the LB-07A core. Shading indicates the ranges of abundances for each element. All data in ppm.

The range for V is the largest seen throughout the core, with a few samples with substantially lower V concentrations than those observed for the upper impactite breccias (see Appendix 4a). This is thought to represent a consequence of the lack of Fe-rich lithologies (with which V would be commonly associated).

4.4.4 Basement Lithologies

The basement lithologies show the most scatter in the contents of Rb, Sr, Zr, Ba and Y out of all the lithologies analysed (Fig. 4.6 D-F; Appendix 4a). Rubidium, Ba and Cs concentrations are highest in the basement lithologies, which likely corresponds to local enrichment in feldspar (e.g., Rollinson, 1993), although owing to the disaggregated state of the core this cannot be conclusively confirmed. One sample (KR7-46; sample depth 530.63 m) contains a substantial relative enrichment in Zr (580 ppm, compared to a range of ca. 90 – 150 ppm for the other basement lithologies), coincident with elevated Ba, Y and Hf concentrations. This most likely represents random sampling of zircon or other accessory minerals, although again this cannot be conclusively confirmed; zircon has been noted only rarely during this study. Vanadium concentrations are variable, similar to those in the polymict breccias. As noted above, V concentrations vary widely throughout the core, and this is most likely a reflection of variation in the abundance of organic-rich shale. Vanadium concentrations have been plotted against shale values in Fig. 4.2 B, and it is apparent that all samples containing shale have consistently high V concentrations, showing that V is concentrated in this phase.

4.4.5 Granophyric-Textured Lithology

The granophyric-textured lithology is characterised by higher Ni, Cr and Co than the majority of the LB-07A samples (Ni contents for the granophyric-textured lithology are higher than 93% of all samples of LB-07A core; Cr contents are higher than 87% of all samples, and Co contents are higher than 94% of all samples; Fig. 4.6 A-C). The

lithophile element abundances of Rb, Sr, Zr and V are all within the range of the impactites (Fig. 4.6 D-F), which reflects the similar mineral composition of the granophyric lithology to the rest of core LB-07A.

4.4.6 Rare Earth Element Data

Rare earth element (REE) data were obtained for 60 samples using INAA (Appendix 4a). The REE concentrations were normalized to the composition of C1 chondrites after Taylor and McLennan (1985). Selected patterns are shown in Fig. 4.7; the impactites all have very similar normalized REE abundances. The normalized data range for most of the sample suite is similar to the values recorded by Koeberl et al. (1998) for the target rock lithologies.

Figure 4.7 shows that the light REE are consistently significantly enriched. Variable Eu anomalies are present throughout the LB-07A core. For example, in Fig. 4.7 B, a positive Eu anomaly is observed for the sample at 364.45 m depth, whereas a distinct negative Eu anomaly is observed for the sample at 360.65 m depth. Most calculated Eu anomaly values (Eu/Eu*) are less than or equal to 1 (Appendix 4a). No correlation can be made between lithology and Eu anomaly, as these may be positive or negative for the same lithology (e.g., metagreywacke) and are most likely related to variable plagioclase contents. Selected samples show very weak Ce anomalies (Appendix 4a). Slight negative Eu and Ce anomalies were also found by Koeberl et al. (1998) in their shale, greywacke and phyllite samples. One basement rock sample of our suite (sample KR7-46, 530.63 m depth) showed significantly higher REE abundances (Fig. 4.7 D), and this sample also showed enrichment in K_2O, as well as Zr, Hf and U, which could mean that the sample is enriched in zircon, as suggested in section 4.4.4. Unfortunately, only a powder mount of this sample could be examined, and the only rock fragments in evidence are altered shale, metagreywacke, and a little carbonate.

No distinct differences were noted with increasing depth, or between the upper impactites, lower impactites and basement metasediments. When the ratios of La/Th (Fig. 4.7 E) and La/Lu (Fig. 4.7 F) are plotted with depth, some scatter is observed for both ratios; average values for La/Lu are ~6, and for La/Th are ~70. The suevites of the upper impactite and the lower impactite cannot be discriminated with respect to their REE signatures and the uppermost basement suevite also falls into the range of REE signatures observed for these impactites. However, the lowermost basement suevite displays a substantially different REE signature; it is less enriched in the REEs than those suevites above it. Additionally, it has higher La/Th (100) and La/Lu (6.62) ratios than the other suevites (Fig. 4.7 E, F). This sample shows evidence of alteration, and a predominance of granophyric-textured fragments. The La/Lu ratio is equivalent to that calculated for the granophyric-textured lithology (Fig. 4.7).

4.5 Cluster Analysis

In order to further process the chemical data, and identify differences between the impactites and basement metasediments which are not readily apparent using 3 variables (i.e., triangular plots), cluster analysis was employed. In this case, all samples ("cases") from the LB-07A core were assessed using the Clustan Graphics 7 software (Wishart, 1997). The data were entered as continuous data, and no weighting was given to any sample. A Z-score transformation was utilized and the data were clustered according to their k-means (MacQueen, 1967), using the Euclidean Sum of Squares.

The cluster analysis employed a combination of 26 major and trace elements. The trace elements were chosen according to those where the majority of the LB-07A samples had values higher than the detection limit. Initially 10 clusters were produced, but it was apparent this was too high a number, as 6 of the groups had 6 members (i.e., samples) or less.

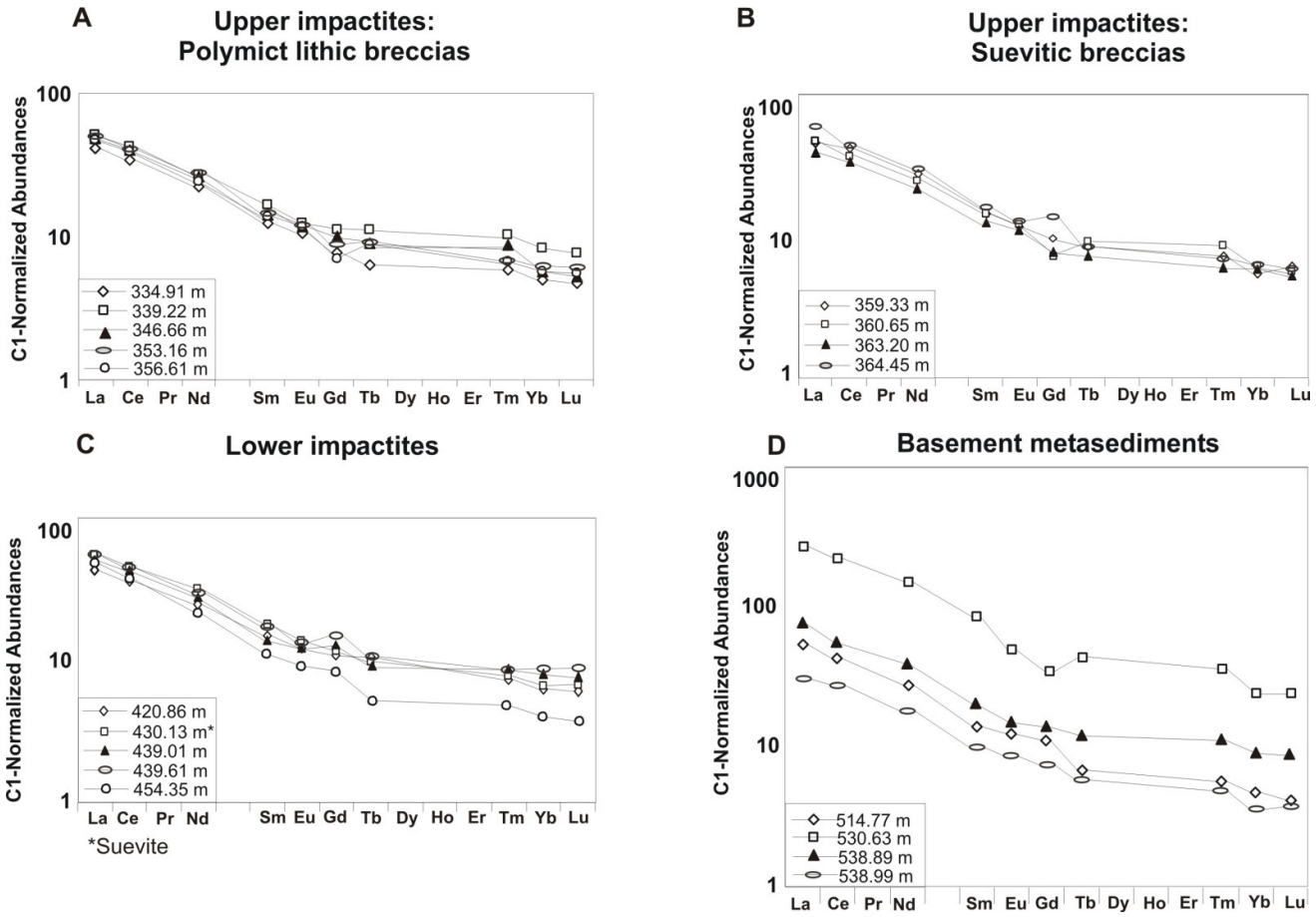

Fig. 4.7: Selected C1 chondrite-normalized rare earth element patterns (normalization factors after Taylor and McLennan, 1985). A) Upper impactite polymict lithic breccias. B) Upper impactite suevite. C) Lower impactite monomict breccias. D) Basement lithologies. Continued on next page.

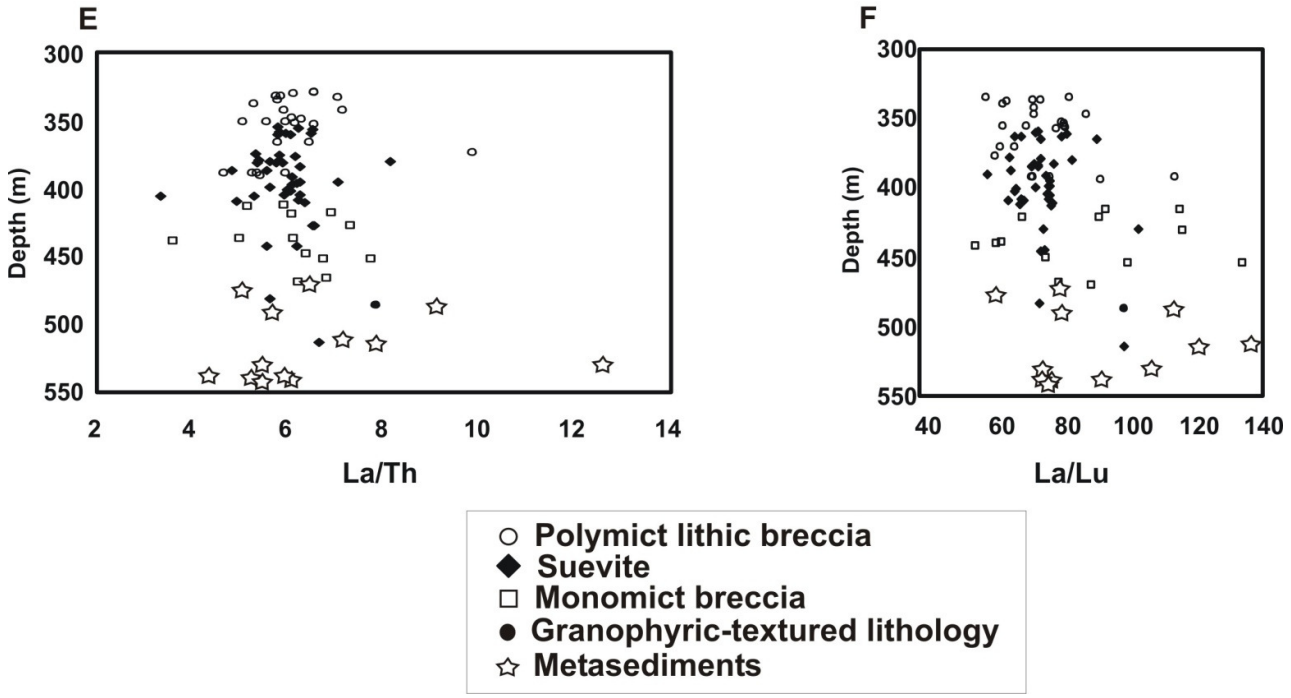

Fig. 4.7 (cont'd): E) La/Th ratios for all samples against depth. F) La/Lu ratios for all samples against depth.

Thus, it was decided to refine the cluster analysis to produce 5 clusters, and even here one group with only 3 members was produced. The results are reported in Table 4.3.

It is immediately apparent from the cluster analysis that the rocks are well-homogenised (Table 4.4), as the data clusters mostly show a variety of lithologies, except for group 5. In some cases (KR7-7, KR7-11, KR7-36, KR7-43, KR7-52), more than 1 part of a sample was analysed – and interestingly, in some cases (i.e., samples KR7-43, KR7-52, KR7-41) not all powders from the individual sample plotted into the same cluster, indicating intra-sample heterogeneity. It has already been emphasized that these samples, being breccias, are heterogeneous with regards to clast size and type variation, which would be responsible for these differences. From Table 4.3 it is evident that few differences do, in fact, exist between the major element components of the groups, but small differences are apparent. In order to investigate this further, a number of geochemical plots of the most variable elements were produced (Fig. 4.8).

Figure 4.8 highlights the differences that exist between the different clusters. In terms of trace elements, it can be observed that cluster 5 is relatively less depleted in Co than the other 4 clusters, whereas cluster 2 is relatively more enriched in Cr (Fig. 4.8 A). Cluster 3 is relatively more enriched in Zr than the other clusters (Fig. 4.8 B), and this would be caused by enrichment of zircon.

It must be noted though, that these differences are on the order of a few percent, with a maximum of 30 %. The major elements show more definitive trends – there is a clear distinction between clusters 2, 3 and 4 in terms of Fe_2O_3 content, and clusters 1, 4 and 5 in terms of MgO content (Fig. 4.8 C).

Table 4.3: Cluster analysis results for 5 cluster groups using 93 cases (i.e., samples) and 26 variables (a combination of major and trace elements, see text for details) and the Euclidean Sum of Squares (k-means). The means, standard deviations of the groups are indicated.

	Cluster 1 (n=8)	**Cluster 2 (n=20)**	**Cluster 3 (n=16)**	**Cluster 4 (n=46)**	**Cluster 5 (n=3)**
SiO_2 (wt%)	54.2±2.8	67.7±5.0	61.1±3.1	62.4±2.1	52.2±5.2
TiO_2 (wt%)	0.48±0.07	0.5±0.06	0.7±0.04	0.6±0.04	0.3±0.06
Al_2O_3 (wt%)	12.5±1.0	13.4±2.3	17.2±1.6	15.5±1.0	6.9±2.5
Fe_2O_3 (wt%)	6.0±0.9	4.5±0.8	6.6±1.0	6.0±0.4	6.6±0.9
MnO (wt%)	0.09±0.03	0.05±0.02	0.05±0.02	0.05±0.01	0.1±0.03
MgO (wt%)	5.6±2.0	1.9±0.6	2.5±0.8	2.8±0.8	12.5±2.6
CaO (wt%)	6.8±1.7	2.5±1.7	1.3±0.7	1.9±0.6	6.0±1.2
Na_2O (wt%)	2.1±1.1	2.7±1.0	2.3±0.5	2.9±0.5	0.4±0.5
K_2O (wt%)	1.2±0.3	1.5±0.5	2.5±0.8	1.8±0.3	0.2±0.4
P_2O_5 (wt%)	0.14±0.04	0.1±0.1	0.08±0.02	0.1±0.02	0.06±0.01
Sc (ppm)	14.3±3.1	8.8±3.3	16.8±4.8	14.7±1.5	17.2±1.4
V (ppm)	112.1±27.8	92.6±20.4	143.1±21.9	122.7±12.5	89.7±6.0
Cr (ppm)	404.1±180.2	103.5±33.6	139.4±41.4	157.7±67.7	1556.7±598.4
Co (ppm)	24.0±6.9	11.3±2.5	18.6±4.5	17.1±2.5	52.7±21.0
Ni (ppm)	202.4±83.7	26.5±20.3	51.7±17.9	70.5±65.8	912.3±441.3
Cu (ppm)	4.3±12.0	23.1±17.2	37.9±11.5	34.0±14.2	65.3±40.8
Zn (ppm)	80.1±8.2	55.6±8.9	85.1±12.7	74.0±6.8	54.0±10.2
Rb (ppm)	56.0±13.6	60.2±17.0	103.6±30.4	74.0±9.9	12.7±16.0
Sr (ppm)	338.0±108.6	323.2±78.4	282.9±65.7	343.2±45.7	276.7±48.4
Zr (ppm)	91.0±16.1	125.6±39.5	163.3±112.1	123.9±13.1	53.3±7.4
Cs (ppm)	2.9±0.9	3.1±0.9	5.2±1.6	3.9±0.5	1.7±1.3
Ba (ppm)	314.4±137.3	432.3±134.2	642.8±151.1	546.0±82.1	181.7±261.9
Hf (ppm)	2.3±0.4	3.0±0.9	4.1±2.8	3.1±0.3	1.2±0.4
Ta (ppm)	0.2±0.07	0.3±0.05	0.5±0.2	0.3±0.05	0.2±0.07
Th (ppm)	2.1±0.5	2.8±0.8	4.2±1.2	3.1±0.4	1.0±0.6
U (ppm)	0.8±0.3	1.0±0.7	1.6±0.9	1.0±0.2	0.5±0.3

Table 4.4: Distribution of the LB-07A lithologies into the 5 clusters produced by cluster analysis of 93 cases and 26 variables and the Euclidean Sum of Squares (k-means). See text for details.

Cluster	# PLB	# SB	# MB	# BM	G
1 (n=8)		3	1	2	1
2 (n=20)	4	6	8	2	
3 (n=16)	2	6	3	5	
4 (n=46)	16	27	1	2	
5 (n=3)	3				

**PLB = polymict lithic breccia; SB = suevite; MB = monomict breccia; BM = basement metasediment; G = granophyric-textured lithology.*

This plot, too, emphasizes that Fe_2O_3 and MgO are not solely dependent on each other and reflect varying degrees of substitution into biotite and chlorite. The CaO contents are reasonably variable between groups, but as the groups are mixtures of various impactites (see Table 4.4), this does not argue for one impactite group containing more pre-impact calcite, or being more affected by post-impact hydrothermal alteration. K_2O content variations are very subtle, but indicate the varying feldspar contents in the various impactites. Again, though, it must be noted that these differences are on the order of 4 wt% in the case of Fe_2O_3, and that this analysis does indeed confirm the observations of the general homogeneity of the impactites.

4.6 Variations in Geochemical Characteristics Between the LB-07A Impactites and Those of the Target Rocks

Koeberl et al. (1998) calculated average compositions of their identified target rocks for the Bosumtwi structure (shale, phyllite-greywacke, granite dykes and Pepiakese granite; Table 4.5). In comparing the ranges of these rocks a number of differences to the new data sets of this study are apparent.

4.6.1 Basement Metasediments *vs.* Target Rock Types

A total of 14 LB-07A basement samples were analyzed, and these are compared to the ranges (see Table 4.5) quoted for the shales and greywacke-phyllites identified by Koeberl et al. (1998).

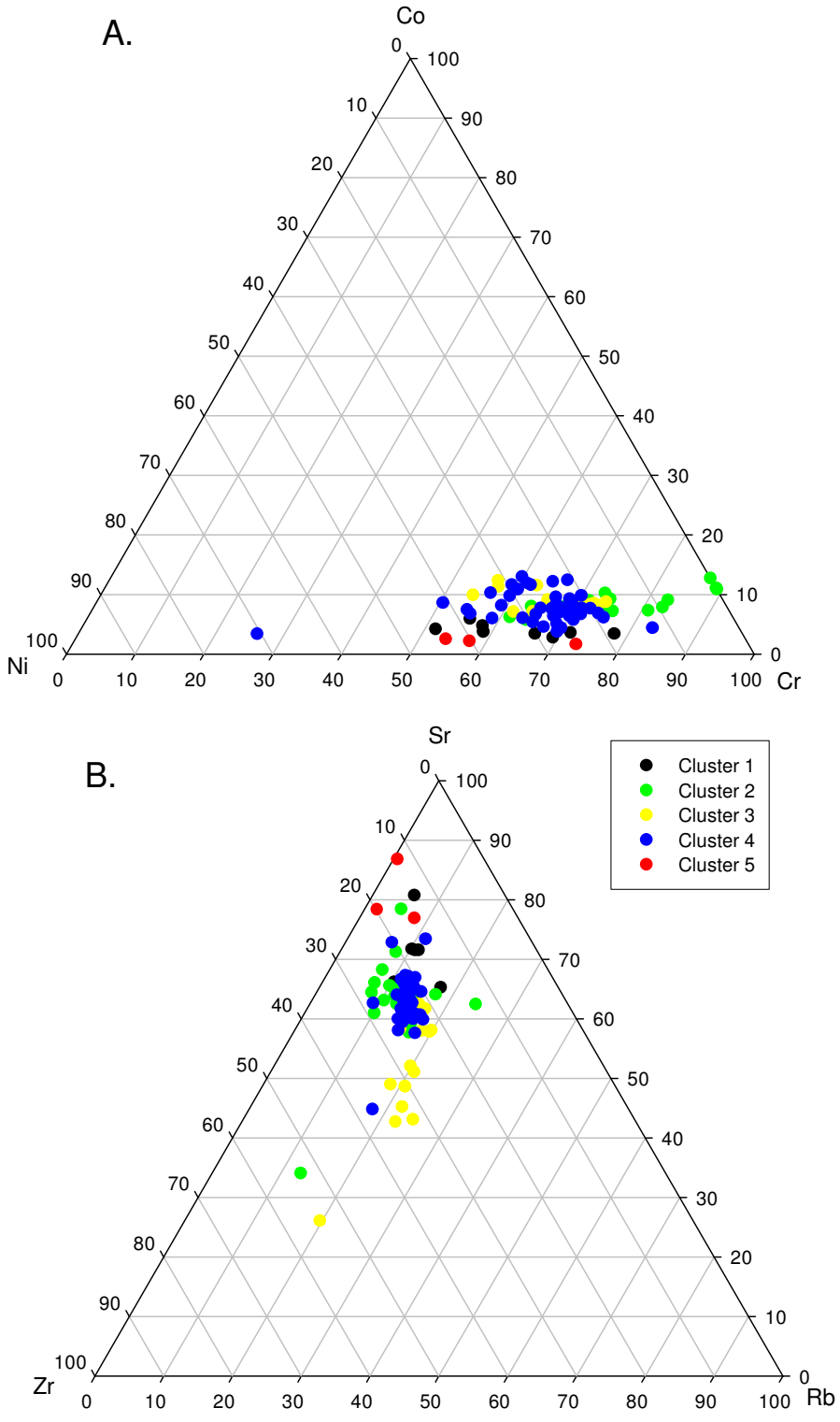

Fig. 4.8: Geochemical plots showing the results of the cluster analysis: 5 clusters produced by cluster analysis of 93 cases and 26 variables and the Euclidean Sum of Squares (k-means): A) Ternary diagram of Co-Ni-Cr. B) Ternary diagram of Sr-Zr-Rb. Continued on next page.

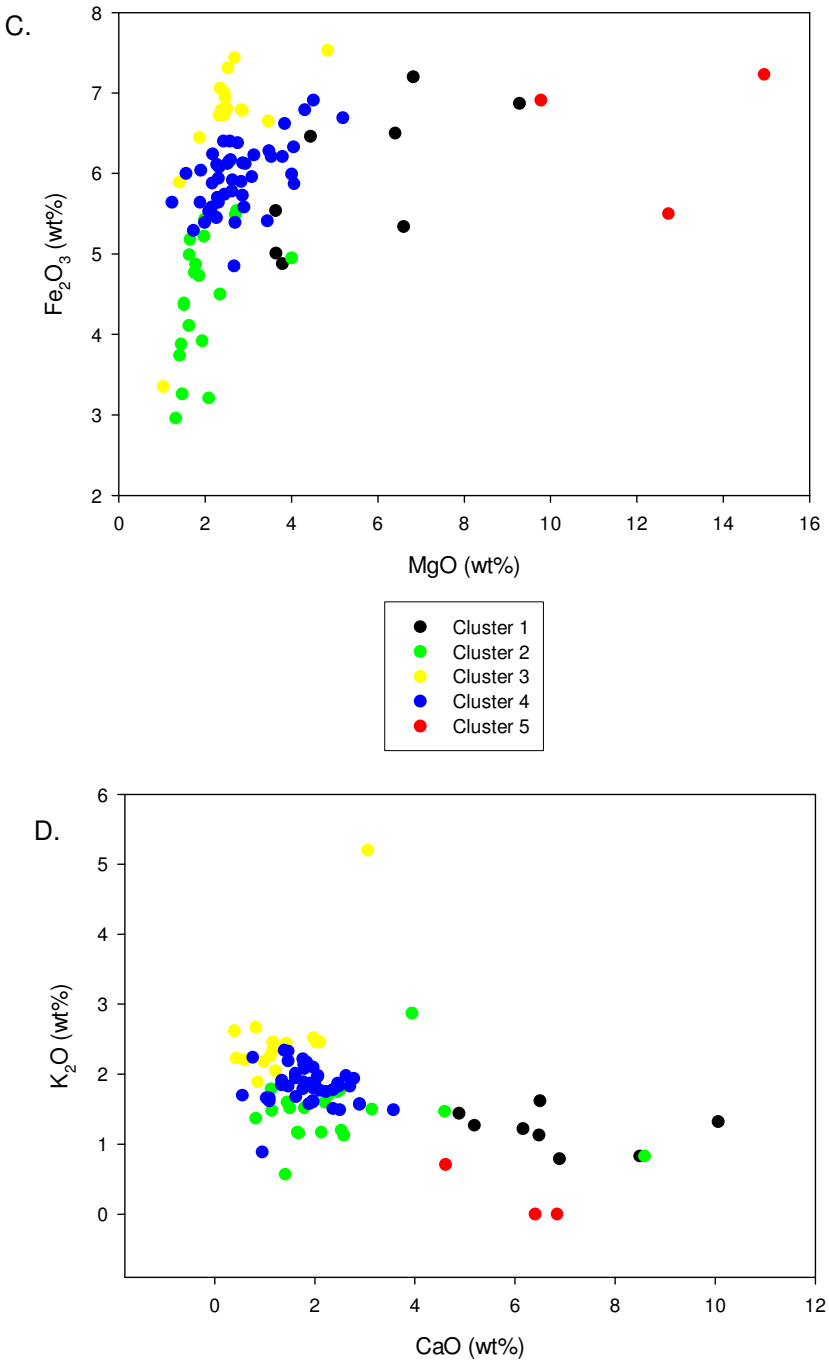

Fig. 4.8 (cont'd): Geochemical plots showing the results of the cluster analysis: 5 clusters produced by cluster analysis of 93 cases and 26 variables and the Euclidean Sum of Squares (k-means): C) Binary diagram of MgO vs. Fe_2O_3. All data in wt%. D) Binary diagram of CaO vs. K_2O. All data in wt%.

Table 4.5: Averages and ranges in major element abundances for the target rocks of the Bosumtwi structure and the Ivory Coast tektites (data in wt%), after Koeberl et al. (1997a, 1998).

	Shale* (Average)	Shale* (Range)	Greywacke-Phyllite* (Average)	Greywacke-Phyllite* (Range)	Granite dyke* (Average)
SiO_2	55.56±1.65	53.56-57.21	66.75±1.77	63.30-69.12	68.74±0.50
TiO_2	0.84±0.10	0.74-0.97	0.66±0.07	0.59-0.77	0.50±0.00
Al_2O_3	19.56±1.89	17.68-22.62	15.27±1.31	12.70-17.02	15.91±0.18
Fe_2O_3	8.54±0.45	7.99-9.14	6.37±0.62	5.64-7.57	3.97±0.31
MnO	0.046±0.008	0.035-0.055	0.028±0.009	0.01-0.037	0.014±0.013
MgO	2.90±0.34	2.40–3.31	2.12±0.25	1.79-2.50	1.44±0.36
CaO	0.09±0.02	0.05- 0.11	0.19±0.13	0.07-0.47	0.31±0.01
Na_2O	1.00±0.68	0.36–2.13	2.26±0.95	0.31-3.07	4.14±0.9
K_2O	2.89±0.16	2.64-3.07	1.80±0.61	0.85-2.72	1.92±0.15
P_2O_5	0.08±0.03	0.04-0.13	0.06±0.03	0.02-0.10	0.06±0.00
LOI	7.91±0.76	6.86-8.99	4.25±0.59	3.49-5.32	2.98±0.33

	Pepiakese granite* (Average)	Pepiakese granite* (Range)	Tektites** (Average)	Tektites** (Range)
SiO_2	57.81±6.28	53.13-66.69	67.58±0.59	66.2-68.5
TiO_2	0.46±0.34	0.06- 0.88	0.56±0.02	0.54-0.61
Al_2O_3	16.45±2.42	14.73-19.87	16.74±0.37	16.3-17.7
Fe_2O_3	6.09±3.97	0.48-9.17	6.16±0.15	5.8-6.5
MnO	0.067±0.047	0.001-0.106	0.06±0.01	0.04-0.07
MgO	6.63±4.61	0.12 – 10.17	3.46±0.35	3.0-4.4
CaO	4.36±2.94	0.23-6.76	1.38±0.11	1.2-1.5
Na_2O	6.04±4.14	2.92-11.88	1.90±0.16	1.5-2.1
K_2O	0.67±0.43	0.27-1.27	1.95±0.11	
P_2O_5	0.10±0.08	0.02-0.21		
LOI	1.48±0.71	0.51-2.22		

**Data from Koeberl et al. (1998); **data from Koeberl et al. (1997a).*

The LB-07A basement metagreywacke was found to have a somewhat different geochemical signature from that of the greywacke-phyllite of Koeberl et al. (1998): the LB-07A metagreywacke shows slightly higher concentrations of MgO, MnO, CaO, P_2O_5 and LOI. The CaO and LOI contents clearly reflect the post-impact carbonate component. The LB-07A metagreywacke also has slightly lower concentrations of SiO_2, TiO_2 and Fe_2O_3, and similar concentrations of Al_2O_3, Na_2O and K_2O in comparison with the greywacke-phyllites.

Thus, the only significant difference between the LB-07A metagreywacke and those of Koeberl et al. (1998) is the CaO content. The LB-07A altered shales are more similar in composition

to the shale compositions of Koeberl et al. (1998) than the metagreywackes are to the greywacke-phyllites, but the shales generally have larger ranges than those quoted by Koeberl et al. (1998). Lower concentrations were observed for TiO_2, Al_2O_3 and Fe_2O_3, and enrichments in CaO and Na_2O exist for the LB-07A shales in comparison to the shales of Koeberl et al. (1998; Table 4.1, 4.5). As with the metagreywackes, the enrichment in CaO is explained by the post-impact carbonate component.

These differences are intriguing in that one would expect near-identical compositions for the basement metasediments to the same target lithologies. For the greywackes, though, it is immediately evident that the fact that Koeberl et al. (1998) combined their geochemical signatures of both greywackes and phyllites which has made a subtle difference to the geochemical signature of metagreywackes observed in the core. Additionally, the rocks in the LB-07A core basement metasediments are finely powderized, and it is not possible to ascribe a distinct lithology to these data.

4.6.2 Polymict/Monomict Impact Breccias *vs.* Target Rocks

Harker plots of the impactite compositions (Fig. 4.9) show that the impactites and basement rocks of the LB-07A core consist of a thoroughly homogenized mixture of target rocks similar to those analyzed by Koeberl et al. (1998). However, a number of samples have outliers (particularly noticeable for Fe_2O_3, CaO and MnO contents) that are more enriched in these elements than the general field defined by the majority of samples.

The CaO contents cannot be only accounted for by utilizing post-impact carbonate, as it is clear that calcite exists both as a pre- and post-impact phase (Chapter 3). The fields that delineate the monomict breccias, the basement metasediments, and the majority of the polymict breccias mirror each other in shape and extent, showing that the LB-07A column is reasonably well homogenized in

terms of the geochemical signature. The most notable difference between the LB-07A impactite concentrations and the target rocks is that they are generally more enriched in CaO than the target samples, except for the Pepiakese granite.

4.7 Siderophile Element Compositions and Possible Meteoritic Component

Chromium, Co and Ni abundances of the rocks of the LB-07A core generally have narrow ranges, with just a few samples showing relative enrichments. For Ni, the range lies between 6 and 200 ppm, with a maximum concentration of 1122 ppm (Fig. 4.6, Appendix 4a). The highest concentrations of Ni (200 - 1122 ppm) occur within the polymict breccias of the upper impactite (Fig. 4.6), and the maximum concentration corresponds to a sample that has a higher concentration of Fe_2O_3 than most other samples (Appendix 4a) and that is intensely iron-stained.

A number of samples (KR7-11, KR7-14, KR7-21) which have Ni contents within the range of 200-1122 ppm Ni contain a substantial proportion of melt particles. However, for other melt-rich units, such as the suevite intercalation at 430.13 m depth (up to 18 vol% melt locally, see sections 3.1.4 and 5.3), very little enrichment in Ni is observed. No substantial and consistent differences in Ni concentration between the polymict lithic breccias and the suevites have been noted, as similar numbers of polymict lithic breccia and suevite have high Ni concentrations. Great variation in Ni concentrations is also observed in the basement rocks, predominantly in the metagreywacke samples and the granophyric-textured rock from 487.12 m depth. The Co and Cr patterns are similar to the Ni pattern. Maximum enrichment in both Co and Cr concentrations (up to 2023 ppm and 77 ppm, respectively; Appendix 4a) coincides with maximum Ni enrichment.

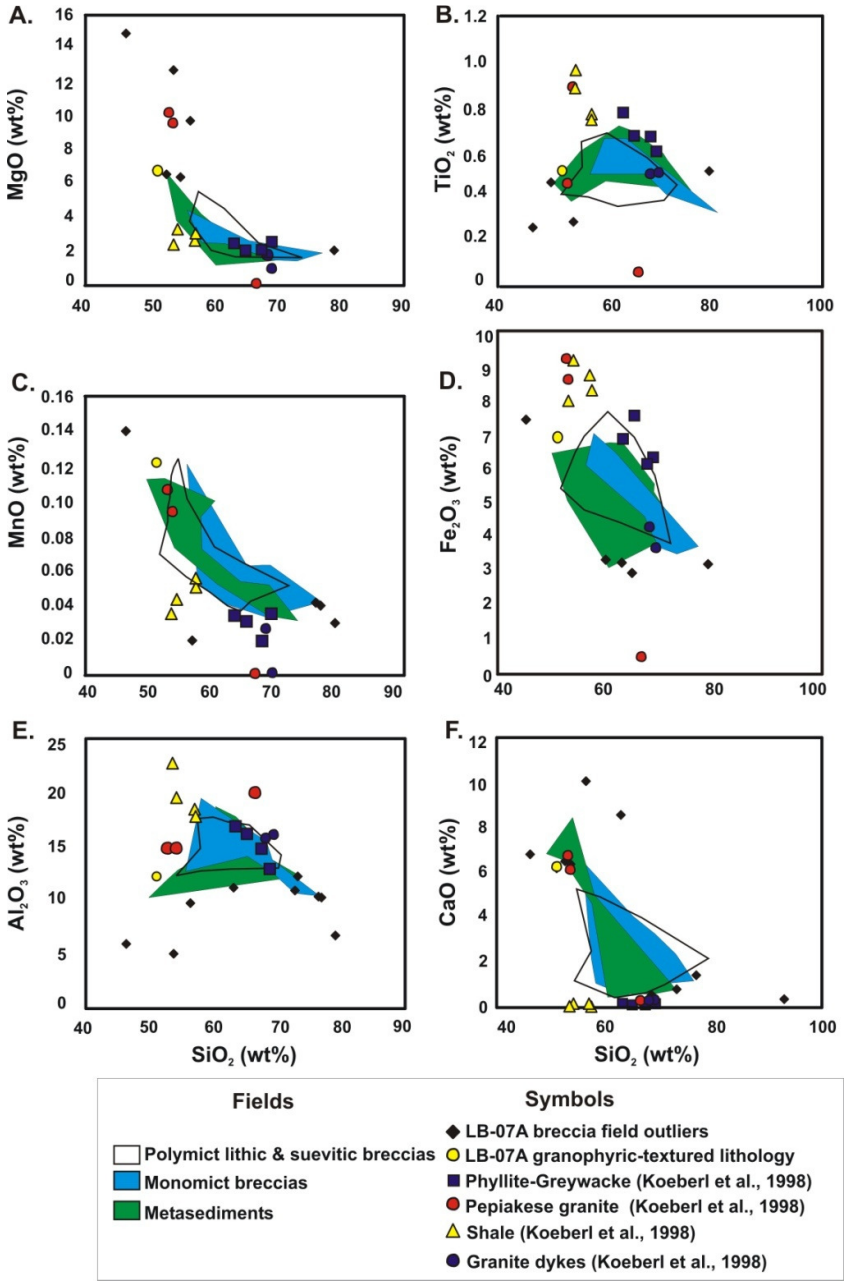

Fig. 4.9: Harker plots for the LB-07A core samples versus "regional target rocks" (Koeberl et al., 1998). Fields delineate the positions of the compositions of the polymict lithic breccias, suevites, monomict breccias and basement metasediments of the LB-07A core. Symbols indicate the positions of LB-07A breccia outliers, the granophyric-textured lithology (of core LB-07A) and the regional target rocks (shale, greywacke-phyllite, granite dyke and Pepiakese granites; Koeberl et al., 1998). All data in wt%.

The average Co concentrations are between 3 and 20 ppm. The Cr values lie in the range of 50 – 200 ppm. Copper concentrations correlate positively with the Cr, Co and Ni concentrations, which is a

strong indication that sulphide, especially the secondary sulphides such as pyrite and chalcopyrite, whose presence is indicated from the petrographic studies (see section 3.2.4), is responsible for the local enrichment of these elements. All iridium results by INAA are below the detection limit of ~2 ppb for carbonate-poor samples and ~0.5 ppb for carbonate-rich samples.

4.7.1 Meteoritic Component

Ten samples with variable siderophile element content were analysed for their PGE content (see Appendix 4b; Fig. 4.10). Of these 10 samples, two were duplicated in order to check for reproducibility. As expected, some of the samples with elevated siderophile element data (for Cr, Co, and Ni) show fairly high PGE contents. For example, suevite KR7-9 (and its duplicate KR7-9d, see Appendix 4b, Fig. 4.10), which has the highest Ni and Cr concentrations, has the highest PGE content of all analysed samples. The Ru/Ir ratio (2.1–2.2) is within a factor of two of the chondritic ratio (1.42; Jochum, 1996) but the Pt/Ir and Pd/Ir ratios in this sample (36.6 and 39.2, respectively) are more than 15 times the corresponding chondritic ratios (e.g., Wasson and Kallemeyn, 1988; Jochum, 1996; Horan and Walker, 2000; McDonald et al., 2001). Similarly, the PGE contents of the Ni-rich samples KR7-11b and KR7-14 (both suevites) are relatively high.

The individual PGE contents vary widely between samples (Appendix 4b). For example, Ir values range from 0.028 to 0.68 ppb, Pt values range from 1.3 to 23.6 ppb and Pd values from 0.87 to 26.2 ppb (Appendix 4b). Gold abundances - of particular interest because the Bosumtwi structure is located near the gold-mineralized zones of the Ashanti Belt (see also Dai et al., 2005) - range from 1.2 to 22.7 ppb. The highest Au values, however, do not correlate with the highest PGE values, indicating that gold may reside in a different carrier phase than the PGEs. Another possibility is that Au, which is

more mobile than the PGEs, was affected by hydrothermal alteration.

The chondrite-normalized PGE and Au abundance patterns for the samples are shown in Fig. 4.10. All samples show fairly similar patterns, which are fractionated and non-chondritic. The lowest abundances are found for those PGEs with the highest volatilization temperature, and patterns have a steep slope, consistent with a positive Pt anomaly. These patterns are representative of many crustal rocks, including sedimentary rocks and basic magmas and associated sulphide mineralization where Pt is enriched over Rh (see e.g., Barnes et al., 1985; Schmidt et al., 1997; McDonald et al., 2001; Farago et al., 2005; Kinnaird, 2005).

Despite the evidence of relatively high Ir and Ru concentrations, the normalized PGE abundance patterns do not provide any unambiguous evidence for the presence of an extraterrestrial component. In contrast, some low-temperature mobility of the PGEs might have influenced the distribution patterns (e.g., Colodner et al., 1993). No distinction can be made between the suevites and basement rocks, even though the overall contents in samples KR7-22 (lower impactites), KR7-29a and KR7-31 (basement shale) are lower than the abundances in the impact breccias. Overall, the PGE contents vary widely, and show no near-chondritic abundance patterns.

Two samples were also analysed for their Os isotope content (Appendix 4b, Fig. 4.11). The signature of both samples (and other samples from core LB-08A and the crater rim) was radiogenic (Allègre and Luck, 1980). Neither of these samples shows any evidence of a meteoritic component, consistent with the PGE results. The results are presented in Fig. 4.11, where $^{187}Os/^{188}Os$ isotopic ratio versus inverse Os content is reported. Figure 4.11 shows that mixing between an unradiogenic Os-rich meteoritic component with

radiogenic, Os-poor crustal rocks would create a linear mixing trend, which is not observed in this diagram, and terrestrial Os clearly dominates the mixtures.

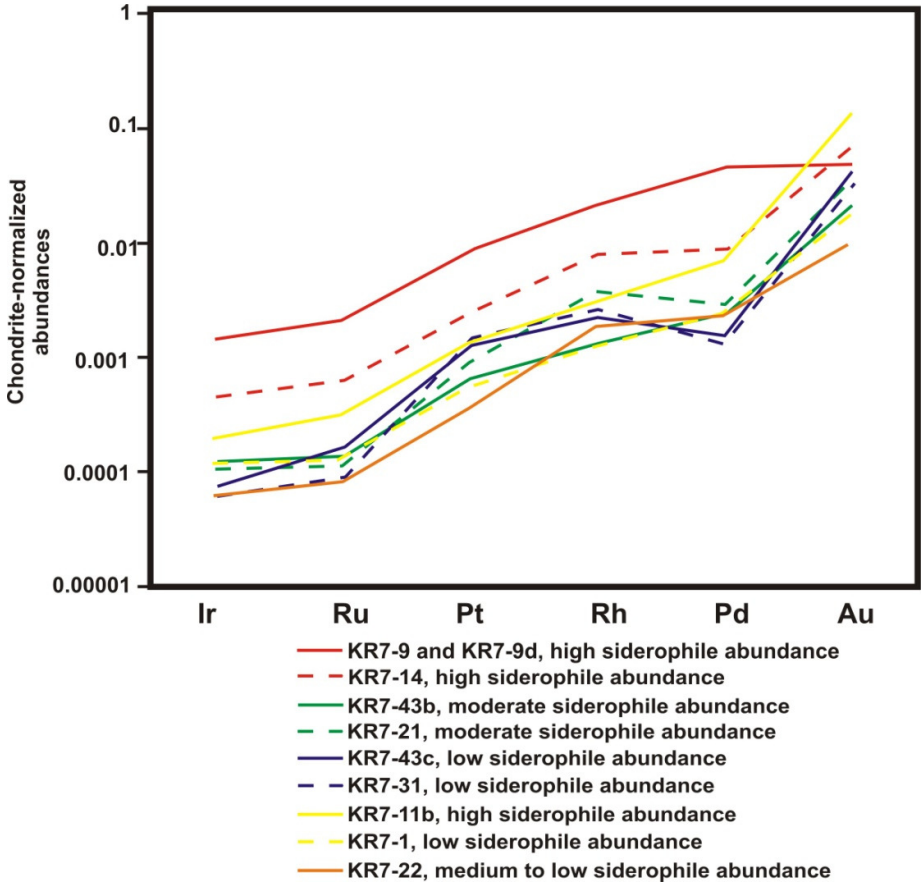

Fig. 4.10: Chondrite-normalized PGE abundance patterns for selected samples from the LB-07A core. Normalization data from Jochum (1996), except for Pd - from Anders and Grevesse (1989).

4.8 Summary

The major and trace element patterns throughout the LB-07A core are, overall, fairly constant with depth. The suevites and the polymict lithic breccias of the LB-07A core are not chemically distinct from each other, and are not substantially different from the average compositions of the monomict breccias and basement rock lithologies (Table 4.1; Fig. 4.1, 4.6, 4.8).

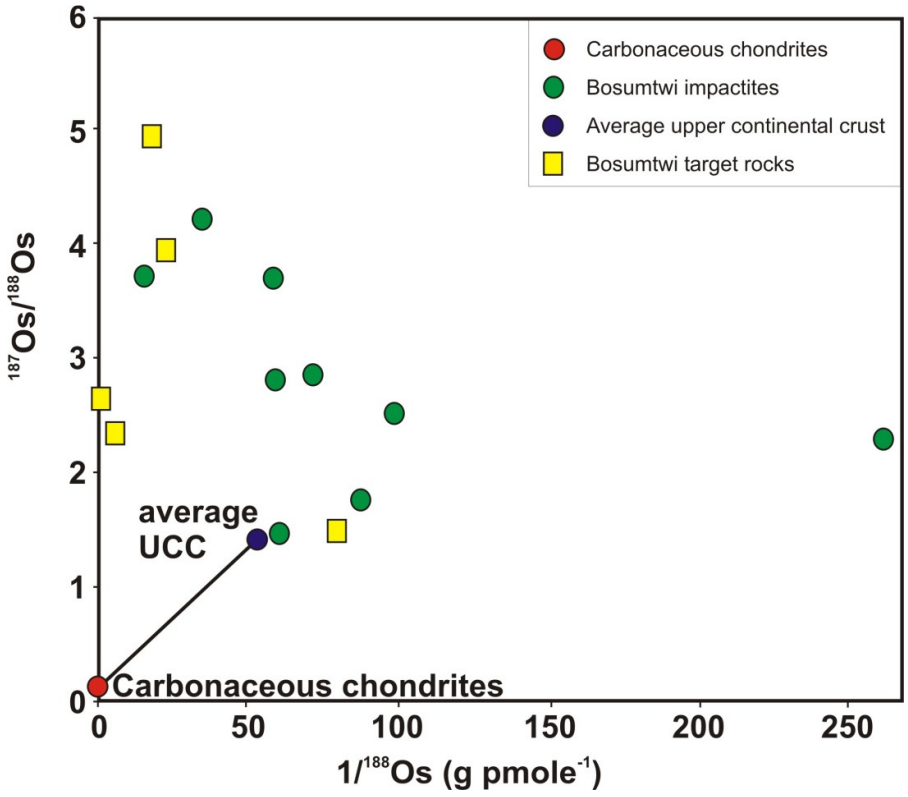

Fig. 4.11: Plot of inverse ^{188}Os concentration ($1/^{188}Os$) versus $^{187}Os/^{188}Os$ for the Bosumtwi drill core samples and target rocks. A straight mixing line between radiogenic, Os-poor (i.e, upper crustal) target rocks (Koeberl and Shirey, 1993) and an unradiogenic, Os-rich component (i.e., carbonaceous chondrites) is shown in order to indicate the ideal mixing line for meteorite and upper continental crust mixing (Peucker-Ehrenbrink and Jahn, 2001).

This observation is not surprising given that the various target lithologies are extremely intercalated, and that such homogenization is usually observed in impactites (Dressler and Reimold, 2001). In addition to the known target rock lithologies (metagreywacke, shale, phyllite, quartz), CaO contents as well as petrographic observations have indicated that there is the presence of carbonate target rock, in addition to a carbonate component caused by post-impact hydrothermal alteration. This has been confirmed by petrographic analysis (Chapter 3).

For a number of the major and trace elements, the scatter in the range of composition increases with depth within the basement lithologies (no obvious difference can be ascertained between the

upper and lower impactites). This provides further evidence for extensive mixing of the target lithologies for the polymict and monomict breccias.

When the LB-07A core impactites are compared to regional target rock samples, it is evident that their geochemical signatures represent a mixture of the known target rocks in addition to a carbonate component.

The PGE and Os isotope study did not provide an indication of the amount of extraterrestrial component, and this is related to the high indigenous siderophile component of the regional Birimian rocks.

Chapter Five: Shock Metamorphism

5.1 Introduction

Shock metamorphic features in minerals and rocks are diagnostic evidence of an impact event (see French, 1998; Koeberl and Martínez, 2003). Not only do they provide definitive diagnosis, but pressure and temperature constraints for the host grains can be ascertained from such features. As documented in Table 1.1, unique features are noted in specific pressure ranges (Stöffler, 1984; Melosh, 1989; Stöffler and Langenhorst, 1994; French, 1998; Montenari and Koeberl, 2000; Koeberl, 2002; Osinski et al., 2008a) including planar deformation features (PDFs; formed at pressures of 5 - 45 GPa in quartz), diaplectic glasses (formed at pressures of 30 – 40 GPa) and mineral and rock melting (formed at pressures of 45 - >70 GPa; pressure ranges for porous and non-porous rocks).

Northern out-of-crater suevites of the Bosumtwi structure have been studied in terms of shock metamorphism (Littler et al., 1961; Chao et al., 1962; Koeberl et al., 1998; Boamah and Koeberl, 2003, 2006). Both Littler et al. (1961) and Chao et al. (1962) noted a high pressure polymorph (coesite) in the out-of-crater suevites (see section 1.4.1). Koeberl et al. (1998) found that only the northern out-of-crater suevites displayed distinctive shock effects, such as PDFs in quartz, whereas country rocks collected in and around the crater area showed no evidence of shock. Melt particles were noted in the out-of-crater suevites (Koeberl et al., 1998). Boamah and Koeberl (2003, 2006) noted a variety of shock effects in the northern out-of-crater suevites. These included variably textured impact glasses of differing composition, which formed up to 20 vol% of the suevites, as well as multiple sets of PDFs (up to 5 sets) in quartz. Additionally, they noted the presence of diaplectic quartz and feldspar glass, kinked phyllosilicates, lechatelierite and ballen-textured quartz in the suevites from north of the crater rim. Boamah and Koeberl (2006) concluded that the shock pressures thus determined ranged from

less than 5 GPa to at least 50 GPa in the northern out-of-crater suevites.

Morrow (2007) performed a detailed shock analysis of quartz in the upper impactite interval of core LB-07A using standard and universal stage optical microscopy and microRaman spectroscopic examination of quartz. He found that there was widespread evidence of heterogeneous shock metamorphism, including mosaicism, the presence of planar microstructures, reduced birefringence, rare diaplectic glass and rare coesite and melting in the upper impactite breccias. He estimated that shock pressures in excess of 20 GPa were widely reached but material that had experienced pressures in excess of 40-45 GPa was rare.

5.1.1 Shock Pressure Dependence of Orientations of PDFs in Quartz

Planar deformation features provide a useful assessment of shock pressure variation in impactites. With increasing shock intensity, PDFs become more abundant and more closely spaced in minerals (Stöffler and Langenhorst, 1994).

Table 5.1 summarizes the usual crystallographic orientations of PDFs that can be measured in quartz. The relative abundance of different PDF orientations varies with shock pressure (Table 5.1).

5.1.2 Shock Dependence of Diaplectic Glasses, High-Pressure Polymorphs and Mineral Melts

Diaplectic glasses, coesite, stishovite and mineral melts form at higher pressures than PDFs in quartz (Fig. 1.8; Stöffler and Langenhorst, 1994). As detailed in section 1.3.3, diaplectic glasses form at pressures between 30 and 40 GPa (e.g., von Engelhardt et al., 1967; Stöffler, 1984; Langenhorst and Deutsch, 1994; Huffman and Reimold, 1996; French, 1998), provided the related shock temperatures stay below the melting point of the mineral. Stishovite

is formed at lower pressures than coesite (12-45 GPa *vs.* 30-60 GPa; Stöffler and Langenhorst, 1994), but preservation of these two phases is largely dependent on the post-shock temperatures, as the high pressure polymorphs are unstable above 400 ^{o}C (for stishovite) and 1100 ^{o}C (for coesite; see Dachille et al., 1963; Skinner and Fahey, 1963; Stöffler and Langenhorst, 1994). Melting of minerals takes place when the shock temperatures are above a mineral's melting point (see section 1.3.4). Generally this takes place at pressures greater than 45 GPa (French, 1998; Koeberl and Martínez, 2003).

Table 5.1: Typical crystallographic orientations of planar deformation features in shocked quartz. Minimum pressures for the generation of some of these features are indicated (modified after Stöffler and Langenhorst, 1994; Langenhorst, 2002).

Symbol	Bravais-Miller indices	Polar angle (angle between pole to plane and quartz c-axis)	Shock pressure
c	*(0001)	0°	>5 GPa
ω	*$\{10\bar{1}3\};\{01\bar{1}3\}$	23°	>10 GPa
π	*$\{10\bar{1}2\};\{01\bar{1}2\}$	32°	>20 GPa
r,z	*$\{10\bar{1}1\};\{01\bar{1}1\}$	52°	>20 GPa
m	$\{10\bar{1}0\}$	90°	
ξ	$\{1\bar{1}\bar{2}2\};\{2\bar{1}\bar{1}2\}$	48°	>22 GPa
s	$\{1\bar{1}\bar{2}1\};\{2\bar{1}\bar{1}1\}$	66°	
a	$\{1\bar{1}\bar{2}0\};\{2\bar{1}\bar{1}0\}$	90°	
	*$\{22\bar{4}1\};\{4\bar{2}\bar{2}1\}$	77°	
t	$\{40\bar{4}1\};\{04\bar{4}1\}$	79°	
k	$\{51\bar{6}0\};\{61\bar{5}0\}$	90°	
x	$\{51\bar{6}1\};\{65\bar{1}1\};$ $\{61\bar{5}1\};\{15\bar{6}1\}$	82°	
-	$\{31\bar{4}1\};\{43\bar{1}1\};$ $\{41\bar{3}1\};\{13\bar{4}1\}$	78°	
-	$\{21\bar{3}1\};\{32\bar{1}1\};$ $\{31\bar{2}1\};\{12\bar{3}1\}$	74°	

**Prominent planes in shocked grains*

5.2 Methodology

In this study, a qualitative and quantitative assessment of the LB-07A core in terms of shock metamorphism has been made. Shock point-counting of a number of representative samples which contain between 60 and 297 quartz grains took place. In this procedure, the

presence and relative abundance of PFs and PDFs in quartz was documented. In the same sections, feldspar grains were examined to ascertain whether they contain PDFs. Additionally, in thin sections of suevites, the number and size of melt particles were determined. In order to measure the crystallographic orientations of PDFs in the upper impactites, lower impactites and basement metasediments, measurements on the universal stage (U-stage; see Langenhorst, 2002) have been performed, so that a shock-pressure profile through the LB-07A core could be constructed. Finally, melt particles from different depths have been analysed by electron microprobe analysis (see section 2.5.5 for detail on the procedures).

5.3 Shock Variation in the LB-07A Core

5.3.1 Quartz and Feldspar – Shock Metamorphic Effects

Quartz grains in the polymict lithic breccias and suevites (occurring as individual quartz grains, polycrystalline aggregates, or within metagreywacke) display planar fractures and PDFs. The results for the quantitative shock point-counting of PDFs in quartz grains are given in Table 5.2. In certain thin sections relatively fewer quartz grains were counted either owing to the presence of larger clasts of non-quartz-bearing lithic material or large numbers of micrometre-scale quartz grains, for which elucidation of shock features was not possible at the optical scale.

Usually only one or two sets of PDFs were observed (Fig. 5.1); only a few grains have been noted containing 3 sets of PDFs in the quartz clasts of the upper impactites. These may or may not be decorated (Fig. 5.2). In contrast, 3 PDF sets in quartz (Fig. 5.2) are somewhat more common in suevite from core LB-08A, which is from the central uplift (Ferrière et al. 2007a). Reduced birefringence (Fig. 5.3 A, B), isotropism, mosaicism and undulatory extinction (Fig. 5.3 C) are common in both quartz and feldspar (all of which form at < 40 GPa, French, 1998; Table 1.1). Toasted quartz is common (Fig. 5.2, Fig. 5.4 D).

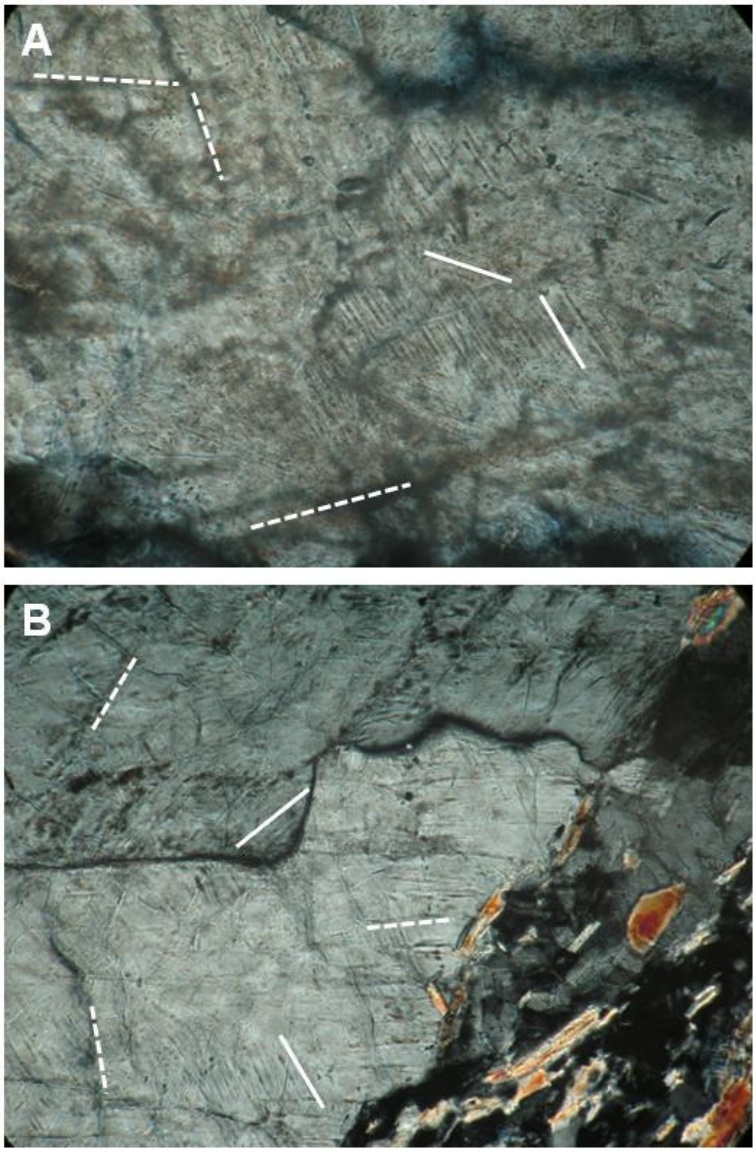

Fig. 5.1: Photomicrographs of planar deformation features in quartz grains. A) Sample KR7-35, suevite, upper impactites, sample depth = 359.33 m; 2 PDF sets, oriented NW-SE and WNW-ESE (indicated with solid lines) and 3 sets of sub-parallel fractures oriented ESE-WNW, ENE-WSW and NW-SE (indicated with dashed lines); image width = 0.25 mm, cross-polarised light (CPL). B) Sample KR7-1, polymict lithic breccia, upper impactites, sample depth = 334.38 m; 2 grains with 1 PDF set each, oriented NE-SW and WNW-ESE (indicated with solid lines), and 3 sets of sub-parallel fractures oriented NNE-SSW, ENE-WSW and NNW-SSE (indicated with dashed lines); image width = 0.25 mm, CPL.

No PDFs in feldspar have been noted; this is consistent with observations from the LB-08A core (Ferrière et al., 2007a).

Undulatory extinction of quartz is evident throughout the drill core samples, as is planar fracturing, but the abundances of these features do not vary consistently with depth.

Both the polymict lithic breccias and the suevites contain similar proportions of shocked quartz (Table 5.2). The proportion of shocked quartz grains containing 1 or 2 or more sets of PDFs, calculated as a percentage of the total number of quartz grains screened per sample, varies between 1.4 and 12.1% for the upper impactites, 2.6 and 6.5% for the lower impactites and 0.6 and 3.3% for the basement metasediments (Table 5.2; Fig. 5.4).

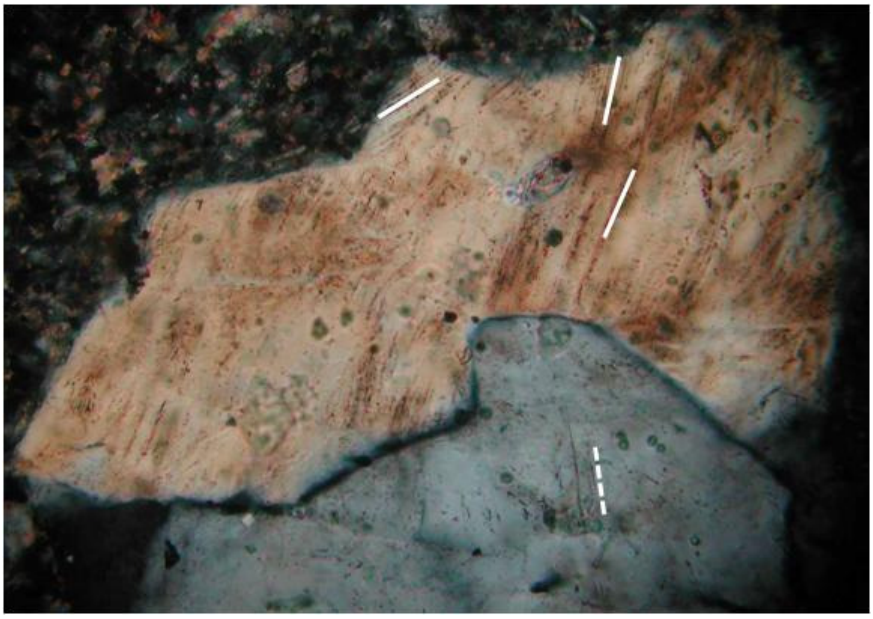

Fig. 5.2: Photomicrograph of decorated planar deformation features and one set of planar fractures in quartz grains. Sample KR7-41, suevite, upper impactites, sample depth = 408.72 m; one set of planar fractures (PF, indicated with dashed line), oriented NNW-SSE; three sets of decorated PDFs in toasted quartz (2 sets oriented NNE-SSW and 1 set oriented NE-SW, indicated with solid lines); image width = 0.20 mm, CPL.

Figure 5.4 shows the variation in the proportion of shocked quartz grains for analysed samples in the LB-07A core. In the upper impactites, there is no clear increase or decrease in the number of PDFs with depth (Fig. 5.4).

Table 5.2: Summary of shock features in quartz grains and melt particle statistics for upper impactite polymict lithic breccia and suevite, lower impactite monomict breccia and suevite and basement metasedimentary lithologies. The basement suevites show no PDFs.

Sample Number /Depth (m)	Total No. quartz grains studied	Total % quartz grains without PDFs or PFs	Total % quartz grains with PFs	Total % quartz grains with 1 set of PDFs	Total % quartz grains with 2 or more sets of PDFs	No. melt fragments < 1 mm	No. melt fragments ±1 mm	No. melt fragments > 1 mm	Rock type	Unit
KR7-1/334.91	144	48.6	41.0	10.4	0	0	0	0	P.L.B.	U.I.
KR7-35/359.33	172	90.7	2.3	5.8	1.2	3	2	2	S.B.	U.I.
KR7-6/360.65	186	90.3	7.5	2.2	0	2	0	1	S.B.	U.I.
KR7-7/363.20	98	92.9	2.0	4.1	1.0	9	1	0	S.B.	U.I.
KR7-36/364.45	143	95.8	2.8	1.4	0	5	0	0	S.B.	U.I.
KR7-8/370.34	118	92.4	2.5	4.2	0.8	0	0	0	P.L.B.	U.I.
KR7-9/377.46	143	97.2	2.8	0	0	0	0	0	P.L.B.	U.I.
KR7-37/379.09	137	96.4	2.2	1.5	0	4	3	0	S.B.	U.I.
KR7-51/383.14	143	90.2	4.2	4.2	1.4	1	2	1	S.B.	U.I.
KR7-13/393.78	133	88.0	0.75	9.8	1.5	0	0	0	P.L.B.	U.I.
KR7-14/398.44	94	89.4	3.2	6.4	1.1	6	2	0	S.B.	U.I.
KR7-40/400.06	233	94.4	2.1	2.1	1.3	4	1	1	S.B.	U.I.
KR7-53/400.58	213	94.4	2.8	4.7	0	2	0	1	S.B.	U.I.
KR7-15/402.73	177	91.5	3.4	4.5	0.6	5	0	0	S.B.	U.I.
KR7-16/404.26	206	85.9	4.4	8.4	1.5	12	2	1	S.B.	U.I.
KR7-17/405.57	181	77.9	9.9	11.0	1.1	13	10	0	S.B.	U.I.
KR7-44/407.77	227	93.4	4.4	1.8	0.4	2	4	2	S.B.	U.I.
KR7-20/408.32	245	90.2	2.9	6.9	0	6	1	0	S.B.	U.I.
KR7-41/408.72	206	85.9	2.4	8.3	3.4	3	2	2	S.B.	U.I.
KR7-71/415.67	123	96.7	0	2.4	0.9	0	0	0	M.B.	L.I.
KR7-73/421.56	291	90.4	3.8	4.5	1.4	0	0	0	M.B.	L.I.
KR7-74/430.03	235	95.3	2.1	1.7	0.9	0	0	0	M.B.	L.I.
KR7-23/430.13	229	92.2	4.3	3.1	0.4	4	4	12	S.B.	L.I.
KR7-75/430.28	108	89.8	3.7	4.6	1.9	1	0	0	S.B.	L.I.
KR7-76/441.60	161	88.9	6.8	3.1	1.2	0	0	0	M.B.	L.I.
KR7-27/468.28	297	62.3	32.3	4.0	1.4	0	0	0	M.B.	L.I.
KR7-28/470.55	137	74.5	24.1	1.5	0	0	0	1	Shale	B.M.
KR7-29A/487.36	174	98.8	0.6	0.6	0	0	0	0	MGW	B.M.
KR7-31/512.15	60	95.0	1.7	3.3	0	0	0	0	MGW	B.M.
KR7-84/538.29	161	85.1	13.0	1.9	0	0	0	0	Shale	B.M.

**Average sample size examined is 1.5 cm^2; % refers to relative % of the total no. of quartz grains. P.L.B. = polymict lithic breccia; S.B. = suevite; M.B. = monomict breccia; MGW = metagreywacke; U.I. = upper impactites; L.I. = lower impactites; B.M. = basement metasediments.*

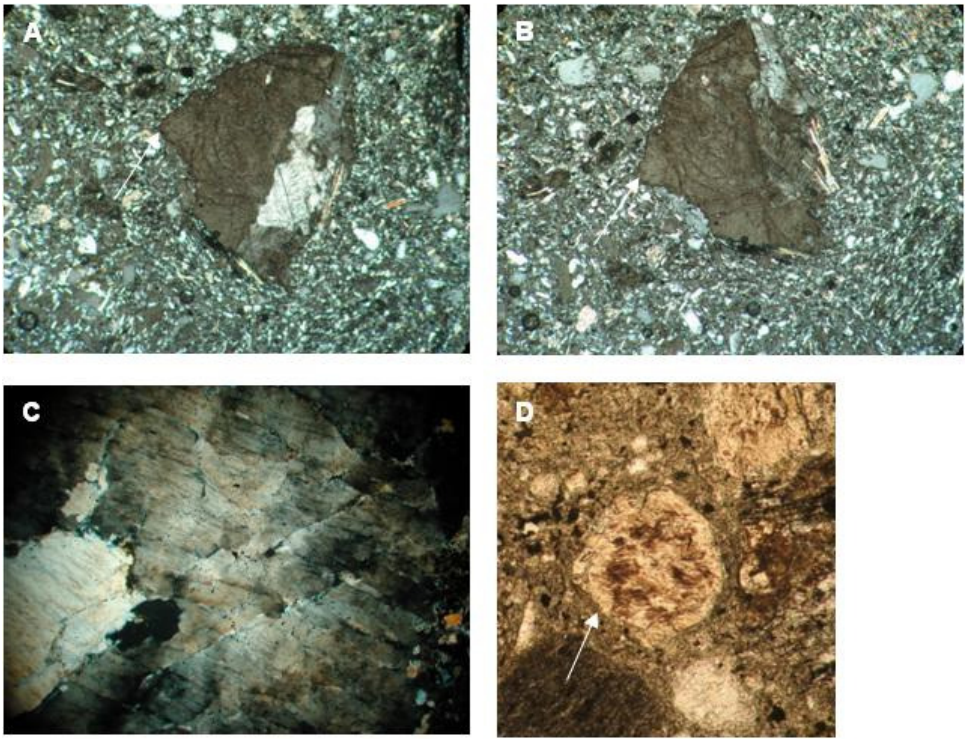

Fig. 5.3: Photomicrographs of various shock features in quartz. A) and B) Photomicrographs of reduced birefringence in quartz grains, with shock fractures (formed at ca. 5 GPa). Sample KR7-41, suevite, upper impactites, sample depth = 408.72 m; image width = 2 mm, CPL. C). Photomicrograph of mosaic extinction in a quartz grain, with 2 sets of sub-parallel fractures oriented NE-SW and NW-SE. Sample KR7-44, suevite, upper impactites, sample depth = 407.77 m; image width = 2 mm, CPL. D) Photomicrograph of toasted quartz. Sample KR7-18, suevite, upper impactites, sample depth = 411.34 m; image width = 1 mm, plane polarized light (PPL).

The suevites in the lower impactites display lower levels of shock than those of the upper impactites (Fig. 5.4), as relatively fewer PDF sets in quartz were observed (Table 5.2; Fig. 5.4).

In the suevites of the basement metasediments, no PDFs in quartz were found. In some monomict breccias and basement metasediment samples, a few discrete grains containing one, or at most two, PDF sets were found (Table 5.2). Owing to the poor recovery within this lower section, and the strongly pulverized nature of the material, full shock evaluation was hampered. Nevertheless, the lower impactites are seemingly shocked to a lower degree than the clasts in the upper impactite sequence (Table 5.2).

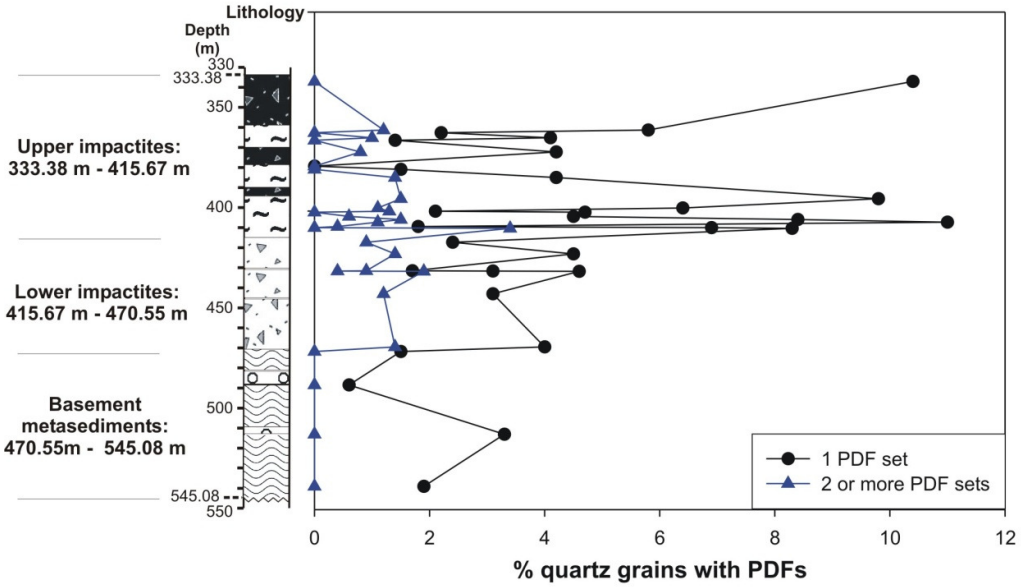

Fig. 5.4: Variation of the proportion of shocked quartz grains with depth through the LB-07A core. % quartz grains with PDFs refers to the relative % of all quartz grains studied for their shock features (compare Table 5.2).

Toasted quartz (see Whitehead et al., 2002b; Fig. 5.3 D) has been noted in suevite and polymict lithic breccia samples (from a depth of about 378 m), and in the lowermost suevite injection where all grains containing PDFs are toasted quartz grains. All toasted grains display either PFs or PDFs. No ballen quartz has been observed in any of the samples of the LB-07A core, in contrast to observations made in the out-of-crater suevites (Chapter 6; Boamah and Koeberl, 2006; Ferrière et al., 2008).

The total number of shocked grains per sample decreases with depth, consistent with an apparent decrease in shock pressure with depth. The clasts of the basement metasediments are shocked to a lower degree than many of the impactite clasts.

5.3.2 PDF Crystallographic Orientations

Crystallographic orientations of PDFs in quartz from the upper impactites, lower impactites and basement metasediments were

measured using the U-stage. This study was conducted for two reasons: to provide a quantitative assessment of shock pressure variation and to compare the statistics of the PDF orientations in clasts of the upper impactites to those obtained by Morrow (2007) for samples from the same interval. It must be noted that not all PDF sets in a particular grain are necessarily visible owing to the orientation of the crystal with respect to the microscope. Another difficulty encountered with some samples was that some of the shocked grains were located at the edge of a thin section, and the mechanical properties of the U-stage would not allow these to be measured. Thus, the shock pressures obtained by the study of the crystallographic orientations of PDFs provide comparative pressure estimates for the different units of the core.

The main difficulty encountered in the U-stage study was the lack of shocked quartz grains in most of the basement metasediments. Only 4 basement metasediment samples displayed shocked quartz grains (Table 5.3), and in these, only rare PDFs were noted (Tables 5.2 and 5.3). However, all possible PDF orientations were measured (Table 5.4; Appendix 5a). In the lower impactites, more quartz grains than in the basement metasediments were found to be shocked (Table 5.4).

Many samples of the lower impactites are extremely fine-grained, and measurements were restricted to those grains where the features could be observed with certainty (grains which were at least 175 μm in size).

In the upper impactites, samples that contain the largest number of documented PDFs were studied, and both polymict lithic breccias and suevites were examined. Histograms of all the results are shown in Fig. 5.5.

Table 5.3: Shock analysis of the basement metasediments. All samples were examined (using the 50x magnification) for evidence of PFs and PDFs in quartz grains, and the orientation of PDF sets were measured using a U-Stage.

Sample	Depth (m)	Lithology	Shock indicators in quartz
KR7-28	470.55	Shale	2 PDF sets
KR7-29	475.76	Shale	None
KR7-81	483.00	Suevite	None
KR7-82	487.12	Granophyric-textured lithology	None
KR7-29A	487.36	Metagreywacke	1 PDF set
KR7-30	491.01	Shale	None (very fine grained)
KR7-31	512.15	Metagreywacke	2 PDF sets
KR7-83	513.90	Suevite	None
KR7-32	514.77	Suevite	None
KR7-46	530.63	Shale	None (very fine grained)
KR7-47	530.79	Shale	None
KR7-84	538.29	Shale	3 PDF sets
KR7-48	538.89	Shale	None
KR7-49	538.99	Metagreywacke	None
KR7-33	542.70	Shale/Slate	None (very fine grained)

For all data sets, absolute frequencies (in %) are reported, where absolute frequency (after von Engelhardt and Bertsch, 1969) is defined as:

$$\textbf{Absolute frequency, } F_{hkil} = (q_{hkil}/Q)*100$$

where q_{hkil} = actual number of measured symmetrically equivalent deformation planes {*hkil*} observed in *n* quartz grains; and Q = total number of all measured sets of planar structures observed in *n* quartz grains.

The PDF orientations in the quartz grains of the basement metasediments (Fig. 5.5 C) are dominated by c (0001), ω $\{10\bar{1}3\}$ and s $\{11\bar{2}1\}$. The other measured orientation is ξ $\{11\bar{2}2\}$. Interestingly, no measurements for orientation π $\{10\bar{1}2\}$ were obtained. However, the results for the basement metasediments are not entirely statistically valid, owing to the limited number of grains counted. It must be emphasized, however, that these were the only shocked grains found, and that there are so few shocked grains is the main finding of the shock characteristics of the basement metasediments.

Table 5.4: Number of PDF sets and absolute frequencies (%) of specific PDF orientations in quartz grains from the basement metasediments, lower impactites and upper impactites of core LB-07A.

	Basement metasediments	Lower impactites	Upper Impactites
No. of sets (Q)	8	56	55
No. of grains (n)	8	45	50
No. of PDF sets/grain (Q/n)	1	1.27	1.1

Indexed orientations	Basement Metasediments (%)	Lower impactites (%)	Upper impactites (%)
c (0001); 0°	25	21.4	9.0
ω $\{10\bar{1}3\}$; 23°	25	28.6	40
π $\{10\bar{1}2\}$; 32°	n.d.	16.1	16.4
r $\{10\bar{1}1\}$; 52°	n.d.	1.8	5.5
m $\{10\bar{1}0\}$; 90°	n.d.	1.8	n.d.
ξ $\{11\bar{2}2\}$; 48°	12.5	n.d.	3.6
s $\{11\bar{2}1\}$; 66°	25	3.6	10.9
$\{22\bar{4}1\}$; 77°	n.d.	8.8	7.3
t $\{40\bar{4}1\}$; 79°	n.d.	1.8	n.d.
x $\{51\bar{6}1\}$; 82°	n.d.	1.8	1.8
$\{21\bar{3}1\}$; 74°	n.d.	3.6	1.8
Unindexed	12.5	10.7	3.6
Total	100	100	100

**Absolute frequencies after von Engelhardt and Bertsch (1969); unindexed orientations are those which provide measurements that do not correspond to the rational PDF crystallographic orientations; n.d. = none detected.*

The PDF orientations of quartz grains from the lower impactites (Fig. 5.5 B) are dominated by the ω $\{10\bar{1}3\}$-equivalent crystallographic plane (28.6%). Basal c (0001) orientations are also abundant, at 21.4%. Other measured PDF orientations, in order of decreasing abundance, include: π $\{10\bar{1}2\}$, $\{22\bar{4}1\}$, s $\{11\bar{2}1\}$, $\{21\bar{3}1\}$ and minor r $\{10\bar{1}1\}$, m $\{10\bar{1}0\}$, t $\{40\bar{4}1\}$ and x $\{51\bar{6}1\}$. In most grains, only single PDF sets occur. In those grains in which more than one PDF set occurs, the most common association is ω $\{10\bar{1}3\}$ and c (0001).

As with the lower impactites, the PDF orientations of the quartz grains of the upper impactites (Fig. 5.5 A) are dominated by the ω $\{10\bar{1}3\}$-equivalent crystallographic plane (40%). This is followed by π $\{10\bar{1}2\}$ and s $\{11\bar{2}1\}$. In order of decreasing abundance, other measured PDF orientations include: c (0001), $\{22\bar{4}1\}$, r $\{10\bar{1}1\}$, ξ $\{11\bar{2}2\}$, x $\{51\bar{6}1\}$ and

{$2\bar{1}3\bar{1}$}. In grains where more than 1 PDF set occurs, no specific orientations are consistently associated together.

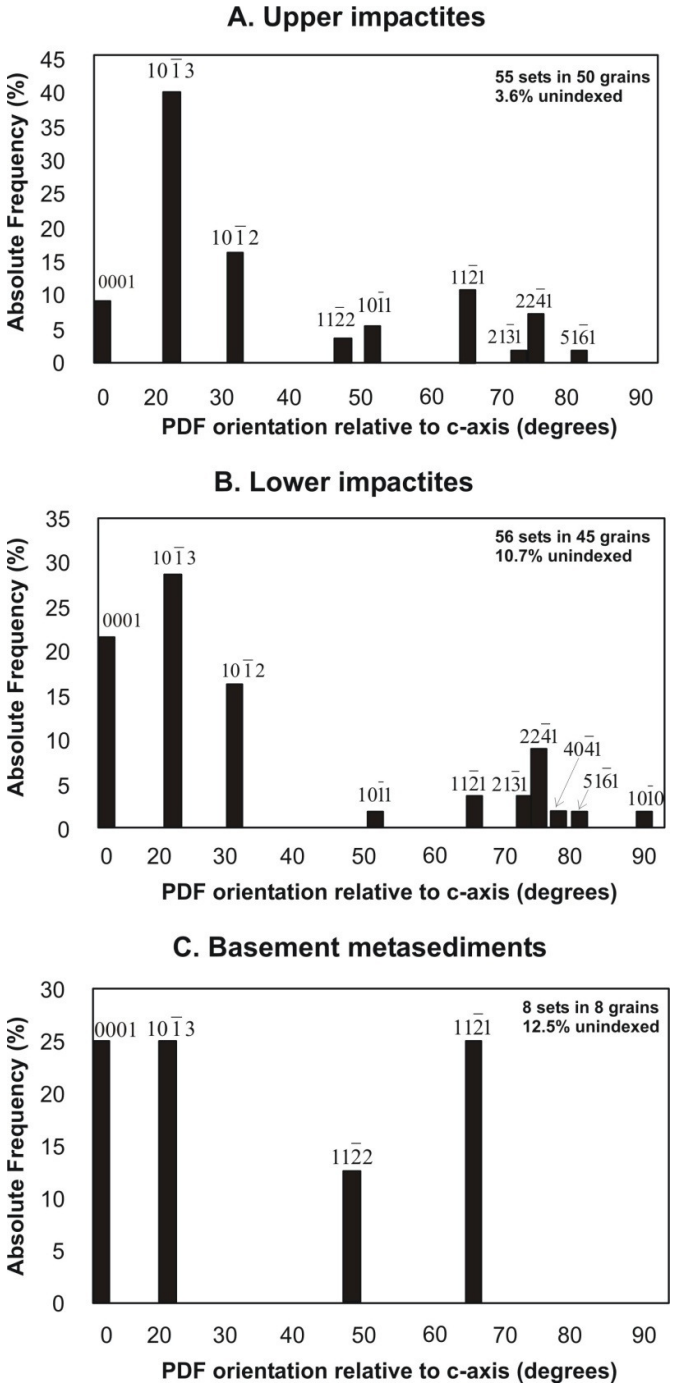

Fig. 5.5: Histograms of crystallographic orientations of planar deformation features in quartz: A) upper impactites, B) lower impactites and C) basement metasediments. Absolute frequencies calculated after von Engelhardt and Bertsch (1969).

It is not surprising that the upper impactites display the most diverse set of orientations, as this unit is made up of a greater variety of material – i.e., shale, metagreywacke, schist, granitoid - than the material of the lower impactites and basement metasediments (shale, phyllite or metagreywacke only). The polymict material in the upper impactites is sourced from all parts of the growing transient crater, and as a result will represent a larger shock pressure range than the material from the lower impactites and basement metasediments which were formed *in situ*.

5.3.3 PDF Crystallographic Orientations – Comparison with Morrow (2007)

The U-stage data for the upper impactites collected in this study can be compared to the work of Morrow (2007), who provided a detailed mineralogical description of the characteristics of shocked quartz from the upper impactites (Table 5.5; Fig. 5.6). The maximum volume percentage of shocked quartz found in this study is 51.4 % for the polymict lithic breccias and 22 % for the suevites, although there is quite considerable variation within the polymict lithic breccias and suevitic breccias. This is roughly comparable to the statistics compiled by Morrow (2007), who found that up to 61 % of quartz grains were shocked in the polymict lithic breccias, compared with up to 20 % in the clasts of the suevites.

It was also noted by Morrow (2007) that the ratios of shocked to unshocked quartz grains probably represent minimum values, as additional PDF-containing quartz grains may not be visible (owing to the crystallographic orientation of the grains relative to the stage orientation).

Morrow (2007) proposed that the average shock pressure increases with depth in the upper impactites as there is an increase in planes parallel to π $\{10\bar{1}2\}$ with depth, together with an increase in the percentage of diaplectic glass.

Table 5.5: Comparison between the U-stage data of Morrow (2007; upper impactites) and averages of data collected in this study (upper impactites, lower impactites, basement metasediments). All data in absolute frequencies (%).

Indexed orientations	Upper impactites (Morrow, 2007)	Upper impactites (this study)	Lower impactites (this study)	Basement metasediments (this study)
c(0001); 0°	4	9	21.4	25
ω $\{10\bar{1}3\}$; 23°	52	40	28.6	25
π $\{10\bar{1}2\}$, 32°	16	16.4	16.1	n.d.
r $\{10\bar{1}1\}$; 52°	5.5	5.5	1.8	n.d.
m $\{10\bar{1}0\}$; 90°	1	n.d.	1.8	n.d.
ξ $\{11\bar{2}2\}$; 48°	2.5	3.6	n.d.	12.5
s $\{11\bar{2}1\}$; 66°	4	10.9	3.6	25
a $\{11\bar{2}0\}$; 90°	1	n.d.	n.d.	n.d.
$\{22\bar{4}1\}$; 77°	0.5	7.3	8.8	n.d.
t $\{40\bar{4}1\}$; 79°	n.d.	n.d.	1.8	n.d.
x $\{51\bar{6}1\}$; 82°	2	1.8	1.8	n.d.
$\{21\bar{3}1\}$; 74°	5.5	1.8	3.6	n.d.
Unindexed	6	3.6	10.7	12.5
Total	100	100	100	100

Additionally, he noted that the distribution of suevite with depth also supports this trend. An increase in the proportion of planes parallel to π $\{10\bar{1}2\}$ with depth has not been noted in this study (see Appendix 5a), which may be a result of the relatively fewer grains counted in this study. An increase in diaplectic glass with depth has been noted in this study, in agreement with the observations made by Morrow (2007).

The orientations of PDFs in quartz for the upper impactites obtained in this study and those of Morrow (2007) are directly comparable, indicating that the clasts of the upper impactites are shocked to similar levels throughout the unit when the relative abundances of PDF orientations are used as a measure of shock degree (Langenhorst, 2002; Table 5.5; Fig. 5.6). The relative proportions of the different orientations are very similar, and are within error of each other.

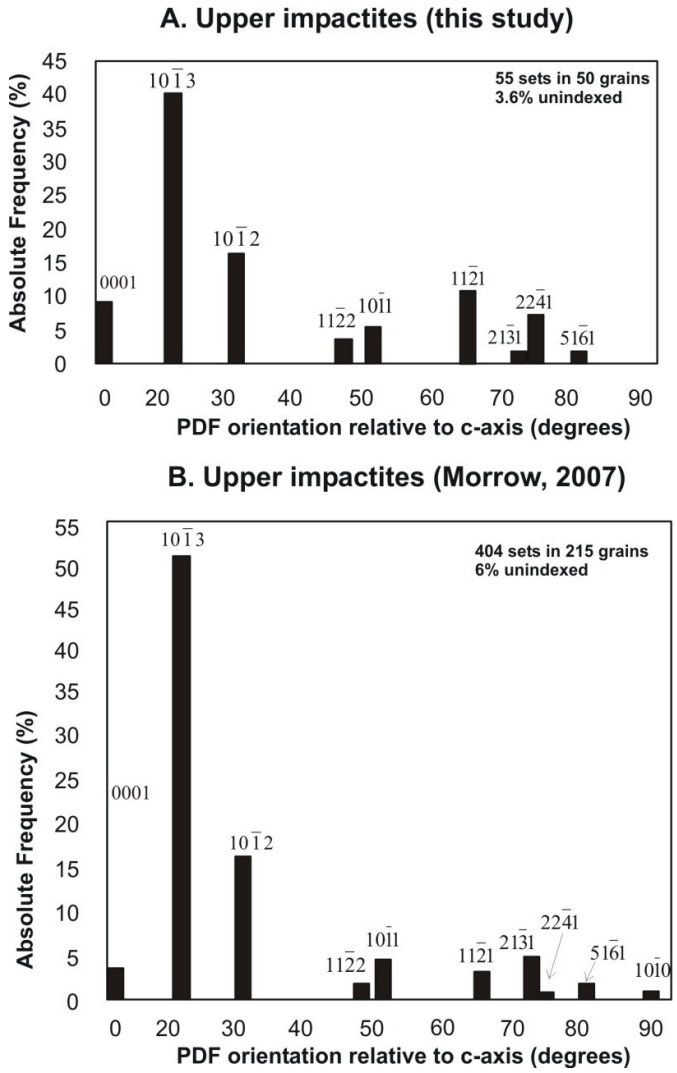

Fig. 5.6: Histograms of crystallographic orientations of planar deformation features in quartz: A) upper impactites (this study) B) upper impactites (Morrow, 2007). Absolute frequencies calculated after von Engelhardt and Bertsch (1969).

5.3.4 Diaplectic Glass

Diaplectic quartz glass (Fig. 5.7 A, B; see Table 3.1) is noted in the impact breccia thin sections from the uppermost part of the core (at 2 vol% of all phases; see Table 3.2). The proportion of diaplectic quartz glass was quantified as a percentage of all clasts (including matrix) in Table 3.2. The proportion of diaplectic quartz glass increases below 400 m to a maximum of 4.0 vol% (of all phases – determined during point-counting of impact breccia samples) at 412.17 m (see Table

3.2). The average amount of diaplectic quartz glass (of all clasts) in the point-counted samples is 2.5 vol% (Table 3.2). Several small diaplectic quartz glass clasts have been observed in the basement suevites. Diaplectic quartz glass is frequently characterised by small fluid inclusions.

Diaplectic feldspar glass is generally rare and has been found in only three sections, at 404.26, 408.72, and 411.34 m depth (Fig. 5.7 C, D), at <1 vol% of all clasts in a thin section out of a total of 60 thin sections. No high pressure polymorphs have been observed in core LB-07A.

Morrow (2007) also found evidence of diaplectic quartz glass at < 1 rel% (relative to the total quartz in the sample) in the polymict lithic breccias, and at a maximum of 2 vol% in the suevites. Thus, he evaluated the proportion of diaplectic quartz glass differently to this study where the proportion of diaplectic quartz glass was determined as a percentage of all clasts (Table 3.2). He noted rare diaplectic feldspar glass in the polymict lithic breccias and suevites. It appears that the percentage of diaplectic quartz glass noted in this study is higher than that noted by Morrow (2007). He also found rare coesite within diaplectic quartz glass clasts in the upper impactites of LB-07A core using microRaman spectroscopic analysis. No coesite was noted in this study; however, microRaman spectroscopic analysis was not utilized.

5.3.5 Carbonate Minerals

Prior to this study, carbonate minerals had not been noted as a major part of the target lithologies at Lake Bosumtwi (see Chapter 3). Evidence for both pre- and post-impact carbonate has been found in this study in core LB-07A. Calcite commonly displays 2 – and more rarely up to 3 - sets of polysynthetic twins (Fig. 5.8), which may be an effect of shock (Deutsch et al., 2007).

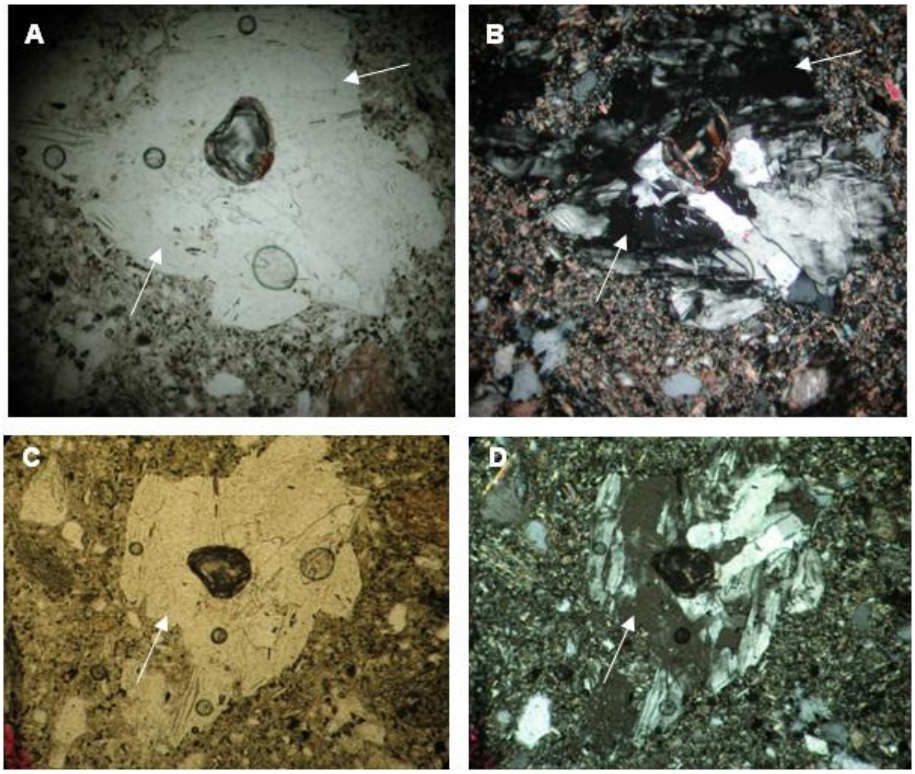

Fig. 5.7: Photomicrographs of diaplectic glass. A) and B) Sample KR7-16, suevite, upper impactites, sample depth = 404.26 m; diaplectic quartz glass (marked by arrows); image width = 1 mm: A) PPL; B) CPL. C) and D) Sample KR7-16, suevite, upper impactites, sample depth = 404.26 m; diaplectic K-feldspar glass (marked by arrow); image width = 1 mm: C) PPL; D) CPL.

Additionally, fracture sets (Fig. 5.8 A-D) similar to PFs in quartz have been noted in calcite grains in the suevites at the following depths: 359.33 m (KR7-35), 363.20 m (KR7-7), 430.28 m (KR7-75) and 513.90 m (KR7-83). This feature has also been observed in a basement metasedimentary sample (KR7-29A, 487.36 m).

5.4 Suevite Melt Particle Characteristics in the LB-07A Core

Suevites, as noted in Chapter 3, have been found in the upper impactites as intercalations with polymict lithic breccia, and as dykes within the lower impactites and basement metasediments. These suevites display different characteristics throughout the core (Table 5.6). The suevites from different depths show differences in the colour of their matrices and melt particles, the sizes of lithic, mineral and melt clasts and overall proportion of shocked quartz grains.

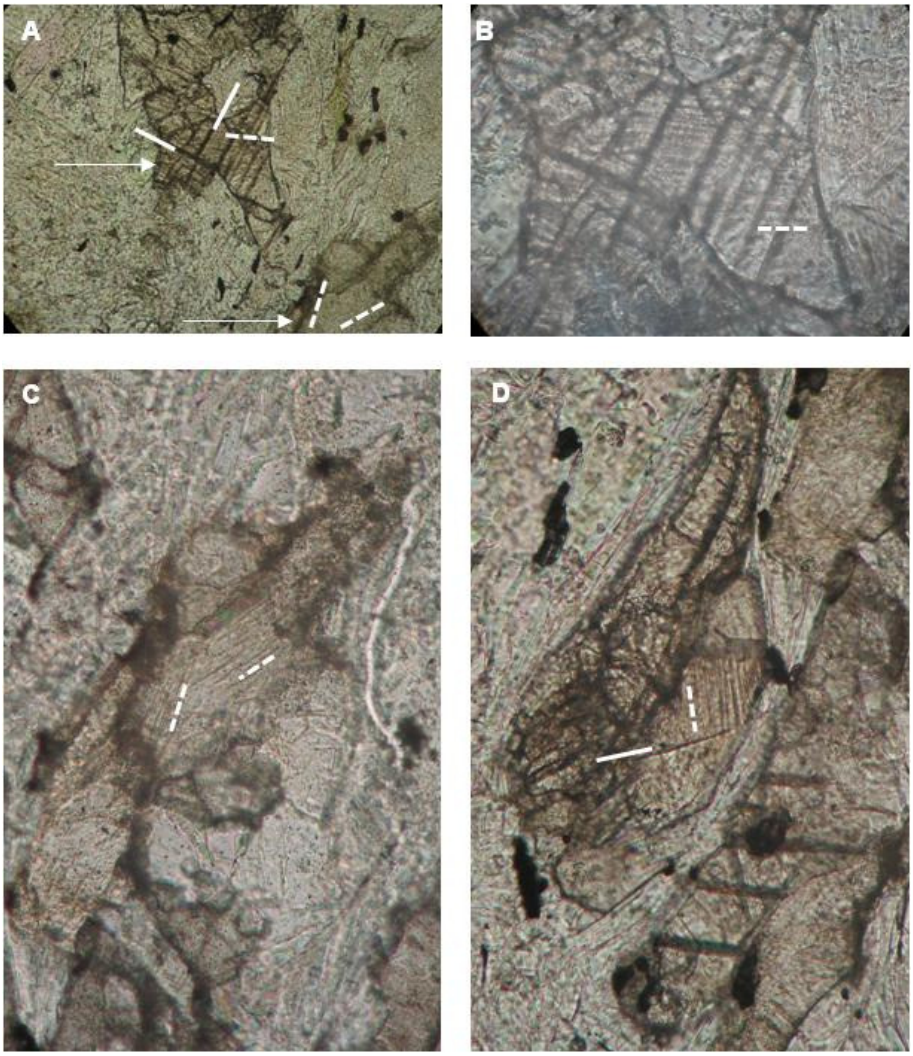

Fig. 5.8: Photomicrographs of fractured and twinned calcite. A-D) Sample KR7-83, suevite, basement metasediments, sample depth = 513.90 m. A) Central grain displays 2 cleavages (indicated with solid lines) oriented NNE-SSW and NW-SE, and one fracture set (indicated with dashed lines) oriented E-W; second grain in lower right corner displays 2 fracture sets oriented NNE-SSW and ENE-WSW; other minerals include quartz and feldspar in image; image width = 1 mm, PPL. B) Close-up of central calcite grain in A); image width = 0.20 mm, PPL. C) Close-up of lower right grain in A); image width = 0.075 mm, PPL. D) Calcite grain with cleavage oriented ENE-WSW and 1 fracture set oriented NNW-SSE; image width = 0.075 mm, PPL.

Scanning electron imagery of the melt particles in the LB-07A core is contained in Appendix 5b.

In the LB-07A core, no carbonate melts were observed, and certainly no carbonate-silicate immiscibility was in evidence, unlike that

described from the Ries crater (Graup, 1999) or the Haughton crater (Osinski and Spray, 2001).

Table 5.6: Differences between suevites along the LB-07A core.

	Upper Impactites	Lower Impactites	Basement suevite (483 m depth)	Basement suevite (513.9 m depth)
Colour of matrix	Grey-brown	Moderate greenish-yellow	Dark grey	Light grey
Colour of melt particles	Grey-brown or whitish	Moderate yellowish-green	Grey-brown	Grey-brown
Size of lithic and mineral clasts	0.1 mm - 2 cm	0.1 - 1 mm	0.1 - 0.5 mm	0.1 - 0.5 mm
Mean size of melt particles	~ 1 mm	~ 0.1 mm (up to 1 cm)	0.1 - 1 mm	0.1 - 0.5 mm
Mean % PDF sets of total quartz grains	5.8 %	5 %	0	0
Maximum % PDF sets of total quartz grains	12.1 %	6.5 %	0	0

**Colours after Munsell (1912).*

5.4.1 Melt Particle Characteristics in the Upper Impactites

Melt particle abundances in the suevites of the upper impactite unit range from 1.5 to 7 vol% (Table 3.2). No variation in either shape or size distribution of the melt particles was detected between the three suevitic breccia units in the upper impactite sequence.

The melt particles range in shape from shard-like (Fig. 5.9 A, B, E, F) to rounded (Fig. 5.9 C, D, I-L). The size of the melt particles is mostly of the order of 1 mm (longest dimension), with a few having maximum widths of 500 µm.

Melt particles in the upper impactites are either mafic (brown-black; with flow structures, with or without vesicles; Fig. 5.9 I-L) or felsic (colourless to white, aphanitic, commonly with flow structures and vesicles; Fig. 3.13 B; Fig. 5.9 I-L). The mafic particles comprise

approximately 95% of all melt particles observed. Some lithic clasts have also been partially melted (Fig. 5.9 H), as part of the original material can be observed (e.g., metagreywacke). No microlites were observed in any of the melt particles in the upper impactites.

Clasts within the melt particles consist of rounded quartz grains (some with planar fractures in the largest grains) that are generally ≤ 50 μm in diameter (Fig. 5.9 F, L).

5.4.2 Melt Particle Characteristics in the Lower Impactites

The upper suevite intercalation (at 430.13 to 430.33 m depth) in the lower impactite unit contains the highest proportion of melt in the LB-07A core. Two thin sections of this sample were examined: one with 36 vol% melt (Fig. 5.10 A) and the other with 18 vol% melt. The largest melt fragment yet observed in the LB-07A core was from the former sample, and it alone is responsible for the large volume percentage. It is a sub-rounded clast with a maximum length of 1 cm and a width of 4 mm (Fig. 5.10 A, B). This estimate of melt abundance is clearly not representative, but it must be emphasized that the other thin section from this depth also contains a substantial proportion of rounded melt particles. The melt particles in the second thin section are 0.2–1.5 mm in diameter and the majority are <1 mm in diameter. Within both thin sections many sub-rounded to sub-angular melt particles with diameters between 100 μm and 5 mm were found (Fig. 5.11 A-L).

The melt particles of the lower impactite suevites contain quartz fragments (angular to rounded; Fig. 5.11 A, B, E-H, J-L) that may contain shock fractures (in some clasts to such a great extent that the particles have a shattered appearance). Some quartz clasts also display undulose extinction. The clasts within the melt fragments of the lower impactites seem to be slightly larger than those observed in melt fragments of the upper impactite suevite (100 μm *vs.* 50 μm).

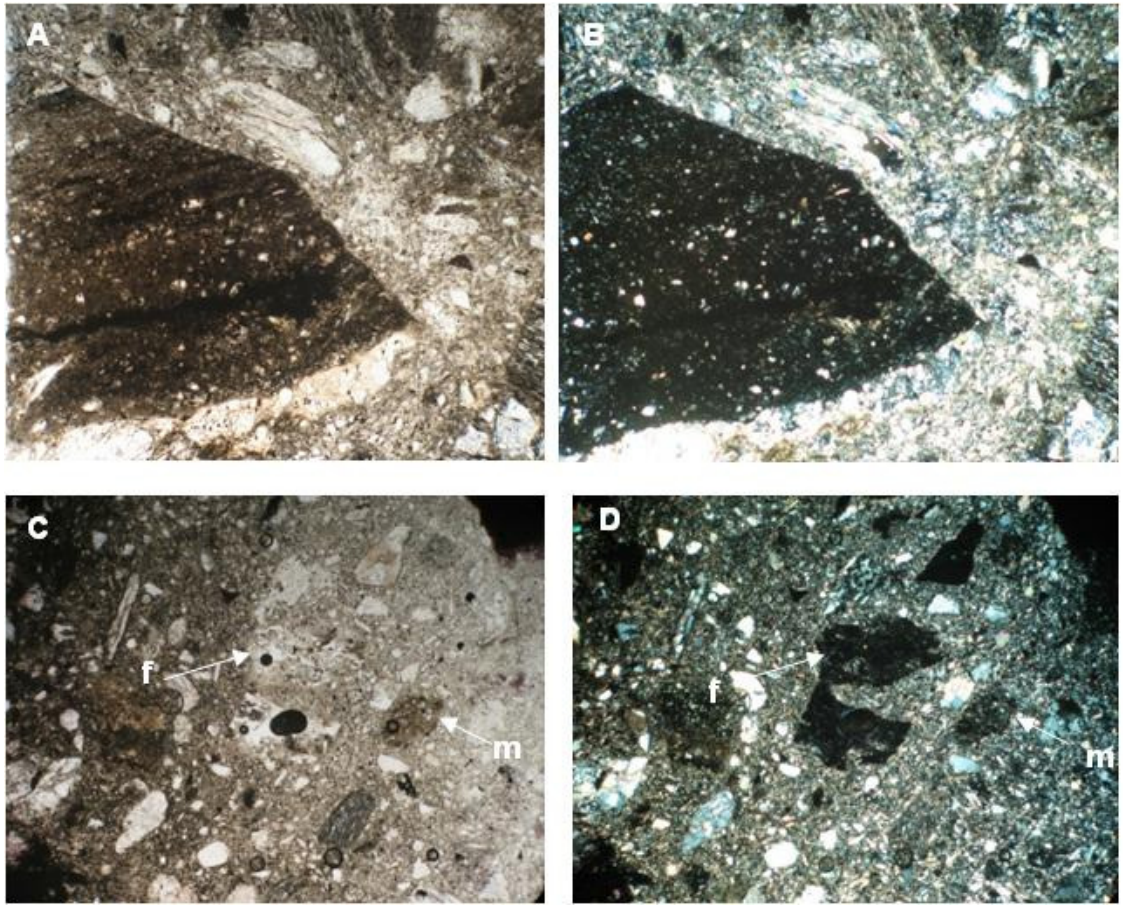

Fig. 5.9: Photomicrographs of melt particles from the upper impactites. A) and B) Sample KR7-6, suevite, upper impactites, sample depth = 360.65 m; angular shard; image width = 3 mm: A) PPL; B) CPL. C) and D) Sample KR7-36, suevite, upper impactites, sample depth = 364.45 m; felsic (f) and mafic (m) melt particles (indicated with arrows); image width = 3 mm: C) PPL; D) CPL. Continued on next page.

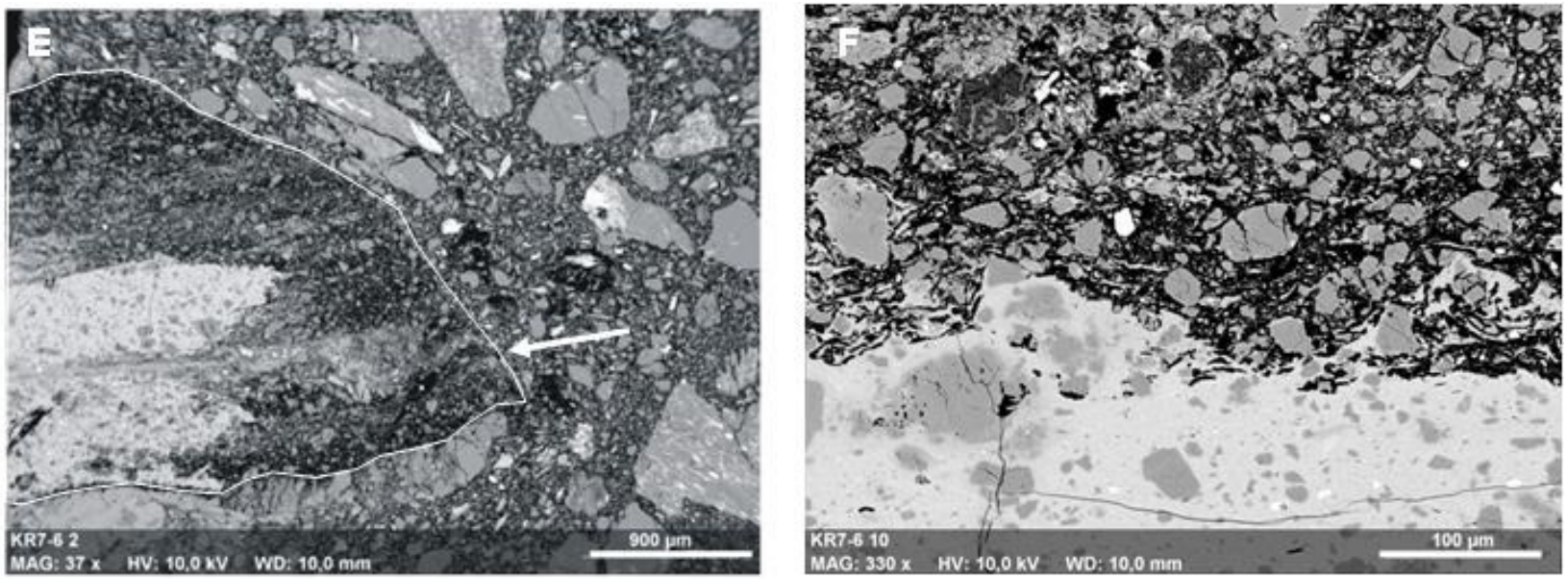

Fig. 5.9 (cont'd): E) - F) Backscattered electron images of melt clasts in upper impactite suevite: the grey fragments correspond to quartz (moderately grey indicates silica-rich lithologies), with lighter white-grey and dark grey indicating the mixed melts. E) and F) Sample KR7-6, suevite, upper impactites, sample depth = 360.65 m; angular shard: E) Angular shard (outlined and indicated by arrow) with highly variable composition indicated by SEM imagery; width of scale bar = 900 µm. F) Enlarged area from E), showing the boundary between felsic and mafic phases in the melt particle, with both phases characterised by quartz inclusions; width of scale bar = 100 µm. Continued on next page.

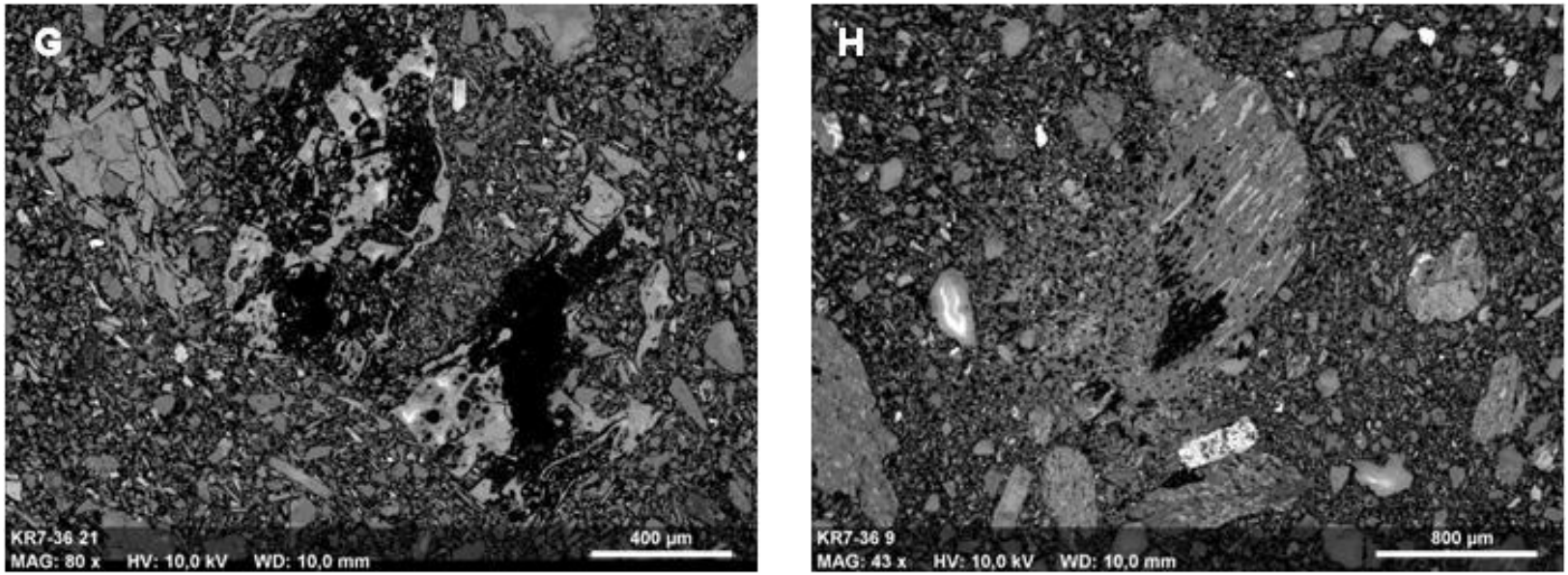

Fig. 5.9 (cont'd): Backscattered electron images of melt clasts in upper impactite suevite. G) and H) Sample KR7-36, suevite, upper impactites, sample depth = 364.45 m: G) Felsic melt particles which are highly vesiculated; width of scale bar = 400 µm. H) Partially melted metagreywacke clast; width of scale bar = 800 µm. Continued on next page.

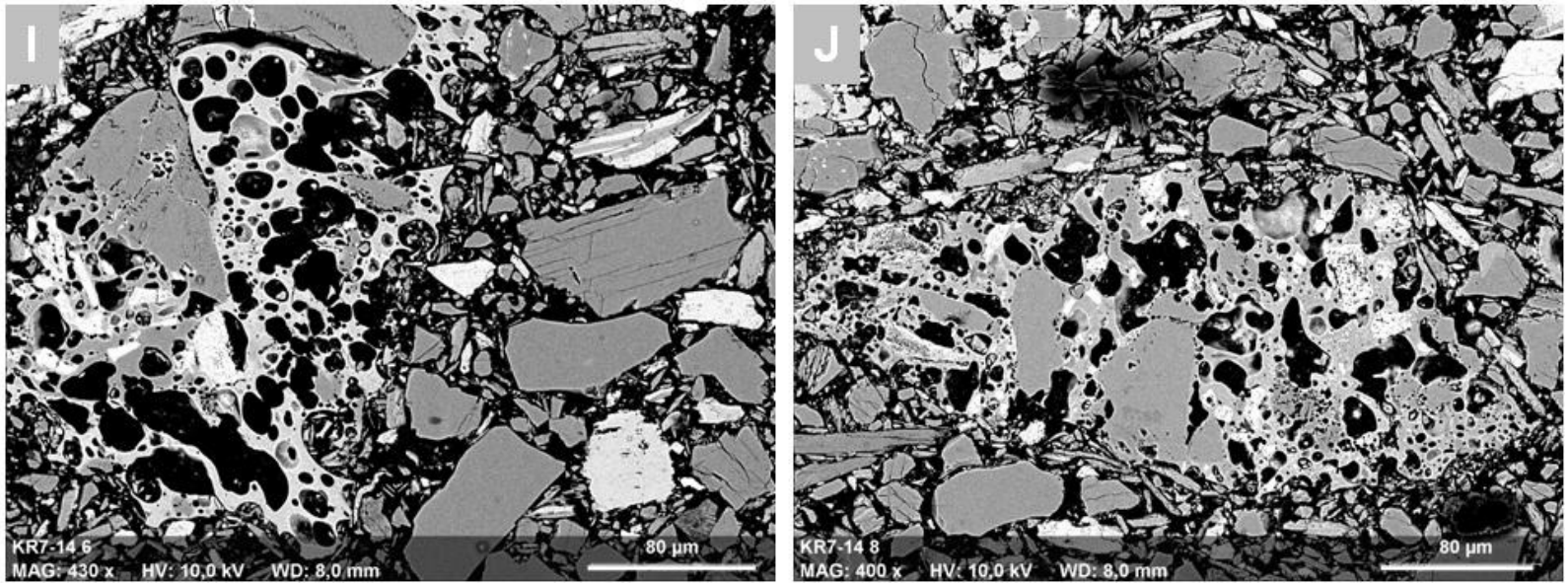

Fig. 5.9 (cont'd): I) – J) Backscattered electron images of melt clasts in upper impactite suevite. Sample KR7-14, suevite, upper impactites, sample depth = 398.44 m: highly vesicular melt particles in clastic matrix which consists of mixed lithologies and minerals; I) and J) width of scale bar = 80 µm. Continued on next page.

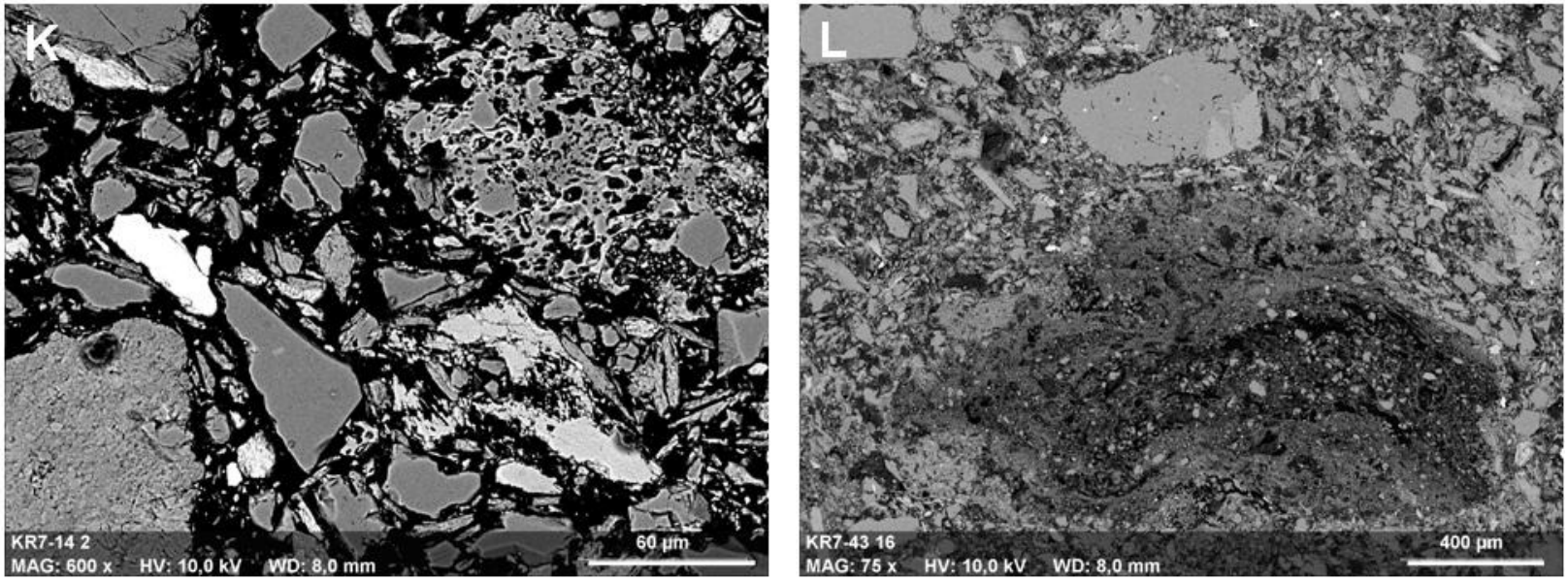

Fig. 5.9 (cont'd): Backscattered electron images of melt clasts in upper impactite suevite. K) Sample KR7-14, suevite, upper impactites, sample depth = 398.44 m: width of scale bar = 60 µm. L) Sample KR7-43, suevite, upper impactites, sample depth = 384.84 m; melt particle which consists of flow bands. The particle is more mafic than the surrounding matrix and the centre of the particle is characterised by numerous quartz clasts; width of scale bar = 400 µm.

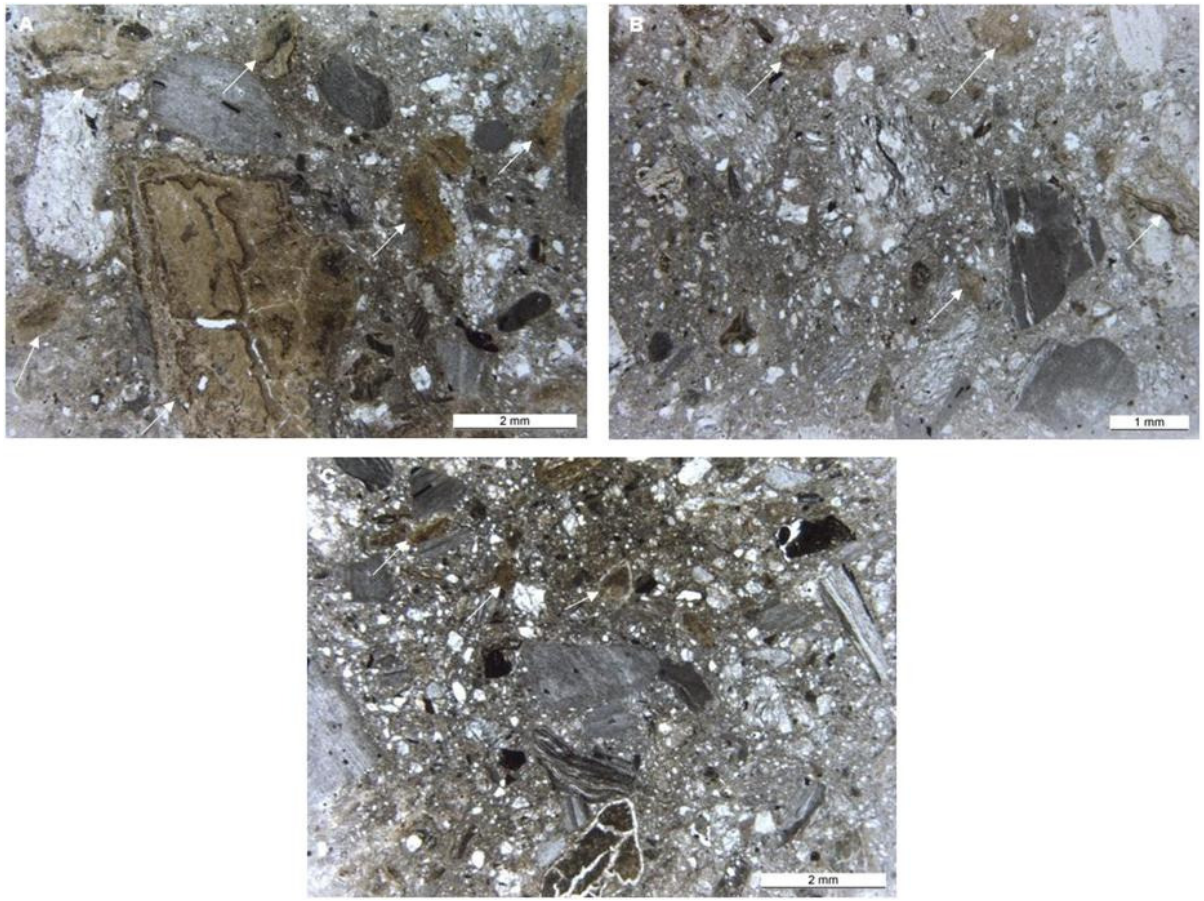

Fig. 5.10: Macro-photographs of the lower impactite suevites. Melt particles (indicated with arrows) are brown in colour. A) and B) Sample KR7-23; suevite, lower impactites, sample depth = 430.13 m; distinct flow structures can be noted in many of the melt particles. C) Sample KR7-45; suevite, lower impactites, sample depth = 445.22 m.

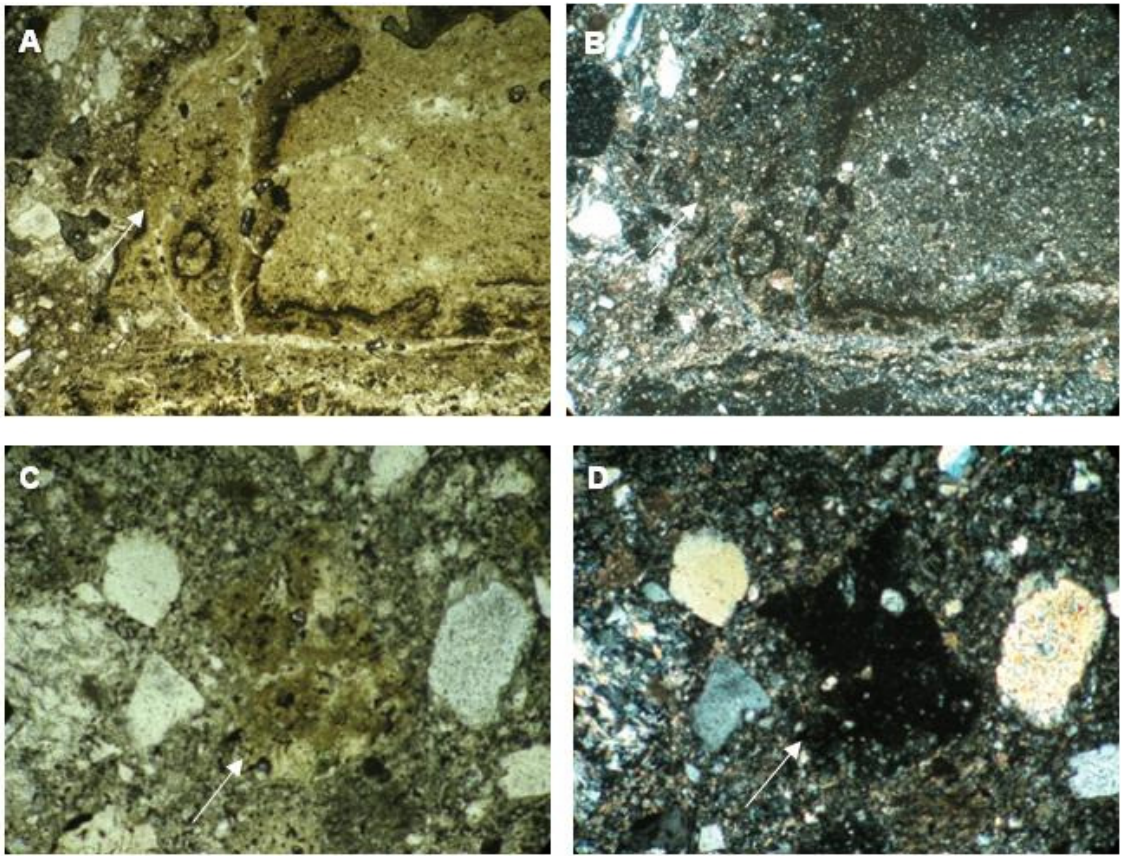

Fig. 5.11: Photomicrographs of melt particles (indicated with arrows) from the lower impactites. Sample KR7-23, suevite, lower impactites, sample depth = 430.13 m. A) and B) Part of the largest recorded melt particle in core LB-07A; image width = 3 mm: A) PPL; B) CPL. C) and D) Melt particle with distinct colour variation and large quartz clasts; image width = 3 mm: C) PPL and D) CPL. Continued on next page.

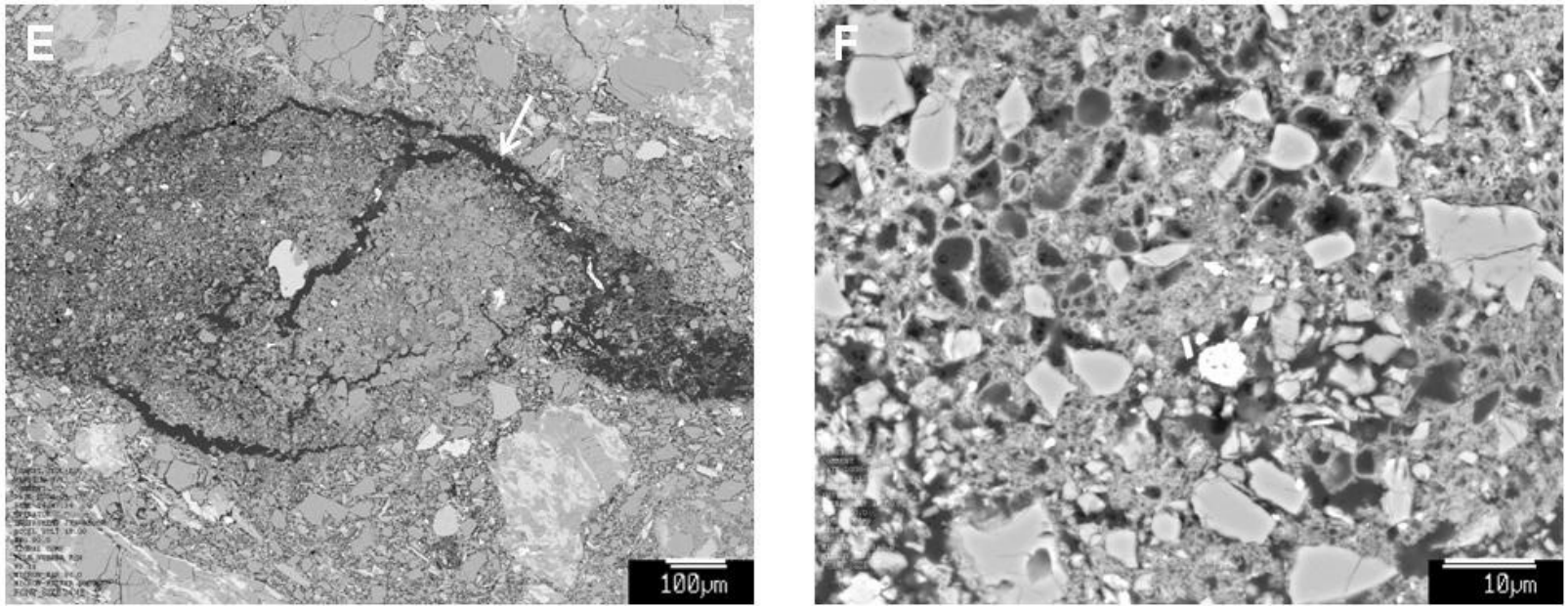

Fig. 5.11 (cont'd): E) – F) Backscattered electron images of melt clasts in lower impactite suevite: the grey fragments correspond to quartz (moderately grey indicates silica-rich lithologies), with lighter white-grey and dark grey indicating the mixed melts. Sample KR7-23, suevite, lower impactites, sample depth = 430.13 m. E) Sub-rounded melt particle with variable composition. Matrix is composed of fine-grained clastic phases, and is not molten; width of scale bar = 100 µm. F) Entire image consists of part of a single melt particle with distinctive sub-rounded quartz clasts and numerous rounded pores; width of scale bar = 10 µm. Continued on next page.

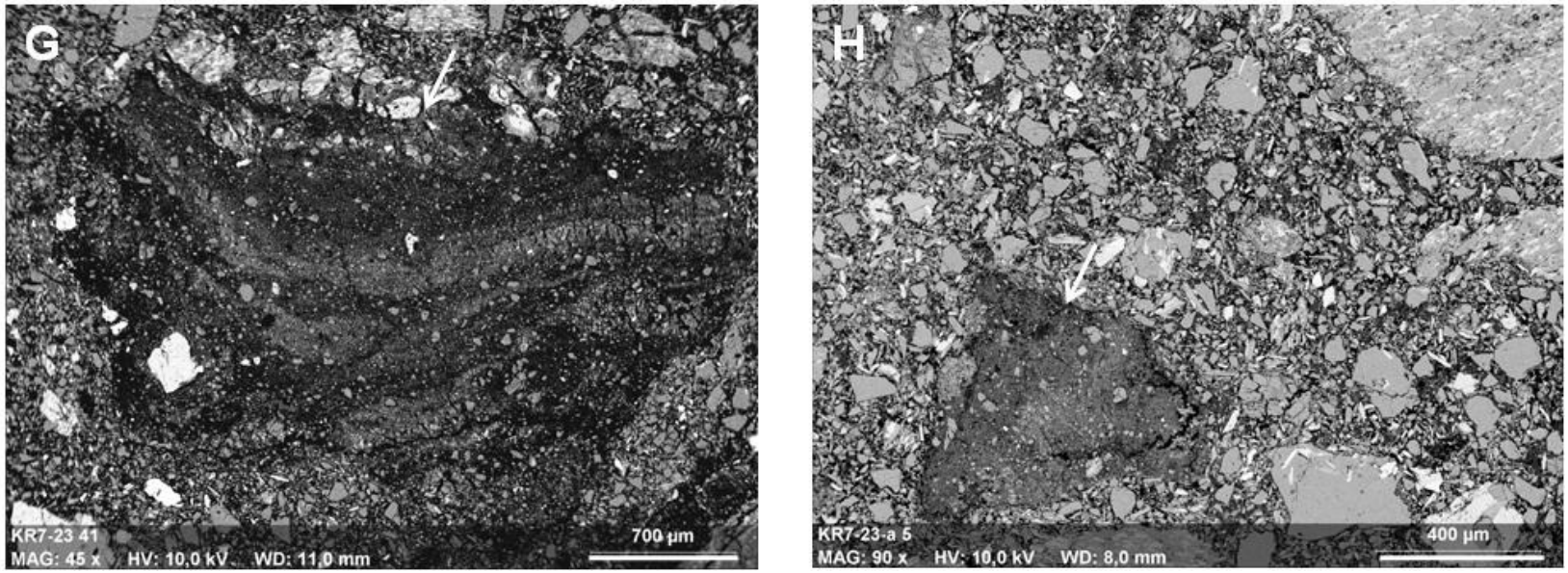

Fig. 5.11 (cont'd): G) – H) Backscattered electron images of melt clasts in lower impactite suevite. Sample KR7-23, suevite, lower impactites, sample depth = 430.13 m. G) and H) Discrete melt particle in clastic matrix (indicated by arrow). Continued on next page.

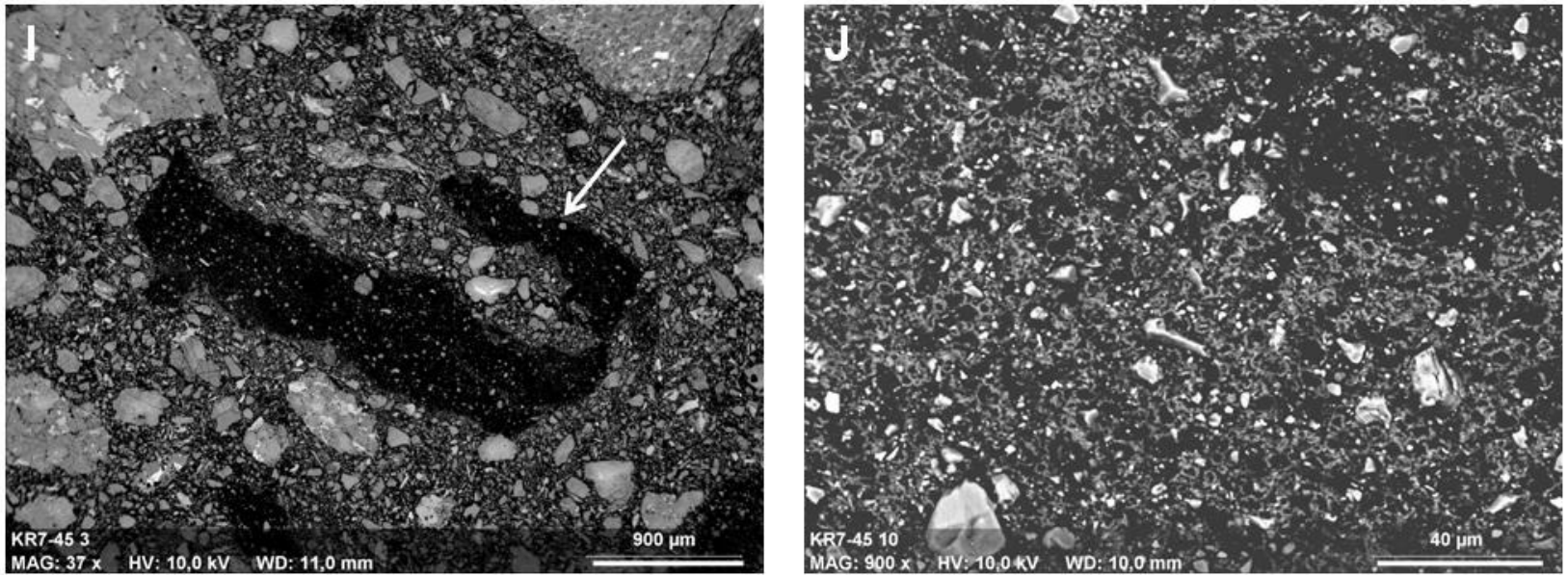

Fig. 5.11 (cont'd): I) - J) Backscattered electron images of melt clasts in lower impactite suevite. Sample KR7-45, suevite, lower impactites, sample depth = 445.22 m; matrix consists of sub-rounded to angular fragments of target rocks and minerals. I) Sub-angular melt particle (indicated by arrow) with a distinct lack of vesicles; width of scale bar = 900 µm. J) Entire image consists of part of a single melt particle with sub-rounded to angular inclusions; width of scale bar = 40 µm. Continued on next page.

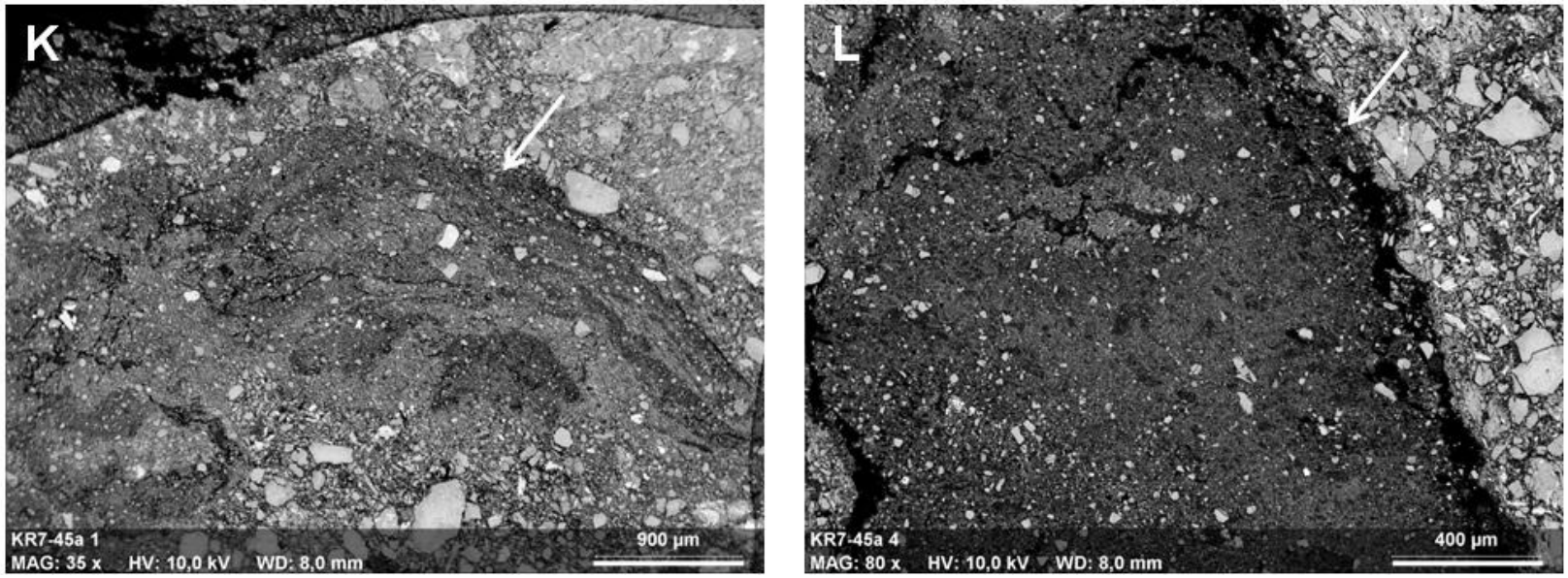

Fig. 5.11 (cont'd): K) - L) Backscattered electron images of melt clasts in lower impactite suevite. Sample KR7-45, suevite, lower impactites, sample depth = 445.22 m; matrix consists of sub-rounded to angular fragments of target rocks and minerals. K) Droplet-shaped melt particle (indicated by arrow) with flow structures of variably mafic composition; width of scale bar = 900 µm. L) Homogeneous melt particle which contains few vesicles; width of scale bar = 400 µm.

No microlites were observed in any of the particles. The melt fragments themselves show evidence of flow (schlieren) and are commonly vesiculated (Fig. 5.11 E) though this effect is far less pronounced than in the melt particles of the upper impactites (Fig. 5.9 I-L). The suevite intercalation at 445.13 m depth has similar matrix and melt fragment characteristics to the intercalation at 430.13 m, although it has a relatively smaller proportion of melt particles (5.6 vol%; Figs. 5.10 C; 5.11 I-L).

5.4.3 Melt Particle Characteristics in the Basement Suevites

In both suevite intercalations of the basement some discrete melt particles display a fine vesicular texture (Fig 5.12 A-F), with a distinct lack of microlites. No felsic melt particles were noted in thin section examination in the basement metasediments. Core disaggregation does not allow good melt particle statistics to be compiled. Melt particles as seen in grain mount are similar in size to the lithic and mineral clasts in the suevites (0.1–0.5 mm; Fig. 5.12 A-D). All particles are rounded to sub-rounded (Fig. 5.12 A-E).

5.4.4 Possible Sources of Alteration in Suevites

The various suevites from the upper and lower impactites, as well as those from the basement section, differ in colour; this seems to be the result of variable alteration. The melt fragments from the upper and lower suevites resemble each other in terms of shape, size and general appearance, and all contain quartz fragments.

The suevites are similar to each other in terms of clast content (see section 3.2) and chemical signatures (see section 4.3.6). It is possible that different phyllosilicate minerals may be responsible for the colour differences of the suevites.

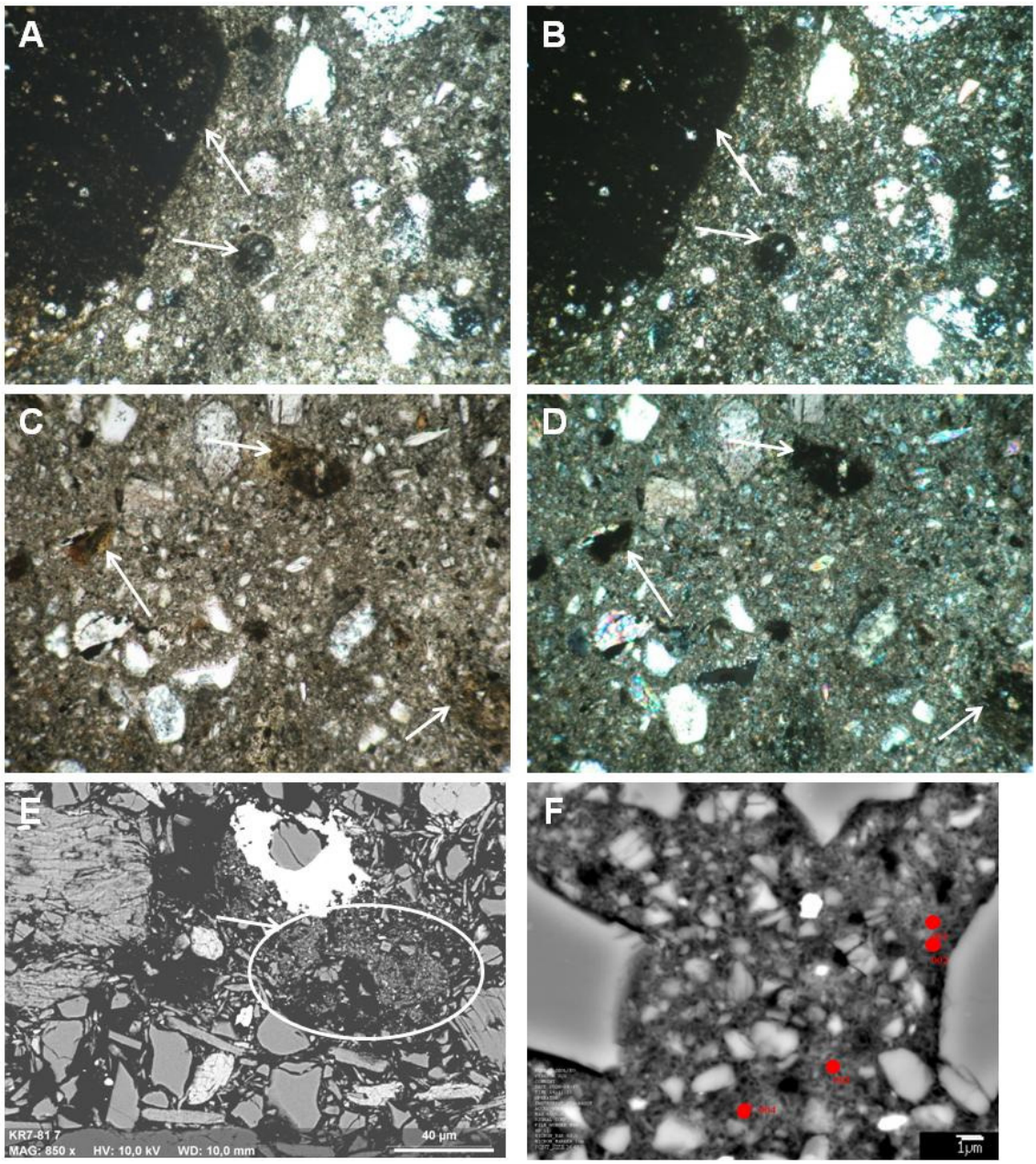

Fig. 5.12: A-D) Photomicrographs of melt particles (indicated with arrows) from the suevite injections into the basement metasediment. A) and B) Sample KR7-81, suevite, basement metasediments, sample depth = 483.00 m; image width = 1.75 mm: A) PPL; B) CPL. C) and D) Sample KR7-83, suevite, basement metasediments, sample depth = 513.90 m; image width = 1.75 mm: C) PPL; D) CPL. E)-F) Backscattered electron image of melt clasts in basement suevite: the single light grey-white fragment is pyrite, grey fragments correspond to quartz (moderately grey indicates silica-rich lithologies), with dark grey indicating the mixed melts. Sample KR7-81, suevite, basement metasediments, sample depth = 483.00 m; E) Highly vesicular melt particle (circled) in clastic matrix; width of scale bar = 40 µm. F) Vesicular material, with the analysed points (by EMPA; red points) indicated; width of scale bar = 1 µm.

In order to examine potential alteration, X-ray diffraction was performed on selected samples from the different units from the following depths: 382.94 m (suevite, upper impactites); 430.13 m (suevite, lower impactites); 483.00 m (suevite, basement); 513.90 m (suevite, basement). These results are presented in Appendix 5c.

Besides comparable quantities (semi-quantitative evaluation) of chlorite, muscovite, illite and quartz in all samples, the major differences noted were that significant plagioclase and calcite occur in the upper impactites, lower impactite suevites and the upper basement suevite, but not in the lowermost basement suevite, and that the lowermost basement suevite contains a minor amount of smectite. It was noted in section 4.3.6 that the lowermost suevite has comparatively higher SiO_2 and lower Al_2O_3, Fe_2O_3, Na_2O, K_2O and P_2O_5 contents than the other suevites. This suevite contains granophyric-textured clasts and muscovite, with little metagreywacke and no shale, and this explains the somewhat different chemical signature. The smectite could represent altered melt – however, the proportion of the melt in the sample is so small that it seems unlikely that it would form a significant phase in XRD analysis. However, no significant differences could be established between the bulk compositions of the different suevites of the core, which might explain the colour variation.

5.4.5 Suevite Melt Particle Compositions

Melt particles in core LB-07A have been divided on the basis of colour and size differences between the upper and lower impactite suevites and suevites of the basement metasediments. Melt particle major element compositions were determined at the Humboldt-University in Berlin using the electron microprobe at the Museum of Natural History using a beam diameter of 10 µm (see Chapter 2 for operating conditions; Appendix 5d). Approximately 272 points were analysed on melt particles in samples from throughout the core; however, many of these analyses displayed poor totals (lower than

60 wt%) which were rejected. These poor totals reflected highly altered areas in the sample (to highly porous phyllosilicate aggregates) and possible analyses of holes. Additionally, results which represented intersections with quartz clasts in the melt (i.e. SiO_2 = 100 wt%) were also removed from the database.

Appendix 5d presents the modified data set (modified with respect to removal of poor analyses and quartz compositions). Compositional data from 3 melt particles from sample KR7-17, 1 particle from sample KR7-7 and 2 particles from sample KR7-35 were collected for the upper impactites. The melt particles of the upper impactites have been shown petrographically to represent both mafic and felsic phases with a predominance of mafic over felsic particles. This study focused on the analysis of the mafic particles from the upper impactites (owing to their predominance; additionally SEM analysis indicated that the felsic particles are highly siliceous). For the lower impactites, 4 particles were analysed in both samples KR7-45 and KR7-23, and for the basement suevite (sample KR7-81), one melt particle was analysed.

For the melt particles of the upper impactites, most of the totals were in the range of 70 to 95 wt%. All data with totals greater than 80 wt% were used. In order to assess that these data are representative of proper compositions, a ternary plot of Al_2O_3-(MgO+FeO)-SiO_2 was plotted with the cut-off totals of 80 wt% and 90 wt% (Fig. 5.13 A). In the case of the lower impactites, the majority of analyses were between 60 wt% and 80 wt% (only one sample had a total of greater than 90 wt%). A ternary plot of Al_2O_3-(MgO+FeO)-SiO_2 was plotted for the lower impactites (Fig. 5.13 B) with the following cut-off totals: 60 wt%, 70 wt%, 80 wt% and 90 wt%.

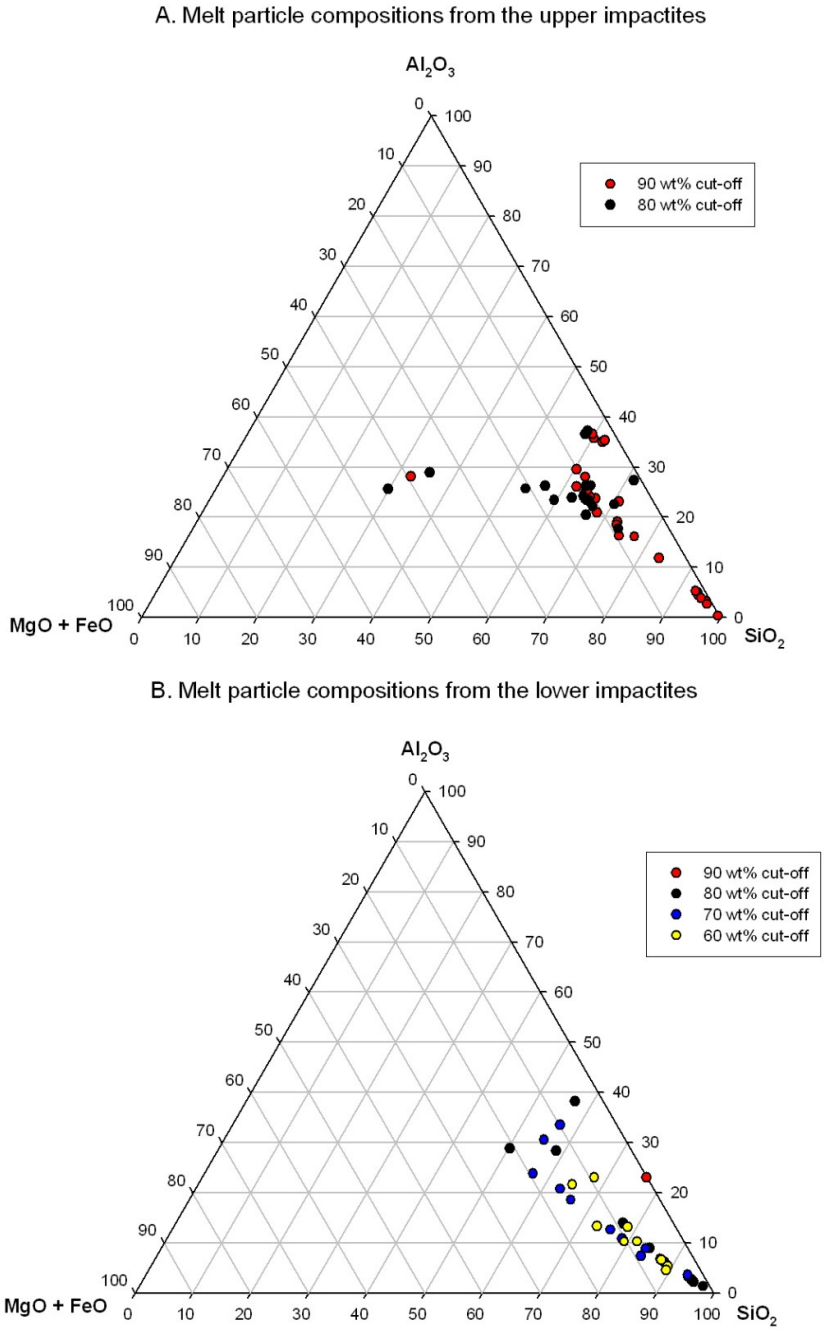

Fig. 5.13: Ternary plots of Al_2O_3-(MgO+FeO)-SiO_2 for A) analyses of melt particles from the upper impactites and B) analyses of melt particles from the lower impactites obtained by electron microprobe analysis (10 µm defocused beam). Cut-off points for the totals are indicated in the legend, in order to test the validity of the melt particle analyses.

For the upper impactites, it was concluded that the entire dataset in the range of 80-99 wt% would be used, as the results are similar regardless of the cut-off total. This, too, was concluded for the lower

impactites. It is clear from these plots (Fig. 5.13) that there is some variation in the melt particle compositions and, for the lower impactites, there is clearly some intra-melt heterogeneity, as the majority of the analyses are from the single large melt particle intersected in sample KR7-23.

Unfortunately, the melt particle analyses from the basement suevite KR7-83 all displayed low totals (between 20 wt% and 51 wt%). Basement suevite KR7-81, however, yielded 4 compositions between 65 and 72 wt%, and these are used here, in order to provide a comparison with the melt particles of the upper and lower suevites. It was noted by optical microscopic analysis that these melt particles are highly vesiculated, one reason why good compositional data could not be collected.

Figure 5.14 shows 4 binary plots of the melt particle compositions, with all the different melt particle data shown separately. The most important trend is the clear internal variation of melt particle compositions – i.e., the samples do not consist of one melt phase, but rather a variety. The melt particles from different samples show a variety of ranges for SiO_2. Analyses from particles in KR7-17 (upper impactites) vary between 40 and 60 wt% SiO_2, those from sample KR7-7 are between 50 and 65 wt%, while those from KR7-35 vary between 50 and 95 wt% (Fig. 5.14 A). These ranges are not insubstantial, and indicate highly variable inputs of SiO_2 between the different particles. The analyses from the particles of the lower impactites vary between 40 and 85 wt% (Fig. 5.14 A), whereas those from the basement suevite show the least variation, of between 40 and 50 wt% (Fig. 5.14 A).

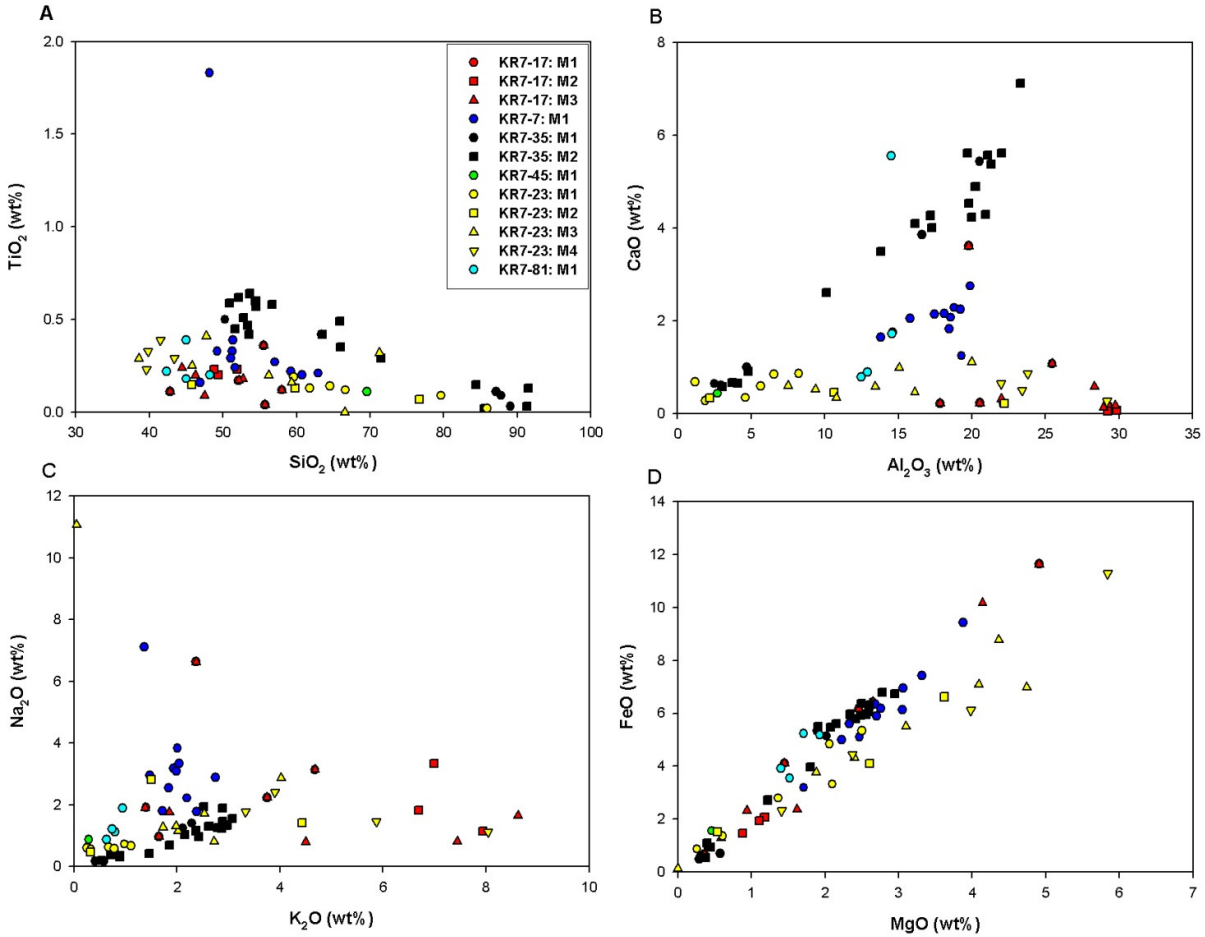

Fig. 5.14: Binary plots of the electron microprobe analyses (10 µm defocused beam): Melt particle phases in the within-crater suevites from core LB-07A. A) SiO_2 vs. TiO_2; B) Al_2O_3 vs. CaO; C) K_2O vs. Na_2O; D) MgO vs. FeO. Data in wt%.

TiO_2 values are generally less than 0.7 wt%, although a single outlier from sample KR7-7 is evident, and may reflect the presence of a Ti-rich mineral such as rutile, which has been noted in the core, and in this sample.

Some positive correlation between CaO and Al_2O_3 can be observed in Fig. 5.14 B, particularly for analyses from sample KR7-35. There is much spread in the data for Al_2O_3, with negligible CaO inputs for melt particles from the lower impactites. The particle analysed from sample KR7-7 has the most similar values intra-sample for CaO and Al_2O_3 (Fig. 5.14 B). Positive correlation between Na_2O and K_2O values are observed in Fig. 5.14 C. It is likely that much of the Al_2O_3, Na_2O, K_2O and CaO may be related to different inputs of the feldspar minerals, which are common in the core (more so in the lithic clasts than as discrete mineral phases). FeO and MgO contents are strongly correlated, as seen with the bulk analyses from the LB-07A core (see Chapter 4), and considerable values of up to 12 wt% FeO with 5 wt% MgO are observed (Fig. 5.14 D). This indicates that FeO and MgO-bearing minerals, such as the phyllosilicates (biotite and chlorite) may have contributed to these melt particle compositions.

Thus, it is evident that the melt particles do not form homogeneous entities (i.e, discrete mineral melts), but rather consist of mixtures of minerals, or even melting of bulk target rock. This is supported by the extensive petrographic and SEM image evidence (see Figs 5.9, 5.10, 5.11) where distinct flow banding and differences in the colour directly related to compositional changes are apparent. The particles of the basement suevite are more homogeneous in composition, which is supported by their optical characteristics (see Fig. 5.12) which indicates less variation in banding and colour.

In order to ascertain more strictly the compositions of the melt particles, and to work out the contributory phases, a number of ternary diagrams were produced (Fig. 5.15). The different melt

particles are indicated together with fields indicating the positions of representative mineral data from Deer et al. (1971) for the suspected contributory mineral phases (quartz, albite, anorthite, K-feldspar, muscovite, biotite, chlorite and calcite) based on the target rocks in the vicinity. Additionally, the proposed target rock lithologies of Koeberl et al. (1998) as well as the position of the average Ivory Coast tektites (Koeberl et al., 1997a) are shown.

Figure 5.15 A indicates that the melt particles form a trend originating from 100% SiO_2 – i.e. quartz. The trend moves towards a central region between Al_2O_3 and (MgO+FeO). This suggests that there may have been input by feldspars and muscovite (located to the right of the trend) as well as the more iron-rich biotite and chlorite (located to the left of the trend). In some cases, direct overlap into the different mineral areas is observed (e.g., plagioclase). The target rock lithologies of shale and phyllite-greywacke fall directly into the central region of the trend. In order to fully understand the different inputs by feldspar material (K-feldspar as well as plagioclase), as well as the newly defined target rock grouping of calcite (this study), a ternary plot of K_2O-Na_2O-CaO was produced (Fig. 5.15 B). There is some direct overlap of the melt particle analyses in these fields; however, most of the analyses plot in a region central to the three apices. Analyses from sample KR7-35 trend towards calcite, which has been defined as a contributory target lithology in this study (Chapters 3, 4). On the whole, it appears that the melt particle analyses represent mixes involving feldspar minerals. It is also known from Fig. 5.15 A that there is some phyllosilicate input, and this may also provide a control over the K_2O contents. In order to elucidate this possibility, Fig. 5.15 C, an AK(FM) diagram, was plotted.

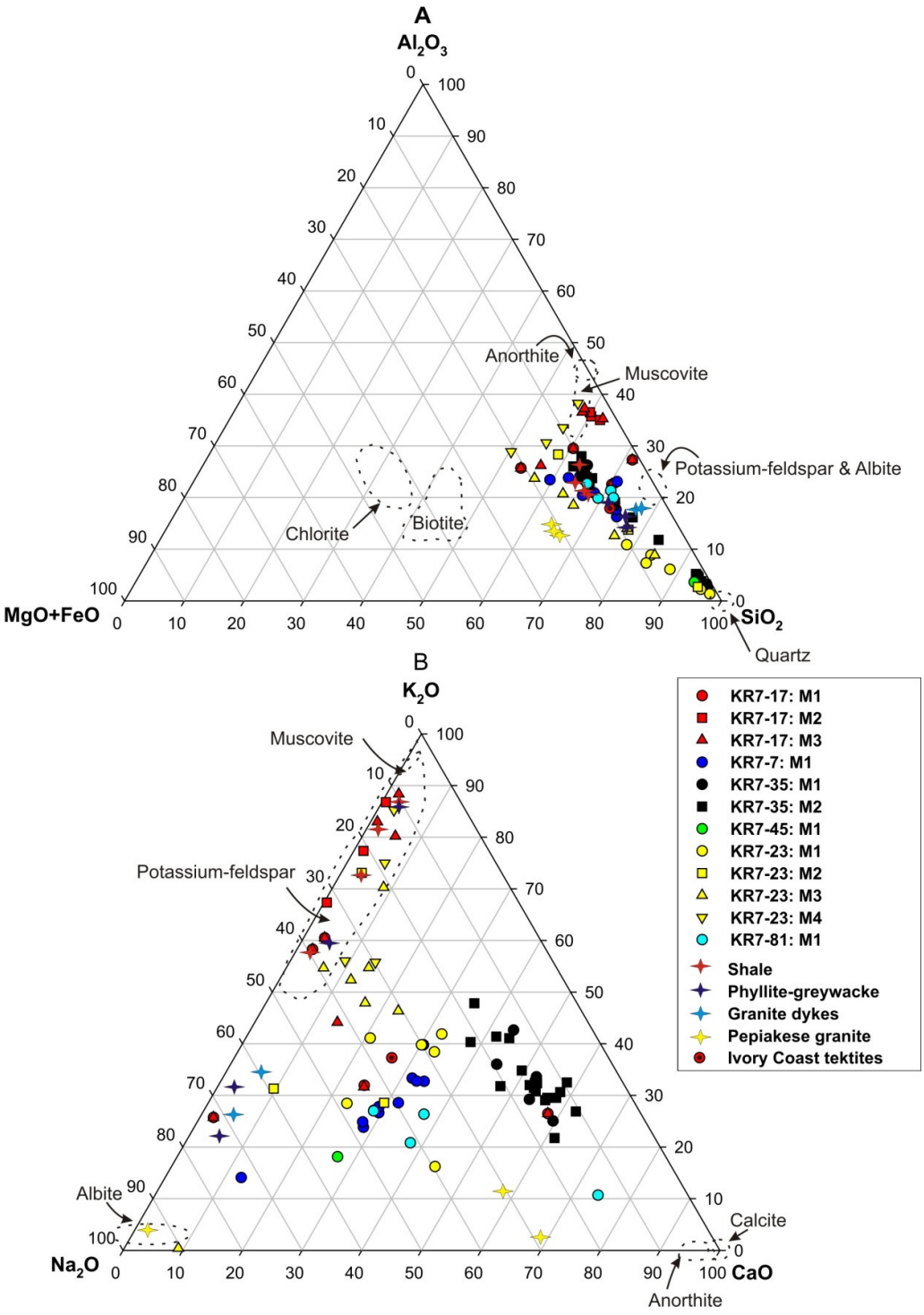

Fig. 5.15: Ternary discrimination diagrams for the electron microprobe analyses (10 µm defocused beam) of the melt particles from core LB-07A. A) Al_2O_3-(MgO+FeO)-SiO_2 and B) K_2O-Na_2O-CaO. Fields for common minerals in the LB-07A core are indicated (after Deer et al., 1971). Average target rock compositions (phyllite-greywacke, shale, granite dykes, Pepiakese granite; after Koeberl et al., 1998) and the Ivory Coast tektites (after Koeberl et al., 1997a) are also plotted. Continued on next page.

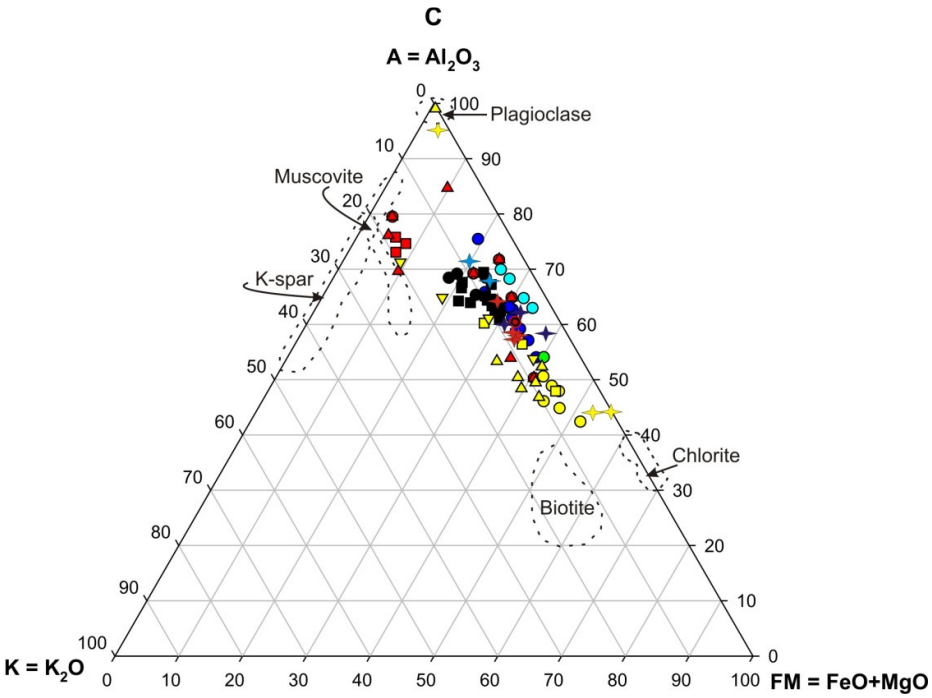

Fig. 5.15 (cont'd): Ternary discrimination diagrams for the electron microprobe analyses (10 µm defocused beam) of the melt particles from core LB-07A. C) AK (FM) diagram.

Nearly all melt particle analyses lie on a trend line between Al_2O_3 and FeO+MgO – in essence, indicating mixing between biotite and chlorite (MgO and FeO-rich minerals) and plagioclase feldspar (Al_2O_3-rich). There are a few outliers from this trend, and these analyses plot closer to the field represented by K-feldspar and muscovite (Fig. 5.15 C), both of which occur in the target rocks.

Thus a number of conclusions can be made from the within-crater melt particle compositional data:

1. Melt particles are not homogeneous and show internal variation (supported by the optical observations).
2. Melt particles are not composed of discrete mineral phases, but rather show evidence of mineral mixes and schlieren.
3. There is more compatibility between the melt particle analyses of the normalized contents of the shales and phyllite-greywackes, and to a lesser extent the granite dykes, with no overlap of the Pepiakese

granite target rock lithology with the melt particle compositions (this supports the observation of the chief core lithologies of metagreywacke and shale in the LB-07A core).

At this stage, it should be noted that the target rock lithologies proposed by Koeberl et al. (1998) are fairly similar in terms of mineral constituents, and it is possible that partial melting of the fine-grained constituents may have produced the melt compositions observed. This will be explored more fully in the Discussion chapter (chapter 7).

As already noted in this chapter, a number of analyses for the lower impactites had totals of less than 75 wt%. In order to ascertain whether these analyses are representative of the melt particle compositions observed so far, another AK(FM) plot was produced (Fig. 5.16). All the data from sample KR7-45 are indicated (this was the only sample with these lower totals). It is evident from the figure that these data lie along the same central trend as observed in Fig. 5.15 C, and that there is much overlap with the data from sample KR7-23 (also of the lower impactites). Thus, these data indicate that there are similarities in the lower total data, and that these lower totals are most likely analyses of pore space in highly vesicular or altered (to porous phyllosilicates) melt.

As the melt particles are clearly quite variable in their major element compositions, and clearly form a multi-variable system, it was decided to perform cluster analysis on particle compositions in order to ascertain how many phases could be differentiated for the melt particles (including the data for the lower totals).

The melt particle analyses (“cases”) were assessed using the Clustan Graphics 7 software (Wishart, 1997), utilizing the same methodology as employed in Chapter 4 (see Section 4.5).

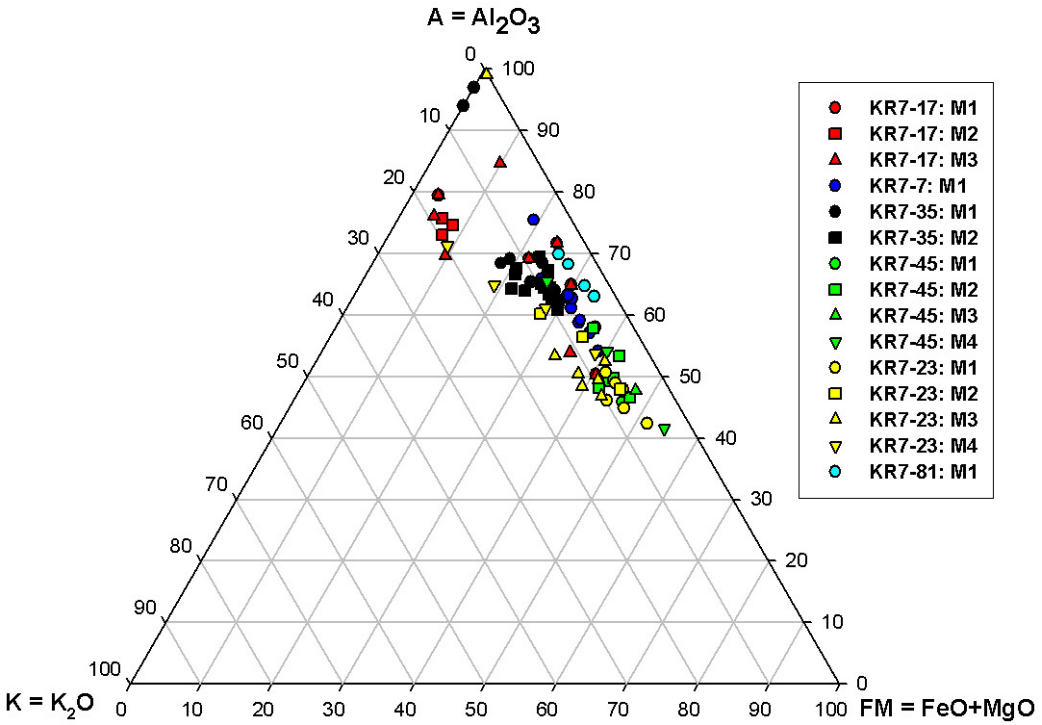

Fig. 5.16: Ternary discrimination diagram for the electron microprobe analyses (10 µm defocused beam) of the melt particles from core LB-07A. AK(FM) diagram.

The data were entered as continuous data, and no weighting was given to any sample. A Z-score transformation was utilized and the data were clustered according to their k-means (MacQueen, 1967), using the Euclidean Sum of Squares. The analysis used all the major element data. Initially 10 clusters were produced, but it was decided to use a 5 cluster analysis instead as this is more representative of the variation in the particles. The results are reported in Table 5.7.

Cluster analysis shows that most analyses are contained within clusters 1-3, with fewer than 10 cases in clusters 4 and 5 (Table 5.7). Cluster 1 is characterised by high CaO contents, with moderate to low concentrations of the other major elements. Cluster 2 contains high SiO_2 values, with low concentrations of the other major elements. Cluster 3 has the highest K_2O contents, moderate Al_2O_3 contents, and all other elements have low concentrations. Cluster 4

is characterised by high FeO and MgO values. Cluster 5 contains high Na_2O values, with moderate SiO_2 and Al_2O_3 contents, and all other elements have low concentrations. The different clusters clearly represent mineral mixes, with the dominant input of certain minerals. It is proposed the cluster 1 represents predominantly anorthite and calcite (supported by Fig. 5.15 B which indicated a clear calcite contribution to the particles of sample KR7-35), cluster 2 represents a predominance of quartz, cluster 3 of K-feldspar and muscovite, cluster 4 of biotite and chlorite and cluster 5 represents predominance of albite. This makes sense given that these minerals form parts of one or more of the target lithologies.

Table 5.7: Cluster analysis results for 5 cluster groups using 90 cases (i.e., samples) and 9 variables (major elements, see text for details) and the Euclidean Sum of Squares (k-means). The means and standard deviations of the groups are indicated (all data in wt%).

	Cluster 1 (n = 31)	**Cluster 2 (n = 34)**	**Cluster 3 (n = 12)**	**Cluster 4 (n = 5)**	**Cluster 5 (n = 5)**
SiO_2	53.6±5.6	65.2±15.8	48.2±6.2	37.0±8.2	55.8±9.07
TiO_2	0.4±0.3	0.2±0.1	0.2±0.06	0.2±0.1	0.09±0.09
Al_2O_3	18.9±3.0	6.5±3.9	26.4±3.6	21.7±2.8	17.8±2.3
FeO	6.1±1.0	3.0±1.8	2.7±2.0	16.0±7.6	3.1±1.7
MnO	0.07±0.04	0.02±0.02	0.01±0.02	0.07±0.04	0.03±0.02
MgO	2.7±0.7	1.3±1.5	1.5±1.2	6.5±2.5	1.2±0.7
CaO	3.5±1.7	0.8±0.5	0.3±0.2	0.3±0.3	0.7±0.5
Na_2O	1.8±0.8	1.1±0.8	1.9±0.9	1.4±1.0	7.2±2.3
K_2O	2.2±0.6	0.9±0.6	5.9±2.0	2.9±1.4	1.6±1.0

The cluster analysis allows us to more fully examine the compositional variation in the different melt particles. Table 5.8 shows the distribution of the clusters in the melt particles. The cluster analysis supports the observations made on the binary and ternary plots that the melt particles show some internal variation. The maximum number of clusters in a sample is 4, while some particles only have compositions in one cluster. Generally, most melt particles are composed of two different clusters, which supports the observations from SEM analysis. The only difference between the particles of the upper and lower impactites is that those from the upper impactites generally contain compositions falling into clusters

1, 3 and 4, whereas those of the lower impactites are dominated more by compositions in cluster 2. The basement suevite melt particles are composed of cluster 2 followed by cluster 1 contents. Thus, the cluster analysis results support the observations made that the melt particles show internal differences.

Table 5.8: Distribution of the clusters in the different melt particles from the within-crater suevites, produced by cluster analysis of 90 cases and 9 variables and the Euclidean Sum of Squares (k-means). See text for details.

Melt particle	Cluster 1	Cluster 2	Cluster 3	Cluster 4	Cluster 5
KR7-17 M1	2		1	1	1
KR7-17 M2			3		
KR7-17 M3	2		4	2	1
KR7-7 M1	9	1			1
KR7-35 M1	2	3			
KR7-35 M2	13	5			
KR7-45 M1		3			
KR7-45 M2		4			
KR7-45 M3		1			
KR7-45 M4		2			1
KR7-23 M1		6			
KR7-23 M2		2	1		
KR7-23 M3	2	3		1	1
KR7-23 M4			3	1	
KR7-81 M1	1	3			

5.4.5.1 Melt particle comparison to the Ivory Coast tektites

The Ivory Coast tektites represent the most distal melts related to the Bosumtwi crater. The major element compositions of the Ivory Coast tektites (Table 4.5; see also Koeberl et al. 1997, 1998) have been plotted against the melt particle phase compositions in Fig. 5.15. The average of the Ivory Coast tektites is compatible with the melt particle analyses for core LB-07A, as it plots in a central region of the analyses. As discussed in section 1.2.5.4, tektites represent melts of surficial material from an impact target sequence (Koeberl and Martínez-Ruiz, 2003). This phase is thought to represent a mixture of all of the target rocks.

5.5 Summary

It is clear that the clasts of the basement metasediments are shocked to a lesser degree (i.e., lower pressures) than the clasts of the

impactite sequence: far fewer shocked grains and a smaller range of PDF orientations are evident. The number of shocked quartz grains in all lithologies decreases with depth through the LB-07A core. The PDF measurements (Table 5.2) indicate that the quartz grains in the upper impactites have an average of 5.9 % displaying 1 or more PDF sets, whereas the lower impactites have an average of 4.4 % and the basement metasediments show an average of 1.8 %.

According to the measured PDF orientations, the basement metasediments were locally shocked to pressures of no more than 30 GPa (constrained by the absence of diaplectic quartz glass). Planar deformation feature orientations of base c (0001), ω $\{10\bar{1}3\}$ and s $\{11\bar{2}1\}$ are common to all three units, and a proportional increase in the orientations of c (0001) is noted with depth. The clasts of the impactites were shocked to higher pressures – this is evident by the more diverse array of measured PDF orientations, together with the presence of abundant melt particles and diaplectic glass.

No PDFs in feldspar have been noted, but rare diaplectic feldspar glass has been observed at various positions in the LB-07A core. Carbonate minerals show evidence of dense twinning and possible shock-generated fractures, and it believed that these fractures are limited to pre-impact calcite, as these features are not seen in the post-impact carbonate veins and pods.

Observations of the crystallographic orientations of PDFs in quartz from the upper impactites are directly comparable to those made by Morrow (2007).

The suevites of the upper impactites have a maximum proportion of 7 vol% melt, whereas the lower impactites vary between 5.6 and at most 36 vol% melt (maximum proportion of melt observed in the

core, from an unrepresentative sample) and less than 5 vol% melt in the basement suevites.

Melt particles in the different units are distinct from each other in terms of colour and, to a lesser degree, chemical composition. Individual melt particles are heterogeneous in their composition and form mixes of the different target rock minerals. A cluster analysis was performed, and it is evident that a number of particles consist of up to 4 different phases, accounting for their internal heterogeneity.

Chapter Six: Out-of-Crater Suevites

6.1 Introduction

Owing to the processes of erosion and weathering, few impact craters on Earth preserve a full range of within- and beyond-crater rim impactites. The Bosumtwi crater is one of only a few craters on Earth where rocks from the crater interior, crater rim region and distal ejecta (the Ivory Coast tektite strewn field) are still in existence (Glass, 1968, 1969; Glass et al., 1991; Koeberl et al., 1997a, 2005, 2006a, 2007a). Comparison of the characteristics of the different impactites allows insight into the formation processes of these rocks.

In February 2007, a sampling visit to Ghana was conducted in order to collect samples of the out-of-crater suevites, from both the northern and southern outcrops (Koeberl and Reimold, 2005; Fig. 6.1; Appendix 1), to allow comparison with the LB-07A suevites, and also to geochemically and petrographically characterise the suevites from south of the crater for the first time. The sampling locations of this study are shown in Fig. 6.1 and GPS coordinates are contained in Appendix 2. Two outcrops were examined in the south (outcrops 1 and 2) and two in the north (outcrops 3 and 4). Additionally, thin sections of some out-of-crater suevites and target rocks (prefix LB-; collected by W.U. Reimold and C. Koeberl; prefix J-; collected by W.B. Jones) were examined so as to more fully investigate the different clast populations of these breccias.

Out-of-crater suevites outside the Bosumtwi crater rim have been noted in various reports (e.g., Chao, 1968; Jones et al., 1981; Koeberl et al., 1998; Boamah and Koeberl, 2003; Koeberl and Reimold, 2005). The suevites from north of the crater have been characterised petrographically and geochemically (Koeberl et al., 1998; Boamah and Koeberl, 2002, 2003, 2006). Although suevites located south of the crater rim have been noted, they have not been studied extensively.

6.2 Methodology

Suevites from the northern and southern outcrops were examined in order to establish differences between those from the north and south in terms of clast populations, sizes and distribution as well as melt particle size, shape and distribution. Any horizontal or vertical variation within a particular outcrop was noted. Sixteen samples of either suevite or of the large (>10 cm) melt particles were collected. Selected samples were crushed for major and trace element analysis. Representative samples were analyzed for their major element content using XRF at the Humboldt-University (Berlin) and trace element content using ICP-MS at the University of the Witwatersrand (Johannesburg). Polished thin sections were made at SGS Lakefields (Johannesburg), and some were also made at the Humboldt-University (Berlin), in order to examine the matrices and melt particles (including clasts within the melt particles). Point-counting of a number of sections as well as “shock point-counting” was conducted.

6.3 Target Rock Lithologies

A number of target rocks (collected from locations outside the crater rim; Fig. 6.1) were examined in thin section, for comparison with the clasts in the LB-07A impactites. Koeberl et al. (1998) suggested (on the basis of a combined geochemical and petrographic study) that 4 groups of target rocks were in existence at the Bosumtwi structure: shale, phyllite-greywacke, granite dykes and Pepiakese granite. The current study re-evaluates the groupings petrographically in order to ascertain if the groupings suggested by Koeberl et al. (1998) are appropriate.

Samples LB-32, J-501, J-502 (Fig. 6.2 A) have been classified as phyllites (Koeberl et al., 1998; Karikari et al., 2007). Common characteristics of these samples are that they are all very fine-grained (< 100 μm) and dark grey.

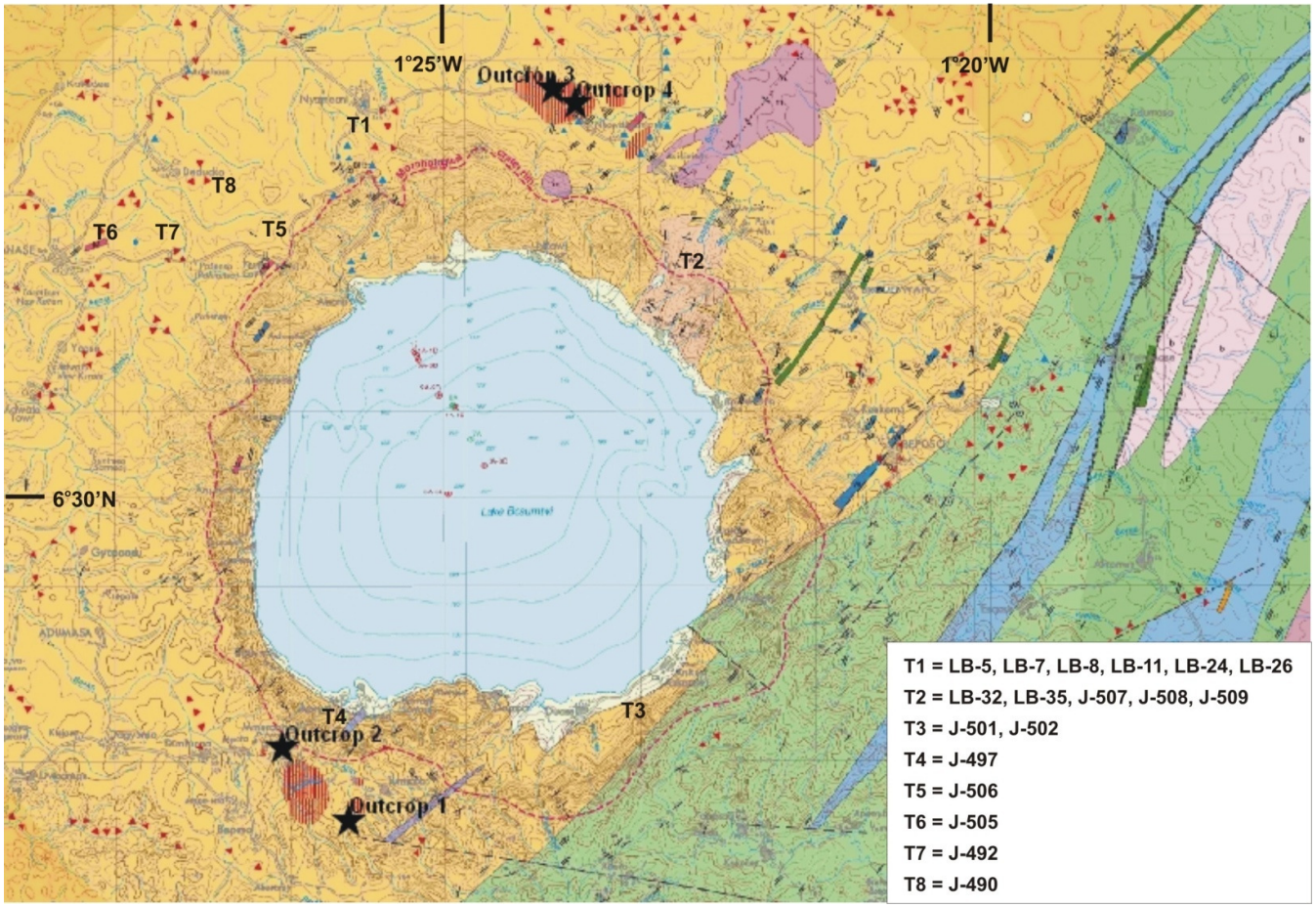

Fig. 6.1: Sampling locations of the suevites from north and south of the crater, superimposed onto the regional geological map of Koeberl and Reimold (2005; Appendix 1). Outcrops 1-4 indicate the positions of the suevites sampled in this study. Points T1-8 indicate the locations where target rocks were collected by W.B. Jones or by W.U. Reimold and C. Koeberl.

The samples contain quartz, feldspar and sericite, with a strong fabric defined by sericite. In general, sericite is the dominant phase, with a maximum modal percentage of 70 vol%, and roughly equal proportions of quartz and feldspar (sub-rounded). Rare (< 1 vol%) opaques are present. In some samples, there is some mylonitization across the samples, defined by finer or coarser bands of quartz.

Metagreywacke samples (LB-7, LB-8, J-492, J-506; Fig. 6.2 B) are composed of quartz, plagioclase (commonly sericitized), biotite and/or muscovite grains set in a matrix of fine-grained (<100 µm) sericite, quartz and feldspar (matrix proportion up to 55 vol%). Quartz is the dominant phase – comprising up to 40 vol% of the rock. The maximum grain size is 2 mm. Plagioclase and K-feldspar have a maximum size of 1.5 mm and form 5 vol% of the rock. Biotite and/or muscovite form less than 1 vol% of the rock. The largest biotite grains are 0.5 mm in size. However, there is some variability in the mineral proportions – in some samples plagioclase may form up to 40 vol% of the sample, and in others biotite may form up to 30 vol% (Appendix 3b).

Shale samples (LB-5, LB-11, J-490, J-497; Fig. 6.2 C) can be divided texturally into those which are carbonaceous or those which are laminated (Appendix 3b). The carbonaceous shales (LB-5, J-490) are very fine-grained (grain size is < 100 µm) and are dark grey to black. They consist of equal proportions of quartz, feldspar and sericite with carbonaceous darker patches. The laminated shales (LB-11, J-497) are dark grey, and the individual grains are larger than those in the other shales. The laminated shales (some converted to slates) are defined by a clear alignment of grains. The slate samples contain a clear crenulation cleavage, defined by quartz (Fig. 6.2 C). There are discrete grains of biotite in evidence. Quartz and feldspar grains constitute 40 vol% of the sample, with phyllosilicates amounting to 60 vol%. The maximum grain size is 1 mm for all phases.

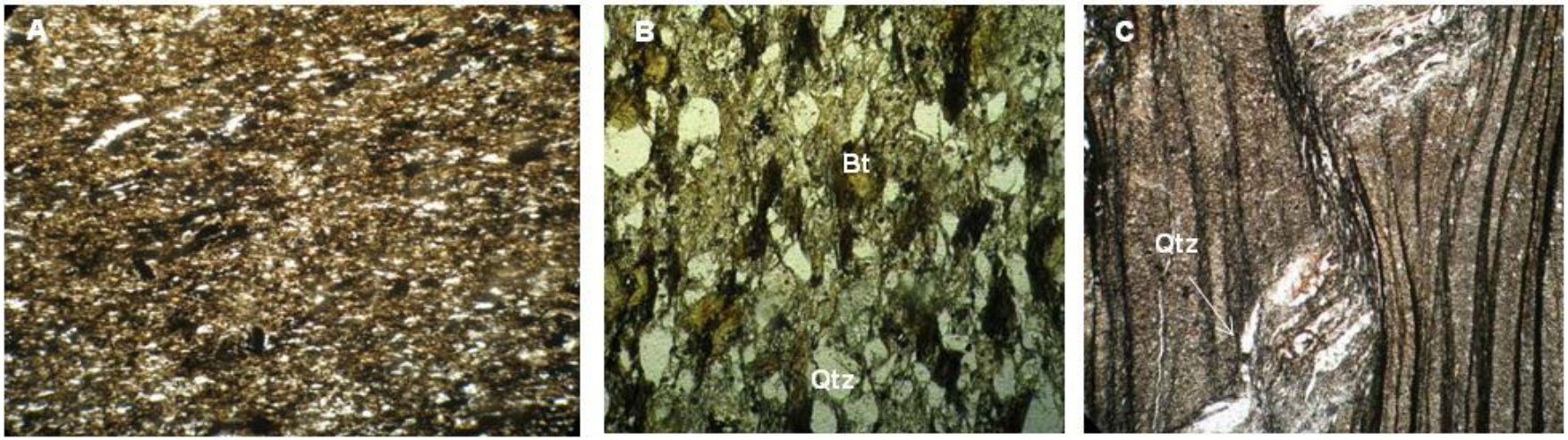

Fig. 6.2: Photomicrographs of target rock lithologies sampled outside of the crater. A) Sample LB-32, phyllite; main minerals are quartz, feldspar and biotite; image width = 3 mm, PPL. B) Sample J-492, greywacke; main minerals are quartz, feldspar and biotite, with a preferred orientation of grains from the top to the bottom of the image; image width = 2.75 mm, PPL. C) Sample J-497, slate, with crenulation cleavage defined by quartz; image width = 2.5 mm, PPL. Continued on next page.

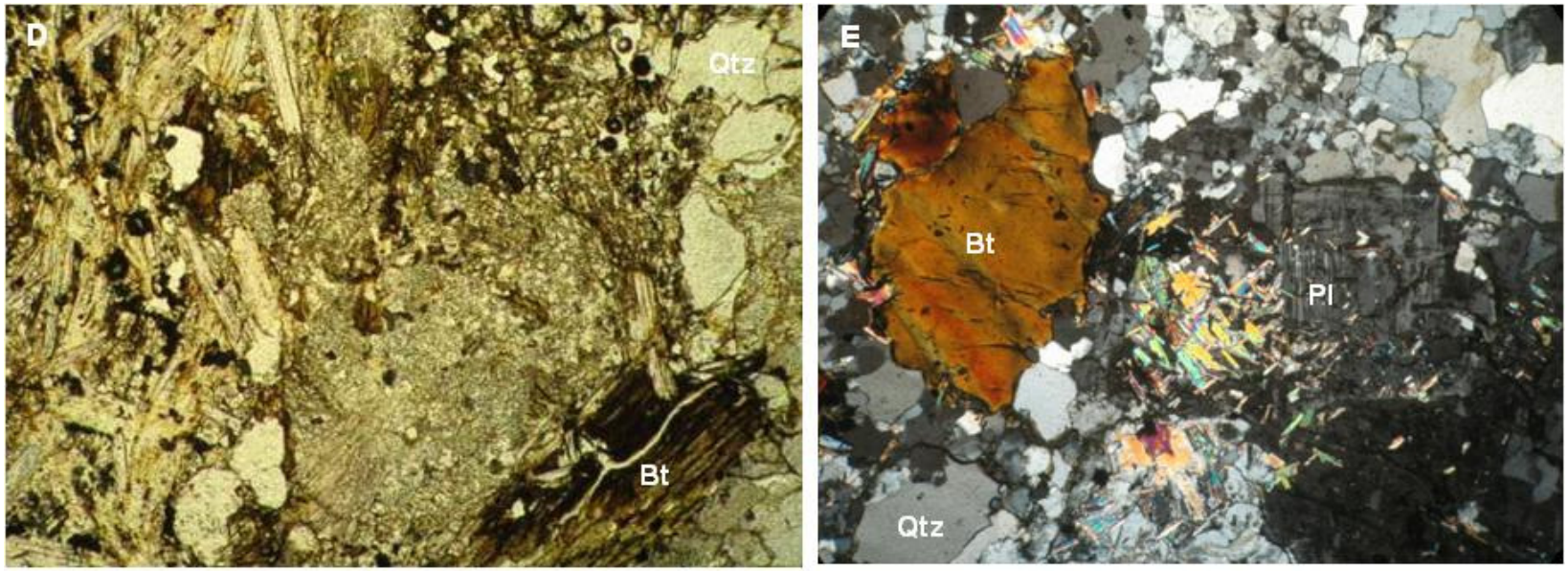

Fig. 6.2 (cont'd): Photomicrographs of target rock lithologies sampled outside of the crater. D) Sample J-505, granite dyke; main minerals are quartz, feldspar, biotite and chlorite, image is dominated by fine-grained quartz-feldspar intergrowth; image width = 2.75 mm, PPL. E) Sample LB-35, Pepiakese granite; main minerals are quartz, sericitized plagioclase, microcline and biotite; image width = 3 mm, CPL.

Local iron-staining is observed. Thus, textural as well as compositional variation is apparent in the shales.

The granite dyke samples (LB-24, LB-26, J-505; Fig. 6.2 D) are variably textured – spherulitic to granophyric in parts (equivalent to the granophyric-textured lithology proposed by Reimold et al., 1998 and in core LB-07A). These samples contain quartz, plagioclase, potassium-feldspar, biotite, sericite and chlorite. Quartz and feldspar (some sericitized) grains are generally intergrown with a granoblastic texture. Their proportions are roughly equal, and constitute about 70 vol% of the rock (Appendix 3b). Biotite is the most common phyllosilicate and has a patchy texture. It forms ca. 30 vol% of the rock. Quartz and feldspar grains have a maximum size of 2 mm, but most grains are ±100 µm in size. The phyllosilicate grains are all on the order of 100 µm or less in size.

Pepiakese granite samples (LB-35, J-507, J-508, J-509; Fig. 6.2 E) are composed of quartz, plagioclase, microcline, muscovite, sericite, biotite and minor chlorite. All grains except for the phyllosilicates are resorbed. Plagioclase is the dominant phase, comprising up to 44 vol% of the rock (Appendix 3b); the grains have a maximum size of 3 mm, and many of the grains are sericitized. Quartz grains constitute 40 vol% of the rock and display a size range of 0.75 - 2 mm. Microcline grains are less than 0.5 mm in size and form 10 vol% of the rock. Biotite grains form the dominant phyllosilicate phase and vary between <0.5 mm to 1 mm in size, and form approximately 5 vol% of the rock, whereas muscovite and sericite form less than 1 vol% of the rock, and are less than 0.5 mm in size. As with the greywacke samples, the mineral proportions are somewhat variable between samples, but either quartz or plagioclase form the dominant phase, each comprising ca. 40 vol%.

It is apparent that there is much overlap between the target rock groupings in terms of mineral proportions, but these proportions are

highly variable within individual lithologies. Chemically, these samples are all similar (they contain varying proportions of the same minerals). As evidenced by this petrographic study, the phyllite and greywacke samples are different both texturally as well as in terms of their general mineral proportions. Thus, it is suggested in this study that the different metasediments should not be grouped together – in particular greywacke and phyllite.

6.4 Suevite Outcrop Locations

The suevites of the southern (Fig. 6.3) and northern (Fig. 6.4) exposures are somewhat different to each other in their macroscopic features, and thus will be dealt with separately. All out-of-crater suevites have been intensely affected by tropical weathering.

In the south, the suevites are exposed in stream beds, south-east of the village of Adumasa (see Appendix 1, Fig. 6.1). Outcrop 1 (Fig. 6.3 A) consists of an approximately 3 to 5 m high, 2 m wide and about 10 m long exposure (total outcrop dimension) next to the river bed. A 0.5 metre-thick weathering horizon caps the exposure. Outcrop 1 is located in thick jungle. Outcrop 2 (Fig. 6.3 B) consists of a 1 m^2 pavement (0.5 m exposed depth) in a stream bed (also with a weathering horizon on top of the pavement). Both sites are similar in their clast content, distribution and melt particle characteristics. Neither site is laterally continuous beyond the dimensions quoted here.

The breccia exposures from the north of the crater are more laterally-extensive than those from the south of the crater. The exposures are 1 to 3 m in vertical thickness. Outcrops are located to the south of the Nyameani-Beposo road (see Appendix 1, Fig. 6.1). Outcrop 3 (Fig. 6.4 is located about 50 to 200 m south of the road (Fig. 6.1). The outcrop covers several hundred square metres, and has variable thickness (1 m to 5 m). The outcrop is a mixture of *in situ* deposits as well as boulders. These observations are consistent with those made

by Boamah and Koeberl (2003) who described these breccias as "large blocks of up to several metres width and as patchy massive deposits". Outcrop 4, consists of a single 2.5 m high and 2 m wide exposure situated in dense jungle.

6.4.1 Suevite from South of the Crater – Outcrop Description

The suevites have a medium dark grey matrix macroscopically (Fig. 6.5 A, B). These breccias are matrix-supported. Macroscopically, only graphitic shale (with internal quartz veining), slate and quartz are identifiable as the main lithic clast phases. Maximum clast size is 10 cm (Fig. 6.3). Melt particles of up to 10 cm diameter are present.

Lateritic material (laterite is a weathering product consisting of clay minerals and enriched in iron and aluminium; Aleva, 1994) is noted as a post-impact alteration product that occurs as rims around a number of shale clasts, and as in-filling in fractures in the suevites. The within-crater suevites lack this lateritic alteration.

No textural differences were noted between the suevites from the two southern sampling localities, and clast populations are similar. In the first section (outcrop 1), which is 5 m in height, there was a distinct upward decrease in melt particle number (from generally 10 % to a minimum of 5 %). The clasts are not preferentially oriented, and lithic clast shapes vary from angular to sub-rounded. Overall, the macroscopic modal proportions are as follows: the matrix composes 85 vol% of the outcrop, while lithic and mineral clasts amount to 5 vol% or less of the outcrop, and melt particles account for 5-10 vol%.

6.4.2 Suevite from North of the Crater – Outcrop Description

In contrast to the suevites from the south, the suevites from the northern exposures have a pale yellow to yellowish-green matrix macroscopically (Fig. 6.6 A, B, C).

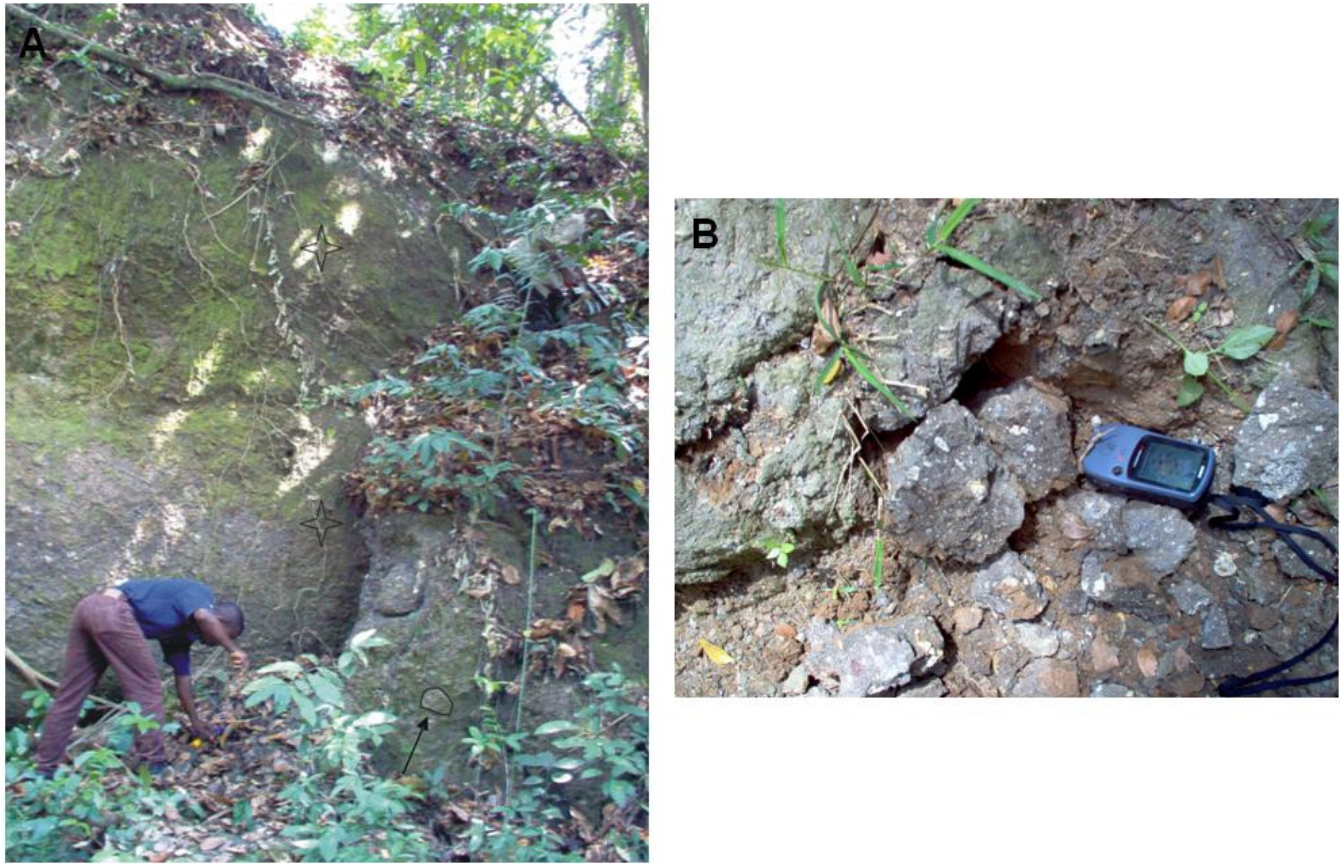

Fig. 6.3: Out-of-crater breccia from the south. A) Outcrop 1: GPS UTM coordinates: 0673437, 0713135 (UTM Zone = 30N). Person for scale. The exposure is located adjacent to a stream bed and consists entirely of suevite, except for the 0.5 m weathering horizon capping the exposure. Maximum clast size is 10 cm, circled, and indicated by arrow. Stars indicate the sampling positions. B) Outcrop 2: GPS UTM coordinates: 0672300, 0714393. GPS for scale. The exposure consists of a 1 m^2 pavement in a stream bed.



Fig. 6.4: Out-of-crater breccia from the north. A) Outcrop 3: GPS UTM coordinates: 0676968, 0725874 (UTM Zone = 30N). Hammer (30 cm long) for scale. The exposure consists entirely of suevite, with clasts up to 25 cm in diameter. A hole from a 15 cm granite clast which has been removed is circled, and indicated by arrow. B) Outcrop 4: GPS UTM coordinates: 0677361, 0725615. The exposure consists of a single boulder, 2.5 m high and 2 m wide.

The suevites from the northern exposures have a different clast population to those from south of the crater. Lithic and mineral clasts are less diverse than those in the south, and include significantly more granitoid, shale, phyllite, schist together with quartz, feldspar and Fe oxides. In general, matrix comprises 70-80 vol% of the outcrop, with up to 20 vol% clasts, and a maximum of 20 vol% melt. Only minor shale is noted in outcrop 3 but is not present in outcrop 4 (shale and slates were observed in the suevites from south of the crater). Granitoid clasts are very large – mostly ~10 cm, but they may be as much as 25 cm in size. Lithic clasts with diameters greater than 20 cm comprise 20% of the total volume of the suevite at outcrop 4. Clast shapes vary from sub-angular to rounded. No preferential orientation of clasts is apparent. At outcrops 3 and 4, no changes in the lithic clast size with height were noted as all clasts are mixed. There are no substantial changes of lithic, melt clast size and shape with height in the individual outcrops.

Unlike the exposures from south of the crater, there is some lateral variation between the two northern localities (outcrops 3 and 4). There is a greater variety of clasts observed at outcrop 3 in comparison to outcrop 4. Melt particle shapes (see section 6.4.5.1) are more variable in outcrop 3 than in outcrop 4 (located SE of outcrop 3, Fig. 6.1), with a dominance of rounded and less elongate shapes being observed in outcrop 4. Melt particles in outcrop 4 are fewer in number, but larger in size (up to 40 cm diameter; sample BS-5, BS-6) than in outcrop 3 (up to 3 cm in size). Proportionally, there are more melt particles in the exposure at outcrop 3 than outcrop 4. These observations may be a factor of the limited exposure at outcrop 4.

Overall clast size in the suevites from north of the crater is substantially larger than that observed in suevites from south of the crater (3 mm minimum, with most clast sizes ranging from 5 to 10 cm).

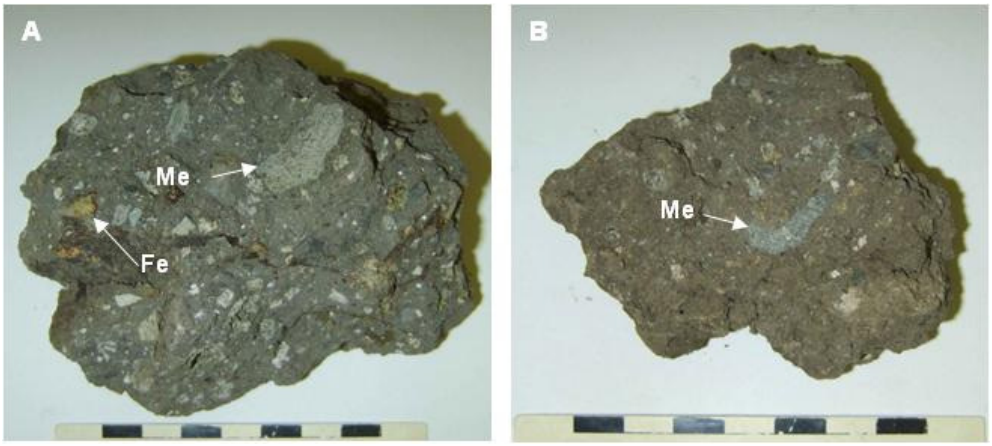

Fig. 6.5: Hand specimen images of suevites from south of the crater. A) Sample BS-1, outcrop 1. B) Sample BS-2, outcrop 1. Both samples are characterised by a medium dark grey matrix. Post-alteration Fe-oxides/-hydroxides are evident on the left side of sample BS-1 (indicated by Fe). Melt particles are indicated (Me). Scale bar in cm.

6.4.3 Suevite from South of the Crater – Microscopic Features

The suevites from south of the crater are characterised by a dark brown to greyish-brown matrix in thin section. The matrix comprises between 32 and 62 vol% of the suevite (determined by point-counting, see Table 6.1). Lithic clasts comprise up to 55 vol% of the suevite. The proportion of melt particles varies between 4 and rarely 57.5 vol%, with an average of 18 vol% (Table 6.1). A more diverse array of lithic and mineral clasts was identified in thin section (Table 6.1) than in the outcrop which includes minor metagreywacke, schist, phyllite, granitoid together with rare feldspar and some phyllosilicates (muscovite, biotite and minor chlorite). Clast shapes vary from angular (shale clasts) to sub-rounded (quartz clasts). The schist clasts display distinct pre-impact cleavage. No carbonate was found in the thin sections either as matrix or clasts.

6.4.4 Suevite from North of the Crater – Microscopic Features

The suevites are matrix-supported and have similar proportions of matrix to those from south of the crater (36 – 59 vol%). The matrix is medium to dark brown in thin section, and clast shapes are sub-rounded to angular. No pre- or post-impact carbonate component was noted. A less diverse array of clasts is observed in the suevites

from north of the crater (see also section 6.4.2; Table 6.1). Table 6.1 also emphasizes the heterogeneity in the clast populations – this is a function of the large size ranges of some of the clasts (sub-mm to over 10 cm size), whereas others only occur at the sub-mm scale.

6.4.4.1 Comparison to previous work on the out-of-crater suevites from the north of the crater

Boamah and Koeberl (2006) examined the suevites from north of the crater for their clast contents. They drilled a number of short (30 m) drill cores in 1999 for the purpose of examining the suevites as well as to determine the thickness of the suevite.

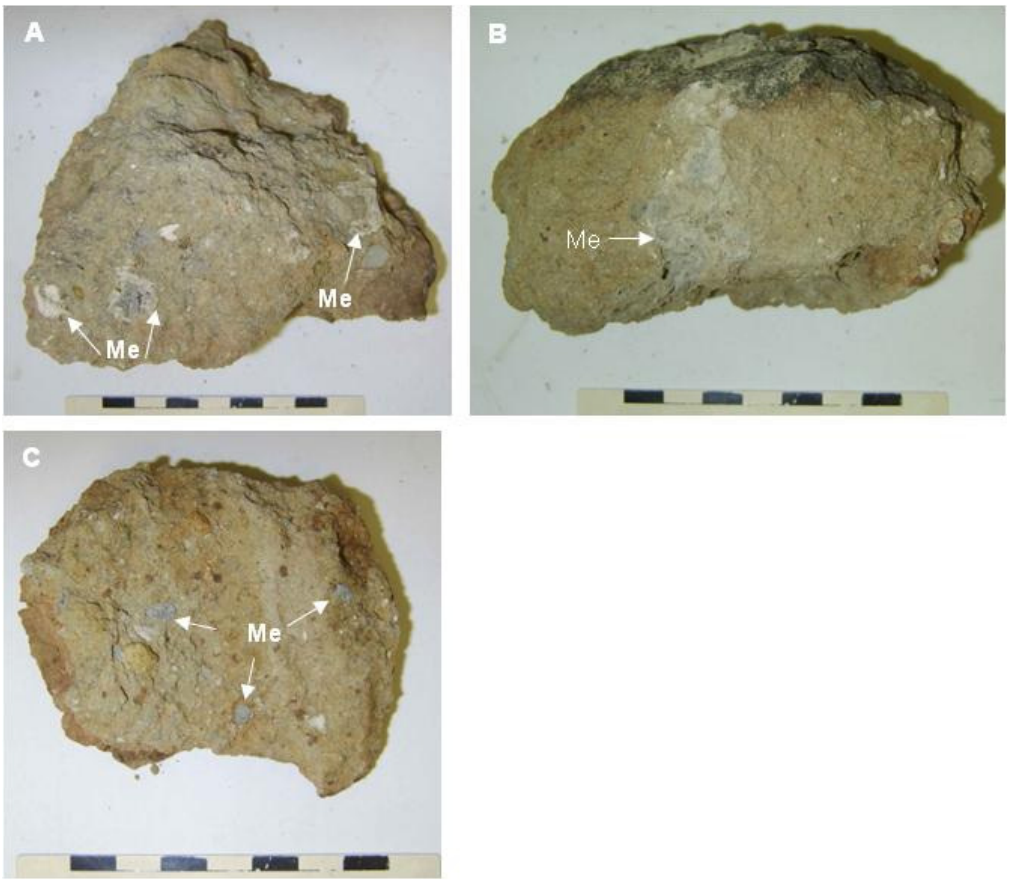

Fig. 6.6: Hand specimen images of suevites from north of the crater. A) Sample BS-12, outcrop 3. B) Sample BS-9, outcrop 3. C) Sample BS-14, outcrop 3. Both samples are characterised by a yellow to yellowish-green matrix. Melt particles are indicated (Me). Scale bar in cm.

Table 6.1: Modal analysis data (in vol%) obtained by point-counting of selected, representative samples of the out-of-crater suevites.

Sample No. **Location w.r.t crater**	**BS-9** **North**	**BS-12** **North**	**BS-15** **North**	**BS-16A** **North**	**LB-47** **North**	**LB-47b** **North**	***Average*** ***North***
Matrix	59.2	39.6	51.1	47.3	55.9	35.6	48.1
Metagreywacke							
Shale					0.7	0.4	0.2
Phyllite	4.1	4.3	2.2		1.2	1.1	2.2
Schist		2.9	2.2	11.2	1.2	1.4	3.2
Granitoid	3.6	4.8	3.6	1.1	4.2	2.8	3.4
Phyllosilicates*							
Quartz*	2.4	1.3	2.2	3.2	3.3	2.8	2.5
Total feldspar*	1.8	0.8	0.7	2.1	0.9	1.4	1.3
Secondary oxides	3.0	1.1	0.7	0.5	2.1	4.0	1.9
Opaques							
Diaplectic Glass*	0.3				0.5	1.0	
Melt & melted clasts	25.7	45.2	37.2	34.6	30.0	49.4	37.0
Total	100.0	100	99.9	100.0	100	99.9	100.1

Sample No. **Location w.r.t. crater**	**LB-39b** **South**	**LB-39 a1** **South**	**LB-39a1/1** **South**	**LB-39a1/2** **South**	**LB-39c** **South**	**BS-1** **South**	**BS-2a** **South**	***Average*** ***South***
Matrix	32.1	38.3	16.4	62.1	46.5	59.2	55.5	44.3
Metagreywacke		4.0	4.2	0.6	1.6	2.2	8.0	2.9
Shale		4.8	3.9	4.1	2.3	5.1	3.6	3.4
Phyllite	5.1	3.8	3.9	9.4	3.7	4.3	0.6	4.4
Schist	2.4	1.2	2.6	2.6	4.6	2.7	3.0	2.7
Granitoid	4.0	17.9	2.0	3.0	9.2	4.1	1.3	5.9
Phyllosilicates*	2.6	0.2	0.9	1.1	0.9			0.8
Quartz*	47.5	7.6	6.4	2.4	9.7	5.6	4.4	11.9
Total feldspar*					<0.1		0.4	<0.1
Secondary oxides	2.4	3.2	2.4	3.4	4.2	3.9	0.6	2.9
Opaques		1.3		1.3	1.1	1.7		0.8
Diaplectic Glass*		0.1			8.4		3.0	1.2
Melt & melted clasts	4.0	17.4	57.5	10.1	7.7	11.3	19.5	18.2
Total	100.1	99.8	100.2	100.1	99.9	100.1	99.9	99.5

**Phyllosilicates = chlorite + biotite + muscovite (primary and secondary); Quartz = quartz + quartzite; Total feldspar = Plagioclase + K-Feldspar, where plagioclase>>K-feldspar; Diaplectic glass = diaplectic quartz glass and diaplectic feldspar glass. Between 500 and 1000 grains counted over 1.5 cm^2 area. x = traces (< 0.1 vol%). Matrix consists of grains which are less than 50 µm in size.*

From their outcrop descriptions (eight 1 m x 1 m outcrop faces examined), Boamah and Koeberl (2006) found that the suevites were composed of up to 70 vol% matrix (defined as all clasts < 2 mm in size) and clasts comprising 8 vol% metagreywacke, 5 vol% metapelite, 3 vol% granitoid and 20 vol% melt (maximum proportions reported). These proportions are similar to those estimated in this study (see section 6.4.2): 70-80 vol% matrix, up to 20 vol% lithic and mineral clasts and up to 20 vol% melt. In their microscopic study (conducted on 19 thin sections from the cores), they found similar

statistics to their macroscopic study. They found that the suevite was composed of up to 70 vol% matrix (mineral clasts, including melt < 0.5 mm in size), 15-20 vol% melt, 10 vol% rock fragments (greywacke, phyllite, shale, schist and granite) and 5 vol% quartz and feldspar clasts (Table 6.2). Some criteria used in the microscopic analysis of this study and that of Boamah and Koeberl (2006) are clearly different: in this study, rock fragments were not grouped, but the different pelitic rock types were distinguished. The size fraction of 0.5 mm for matrix material is different to that used in this study (0.05 mm; see Table 6.1). However, when the averages of this study are re-calculated (Table 6.2) according to the specifications used by Boamah and Koeberl (2006) to make the data sets comparable, similar results are obtained.

Table 6.2: Comparison between the petrographic data for the northern out-of-crater suevites of this study and that of Boamah and Koeberl (2006). All populations in vol%.

	This study	Boamah & Koeberl (2006)
Matrix	48.1	70
Rock fragments	8.5	10
Mineral fragments*	3.8	5
Melt*	37.3	15-20

**Mineral fragments include quartz, feldspar, iron hydroxides and opaques; Melt includes diaplectic glass.*

The only difference between the data sets is the higher volumes of melt (37 vol% *vs.* 20 vol%) and the lower volumes of matrix (48.1 vol% *vs.* 70 vol%) noted in this study. The reason for this difference is that these suevites are very heterogeneous in terms of clast size and this would be reflected in the thin section evaluation. It must be noted that samples selected for point-counting were chosen specifically to observe as much matrix as possible.

6.4.5 Shock Metamorphism of the Out-of-Crater Suevites

"Shock point-counting" of quartz grains reveals no significant difference between the out-of-crater suevites from south and north of the crater (Table 6.3). Quartz grains contain anything between none

and 4 PDF sets with 1 PDF set being the most common (see Table 6.1). The PDFs may be decorated (Fig. 6.7 A), but this is generally quite rare. Quartz is commonly toasted. It must be noted that the out-of-crater suevites have a greater variety of clasts within their melt particles than those in the LB-07A core; including quartz, feldspars, as well as discrete target rock fragments (schist, granite). The micro-clasts within the melt particles show no evidence of shock. Ballen quartz (Fig. 6.7 B) was noted in most samples, which was not noted at all in the LB-07A core. Suevites from both the southern and northern exposures contain diaplectic quartz glass.

Table 6.3: Summary of shock features in quartz grains of selected, representative samples of the out-of-crater suevites.

Sample No.	Total No. qtz* grains studied	Total % qtz without PDFs or PFs	Total % qtz grains with PFs	Total % qtz grains with 1 PDF set	Total % qtz grains with ≥2 PDF sets	Location w.r.t. crater
BS-2A	67	76.1	6.0	14.9	3.0	South
LB-39a1/1	123	73.9	6.5	13.0	6.5	South
LB-39a1/2	150	80.0	2.7	14.6	2.7	South
LB-39b	42	52.4	7.2	26.2	14.3	South
BS-9	92	84.8	8.7	4.3	2.2	North
BS-13	64	75.0	4.7	9.4	10.9	North
BS-16B	79	73.4	6.3	12.7	7.6	North
LB-30a	127	70.9	7.1	15.7	6.3	North

**qtz = quartz; average section size examined is 1.5 cm^2; percent/% refers to relative % of the total.*

6.4.5.1 Melt particle characteristics

In the suevites from south of the crater, melt particles are round to ovoid, with embayed edges. They are commonly strongly vesiculated and have a maximum size of 3 cm in thin section (cf. 10 cm in outcrop, section 6.4.1). Vesicles are present in all melt particles, and reach a maximum size of 300 µm. Two distinct colours of melt particles are noted in hand-specimen – white-grey and green-grey. In thin section, melt particles are white to brown, and vary in shape from sub-angular to sub-rounded, and particles are rarely larger than a few mm.

In contrast, the melt particles in suevites from north of the crater are macroscopically light to dark brown, and contain large sub-rounded

vesicles (Fig. 6.8 A-D). Within a particular melt particle, colour variation highlights the internal flow structures (Fig. 6.8 D). In thin section, these melt particles vary from white to light grey. A few melt particles have slightly yellow patches (a result of iron staining). In outcrop, the size of the melt particles is sub-cm to ca. 40 cm.

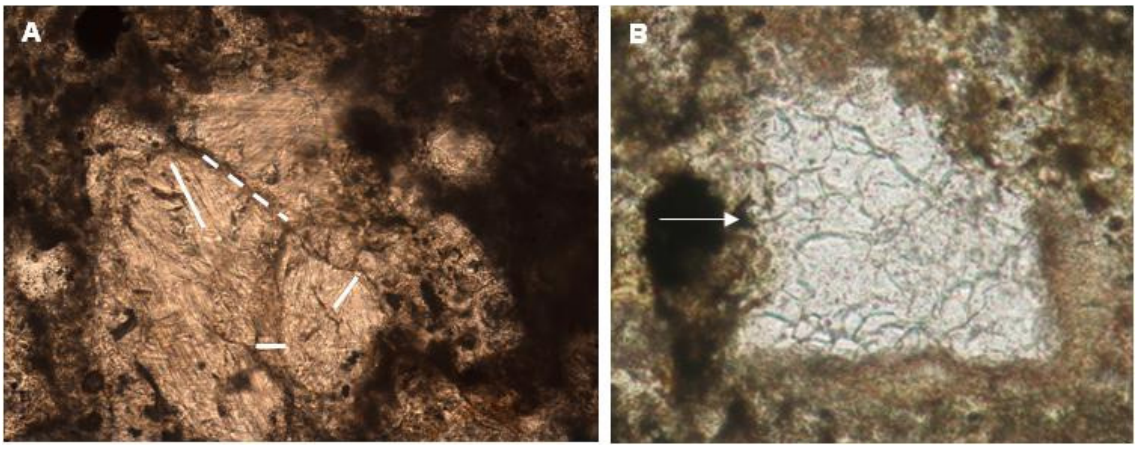

Fig. 6.7: Photomicrographs of various features in the out-of-crater suevites. A) Sample BS-5, 3 PDF sets in a quartz grain, oriented NNW-SSE, E-W and NE-SW (indicated with solid lines), 1 set of sub-parallel fractures oriented NW-SE (indicated with dashed lines); image width = 0.52 mm, PPL. B) Sample LB-31; ballen quartz; image width = 0.5 mm, PPL.

The melt clasts have well-defined margins, and display much vesiculation, which is generally coarser at the margin of a fragment, with smaller vesicles in the interior. Melt particles have a variety of shapes, ranging from rounded to irregular, irregularly-shaped (Fig. 6.8 A) to elongate shapes (pancake-shaped in 3D; Fig. 6.8 B, C). The large clasts in the particles consist of quartz or weathered material.

Thin section images of suevites from the south and north of the crater are shown in Fig. 6.9. The larger melt particles are circled, and indicated by arrows. Some thin sections of the northern suevite exposures have matrices which consist entirely of agglomerated melt particles (e.g., sample LB-41; Fig. 6.10 A).

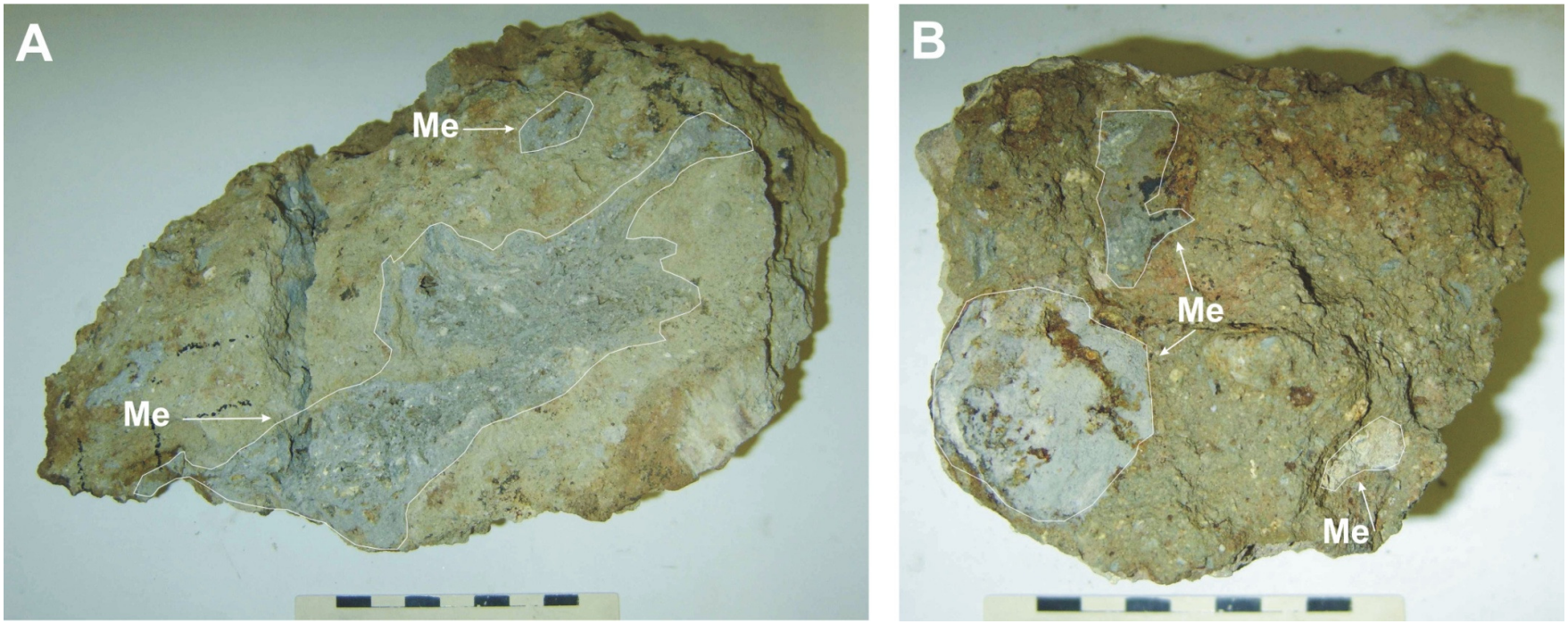

Fig. 6.8: Hand specimen images of large melt particles in suevites from north of the crater (outlined, indicated by Me). A) Sample BS-16, Outcrop 3; irregular to elongate-shaped melt particle, with quartz-filled vesicles. B) Sample BS-13, Outcrop 3; sub-rounded to sub-angular melt particles. Scale bar in cm. Continued on next page.

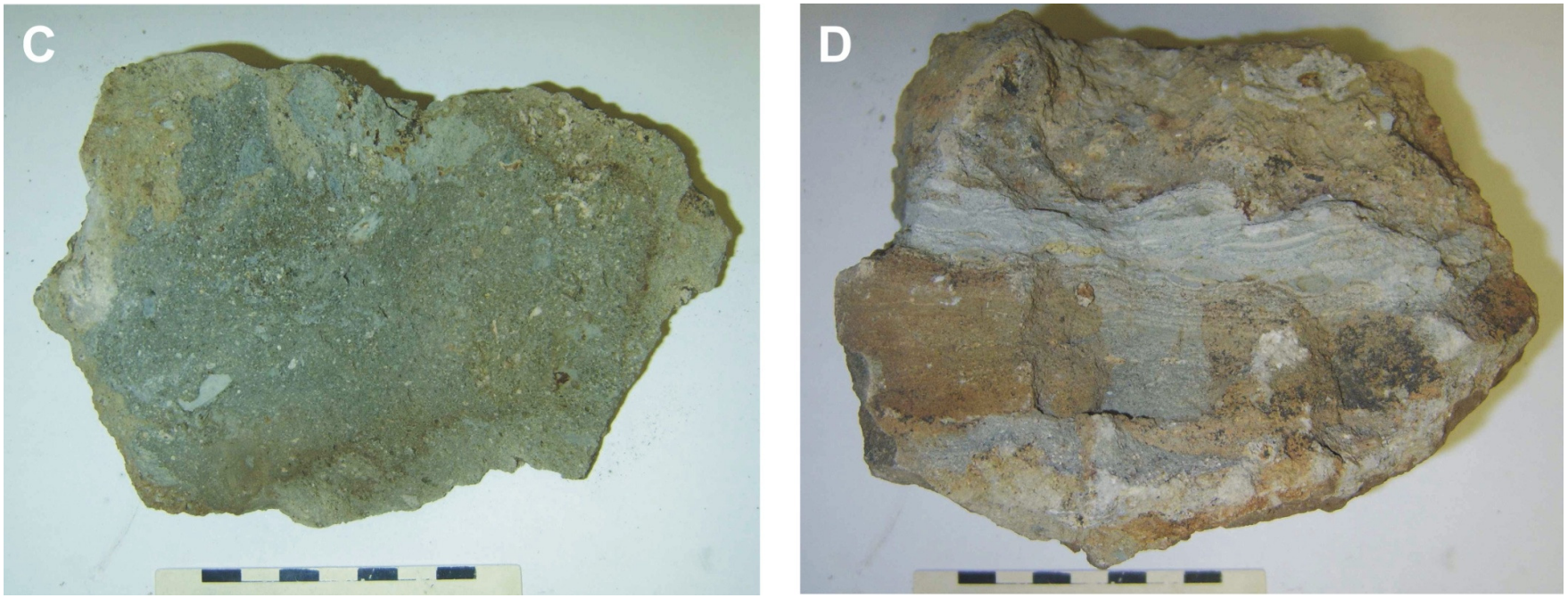

Fig. 6.8 (cont'd): Hand specimen images of large melt particles in suevites from north of the crater. C) Sample BS-5, Outcrop 4; entire sample consists of a pancake-shaped melt particle (oriented horizontally in outcrop). D) Sample BS-4, Outcrop 3; entire sample consists of a melt particle with definitive flow structures (of different composition), defined by slightly different colouring of melt bands. Scale bar in cm.

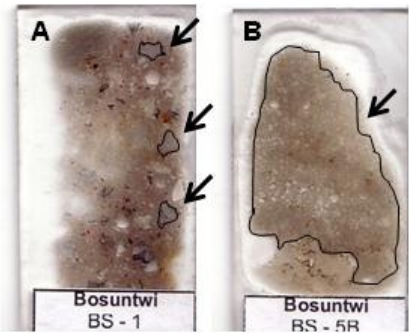

Fig. 6.9: Thin section images of the suevites from A) south of the crater (sample BS-1; outcrop 1) and B) north of the crater (sample BS-5; outcrop 4). Melt particles are circled and indicated by arrows. Note the extensive and variable size of vesiculation in the melt particle from the north of the crater.

Melt agglomerates consist of variably coloured (light to dark brown) melt particles that are apparently fused together, with variably sized vesicles (Fig. 6.10 A, C). The vesicle size varies between 300 µm and 1.5 mm. Vesicles are locally filled with Fe oxides and angular micro-fragments of melt. The latter are the result of spalling during the thin-sectioning process. The matrices also show feldspar microlites (Fig. 6.10 B-F) crystallized from the melt. The matrices of all the suevites are entirely clastic (Fig. 6.10 G-L), and not molten, as observed for suevites from the Ries crater (Osinski et al., 2004). Melt particles are present as discrete entities (Fig. 6.10 G, K, L). This is similar to the observations made for the within-crater suevites (see Chapter 5). Melt particles from south of the crater display distinctive flow banding, which indicates that these melt particles are not homogeneous in composition (Fig. 6.10 H, J-L). This concept will be examined in section 6.5.3.

6.5 Chemical signatures of the out-of-crater suevites

All major and trace element values for the out-of-crater breccias of this study are reported in Appendix 6a. Only selected samples were analysed – 3 samples for the southern out-of-crater suevites (only 3 were collected from the 2 localities: outcrop 1 was homogeneous in clast and in general melt particle distribution; 2 samples were collected there, and outcrop 2 had limited exposure).

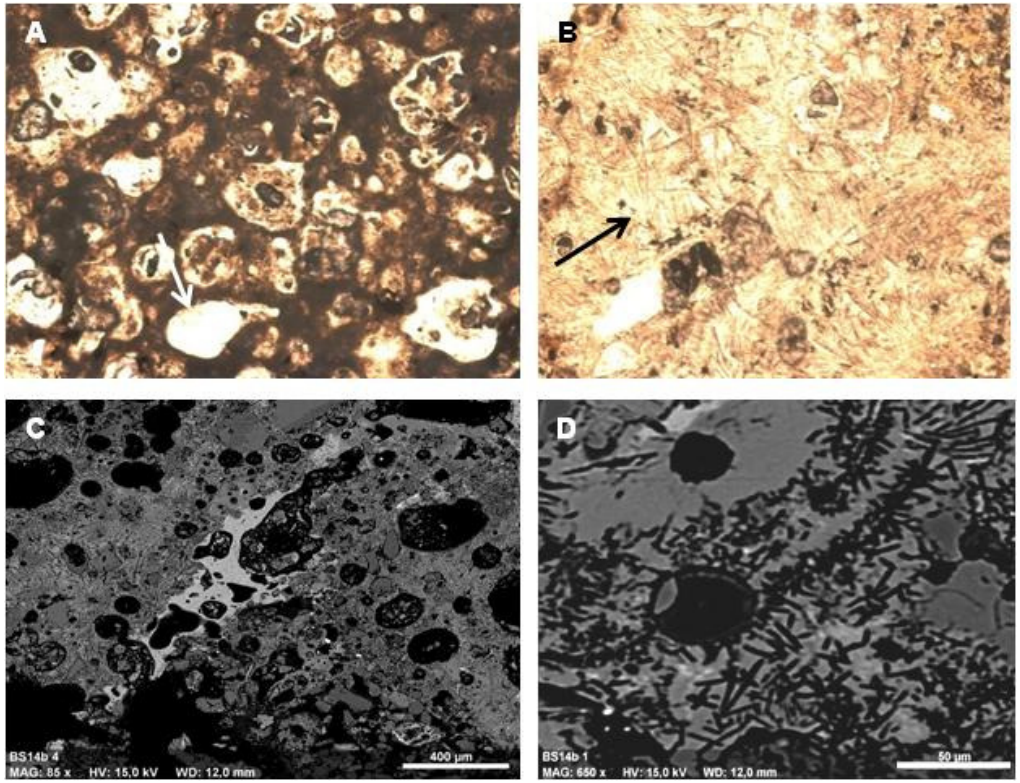

Fig. 6.10: A) Photomicrograph consists entirely of a melt agglomerate from suevite from north of the crater with white, sub-rounded vesicles (indicated by arrow). Sample BS-4; image width = 0.52 mm, PPL. B) Photomicrograph of microlites (indicated by arrow) in melt in suevite from north of the crater. Sample BS-4; image width = 0.52 mm, PPL. C) and D) Backscattered electron images of melt with microlites in Fe-rich melt from north of the crater: the grey fragments correspond to quartz (moderately grey indicates silica-rich melt), with lighter white-grey and dark grey indicating the mixed melts, and black for the vesicles. Sample BS-14B. C) Width of scale bar = 400 µm. D) Entire image shows microlites in melt (mesostasis); width of scale bar = 50 µm. Continued on next page.

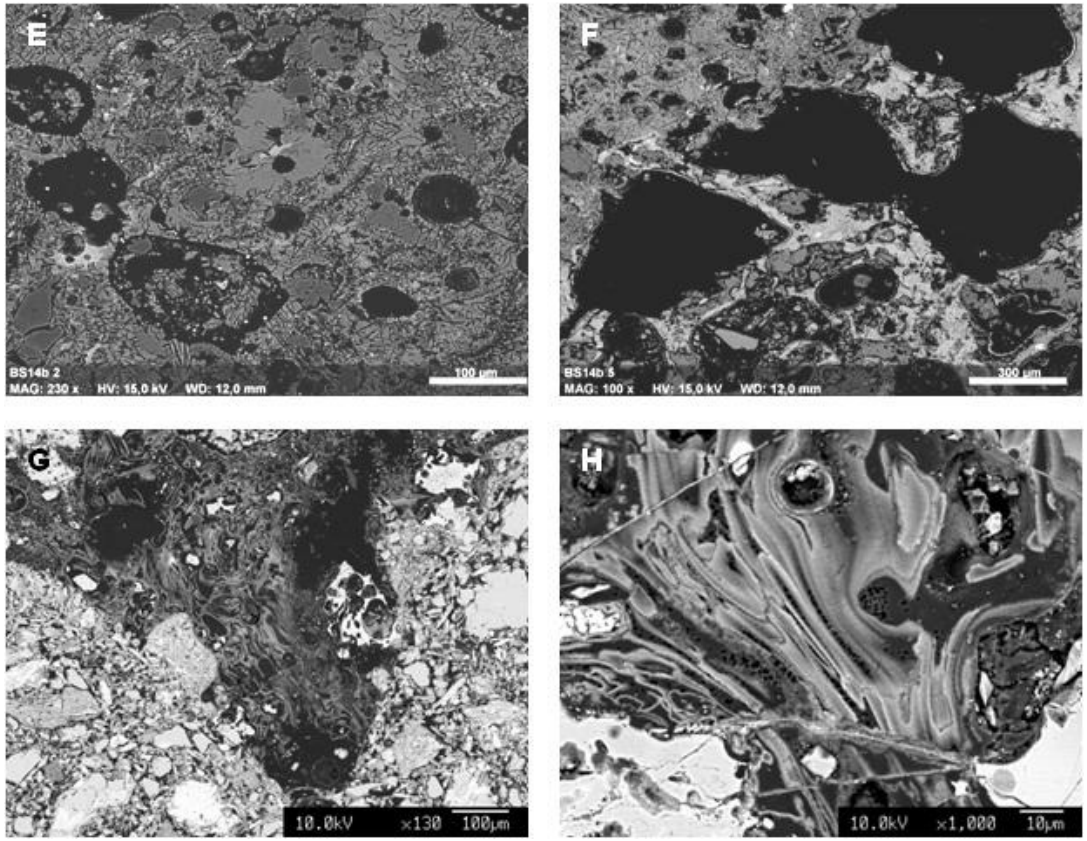

Fig. 6.10 (cont'd): E) and F) Backscattered electron images of melt with microlites in Fe-rich melt from north of the crater. Sample BS-14B. E) Extensive development of microlites in melt agglomerate. In parts, the microlites form radiating fans; width of scale bar = 100 µm. F) Melt agglomerate with flow texture between vesicles; width of scale bar = 300 µm. G) and H) Backscattered electron images of melt particles from south of the crater. Sample BS-2A. G) Discrete melt particle in clastic matrix from south of the crater; width of scale bar = 100 µm. H) Flow banding of different compositions in melt particle. Width of scale bar = 10 µm. Continued on next page.

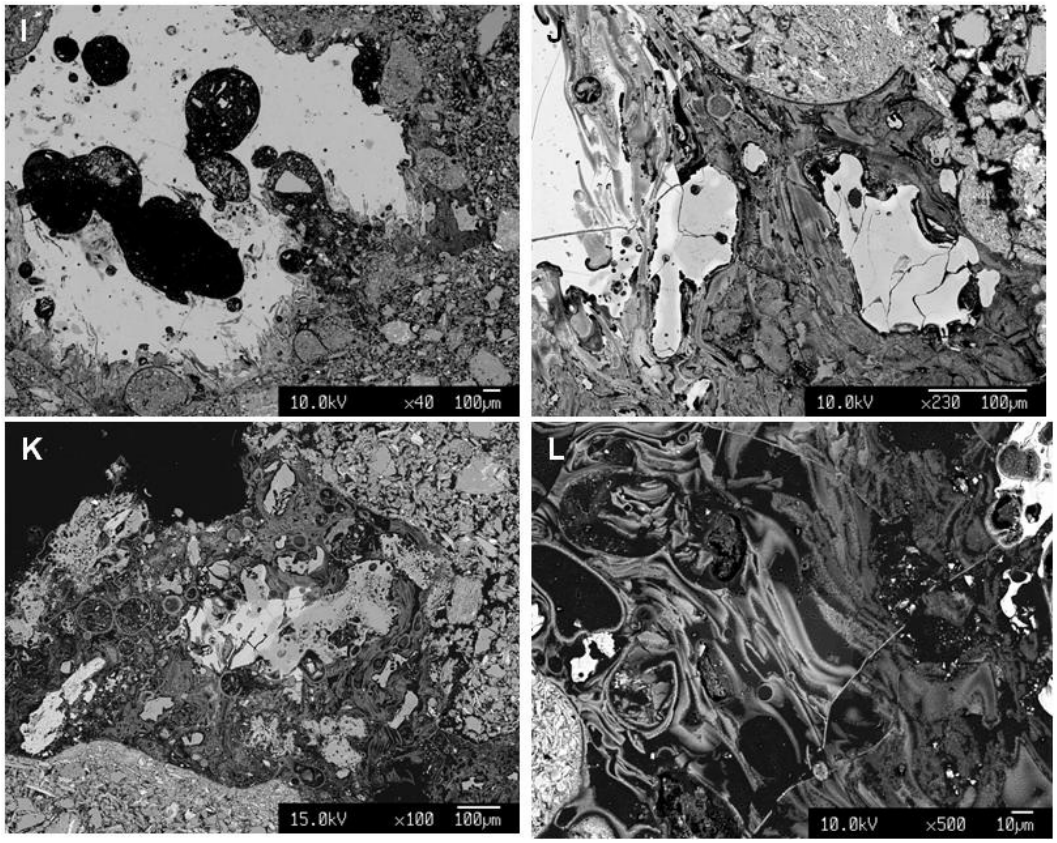

Fig. 6.10 (cont'd): Backscattered electron images of discrete melt particle in clastic matrix from south of the crater. Sample BS-2A. I) Melt particle with large vesicles, mafic composition in clastic matrix; width of scale bar = 100 µm. J) Angular melt particle containing large glassy areas, internally variable in composition; width of scale bar = 100 µm. K) Melt particle with highly variable composition; width of scale bar = 100 µm. L) Close up of an area of the melt particle in G, showing the flow textures with different composition; width of scale bar = 10 µm.

For the northern out-of-crater suevites, 6 samples from the 2 localities were analysed in order to check suevite and melt particle compositions and matrix variations.

6.5.1 Whole Rock Analysis

Harker plots of the out-of-crater suevites are shown in Fig. 6.11. There are no substantial differences in composition between the out-of-crater suevites from north and south of the crater for the elements SiO_2 (Fig. 6.11 A-H), TiO_2 (Fig. 6.11 A), Fe_2O_3 (Fig. 6.11 C) and K_2O (Fig. 6.11 H). The major element ranges for SiO_2 concentrations of the suevites from north and south of the crater are the same: 63 - 67 wt%. TiO_2 compositions range from 0.56 wt% to 0.68 wt% for the suevites from south of the crater, whereas the suevites from north of the crater have a slightly larger range from 0.52 to 0.77 wt% (Fig. 6.11 A). Fe_2O_3 concentrations vary between 4.72 and 8.17 wt% for the suevites from north of the crater which is comparable to the range of Fe_2O_3 values from south of the crater: 6.24 - 7.84 wt% (Fig. 6.10 C). The maximum value for K_2O for the suevites from south of the crater is 1.68 wt%, whereas for the suevites from the northern sector, 2.14 wt% is the maximum (Fig. 6.10 H). The suevites from south of the crater have slightly lower concentrations of CaO (0.53 - 0.92 wt%) in comparison to the concentrations in the suevites from north of the crater (1.4 - 2.45 wt%; Fig. 6.11 F).

The suevites from south of the crater have higher concentrations of P_2O_5 (between 0.09 and 0.13 wt%), and far higher concentrations of MgO (Fig. 6.11 E) and MnO (Fig. 6.11 D) than the samples from the northern sector. The suevites from north of the crater have MgO values of between 0.62 and 1.03 wt% in comparison to those from south of the crater whose concentrations vary between 2.13 and 2.80 wt% (Fig. 6.11 E).

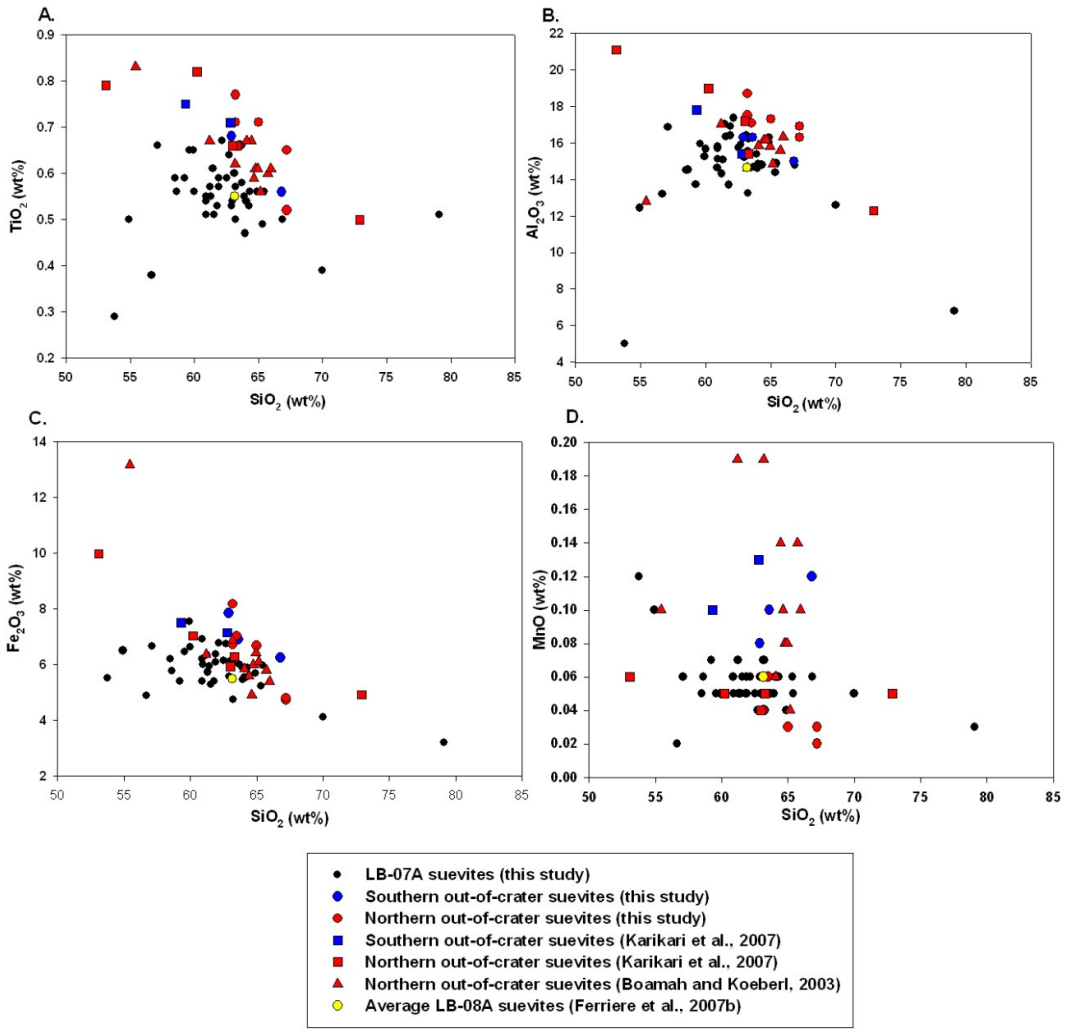

Fig. 6.11: Harker plots for the out-of-crater suevites, indicating the differences between the suevites from the south and north of the crater. Data for the LB-07A suevites, average of the LB-08A suevites (Ferrière et al., 2007b), and out-of-crater suevites from the studies of Karikari et al. (2007) and Boamah and Koeberl (2003) are indicated. All elements are plotted against SiO_2. A) TiO_2; B) Al_2O_3; C) Fe_2O_3; D) MnO. All data in wt%. Continued on next page.

The maximum concentration of MnO in the suevites from north of the crater is 0.06 wt%, which is substantially lower than the maximum for the suevites from south of the crater which is 0.12 wt% (Fig. 6.11 D). The suevites from north of the crater have slightly higher concentrations of Na_2O (Fig. 6.11 G; 2.3 - 3.6 wt%) and Al_2O_3 (Fig. 6.11 B; 16.9 - 18.7 wt%) than the suevites from south of the crater which have Na_2O and Al_2O_3 ranges of 15 - 16.3 wt% and 1.96 - 2.66 wt% respectively. In terms of lithological differences, both sample

sets are similar in their clast distribution, with slightly elevated proportions of shale, granitoid and metagreywacke in the samples from south of the crater. The elevated MgO and MnO values are a direct consequence of the higher proportions of shale (cf. Table 4.5).

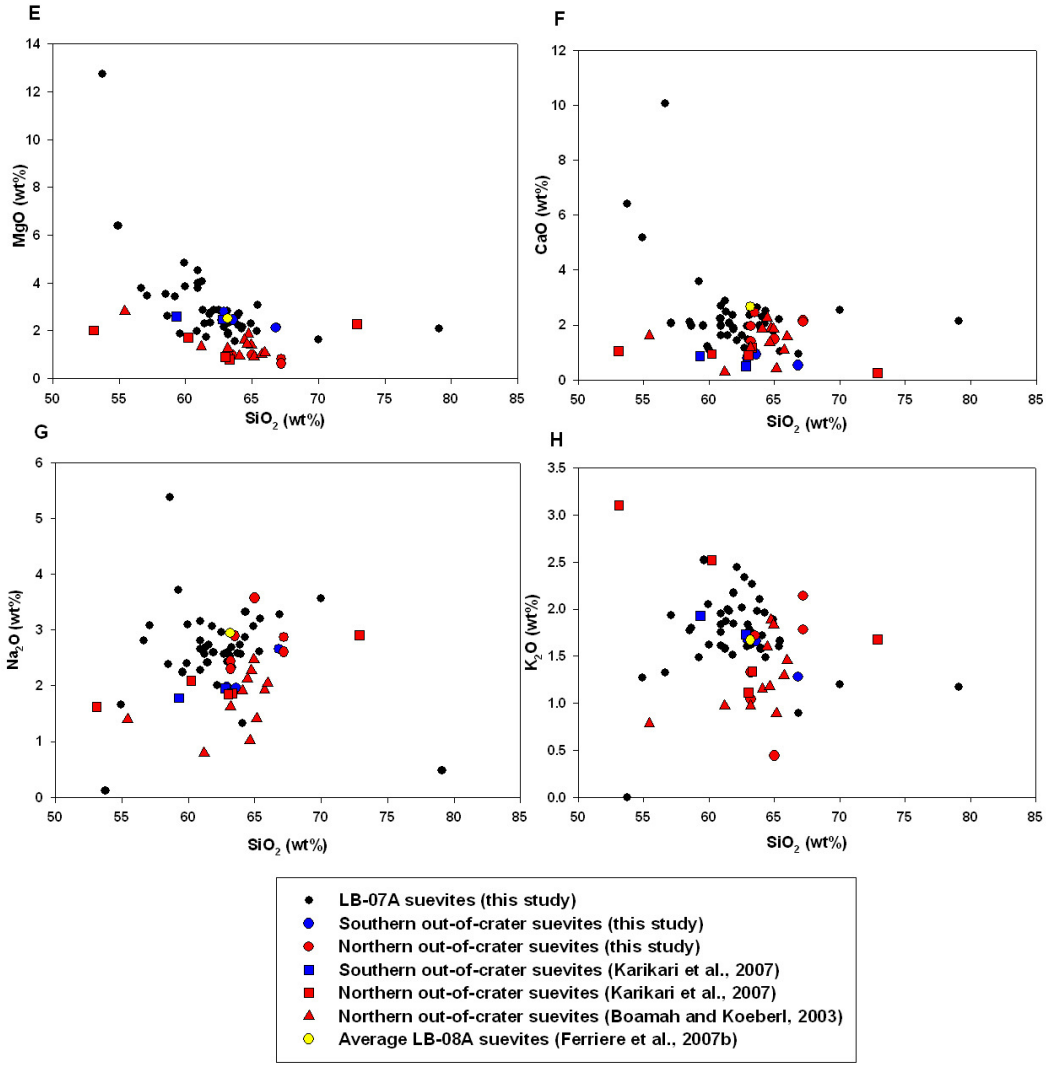

Fig. 6.11 (cont'd): Harker plots for the out-of-crater suevites, indicating the differences between the suevites from the south and north of the crater. Data for the LB-07A suevites, average of the LB-08A suevites (Ferrière et al., 2007b), and out-of-crater suevites from the studies of Karikari et al. (2007) and Boamah and Koeberl (2003) are indicated. All elements are plotted against SiO_2. E) MgO; F) CaO; G) Na_2O and H) K_2O. All data in wt%.

6.5.1.1 Major element differences between the out-of-crater suevites and the within-crater suevites

The compositional data for the LB-07A suevites and the average for the LB-08A suevites (Ferrière et al., 2007b) are indicated on Fig. 6.11. The suevites from both the LB-07A and LB-08A cores show slightly more overlap with the compositions of the suevites from out of the crater, and this is significant for Al_2O_3 (Fig. 6.11 B), MgO (Fig. 6.11 E) and K_2O (Fig. 6.11 H). TiO_2 concentrations (Fig. 6.11 A) for the out-of-crater suevites are higher than for the within-crater suevites.

The suevites from north of the crater are more enriched in Al_2O_3 (Fig. 6.11 B) than the within-crater suevites, caused by the higher granitoid contents. The CaO contents (Fig. 6.11 F) of the out-of-crater suevites fall within the lowest CaO values of the within-crater suevites (consistent with the observation of a lack of calcite in the out-of-crater suevites). Much overlap for all three groups is apparent for Fe_2O_3 contents and MnO (due to low concentrations; Fig. 6.11 C-D). K_2O contents (Fig. 6.11 H) are highly variable for the suevites from north of the crater, which may again reflect the variable granitoid component in these suevites.

6.5.1.2 Comparison of the major element results for the out-of-crater suevites with previous studies

In addition to the major element analyses from this study, the results of out-of-crater suevites analysed by Karikari et al. (2007) and Boamah and Koeberl (2003) are shown. Table 6.4 documents the ranges of the different studies of the out-of-crater suevites.

As expected, the ranges of the major element compositions between this study, and the studies of Boamah and Koeberl (2006) and Karikari et al. (2007) are similar (Fig. 6.11), and overlap is observed for all elements. Overlap in the values for the northern out-of-crater suevites of all studies is significant. For the suevites from south of the

crater, overlap is generally good (between the results from this study and those of Karikari et al., 2007).

Table 6.4: Comparison of major element ranges of out-of-crater suevites in this study to those of Boamah and Koeberl (2006) and Karikari et al. (2007).

	Suevites from north of the crater *	Suevites from south of the crater*	Out-of-crater suevites**	Out-of-crater suevites***
SiO_2	62.9 - 66.8	63.2 - 67.2	55.4-66.0	53.1–72.9
TiO_2	0.56 - 0.68	0.52 - 0.77	0.56-0.83	0.50-0.82
Al_2O_3	15.0 - 16.3	16.3 - 18.7	12.8-17.1	12.3-21.1
Fe_2O_3	6.24 - 7.84	4.72 - 8.17	4.91-13.1	4.91-9.97
MnO	0.08 - 0.12	0.02 - 0.06	0.04-0.14	0.04-0.13
MgO	2.13 - 2.80	0.62 - 1.03	0.92-2.81	0.79-2.61
CaO	0.53 - 0.92	1.40 - 2.45	0.29-2.24	0.26–1.17
Na_2O	1.96 - 2.66	2.30 - 3.57	0.79-2.47	1.62–2.91
K_2O	1.28 - 1.68	0.44 - 2.13	0.78-1.89	1.11–3.10
P_2O_5	0.09 - 0.13	0.04 - 0.10	0.04-0.12	0.06-0.15
LOI	3.80 - 4.70	2.60 - 4.10	4.89-11.2	3.43-8.75

**Data from this study; **Data from Boamah and Koeberl (2006); ***Data from Karikari et al. (2007).*

In general, the ranges (Table 6.4) for the suevites of the other studies are larger than for those of this study, and this is thought to represent variations in the clast contents of the breccias. As shown in Table 6.1, the suevites are highly heterogeneous in terms of clast content and proportion, and thus differences are to be expected in the related chemical data. In terms of MgO content, the values for the suevites from north of the crater are much higher than for the suevites from south of the crater and those of the other studies.

LOI contents are much higher for the suevites of Boamah and Koeberl (2006) and this could be a factor of local phyllosilicate differences (specific proportions were not documented by Boamah and Koeberl, 2006). It is thought that any differences between the sample ranges are reflective of the extensive clast variation.

6.5.2 Trace Element Analysis

The XRF and ICP-MS results (see Appendix 6a) reveal few differences between the trace element signatures of the out-of-crater suevites from the north and south of the crater (Fig. 6.12). The

suevites from south of the crater have slightly higher V contents than the suevites from north of the crater (Fig. 6.12 A). In general, Cu, Zn, Co and Cr (Fig. 6.12 B-C) contents are directly comparable. The suevites from north of the crater have somewhat higher Sr contents (related to plagioclase variations), but comparable Rb contents than those from south of the crater (Fig. 6.12 D). Thorium and Ba contents are notably less for the suevites from south of the crater (Fig. 6.12 E-F), which may be related to trace minerals such as monazite. There is some enrichment in Zr contents for the suevites from south of the crater compared to those from the north, but this may be a result of accidental sampling of zircon.

Siderophile contents do not differ substantially between the northern and southern suevites. Overall, Cr contents vary between 101 ppm and 172 ppm, Ni contents are between 41 ppm and 64.7 ppm, and the range of Co contents is 16-25.5 ppm (Appendix 6a). The siderophile elements generally correlate positively with Fe_2O_3 and MgO contents, but some exceptions are observed. Larger ranges of trace element abundances are evident for the suevites from the northern sector as opposed to those from the south (Appendix 6a), but this may be a factor of sample statistics.

6.5.2.1 Rare earth elements

Chondrite-normalized rare earth element plots (Fig. 6.13; Taylor and McLennan, 1985) reveal few differences between the suevites from south of the crater and those from north of the crater. Both the suevite groups from south and north of the crater form reasonably steep patterns, and have high absolute abundances. The patterns have similar shapes and slopes. The heavy rare earth elements (HREE) have reasonably flat slopes and there is comparative enrichment in the light rare earth elements (LREE).

The suevites from south of the crater display small, positive Ce anomalies.

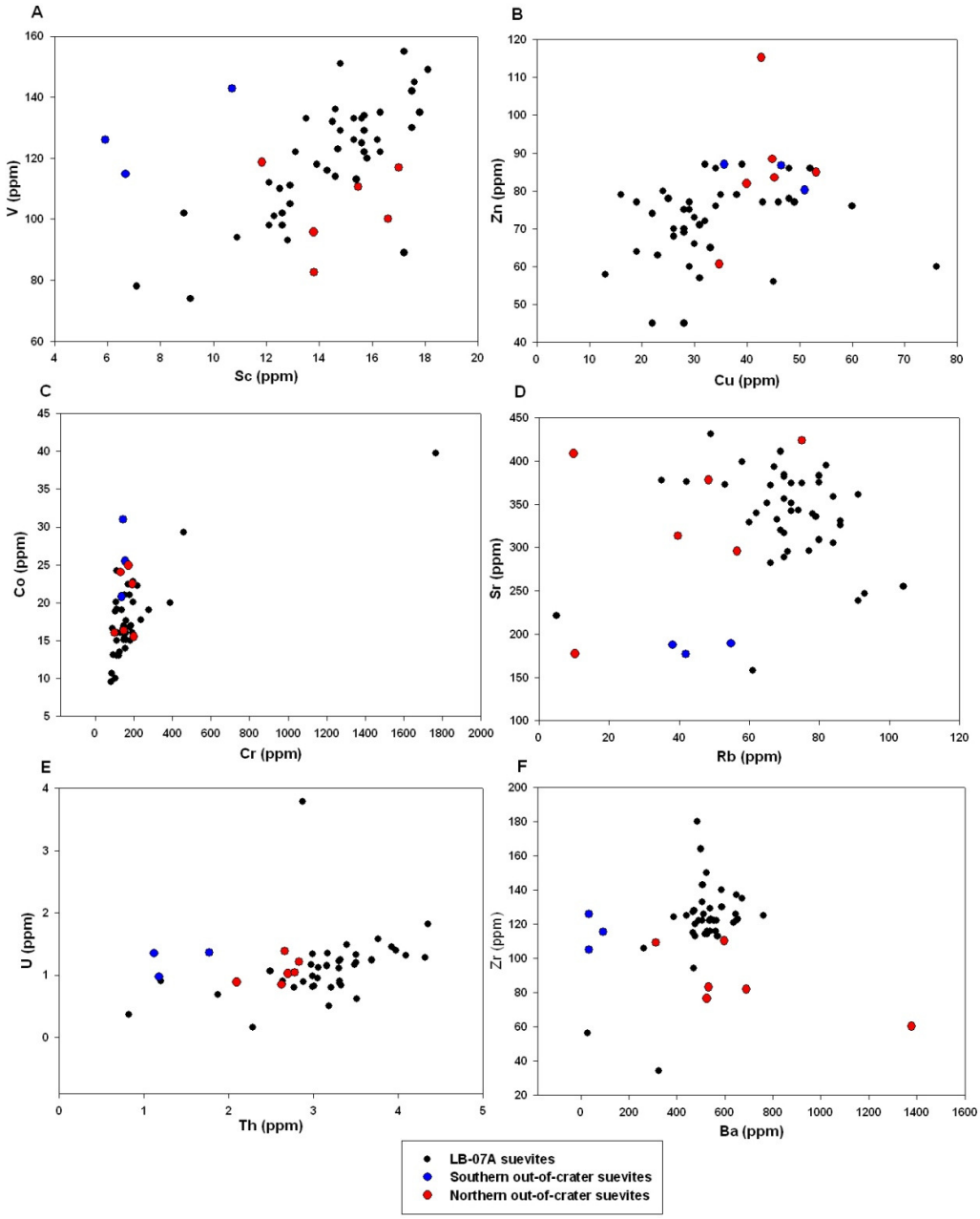

Fig. 6.12: Trace element plots for the within-crater and out-of-crater suevites, indicating the differences between the suevites from the south and north of the crater. A) Sc vs. V; B) Cu vs. Zn; C) Cr vs. Co; D) Rb vs. Sr; E) Th vs. U and F) Ba vs. Zr. All data in ppm.

This is explained by the large amounts of organic material (predominantly present in the shales), which will affect the REE signature (Leleyter et al., in press). When organic matter is present in a sample, it absorbs significant amounts of REE except Ce (as Ce tends to show an affinity towards oxides). Thus, it effectively

"removes" all REE except Ce from the bulk host rock. When the sample from the "bulk host rock" is then analysed, it will be comparatively enriched in Ce (the undissolved organic matter thus contains comparatively little Ce), and thus the REE pattern produced by a bulk analysis will be affected, as a positive Ce "anomaly" is produced. Very small Eu anomalies are apparent for these samples.

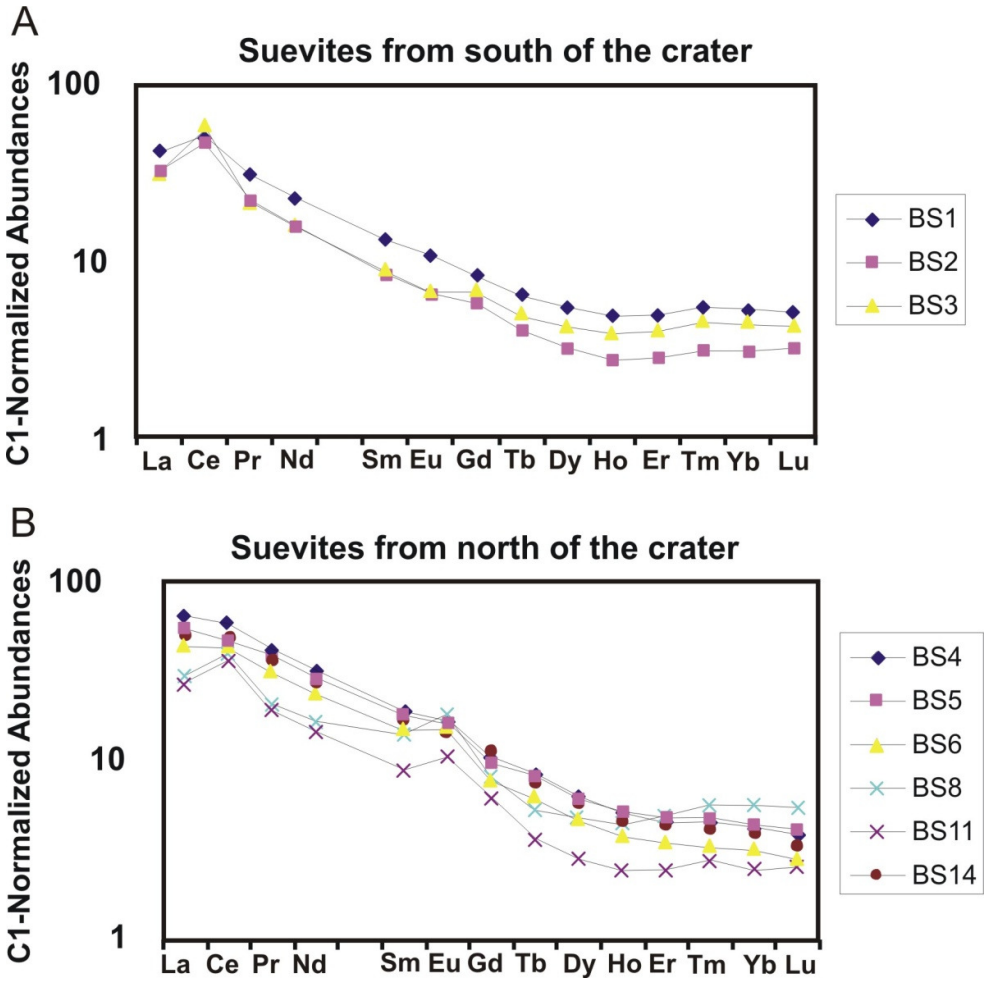

Fig. 6.13: Selected C1 chondrite-normalized rare earth element patterns (normalization factors after Taylor and McLennan, 1985). A) Out-of-crater suevites from south of the crater. B) Out-of-crater suevites from north of the crater.

In contrast, only two suevite samples from north of the crater display Ce anomalies, and this is caused by the general lack of organic matter in these samples. Generally these samples all display positive

Eu anomalies – caused by enrichment in the feldspar minerals (see Table 6.1).

6.5.2.2 Trace element differences between the out-of-crater suevites and the within-crater suevites

In general, the trace element compositions of the within-crater suevites are similar to those from north and south of the crater (Fig. 6.12). The most notable difference is relative enrichment of V in the suevites from south of the crater in comparison to those from north of the crater and the within-crater suevites. This may be explained by the comparatively higher shale component in the suevites from south of the crater (Fig. 6.12 A). There are some differences in Sr and Rb contents (Fig. 6.12 D) from the majority of the within-crater suevite compositions, and this is most likely related to fluctuations in the plagioclase content of the samples (controlled by granite and metagreywacke target rock components).

Ternary plots of Hf-Th-Co and Cr-Zr-La (Fig. 6.14) have been made in order to further assess the trace element patterns. There is much overlap in the normalized trace element patterns of the LB-07A lithologies with the out-of-crater suevites and target rock lithologies (Koeberl et al., 1998). The out-of-crater suevites are somewhat more enriched in Co than the other lithologies, particularly the granite dykes and phyllite-greywackes (Fig. 6.14 A). In Fig. 6.14 B, nearly all lithologies lie along a line between Cr and Zr.

Figures 6.14 C and D show the LB-07A suevites and the out-of-crater suevites. The suevites from north of the crater have very similar trace element signatures to those from within the crater; however, the results for the southern out-of-crater suevites indicate that they have a slightly different trace element signature to the other suevites.

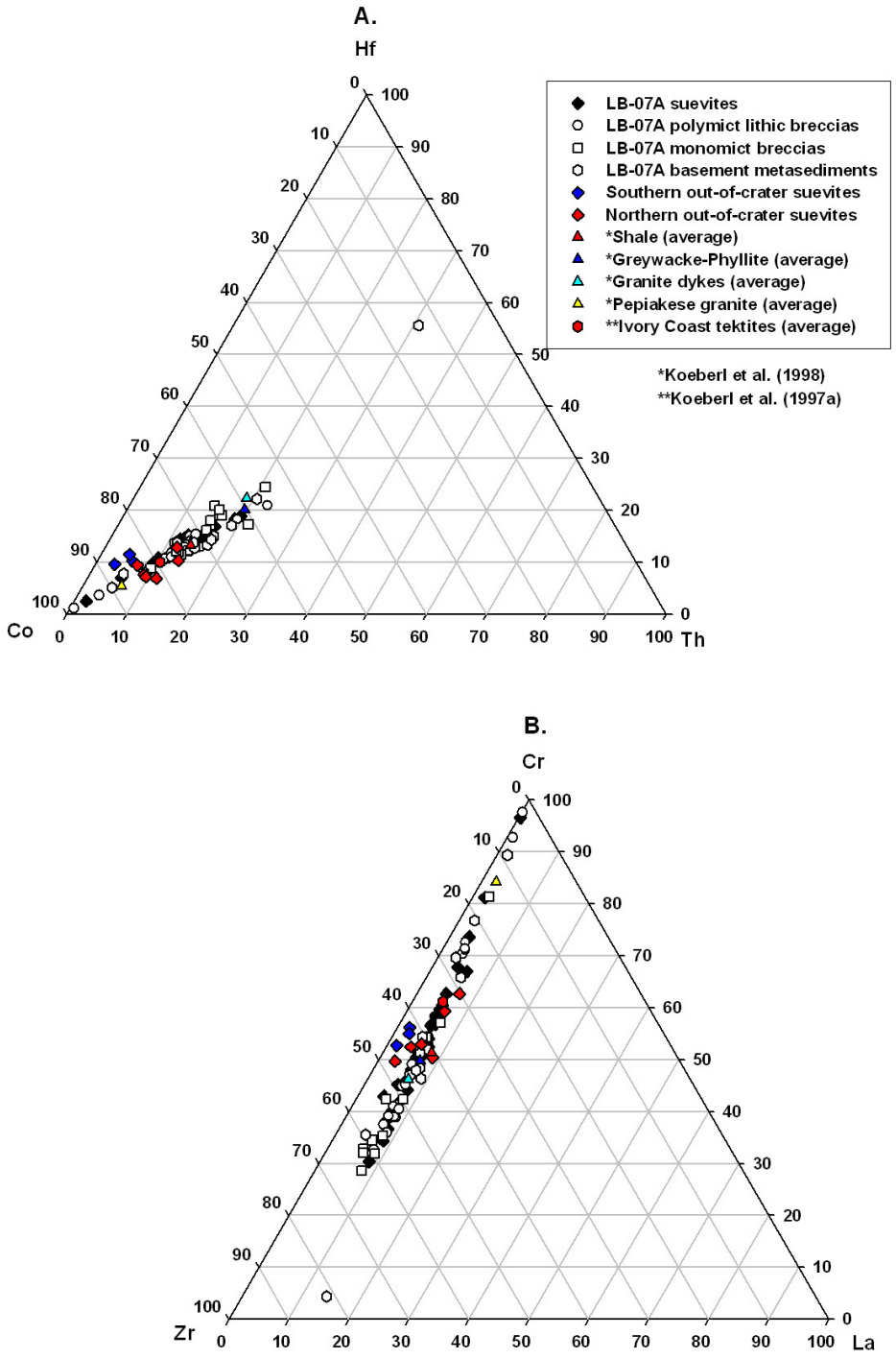

Fig. 6.14: Trace element ternary plots. A) Hf-Co-Th. B) Cr-Zr-La. For A) and B) analyses from all impactite lithologies from LB-07A core, together with the out-of-crater suevites (this study) are indicated as well as averages of the target rock types of Koeberl et al. (1998) and the average Ivory Coast tektite composition (Koeberl et al., 1997a). Continued on next page.

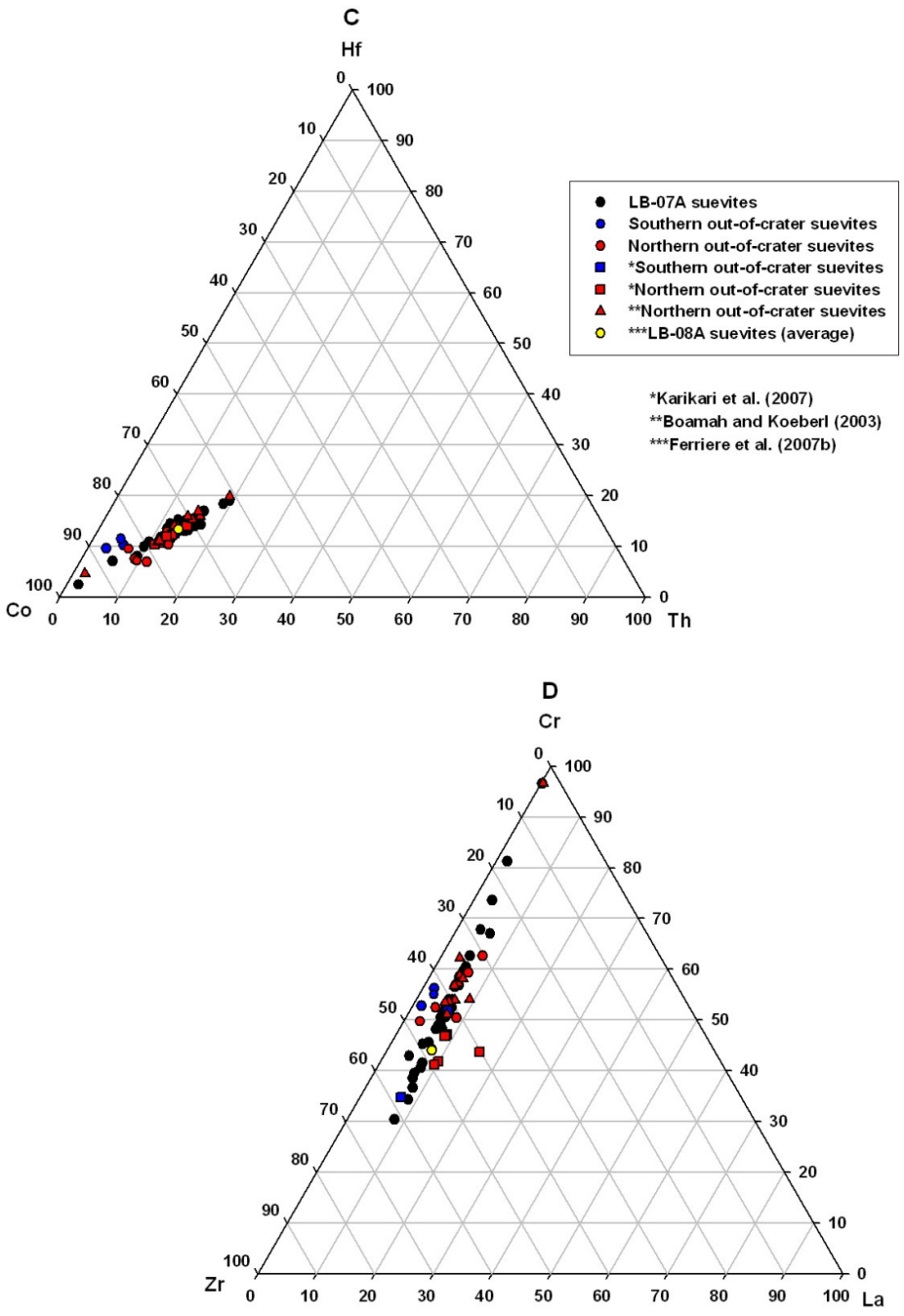

Fig. 6.14 (cont'd): Trace element ternary plots. C) Hf-Co-Th. D) Cr-Zr-La. For C) and D) only suevite analyses from LB-07A core, together with the out-of-crater suevites (this study) are indicated as well as out-of-crater suevite analyses of Karikari et al. (2007), Boamah and Koeberl (2003) and the average of the LB-08A suevite analyses from core LB-08A (Ferrière et al., 2007b).

In order to further compare the geochemical signatures of the impactites and basement rocks of LB-07A, a plot of the averaged C1-

normalised REE signatures for the different lithologies in LB-07A (Fig. 6.15 A) is compared to the averages for the target (Fig. 6.15 B), Ivory Coast tektites (Fig. 6.15 C) of Koeberl et al. (1998) and out-of-crater suevites of this study and those of Boamah and Koeberl (2003; Fig. 6.15 D). As noted in Chapter 4, the within-crater impactites have very similar normalized REE abundances to each other (Fig. 4.7; Fig. 6.15 A). These normalized abundances, however, are slightly lower than those for the average shale and greywacke-phyllites (Fig. 6.15 B). Furthermore, the Pepiakese granite has lower REE abundances than the LB-07A rocks (Fig. 6.15 B). The out-of-crater suevite compositions are close to those of the LB-07A rocks, although the REE patterns from core BH1 (Boamah and Koeberl, 2003) are most similar to those of the greywacke-phyllites (Fig. 6.15 D). The average granite, however, has intermediate compositions comparable to the breccias and basement metasediments from core LB-07A. The REE abundance patterns of the Ivory Coast tektites are slightly elevated in comparison to the REE abundances of the LB-07A core.

The REE abundance patterns of the out-of-crater suevites of this study are mostly comparable with the LB-07A within-crater lithologies, though a number of elements appear to be less enriched in the heavy rare earth elements, although this cannot be fully verified as the analytical methods for the out-of-crater and within-crater suevites were different (see Chapter 2).

Smaller ranges are apparent for the siderophile element contents for the out-of-crater suevites in comparison to the within-crater suevites. The highest concentration of Cr is 1765 ppm for the within-crater suevites (*vs.* 173.7 ppm for the out-of-crater suevites). Cobalt and Ni concentrations reach 39.7 ppm and 466 ppm respectively for the within-crater suevites (*vs.* 31 ppm and 64.7 ppm for the out-of-crater suevites).

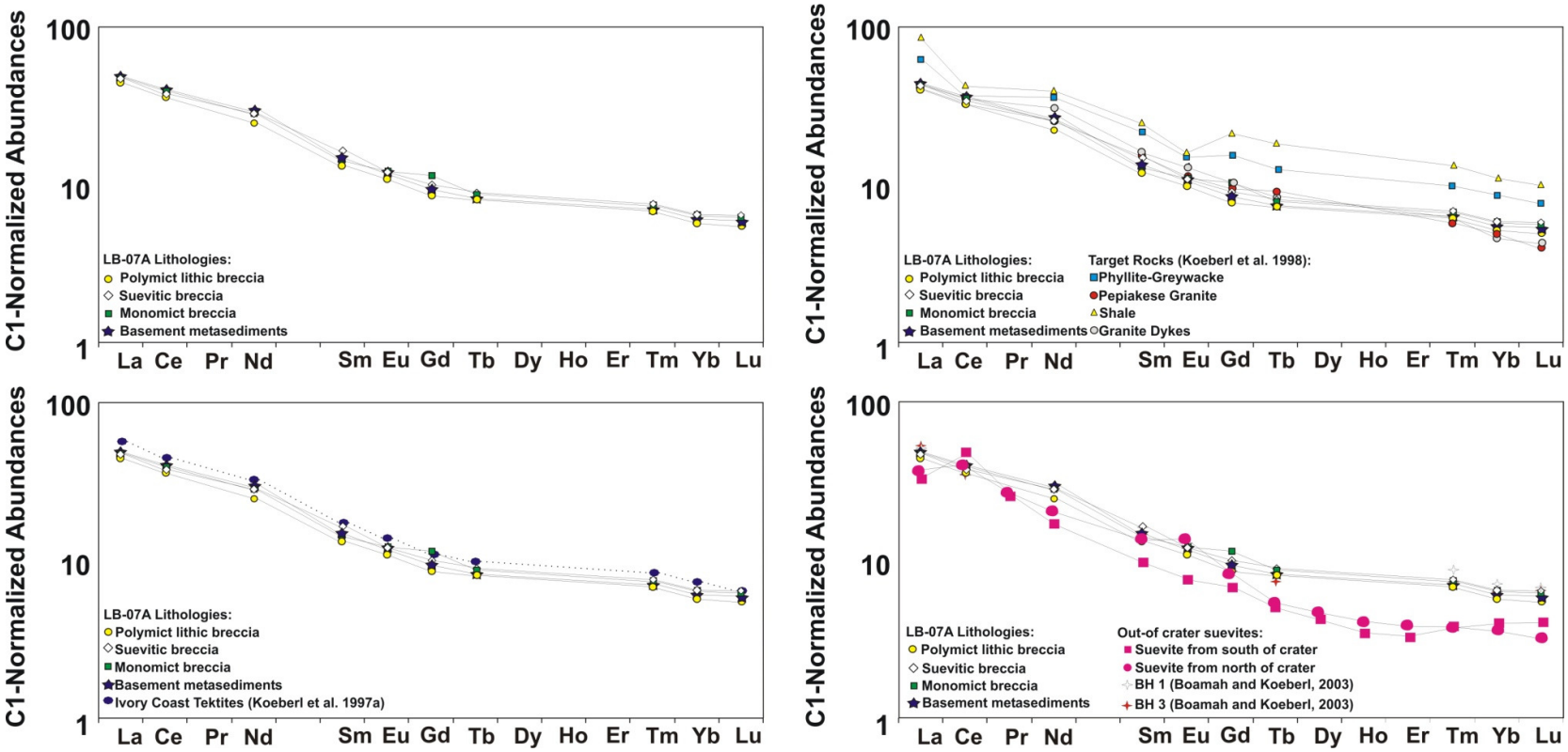

Fig. 6.15: C1 chondrite-normalized average rare earth element patterns (normalization factors after Taylor and McLennan, 1985). A) LB-07A polymict lithic, suevitic and monomict breccias and basement lithologies. B) LB-07A impactites with average target rocks (Koeberl et al., 1998). C) LB-07A impactites with Ivory Coast tektites (Koeberl et al., 1997a). D) LB-07A impactites with out-of-crater average suevites from north of the crater (this study; Boamah and Koeberl, 2003) and south of the crater (this study).

6.5.2.3 Comparison of the trace element results for the out-of-crater suevites with previous studies

In terms of trace element analysis (Fig. 6.16), similar clustering of values to the major elements is observed (Fig. 6.16 A-C; E). The results of different studies are highly compatible.

Strontium (Fig. 6.16D) and Zr (Fig. 6.16 F) values show the most variation for the trace elements results of the different studies: this is most likely related to accidental sampling of zircon for the Zr results, and to differing plagioclase abundances for the Sr results.

In Figures 6.14 C and D, the suevites from this study (both within and out-of-crater) have been plotted together with the out-of-crater suevites of Karikari et al. (2007) and Boamah and Koeberl (2003), as well as the average for the LB-08A suevites (from Ferrière et al., 2007b). The results for the northern out-of-crater suevites for all studies are highly comparable (Fig. 6.14 C-D) and are very similar to data for the LB-07A suevites (as well as the average of the LB-08A suevites). The Karikari et al. (2007) results for 2 suevite analyses from south of the crater are similar to those obtained here, but their results do not overlap as significantly as those from north of the crater (Fig. 6.14 C-D).

Cerium anomalies were noted previously by Boamah and Koeberl (2002) in their analyses of soil samples from the Bosumtwi structure, which they attributed to variable weathering conditions. However, no Ce anomlies were noted in their study of suevites from north of the crater (Boamah and Koeberl, 2003), which is consistent with this study.

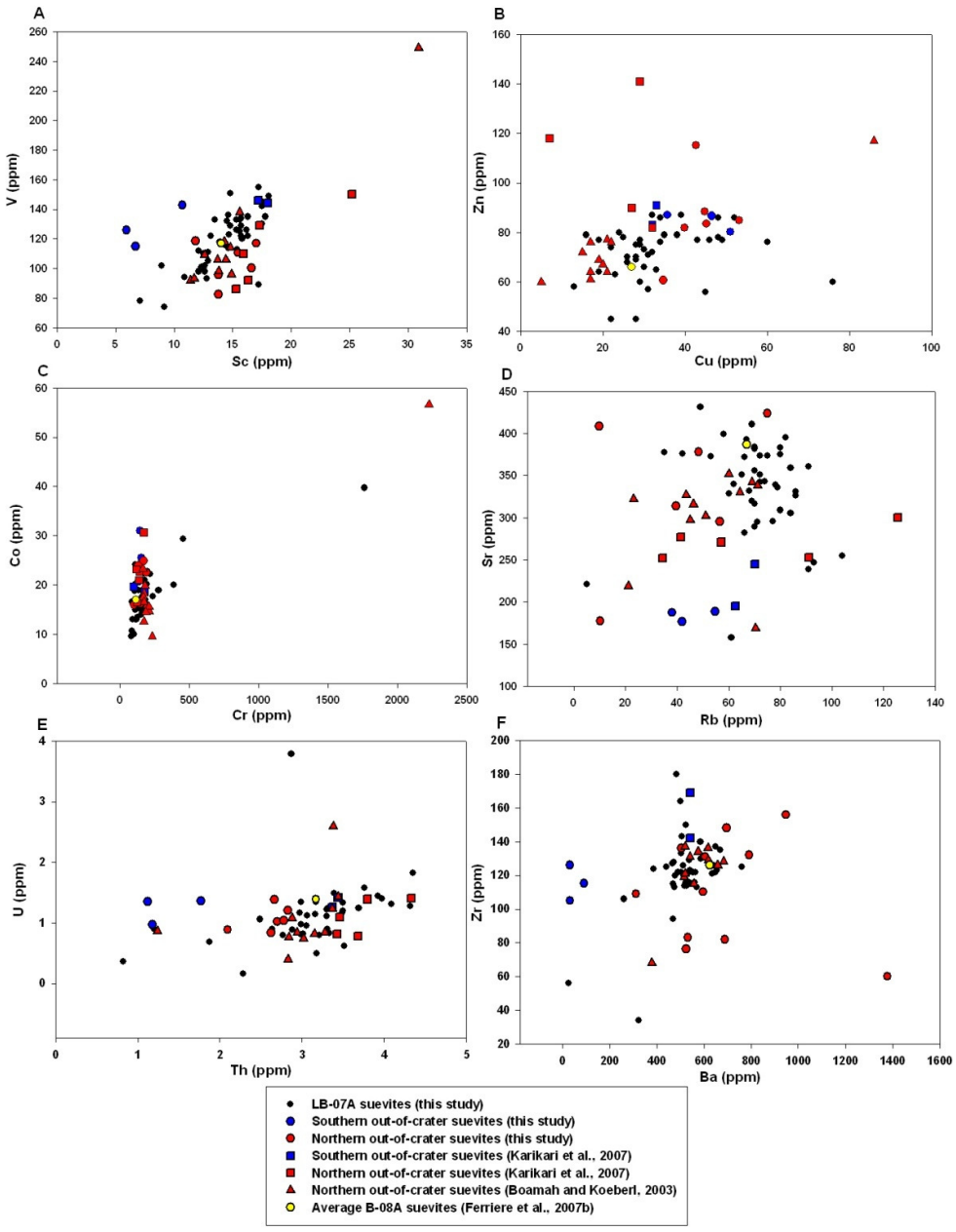

Fig. 6.16: Binary plots of trace element analyses of within-crater (LB-07A from this study; LB-08A average from Ferriere et al., 2007b) and out-of-crater suevites (this study; Karikari et al., 2007; Boamah and Koeberl, 2003). A) Sc vs. V; B) Cu vs. Zn; C) Cr vs. Co; D) Rb vs. Sr; E) Th vs. U and F) Ba vs. Zr. All data in ppm.

6.5.3 Suevite Melt Particle Compositions

Melt particles from the suevites from south and north of the crater were analysed for their major element compositions by electron microprobe analysis (EMPA) at the Humboldt-University in Berlin (see Chapter 2 for operating conditions). Extra SEM images are contained in Appendix 6b. The samples were first analysed by scanning electron microscopy (SEM) in order to obtain semi-quantitative data and ascertain if the particles were suitable to be analysed by EMPA. More analyses were obtained for melt particles for suevites from south of the crater as these have, until now, not been analysed by EMPA analysis. Melt particles from suevites from north of the crater have been previously analysed by Boamah (2001), and the results from this study are used to provide a comparison to his data as well as to the data obtained here for the melt particles of the suevites from within and south of the crater.

6.5.3.1 Melt particles from suevites from south of the crater

Melt particles were analysed from two samples: BS-1 and BS-2 (Appendix 2). The first thin section for sample BS-1 (BS1-A) contained a number of melt particles which yielded variable results (owing to alteration and point intersection with quartz clasts). Of 110 measurement spots analysed, 47 points could be used (all totals > 90 wt%) and are reported in Appendix 5d (4 particles were analysed). Figure 6.17 presents SEM images of areas covering most of the spots analysed in the different particles of sample BS-1A.

The second thin section for sample BS-1 (BS1-B) contained 3 melt particles (Fig. 6.18). The first grain (Fig. 6.18 A) was composed of Si with a small contribution of Al. It contained greater than 60 vol% vesicles, and as it was entirely homogeneous, was not analysed quantitatively. Its composition demonstrates that this particle is composed of lechaterlierite. The second grain (Fig. 6.18 B) was also composed entirely of Si, with remnants of another phase. However, this melt phase was so vesicular that it produced only poor analyses.

The third grain (Fig. 6.18 C-F) could be analysed quantitatively; however most totals were lower than 95 wt%, as this particle is extensively altered. Three areas were analysed on the grain (Fig. 6.18 C-E). Of 55 points analysed, only 7 points could be used, as most totals were lower than 80 wt%, and a number of quartz clasts were analysed. All totals over 90 wt% are reported here (Appendix 5d).

Sample BS-2 contained 4 areas which were assessed. Initially, element mapping was performed in order to ascertain if the particles were spatially homogeneous or not. Element maps for particles 2 and 3 are presented in Fig. 6.19. The element mapping showed that the particles are heterogeneous with respect to their major element concentrations (Fig. 6.19). The backscattered electron image of particle 2 (Fig. 6.19 A) indicates that this particle consists of 3 main phases: dark grey schlieren in a lighter grey phase, together with a more moderately grey phase (located to the right of the image). A number of round, dark grey to black vesicles can be observed. The 3 phases are clearly distinguishable with the application of the element mapping. The moderately grey phase is characterised by high Si values (Fig. 6.19 B), but a lack of enrichment for any other element – thus this is most likely a pure Si glass phase. The light grey phase is characterised by moderate Si and K values, high Al and low Fe and Mg (Fig. 6.19 B-H). The schlieren have relatively lower Si and Al, moderate K and lower Fe, Mg and Na (Fig. 6.19 B-H). Neither phase is highly enriched in Ca (Fig. 6.19 F). It is possible that these 2 phases represent mineral melts, or mixed mineral melts. This concept will be examined in the chemical analyses.

Particle 3 indicates that there are 2 main phases (Fig. 6.19 I-O) and that there is little difference in the Mg, K, Ca and Na contents of these phases. The main phase consists of moderate Si and Al with low Fe whereas the minor phase consists of low Si and Al and moderate Fe.

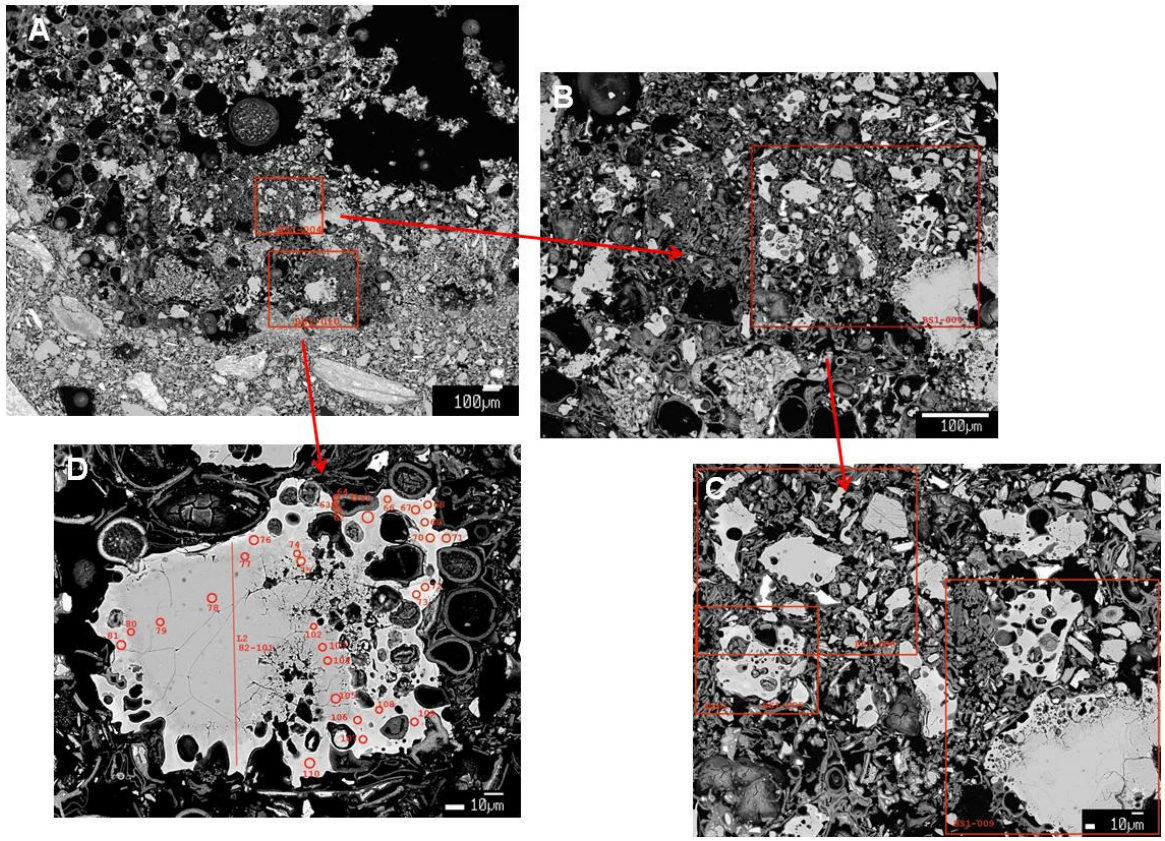

Fig. 6.17: Backscattered electron images of melt particles analysed from sample BS-1, thin section BS-1A suevite from south of the crater: the lightest fragments correspond to rutile, moderately grey indicates silica-rich lithologies, with lighter white-grey and dark grey indicating the mixed melts, and black for the vesicles. A) Area of melt particle analyses, showing two portions analysed; width of scale bar = 100 µm. B) Enlargement of portion 1; width of scale bar = 100 µm. C) Enlargement of portion 1; showing melt particles 1-3; width of scale bar = 10 µm. D) Enlargement of portion 2, showing points analysed on melt particle 4; width of scale bar = 10 µm. Continued on next page.

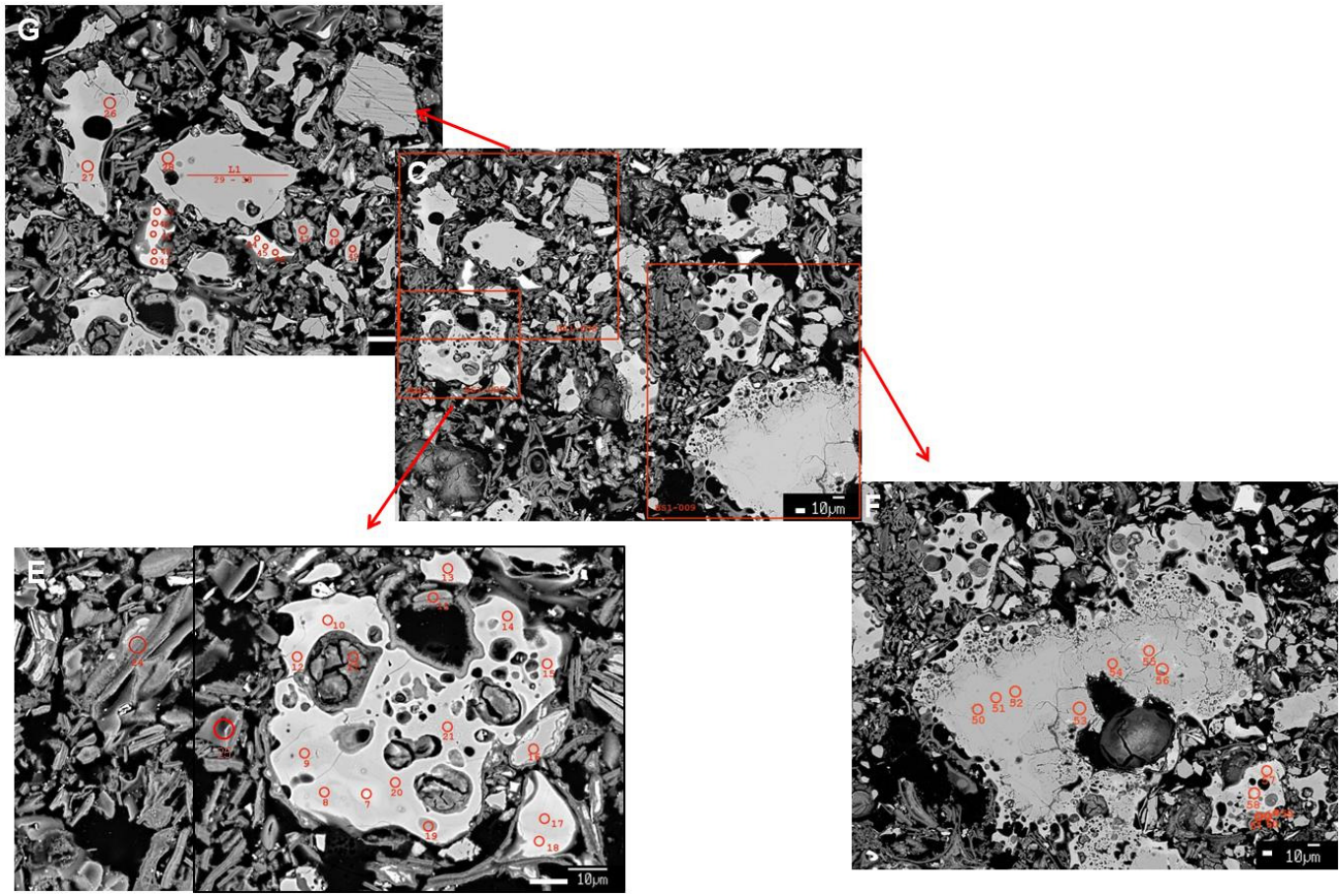

Fig. 6.17 (cont'd): C) Enlargement of portion 1; showing melt particles 1-3; width of scale bar = 10 µm. E) Points analysed on melt particle 1; width of scale bar = 10 µm. F) Points analysed on melt particle 3; width of scale bar = 10 µm. G) Points analysed on melt particle 2; width of scale bar = 10 µm.

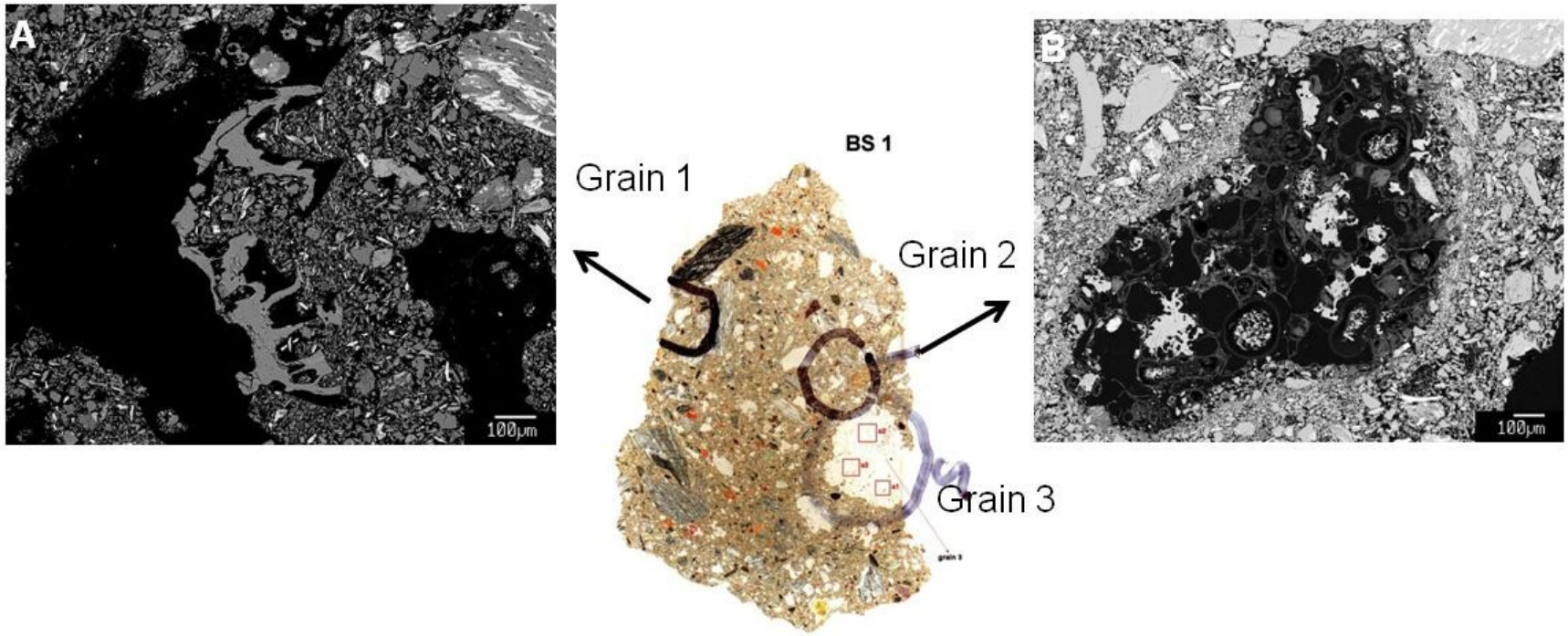

Fig. 6.18: Thin section and backscattered electron images of melt particles analysed from sample BS-1, thin section BS-1B, suevite from south of the crater: the lightest fragments correspond to rutile, moderately grey indicates silica-rich lithologies, with lighter white-grey and dark grey indicating the mixed melts, and black for the vesicles. Three grains were identified in thin section. A) Grain 1. B) Grain 2. Continued on next page.

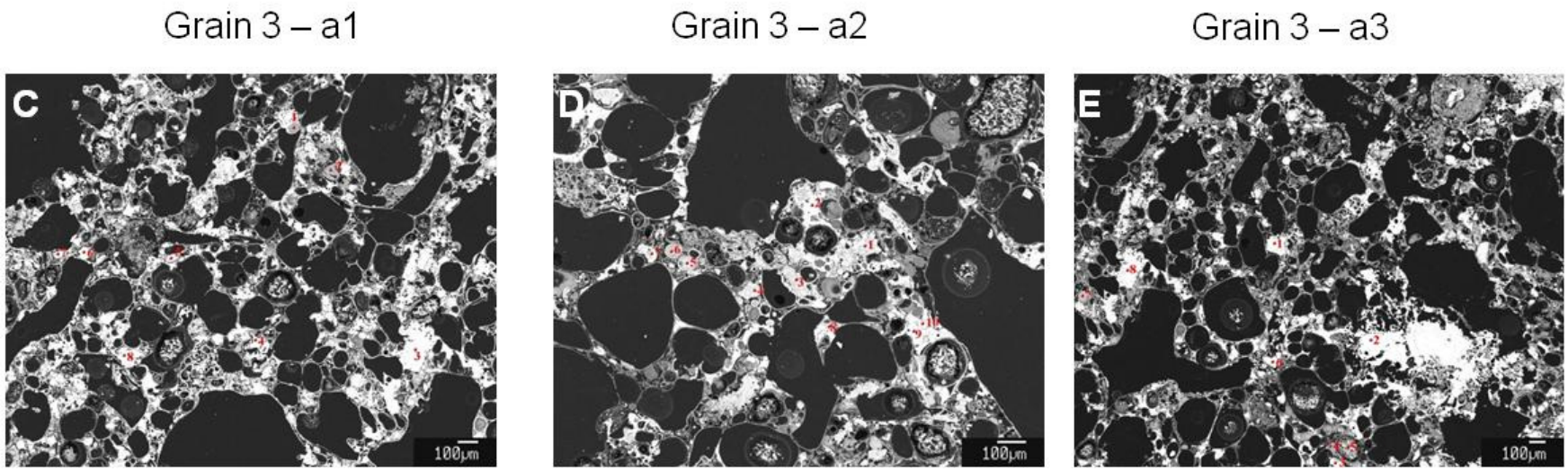

Fig. 6.18 (cont'd): Thin section and backscattered electron images of melt particles analysed from sample BS-1, thin section BS-1B, suevite from south of the crater. C) Grain 3, area 1. D) Grain 3, area 2. E) Grain 3, area 3. The points analysed are indicated in red (see text for details). Width of scale bar = 100 µm.

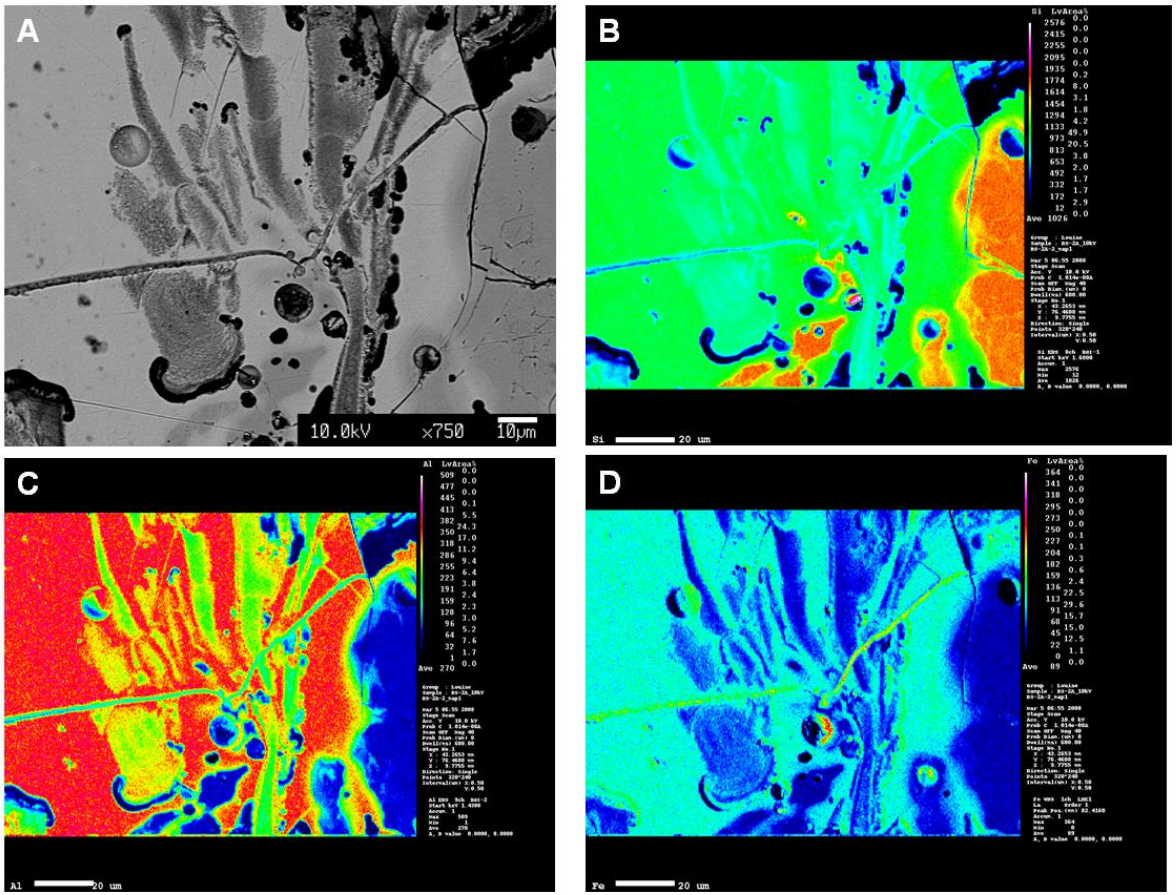

Fig. 6.19: Element maps from sample BS-2, melt particles 2 and 3. Element maps produced by electron microprobe analysis at a current of 10 kV. A) Backscattered electron image of melt particle 2; width of scale bar = 10 µm. B) Si for particle 2; width of scale bar = 20 µm. C) Al for particle 2; width of scale bar = 20 µm. D) Fe for particle 2; width of scale bar = 20 µm. Continued on next page.

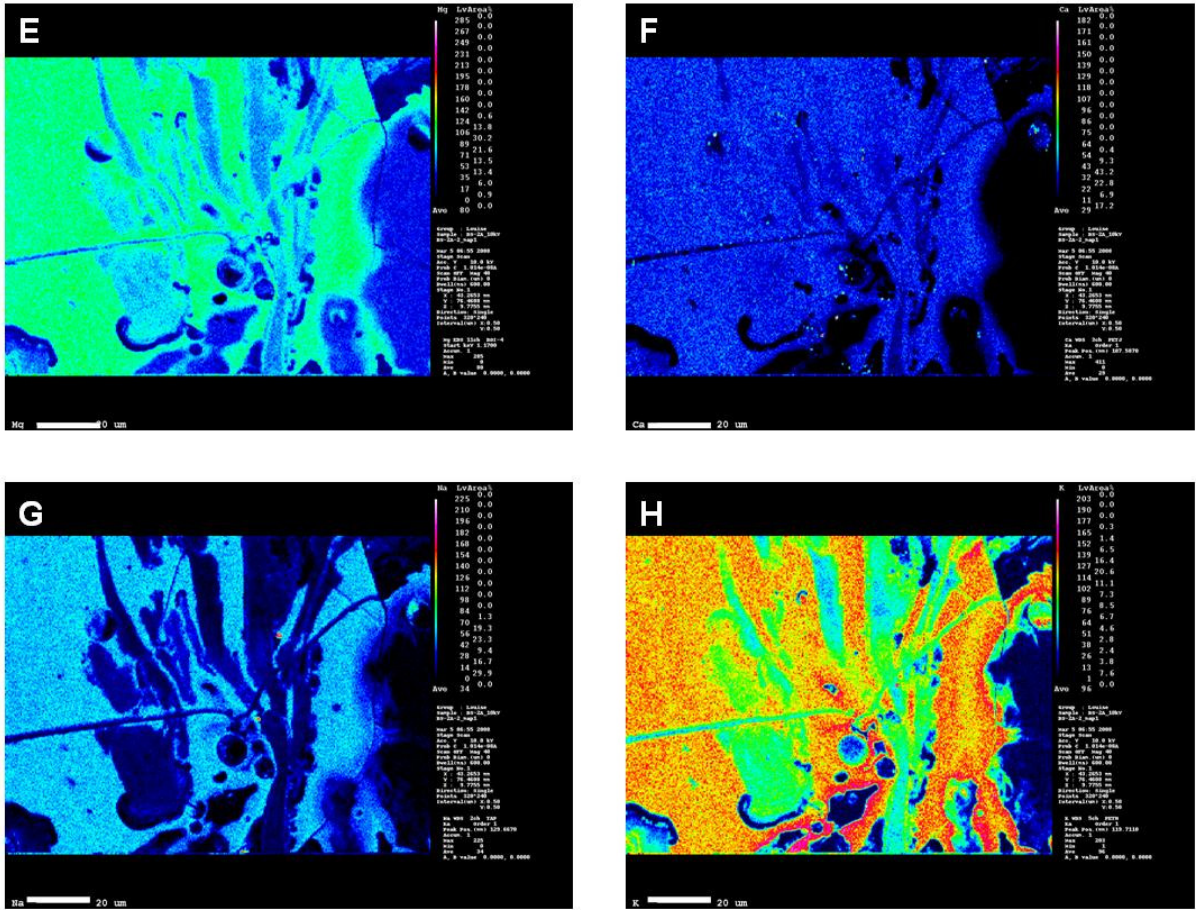

Fig. 6.19 (cont'd): E) Mg for particle 2; width of scale bar = 20 µm. F) Ca for particle 2; width of scale bar = 20 µm. G) Na for particle 2; width of scale bar = 20 µm. H) K for particle 2; width of scale bar = 20 µm. Continued on next page.

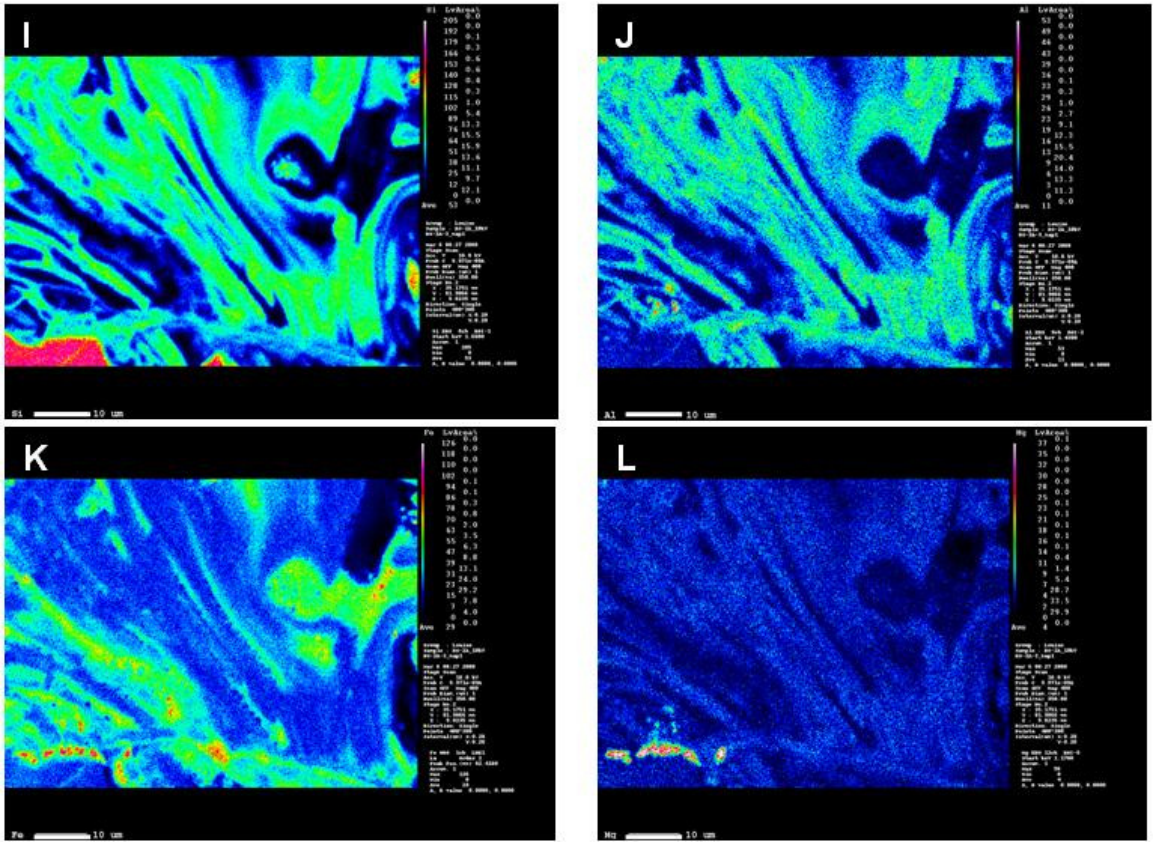

Fig. 6.19 (cont'd): I) Si for particle 3; width of scale bar = 20 µm. J) Al for particle 3; width of scale bar = 20 µm. K) Fe for particle 3; width of scale bar = 20 µm. L) Mg for particle 3; width of scale bar = 20 µm. Continued on next page.

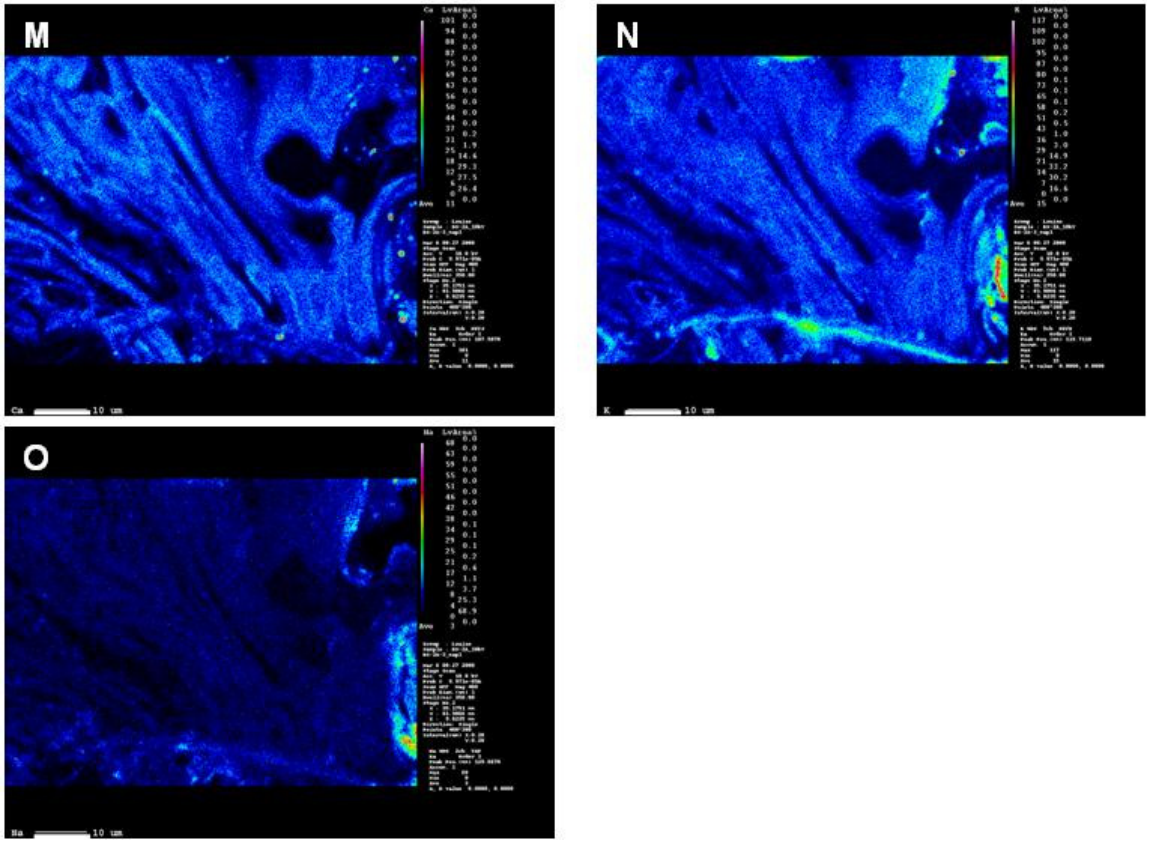

Fig. 6.19 (cont'd): M) Ca for particle 3; width of scale bar = 20 µm. N) K for particle 3; width of scale bar = 20 µm. O) Na for particle 3; width of scale bar = 20 µm.

Following the element mapping, it was decided to analyse particles 2 (BS2-2) and 4 (BS2-4) for their major element compositions. The results are provided in Appendix 5d – 71 analyses (from 95 points analysed) are reported for 2 particles in area 2 and 29 analyses (from 34 points analysed) from a single melt particle are reported for area 4 (after removal of poor analyses and quartz clasts).

The EMPA data will be examined in a similar way to the data for the melt particles of the within-crater suevites (section 5.4.2), although more spatial control on the data exists as the locations of the points have been constrained. Binary plots of the different melt particles are shown in Figure 6.20. As with the melt particles from within the crater, there is some internal heterogeneity in the individual particles – particularly in particles from sample BS-1A and BS-1B. The particles in samples BS2-2 and BS2-4 are more homogeneous, though 2 distinct populations in terms of Na_2O contents are apparent for sample BS2-4.

SiO_2 values vary between 50 and 90 wt%, while TiO_2 values are generally less than 1.5 wt%, though 1 sample displays a TiO_2 value of 2.7 wt% (Fig. 6.20 A). In terms of overall trends, there is some positive correlation between CaO and Al_2O_3, which may reflect variation in anorthite (Fig. 6.20 B). There are two distinct trends between K_2O and Na_2O – the first is a positive correlation between K_2O and Na_2O, while the second shows high K_2O values for lower Na_2O values (Fig. 6.20 C). Interestingly, all the particles analysed from sample BS2 form part of the high K_2O trend. Positive correlation between FeO and MgO is again observed (Fig. 6.20 D), notably with the high K_2O values of sample BS2-4 correlated with the highest MgO and FeO values, which indicates that biotite may have been involved in possibly contributing to its composition.

Thus, as with the within-crater suevites, it is apparent that the melt particles do not form discrete mineral melts.

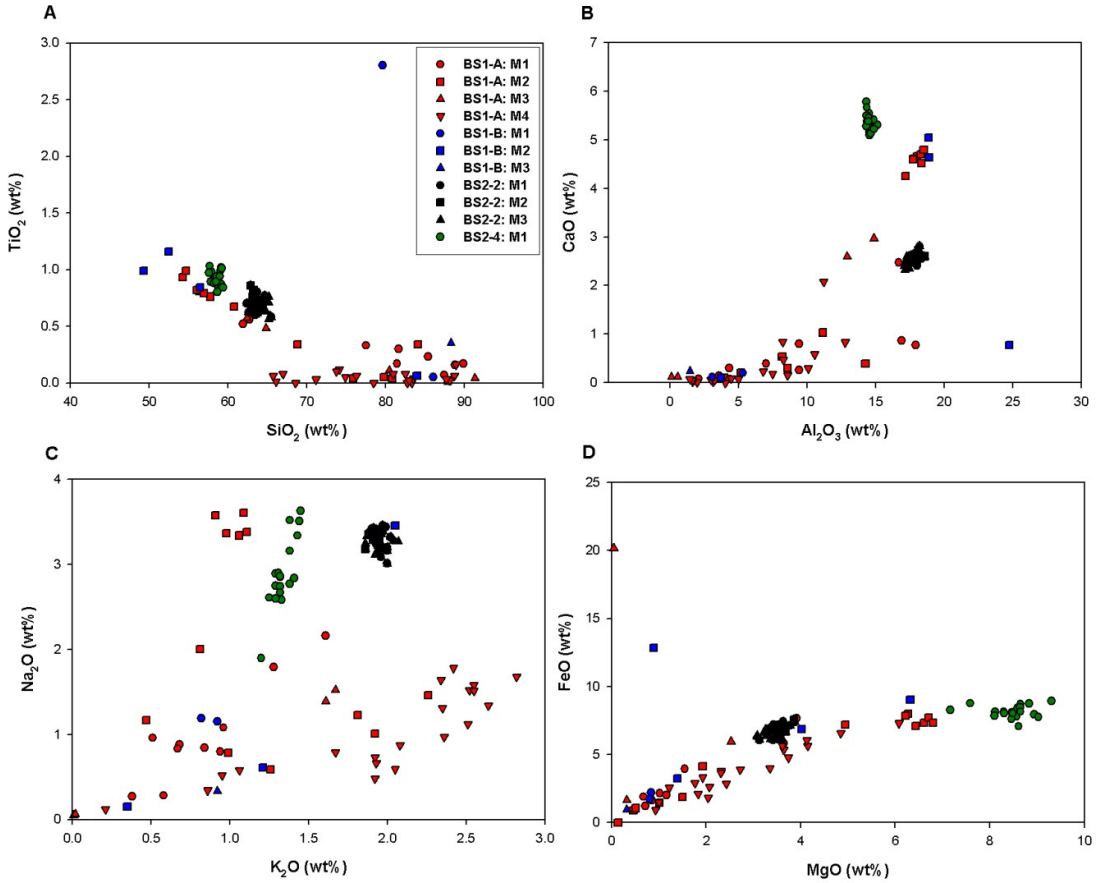

Fig. 6.20: Binary plots of the electron microprobe analyses for melt particles (10 µm defocused beam): melt particles in the out-of-crater suevites from south of Lake Bosumtwi. A) SiO_2 vs. TiO_2; B) Al_2O_3 vs. CaO; C) K_2O vs. Na_2O; D) MgO vs. FeO. Data in wt%.

In order to ascertain the different contributory phases, a number of ternary plots were produced (Fig. 6.21). The separate melt particles are indicated together with possible contributory mineral phases (quartz, albite, anorthite, potassium-feldspar, muscovite, biotite, chlorite and calcite) and the proposed target rock lithologies of Koeberl et al. (1998) and the position of the average Ivory Coast tektites (Koeberl et al., 1997a).

Fig. 6.21 A indicates that the melt particles form a similar trend to those from within the crater (Fig. 5.15 A) in that they originate from the 100 % SiO_2 apex (i.e., quartz). The trend moves towards a central region between Al_2O_3 and (MgO+FeO), which is slightly shifted towards the Al_2O_3 apex. There is overlap in the compositions of the phyllite-greywackes, shales and granite dykes for the relative Al_2O_3-(MgO+FeO)-SiO_2 contents. Figure 6.21 B shows the relative K_2O-Na_2O-CaO contents, which can be used to differentiate between the different feldspars, calcite and muscovite. There is some overlap between the melt particle compositions from sample BS1-A and potassium-feldspar, but analyses from sample BS2 show a trend towards CaO and are more enriched in Na_2O than K_2O. This possibly indicates more plagioclase-enrichment in these analyses. The final ternary diagram (Fig. 6.21 C) presents an AK(FM) plot, and indicates that the melt particles fall between biotite-chlorite and plagioclase-muscovite. In this plot, there is some overlap with the Pepiakese granite phase, which was not indicated in the previous ternary diagrams.

6.5.3.2 Melt particles from suevites from north of the crater

The major element chemical compositions of melt particles (Figs 6.10 A-F) from 3 samples (BS-8, BS-14B and BS-16B) from suevites from north of the crater were obtained using electron microprobe analysis. Each sample consisted entirely of single, large melt particles. Approximately 88 points were analysed from the 3 particles.

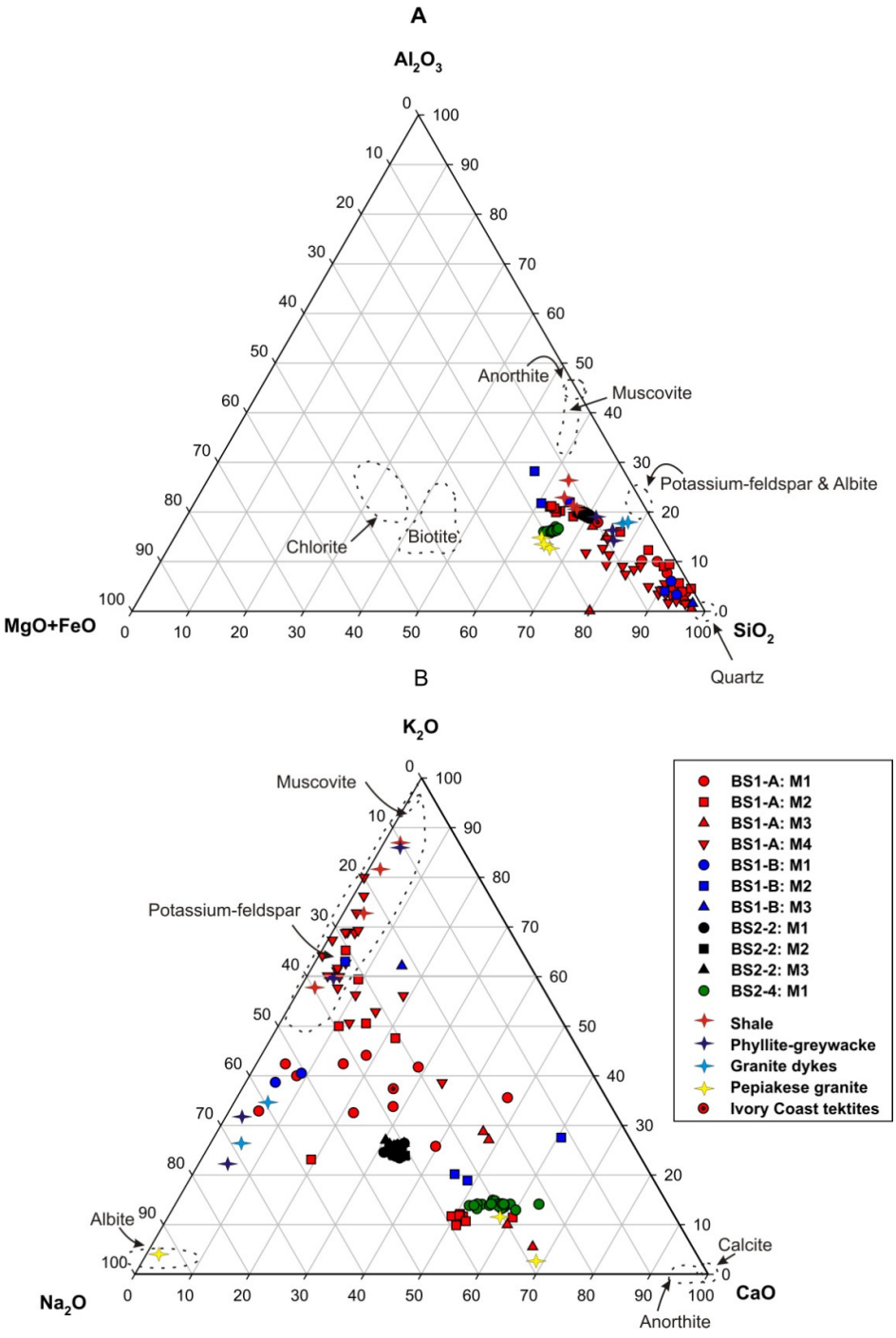

Fig. 6.21: Ternary discrimination diagrams for the electron microprobe analyses (10 µm defocused beam) of melt particle phases in the out-of-crater suevites from south of Lake Bosumtwi. A) Al_2O_3-(MgO+FeO)-SiO_2 and B) K_2O-Na_2O-CaO. Fields for common minerals in the suevites are indicated (after Deer et al., 1971). Average target rock lithologies (phyllite-greywacke, shale, granite dyke and Pepiakese granite; after Koeberl et al., 1998) and the average composition of the Ivory Coast tektites (after Koeberl et al., 1997a) are also plotted. Continued on next page.

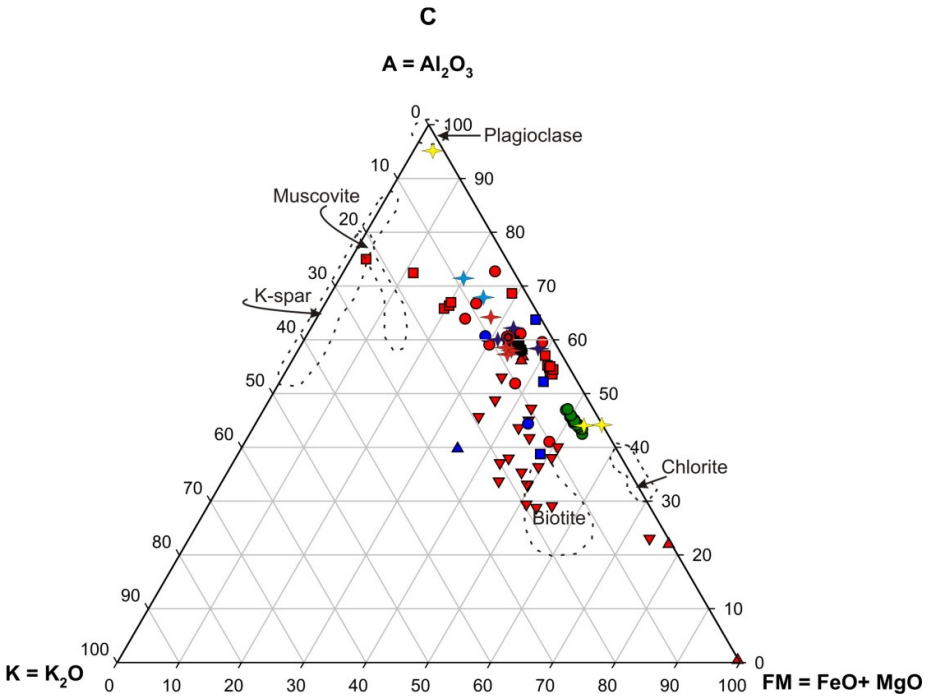

Fig. 6.21 (cont'd): Ternary discrimination diagrams for the electron microprobe analyses (10 µm defocused beam) of melt particle phases in the out-of-crater suevites from south of Lake Bosumtwi. C) AK(FM) diagram.

Good totals (particularly in comparison to the melt particles of the within-crater suevites) were obtained, with nearly all totals above 90 wt%, and all totals below 90% were discarded, lowering the data set to 63 analyses, which is presented in Appendix 5d.

The melt particles differ from those from the suevites from south of the crater and within the crater in that they contain distinct phases of microlites as well as melt (mesostasis; Fig. 6.10 A-F). Once the melt particles were analysed, the analytical spots were characterised visually in terms of the proportion of microlites relative to the amount of melt (mesostasis) – this information is contained in Appendix 5d. In order to check for compositional variation between these phases, the results from samples BS-14B, BS-16B and BS-8 were plotted on Al_2O_3-(FeO+MgO)-SiO_2 diagrams (Fig. 6.22 A-C).

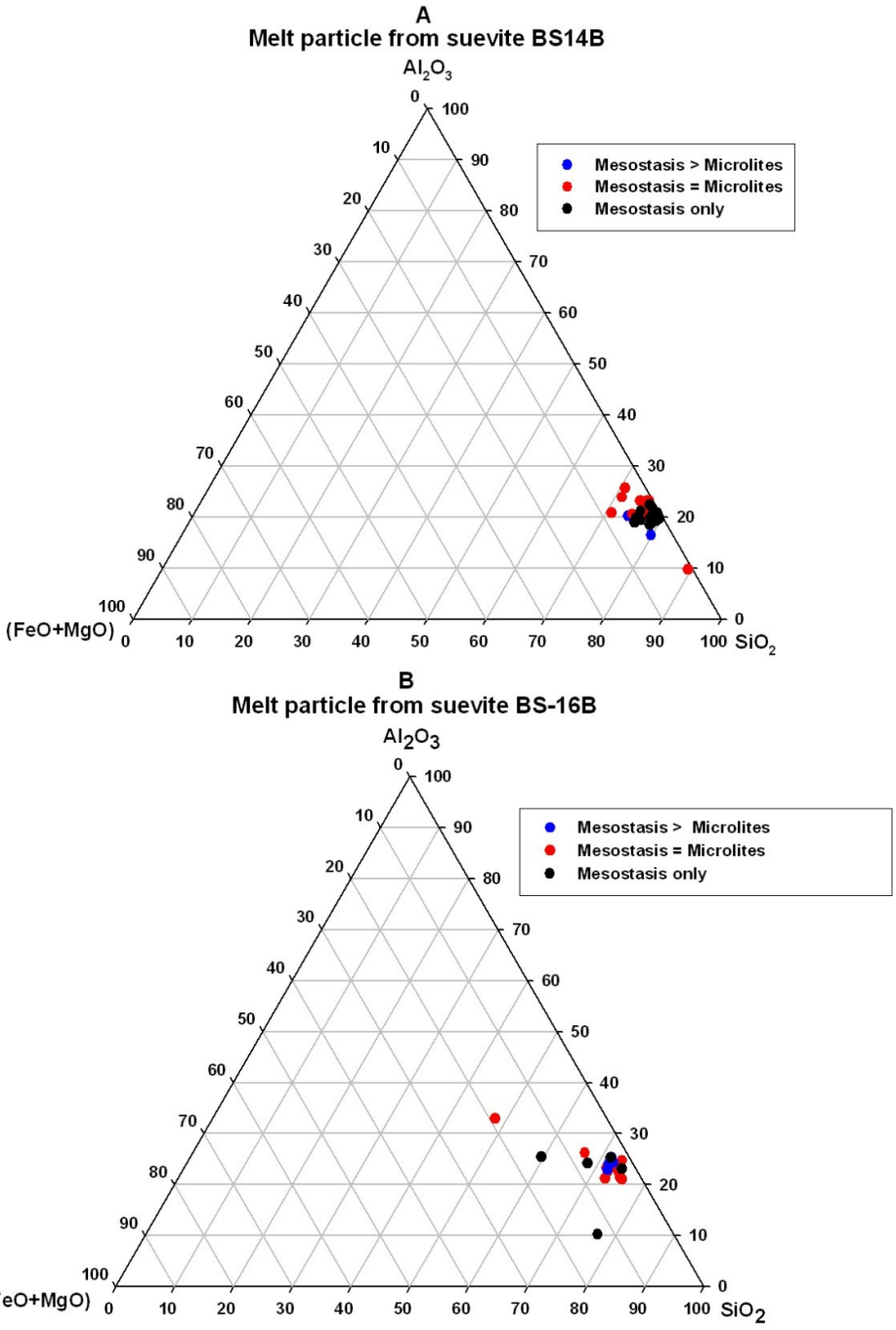

Fig. 6.22: Al_2O_3-(FeO+MgO)-SiO_2 diagrams showing the various phases analysed from melt particles using the electron microprobe (10 µm defocused beam) from A) sample BS-14B; B) sample BS-16B. The phases were identified from assessment of spots analysed with the microprobe, and include where the area % of mesostasis present is greater than the area % of microlites (mesostasis>microlites); where both phases are equal in abundance (mesostasis = microlites), and where only mesostasis is present. Continued on next page.

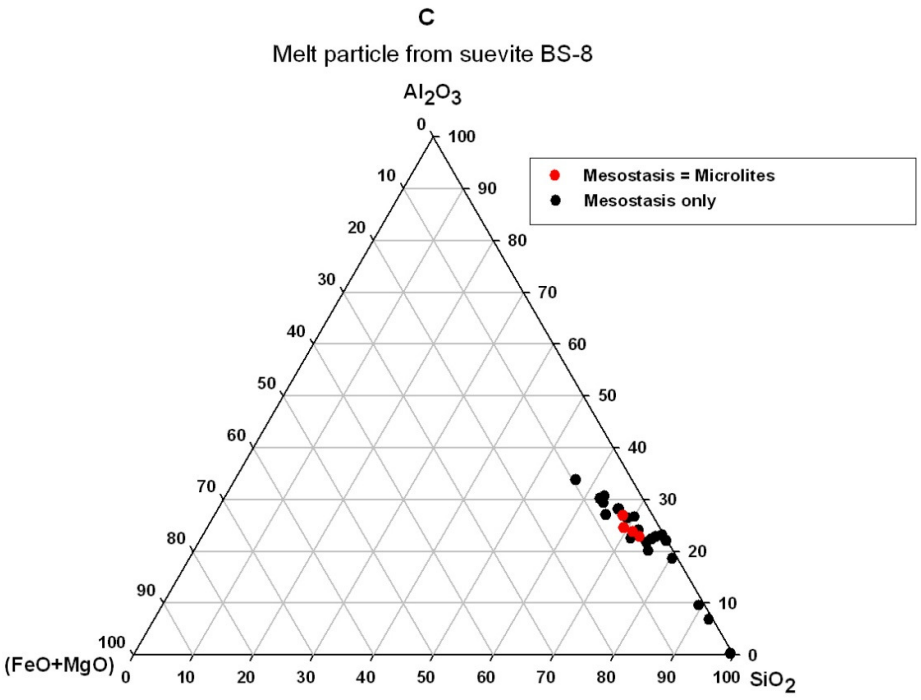

Fig. 6.22 (cont'd): Al_2O_3-(FeO+MgO)-SiO_2 diagrams showing the various phases analysed from melt particles from C) sample BS-8.

Little compositional variation is apparent between the microlite-rich and microlite-poor phases, particularly for the melt particle from sample BS-14B (Fig. 6.22 A). More variation is evident within the melt particle from sample BS-16B (Fig. 6.22 B), and these data points are more iron-rich in composition. The melt particle from sample BS-8 (Fig. 6.22 C) also shows some variation, but the overlap of the two phases is distinct.

It is known that the melt particles do vary in composition as evidenced by the SEM imagery (Fig. 6.10 A-L), so this variation is not unexpected. It must be noted that these phases show far less variation that the compositional data of melt particles from the suevites from south of the crater (Figs 6.20, 6.21). Figure 6.23 presents binary diagrams for the melt particles (indicating the different textural phases).

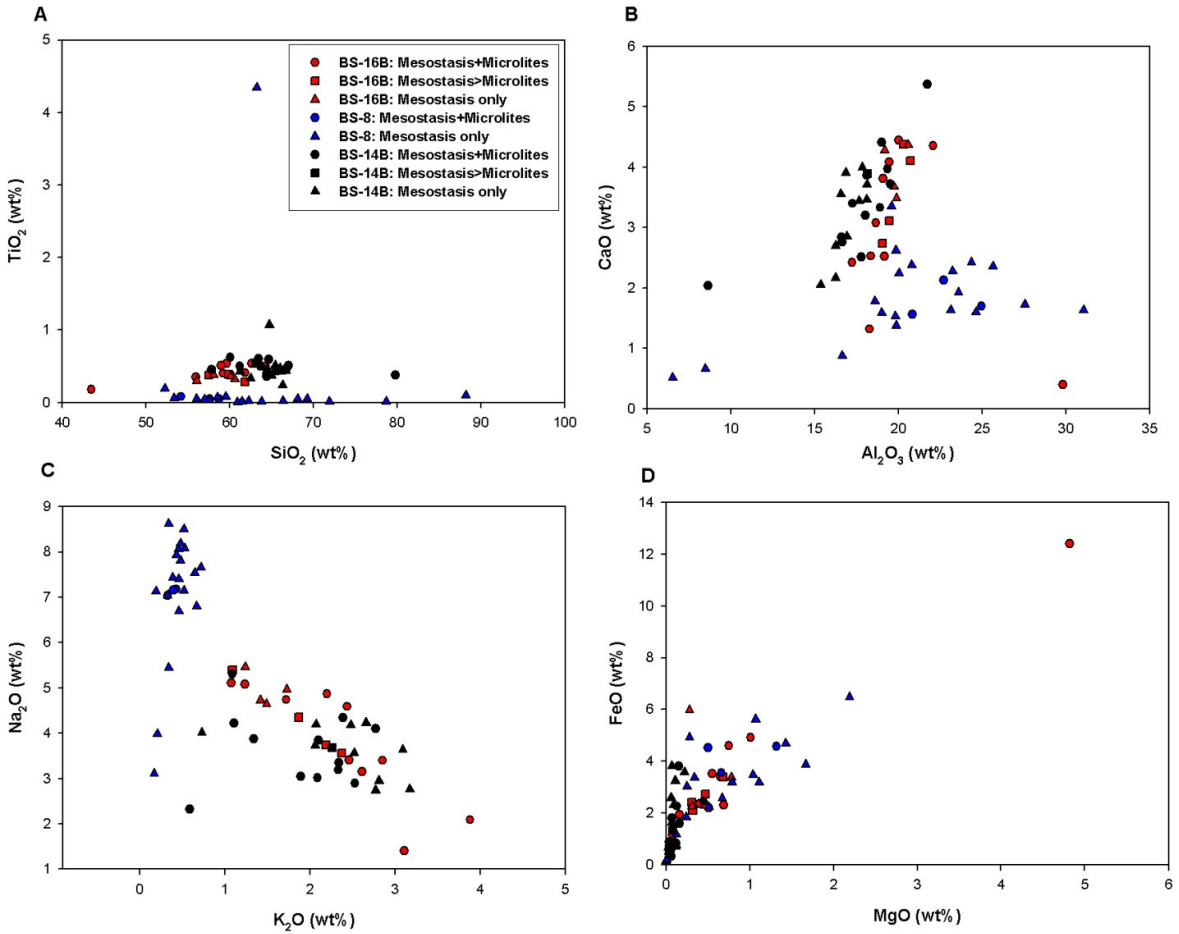

Fig. 6.23: Binary plots of the electron microprobe analyses (10 µm defocused beam): Melt particle phases in the out-of-crater suevites from north of Lake Bosumtwi. A) SiO_2 vs. TiO_2; B) Al_2O_3 vs. CaO; C) K_2O vs. Na_2O; D) MgO vs. FeO. Data in wt%.

It is evident from all the binary plots that the compositions of the different textures in the individual melt particles do not have distinctly different chemical compositions from each other. The compositions of melt particles from samples BS-14B and BS-16B are very similar to each other. For all samples, SiO_2 values are generally between 55 and 70 wt% (Fig. 6.23 A), with only a few outliers observed. TiO_2 values are generally less than 1 wt% (Fig. 6.23 A). Figure 6.23 B plots Al_2O_3 *vs.* CaO, and it is immediately evident that CaO values are very low for sample BS-8, whereas CaO and Al_2O_3 are positively correlated for samples BS-16B and BS-14B.

Sample BS-8 is particularly Na_2O-enriched and K_2O-depleted in comparison to the other samples (Fig. 6.23 C). All samples have noticeably low FeO and MgO contents; however, these elements are still positively correlated (Fig. 6.23 D).

Figure 6.24 presents three ternary diagrams of the data of melt particles from north of Lake Bosumtwi. Fields for the possible contributory minerals as well as symbols for the target rock lithologies of Koeberl et al. (1998) and the average of the Ivory Coast tektites (Koeberl et al., 1997a) are shown. The particles, in general, plot in small, confined areas on the diagrams. Figure 6.24 A indicates that all the particles are depleted in (MgO+FeO) in comparison to their Al_2O_3 and SiO_2 contents, confirming the information presented in the binary diagrams (Fig. 6.23 A, B, D). The compositions are most similar to those of the granite dykes. In the second ternary plot (Fig. 6.24 B), it is evident that the analyses from sample BS-8 are most similar to albite compositions, whereas the other 2 samples plot in a more central region. When the AK(FM) diagram (Fig. 6.24 C) is examined, the analyses plot in a small region closest to plagioclase and away from biotite and chlorite.

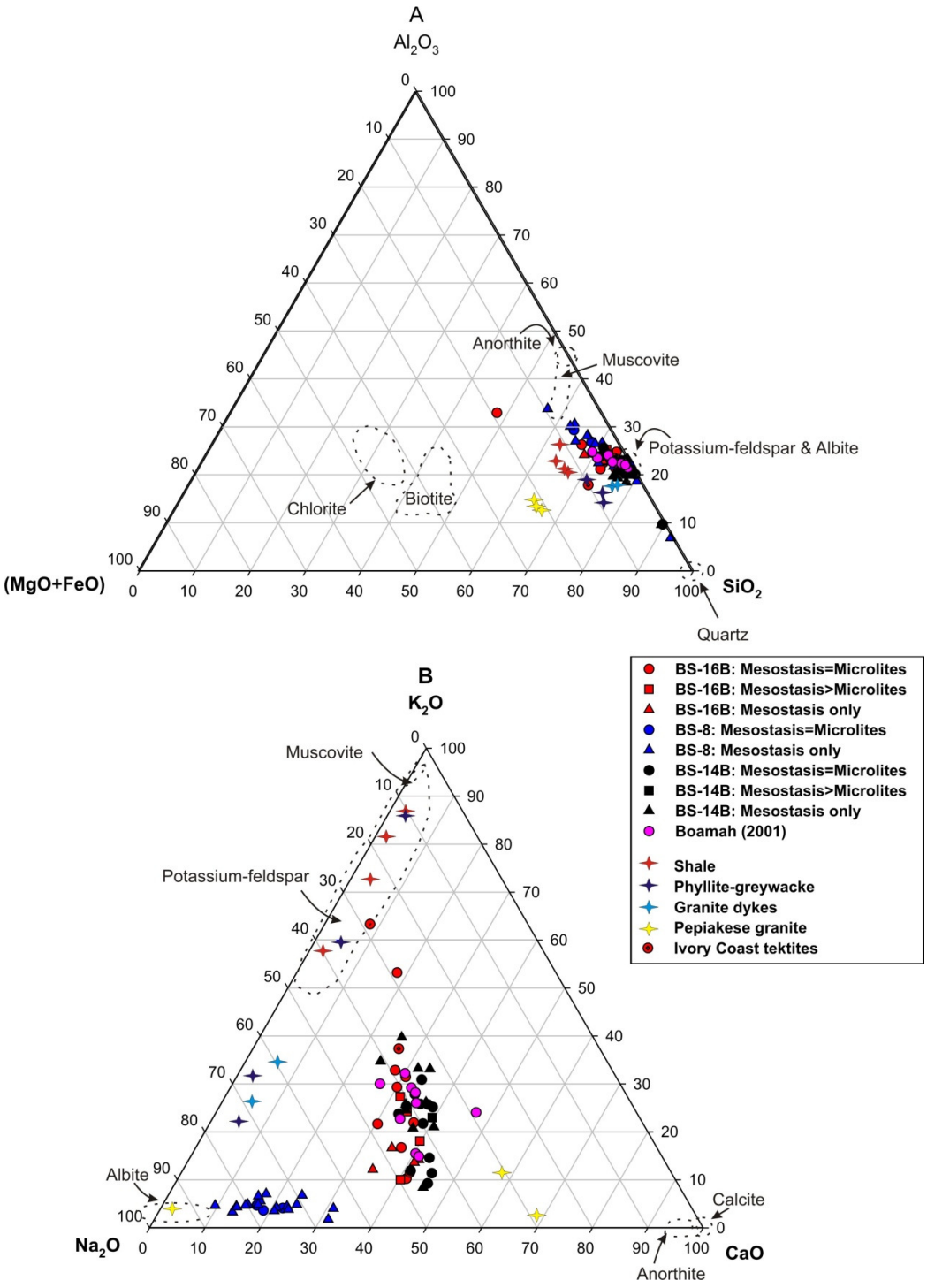

Fig. 6.24: Ternary discrimination diagrams for the electron microprobe analyses (10 µm defocused beam) of melt particle phases in the out-of-crater suevites from north of Lake Bosumtwi. A) Al_2O_3-(MgO+FeO)-SiO_2 and B) K_2O-Na_2O-CaO. Fields for common minerals in the suevites are indicated (after Deer et al., 1971). Average target rock lithologies (phyllite-greywacke, shale, granite dyke and Pepiakese granite; after Koeberl et al., 1998) and the average composition of the Ivory Coast tektites (after Koeberl et al., 1997a) are also plotted. Continued on next page.

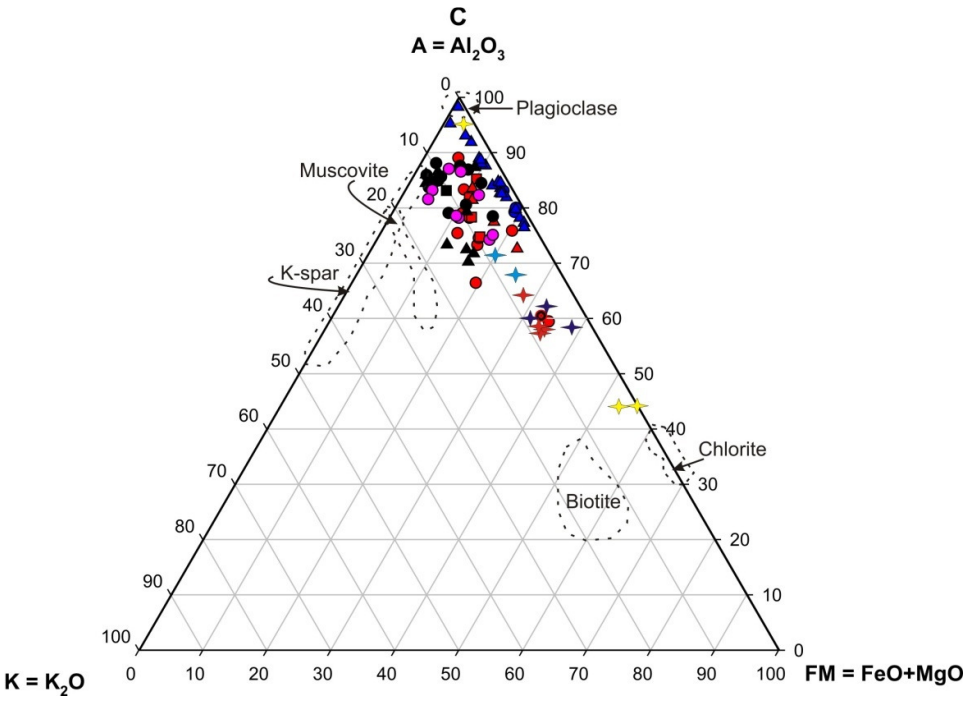

Fig. 6.24 (cont'd): Ternary discrimination diagrams for the electron microprobe analyses (10 µm defocused beam) of melt particle phases in the out-of-crater suevites from north of Lake Bosumtwi. C) AK(FM) diagram.

The position of the average of the Ivory Coast tektites is compatible with the melt particle analyses in Figs 6.24 A and B, but is more enriched in the FeO and MgO component in comparison to the analyses (Figs 6.24 A and C).

6.5.3.2.1 Comparison to previous studies Boamah (2001) obtained EMPA data for melt particles from suevites from north of the crater (from the two boreholes BH1 and BH3). The results of his study are plotted in Fig. 6.24. The results of this study for the melt phases from north of the crater and his study are highly compatible as extensive overlap is observed between the 2 datasets.

6.5.3.3 Comparison of melt particle phases from north of the crater and south of the crater

From the discussion above, it is immediately apparent that a number of distinct differences exist between the data for melt particles from south and north of the crater:

1. The melt particles from north of the crater are more homogeneous in their composition than those from south of the crater, though internal variation is still apparent.
2. The particles from both south and north of the crater are composed of mineral mixes.
3. The melt particles from north of the crater are depleted in (FeO+MgO) relative to the other elements and also with respect to the particles from south of the crater.

In order to diagrammatically display these differences, an AK(FM) diagram was produced (Fig. 6.25). The diagram shows two distinct populations – one more Al_2O_3-rich (the particles from north of the crater), and the other more (FeO+MgO)-rich (the particles from south of the crater). There is some overlap, which is not surprising as the particles are heterogeneous, and do not form a single distinct composition.

It is evident that the particles do not form discrete mineral melts, but rather mineral mixes. There is overlap of the target rock lithologies with some of melt particle compositions; however, this is not unexpected as the target rocks are composed of similar minerals to each other, and vary only in terms of grain size and the relative proportion of minerals (section 6.3). The possible reasons for the differences between the compositions of the melt particles from suevites from north and south of the crater will be examined in the Discussion chapter (chapter 7).

6.5.3.4 Cluster Analysis

In order to further assess the heterogeneity of the out-of-crater suevites, the results were combined into a cluster analysis.

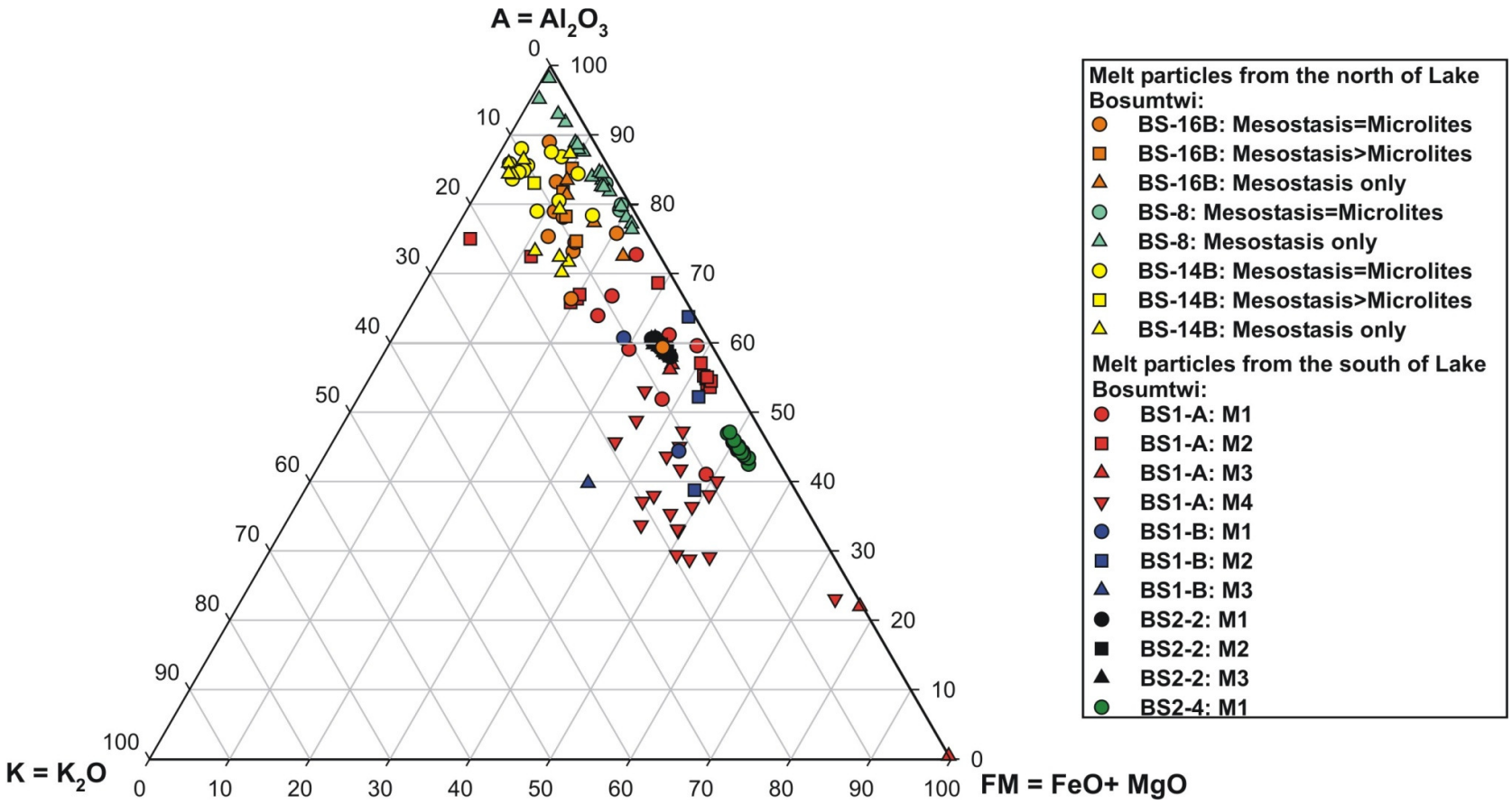

Fig. 6.25: An AK(FM) discrimination diagram for the electron microprobe analyses (10 µm defocused beam) of melt particle phases in the out-of-crater suevites from south and north of Lake Bosumtwi.

The melt particle analyses ("cases") were assessed using the Clustan Graphic 7 software, utilizing the same methodology as employed previously (see Section 4.5). The data were entered as continuous data, and no weighting was given to any sample. A Z-score transformation was utilized and the data were clustered according to their k-means (MacQueen, 1967), using the Euclidean Sum of Squares. The analysis utilized all the major element data. As before, 10 clusters were produced, and then a 5 cluster analysis was chosen as this is more representative of the variation in the particles. The results are reported in Table 6.5.

Table 6.5: Cluster analysis results for 5 cluster groups using 216 cases (i.e. samples) and 9 variables (major elements, see text for details) and the Euclidean Sum of Squares (k-means). The means and standard deviations of the groups are indicated. All data in wt%.

	Cluster 1 (n = 37)	**Cluster 2 (n = 2)**	**Cluster 3 (n = 38)**	**Cluster 4 (n = 21)**	**Cluster 5 (n = 118)**
SiO_2	62.7±2.9	71.4±11.6	81.9±6.0	60.1±5.3	61.7±3.7
TiO_2	0.5±0.1	3.6±1.1	0.1±0.1	0.07±0.1	0.7±0.2
Al_2O_3	18.4±1.4	12.6±10.3	5.4±3.3	22.3±3.4	17.0±2.3
FeO	2.1±1.2	3.3±2.3	3.0±3.3	3.3±1.8	7.2±1.1
MnO	0.02±0.02	0.0±0.0	0.04±0.06	0.02±0.02	0.1±0.1
MgO	0.3±0.2	0.5±0.4	1.5±1.2	0.6±0.0	2.2±0.9
CaO	3.4±0.8	0.8±0.8	0.3±0.4	2.2±0.8	3.3±1.4
Na_2O	3.9±0.8	4.9±5.3	1.0±0.8	7.2±0.9	3.0±0.6
K_2O	2.2±0.7	0.6±0.4	1.3±0.8	0.5±0.2	1.7±0.4

The cluster analysis shows that the majority of the analyses are constrained within cluster 5, followed by clusters 3, 1 and 4 (Table 6.5). Only 2 analyses are represented in cluster 2. The main differences between the clusters are as follows: Cluster 1 represents high K_2O and CaO values (probably from K-feldspar and anorthite), cluster 2 represents high TiO_2 values (cf. Figs 6.20 A and 6.23 A; possibly derived from rutile and other mineral phases), cluster 3 represents high SiO_2 values (after quartz), cluster 4 represents high Al_2O_3 and Na_2O values (possibly derived from albite) and cluster 5 represents high MgO, FeO and MnO values (probably after biotite and chlorite). Table 6.6 shows the distribution of the different clusters in the melt particles. As expected, nearly all analyses from the

suevites from south of the crater are dominated by cluster 5 (see Fig. 6.25). The melt particles from south of the crater also fall into cluster 3. Some of the melt particles fall solely into cluster 5. The melt particles from the samples BS-14B and BS-16B are very similar to each other in terms of the cluster analysis, and fall chiefly into cluster 1, whereas the analyses from sample BS-8 (shown to be different chemically) are dominated by cluster 4. Thus, the cluster analysis emphasizes the previous graphical results in that the melt particles are themselves compositionally heterogeneous and that the particles from north of the crater are more enriched in Al_2O_3 and K_2O than those from south of the crater which are more FeO and MgO rich.

Table 6.6: Distribution of the clusters in the different melt particles from the out-of-crater suevites, produced by cluster analysis of 216 cases and 9 variables and the Euclidean Sum of Squares (k-means). See text for details.

Melt particle	Cluster 1	Cluster 2	Cluster 3	Cluster 4	Cluster 5
BS1-A M1			7		3
BS1-A M2			6		7
BS1-A M3			2		2
BS1-A M4			17		3
BS1-B M1		1	1		
BS1-B M2			1		3
BS1-B M3			1		
BS2-2 M1					24
BS2-2 M2					5
BS2-2 M3					41
BS2-4 M1					29
BS-16B	15			2	1
BS-8		1	2	19	
BS-14B	22		1		

6.6 Summary

Two sets of out-of-crater suevites have been identified at the Bosumtwi crater: those occurring north of the crater, and those occurring south of the crater. The out-of-crater suevites are distinct from each other in terms of petrographic characteristics (colour of matrices, clast population) and chemical composition (for the breccias as well as the melt particles). Both contain significantly more melt particles than the within-crater suevites of the LB-07A core;

however the compositions of the melt particles from south of the crater is similar to those from the core.

Clast and melt particle sizes are significantly larger than those for the LB-07A core, and granitoid is a significant component in the clast populations of the out-of-crater suevites. There is a distinct lack of carbonate clasts, but laterite is present as a post-impact alteration phase.

The out-of-crater suevites have clasts that are more intensely shocked than those from the within-crater suevites. Up to 4 PDF sets in quartz grains have been observed, ballen quartz (absent in core LB-07A) and diaplectic quartz glass is common. Melt particles in the out-of-crater suevites can be as large as 40 cm. They are more vesiculated, and some contain microlites as well as melt phases. A more diverse array of clasts in the out-of-crater suevite melt particles (than those from core LB-07A) is apparent: quartz, feldspars and discrete rock fragments; whereas the melt particles from the LB-07A core contain quartz micro-clasts only. The melt particles of the suevites from south and north of the crater display much internal heterogeneity – particularly noticeable for those from south of the crater.

A few differences have been noted in terms of modal variation in the suevites from north of the crater of this study and that conducted by Boamah and Koeberl (2006): more melt and less matrix was noted in the samples studied here. However, the mineral and lithic clasts proportions were comparable, and it is thought the other differences represent local clast size variability, as these suevites are heterogeneous in these aspects.

Distinct variability was noted in the chemical compositions of the melt particles from south and north of the crater. The melt particles are, themselves, heterogeneous, and both the analyses from south and

north of the crater are distinctly different from each other. The analyses from south of the crater are more enriched in (FeO+MgO) and relatively depleted in Al_2O_3 in comparison to those from north of the crater. Cluster analysis of all the particles has emphasized these differences.

Chapter Seven: Discussion and Conclusions

The Bosumtwi impact crater, Ghana, is one of the best preserved craters of its size and age. A variety of impactites have been preserved. The drilling of the Bosumtwi impact structure by the International Continental Scientific Drilling Program (ICDP) has allowed comparison of shocked rocks from the basement of the structure and monomict and polymict lithic breccias from the crater interior as well as suevites from both the interior and exterior of the crater. These are also compared to the geochemical characteristics and the distribution of the distal impact melt (Ivory Coast tektites).

The primary material investigated in this study is from hard rock core LB-07A, drilled through the deepest part of the crater fill. Additionally, samples of the out-of-crater breccias from both north and south of the crater were collected in order to compare with the within-crater breccias.

This study involved five principal components:

1. Production of the LB-07A lithostratigraphic profile and comparison to that of the LB-08A core (located on the central uplift, Fig. 1.17).
2. Petrographic (clast types, shock degree of clasts, melt particle characteristics) and geochemical characterisation and comparison of the different impactites in the LB-07A core, LB-08A core and the out-of-crater suevites; including the determination of the target rock lithologies for the impactites.
3. Petrographic characterisation of post-impact hydrothermal alteration phases in the impactites in the LB-07A core.
4. Geochemical investigation of the presence of meteoritic projectile matter in the impactites of the LB-07A core.
5. Interpretation of these findings in the context of a model for the formation and modification of the impactites of the Bosumtwi impact crater, and the proposed sequence of events.

The results and main findings under each of these objectives are discussed below.

7.1 Petrographic Characterisation and Comparison of the Impactites in the LB-07A Core, LB-08A Core and the Out-of-Crater Suevites

The LB-07A core provides a cross-section through the fill of and floor to the moat surrounding the central uplift (less than 1 km from the central uplift) of this complex impact structure. Borehole LB-08A was drilled into the flank of the central uplift, approximately 750 m southeast of the LB-07A drill site (Fig. 1.17). The LB-08A core was recovered between 235.60 and 451.33 m below lake level. The impactite sequence is far thicker in the LB-07A core than in the LB-08A core, which befits its location in the moat surrounding the central uplift (Fig. 7.1; for LB-08A core description see Ferrière et al., 2007a; Deutsch et al., 2007).

Core LB-07A has been divided into three sequences: the upper impactites, lower impactites and basement metasediments. The LB-08A core is divided into a thin (~ 25 m *vs.* ~84 m in LB-07A) impactite unit and is underlain by fractured/brecciated metasediments. The uppermost parts of both cores consist of intercalated polymict lithic breccias and suevites. These are matrix-supported in LB-07A (matrix defined as all clasts less than 50 µm in size), but clast-supported in LB-08A (Ferrière et al., 2007a; Deutsch et al., 2007). The clast populations of the impact breccias of both cores are similar and include metagreywacke, phyllite, slate, quartzite, carbonaceous shale, calcite and minor phyllosilicates, epidote, sphene and opaque minerals. The total thickness of the melt-bearing suevites of the uppermost part of LB-08A (<10 m) is substantially different from LB-07A (nearly 50 m). Additionally, the polymict lithic breccia is about two times thicker in the LB-07A core (~35 m) than in the LB-08A core (~16 m).

A significant unit of monomict breccias (~ 55 m; the lower impactites) occurs in core LB-07A, whereas very little monomict breccia has been found in core LB-08A (~1 m; actually described as part of the basement section; Ferrière et al., 2007a). The monomict breccias in core LB-07A are either metagreywacke- or shale-derived; those in core LB-08A originate solely from metagreywacke (Ferrière et al., 2007a). These monomict breccias are thus truly monomict as mixing of different precursor lithologies is not observed.

In contrast to the shale-dominated basement in the LB-07A core, the basement metasediments of the LB-08A core are dominated by metagreywacke (fine-grained to gritty).

In LB-07A, no gritty metagreywacke (following the designation used by Ferrière et al., 2007a) was found. Given the steep regional dip of layering in the Birimian target rocks (~80°; see Boamah and Koeberl, 2003) and the mixed lithostratigraphy (section 1.5), such heterogeneity in the basement in the two cores is not unexpected. A full assessment of the stratigraphic and structural (i.e., presence of folds and faults) relationships could not be made owing to the highly fractured and powderised nature of the basement in the LB-07A core. Both basement sections contain volumetrically limited suevites, as well as small components of similar granophyric-textured lithologies. These granophyric-textured intercalations are thought to represent hydrothermally altered intrusions of the granophyric granitoid lithology described by Reimold et al. (1998) as dykes also occurring in outcrop of the inner crater rim, although they differ slightly from the latter in that they contain patchy calcite. Only one such intercalation was intersected in core LB-07A, whereas three were noted in core LB-08A (Ferrière et al., 2007a); this may be due to the fact that a larger section of basement lithologies was intersected in LB-08A but also demonstrates the obviously heterogeneous basement composition.

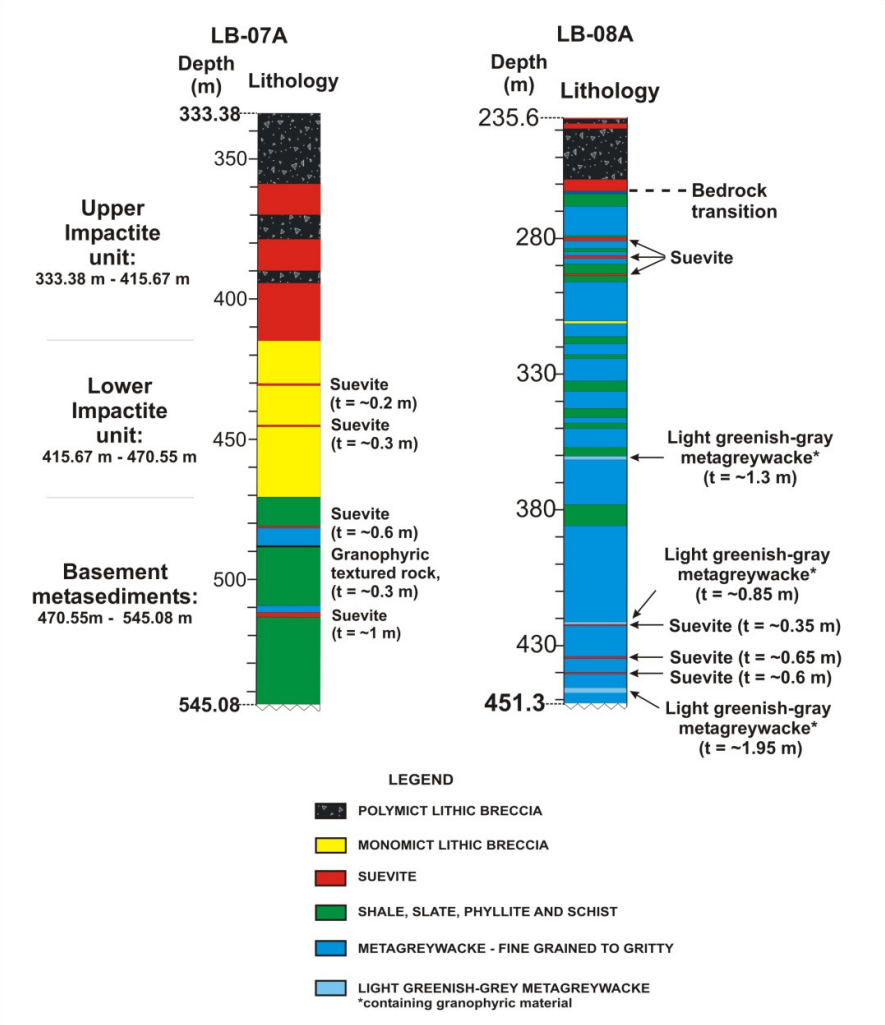

Fig. 7.1: Comparison of the LB-07A and LB-08A stratigraphies (LB-08A after Ferrière et al., 2007a); t = thickness.

The clast populations in the impact breccias in both the LB-07A and LB-08A core samples (Table 7.1) were primarily derived from metasedimentary precursors, consistent with the composition of the basement as intersected in the cores (Chapter 3; see also Ferrière et al., 2007a). No differences in terms of the relative clast proportions were noted between the clast populations of the polymict lithic breccias and suevites of core LB-07A (section 3.2.1; Table 7.1). In contrast, the LB-08A suevites are dominated by metagreywacke over phyllite, and the opposite holds for the polymict lithic breccias (Ferrière et al., 2007b), i.e., the overall clast population of both cores are the same, but the relative proportions of the component clasts

differ in core LB-08A in the different impactites. A significant carbonate (calcite) target component has also been identified in the suevites in LB-07A and LB-08A that was previously unknown from studies of suevites and country rocks from outside the crater rim (Table 7.1; see Reimold et al., 1998; Koeberl et al., 1998; Boamah and Koeberl, 2003, 2006).

Table 7.1: Average modal analyses of within-crater suevites from the LB-07A core (this study), the LB-08A core (Ferrière et al., 2007a) and the out-of-crater suevites (this study). All data in vol%.

	LB-07A*	LB-08A**	Suevites from south of the crater*	Suevites from north of the crater*
Matrix	58.0	42.0	44.3	48.1
Metagreywacke	15.3	29.0	2.9	
Shale	7.4	3.2	3.4	0.2
Phyllite+Slate	3.6	14.1	4.4	2.2
Schist	1.1		2.7	3.2
Granitoid	0.6		5.9	3.4
Quartz	4.0	2.2	11.9	2.5
Feldspar	0.6	1.1	<0.1	1.3
Primary phyllosilicates	0.6		0.8	
Calcite	1.7	1.4		
Secondary phyllosilicates			2.9	1.9
Opaques			0.8	
Melt	5.4***	8.0	19.4	37.3

**Data from this study; ** data from Ferrière et al. (2007a); ***average melt for LB-07A does not include the proportion from non-representative sample KR7-23 (cf. section 5.4.2); average melt includes diaplectic glasses.*

Granite is not a significant component of the within-crater impact breccias and has been found irregularly and only in small amounts (0.5 vol%, on average, in the LB-07A core) or is absent (LB-08A core; Deutsch et al., 2006; Ferrière et al., 2007a; Table 7.1). In contrast, large (up to 25 cm diameter) granitic clasts have been found in the out-of-crater suevites from north of the crater, and up to 5 cm in the out-of-crater suevites from south of the crater (section 6.4.2). It should be noted that the point-counting results obtained on thin sections only present the average population of clasts that are less than 2 cm in size. This is important when examining breccia with a high variability of clast sizes, as both the macroscopic and

microscopic observations need to be taken into account when estimating total clast populations. The maximum percentage of granitoid component found in point-counting of this material in the out-of-crater suevites is 40.5 vol%, compared to 6.5 vol% in the LB-07A core. Another point to consider is the suggested composition of the Ivory Coast tektites (Koeberl et al., 1998), which was estimated by applying harmonic least-squares mixing (Stöckelmann and Reimold, 1989) to the geochemical data: Koeberl et al. (1998) suggested that the Ivory Coast tektites were derived from a mixture of 70 % phyllite-greywacke and 30 % granite (from both the Pepiakese granite and granite dykes).

Previous studies estimated the total granitoid component in the region as no more than 2% from lithological variation in the vicinity of the crater (Reimold et al., 1998), which reflects the clast population of the within-crater suevites (Table 3.2), but not those of the out-of-crater suevites (Table 6.1). The implications of the petrographic results with respect to the composition of the target material will be discussed in section 7.3.

7.2 Geochemical Characterisation and Comparison of the Impactites in the LB-07A Core, LB-08A Core and the Out-of-Crater Suevites

The compositions of the impactites of the LB-07A and LB-08A cores and the out-of-crater suevites have been investigated with a number of geochemical plots of major and trace element abundances (Figs. 6.16, 6.17, 7.2). The impactites are all very similar, with minor differences related to differing clast proportions (e.g., granitoid). This similarity is perhaps not surprising, given the generally fine intercalation of the sedimentary rocks in the target stratigraphy.

The only notable difference between the geochemical characteristics of the impactites from the two cores is that there are more chemical differences for the different impact breccias in the LB-08A core than

in the LB-07A core. This is observed for elements such as SiO_2, CaO, Al_2O_3, Fe_2O_3 and MgO. Ferrière et al. (2007b) attributed this to mineral clast variations, as also observed for the impactites of the LB-07A core, though these do not display such distinctive differences.

Figure 7.2 shows a comparison of Harker plots for cores LB-07A and LB-08A (from Ferrière et al., 2007b) as well as average data for out-of-crater suevites (from this study, Chapter 6). Interestingly, the shales of LB-07A show a greater compositional variability than those from the LB-08A core, whereas the metagreywackes in LB-08A show more variability than those in LB-07A. This is most likely a function of the number of samples in both cores, and thus reflects the fact that the two cores have different proportions of the respective basement lithologies which are intercalated at a metre to centimetre scale. The out-of-crater suevites from both north and south of the crater have CaO values that are comparable to the lowest CaO values obtained from the two cores. This reflects the presence of calcite (both pre- and post-impact) in the core samples. It is unlikely that the variability in CaO values reflects differing proportions of plagioclase, as the proportions of this mineral do not vary substantially between the within and out-of-crater suevites. The SiO_2 and Fe_2O_3 contents for the out-of-crater suevites are within the range of both core datasets.

Table 7.2 shows the averages, standard deviations and ranges for the compositions of the LB-07A (this study) and LB-08A (Ferrière et al., 2007b) suevites as well as those of the out-of-crater suevites (this study).

The similarities between the major element averages are immediately evident, and the ranges for both data sets show significant overlap. Minor differences exist for TiO_2, Al_2O_3, Fe_2O_3, MnO, MgO and CaO values in particular, but these are within the standard deviations of the data, and seemingly relate to different

clast populations (e.g., calcite, granite) in the respective sample materials.

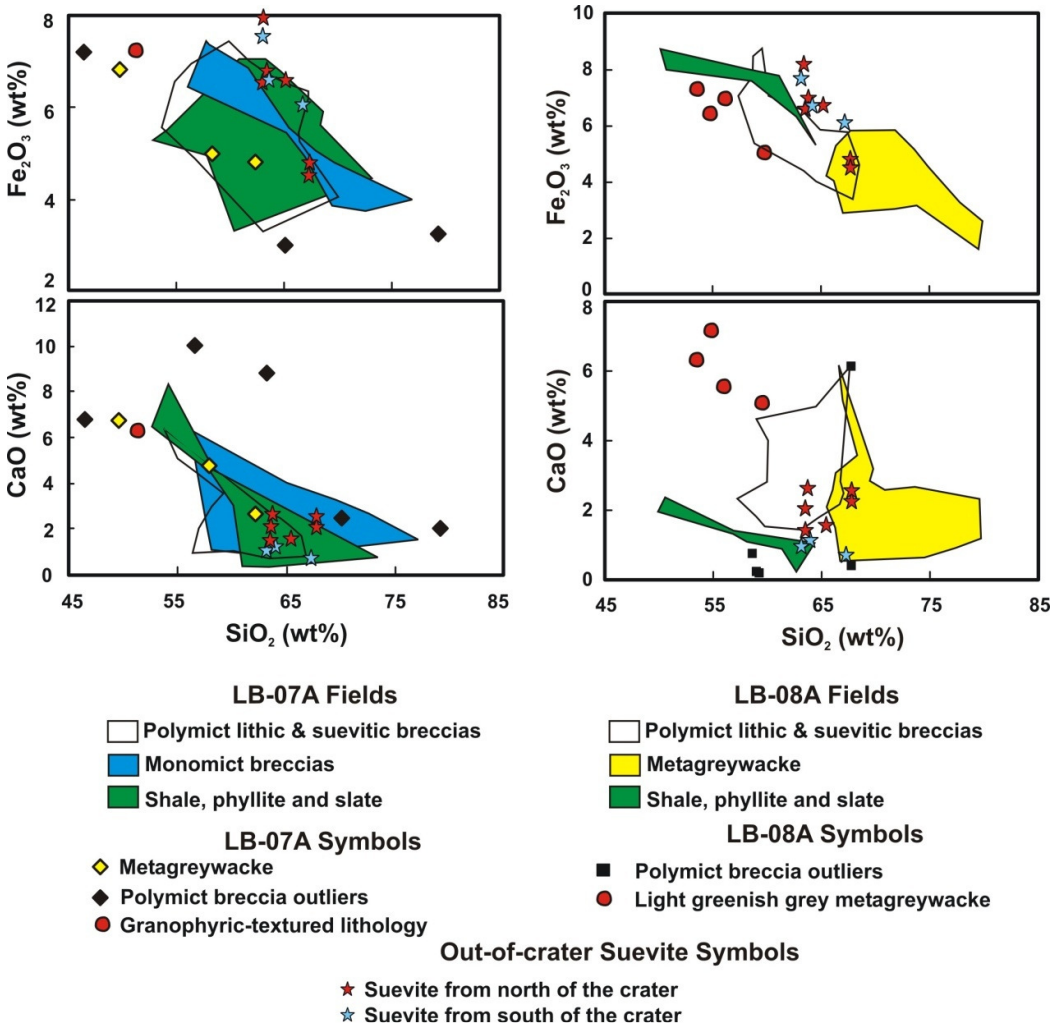

Fig. 7.2: Harker plots of Fe_2O_3 and CaO (wt%) comparing polymict lithic, suevitic and monomict breccias, granophyric-textured lithologies, metagreywacke and phyllite, slate and shale of LB-07A (this work) and LB-08A (data from this study and Ferrière et al., 2007b), shown together with the out-of-crater suevite averages of this study.

Trace element abundances are very similar in the impactites from both cores – enrichment in comparison to background values in Cr, Ni and As are noted in the rocks of both cores (reflecting the presence of mostly secondary sulphides).

Table 7.2: Averages and standard deviations (in wt%) for the LB-07A suevites (this study), LB-08A suevites (Ferrière et al., 2007b) and the suevites from south and north of the crater collected in this study.

	LB-07A* n = 42	**LB-08A** n = 20**	**Suevites from south of the crater* n = 3**	**Suevites from north of the crater* n = 6**
SiO_2	62.3±4.03	63.16±2.44	64.4±2.08	64.8±1.91
TiO_2	0.55±0.07	0.55±0.09	0.63±0.06	0.67±0.09
Al_2O_3	14.70±2.30	14.65±1.01	15.9±0.75	17.3±0.80
Fe_2O_3	5.87±0.76	5.49±0.74	6.99±0.80	6.35±1.35
MnO	0.06±0.02	0.06±0.01	0.10±0.02	0.04±0.01
MgO	3.04±1.82	2.50±0.93	2.46±0.34	0.89±0.15
CaO	2.35±1.57	2.67±0.98	0.75±0.20	1.92±0.41
Na_2O	2.63±0.81	2.94±0.36	2.20±0.40	2.78±0.45
K_2O	1.73±0.43	1.67±0.36	1.54±0.23	1.41±0.61
P_2O_5	0.11±0.07	0.11±0.02	0.11±0.02	0.07±0.02
LOI	6.19±2.32	5.25±0.87	4.33±0.47	3.28±0.53

**Data for the LB-07A suevites, suevites from north and south of the crater from this study. **Data for the LB-08A suevite from Ferrière et al. (2007b).*

Much variation in Rb, Sr and Ba is noted throughout both cores. No significant differences between polymict lithic breccia and suevite are observed. Rare earth element patterns are similar for all lithologies in both cores, as well as those of the out-of-crater suevites (Fig. 7.3 A, B).

The granophyric-textured intercalations noted in this study and those of Ferrière et al. (2007b) display comparable chemical compositions: low SiO_2, K_2O and high CaO, LOI, MgO, Ni, Cr and Co. These chemical results, in addition to the petrographic observations (in that these rocks are comparable to the hydrothermally altered lithology described by Reimold et al.,1998), support their interpretation as a hydrothermally altered lithology.

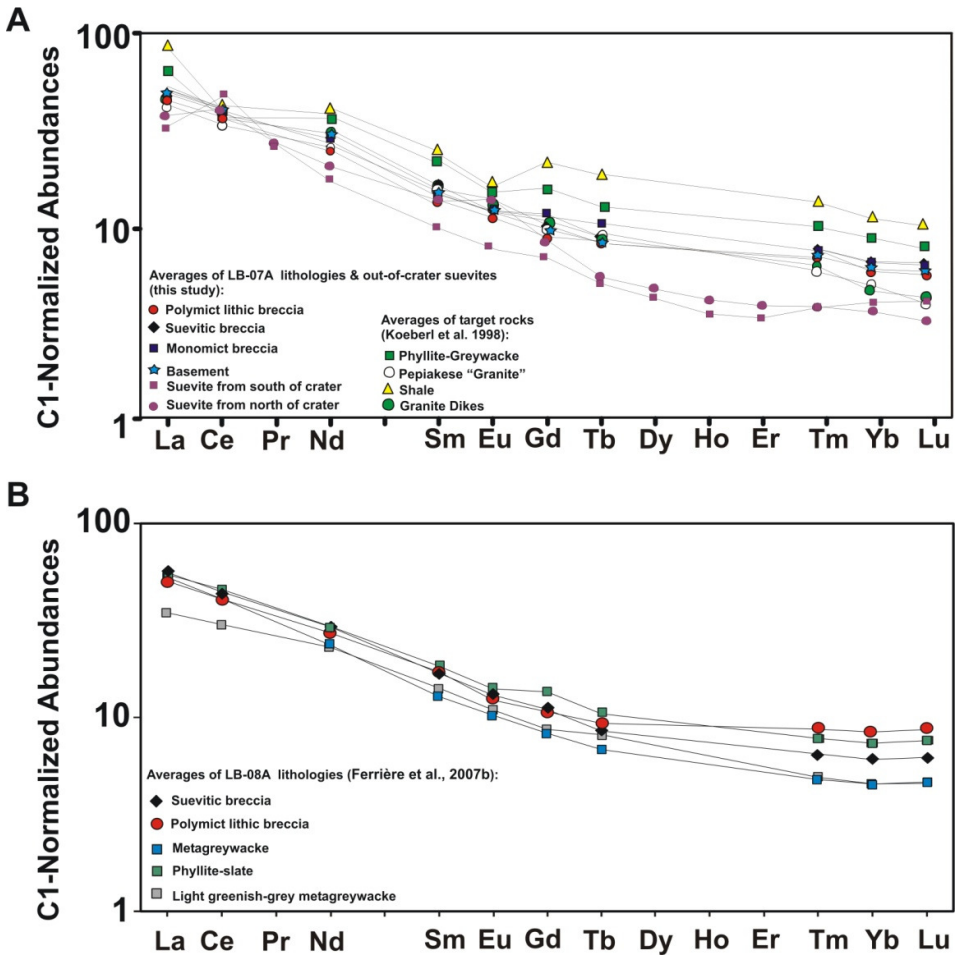

Fig. 7.3: Rare earth element comparisons. A) Averages calculated for polymict lithic, suevitic, monomict breccias as well as basement lithologies from core LB-07A (this study), out-of-crater suevites (this study) and regional target rock lithologies (Koeberl et al., 1998). B) Averages for polymict lithic breccias and suevites, metagreywacke, phyllite-slate and light greenish-grey metagreywacke from core LB-08A (data from Ferrière et al., 2007b).

7.3 Composition of the Target Volume

The overall lithological proportions (in terms of the respective stratigraphies) of the LB-07A and LB-08A cores are compared in Table 7.3; both cores have substantially different proportions of all lithologies. However, this is to be expected given the heterogeneity of the basement rocks. Additionally, the LB-07A core intersects a larger proportion of crater fill, whereas the LB-08A core intersects a larger proportion of basement lithologies as part of the central uplift.

Table 7.3: Comparison of the overall proportions of principal lithologies in the LB-07A (this study) and LB-08A (Ferrière et al., 2007a) cores (bulk stratigraphies).

	LB-07A	LB-08A
Metagreywacke	3.2 %	65 %
Shale, slate, phyllite	31.2 %	21 %
Polymict breccia (lithic and suevite)	39.9 %	13.5 %
Monomict breccias	25.7 %	0.5 %

If one factors in clast compositions of the polymict and monomict breccias, an "average" composition of the entire LB-07A core emerges: 43.6 % metagreywacke, 40.9 % shale, 5.9 % phyllite, 4.8 % quartz and 1.6 % carbonate. Other contributors which make up the remaining 3.2 % involve phyllosilicates, feldspar, granite, schist and impact breccias (too small to estimate the proportions of the different lithologies). Metagreywacke makes up the dominant clast type in the LB-08A core (both in the suevites and basement lithologies; Ferrière et al., 2007a). The country rock in the immediate environs of the crater is also dominated by metagreywacke (see Koeberl and Reimold, 2005). However, the out-of-crater suevites are composed of relatively minor volumes of metagreywacke, and more granitoid (particularly in the north), phyllite, schist and shale (particularly in the south). Thus, the impactites are heterogeneous, which may reflect variation in the regional geology and heterogeneous sampling for the within-crater and the out-of-crater impact breccias.

In order to assess this further, an estimate of the regional target rock distribution has been made, by calculating the relative areas of the different target lithologies from Appendix 1 (Table 7.4). In this procedure, a total area of 395 km^2 was examined after subtracting the areas of the lake and out-of-crater suevites. This number was chosen as a value ~4.5 times the area of the lake (assuming the crater was circular, with a radius of 5.25 km, the crater would cover an area of ~87 km^2) in order to provide as representative a value of the heterogeneous geology as possible. This two-dimensional view indicates that the Birimian metasediments and metavolcanics are the

most abundant rocks in the region, followed by the Tarkwaian Supergroup sediments (termed “Proportion 1” in Table 7.4). However the metavolcanics and Tarkwaian Supergroup sediments do not contribute significantly to the suevite (both out-of-crater and within-crater) compositions as evidenced by their respective clast compositions. After removal of these components, it can be estimated that the metasediments contribute over 90% to the impact breccia, with minor granite (together termed “Proportion 2” in Table 7.4). This is in keeping with the observations made in the two cores.

Table 7.4: Comparison of proportions of regional target lithologies.

Lithology	Proportion 1	Proportion 2
Birimian metasediments	64.8%	92.7%
Birimian metavolcanics	21.7%	-
Tarkwaian Supergroup	8.4%	-
Granite	4.9%	7.0%
Carbonated intermediate dykes	<0.1%	<0.2%
Intrusives	<0.1%	<0.2%

**Granite includes the Kumasi, Bansu and Trobokro batholiths, and granite dykes.*

7.4 Shock Petrographic Comparison of the LB-07A and LB-08A Cores and the Out-of-Crater Suevites

Amongst the within-crater breccias, three sources of data can be examined in order to ascertain the shock metamorphic degree of the clasts: a lapilli-rich layer from core LB-05B (Koeberl et al., 2007b), core LB-07A (this study; Morrow, 2007) and core LB-08A (Ferrière et al., 2007a; Deutsch et al., 2007).

Koeberl et al. (2007b) described a thin (ca. 30 cm), lapilli-rich layer, which occurs in core LB-05B (Fig. 1.17) directly below the post-impact sediments and shows a higher proportion of intensely shocked material at the top of the impactite sequence than the impactites below it. The top 10 cm of the layer comprise “accretionary” lapilli, microtektite-like glass particles and shocked quartz. In the coarser size fraction (> 125 µm), glass particles make up between 70 and 78 % of all particles in this layer. About half of the shocked quartz grains contain 3 or more PDF sets, and up to 23 % of

potassium-feldspar grains are shocked with PDFs. The proportion of shocked grains decreases with depth in the layer.

Several similarities exist between the LB-07A (this work; Morrow, 2007) and LB-08A (Ferrière et al., 2007a; Deutsch et al., 2007) cores. Shocked quartz with similar numbers of PDF sets (although up to 4 sets have been observed rarely in LB-08A *vs.* a maximum of 3 sets in LB-07A) are noted, as well as toasted quartz in both cores. The clasts in the LB-07A suevites were shocked to maximum pressures of 45 to 70 GPa (see Table 1.1) as the suevites contain melt particles, rare diaplectic quartz glass, diaplectic feldspar glass and shocked quartz with PDFs (this study; also observed by Morrow, 2007).

The presence of up to 4 sets of PDFs has been noted in quartz clasts in the out-of-crater suevites (section 6.4.3), and there are significant amounts of quartz diaplectic glass and ballen quartz (section 6.4.3; see also Boamah and Koeberl, 2006). Recent work by Ferrière et al. (2009) has reclassified the "ballen quartz" as "ballen cristobalite". They interpret the formation of the ballen cristobalite to have taken place as a solid-solid transformation of α-quartz to diaplectic quartz glass to ballen cristobalite (consisting of β-cristobalite; Ferrière et al., 2008). Ferrière et al. (2009) suggest that temperatures and pressures would have exceeded 1200 °C (based on annealing experiments; see Short, 1970 and Rehfeldt-Oskierski, 1986) and ~35 GPa (based on the formation of diaplectic quartz; see Stöffler and Langenhorst, 1994) respectively. The presence of ballen cristobalite in addition to the diaplectic glasses and shocked quartz in the out-of-crater suevites provides evidence for greater shock pressures and temperatures than those experienced by the within-crater suevites (which contain no ballen cristobalite and smaller proportions of the other shocked material). A maximum of 40.5 % of quartz grains display 1 or more PDF sets (average: 20.5 % of all quartz grains counted in a sample; Table 6.3), which is distinctly

higher than the maximum for the suevites in the LB-07A core, which is 12.1 %. The average amount of quartz grains displaying 1 or more PDF sets in the LB-07A suevites is 5.7 % (see Table 5.2). Thus, the out-of-crater suevites contain a far higher proportion of shocked quartz and overall more highly shocked material than those from within the crater. The implications of the differing shock characteristics of the within-crater and out-of-crater material will be discussed in section 7.7.3 (model constraints for the Bosumtwi cratering event).

The polymict lithic breccias in both cores do not contain melt particles or diaplectic quartz glass, and only quartz clasts show shock deformation in the form of PFs and PDFs (on average 11.8 % of all quartz grains display PFs whereas 6.7 % display 1 or more PDF sets in the LB-07A core; no statistics provided for the LB-08A core). These clasts have been shocked to a maximum of 30 GPa (Stöffler and Langenhorst, 1994; Huffman and Reimold, 1996). Ferrière et al. (2007a) also proposed lower shock pressures for the clasts of the polymict lithic breccias in comparison to those of the suevites owing to the absence of melt particles in the LB-08A polymict lithic breccias.

Measurements of the crystallographic orientations of PDFs in quartz indicate a dominance of ω $\{10\bar{1}3\}$ planes in the LB-07A core (25 – 40 %; this study; Morrow, 2007) and in core LB-08A (60 - 68 %; Ferrière et al., 2007a). Also, very few basal PDF sets were found in the uppermost sequence of LB-08A. Nearly all the PDF orientations noted by Ferrière et al. (2007a) were also found in this study, except for the $\{11\bar{2}0\}$ orientation, which was noted rarely in the quartz clasts of core LB-08A and was absent in the quartz clasts in core LB-07A. This indicates that the quartz clasts of the uppermost part of core LB-08A were shocked to similar pressures to those observed in the upper impactites of core LB-07A.

The basement section of LB-07A yielded very small percentages of shocked quartz (maximum 3.3 % quartz with PDFs). In contrast, the basement section of the LB-08A core yielded a maximum of 38% shocked quartz (Ferrière et al. 2007a). Ferrière et al. (2007a) noted a slight decrease in shock degree of the metasediments with increasing depth in core LB-08A, based on the abundances of shocked quartz grains with depth. At 271 m, 38 % of quartz grains contained PFs and PDFs (up to 4 sets of PDFs per grain); this decreased to 20 % at 354 m (up to 2 sets of PDFs per grain) and 5 % at 451 m (PFs only). This trend was not observed in the clasts of LB-07A. However, very few clasts in the basement metasediments of this core were shocked. These observations agree with previous studies which indicate that shock pressures (and thus, their effects) are largely confined to the central uplift (e.g., Robertson, 1975) in comparison to the crater fill material.

As noted in section 5.3.2, most of the quartz grains examined for their PDF orientations contained single PDF orientations only. In order to further examine shock pressure variation, Table 7.5 indicates the amount of grains for the different impactite units where the (0001) orientation was encountered only and those where the (0001) orientation was found together with higher order orientations. This can be used to provide basic pressure differences between the different impactite units (Stöffler and Langenhorst, 1994; Langenhorst, 2002). No grains with multiple PDF orientations were encountered in the basement metasediments, and only a few grains with multiple orientations were counted in the upper impactites, although it must be noted that most single PDF sets were of higher order orientations than the (0001) orientation (cf. Table 5.4). It is evident from Tables 7.5 and 5.4, that the clasts of the upper and lower impactites experienced pressures in excess of 20 GPa whereas those from the basement metasediments experienced pressures of less than 10 GPa (Stöffler and Langenhorst, 1994; Langenhorst, 2002).

Table 7.5: PDF associations in the LB-07A core.

PDF orientations	Upper impactites	Lower impactites	Basement metasediments*
c (0001) only	1	5	2
c (0001) and ω $\{10\bar{1}3\}$		4	
c (0001) and π $\{10\bar{1}2\}$		1	
c (0001) and higher	2	1	
ω $\{10\bar{1}3\}$ and π $\{10\bar{1}2\}$	1	1	

**No grains with multiple PDFs were encountered in the basement metasediments*

The pressure constraints provided by the PDF orientations are confirmed by the observation that the LB-07A basement metasediments do not contain diaplectic glass and were, thus, on average, shocked to lower pressures (< 30 GPa; see Table 1.1; French, 1998; Koeberl and Martínez, 2003) than the upper and lower impactites. The suevite dykes in the basement metasediments also lack diaplectic glass and contain only a minor amount of melt particles (see Table 5.6, Section 5.4.3). That suevites from the lower parts of the core seemingly contain less severely shocked grains than the upper part could be a function of admixture of basement material during the injection of such veinlets (i.e., dilution by other material). Deutsch et al. (2007) concluded that, owing to the lack of diaplectic glass, the clasts of the basement lithologies of LB-08A were shocked to < 26 GPa, whereas Ferrière et al. (2007a) suggested shock pressures in the range of 25-30 GPa. Thus, all three studies conclude that the maximum shock pressures observed in the basement lithologies of the central uplift could not have exceeded 30 GPa.

7.4.1 Melt Particle Characteristics

Melt particle populations are notably different for the out-of-crater suevites compared to the within-crater breccias (Table 7.6). As already noted, melt particles are macroscopically significant in the out-of-crater breccias (Table 7.6). Proportionally there is relatively more highly shocked material in the out-of-crater suevites than in the within-crater suevites (Tables 6.1, 7.6). Owing to the presence of

melt particles, an upper limit of between 45 and 70 GPa (Table 1.1; French, 1998; Koeberl and Martínez, 2003) for the shock pressures may be estimated for both the within-crater and out-of-crater suevites.

The melt particle statistics from the two cores are similar to each other (Table 7.6): maximum proportions of melt are 36 vol% (in an unrepresentative sample; 18 vol% in a representative sample) in LB-07A and 15 vol% in LB-08A (Ferrière et al., 2007a).

All melt particles are vesiculated (on the microscopic scale), but those from the out-of-crater suevites are macroscopically vesiculated as well. This indicates that the out-of-crater suevites potentially contained more volatiles than those from within the crater. Additionally, the melt particles from the out-of-crater suevites are locally altered to phyllosilicate minerals. This was observed rarely for the melt particles of the within-crater suevites.

Table 7.6: Melt particle differences for the suevites from the LB-07A (this study) and LB-08A (Ferrière et al., 2007a) cores, as well as the out-of-crater suevites from the south and north of Lake Bosumtwi (this study).

	Melt particles of suevites from LB-07A*	**Melt particles of suevites from LB-08A****	**Melt particles of suevites from south of the crater***	**Melt particles of suevites from north of the crater***
Max. size (cm)	1	1	3	40
Average proportion of melt (vol%)	5.4	8	18.2	37.3
Colour	White, grey brown, moderate yellowish-green	Grey to brown	White, light to dark brown	Light to dark brown
Shape	Sub-angular to rounded	Sub-angular to sub-rounded	Sub-angular to sub-rounded to ovoid to irregular shapes	Sub-rounded to elongate to irregular shapes
Clasts in melt particles	Quartz	Quartz	Quartz, feldspar, schist, granite	Quartz, feldspar, schist, granite

**Max. = maximum; *data from this study; **data from Ferrière et al. (2007a).*

The melt particles are somewhat different in composition in the within-crater and out-of-crater suevites, but are themselves compositionally heterogeneous (also noted for the suevites from north of the crater by Boamah, 2001). Figure 7.4 shows a number of ternary diagrams with fields for the melt particles from the different suevite groups. The different minerals from the target rocks have been plotted on the various diagrams (Fig. 7.4). It is evident for some minerals (e.g., biotite and chlorite) that these cannot be fully distinguished from each other in, for example, Fig. 7.4 A; however, these can be distinguished on Fig. 7.4 C. For the purposes of completeness, all phases that can be plotted on the various diagrams are indicated. However, some of these phases will nonetheless remain indistinguishable from each other owing to their similar compositions on all diagrams, e.g., potassium-feldspar and muscovite, and hence melts of these minerals will be indistinguishable. For the first ternary diagram (Fig. 7.4 A), much overlap between all three groupings is observed, trending away from SiO_2 towards the other apices. The melt analyses from within and south of the crater are relatively more enriched in FeO and MgO than those from north of the crater. In Figure 7.4 B, far larger fields for the different groupings are evident. This emphasizes the heterogeneity within individual melt particles. The analyses from north of the crater have comparatively less K_2O than those from south of and within the crater; conversely, these are relatively depleted in Na_2O in comparison to the analyses from north of the crater. The AK(FM) diagram in Fig. 7.4 C indicates that the suevites from north of the crater are comparatively enriched in alkali elements, in comparison to those from the south which are more enriched in (FeO+MgO). The suevites from within the crater straddle the boundaries of these two fields. Thus, subtle differences are evident between the analyses from different parts of the crater.

A first-order observation is that the Bosumtwi melt data demonstrate strong heterogeneity. The melt particle compositions of all the suevite

types mostly reflect mineral mixing – i.e., they do not represent the melting of discrete minerals (which would result in overlap of the melt data with the mineral data), although occasionally pure SiO_2 melt has been observed. Cluster analysis (sections 5.4.5 and 6.5.3.4) indicates that most melt particles from all the suevites consist of 2 or more phases with distinct chemical compositions. These have been shown to represent the melting and the mixing of melts of the main mineral types (quartz, feldspars and phyllosilicates), in varying proportions. Overall, the melt particles from within the crater are dominated by 3 different clusters: a CaO-dominated melt, a SiO_2-rich melt and a high K_2O and moderate Al_2O_3 melt. The individual particles themselves do not consist of a single melt type, but rather a mix of them. In contrast, the melt particles from the out-of-crater suevites are generally dominated by 2 clusters, which differ in the north and south. Those in the south are dominated by a (MgO-FeO-MnO)-rich melt and a SiO_2-rich melt. Those in the north are dominated by either a (K_2O-CaO)-rich melt or an (Al_2O_3-Na_2O)-rich melt.

The melt particles do not represent discrete target rock melts (Figs. 5.15, 6.22, 6.25). Furthermore, with the exception of the pure SiO_2 melts, the melt particles also do not represent individual mineral melts. Rather, melt particle compositions represent mixes of mineral melts which themselves may not be fully homogenised. Fully homogeneous mineral mixes would represent whole-rock melting, and would plot as average target rock compositions. Also, the chemical compositions as given by the cluster analysis do not equate to the same compositions of specific mineral melts (or mixes thereof). Shock melting is achieved at a grain scale (as opposed to a bulk rock scale; French, 1998). Melt composition will be controlled by the extent of mixing between individual mineral melts.

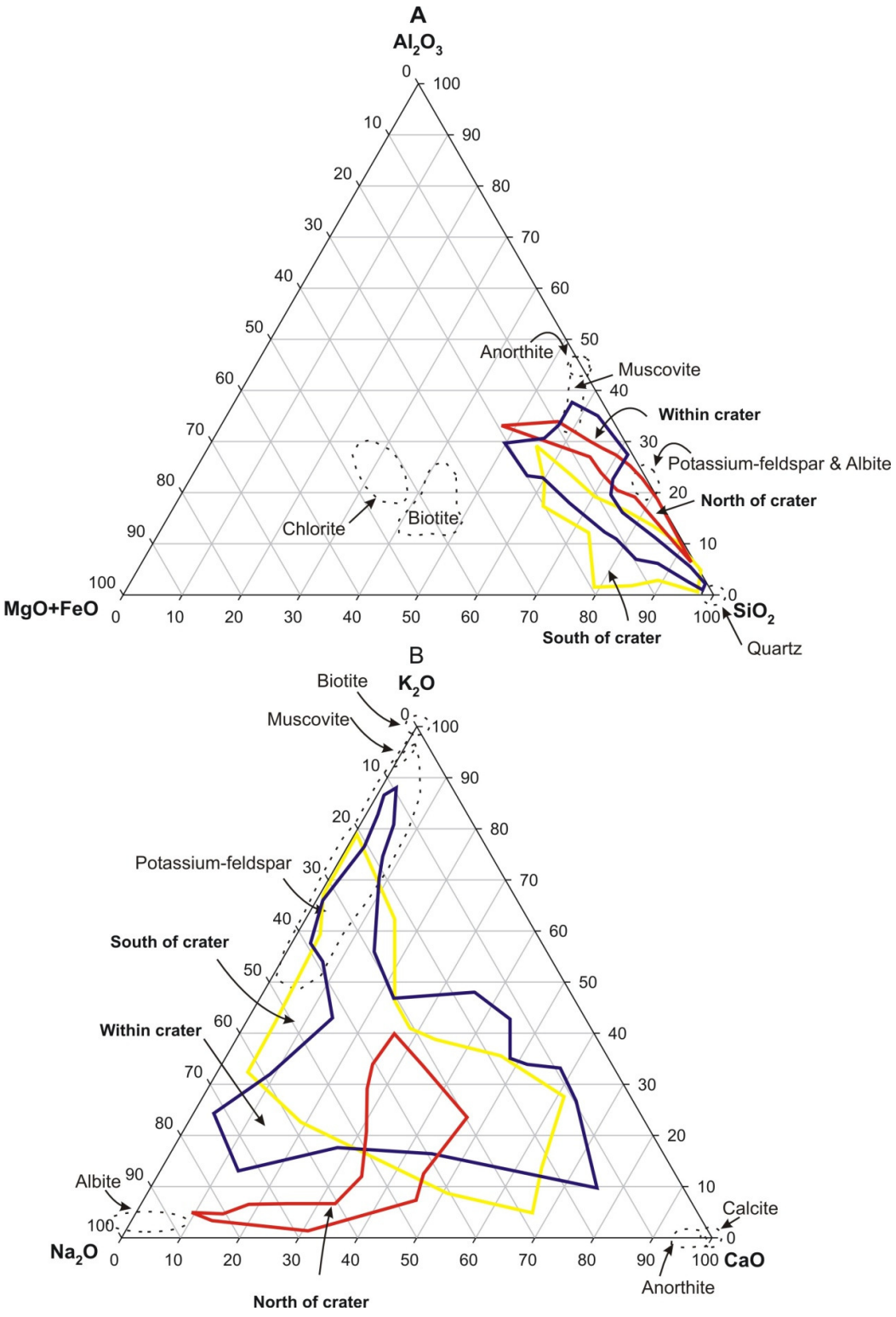

Fig. 7.4: Ternary discrimination diagrams for the electron microprobe analyses (10 µm defocused beam) of melt particle phases from within and out of the crater. A) Al_2O_3-(MgO+FeO)-SiO_2 and B) K_2O-Na_2O-CaO. Continued on next page.

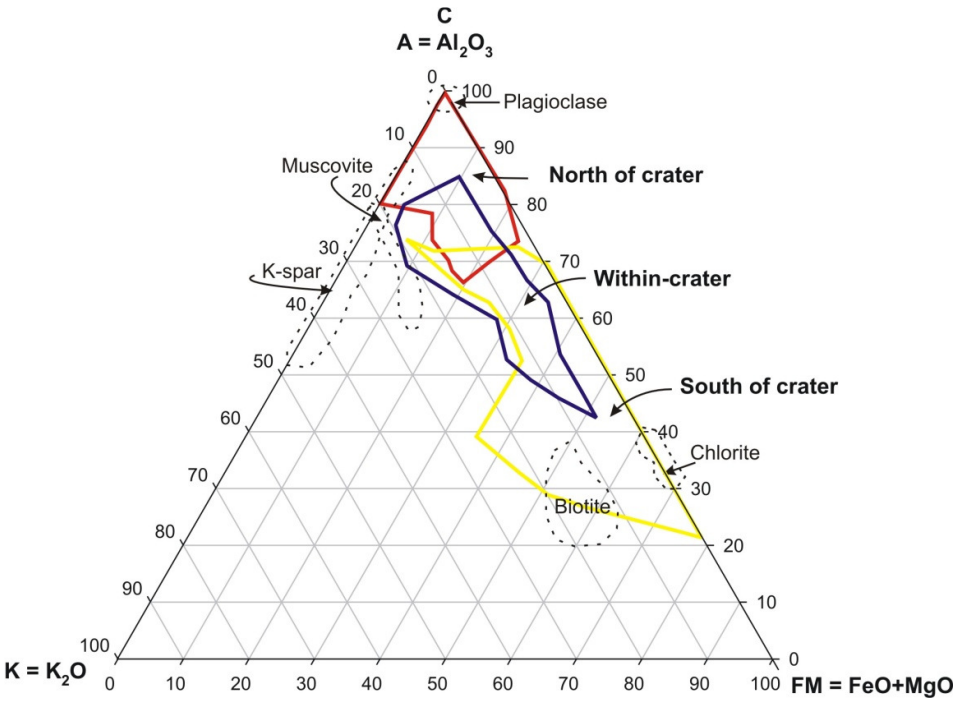

Fig. 7.4 (cont'd): Ternary discrimination diagrams for the electron microprobe analyses (defocused 10 µm beam) of melt particle phases from within and out of the crater C) AK(FM) discrimination diagram for the electron microprobe analyses (10 µm defocused beam) of the melt particles from within and out of the crater.

This mixing, in turn, is controlled by a number of factors including the grain size of the minerals, degree of heating (proximity to the impact site) and duration of heating (time before quenching; affected by the cratering process). For example, a mineral melt may cool quickly when ejected from the crater or may cool slowly if surrounded by heated material. These factors will ultimately control the extent of the mixing of mineral melts, and thus the heterogeneity or homogeneity of the final chemical composition. Thus, where the mineral melts are highly heterogeneous, it may be proposed that these mineral melts cooled faster or were not heated to the extent of more homogeneous material. Overall, it appears that the melt particles from the within-crater suevites are more heterogeneous than those from the out-of-crater suevites (indicated by the cluster analysis; see above) and thus it is proposed that the within-crater melts either cooled quicker or were not heated to the same extent as the out-of-crater melt particles. The implications of this will be discussed in section 7.7.3.

7.5 Petrographic and Geochemical Characterisation of Alteration of Impactites in the LB-07A Core

On a regional scale, extensive evidence of pre-impact hydrothermal alteration has been found (see Yao and Robb, 2000). This hydrothermal activity is implicated in the genesis and modification of the regional gold mineralization in the Ashanti region (at ~2100 Ma, see Yao and Robb, 2000). Yao and Robb (2000) cited as evidence for regional hydrothermal alteration quartz veins/stockworks and pervasive alteration zones throughout the country rocks, sericitization and the widespread occurrence of secondary sulphides (pyrite, chalcopyrite, pyrrhotite and arsenopyrite) and carbonates.

7.5.1 Pre-impact Hydrothermal Mineralization

Evidence of pre-impact hydrothermal alteration is apparent as cross-cutting quartz and carbonate veins restricted to individual lithic clasts in the breccias. Sericitization of plagioclase (confined to cleavage directions in discrete grains) and the development of secondary chlorite after biotite are common. In the target lithologies, Pepiakese granite and granite dykes both contain chlorite after biotite (section 6.3; also noted for the Pepiakese granite by Koeberl et al., 1998), but sericitization is common in the greywackes and phyllites, in addition to the Pepiakese granite and granite dykes (also noted by Moon and Mason, 1967 and Karikari et al., 2007). The latter authors suggested that the pre-impact hydrothermal system was localized in shear zones.

The granophyric-textured lithology is also suggested to represent a unit that experienced pre-impact alteration. This unit was compared to the two types of granite identified by Koeberl et al. (1998) in order to elucidate its possible origin. The granite dykes consist of a quartz-potassium-feldspar-plagioclase-biotite±sericite-chlorite assemblage (feldspars are locally sericitized; section 6.3). The Pepiakese granite is composed of a similar assemblage, with additional muscovite. The granophyric-textured lithology in this study consists of a biotite-

absent quartz-feldspar-muscovite-calcite assemblage. The mineral content of the granophyric-textured lithology suggests that it may be related to the Pepiakese granite.

Pyrite and chalcopyrite (pyrite>chalcopyrite) with minor pyrrhotite and arsenopyrite (also seen in the Birimian rocks, see Yao and Robb, 2000) have been identified as the chief sulphide phases in the breccias (discrete occurrences, and in shale clasts). Pre-impact opaques are evident as phases within the clasts (rutile in shale; section 3.2.4) or as discrete euhedral minerals in the breccias (Figs. 3.9 B; 3.15 A).

7.5.2 Post-impact Alteration

Hydrothermal alteration triggered by impact is a common occurrence in impact structures (e.g., Naumov, 2002; Koeberl and Reimold, 2004; Ames et al., 2004; Reimold et al., 2005). As evidenced by this study and others, the Birimian Supergroup experienced extensive pre-impact greenschist facies alteration. Distinct evidence of post-impact hydrothermal alteration in core LB-07A (this study) and core LB-08A (Ferrière et al., 2007a) includes the occurrence of both macroscopic and microscopic fine-grained carbonate segregations, calcite veins and pods, cross-cutting quartz veins and minor sulphide occurrences (networks in the matrices of the breccias and basement rocks).

Minor pyrrhotite (associated with rutile in shale clasts) has been found in this study, in agreement with the findings of Kontny and Just (2006) and Kontny et al. (2007). Kontny et al. (2007) suggested that <10 µm ferromagnetic pyrrhotite (< 1 vol%) relics within pyrite, minor magnetite and anomalous pyrrhotite of post-impact origin were the main carriers of the rock magnetic signature. The pyrrhotite was termed “anomalous” as it is an alteration product of the pre-impact opaque minerals, and existed as a magnetic phase with a Curie temperature of between 330 and 350 ^{o}C (see Kontny et al., 2007).

Very little post-impact alteration is evident in the LB-07A monomict breccias of the lower impactites, and their chemical compositions reflect the basement metasediments – i.e., the rocks from which they are derived. No particular set of impactites provided a channel for the hydrothermal fluids - however, localized alteration is found throughout the core.

In order to constrain the post-impact temperatures of the hydrothermal system, two constraints are evident: the production of calcite and quartz veining, and the level of post-impact metamorphism. Two studies have suggested post-impact temperatures for the Bosumtwi crater: Kontny et al. (2007) proposed that post-impact temperatures did not exceed 250 ^{o}C. They suggested that the impactites lost their pre-shock remanence and acquired a new stable magnetization during shock-induced grain size reduction. Kontny et al. (2007) suggested that this temperature is constrained by the temperatures that would be required to produce brittle microstructures of the sulphides (below the Curie temperature of ferrimagnetic pyrrhotite, which is 310 ^{o}C).

Petersen et al. (2007) examined post-impact alteration veins from cores LB-07A, LB-08A and LB-05B. They found the veins contained secondary sericitic muscovite (and $2M_1$-muscovite), together with chlorite, in all cores, and illite (only found in LB-08A and accretionary lapilli of LB-05B). They suggested that the temperature for the event was between 280 ^{o}C (constrained by $2M_1$-muscovite, illite and chlorite) and 900 ^{o}C (constrained by the absence of recrystallized quartz and feldspar).

Both studies, though, did not take into account the substantial carbonate vein formation. Experimentally-determined pressure-temperature conditions indicate that quartz and carbonate are stable at low pressures up to a maximum temperature of 600 ^{o}C (Harker and Tuttle, 1956). The temperatures of the post-impact system would

have been constrained by the temperatures of the shocked material (the heat source). Studies have shown that the post-shock temperature range of 500–3000 ^{o}C is typical for most craters (Koeberl and Martínez-Ruiz, 2003). No evidence of upper greenschist to amphibolite facies metamorphism was found in the impactites precluding such high temperatures. Retrogression of biotite to chlorite indicates lower greenschist facies. Thus, this study proposes that the Peterson et al. (2007) upper limit on the post-impact hydrothermal system is too high, and that the limits would be between 250 ^{o}C and a maximum of 300 ^{o}C (following the limit of the lower greenschist facies; see Yardley, 1989).

7.6 Presence of a Meteoritic Component in the Impactites of the LB-07A Core

A number of studies have been undertaken in attempt to detect the presence or absence of a meteoritic component in the Bosumtwi impactites (Palme et al., 1978; Jones, 1985a; Koeberl and Shirey, 1993; Dai et al., 2005; Goderis et al., 2007). So far, evidence for a meteoritic component has been found only in the Ivory Coast tektites (Palme et al., 1978; Koeberl and Shirey, 1993; Koeberl et al., 2004), but not in the out-of-crater suevites at Lake Bosumtwi (e.g., Dai et al., 2005). The meteoritic component in the Ivory Coast tektites was concluded on the basis of $^{187}Os/^{188}Os$ ratios, which are in the range of 0.153 to 0.209 (Koeberl and Shirey, 1993). Koeberl and Shirey (1993) showed that these ratios resulted from mixing of crustal rocks with a meteorite. From the isotope ratios a meteoritic contribution not exceeding 0.1 wt% was estimated for the Ivory Coast tektites (Koeberl and Shirey, 1993).

The PGE and Os isotope study that is a part of this work (section 4.7.1) did not provide unambiguous evidence for the presence of an extraterrestrial component in the LB-07A core impactites. This result is similar to that of Goderis et al. (2007) and may be attributed to the high concentrations of terrestrial PGE in the Bosumtwi crater target

rocks. Dai et al. (2005) showed that it is likely that the Birimian mineralization must be held responsible for the elevated Pt, Pd and Au abundances. More intriguing, though, are the Ir contents, which do not attain high concentrations in the Birimian target rocks (Dai et al., 2005). Impactite samples which do contain appreciable Ir (such as KR7-9, at ca. 0.7 ppb Ir) could contain several tenths of a percent of meteoritic component. However, as the meteoritic component is best identified from a combination of ratios (not exclusively from Ir; Koeberl, 2007), this component cannot be confirmed, as the other PGE elements have high concentrations that are, at least in part, due to the high indigenous PGE component.

The Os isotopic compositions of the LB-07A and LB-08A core samples did not reveal a meteoritic component even though this method is more sensitive than the PGE technique (see Dai et al., 2005; McDonald et al., 2007). This is again related to the high PGE contents of the target rocks, which have been shown to mask the possible small meteoritic component in the Bosumtwi crater rocks.

A possible explanation for the lack of a detectable meteoritic component in the within-crater suevites but its presence in the distal tektites is the suggestion made by Artemieva et al. (2004) that, in the event of an oblique impact (at an angle of 20-45° from the horizontal), some of the meteoritic component would be preferentially incorporated into the distal ejecta. This proposal would certainly support the observation that the tektites seemingly contain meteoritic material, whereas the out-of-crater and within-crater suevites do not (Pierazzo and Melosh, 1999; Dai et al., 2005; McDonald et al., 2007; Goderis et al., 2007). Thus, it may be concluded that the tektites were formed from material that was closest to the point of impact, in agreement with general theory about the origin of tektites (see section 1.2.5.4; Koeberl and Martínez-Ruiz, 2003).

7.7 The Bosumtwi Cratering Event

7.7.1 Impactite Distribution

The Bosumtwi crater is one of only a few terrestrial craters that preserve a variety of distal and proximal impact ejecta. The irregular ejecta distribution (Fig. 1.11) allows us, inter alia, to evaluate the impact angle. The irregular impactite distribution involves out-of-crater suevites north and south of the crater, and tektites and microtektites to the north-northwest and south-west, respectively. Boamah and Koeberl (2003, 2006) determined that the thickness of the out-of-crater suevite was ≤15 m and that it occupied an area of ~1.5 km^2 to the north of the crater. However, Boamah and Koeberl (2006) also discussed that the current distribution of suevite could result from differential erosion of suevites (also proposed by Wagner et al., 2002), though they could not provide an estimate of the extent of erosion.

In order to examine whether potential out-of-crater suevites to the east and west of the crater existed and were subsequently eroded, the geological map and topographic projection of Lake Bosumtwi were examined (Appendix 1). It has been shown that differential erosion may take place post-impact (caused by recent tectonic activity; e.g., Popigai crater, see Masaitis et al., 2005). No significant changes regarding the topographic level of the crater rim or the surrounding areas are apparent around the entire crater, which indicates that, if erosion of suevites took place, then it would be unlikely that suevites to the north and south of the crater would be preferentially preserved whilst those to the east and west were eliminated. The crater is hydrologically closed owing to its high crater rim and, thus, there is a distinct lack of drainage into the surrounding area (see section 1.8.1). Variably oriented thrust-faults have been noted in the northwestern part of the crater (Reimold et al., 1998; section 1.5). No difference in the degree of faulting has been noted around the lake. It is possible, owing to the limited exposure, that some out-of-crater suevite has yet to be found, for example below

the outer crater rim talus and lateritic weathering horizons surrounding the crater. However, it is thought that the current distribution of suevites might well reflect the initial distribution.

In the case of an oblique impact, the geometry of the ejecta blanket is strongly affected. As the impact angle decreases from 90° to 60°, the ejecta first show a concentration on the downrange side of the crater (Melosh, 1989; see Fig. 7.5 A). When the angle is less than 45°, a wedge-shaped zone of no deposition (the "forbidden zone"; Gault and Wedekind, 1978) develops uprange of the crater (Fig. 7.5 B) and, as the angle approaches 0°, a second ejecta-free zone develops downrange of the crater (Fig. 7.5 C, D). This pattern is known as a "butterfly pattern" (Gault and Wedekind, 1978) and is created as the shock wave throws the ejecta out of its path (see section 1.2.5.3).

It is possible that the Bosumtwi impactite distribution (but not the characteristics of the impactites) might be explained by a strongly oblique impact. The distribution of the tektites and microtektites together with the out-of-crater suevites could be in the shape of the "butterfly pattern" with respect to the position of the Bosumtwi crater (Fig. 7.5 E). The crater shape will still remain round, as the shape is dependent more on parameters such as the structure (degree of fracturing, jointing) and strength of the target rocks (see section 1.2.2).

No evidence has been found of out-of-crater suevites to the east and west of the crater. This would imply an impact angle of between 45° and 20°, and the impact originating from the east (as ejecta deposits occur west of the crater).

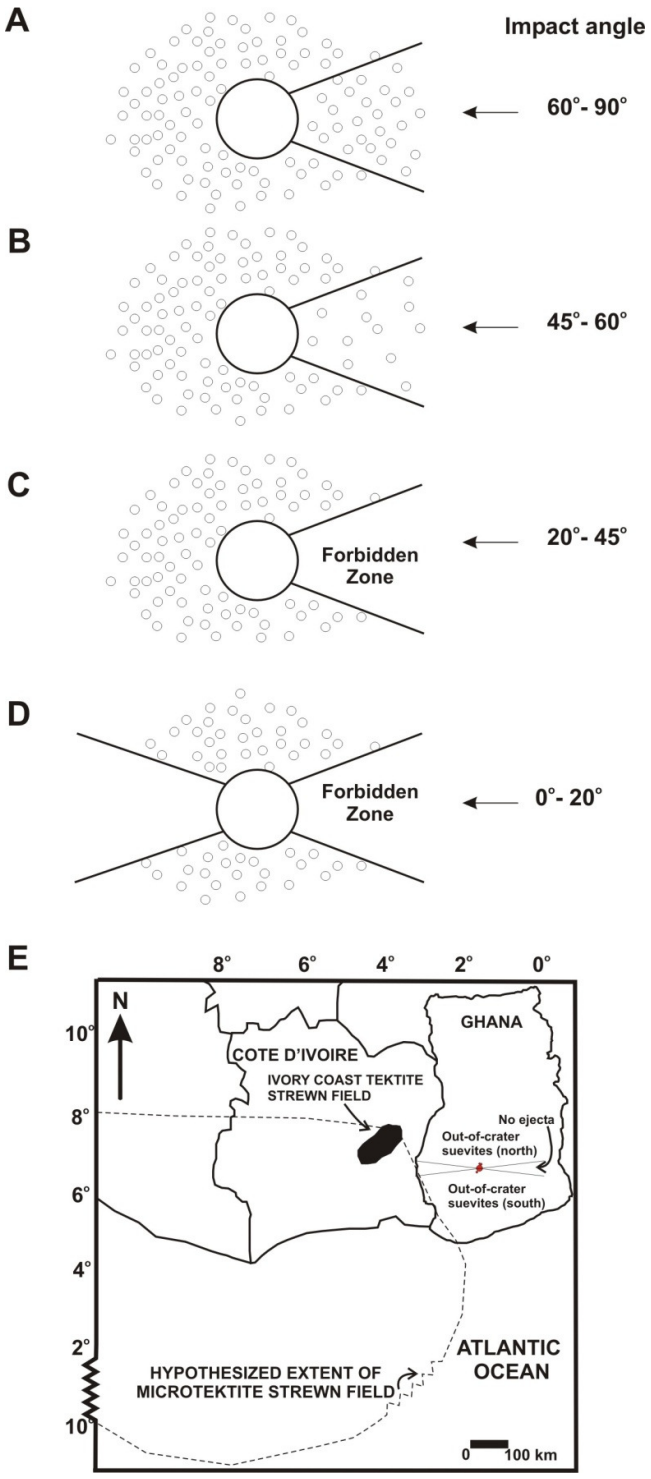

Fig. 7.5: Ejecta patterns caused by oblique impact. Large circle indicates the crater, and small circles indicate the ejecta distribution. A) Oblique impact angle between 60 and 90°. B) Oblique impact angle between 45 and 60°. C) Oblique impact angle between 20 and 45°. D) Oblique impact angle between 0 and 20°. E) Ejecta pattern of the Bosumtwi crater (modified after Koeberl et al., 2007a).

The tektites represent the most intensely shocked material, and the distribution of these is clearly not directly to the west of the crater (Fig. 1.1, 7.5 E), but more to the north-northwest. The entire strewn field incorporating the microtektites, however, includes the area to the west of the crater (Fig. 7.5 E). The distribution of the Bosumtwi impactites would, thus, be created by an impact of a low angle (20° to 45°) which entered the atmosphere from the east (Gault and Wedekind, 1978; Melosh, 1989).

The low-angle impact scenario also agrees with the observed lack of a detectable meteoritic component in the within-crater and out-of-crater suevites, with this meteoritic component being more likely to be preferentially incorporated into the distal ejecta during a low-angle impact (Artemieva et al., 2004; see section 7.6).

7.7.1.1 Average volume of melt in the proximal ejecta – assessment with respect to the numerical modeling

A tentative estimation of the average amount of melt in the proximal ejecta (i.e., the within and out-of-crater suevites) can be made in order to further quantify the Bosumtwi cratering event. As only two cores from the crater were obtained, this assumes homogeneous characteristics across the different sections of the crater. Table 7.7 provides the parameters used for the different melt volume estimations. Estimates of the area and thickness of the out-of-crater suevites from north of the crater are after Boamah and Koeberl (2003). The estimate for the area of the suevites from south of the crater is calculated from the map of Koeberl and Reimold (2005), and the thickness is estimated from the field work undertaken in this study. The estimate of the area for the central uplift is taken from Karp et al. (2002), whereas the estimate for the area of the crater moat has been calculated by subtracting the area of the central uplift from the area of the lake. The thicknesses of the suevites from the crater moat and the central uplift are after the LB-07A core (this study) and the LB-08A core (Ferrière et al., 2007a), respectively.

Average volume percentages of melt are from this study, except for the suevites from the LB-08A core (central uplift; from Ferrière et al., 2007a). The average volume percent of melt includes a calculated average from the melt contained in the suevite matrices – this has been estimated at a maximum of 5 vol%, and an average of 2 vol% for the matrices of the LB-07A core (section 3.2.1). No estimate has been provided for the LB-08A core, but for the purposes of this study, it has been assumed to be the same as the LB-07A core.

Once the averages for the different volume percentages were calculated, a total volume percent of melt in the suevites from within and out of the crater was estimated at approximately 0.189 km^3. This forms approximately 6.87 % of the total volume of suevite (2.76 km^3).

Table 7.7: Parameters used for the calculation of the average melt volume in the proximal ejecta at Lake Bosumtwi. Data for the suevites from the crater moat is estimated from the LB-07A core (this study); for the central uplift from the LB-08A core (Ferrière et al., 2007a).

	Crater Moat (LB-07A)	**Central Uplift (LB-08A)**	**Out-of-crater suevites from the south of Lake Bosumtwi**	**Out-of-crater suevites from the north of Lake Bosumtwi**
Area (km^2)	53.9	2.8	1.5	1.5
Thickness of suevite (km)	0.05	0.011	0.005	0.015
Average vol% of melt	6.6	8.8	19.4	37.3
Volume of suevite (km^3)	2.70	0.03	0.007	0.02
Average volume of melt in suevite (km^3)	0.177	0.003	0.001	0.008

Estimates of areas for the out-of-crater suevites from Boamah and Koeberl (2003) and the map of Koeberl and Reimold (2005); estimate of area for the central uplift from Karp et al. (2002); estimate for area of crater moat calculated from the area of lake minus area of central uplift (see Chapter 1). Thickness of suevite for out-of-crater suevites from north of the crater from Boamah and Koeberl (2003); for the out-of-crater suevites from south of the crater, values from this study were used; for the crater moat, values from the LB-07A core were used (this study), and for the central uplift, values from the LB-08A core were used (Ferrière et al., 2007a). Average volume percentages of melt are from this study, except for the suevites from the LB-08A core (central uplift; from Ferrière et al., 2007a).

Scaling relationships (Grieve and Cintala, 1992) predict that for a crater with a 10 km diameter, an approximate melt volume of 5 km^3

would be observed, which is substantially higher than the melt volume calculated in this study. However, it must be noted that all of the predictions made by Grieve and Cintala (1992) were consistently higher than the observed volume of melt in terrestrial craters (also observed by Artemieva, 2007). Also, Grieve and Cintala (1992) used a granitic target in all their modeling calculations, which is not the case at Lake Bosumtwi in which metasediments comprise the target rocks.

Furthermore, it should be noted that discrepancies between the amount of melt intersected and that predicted by scaling relationships for terrestrial impact craters have also been observed for the Chesapeake Bay crater, even though much of the target there consisted of crystalline lithologies (Wittmann and Reimold, 2008). Wittmann and Reimold (2008) extrapolated their calculated amount of melt (that was retained in the crater) to 10.5 km^3. This is in agreement with gravity and magnetic modeling data (Shah et al., 2005). This amount is substantially less than that predicted by the estimate of Grieve and Cintala (1992), which was approximately 230 km^3. Wittmann and Reimold (2008) suggested that factors such as reworking of melt by resurge flow, impact parameters (angle and velocity), and the proportion of sedimentary material to the target may have contributed to the melt deficiency. This example supports the observations made for the Bosumtwi crater in that all factors in crater formation (impactor characteristics, target lithologies, post-impact reworking) clearly play a role in the proportion of melt.

The calculated amount of melt of this study can be compared to previous numerical modeling results (Artemieva et al., 2004) which predicted the amount of melting and the maximum degree of shock that materials would have experienced during the Bosumtwi impact. From modeling of tektite formation (Artemieva, 2002), it was suggested that the impact angle for the Bosumtwi cratering event was 30-45°, and an impact velocity of 15 km/s was utilized in order to

predict how much melt would be retained in the crater. Artemieva et al. (2004) predicted a total melt volume of 2.6-3.9 km^3 (i.e., 100–200 m of impact melt should have accumulated above and around the central uplift), and suggested that 68 % of the total melt would be found in the crater. Their study did show, though, that in the case of a vertical impact, the amount of melt retained in the crater would be 65-70 % of the total melt produced – i.e., not substantially different from that produced by an oblique impact.

Of the total melt, they predicted that between 0.54 km^3 and 1 km^3 of melt would be found outside the crater (Artemieva et al., 2004) – depending on the target rock configuration (granite *vs.* sediments). If one assumes that all of the melt ejected outside of the crater was emplaced as the tektites and microtektites, this leaves a remainder of between 1.8 and 2.7 km^3 melt in the crater. Although this estimate is somewhat excessive, given that melt occurs in the out-of-crater suevites, is still indicates that the amount of melt predicted is far higher than the amount of melt calculated by this study (0.189 km^3). Thus, there exists a discrepancy between the amount of melt predicted by the numerical modeling and the actual volume of melt intersected in the cores and outside of the crater.

Artemieva (2007) suggested a number of different scenarios to explain the apparent melt deficiency in the Bosumtwi crater, including characteristics of the projectile (low impact velocity, low impact angle) and target properties (composition, high porosity, high volatile content). Previously, it has been proposed that shock pressures will decrease more rapidly in porous rocks owing to the additional work needed to traverse pore spaces – thus a smaller crater and less shocked impactites (i.e, less melt) might be expected for porous rocks given a certain set of impact parameters (Love et al., 1993; Wünnemann et al., 2005). However, Wünnemann and Collins (2006) and Wünnemann et al. (2008) have shown that the opposite will hold for porous target rocks – melt production increases with increasing

porosity (as the porous nature of the rocks will decrease the pressure needed for melting). Thus, the small amount of melt in the crater must be caused by something other than the target rock porosity.

One of the discrepancies of the original modeling performed by Artemieva et al. (2004) was the assumption that the target was a homogeneous crystalline layer, namely, granite. After the ICDP drilling, it was shown that granite, in fact, forms a minor part of the target and that the target lithological composition is far more complex than a single-layer scenario.

Artemieva (2007) discussed that the dispersion of impactites could be due to the vaporisation of pore water, which was not included in the model of Artemieva et al. (2004). Artemieva (2007) suggested that impactites could be turbulently dispersed by the vaporisation of water (and other volatiles, e.g., from carbonate in the target sequence). However, in the case of the Bosumtwi crater, this would require 10 vol% of water to a depth of several kilometres in the target (in order for this process to take place; Artemieva, 2007). In the basement rocks of LB-07A (most indicative of the target lithologies), average LOI values of only 9.5±4.2 wt% are observed for the metagreywackes and 5.6±3.0 wt% for the shales (see Table 4.1). However, in LB-08A core (which intersects a larger basement section than the LB-07A core), LOI values for the metagreywacke are 3.1±1.6 wt% and, for the phyllite-slate, they are 4.9±2.1 wt% (Ferrière et al., 2007b). As discussed in section 4.4.7, the LOI values represent losses from carbonate and phyllosilicate phases – mainly CO_2, H_2O and, thus, can provide a qualitative estimate of the porosity. Combining both studies, this indicates that the LOI varies between 3.1 and 9.5 wt%. An average density value of 2610 kg/m^3 was calculated for the metasediments of the LB-07A and LB-08A cores by Elbra et al. (2007), and by using this value combined with the LOI values, porosities of between 8.1 and 25 vol% can be estimated for the basement rocks of the Bosumtwi crater.

Additionally, Elbra et al. (2007) stated that the average porosity of the metasedimentary target rocks is 8.8 %, and only noted higher values (> 20 %) for the impactites. The high variation in the LOI contents of the target rocks indicates that there is much variation in the porosities and, thus, in the amount of matter which could be volatilized. Although these values are comparable to the stipulations required by Artemieva (2007), the average porosity calculated by Elbra et al. (2007) is below 10 vol% and there may not have been sufficient pore water to have produced the dispersion of impactites and low melt volumes, and, thus, this suggestion of vaporisation of pore water by Artemieva (2007) seems unsatisfactory. It is likely that the discrepancy in the melt volumes must be influenced by other factors in addition to the nature of the target rocks.

A recent study by Osinski et al. (2008b) discussed the varying proportions of melt predicted by numerical modeling and observed melt proportions in craters with different target lithologies. They found that there was little evidence of substantially different volumes of melt being produced by impacts into crystalline or sedimentary rocks and that it was rather the interaction of the melt produced with the clastic debris (in terms of mixing and homogenisation) that would govern the final proportion of melt. Osinski et al. (2008b) proposed that less assimilation of clastic debris owing to the properties of sedimentary rocks may result in an overall smaller proportion of melt than observed for a similar sized crater formed in crystalline rocks. This certainly is a possible option for the melt deficiency observed in the Bosumtwi crater suevites, and warrants further investigation.

Another argument that can be made is that the placement of the two drillholes might have resulted in them missing the “melt body” which had been postulated to cause the magnetic anomaly observed in the Bosumtwi crater (Fig. 1.15; Plado et al., 2000; Danuor and Menyeh, 2007; Ugalde et al., 2007b). Several studies have proposed alternatives to a melt sheet scenario for the source of the magnetic

anomaly (Ugalde et al., 2007b; Danuor and Menyeh, 2007). Ugalde et al. (2007b) suggested that highly magnetic bodies were located in the northeast sector of the structure, rather than underneath the drilling sites. They suggested that these bodies corresponded to a southerly extension of the Kumasi granitoid batholith (located to the northeast of the structure; Fig. 1.11). Danuor and Menyeh (2007) suggested that the causative bodies were located north of the central uplift, but proposed that they were impactites. Only further drilling will elucidate the origin of the magnetic anomalies, but it seems unlikely, given the results of the 2004 ICDP drilling, that a coherent melt sheet actually exists.

7.7.2 Assessment of Other Ideas Pertaining to the Degree of Shock of Clasts in the Basement Material at Lake Bosumtwi

Shock petrographic studies from the two cores (this study; Deutsch et al., 2007; Ferrière et al., 2007a) suggest that the basement metasediments were shocked to < 30 GPa (due to the absence of diaplectic quartz glass; see section 7.2.2). This is less than that predicted from numerical modeling and geophysical studies (> 40 GPa; e.g., Karp et al., 2002; Artemieva et al., 2004). Deutsch (2006) suggested that this discrepancy may be related to the obliquity of the impact rather than any intrinsic properties of the target materials. This work was extended when Deutsch et al. (2007) conducted a number of shock experiments on porous, carbonate-rich greywacke in order to explain the low shock levels observed in the basement lithologies of the central uplift of the Bosumtwi crater. They found that near complete transformation of quartz to diaplectic quartz glass took place at both 34 and 39.5 GPa in the greywackes, and excluded the properties of the porous greywacke as the main reason for the low shock levels.

Other impact structures, for example the Ries, Rochechouart-Chassenon, Slate Islands and Charlevoix structures, record maximum shock pressures between 23 and 30 GPa for uplifted

basement (e.g., von Engelhardt and Graup, 1977; Robertson and Grieve, 1977; Lambert, 1977), so the moderate shock pressures observed in the Bosumtwi structure are not uncommon.

7.7.3 Model Constraints

The target rocks for the Bosumtwi crater, the Birimian Supergroup, have been shown by various studies to consist of a number of different metasedimentary components with granitoid intrusions (sections 1.5; 7.3). Not only is there a diverse suite of rock types present, but they are heterogeneously interbedded on a metre to centimetre scale, and are steeply (~80°) dipping (as opposed to horizontal layering). It has been discussed that distinct differences exist between the lithological compositions of the within-crater and out-of-crater suevites (section 7.1). The within-crater suevite packages appear to be derived primarily from metasedimentary precursors, whereas the out-of-crater suevites incorporate both metasedimentary and granitic components (Table 7.1). The steep dips infer that there is no vertically changing target stratigraphy that the growing transient crater would have encountered.

A number of constraints have to be accommodated within a model for the Bosumtwi cratering event, namely:

1. Petrographic differences between the within-crater and out-of-crater suevites (i.e., distribution of the target granitoid component);
2. shock petrographic differences between the clasts of the within-crater and out-of-crater suevites (i.e., more moderately to highly shocked material in the out-of-crater suevites); and
3. melt volume differences between the within-crater and out-of-crater suevites, and the discrepancy between the observed melt volumes and the amount of melt proposed by numerical modeling.

7.7.3.1 Constraint 1: Petrographic differences

In order to explain the differences in the granitoid content between the out-of-crater and within-crater suevites, a number of different scenarios may be proposed:

Option 1: The transient cavity did not intersect significant granite.

Option 2: All granite was ejected in the ejecta curtain and/or ejecta plume, and was largely deposited out of the crater.

Option 3: The out-of-crater suevites formed by contributions from the ejecta curtain and/or ejecta plume whereas the material that forms the within-crater suevites did not originate from the ejecta curtain and/or ejecta plume (but rather from another source).

Option 4: The ejecta curtain and/or ejecta plume was laterally or radially differentiated, leading to dispersal of different rays of ejecta, some of which contained significant granitoid material. In a laterally differentiated scenario, different ejecta rays radiating away from the crater may have different compositions from each other. In a radially differentiated scenario, ejecta rays are themselves differentiated along their path perpendicular to the crater.

Option 1 can be immediately discarded, as there is significant granite in the out-of-crater suevites, and this material originated from the ejecta curtain and/or ejecta plume (shown by the irregular shapes of the melt particles – Figs. 6.5, 6.6, 6.8, and following traditional crater formation processes; see Melosh, 1989). Further evidence for their formation from the ejecta curtain and/or ejecta plume is that these melt particles have irregular to elongate to bomb-like shapes (Fig. 6.8 C), and are themselves internally layered (Fig. 6.8 D). Additionally, both vertical (in the suevites from south of the crater; see section 6.4.1) and lateral (in the suevites from north of the crater; see section 6.4.2) variation in the amount of melt particles is apparent, consistent

with their origin from the ejecta curtain and/or ejecta plume. Moreover, it is known that granites occur as plutons, batholiths and dykes around the crater (e.g., Reimold et al., 1998; Koeberl et al., 1998; Koeberl and Reimold, 2005) and small dykes have been drilled below the crater. Option 2 also seems unlikely in view of the evidence from the LB-07A core, in that a small, although minor, proportion of granitic material is in evidence. Furthermore, it seems unlikely that a large mass of granite would be ejected into the ejecta curtain and/or ejecta plume without some material falling back into the crater. It seems that the only way the deficiencies in the granitoid contents of the within-crater and out-of-crater suevites can be explained is by proposing two different mechanisms for formation of the within-crater and out-of-crater suevites (option 3). In addition, the out-of-crater suevites differ from each other (in terms of shale contents), and thus it seems likely that a laterally and/or radially differentiated (in terms of clast populations) ejecta curtain and/or ejecta plume existed (option 4). Given the limited outcrop, this study favours lateral as opposed to radial differentiation given the different compositions of suevites north and south of the crater. Similar observations (differing composition of impactites reflecting heterogeneous target rock stratigraphy) have been made at the Rochechouart-Chassenon structure, France (Lambert, 2008), indicating that, where a differentiated target is in evidence, impactites will reflect that heterogeneity. This is also apparent for impactites of the Popigai crater, Russia, where Vishnevsky and Montanari (1999) differentiated 4 types of suevite, which varied in their clastic content, reflecting the distinct target rock lithologies (crystalline basement overlain by sediments; see Masaitis et al., 2005). The different impactites displayed different degrees of shock, and they thus proposed two different mechanisms to explain the differences between those with lower proportions of shocked material from those containing higher proportions. They suggested that the crater-fill impactites formed by two mechanisms: some formed as part of a flow deposit (impactites with lower proportions of shocked material) and

others originated as ballistically-transported debris from a complex ejecta cloud (impactites with higher proportions of shocked material).

Thus, it is apparent that potentially the “source material” for the within-crater suevites did not originate directly from the ejecta curtain and/or ejecta plume. One possibility is that the source material never left the crater – it was moved and emplaced by a type of ground-surge mechanism. Another is that the source rocks for the within-crater suevites incorporated material from slumping off the transient crater walls.

7.7.3.2 Constraints 2 and 3: Shock petrographic and melt volume differences

It is evident that the most intensely shocked material has been incorporated into the out-of-crater suevites, which implies that this material originated from the ejecta curtain and/or ejecta plume. During crater formation (see section 1.2.4), the most intensely shocked material – in this case the Ivory Coast tektites and microtektites - is ejected first (Melosh, 1989). Following this, intensely shocked material is ejected as part of the ejecta plume and curtain. It is likely that much of the shocked material incorporated in the out-of-crater suevites (as some of the melt particles which display irregular to elongate to bomb-like shapes that indicate that they were shaped by movement through air; Figs. 6.5, 6.6, 6.8) originated from the ejecta curtain and/or ejecta plume. However, this does not explain the comparatively smaller volumes of melt and granitoid in the within-crater suevites, as it seems unlikely that the impactites in the crater were formed by a typical “fallback” mechanism. A differentiated ejecta curtain and/or ejecta plume seems to be the only option available to explain the large volumes of granitoid and melt in the out-of-crater suevites.

The within-crater suevites display lower levels of shock recorded in clasts, contain fewer melt particles, and are essentially derived from

metagreywacke and shale. The lower proportion of shocked material is satisfied if the mechanism by which the within-crater suevite formed incorporates ground-surge in addition to slumping from transient crater walls rather than incorporating fallback material (i.e., material from the ejecta curtain and/or ejecta plume). Material which experienced energies sufficient to eject it from the crater would be expected to contain higher proportions of shocked material and may display higher levels of shock in clasts whereas material which was not expelled from the crater would contain less shocked material, and potentially material displaying lower levels of shock. This can be explained by a model which suggests that the within-crater suevites formed more or less *in situ* - i.e., they were not expelled to great distances from where they originated. The fact that the material within the crater does contain shock indicators such as melt particles and diaplectic quartz glass does indicate that this material was moved and shocked – i.e., by ground-surge and/or transient crater wall slumping. However, a small proportion of the material within the crater does originate from "fallback" from the ejecta curtain and/or ejecta plume - a 30 cm lapilli-rich layer which occurs on top of the impactite sequence (found in core LB-05B; described by Koeberl et al., 2007b; see section 7.4). This is the only evidence within the crater of fallback material. This is not representative of the main impactite packages described from cores LB-07A (this study) and LB-08A (Ferrière et al., 2007a).

7.7.4 Proposed Model for the Formation of the Bosumtwi Impactites

The differing characteristics of the distal ejecta and the out-of-crater and within-crater impactite material directly represents the variable target rock material from which these impactites were derived. Thus, the following sequence of events is suggested from the data collected in this project and the available literature data in order to explain the impactite differences:

1. The target rocks for the Bosumtwi crater consist predominantly of metasediments, together with minor granitic intrusions (Fig. 7.6 A).
2. The crater was formed by an oblique (20-45°) impact, with the bolide travelling from east to west (Fig. 7.6 A). This accounts for the strongly asymmetrical impactite distribution (see Fig. 7.5). A major portion of the meteoritic component was imparted into the most energetic ejecta (i.e., those creating the distal ejecta; see section 7.6; Fig. 7.6 B). Formation of the Ivory Coast tektites and microtektites (Fig. 7.6 B).
3. A high-energy ejecta curtain and/or ejecta plume was created (Fig. 7.6 B), which produced the material for the accretionary lapilli layer (i.e, uppermost fallback from the curtain and/or ejecta plume; Koeberl et al., 2007b) and out-of-crater suevites (Fig. 7.6 C and D), as well as, presumably, a limited contribution to the within-crater suevites.
4. The ejecta curtain and/or ejecta plume was laterally differentiated, reflecting the regional stratigraphic variation, and the out-of-crater suevites were formed by “ejecta rays” of differing composition. This would explain the higher granitoid content (and variable shale) in the out-of-crater suevites and the lower granitoid content in the within-crater suevites. The out-of-crater suevites consist of a higher proportion of shocked material than the within-crater suevites as they originate from the ejecta curtain and/or ejecta plume (whereas the within-crater suevites do not; Fig. 7.6 A, C).
5. The within-crater suevites, which are relatively granitoid-deficient and contain significantly smaller melt clasts and less strongly shocked lithic clasts than those of the out-of-crater suevites, were formed in close proximity to the impact site. Either this material was “washed” around the crater in a ground-surge incorporating a large proportion of comparatively weakly shocked material and/or material derived from slumping off the crater walls. Both mechanisms could result in subhorizontal layering (intercalation) of melt-rich (i.e, suevite) and melt-deficient (i.e., polymict lithic breccia) material. The suevites contain proportionally less shocked

material, as this material contains few contributions from the ejecta curtain and/or ejecta plume (Fig. 7.6 C).

6. The within-crater monomict breccias are a parautochthonous unit, whereas the basement material is autochthonous (Fig. 7.6 B and C). The material was fractured and brecciated by the transition of the shock wave, and the different natures of the breccias and the basement material directly represent the decreasing energy of the shock wave with depth.
7. The formation of suevitic intercalations in the monomict breccias and basement rocks takes place by breccia injection (which exploits fractures produced during the crater collapse in the extensional phase of impact cratering). The origin of the suevite is from the ground surge and/or material derived from slumping off crater walls as the central uplift forms (Fig. 7.6 C). These suevite intercalations are essentially comparable to the upper impactite suevites.
8. The uppermost impact fallback layer (consisting of relatively fine-grained accretionary lapilli and glass spherules in addition to moderately shocked clastic debris; typified by LB-05B) was formed by terminal fallback of the finest material in the ejecta curtain and/or ejecta plume (Fig. 7.6 D).
9. Following the final modification of the crater, a small hydrothermal system (< 300 ^{o}C) produced limited overprint (sulphides, chlorite, calcite and quartz veining; Fig. 7.6 E).

7.8 Suevites of the Bosumtwi and Ries Craters – a Comparison

The 14.5 Ma old Ries crater in Germany (24 km in diameter) is the type locality for suevite, thus providing a useful crater against which to test some of the observations made in this study. It is also associated with a tektite (“moldavite”) strewn field (Hörz, 1982; von Engelhardt et al., 1987; Stöffler et al., 2002).

The Ries crater is just over twice the size of the Bosumtwi crater, and its characteristics have been well documented (see, e.g., Kring, 2005 for details).

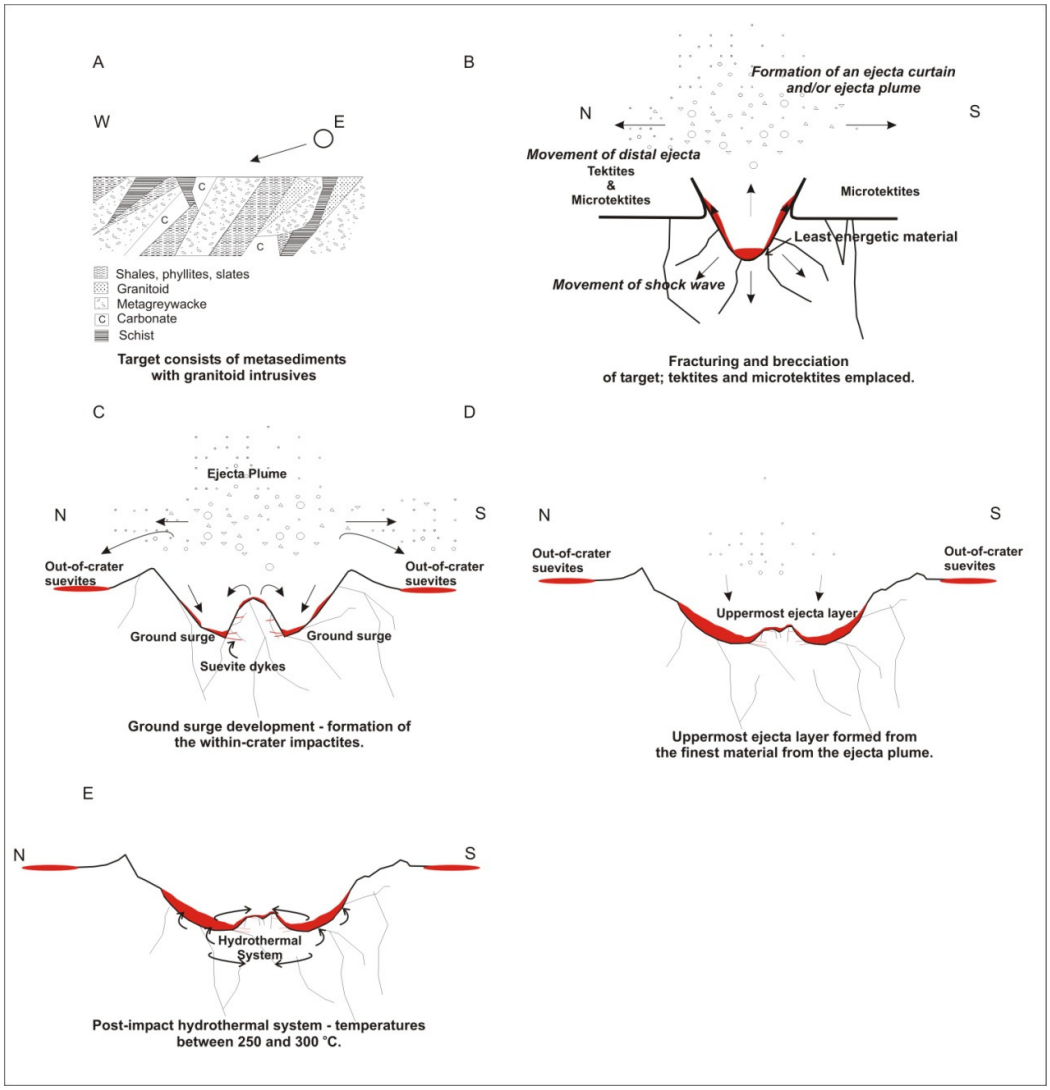

Fig. 7.6: Model for the emplacement of the impactites at the Bosumtwi crater. A) An oblique impact, travelling from east to west makes contact with the Birimian target rocks. Note the heterogeneous nature of the target geology. B) Ejection of the Ivory Coast tektites and microtektites; formation of ejecta curtain and/or ejecta plume; fracturing and brecciation of the target rocks by the progression of the shock wave. C) Formation of the central uplift and out-of-crater and within-crater suevites by contributions from the ejecta curtain and/or ejecta plume and ground surge/slumping, respectively. D) Formation of the uppermost impact fallback layer (fine-grained material from the ejecta plume). E) Post-impact hydrothermal system affects entire crater fill.

The target lithologies prior to impact consisted of a crystalline basement (Hercynian), unconformably covered by 600-700 m of sediments (Mesozoic; see Pohl et al., 1977) – forming, in essence, two horizontal, yet complex, layers. Thus, the Ries crater differs from the Bosumtwi crater, where, in essence, a single layer of relatively steeply dipping metasediments with subsidiary granitoid intrusions is in evidence. A number of impactites have been identified in the Ries crater: monomict breccias and megablocks, Bunte Breccia, fallout and crater suevite (Pohl et al., 1977), and are compared to the impactites observed at the Bosumtwi crater.

Monomict breccias and megablocks are found in an uplifted rim at the Ries crater (von Engelhardt, 1990), the position of which represents the hypothesized edge of the transient crater (see Kring, 2005). The monomict breccias and megablocks have been shocked to pressures less than 10 GPa, and the megablocks themselves are internally brecciated (see Kring, 2005). The block size (1 – 2 km) decreases with increasing distance from the crater centre (Gall et al., 1975; von Engelhardt, 1990). This impactite type is analogous to the so-called Zone 3 (thought to represent a megabreccia zone on the crater rim) at the Bosumtwi structure reported by Reimold et al. (1998), in which decreasing block size occurs towards the rim crest, i.e., away from the crater centre (Fig. 1.12; section 1.5).

A polymict breccia, which is composed of the sedimentary rocks at the Ries crater, is associated with the megablocks. It is known as the "Bunte Breccia" (Schneider, 1971; Hörz et al., 1977, 1983), and in general the clasts have experienced low levels of shock (< 10 GPa). Polymict breccia located to the north-northeast of the Bosumtwi crater displaying low levels of shock and a distinct lack of melt particles (which would then classify it as a suevite) has been identified as a potential candidate for a Bunte Breccia equivalent (Koeberl and Reimold, 2005), but this still has to be confirmed through further work.

The Ries within-crater suevites are more complex than those in Bosumtwi core LB-07A: subdivisions based on melt and clast content, texture, and degree of remanent magnetization (see Stöffler et al., 1977; von Engelhardt and Graup, 1984; Kring, 2005) have been described. This is in contrast to the Bosumtwi suevites, in which seemingly little change with depth takes place. The crater suevites at the Ries crater are far thicker (> 200 m; Stöffler et al., 1977; von Engelhardt and Graup, 1984; Kring, 2005) than those at the Bosumtwi structure (~ 84 m in LB-07A) and display significant variation which Stöffler et al. (1977) suggested reflects different depositional histories: the bottom unit formed by ground surge of melt-poor suevite with the crystalline basement, the middle unit formed by fallback (melt proportion decreases with depth) and the upper unit formed by slumping of material from the crater walls (variable melt content). Also, Pohl et al. (2008) examined the recently drilled Enkingen core (located near the inner edge of the crater rim), and found that textural relationships in the suevite favour a significant contribution of fallback from the vapour plume. In contrast, the suevites from within the Bosumtwi crater cannot be subclassified by the parameters used for the Ries crater suevites. The within-crater suevites from the Bosumtwi crater have been proposed by this study to have formed from two different mechanisms: primary formation from ground-surge and/or slumping off the transient crater walls together with a minor amount of fallback (< 1% contribution) from the ejecta curtain and/or ejecta plume. The within-crater suevites in the Bosumtwi crater contain between 5 and 8 vol% melt (LB-07A *vs.* LB-08A proportions; see Table 7.1) which is not significantly different to the proportions from the Ries crater suevites which vary between 2 and 9 vol% (see von Engelhardt and Graup, 1984; Kring, 2005). Bulk chemical analyses of the melt particles from the Ries crater indicate that these phases are very similar (see Dressler and Reimold, 2001) to each other, but are themselves internally heterogeneous (composed of schlieren of different compositions; Stähle, 1972). Additionally, carbonate melts (Osinski, 2003) have also been noted

in the suevites (not noted as part of the melt assemblage of the Bosumtwi crater). Overall, however, the Ries suevite glasses are similar to each other in their bulk composition. The small size of the glass particles for the within-crater suevites at Lake Bosumtwi has not allowed bulk glass compositions to be determined.

The melt particles from the fallout suevites from the Ries crater show different chemical characteristics to those from within the crater (similar to the observations made in this study for the melt particles from the Bosumtwi crater). The out-of-crater suevites from the Ries crater vary from a few metres to 25-30 m in thickness (Osinski, 2003), and a number of different types of melt particles have been identified and investigated (Osinski, 2003). Some of the melt particles (termed "Type 1 Glasses" by Osinski, 2003) directly reflect a homogeneous mixture of 3 of the rock types at the Ries crater (amphibolite, granite and minor Al-rich gneisses). Other types (types 2, 3 and 4) may either reflect melting of minerals, the basement or of the sedimentary cover – and most are chemically heterogeneous. The melt particles at the Bosumtwi crater (both within and out-of-crater) have been shown to be derived from mineral mixes and not whole-rock melts (see section 7.4.1).

In terms of groundmass comparisons, Osinski et al. (2004) conducted a detailed study of different phases in out-of-crater suevite at the Ries crater. They identified a number of different textural characteristics of the suevite matrices, including flow textures between different groundmass phases, globules of phases within other phases and quench-textured crystallites in the groundmass. They found that, in some cases, discrimination of the glass clasts and matrix was impossible, and that textural relations of the matrix indicated that it was once molten – the minerals that compose the matrix consisted of a series of "impact-generated melts" (Osinski et al., 2004) and that these observations are inconsistent with the traditional nomenclature of suevite ("a polymict impact breccia that

includes melt particles (glassy or crystallized) in a mostly clastic matrix containing lithic and mineral clasts in various stages of shock metamorphism"; see Stöffler and Grieve, 2007). The matrices of the Bosumtwi crater suevites are not molten and show no evidence of (re)crystallisation on the scale that Osinski et al. (2004) described. Instead it has been demonstrated that discrete melt particles are set in a clastic matrix (see Fig. 3.13 B, C), in keeping with the definition of Stöffler and Grieve (2007).

7.9 Conclusions

The ICDP drilling has provided a three-dimensional perspective of the Bosumtwi impact crater, which is one of only a few well-preserved, relatively accessible, medium-sized terrestrial impact craters. The study of core LB-07A through the thick fill of the crater moat, together with the comparison to the impactites outside the crater, has allowed investigation of cratering processes and emplacement mechanisms for these different impactites.

The main findings of this project are as follows:

1. The drilling into the crater has redefined the target composition: granite forms a more minor part of the target than previously assumed by Koeberl et al. (1998), whereas a small (< 5 vol%), previously unknown carbonate (calcite) component of the target rocks has been identified. A comprehensive lithostratigraphic section has been produced, and has provided a tool for correlation with geophysical and geochemical observations (see Meteoritics and Planetary Science, volume 42, 2007).
2. Suevites, polymict lithic breccias and monomict breccias as well as deformed basement rock have been intersected in core LB-07A. These impactites formed chiefly from metasediments (metagreywacke, phyllite and shale) with minor granitoid. The suevites and polymict lithic breccias alternate and form what has been termed the upper impactites unit. They differ by the presence or

absence of melt particles. The upper impactites are underlain by the lower impactites, which comprise monomict breccias after either metagreywacke or shale. The impactites are underlain by deformed basement rock (metagreywacke, shale and phyllite), and a number of suevite injections are found in both the lower impactites and basement metasediments.

3. Evidence of pre- and post-impact alteration is apparent. The pre-impact alteration includes quartz veining, formation of oxides in metasediments, sulphide formation, sericitization of feldspars and chloritization of biotite. The post-impact alteration, in the form of an impact-induced hydrothermal system, produced carbonate (calcite) in the form of veins and pods, quartz and chlorite veining and sulphide formation in the breccia matrices, which collectively constrain an upper temperature limit of 300 ^{o}C.

4. Traces of the meteoritic projectile were not found in the within-crater polymict breccias by PGE and Os isotope analysis. This is likely owing to high target rock indigenous abundances, which seem to mask any possible meteoritic signature. Also, it is possible that a low angle of impact may have influenced the distribution of any meteoritic projectile.

5. The out-of-crater suevites are distinct from the within-crater suevites in terms of clast composition, geochemistry, melt proportion and shock state of clasts. They contain substantially more granite clasts than the within-crater suevites, and lack carbonate clasts. The melt particles are substantially more abundant and larger than those from within the crater. There is a higher proportion of moderately to highly shocked clastic material in the out-of-crater suevites.

6. Melt particle compositions of the within-crater and out-of-crater suevites indicate that these particles were formed as mixes of minerals from the different target rocks, rather than as bulk target rock melts. The melt particle compositions of the suevites from south of the crater are very similar to those from within the crater and are distinct from the melt particle compositions from the north of the crater.

7. The shock pressures experienced by clasts in the crater-fill material are substantially lower than predicted by pre-drilling numerical modeling.
8. No melt sheet has been intersected.
9. The impactite distribution is consistent with a low-angle oblique impact with the projectile impacting from the east.
10. It is likely that the apparent intercalation of the within-crater suevites and polymict lithic breccias resulted from either slumping off the crater walls or from lateral movement of material within the crater, combined with minor admixture of fallback material from the ejecta curtain and/or ejecta plume. This would result in a lower average shock state than for the material from outside of the crater, which could represent material deposited from the ejecta curtain and/or ejecta plume.
11. The local geological differences in different sectors of the transient crater may be responsible for the different clast populations in the within-crater and out-of-crater suevites. Additionally, the differences in the clast content between the out-of-crater suevites may have resulted from a laterally differentiated ejecta curtain and/or ejecta plume.

Observations of petrographic and geochemical characteristics of impactites provide first order insight into the differences and similarities of impactites. These, in turn, substantiate or negate modeling results concerning impact cratering processes. These detailed studies of the Bosumtwi crater impactites reveal that much is still unknown about specific impactite-forming processes, such as the controls over the variable contributions from the ejecta curtain and/or ejecta plume to within and out-of-crater impactites.

Crater-forming processes are dependent upon a complex set of factors. These include the type of target rocks, how they occur with respect to each other (intrusives) and the angle of impact. The immediate effects of an impact event can currently only be

generalized, and it is evident that only through the continued study of craters with different characteristics (i.e., target rock architecture and type) can further understanding into crater- and impactite-forming processes be gained.

7.10 Recommendations

There are a number of target areas which have been highlighted from this study and should be addressed in future studies of the Bosumtwi impact crater and surrounds. As has been noted, there is a lack of outcrop of impactite units around Lake Bosumtwi – either owing to non-deposition of impactites or elimination of these units through extensive tropical weathering. In particular, an equivalent for the "Bunte Breccia" of the Ries crater has been proposed, but not fully investigated. It is proposed that further studies of the impactites of the Bosumtwi crater focus on extensive fieldwork and detailed mapping, possibly with drilling of a number of short boreholes in all areas surrounding the crater (i.e., not constrained to known suevite sites). This would help to establish the extent of continuity of the impactite units and identify new impactite units.

Another problem has been the lack of detectable meteoritic component and the difficulty in finding such a component in the within and out-of-crater impactites. It is proposed that detailed laser ablation ICP-MS on melt particles from both within and in particular out-of-crater suevites be conducted, as it has been proposed that much of the meteoritic component was ejected from the crater into the distal ejecta (tektites).

Finally, in order to establish lateral continuity of the impactite units within the crater, drilling to the east and/or south of the previous drill sites within the crater is recommended.

References

Ahrens T.J. and O'Keefe J.D. (1978). Energy and mass distributions of impact ejecta blankets on the moon and Mercury. Proceedings of the 9th Lunar and Planetary Science Conference, 3787-3802.

Aleva G.J. (ed.) (1994). Laterites. Concepts, Geology, Morphology and Chemistry. International Soil Reference and Information Centre. Wageningen, Netherlands, 169 pp.

Allaby A. and Allaby M., eds. (1999). *Dictionary of Earth Sciences*, 2nd edition. Oxford University Press, Oxford, 619 pp.

Allègre C.J. and Luck J-M. (1980). Osmium isotopes as petrogenetic and geological indicators. Earth and Planetary Science Letters, **48**, 148-154.

Alvarez W. (1996). Trajectories of ballistic ejecta from the Chicxulub crater. In *The Cretaceous-Tertiary event and other catastrophes in Earth history* (G. Ryder, D. Fastovsky and S. Gartner, eds.). Geological Society of America Special Paper, **307**, 141-150.

Alvarez W., Claeys P. and Kieffer S.W. (1995). Emplacement of Cretaceous-Tertiary boundary shocked quartz from Chicxulub crater. Science, **269**, 930-935.

Ames D.E., Kjarsgaard I.M., Pope K.O., Dressler B. and Pilkington M. (2004). Secondary alteration of the impactite and mineralization in the basal Tertiary sequence, Yaxcopoil-1, Chicxulub impact crater, Mexico. Meteoritics and Planetary Science, **39**, 1145-1167.

Anders E. and Grevesse N. (1989). Abundances of the elements: Meteoritic and solar. Geochimica et Cosmochimica Acta, **53**, 197-214.

Artemieva N. (2002). Tektite origin in oblique impact: Numerical modelling. In *Impacts in Precambrian shields* (J. Plado and L. Pesonen, eds.). Impact Studies, **2,** Springer-Verlag, Berlin, 257-276.

Artemieva N. (2007). Possible reasons of shock melt deficiency in the Bosumtwi drill cores. Meteoritics and Planetary Science, **42**, 883-894

Artemieva N.A., Karp T. and Milkereit B. (2004). Investigating the Lake Bosumtwi impact structure: Insight from numerical modeling. Geochemistry, Geophysics, Geosystems, **5**, doi: 10.1029/2004GC000733.

Bajpai A.C., Mustoe L.R. and Walker D. (1974). *Engineering Mathematics.* Wiley, London, 793 pp.

Barnes S.-J., Naldrett A.J. and Gorten M.P. (1985). Origin of the fractionation of platinum-group elements in terrestrial magmas. Chemical Geology, **53**, 197-214.

Bischoff L. and Oskierski W. (1987). Fractures, pseudotachylite veins, and breccia dikes in the crater floor of the Rochechouart impact structure, SW-France, as indicators of crater-forming processes. In *Research in terrestrial impact structures* (J. Pohl, ed.), Earth Evolution Science, International Monograph Series, Friedrich Vieweg and Son, Wiesbaden, 5-29.

Boamah D. (2001). *Bosumtwi Impact Structure, Ghana : Petrography and geochemistry of target rocks and impactites, with emphasis on shallow drilling project around the crater*. PhD Thesis, unpublished, University of Vienna, Vienna, Austria, 262 pp.

Boamah D. and Koeberl C. (2002). Geochemistry of solids from the Bosumtwi impact structure, Ghana, and relationship to radiometric airborne geophysical data. In *Impacts in Precambrian shields* (J. Plado and L. Pesonen, eds.). Impact Studies, **2**, Springer-Verlag, Berlin, 211-255.

Boamah D. and Koeberl C. (2003). Geology and geochemistry of shallow drill cores from the Bosumtwi impact structure, Ghana. Meteoritics and Planetary Science, **38**, 1137-1159.

Boamah D. and Koeberl C. (2006). Petrographic studies of "fallout" suevite from outside the Bosumtwi impact crater, Ghana. Meteoritics and Planetary Science, **41**, 1761-1774.

Brandt D. (1999). The Tswaing Crater: One of the World's Best Preserved and Museum Plans for the Site. Meteoritics, **34**, A17.

Brandt D. and Reimold W.U. (1995). The geology of the Pretoria Saltpan impact structure and the surrounding area. South African Journal of Geology, **98**, 287-303.

Brooks K., Scholz C.A., King J.W., Peck J., Overpeck J.T., Russell J.M. and Amoako P.Y.O. (2005). Late-Quaternary low-stands of Lake Bosumtwi, Ghana: evidence from high-resolution seismic reflection and sediment-core data. Palaeogeography, Palaeoclimatology, Palaeoecology, **216**, 235-249.

Bunch T.E., Dence M.R. and Cohen A.J. (1967). Natural terrestrial maskelynite. American Mineralogist, **52**, 244-253.

CANMET (1994). Catalogue of Certified Reference Materials. Canadian Certified Reference Materials project **94-1E**, 82 pp.

Channell J., Mazaud A., Sullivan P., Turner S. and Raymo M. (2002). Geomagnetic excursions and paleointensitites in the 0.9-2.15 MA interval of the Matuyama Chron at ODP Site 983 and 984 (Iceland basin). Journal of Geophysical Research, **107**, 1-14, doi: 10.1029/2001 JB000491.

Chao E.C.T. (1968). Pressure and temperature histories of impact metamorphosed rocks – based on petrographic observations. In *Shock metamorphism of natural materials* (B.M. French and N.M. Short, eds.). Mono Book Corporation, Baltimore, 135-158.

Chao E.C.T., Fahey J.J. and Littler J. (1961). Coesite from Wabar Crater, near Al Hadida, Arabia. Science, **133**, 882-883.

Chao E.C.T., Fahey J.J., Littler J. and Milton D.J. (1962). Stishovite, SiO_2, a very high pressure new mineral from Meteor Crater, Arizona. Journal of Geophysical Research, **67**, 419-421.

Chayes, F. (1949). A simple point counter for thin-section analysis. American Mineralogist, **34**, 1-11.

Chen M., Sharp T.G., El Goresy A.E., Wopenka B. and Xie X. (1996). The majorite-pyrope + magnesiowüstite assemblage: constraints on the history of shock veins in chondrites. Science, **271**, 1570–1573.

Cintala M.J. and Grieve R.A.F. (1994). The effects of differential scaling of impact melt and crater dimensions on lunar and terrestrial craters: Some brief examples. In *Large meteorite impacts and planetary evolution* (B.O. Dressler, R.A.F. Grieve and V.L. Sharpton, eds.). Geological Society of America Special Paper, **293**, 51–59.

Cintala M.J., Berthoud L. and Hörz F. (1999). Ejection-velocity distributions from impacts into coarse-grained sand. Meteoritics and Planetary Science, **34**, 605-623.

Collins G.S., Melosh H.J., Morgan J.V. and Warner M.R. (2002). Hydrocode simulations of Chicxulub crater collapse and peak-ring formation. Icarus, **157**, 24-33.

Colodner D.C., Boyle E.A. and Edmond J.M. (1993). Determination of rhenium and platinum in natural waters and sediments and iridium in sediments by flow injection isotope dilution inductive coupled plasma mass spectrometry. Analytical Chemistry, **65**, 1419-1425.

Dachille F., Zeto R.J. and Roy R. (1963). Coesite and stishovite: Stepwise reversal transformations. Science, **140**, 991-993.

Dai X., Boamah D., Koeberl C., Reimold W.U., Irvine G. and McDonald I. (2005). Bosumtwi impact structure, Ghana: Geochemistry of impactites and target rocks, and search for a meteoritic component. Meteoritics and Planetary Science, **40**, 1493–1511.

Danuor S.K. (2004). *Geophysical investigations of the Bosumtwi impat crater and comparison with terrestrial meteorite craters of similar age and size.* PhD thesis, unpublished, Kwame Nkrumah University of Science and Technology, Kumasi, Ghana, 132 pp.

Danuor S.K. and Menyeh, A. (2007). Results of pre-drilling potential field measurements at the Bosumtwi crater. Meteoritics and Planetary Science, **42**, 541-547.

Davis G.H. and Reynolds S.J. (1996*). Structural Geology of Rocks and Regions*, 2nd Edition. John Wiley and Sons, New York, 776 pp.

Davis D.W., Hirdes W., Schaltegger U. and Nunoo E.A. (1994). U-Pb age constraints on deposition and provenance of Birimian and gold-bearing Tarkwaian sediments in Ghana, West Africa. Precambrian Research, **67**, 89-107.

Deer W.A., Howie R.A. and Zussman J. (1971). *An Introduction to the Rock Forming Minerals.* Longman Group Limited, London, 528 pp.

Dence M.R. (1968). Shock zoning at Canadian craters: Petrography and structural implications. In *Shock metamorphism of natural materials* (B.M. French and N.M. Short, eds.). Mono Book Corporation, Baltimore, 169-184.

DePaolo D.J. and Wasserburg G.J. (1979). Petrogenetic mixing models and Nd-Sr isotopic patterns. Geochimica et Cosmochimica Acta, **43**, 615-627.

Deutsch A. (2006). Lake Bosumtwi drilling project: Shock metamorphism in rocks from core BCDP-8A versus experimental data (abstract #1327). 37th Lunar and Planetary Science Conference. CD-ROM.

Deutsch A., Heinrich V. and Luetke S. (2006). The Lake Bosumtwi Impact Crater Drilling Project (BCDP): Lithological profile of wellhole BCDP-8A (abstract #1292). 37th Lunar and Planetary Science Conference. CD-ROM.

Deutsch A., Luetke S. and Heinrich V. (2007). The ICDP Lake Bosumtwi impact crater scientific drilling project (Ghana): Core LB-08A litho-log, related ejecta, and shock recovery experiments. Meteoritics and Planetary Science*,* **42**, 635-654.

Dressler B.O. and Sharpton V.L. (1997). Breccia formation at a complex impact crater: Slate Islands, Lake Superior, Ontario, Canada. Tectonophysics, **275**, 285-311.

Dressler B.O. and Reimold W.U. (2001). Terrestrial impact melts and glasses. Earth-Science Reviews, **56**, 205-284.

Dressler B.O. and Reimold W.U. (2004). Order or chaos? Origin and mode of emplacement of breccias in floors of large impact structures. Earth-Science Reviews, **67**, 1-54.

Dressler B.O., Grieve R.A.F. and Sharpton V.L., eds. (1994). Large Meteorite Impact and Planetary Evolution. Geological Society of America Special Paper, **293**, 348 pp.

Durrani S.A. and Khan H.A. (1971). Ivory Coast microtektites: Fission track age and geomagnetic reversals. Nature, **232**, 320-322.

Earth Impact database: http://www.unb.ca/passc/ImpactDatabase/index.html

Elbra T., Kontny A., Pesonen L.J., Schleifer N. and Schell C. (2007). Petrophysical and paleomagnetic data of drill cores from the Bosumtwi impact structure, Ghana. Meteoritics and Planetary Science, **42**, 829-838.

El Goresy A. (1966). Metallic spherules in Bosumtwi crater glasses. Earth and Planetary Science Letters, **1**, 23-24.

El Goresy A., Fechtig H. and Ottemann T. (1968). The opaque minerals in impactite glasses. In *Shock metamorphism of natural materials* (B.M. French and N.M. Short, eds.). Mono Book Corporation, Baltimore, 531-554.

El Goresy A., Dubrovinsky L., Sharp T.G., Saxena S.K., Chen M. (2000). A monoclinic post-stishovite polymorph of silica in the Shergotty meteorite. Science, **288**, 1632–1634.

Evans N.J., Gregoire D.C., Grieve R.A.F., Goodfellow W.D. and Veizer J. (1993). Use of platinum-group elements for impactor identification: Terrestrial impact craters and Cretaceous-Tertiary boundary. Geochimica et Cosmochimica Acta, **57**, 3737–3748.

Farago M.E., Hutchinson E.J., Simpson P.R. and Thornton I. (2005). Recent increases in platinum metals in the environment from vehicle catalytic converters. Applied Earth Science (IMM Transactions section B), **114**, 182-192.

Fergusson M. (1902). Lake Bosumchwi. Geographical Journal, **19**, 370-372.

Ferrière L., Koeberl C. and Reimold W.U. (2007a). Drill core LB-08A, Bosumtwi impact structure, Ghana: Petrographic and shock metamorphic studies of material from the central uplift. Meteoritics and Planetary Science, **42**, 611-633.

Ferrière L., Koeberl C., Reimold W.U. and Mader D. (2007b). Drill core LB-08A, Bosumtwi impact structure, Ghana: Geochemistry of fallback breccia and basement samples from the central uplift. Meteoritics and Planetary Science, **42**, 689-708.

Ferrière L., Koeberl C. and Reimold W.U. (2009). Characterization of ballen quartz and cristobalite in impact breccias: new observations and constraints on ballen formation. European Journal of Mineralogy*, in press*.

Feybesse J.-L., Billa M., Guerrot C., Duguey E., Lescuyer J.-L., Milesi J.-P. and Bouchot V. (2006).The Paleoproterozoic Ghanaian province: Geodynamic model and ore controls, including regional stress modeling. Precambrian Research, **149**, 149-196.

Fredriksson K., Dube A., Milton D.J. and Balasundaram M.S. (1973). Lonar Lake, India: An impact crater in basalt. Science, **180**, 862-864.

French B.M. (1968). Shock metamorphism as a geological process. In *Shock metamorphism of natural materials* (B.M. French and N.M. Short, eds.). Mono Book Corporation, Baltimore, 1-17.

French B.M. (1990). 25 years of the impact-volcanic controversy: Is there anything new under the sun or inside the Earth. EOS Transactions of the American Geophysical Union, **71**, 411-414.

French B.M. (1998). Traces of Catastrophe: A Handbook of Shock-Metamorphic Effects in Terrestrial Meteorite Impact Structures. Lunar and Planetary Institute Contribution No. **954**, Lunar and Planetary Institute, Houston, Texas, 120 pp.

French B.M. and Short N.M., eds. (1968). *Shock Metamorphism of Natural Materials.* Mono Book Corporation, Baltimore, 644 pp.

French B.M., Koeberl C., Gilmour I., Shirey S.B., Dons J.A. and Naterstad J. (1997). The Gardnos impact structure, Norway: Petrology and geochemistry of target rocks and impactites. Geochimica et Cosmochimica Acta, **61**, 873-904.

Gall H., Müller D., Stöffler D. (1975). Verteilung, Eigenschaften und Entstehung der Auswurfmassen des Impaktkraters Nördlinger Ries. Geologische Rundschau, **64**, 915-974.

Garvin J.B. and Schnetzler C.C. (1994). The Zhamanshin impact feature: a new class of complex crater? In *Large meteorite impacts and planetary evolution* (B.O. Dressler, R.A.F. Grieve, V.L. Sharpton, eds.). Geological Society of America Special Paper, **293,** 249-257.

Gault D.E. and Wedekind J.A. (1978). Experimental studies of oblique impact. Proceedings of the 9th Lunar and Planetary Science Conference, 3843-3875.

Gault D.E, Quaide W.L. and Overbeck V.R. (1968). Impact cratering mechanisms and structures. In *Shock metamorphism of natural materials* (B.M. French and N.M. Short, eds.). Mono Book Corporation, Baltimore, 87-99.

Gentner W., Lippolt H.J. and Müller O. (1964). Das Kalium-Argon-Alter der Bosumtwi Kraters in Ghana und die chemische Beschaffenheit seiner Gläser. Zeitschrift für Naturforschung, **19A**, 150-153.

Gentner W., Kleinmann B. and Wagner G.A. (1967). New K-Ar and fission track ages of impact glasses and tektites. Earth and Planetary Science Letters, **2**, 83-86.

Glass B.P. (1968). Glassy objects (microtektites?) from deep-sea sediments near the Ivory Coast. Science, **161,** 891-893.

Glass B.P. (1969). Chemical composition of Ivory Coast microtektites. Geochimica et Cosmochimica Acta, **33**, 1135-1147.

Glass B.P., Kent D.V., Schneider D.A. and Tauxe L. (1991). Ivory Coast microtektite strewn field: Description and relation to the Jaramillo geomagnetic event. Earth and Planetary Science Letters, **107**, 182-196.

Glass B.P., Liu S., Leavens P.B. (2002). Reidite: An impact-produced high-pressure polymorph of zircon found in marine sediments. American Mineralogist, **87**, 562–565.

Goderis S., Tagle R., Schmitt R.T., Erzinger J. and Claeys P. (2007). Platinum group elements provide no indication of a meteoritic component in ICDP cores from the Bosumtwi crater, Ghana. Meteoritics and Planetary Science, **42**, 731–741.

Goltrant O., Cordier P. and Doukhan J.-C. (1991). Planar deformation features in shocked quartz: A transmission electron microscopy investigation. Earth and Planetary Science Letters, **106**, 103-115.

Goltrant O., Leroux H., Doukan J.-C. and Cordier P. (1992). Formation mechanisms of planar deformation features in naturally shocked quartz. Physics of the Earth and Planetary Interiors, **74**, 219-240.

Govindaraju, K. (1989). 1989 compilation of working values and sample description for 272 geostandards. Geostandards Newsletter, **13**, 1-113.

Gratz A.J., Nellis W.J., Christie J.M., Brocious W., Swegle J., Cordier P. (1992). Shock metamorphism of quartz with initial temperatures – 170 to +1000°C. Physics and Chemistry of Minerals, **19**, 267–288.

Graup G. (1999). Carbonate-silicate immiscibility upon impact melting: Ries crater, Germany. Meteoritics and Planetary Science, **34**, 425-438.

Grieve R.A.F. (1987). Terrestrial impact structures. Annual Review of Earth and Planetary Sciences, **15**, 245-270.

Grieve R.A.F. (1990). Impact cratering on the Earth. Scientific American, **262**, 66-73.

Grieve R.A.F. (1991). Terrestrial impact: the record in the rocks. Meteoritics, **26**, 175-194.

Grieve R.A.F. and Therriault A. (2000). Vredefort, Sudbury, Chicxulub: Three of a kind? Annual Reviews of Earth and Planetary Science, **28**, 305-338.

Grieve R.A.F. and Cintala M.J. (1992). An analysis of differential impact melt-crater scaling and implications for the terrestrial impact record. Meteoritics, **27**, 526-538.

Grieve R.A.F., Robertson P.B., and Dence M.R. (1981). Constraints on the formation of ring impact structures, based on terrestrial data. In *Multi-ring basins: formation and evolution,* (P.H. Schultz and R.B. Merrill, eds.). *Proceedings of the Lunar and Planetary Science Conference* **12A**, Pergamon, New York, 37-57.

Grieve R.A.F., Langenhorst F. and Stöffler D. (1996). Shock metamorphism of quartz in nature and experiment: II. Significance in geoscience. Meteoritics and Planetary Science, **31**, 6-35.

Hall J.B., Swaine M.D. and Talbot M.R. (1978). An early Holocene leaf flora from Lake Bosumtwi, Ghana. Palaeogeography, Palaeoclimatology, Palaeoecology, **24**, 247-261.

Harker R.I. and Tuttle O.F. (1956). Experimental data on the PCO_2-T curve for the reaction: calcite + quartz = wollastonite + carbon dioxide. American Journal of Science, **254**, 239-256.

Hassler, D.R., Peucker-Ehrenbrink, B. and Ravizza, G.E. (2000). Rapid determination of Os isotopic composition by sparging OsO_4 into a magnetic-sector ICP-MS. Chemical Geology, **166**, 1-14.

Henkel H. and Pesonen L.J. (1992) Impact craters and craterform structures in Fennoscandia. Tectonophysics, **216**, 31-40.

Hildebrand A.R., Penfield G.T., Kring D.A., Pilkington M., Camargo Z, A., Jacobsen S.B. and Boynton W.V. (1991). Chicxulub crater: A possible Cretaceous/Tertiary boundary impact crater on the Yucatán Peninsula, Mexico. Geology, **19**, 867-871.

Hirdes W. and Nunoo B. (1994). The Proterozoic paleoplacers at Tarkwa gold mine, SW Ghana: Sedimentology, mineralogy, and precise age dating of the Main Reef and West Reef, and bearing of the investigations on source area aspects. In *Metallogenesis of selected gold deposits in Africa*. Geologisches Jahrbuch, **D100**, 247-311.

Hirdes W., Davis D.W., Lüdtke G. and Konan G. (1996). Two generations of Birmian (Paleoproterozoic) volcanic belts in northeastern Côte d'Ivoire (West Africa): consequences for the "Birimian controversy". Precambrian Research, **80**, 173-191.

Horan M.F. and Walker R.J. (2000). Abundances of highly siderophile elements in chondrites (abstract # 1375). 31st Lunar and Planetary Science Conference. CD-ROM.

Hörz F. (1982). Ejecta of the Ries crater, Germany. In *Geological implications of impacts of large asteroids and comets on the Earth* (L.T Silver and P.H. Schultz, eds.). Geological Society of America Special Paper, **190**, 39-55.

Hörz F., Horst G., Hüttner R. and Oberbeck V.R. (1977). Shallow drilling in the "Bunte Breccia" impact deposits, Ries Crater, Germany. In *Impact and explosion cratering* (D.J. Roddy, R.O. Pepin and R.B. Merrill, eds.). Pergamon Press, New York, 425-448.

Hörz F., Ostertag R. and Rainey D.A. (1983). Bunte Breccia of the Ries: continuous deposits of large impact craters. Reviews of Geophysics and Space Physics, **21**, 1667-1725.

Hough R.M., Pillinger C.T., Gilmour I., Langenhorst F. and Montanari A. (1997). Diamonds from the iridium rich K-T boundary layer at Arroyo el Mimbral, Tamaulipas, Mexico. Geology, **11**, 1019–1022.

Huffman A.R. and Reimold W.U. (1996). Experimental constraints on shock-induced microstructures in naturally deformed silicates. Tectonophysics, **256**, 165-217.

Ivanov B.A., Badukov D.D., Yakovlev O.I., Gerasimov M.V., Dikov Y.P., Pope K.O. and Ocampo A.C. (1996). Degassing of sedimentary rocks due to Chicxulub impact: Hydrocode and physical simulations. In *The Cretaceous - Tertiary event and other catastrophes in Earth history* (G. Ryder, D. Fastovsky and S. Gartner, eds.). Geological Society of America, Boulder, 125-139.

Jarosewich, E., Clarke, R.S. Jr. and Barrows, J.N., eds. (1987). The Allende meteorite reference sample. Smithsonian Contribution to Earth Science, **27**, 1-49.

Jochum K. (1996). Rhodium and other platinum-group elements in carbonaceous chondrites. Geochimica et Cosmochimica Acta, **60**, 3353–3357.

Jones W.B. (1985a). Chemical analyses of Bosumtwi crater target rocks compared with Ivory Coast tektites. Geochimica et Cosmochimica Acta, **49**, 2569-2576.

Jones W.B. (1985b). The origin of the Bosumtwi crater, Ghana – an historical overview. Proceedings of the Geological Association (London), **96,** 275-284.

Jones W.B., Bacon M. and Hastings D.A. (1981). The Lake Bosumtwi impact crater, Ghana. Geological Society of America Bulletin, **92**, 342-349.

Junner N.R. (1937). The geology of the Bosumtwi caldera and surrounding country. Gold Coast Geological Survey Bulletin, **8**, 1-38.

Karikari F., Ferrière L., Koeberl C., Reimold W.U. and Mader D. (2007). Petrography, geochemistry and alteration of target rocks from the Bosumtwi impact structure, Ghana. Meteoritics and Planetary Science*,* **42**, 513-540.

Karp T., Milkereit B., Janle J., Danuor S.K., Pohl J., Berckhemer H. and Scholz C.A. (2002). Seismic investigation of the Lake Bosumtwi impact crater: Preliminary results. Planetary Space Science, **50**, 735-742.

Kesse, G.O. (1985). *The Mineral and Rock Resources of Ghana.* Balkema, Rotterdam, 610 pp.

Kieffer S.W. and Simonds C.H. (1980). The role of volatiles and lithology in the impact cratering process. Reviews of Geophysics and Space Physics, **18**, 143-181.

Kieffer S.W., Phakey P.P. and Christie J.M. (1976). Shock processes in porous quartzite: Transmission electron microscope observations and theory. Contributions to Mineralogy and Petrology, **59**, 41–93.

Kinnaird J.A. (2005). Geochemical evidence for multiphase emplacement in the southern Platreef. Applied Earth Science (IMM Transactions section B), **114**, 225–242.

Kitson A.K. (1916). The Gold Coast: some consideration of its structure, people and natural history. Geographical Journal, **48**, 369-392.

Koeberl C. (1993). Instrumental neutron activation analysis of geochemical and cosmochemical samples: A fast and reliable method for small sample analysis. Journal of Radioanalytical and Nuclear Chemistry, **168**, 47-60.

Koeberl C. (1994a). African meteorite impact craters: Characteristics and geological importance. Journal of African Earth Science, **18**, 263-295.

Koeberl C. (1994b). Neutron Activation Analysis. In *Advanced mineralogy, volume 2 Methods and instrumentations: results and recent developments* (A.S. Marfunin, ed.). Springer Verlag, Berlin, 322-329.

Koeberl C. (2002). Mineralogical and geochemical aspects of impact craters. Mineralogical Magazine, **66**, 745-768.

Koeberl C. (2007). The geochemistry of impacts and cosmochemistry of impacts. In *Treatise of Geochemistry*, online edition, volume **1** (A. Davis, ed.). Elsevier, p. 1.28.1-1.28.52, doi: 10.1016/B978-008043751-4/00228-5.

Koeberl C. and Martínez-Ruiz F. (2003). The Stratigraphic Record of Impact Events: A Short Overview. In *Impact markers in the stratigraphic record* (C. Koeberl and F. Martínez-Ruiz, eds.). Impact Studies Series, Springer-Verlag, Berlin, 1-40.

Koeberl C. and Shirey S.B. (1993). Detection of a meteoritic component in Ivory Coast tektites with rhenium-osmium isotopes. Science, **261**, 595-598.

Koeberl C. and Reimold W.U. (2004). Post-impact hydrothermal activity in meteorite impact craters and potential opportunities for life. In *Bioastronomy 2002: life among the stars* (R.P. Norris and F.H. Stootman, eds.). Astronomical Society of the Pacific, San Francisco, 299–304.

Koeberl C. and Reimold W.U. (2005). Bosumtwi impact crater, Ghana (West Africa): An updated and revised geological map, with explanations. Jahrbuch der Geologischen Bundesanstalt, Wien (Yearbook of the Geological Survey of Austria) Vienna, **145**, 31-70 and 1 map, 1:50,000.

Koeberl C. and Milkereit B. (2007). Continental Drilling and the Study of Impact Craters and Processes - an ICDP Perspective. In *Continental Scientific Drilling* (U. Harms, C. Koeberl and M.D. Zoback, eds.). Springer, Heidelberg, 95-161.

Koeberl C., Sharpton V.L., Schuraytz B.C., Shirey S.B., Blum J.D. and Marin L.E. (1994a). Evidence for a meteoritic component in impact melt rock from the Chicxulub structure. Geochimica et Cosmochimica Acta, **58**, 1679–1684.

Koeberl C., Reimold W.U., Shirey S.B. and Le Roux F.G. (1994b). Kalkkop crater, Cape Province, South Africa: confirmation of impact origin using osmium isotope systematics. Geochimica et Cosmochimica Acta, **58**, 1229–1234.

Koeberl C., Bottomley R.J., Glass B.P. and Storzer D. (1997a). Geochemistry and age of Ivory Coast tektites and microtektites. Geochimica and Cosmochimica Acta, **61**, 1745-1772.

Koeberl C., Masaitis V.L., Shafranovsky G.I., Gilmour I., Langenhorst F. and Schrauder M. (1997b). Diamonds from the Popigai impact structure, Russia. Geology, **25**, 967–970.

Koeberl C., Bottomley R.J., Glass B.P. and Storzer D. (1997c). New studies of the Bosumtwi impact structure, Ghana: The 1997 field season (abstract). Meteoritics and Planetary Science, **32**, A72-A73.

Koeberl C., Reimold. W.U., Blum J.D. and Chamberlain C.P. (1998). Petrology and geochemistry of target rocks from the Bosumtwi impact structure, Ghana, and comparison with Ivory Coast tektites. Geochimica et Cosmochimica Acta, **62**, 2179-2196.

Koeberl C., Shukolyukov A. and Lugmair G. (2004). An ordinary chondrite impactor composition for the Bosumtwi impact structure, Ghana, West Africa: Discussion of siderophile element contents and Os and Cr isotope data (abstract #1256). 35th Lunar and Planetary Science Conference. CD-ROM.

Koeberl C., Milkereit B., Overpeck J.T., Scholz C.A., Peck J. and King J. (2005). The 2004 ICDP Bosumtwi impact crater, Ghana, West Africa, drilling project: A first report (abstract #1830). 36th Lunar and Planetary Science Conference. CD-ROM.

Koeberl C., Milkereit B., Overpeck J.T., Scholz C.A., Reimold W.U., Amoako P.Y.O., Boamah D., Claeys, P., Danuor S., Deutsch A., Hecky R.E., King J., Newsom H., Peck J. and Schmitt D.R. (2006a). An international and multidisciplinary drilling project into a young complex impact structure: The 2004 ICDP Bosumtwi impact crater, Ghana, drilling project—An overview (abstract #1859). 37th Lunar and Planetary Science Conference. CD-ROM.

Koeberl C., Brandstätter F., Hecht L., Reimold W. U., Peck J. and King J. (2006b). Uppermost impact fallout layer in a drill core at the Bosumtwi impact crater (Ghana): A preliminary study (abstract # 1552). 37th Lunar and Planetary Science Conference. CD-ROM.

Koeberl C., Milkereit B., Overpeck J. T., Scholtz C. A., Amoako P. Y. O., Boamah D., Danuor S., Karp T., Kueck J., Hecky R. E., King J. W. and Peck J. (2007a). An international and multidisciplinary drilling project into a young complex impact structure: The 2004 ICDP Bosumtwi Crater Drilling Project - An overview. Meteoritics and Planetary Science, **42**, 483-511.

Koeberl C., Brandstätter F., Glass B.P., Hecht L., Mader D. and Reimold W.U. (2007b). Uppermost impact fallback layer in the Bosumtwi crater (Ghana): Mineralogy, geochemistry, and comparison with Ivory Coast tektites. Meteoritics and Planetary Science, **42**, 709-729.

Kolbe P., Pinson W. H., Saul J. M. and Miller E.W. (1967). Rb-Sr study on country rocks of the Bosumtwi crater, Ghana. Geochimica et Cosmochimica Acta, **31**, 869–875.

Kontny A. and Just J. (2006). Magnetic mineralogy and rock magnetic properties of impact breccias and crystalline basement rocks from the BCDP-drillings 7A and 8A (abstract #1343). 37th Lunar and Planetary Science Conference. CD-ROM.

Kontny A. Elbra T., Just J., Pesonen L.J., Schleicher A.M. and Zolk J. (2007). Petrography and shock-related remagnetization of pyrrhotite in drill cores from the Bosumtwi Impact Crater Drilling Project, Ghana. Meteoritics and Planetary Science, **42**, 811–827.

Kretz R. (1983). Symbols for rock-forming minerals. American Mineralogist, **68**, 277-279.

Kring D.A. (2005). Hypervelocity collisions into continental crust composed of sediments and an underlying crystalline basement: Comparing the Ries (~24 km) and Chicxulub (~180 km) impact craters. Chemie der Erde, **65**, 1–46.

Kring D.A. (2007). Guidebook to the Geology of Barringer Meteorite Crater (a.k.a. Meteor Crater). Lunar and Planetary Institute Contribution No. 1355, Lunar and Planetary Institute, Houston, 154 pp.

Lacroix A. (1934). Sur la découverte de tektites à la Côte d'Ivoire. Comptes Rendus de l'Academie des Sciences Paris, **199**, 1539-1542.

Lambert P. (1977). The Rochechouart crater: Shock zoning study. Earth and Planetary Science Letters, **35**, 258–268.

Lambert P. (1981). Breccia dikes: Geological constraints on the formation of complex craters. In *Multi-ring basins: formation and evolution* (P.H. Schultz and R.B. Merrill, eds.). Proceedings of the Lunar and Planetary Science Conference, **12A,** Pergamon, New York, 59-78.

Lambert P. (2008). Impact deposits at Rochechouart-Chassenon (abstract). In *Large Meteorite Impacts and Planetary Evolution IV*, Lunar and Planetary Institute Contribution No. **1423**, Lunar and Planetary Institute, Houston, 122-123.

Langenhorst F. (1994). Shock experiments on α- and β- quartz: II. X-ray investigations. Earth and Planetary Science Letters, **128**, 638–698.

Langenhorst F. (2002). Shock metamorphism of some minerals: Basic introduction and microstructural observations. Bulletin of the Czech Geological Survey, **77**, 265-282.

Langenhorst F. and Deutsch A. (1994). Shock experiments on pre-heated α-and β- quartz: I. Optical and density data. Earth and Planetary Science Letters, **125**, 407–420.

Langenhorst F. and Poirier J.P. (2000). Anatomy of black veins in Zagami: Clues to the formation of high-pressure phases. Earth and Planetary Science Letters, **184**, 37–55.

Langenhorst F., Joreau P. and Doukhan J.C. (1995). Thermal and shock metamorphism of the Tenham meteorite: a TEM examination. Geochimica et Cosmochimica Acta, **59**, 1835–1845.

Lapidus D.F. and Winstanley I. (1990). *Collins Dictionary of Geology*. Collins, London, 565 pp.

Leleyter L., Probst J-L., Depetris, P., Haida S., Mortatti J., Rouault R. and Samuel J. (2007). Trace element speciation in river sediments. International Journal of Environmental and Analytical Chemistry, *in press.*

Leroux H., Reimold W.U. and Doukhan J.-C. (1994). A TEM investigation of shock metamorphism in quartz from the Vredefort dome, South Africa. Tectonophysics, **230**, 223-239.

Leube A., Hirdes W., Mauer R. and Kesse G.O. (1990). The Early Proterozoic Birimian Supergroup of Ghana and some aspects of its associated gold mineralization. Precambrian Research, **46,** 136-165.

L'Heureux E. and Milkereit B. (2007). Impactites as a random medium—Using variations in physical properties to assess heterogeneity within the Bosumtwi meteorite impact crater. Meteoritics and Planetary Science, **42**, 849–858.

Lippolt H.J. and Wasserburg G.J. (1966). Rubidium-Strontium-Messungen an Gläsern vom Bosumtwi-Krater und an Elfenbeinküsten-Tektiten. Zeitschrift für Naturforschung, **12A**, 226-231.

Littler J., Fahey J.J., Dietz R.S. and Chao E.C.T. (1961). Coesite from the Lake Bosumtwi crater, Ashanti, Ghana. Geological Society of America Special Paper, **68**, 218.

Love S.G., Hörz F. and Brownlee D.E. (1993). Target porosity effects in impact cratering and collisional disruption. Icarus, **105**, 216–224.

Maier W.D., Andreoli M.A.G., McDonald I., Higgins M.D., Boyce A.J., Shukolyukov A., Lugmair G.W., Ashwal L.D., Graser P., Ripley E.M. and Hart R.J. (2006). Discovery of a 25-cm asteroid clast in the giant Morokweng impact crater, South Africa. Nature, **441**, 203-206.

Maclaren M. (1931). Lake Bosumtwi, Ashanti. Geographical Journal, **78**, 270-276.

MacQueen J.B. (1967). Some methods for classification and analysis of multivariate observations. In *Proceedings of the 5th Berkeley symposium on mathematical statistics and probability*, University of California Press, Berkeley, 281-297.

Masaitis V.L., Shafranovsky G.I., Ezersky V.A. and Reshetnyak N.B. (1990). Impact diamonds in ureilites and impactites. Meteoritika, **49**, 180–195.

Masaitis V.L., Naumov M.V. and Mashchak M.S. (1999a). Anatomy of the Popigai impact crater, Russia. In *Large meteorite impacts and planetary evolution II* (B.O. Dressler and V.L. Sharpton, eds.). Geological Society of America Special Paper, **339**, 1-17.

Masaitis V.L., Shafranovsky G.I., Grieve R.A.F., Langenhorst F., Peredery W.V., Therriault A.M., Balmasov E.L. and Federova I.G. (1999b). Discovery of impact diamonds in black Onaping suevites, Sudbury structure, Ontario, Canada. In *Large meteorite impacts and planetary evolution II* (B.O. Dressler and V.L. Sharpton, eds.). Geological Society of America Special Paper, **339**, 317-321.

Masaitis V.L., Naumov M.V. and Mashchak M.S. (2005). Original diameter and depth of erosion of the Popigai impact crater, Russia. In *Large meteorite impacts III* (T. Kenkmann, F. Hörz and A. Deutsch, eds.). Geological Society of America Special Paper, **384**, 131-140.

Master S. and Reimold W.U. (2000). The impact cratering record of Africa: An updated inventory of proven, probable, possible, and discredited impact structures on the African continent (abstract). In *Catastrophic events and mass extinctions: impacts and beyond,* Lunar and Planetary Institute Contribution No. **1053**, Lunar and Planetary Institute, Houston, 133–134.

McDonald I. (2002). Clearwater East structure: A re-interpretation of the projectile type using new platinum-group element data from meteorites. Meteoritics and Planetary Science, **37**, 459–464.

McDonald I. and Viljoen K.S. (2006). Platinum-group element geochemistry of mantle eclogites: A reconnaissance study of xenoliths from the Orapa kimberlite, Botswana. Applied Earth Science (IMM Transactions section B), **115**, 81–93.

McDonald I., Andreoli M.A.G., Hart R.J. and Tredoux M. (2001). Platinum-group elements in the Morokweng impact structure, South Africa: Evidence for the impact of a large ordinary chondrite projectile at the Jurassic-Cretaceous boundary. Geochimica et Cosmochimica Acta, **65**, 299–309.

McDonald I., Peucker-Ehrenbrink B., Coney L., Ferriere L., Reimold W.U. and Koeberl C. (2007). Search for a meteoritic component in drill cores from the Bosumtwi impact structure, Ghana: Platinum group element contents and osmium isotopic characteristics. Meteoritics and Planetary Science, **42**, 743–753.

McGetchin T.R., Settle M. and Head J.W. (1973). Radial thickness variation in impact crater ejecta: Implications for lunar basin deposits. Earth and Planetary Science Letters, **20**, 226-236.

Melosh H.J. (1982). A schematic model of crater modification by gravity. Journal of Geophysical Research, **87**, 371-380.

Melosh H.J. (1989). *Impact Cratering: A Geologic Process.* Oxford University Press, New York, 245 pp.

Melosh H.J. and Ivanov B.A. (1999). Impact crater collapse. Annual Review of Earth and Planetary Science, **27**, 385-415.

Meteoritics and Planetary Science (2007). Volume **42**, Issues 4 and 5, 477-896.

Moon P.A. and Mason D. (1967). The geology of 1/4° field sheet s nos. 129 and 131, Bompata S.W. and N.W Ghana. Ghana Geological Survey Bulletin, **31**, 1-51.

Montanari A. and Koeberl C. (2000). *Impact Stratigraphy: The Italian Record*. Springer-Verlag, Berlin, 364 pp.

Morgan J. W., Higuchi H., Ganapathy R. and Anders E. (1975). Meteoritic material in four terrestrial meteorite craters. Proceedings of the 6th Lunar and Planetary Science Conference, 1609–1623.

Morgan J., Warner M. and Grieve R.A.F (1997). Size and morphology of the Chicxulub impact crater. Nature, **390**, 472-476.

Morrow J.R. (2007). Shock-metamorphic petrography and microRaman spectroscopy of quartz in upper impactite interval, ICDP drill core LB-07A, Bosumtwi impact crater, Ghana. Meteoritics and Planetary Science, **42**, 591-610.

Morris W.A., Ugalde H., Clark C. (2007a). Physical property measurements: ICDP boreholes LB-07A and LB-08A, Lake Bosumtwi impact structure, Ghana. Meteoritics and Planetary Science, **42**, 801-809.

Morris W.A., Ugalde H., Clark C., and Miles B. (2007b). Clast fabric examination of impact-generated breccias, borehole LB-07A, Bosumtwi, Ghana. Meteoritics and Planetary Science, **42**, 769–778.

Munsell A.H. (1912). A pigment color system and notation. The American Journal of Psychology, **23**, 236-244.

Naumov M.V. (2002). Impact-generated hydrothermal systems: Data from Popigai, Kara, and Puchezh-Katunki impact structures. In *Impacts in Precambrian Shields* (J. Plado and L.J. Pesonen, eds.). Impact Studies Series, Springer-Verlag, Berlin-Heidelburg, 117-171.

Nesbitt H.W. and Young G.M. (1982). Early Proterozoic climates and plate motions inferred from major element chemistry of lutites. Nature, **299**, 715-717.

Nicolaysen L.O. and Reimold W.U. (1999). Vredefort shatter cones revisited. Journal of Geophysical Research, **104**, 4911-4930.

Oberthür T., Vetter U., Davis D.W. and Amanor J.A. (1998). Age constraints on gold mineralization and palaeoproterozoic crustal evolution in the Ashanti belt of southern Ghana. Precambrian Research, **89**, 129-143.

Ojamo H., Pesonen L.J., Elo S., Hautaniemi H., Koeberl C., Reimold W.U. and Plado J. (1997). The Bosumtwi impact structure, Ghana : International geophysical co-operation at the best (abstract). In *Sovelletun geofysiikan XI neuvottelupäivät* (P. Kaikkonen, K. Komminaho and H. Salmirinne, eds.). Oulun yliopisto, Oulu, 10-11.

O'Keefe J.D. and Ahrens T.J. (1999). Complex craters: Relationship of stratigraphy and rings to impact conditions. Journal of Geophysical Research-Planets, **E 11**, 27091-27104.

Osae S., Kase K. and Yamamoto M. (1995). A geochemical study of the Ashanti gold deposit at Obuasi, Ghana. Okayama University Earth Science Reports, **2**, 81–90.

Osae S., Misra S., Koeberl C., Sengupta D. and Ghosh S. (2005). Target rocks, impact glasses, and melt rocks from the Lonar impact crater, India: Petrography and geochemistry. Meteoritics and Planetary Science, **40**, 1473 - 1492.

Osinski G.R. (2003). Impact glasses in fallout suevites from the Ries impact structure, Germany: An analytical SEM study. Meteoritics and Planetary Science, **38**, 1641-1667.

Osinski G.R. and Spary J.G. (2001). Impact-generated carbonate melts: evidence from the Haughton structure, Canada. Earth and Planetary Science Letters, **194**, 17-29.

Osinski G.R., Grieve R.A.F and Spray J.G. (2004). The nature of the groundmass of surficial suevite from the Ries impact structure, Germany, and constraints on its origin. Meteoritics and Planetary Science, **39**, 1655-1683.

Osinski G.R., Spray J.G. and Grieve R.A.F. (2008a). Impact melting in sedimentary targets: An assessment. In *The Sedimentary Record of Meteorite Impacts* (K. Evans, W. Horton, J. Morrow and J. Warme, eds.). Geological Society of America Special Paper, **437**, 1-18.

Osinski G.R., Grieve R.A.F., Collins G.S., Marion C. and Sylvester P. (2008b). The effect of target lithology on the products of impact melting. Meteoritics and Planetary Science, **43**, *in press*.

Palme H. (1982). Identification of projectiles of large terrestrial impact craters and some implications for the interpretation of Ir-rich Cretaceous/Tertiary boundary layers. In *Geological implications of impacts of large asteroids and comets on the Earth* (L. T. Silver and P. H. Schultz, eds.). Geological Society of America Special Paper, **190**, 223–233.

Palme H., Janssens M.J., Takahashi H., Anders E. and Hertogen J. (1978). Meteorite material at five large impact craters. Geochimica et Cosmochimica Acta, **42**, 313–323.

Palme H., Göbel E. and Grieve R.A.F. (1979). The distribution of volatile and siderophile elements in the impact melt of East Clearwater (Quebec). Proceedings of the 10th Lunar and Planetary Science Conference, 2465–2492.

Peck J.A., Green R.R., Shanahan T., King J.W., Overpeck J.T. and Scholz C.A. (2004). A magnetic mineral record of Late Quaternary tropical climate variability from Lake Bosumtwi, Ghana. Palaeogeography, Palaeoclimatology, Palaeoecology, **215**, 37-57.

Peredery W.V. (1972). Chemistry of fluidal glasses and melt bodies in the Onaping Formation. In *New developments in Sudbury geology* (J.V. Guy-Bray, ed.). Geological Association of Canada Special Paper, **10**, 49-59.

Pesonen L.J. and Henkel H., eds. (1992). Terrestrial impact craters and craterform structures, with a special focus on Fennoscandia. Tectonophysics, **216**, 1-234.

Pesonen L.J., Koeberl C., Ojamo H., Hautaniemi H., Elo S. and Plado J. (1998). Aerogeophysical studies of the Bosumtwi impact structure, Ghana. Geological Society of America Abstracts with Programs, **30**, A-190.

Pesonen L.J., Plado J., Koeberl C. and Elo, S. (1999). The Lake Bosumtwi meteorite impact structure, Ghana: Magnetic modelling. Meteoritics and Planetary Science, **34**, supplement, A91-A92.

Petersen M.T., Newsom H.E., Nelson M.J. and Moore D.M. (2007). Hydrothermal alteration in the Bosumtwi impact structure: Evidence from 2M1-muscovite, alteration veins, and fracture fillings. Meteoritics and Planetary Science, **42**, 655–666.

Peucker-Ehrenbrink B. and Jahn B.-M. (2001). Rhenium-osmium isotope systematics and platinum group element concentrations: Loess and the upper continental crust. Geochemistry, Geophysics, Geosystems, **2**, doi: 10.1029/2001GC000172.

Peucker-Ehrenbrink B., Bach W., Hart S.R., Blusztajn J.S. and Abbruzzese T. (2003). Rhenium-osmium isotope systematics and platinum group element concentrations in oceanic crust from DSDP/ODP Sites 504 and 417/418. Geochemistry, Geophysics, Geosystems, **4**, doi: 10.1029/2002GC000414.

Philpotts A.R. (1964). Origin of pseudotachylites. American Journal of Science, **262**, 1008-1035.

Pierazzo E. and Melosh H.J. (1999). Hydrocode modeling of Chicxulub as an oblique impact event. Earth and Planetary Science Letters, **165**, 163-176.

Pierazzo E. and Melosh H.J. (2000). Hydrocode modeling of oblique impacts: the fate of the projectile. Meteoritics and Planetary Science, **35**, 117-130.

Pierazzo E., Kring D.A. and Melosh H.J. (1998). Hydrocode simulation of the Chicxulub impact event and the production of climatically active gases. Journal of Geophysical Research, **103**, 28607-28626.

Pierazzo E., Hahmann A.N. and Sloan L.C. (2003). Chicxulub and climate: Radiative perturbations of impact-produced S-bearing gases. Astrobiology, **3**, 99-118.

Plado J., Pesonen L.J., Koeberl C. and Elo S. (2000). The Bosumtwi meteorite impact structure, Ghana: A magnetic model. Meteoritics and Planetary Science, **35**, 723-732.

Poag C.W., Hutchinson D.R., Colman S.M. and Lee M.W. (1999). Seismic expression of the Chesapeake Bay impact crater: Structural and morphologic refinements based on new seismic data. In *Large meteorite impacts and planetary evolution II* (B.O. Dressler and V.L. Sharpton, eds.). Geological Society of America Special Paper, **339**, 149-164.

Poag C.W., Koeberl C. and Reimold W.U. (2004). The Chesapeake Bay Crater: Geology and Geophysics of a Late Eocene Submarine Impact Structure. *Impact Studies Series,* Springer, Berlin-Heidelberg, 522 pp.

Pohl J., Stöffler D., Gall H. and Ernston K. (1977). The Ries impact crater. In *Impact and explosion cratering* (D.J. Roddy, R.O. Pepin and R.B. Merrill, eds.). Pergamon Press, New York, 343–404.

Pohl J., Poschlod K., Reimold W.U. and Crasselt C. (2008). Ries crater, Germany: the Enkingen magnetic anomaly and associated drill core SUBO 18. In *Large Meteorite Impacts and Planetary Evolution IV*, Lunar and Planetary Institute Contribution No. **1423**, Lunar and Planetary Institute, Houston, 178-179.

Ravizza, G.E. and Pyle, D. (1997). PGE and Os isotopic analyses of single sample aliquots with NiS fire assay preconcentration. Chemical Geology, **141**, 251-268.

Rehfeldt-Oskierski A. (1986). *Stosswellenexperimente an quartz-einkristallen und thermisches verhalten von diaplektischen quarzgläsern.* PhD Thesis, unpublished, University of Münster, Münster, Germany, 145 pp.

Reimold W.U. (1995). Pseudotachylite in impact structures generation by friction melting and shock brecciation? A review and discussion. Earth-Science Reviews, **39**, 247-264.

Reimold W.U. (1998). Exogenic and endogenic breccias: A discussion of major problematics. Earth-Science Reviews, **43**, 25-47.

Reimold W.U. and Gibson R.L. (2001). *The Vredefort Impact Structure, South Africa: The scientific evidence and a two-day excursion guide.* Memoir **92**, Council for Geoscience, Pretoria, 99 pp.

Reimold W.U. and Gibson R.L. (2005). "Pseudotachylites" in large impact structures. In *Impact tectonics, Impact Studies Series* **8** (C. Koeberl, H. Henkel, eds.). Springer, Berlin-Heidelberg, 1-53.

Reimold W.U. and Gibson R.L. (2006). The melt rocks of the Vredefort impact structure – Vredefort Granophyre and pseudotachylitic breccias: Implications for impact cratering and the evolution of the Witwatersrand Basin. Chemie der Erde, **66**, 1-35.

Reimold W.U., Koeberl C. and Bishop J. (1994). Roter Kamm impact crater, Namibia: Geochemistry of basement rocks and breccias. Geochimica et Cosmochimica Acta, **58**, 2689-2710.

Reimold W.U., Brandt D. and Koeberl C. (1998). Detailed structural analysis of the rim of a large, complex impact crater: Bosumtwi crater, Ghana. Geology, **26**, 543-546.

Reimold W.U., Koeberl C., Gibson R.L. and Dressler B.O. (2005). Economic mineral deposits in impact structures: A review. In *Impact tectonics, Impact Studies Series* **8** (C. Koeberl, H. Henkel, eds.). Springer, Berlin-Heidelberg, 479-552.

Robertson P.B. (1975). Zones of shock metamorphism at the Charlevoix impact structure, Quebec. Geological Society of America Bulletin, **86**, 1630–1638.

Robertson P.B. and Grieve R.A.F. (1977). Shock attenuation at terrestrial impact structures. In *Impact and explosion cratering* (D.J. Roddy, R.O. Pepin and R.B. Merrill, eds.). Pergamon Press, New York, 687-702.

Robertson P.B., Dence M.R. and Vos M.A. (1968). Deformation in rock-forming minerals from Canadian craters. In *Shock metamorphism of natural materials* (B.M. French and N.M. Short, eds.). Mono Book Corp., Baltimore, 433-452.

Roddy D.J. and Davis L.K. (1977). Shatter cones formed in large-scale experimental explosion craters. In *Impact and explosion cratering: planetary and terrestrial implications* (D.J. Roddy, R.O. Pepin and R.B. Merrill, eds.). Pergamon, New York, 715-750.

Roddy D.J., Pepin R.O. and Merrill R.B., eds. (1977). *Impact and Explosion Cratering: Planetary and Terrestrial Implications.* Pergamon, New York, 1301 pp.

Rohleder H.P.T. (1936). Lake Bosumtwi, Ashanti. Geographical Journal, **87**, 51-65.

Rollinson H. 1993. Using *Geochemical Data: Evaluation, Presentation, Interpretation.* Longman Group UK Limited, London, 352 pp.

Schell C., Schleifer N. and Elbra T. (2007). Characterization of the log lithology of cores LB-07A and LB-08A of the Bosumtwi impact structure by using the anisotropy of magnetic susceptibility. Meteoritics and Planetary Science, **42**, 839–847.

Schmidt G., Palme H. and Kratz K.-L. (1997). Highly siderophile elements (Re, Os, Ir, Ru, Rh, Pd, Au) in impact melts from three European impact craters (Sääksjärvi, Mien and Dellen): Clues to the nature of the impacting bodies. Geochimica et Cosmochimica Acta, **61**, 2977–2987.

Schmitt D.R., Milkereit B., Karp T., Scholz C., Danour S., Meillieux D. and Welz M. (2007). In situ seismic measurements in borehole LB-08A in the Bosumtwi impact structure, Ghana: Preliminary interpretation. Meteoritics and Planetary Science, **42**, 755-768.

Schmitt R.T., Wittmann A. and Stöffler D. (2004). Geochemistry of drill core samples from Yaxcopoil-1, Chicxulub impact crater, Mexico. Meteoritics and Planetary Science, **39**, 979–1001.

Schneider W. (1971). Petrologische Untersuchungen der Bunten Breccie im Nördlingen Ries. Neues Jahrbuch für Mineralogie - Abhandlungen, **114**, 136-180.

Schnetzler C.C., Pinson W.H. and Hurley P.M. (1966). Rubidium-strontium age of the Bosumtwi crater area, Ghana, compared with the age of the Ivory Coast tektites. Science, **151**, 817-819.

Schnetzler C.C., Philpotts J.A. and Thomas H.H. (1967). Rare earth and barium abundances in Ivory Coast tektites and rocks from the Bosumtwi crater area, Ghana. Geochimica et Cosmochimica Acta, **31**, 1987–1993.

Scholz C.A., Karp T., Brooks K.M., Milkereit B., Amoako P.Y.A. and Arko J.A. (2002). Pronounced central uplift identified in the Lake Bosumtwi impact structure, Ghana, using multichannel seismic reflection data. Geology, **30**, 939-942.

Scholz C.A., Karp T. and Lyons R.P. (2007). Structure and morphology of the Bosumtwi impact structure from seismic reflection data. Meteoritics and Planetary Science, **42**, 549-560.

Schultz P.H. (1996). Effect of impact angle on vaporization. Journal of Geophysical Research, **100**, 21117-21135.

Schultz P.H. and Gault D.E. (1982). Impact ejecta dynamics in an atmosphere: Experimental results and extrapolations. Geological Society of America Special Paper, **190**, 153-174.

Schuraytz B.C., Sharpton V.L. and Marin L.E. (1994). Petrology of impact-melt rocks at the Chicxulub multiring basin, Yucatán, Mexico. Geology, **22**, 868–872.

Shah A.K., Brozena J., Vogt P., Daniels D. and Plescia J. (2005). New surveys of the Chesapeake Bay impact structure suggest melt pockets and target-structure effect. Geology, **33**, 417-420.

Shanahan T.M., Overpeck J.T., Wheeler C.W., Beck J.W., Pigati J.S., Talbot M.R., Scholz C.S., Peck J. and King J.W. (2006). Paleoclimatic variations in West Africa from a record of late Pleistocene and Holocene lake level stands of Lake Bosumtwi, Ghana. Palaeogeography, Palaeoclimatology, Palaeoecology, **242**, 287–302.

Sharp T.G., El Goresy A., Wopenka B. and Chen M. (1999). A post-stishovite SiO_2 polymorph in the meteorite Shergotty: implications for impact events. Science, **284**, 1511–1513.

Sharpton V.L., Dalrymple G.B., Marin L.E., Ryder G., Schuraytz B.C. and Urrutia-Fucugauchi J. (1992). New links between the Chicxulub impact structure and the Cretaceous/Tertiary boundary. Nature, **359**, 819-821.

Sharpton V.L., Dressler B.O., Herrick R.R., Schneiders B. and Scott J. (1996). New constraints on the Slate Islands impact structure, Ontario. Geology, **24**, 851-854.

Shaw H.F. and Wasserburg G.J. (1982). Age and provenance of the target materials for tektites and possible impactites as inferred from Sm-Nd and Rb-Sr systematics. Earth and Planetary Science Letters, **60**, 155–177.

Shoemaker, E.M. (1977). Why study impact craters? In *Impact and explosion cratering: planetary and terrestrial implications* (D.J. Roddy, R.O. Pepin and R.B. Merrill, eds.). Pergamon, New York, 1-10.

Short N.M. (1970). Progressive shock metamorphism of quartzite ejecta from the Sedan nuclear explosion crater. Journal of Geology, **78**, 705-723.

Shuvalov V. (2003). Displacement of target material during impact cratering. In *Impact markers in the stratigraphic record* (C. Koeberl and F. Martínez-Ruiz, eds.). Springer Verlag, Heidelberg, 121-135.

Shuvalov V. and Dypvik H. (2004): Ejecta formation and crater development of the Mjølnir impact. Meteoritics and Planetary Science, **39**, 467-479.

Sibson R.H. (1975). Generation of pseudotachylite by ancient seismic faulting. Geophysical Journal of the Royal Astronomical Society, **43**, 775-794.

Skinner B.J. and Fahey J.J. (1963). Observations on the inversion of stishovite to silica glass. Journal of Geophysical Research, **68**, 5595-5604.

Smit J. (1999). The global stratigraphy of the Cretaceous-Tertiary boundary impact ejecta. Annual Reviews of Earth and Planetary Science, **27**, 75-113.

Spray J.G. (1995). Pseudotachylyte controversy: Fact or friction? Geology, **23**, 1119-1122.

Spudis P.D. (1993). *The Geology of Multi-Ring Basins*. Cambridge University Press, New York, 263 pp.

Stähle V. (1972). Impact glasses from the suevite of the Nördlinger Ries. Earth and Planetary Science Letters, **17**, 275-293.

Stöckelmann D. and Reimold W.U. (1989). The HMX mixing calculation program. Mathematical Geology, **21**, 853–860.

Stöffler D. (1971a). Progressive metamorphism and classification of shocked and brecciated crystalline rocks at impact craters. Journal of Geophysical Research, **76**, 5541-5551.

Stöffler D. (1971b). Coesite and stishovite in shocked crystalline rocks. Journal of Geophysical Research, **76**, 5474-5488.

Stöffler D. (1972). Deformation and transformation of rock-forming minerals by natural and experimental shock processes: I. Behaviour of minerals under shock compression. Fortschritte der Mineralogie, **49**, 50-113.

Stöffler D. (1974). Deformation and transformation of rock-forming minerals by natural and experimental shock processes: II. Physical properties of shocked minerals. Fortschritte der Mineralogie, **51**, 256-289.

Stöffler D. (1984). Glasses formed by hypervelocity impact. Journal of Non-Crystalline Solids, **67**, 465-502.

Stöffler D. and Langenhorst F. (1994). Shock metamorphism of quartz in nature and experiment: I. Basic observation and theory. Meteoritics, **29**, 155-181.

Stöffler D. and Reimold W.U. (2006). Geologic setting, properties, and classification of terrestrial impact formations (abstract). In *Papers to first international conference on impact cratering in the Solar System,* Noordwijk, Netherlands. CD-ROM, ESLAB-40, WPP-266, 6 pp.

Stöffler D. and Grieve R.A.F. (2007) Impactites, Chapter 2.11 in Metamorphic Rocks: A Classification and Glossary of Terms, Recommendations of the International Union of Geological Sciences (D. Fettes and J. Desmons, eds.). Cambridge University Press, Cambridge, 82-92, 111-125, and 126-242.

Stöffler D., Gault D.E., Wedekind J.A., Polkowski G. (1975). Experimental hypervelocity impact into quartz sand: Distribution and shock metamorphism of ejecta. Journal of Geophysical Research, **80**, 4062-4077.

Stöffler D., Ewald U., Ostertag R. and Reimold W. U. (1977). Research drilling Nördlingen 1973 (Ries): Composition and texture of polymict impact breccias. Geologica Bavarica, **75**, 163–189.

Stöffler D., Bischoff L., Oskierski W. and Wiest B. (1988). Structural deformation, breccia formation, and shock metamorphism in the basement of complex terrestrial impact craters: implications for the cratering process. In *Deep drilling in crystalline bedrock, volume 1: the deep gas drilling in the Siljan impact structure, Sweden, and astroblemes* (A. Bodén and K.G. Eriksson, eds.). Springer-Verlag, New York, 277-297.

Stöffler D., Artemieva N.A., Pierazzo E. and Ivanov B.A. (2001). Ries Crater, Germany: Geology and numerical modeling of Impact Cratering. Meteoritics and Planetary Science, **36**, supplement A199.

Stöffler D., Artemieva N.A. and Pierazzo E. (2002). Modeling the Ries-Steinheim impact event and the formation of the moldavite strewn field. Meteoritics and Planetary Science, **37**, 1893-1907.

Stöffler D., Artemieva N.A., Ivanov B. A., Hecht L., Kenkmann T., Schmitt R.T., Tagle R. A. and Wittmann A. (2004). Origin and emplacement of the impact formations at Chicxulub, Mexico, as revealed by the ICDP deep drilling Yaxcopoil-1 and by numerical modeling. Meteoritics and Planetary Science, **39**, 1035-1068.

Storzer D. and Wagner G.A. (1977). Fission track dating of meteorite impacts. Meteoritics, **12**, 368-369.

Tagle R. and Claeys Ph. (2005). An ordinary chondrite impactor for the Popigai crater, Siberia. Geochimica et Cosmochimica Acta, **69**, 2877–2889.

Talbot M.R. and Delibrias G. (1977). Holocene variations in the level of Lake Bosumtwi. Nature, **268**, 722-724.

Talbot M.R. and Delibrias G. (1980). A new Late Pleistocene-Holocene water level curve for Lake Bosumtwi, Ghana. Earth and Planetary Science Letters, **47**, 336–344.

Talbot M.R. and Kelts K. (1986). Primary and diagenetic carbonates in the anoxic sediments of Lake Bosumtwi, Ghana. Geology, **14**, 912-916.

Talbot M. R., Livingston D. A., Palmer P. A., Maley J., Melack J. M., Delibrias G. and Gulliksen S. (1984). Preliminary results from sediment cores from Lake Bosumtwi, Ghana. Paleoecology of Africa and the Surrounding Islands, **16**, 173–192.

Taylor P.N., Moorbath S., Leube A. and Hirdes W. (1992). Early Proterozoic crustal evolution in the Birimian of Ghana: Constraints from geochronology and isotope geochemistry. Precambrian Research, **56**, 97–111.

Taylor S.R. and McLennan S.M. (1985). *The Continental Crust: Its Composition and Evolution*. Blackwell Scientific, Oxford, 312 pp.

Turner B.F., Gardner L.R. and Sharp W.E. (1996a). The hydrology of Lake Bosumtwi, a climate-sensitive lake in Ghana, West Africa. Journal of Hydrology, **183**, 243-261.

Turner B.F., Gardner L.R., Sharp W.E. and Blood E.R. (1996b). The geochemistry of Lake Bosumtwi, a hydrologically closed basin in the humid zone of tropical Ghana. Limnology and Oceanography, **41**, 1415-1424.

Ugalde H., Danuor S.K. and Milkereit B. (2007a). Integrated 3-D model from gravity and petrophysical data at the Bosumtwi impact structure, Ghana. Meteoritics and Planetary Science, **42**, 856-866.

Ugalde H., Morris W.A., Pesonen L.J. and Danuor S.K. (2007b). The Lake Bosumtwi meteorite impact structure, Ghana – Where is the magnetic souce? Meteoritics and Planetary Science, **42**, 867-882.

Vishnevsky S. and Montanari A. (1999). The Popigai impact crater (Arctic Siberia, Russia): geology, petrology, geochemistry, and geochronology of glass-bearing impactites. In *Large meteorite impacts and planetary evolution II* (B.O. Dressler and V.L. Sharpton, eds.). Geological Society of America Special Publication, **339**, 19-60.

Von Engelhardt W. (1990). Distribution, petrography and shock metamorphism of the ejecta of the Ries crater in Germany – A review. Tectonophysics, **171**, 259-273.

Von Engelhardt W. (1997). Suevite breccia of the Ries impact crater, Germany: Petrography, chemistry, and shock metamorphism of crystalline rock clasts. Meteoritics and Planetary Science, **32**, 545-554.

Von Engelhardt W. and Bertsch W. (1969). Shock induced planar deformation structures in quartz from the Ries crater, Germany. Contributions to Mineralogy and Petrology, **20**, 203-234.

Von Engelhardt W. and Graup G. (1977). Stosswellenmetamorphose im Kristallin der Forschungsbohrung Nördlingen 1973. Geologica Bavarica, **55**, 255–272.

Von Engelhardt W. and Graup G. (1984). Suevite of the Ries Crater, Germany: Source rocks and implications for cratering mechanics. Geologische Rundschau, **73**, 447-481.

Von Engelhardt W., Arndt J., Stöffler D., Müller W.F., Jeziorkowski H. and Gubser R.A. (1967). Diaplektische Gläser in den Breccien des Ries von Nördlingen als Anzeichen für Stoßwellenmetamorphose. Contributions to Mineralogy and Petrology, **15**, 93-102.

Von Engelhardt W., Stöffler D. and Schneider W. (1969). Petrologische Untersuchungen im Ries. Geologica Bavarica, **61**, 229-295.

Von Engelhardt W., Luft E., Arndt J., Schock H. and Weiskirchner W. (1987). Origin of moldavites. Geochimica et Cosmochimica Acta, **51**, 1425-1443.

Wagner R., Reimold W.U. and Brandt D. (2002). Bosumtwi impact crater: Ghana: A remote sensing investigation. In *Meteorite impacts in Precambrian shields. Impact Studies, volume 2,* (J. Plado and L.J. Pesonen, eds.). Heidelberg, Springer Verlag, 189-210.

Wasson J.T. and Kallemeyn G.W. (1988). Compositions of chondrites. Philosophical Transactions of the Royal Society of London, **A352**, 535-544.

Watkins A.P., Iliffe J.E. and Sharp W.E. (1993). The effects of extensional and transpressional tectonics upon the development of the Birimian sedimentary facies in Ghana, W. Africa: Evidence from the Bomfa/Beposo District, near Konongo. Journal of African Earth Sciences, **17**, 457-478.

Whitehead J., Grieve R.A.F. and Spray J. (2002a). Mineralogy and petrology of melt rocks from the Popigai impact structure, Siberia. Meteoritics and Planetary Science, **37**, 623-648.

Whitehead J., Spray J.G., and Grieve R.A.F. (2002b). Origin of “toasted” quartz in terrestrial impact structures. Geology, **30**, 431–434.

Wieland F., Reimold W.U. and Gibson R.L. (2006). New observations on shatter cones in the Vredefort impact structure, South Africa, and evaluation of current hypotheses for shatter cone formation. Meteoritics and Planetary Science, **41**, 1737-1759.

Wishart D. (1997). ClustanGraphics: Interactive Graphics for Cluster Analysis. Computing Science and Statistics, **29**, 48-51.

Wittmann A. and Reimold W.U. (2008). The volume of impact melt in the Chesapeake Bay crater (abstract). In *Large Meteorite Impacts and Planetary Evolution IV*, Lunar and Planetary Institute Contribution No. **1423**, Lunar and Planetary Institute, Houston, 215-216.

Woodfield P.D. (1966). The Geology of the 1/4 Field Sheet 91, Fumso, N.W. Ghana. Geological Survey Bulletin, **30**.

Wright J.B., Hastings D.A., Jones W.B. and Williams H.R. (1985). *Geology and Mineral Resources of West Africa*. George Allen and Unwin, London, 38-45.

Wünnemann K. and Ivanov B.A. (2003). Numerical modelling of the impact crater depth-diameter dependence in an acoustically fluidized target. Planetary and Space Science, **51**, 831-845.

Wünnemann K. and Collins G.S. (2006). The effect of porosity on meteorite impact process (abstract #EGU06-A-03991). Geophysical Research Abstracts **8**, 2 pp.

Wünnemann K., Collins G.S. and Melosh H.J. (2005). A strain-based porosity model for use in hydrocode simulations of impacts and implications for transient crater growth in porous targets. Icarus, **180**, 514–527.

Wünnemann K., Collins G.S. and Osinski G.R. (2008). Numerical modeling of impact melt production in porous rocks. Earth and Planetary Science Letters, doi: 10.1016/j.epsl.2008.03.007.

Yao Y. and Robb L. (2000). Gold mineralization in Palaeoproterozoic granitoids at Obuasi, Ashanti region, Ghana: Ore geology, geochemistry and fluid characteristics. South African Journal of Geology, **103**, 255–278.

Yardley B.W.D. (1989). *An Introduction to Metamorphic Petrology*. Longman Earth Science Series, Prentice Hall, Harlow, 248 pp.